UNIVERSITY OF CALIFORNIA, SAN DIEGO

Numerical Simulations and Shaking Table Tests of Geosynthetic Reinforced Soil Bridge Abutments

A dissertation submitted in partial satisfaction of the requirements for the degree

Doctor of Philosophy

in

Structural Engineering

by

Yewei Zheng

Committee in charge:

Professor Patrick J. Fox, Chair
Professor John S. McCartney, Co-Chair
Professor Ahmed M. Elgamal
Professor Peter M. Shearer
Professor P. Benson Shing

2017

The Dissertation of Yewei Zheng is approved, and it is acceptable in quality and form for publication on microfilm and electronically:

_____

_____

_____

_____

Co-Chair

_____

Chair

University of California, San Diego

2017

DEDICATION

To my parents for their everlasting love and support.

EPIGRAPH

Now this is not the end.

It is not even the beginning of the end.

But it is, perhaps, the end of the beginning.

– Winston Churchill

TABLE OF CONTENTS

LIST OF FIGURES

LIST OF TABLES

ACKNOWLEDGEMENTS

First of all, I would like to express my deepest appreciation to my advisors, Professor Patrick Fox and Professor John McCartney, for their patient guidance, insightful advice, warm encouragement, continuous support, and enormous help. I feel truly lucky and honored to have two great advisors, Pat and John. Their enthusiasm on research ignites my passion on learning and research, their rigorous attitude towards research inspires me to pursue excellence, and their continuous guidance leads me to become a better researcher.

I would like to thank Professor Benson Shing for his valuable suggestions on the shaking table testing program, and my committee members, Professor Ahmed Elgamal and Professor Peter Shearer, for their time and comments on my research.

I also thank the staff at the UCSD Powell Structural Laboratories, Dr. Christopher Latham, Darren McKay, Noah Aldrich, and Michael Sanders for their help with the design and setup for the shaking table tests, and undergraduate research assistants, Bernardo Ambriz and Wante Lu for their help with the construction of the abutment specimens.

My sincere gratitude also goes to my friends and fellow graduate students at UCSD for their continuous help, emotional support, and sincere friendship. I would particularly like to thank Dr. Hefu Pu, Dr. Yong Li, Dr. Xiaowei Deng, Dr. Weian Liu, Dr. Xuan Zhu, Dr. Jinhui Yan, Wenyong Rong, Lan Luo, Andrew Sander, Kaitlin Hall, Tugce Baser, Ismaail Ghaaowd, Leticia Nocko, and Radhavi Samarakoon.

Finally, I would like to dedicate this dissertation to my parents for their everlasting love and support during my life. I would not be able to finish the odyssey without the support from my family. I also have to thank my beloved girl whom I may have not met yet. Thanks to everything in my life which does not kill me but makes me stronger.

Financial support for this research was provided by the California Department of Transportation (Caltrans) and Federal Highway Administration (FHWA) Pooled Fund Project 65A0556, and is gratefully acknowledged. I am also grateful for the Jacobs Fellowship from Jacobs School of Engineering at UCSD and the GSI Fellowship from Geosynthetic Institute.

Chapter 3 of this dissertation is based on materials published by the Journal of Geotechnical and Geoenvironmental Engineering titled "Numerical Investigation of Geosynthetic-Reinforced Soil Bridge Abutments under Static Loading" with authors, Yewei Zheng and Patrick J. Fox (2016). The dissertation author is the first author of this paper.

Chapter 4 of this dissertation is based on materials published by the Journal of Geotechnical and Geoenvironmental Engineering titled "Numerical Investigation of the Geosynthetic Reinforced Soil-Integrated Bridge System under Static Loading" with authors, Yewei Zheng and Patrick J. Fox (2017). The dissertation author is the first author of this paper.

Chapter 5 of this dissertation is based on materials from a manuscript in review titled "Numerical Simulation of Load-Deformation and Failure Behavior of Geosynthetic-Reinforced Soil Bridge Abutments" with authors, Yewei Zheng, Patrick J. Fox, and John S. McCartney (2017). The dissertation author is the first author of this paper.

Chapter 6 of this dissertation is partially based on materials from a manuscript in review titled "Shaking Table Test of a Half-Scale Geosynthetic Reinforced Soil Bridge Abutment" with authors, Yewei Zheng, Andrew C. Sander, Wenyong Rong, Patrick J. Fox,

P. Benson Shing, and John S. McCartney (2017). The dissertation author is the first author of this paper.

Chapter 7 of this dissertation is based on materials from two manuscripts in preparation for publication, tentatively titled "Large-Scale Model Tests of Geosynthetic Reinforced Soil Bridge Abutments. I: Static Loading," and "Large-Scale Model Tests of Geosynthetic Reinforced Soil Bridge Abutments. II: Longitudinal Shaking," respectively, with a preliminary author list of Yewei Zheng, John S. McCartney, P. Benson Shing, and Patrick J. Fox (2017). The dissertation author is the first author of these paper.

Chapter 8 of this dissertation is based on material from a manuscript in preparation for publication, tentatively titled "Large-Scale Model Tests of Geosynthetic Reinforced Soil Bridge Abutments. III: Transverse Shaking," with a preliminary author list of Yewei Zheng, John S. McCartney, Patrick J. Fox, and P. Benson Shing (2017). The dissertation author is the first author of this paper.

VITA AND PUBLICATIONS

2011	Bachelor of Engineering in Civil Engineering
	Huazhong University of Science and Technology, Wuhan, China
2013	Master of Science in Civil Engineering
	University of Oklahoma, Norman, USA
2017	Doctor of Philosophy in Structural Engineering
	University of California, San Diego, La Jolla, USA

Journal Publications

1. Zheng, Y., and Fox, P.J. (2016). "Numerical investigation of geosynthetic-reinforced soil bridge abutments under static loading." *Journal of Geotechnical and Geoenvironmental Engineering*, 10.1061/(ASCE)GT.1943-5606.0001452, 04016004.
2. Zheng, Y., and Fox, P.J. (2016). Closure to "Numerical investigation of geosynthetic-reinforced soil bridge abutments under static loading." By Yewei Zheng, and Patrick J. Fox. *Journal of Geotechnical and Geoenvironmental Engineering*, 10.1061/(ASCE)GT.1943-5606.0001623, 07016032.
3. Zheng, Y., and Fox, P.J. (2017). "Numerical investigation of the geosynthetic reinforced soil-integrated bridge system under static loading." *Journal of Geotechnical and Geoenvironmental Engineering*, 10.1061/(ASCE)GT.1943-5606.0001665, 04017008.
4. Zheng, Y, Sander, A.C., Rong, W., Fox, P.J., Shing, P.B., and McCartney, J.S. "Shaking table test of a half-scale geosynthetic-reinforced soil bridge abutment." *Geotechnical Testing Journal*, in review.
5. Trautner, C.A., Zheng, Y**.**, McCartney, J.S., and Hutchinson, T.C. "An approach for shake table performance evaluation during repair and retrofit actions." *Earthquake Engineering and Structural Dynamics*, in review.
6. Zheng, Y., Fox, P.J., and McCartney, J.S. "Numerical simulation of load-deformation and failure behavior of geosynthetic-reinforced soil bridge abutments." *Journal of Geotechnical and Geoenvironmental Engineering*, in review.
7. Zheng, Y., McCartney, J.S., Fox, P.J., and Shing, P.B. "Large-scale model tests of geosynthetic reinforced soil bridge abutments. I: Static loading." *Journal of Geotechnical and Geoenvironmental Engineering*, in preparation.

8. Zheng, Y., McCartney, J.S., Fox, P.J., and Shing, P.B. "Large-scale model tests of geosynthetic reinforced soil bridge abutments. II: Longitudinal shaking." *Journal of Geotechnical and Geoenvironmental Engineering*, in preparation.

9. Zheng, Y., McCartney, J.S., Fox, P.J., and Shing, P.B. "Large-scale model tests of geosynthetic reinforced soil bridge abutments. III: Transverse shaking." *Journal of Geotechnical and Geoenvironmental Engineering*, in preparation.

10. Zheng, Y., Rong, W., McCartney, J.S., and Fox, P.J. "Numerical investigation of 3D effects on static response of geosynthetic reinforced soil bridge abutments." *Journal of Geotechnical and Geoenvironmental Engineering*, in preparation.

Conference Publications

1. Zheng, Y., Fox, P.J., and Shing, P.B. (2014). "Numerical simulations for response of MSE wall-supported bridge abutment to vertical load." *GeoShanghai 2014, International Conference on Geotechnical Engineering 2014*, Shanghai, China, 493-502.

2. Zheng, Y., Fox, P.J., and Shing, P.B. (2015). "Verification of numerical model for static analysis of geosynthetic-reinforced soil bridge abutments." *Geosynthetics 2015*, Portland, OR, USA, 152-160.

3. Zheng, Y., Fox, P.J., and Shing, P.B. (2015). "Numerical study of deformation behavior for a geosynthetic-reinforced soil bridge abutment under static loading." *IFCEE 2015, International Foundations Congress & Equipment Exposition 2015*, San Antonio, TX, USA, 1503-1512.

4. Zheng, Y., and Fox, P.J. (2016). "Effects of reinforcement parameters on performance of geosynthetic-reinforced soil bridge abutments under static loading." *GeoAmericas 2016, 3rd Pan-American Conference on Geosynthetics*, Miami Beach, FL, USA, 900-910.

5. Zheng, Y., Fox, P.J., and McCartney, J.S. (2017). "Numerical study of compaction effect on the static behavior of geosynthetic reinforced soil-integrated bridge system." *Geotechnical Frontiers 2017*, Orlando, FL, USA, 33-43.

6. Rong, W., Zheng, Y., McCartney, J.S., and Fox, P.J. (2017). "3D deformation behavior of geosynthetic reinforced soil bridge abutments." *Geotechnical Frontiers 2017*, Orlando, FL, USA, 44-53.

7. Zheng, Y., Sander, A.C., Rong, W., McCartney, J.S., Fox, P.J., and Shing, P.B. (2017). "Experimental design for half-scale shaking table test of a geosynthetic-reinforced soil bridge abutment." *Geotechnical Frontiers 2017*, Orlando, FL, USA, 54-63.

ABSTRACT OF THE DISSERTATION

Numerical Simulations and Shaking Table Tests of Geosynthetic Reinforced Soil Bridge Abutments

by

Yewei Zheng

Doctor of Philosophy in Structural Engineering

University of California, San Diego, 2017

Professor Patrick J. Fox, Chair

Professor John S. McCartney, Co-Chair

Geosynthetic reinforced soil (GRS) bridge abutments are becoming widely used in transportation infrastructure and provide many advantages over traditional pile-supported designs, including lower cost, faster and easier construction, and smoother transition between the bridge and approach roadway. Seismic events represent a severe loading condition and experimental testing and evaluation are needed to understand the potential issues and performance characteristics. This study involves a comprehensive evaluation of the performance of GRS bridge abutments for the service limit state, the strength limit state,

and an extreme event limit state (i.e., seismic loading conditions) using both numerical simulations and physical modeling experiments.

A numerical model was developed for GRS bridge abutments under service loading conditions and was validated using field measurements. Simulation results indicate that the horizontal restraining forces generated from the bridge structure can have an important effect on reducing lateral facing displacements and bridge seat settlements of GRS bridge abutments. Parametric studies were conducted to investigate the effects of various design parameters on the performance of GRS bridge abutments for service loading conditions, and the results indicate that reinforcement spacing, reinforcement stiffness, bridge load, and abutment height have the most significant effects on the lateral facing displacements and bridge seat settlements.

The numerical model was enhanced by incorporating the strain softening behavior for backfill soil and the rate-dependent behavior for geosynthetic reinforcement to simulate the load-deformation behavior of GRS bridge abutments up to failure condition. A linearly elastic reinforcement model can capture the deformation behavior of GRS bridge abutments for service loads, but not for larger applied loads approaching failure. The geometry parameters for GRS bridge abutments have important effects on the internal failure surface of the GRS bridge abutments, and the internal failure surface manifests as a bilinear surface that starts at the heel of the bridge footing, moves vertically downward to mid-height of the GRS bridge abutment, and then linearly to the toe of the GRS bridge abutment.

The seismic response of GRS bridge abutments was evaluated using an experimental testing program. Shaking table tests were conducted on six half-scale GRS

bridge abutments by application of a series of shaking events in the directions longitudinal and transverse to the bridge beam. Experimental design of the model specimen followed established similitude relationships for shaking table testing of reduced-scale models in a 1*g* gravitational field, including scaling of model geometry, geosynthetic reinforcement stiffness, backfill soil modulus, bridge load, and characteristics of the earthquake motions. Experimental results indicate that the seismic facing displacements and bridge seat settlements for GRS bridge abutments are small and will likely not have a major effect on the bridge performance. Reinforcement spacing and stiffness have the most important effects on the seismic performance of GRS bridge abutments.

Chapter 1

Introduction

1.1 Background and Motivation

The inclusion of reinforcements that are strong in tension into soils produces a composite material that has better mechanical behavior than soil alone. The use of soil reinforcements dates back to prehistoric times. For instance, ancient people used natural reinforcements (e.g., straws and roots) to reinforce earth dikes (Berg et al. 2009). Modern reinforced soil technology was developed by Henri Vidal in the early 1960s after which a significant amount of research and observation of constructed facilities has expanded the use of reinforced soil technology in a number of applications, including reinforced slopes, retaining walls, and bridge abutments.

A reinforced soil retaining structure consists of three main components: backfill material, reinforcements, and facing elements. Well-graded granular materials are typically used as the backfill material to ensure adequate soil-reinforcement interaction and good

drainage conditions for the system. The reinforcements are typically classified into two categories: in-extensible reinforcements (e.g., steel strips, steel bar mats, steel welded wire mesh) and extensible reinforcements (e.g., geogrids, geotextiles, geocells). There are also a variety of choices for facing elements, including full-height panels, precast segmental panels, modular blocks, wrap-around geosynthetic facing, gabions constructed from welded wire mesh, and sprayed-on shotcrete.

Since the early 1980s, the use of geosynthetics for retaining structures has gained increasing popularity due to cost savings. Geosynthetic reinforced soil (GRS) retaining walls have been used extensively in transportation infrastructure and provide many advantages over conventional retaining walls in many situations, including lower cost, faster and easier construction, and better performance under static and seismic loading. In recent years, GRS retaining walls also have been developed as bridge abutments where bridge loads are applied directly to the top of the reinforced soil mass. Similar to GRS retaining walls, GRS bridge abutments offer significant cost savings in comparison to traditional pile-supported designs and can reduce differential settlements between the bridge and approach roadway (Abu-Hejleh et al. 2002).

GRS bridge abutments are typically subjected to much larger surcharge loads than conventional GRS retaining walls and, as such, the allowable bearing pressure and resulting deformations are important issues for design. Several case histories for in-service GRS bridge abutments have been reported and each shows good field performance (Won et al. 1996; Wu et al. 2001; Abu-Hejleh et al. 2002; Adams et al. 2007, 2008, 2011a). Numerical studies have also been conducted on GRS bridge abutments under service load conditions, which generally considered perfectly plastic soil behavior and linearly elastic

geosynthetic reinforcement behavior (Helwany et al. 2003, 2007; Fakharian and Attar 2007; Ambauen et al. 2016). Results from these investigations showed relatively small lateral facing displacements and bridge seat settlements for the service limit state. However, detailed investigations are needed to better understand the effects of various design parameters on the performance of GRS bridge abutments.

Numerical modeling efforts to understand the load-deformation behavior and bearing capacity of GRS bridge abutments corresponding to the strength limit state, including large deformations up to failure condition, is more limited and has also assumed perfectly plastic soil and linearly elastic geosynthetic reinforcement (Wu et al. 2006a, 2006b). Based on other related research findings (e.g., Walters et al. 2002; Hatami and Bathurst 2006; Liu and Ling 2012; Yang et al. 2012), strain softening of backfill soil and nonlinear response of geosynthetic reinforcement would be expected to have important effects on the behavior of GRS bridge abutments under high load conditions. Therefore, numerical models that incorporate the strain softening behavior of soil and the nonlinear behavior of reinforcement are needed to simulate the load-deformation and failure behavior of GRS bridge abutments for the strength limit state.

Although GRS bridge abutments are becoming widely used across the United States, this technology has not been adopted in highly seismic areas like California. Seismic events represent a severe loading condition (i.e., an extreme event limit state) and experimental testing and evaluation are needed to understand the potential issues and performance characteristics for different design variables (e.g., bridge load, reinforcement spacing, reinforcement stiffness, etc.). Seismic compression of the backfill in the GRS bridge abutment and associated settlement of the bridge seat, are of particular concern as

they may have an important impact on the performance of the bridge and approach roadway. Yen et al. (2011) conducted post-earthquake reconnaissance for the 2010 Maule Earthquake, and found that a GRS bridge abutment exhibited no signs of lateral or vertical movements after shaking, while the bridge suffered minor damage that may have resulted from the severe bridge skew angle. Shaking table tests conducted by Helwany et al. (2012) on a 3.6 m-high GRS bridge abutment indicated no significant distress during shaking with horizontal accelerations up to 1*g*. Despite the limited information on the seismic performance in the field and in previous shaking table testing program, more investigations are warranted on the seismic response of GRS bridge abutments for various configurations and loading conditions.

1.2 Research Objectives

The specific objectives of this research are to:

1. Develop and validate a numerical model for GRS bridge abutments for the service limit state;
2. Investigate the performance of geosynthetic reinforced soil-integrated bridge system (GRS-IBS) for the service limit state;
3. Develop a numerical model for GRS bridge abutments for the strength limit state;
4. Investigate the load-deformation and failure behavior of GRS bridge abutments up to the strength limit state;
5. Conduct shaking table tests on reduced-scale GRS bridge abutments subjected to shaking in the longitudinal and transverse directions;
6. Understand the behavior of GRS bridge abutments under an extreme event limit state (i.e., seismic loading conditions).

1.3 Dissertation Organization

This dissertation was prepared as a paper-based dissertation, with the different chapters presenting excerpts of journal publications submitted or published in international journals. The remainder of this dissertation is organized as follows:

Chapter 2 presents a literature review of past work related to the research topic.

Chapter 3 presents the development and validation of a numerical model for GRS bridge abutments for the service limit state, and a parametric study on the effects of bridge contact friction coefficient, backfill soil relative compaction, backfill soil cohesion, reinforcement spacing, reinforcement length, reinforcement stiffness, and bridge load.

Chapter 4 presents a numerical investigation on the static response of the geosynthetic reinforced soil-integrated bridge system (GRS-IBS). This chapter also includes a parametric study on the effects of backfill soil compaction, reinforcement length, reinforcement stiffness, bearing bed reinforcement, bridge seat setback distance, bridge load, and abutment height.

Chapter 5 presents the development of a numerical model for GRS bridge abutments for the strength limit state, and a parametric study on the effects of reinforcement, backfill soil, and abutment geometry parameters on the load-deformation and failure behavior of GRS bridge abutments.

Chapter 6 presents a detailed description of the shaking table testing program, including similitude relationships, material properties, test configuration, instrumentation, construction, and input motions.

Chapter 7 presents results and analysis for GRS bridge abutments subjected to a series of shaking events in the longitudinal direction, including facing displacements, bridge seat and bridge beam displacements, acceleration responses, lateral and vertical stresses, reinforcement strains, and contact forces between the bridge seat and bridge beam.

Chapter 8 presents results and analysis for a GRS bridge abutment subjected to a series of shaking events in the transverse direction, including facing displacements, bridge seat and bridge beam displacements, acceleration responses, lateral and vertical stresses, reinforcement strains, and contact forces between the bridge seat and bridge beam.

Finally, Chapter 9 presents conclusions and recommendations for future research.

Chapter 2

Literature Review

2.1 Geosynthetic Reinforced Soil Retaining Structures

2.1.1 Reinforced Soil Mechanisms

Transfer of loads between soil and an embedded reinforcement involves two mechanisms, friction and passive bearing resistance, as shown in Figure 2.1. Frictional forces are mobilized at the soil-reinforcement interface or within the soil near the interface along the reinforcement length due to relative displacements between the soil and reinforcement. The passive bearing resistance forces are generated on the transverse ribs (e.g., steel bar mats, welded wire mesh, geogrids, etc.). The contribution of each

mechanism depends on the magnitude of normal force and the material properties of the soil and reinforcement (Berg et al. 2009).

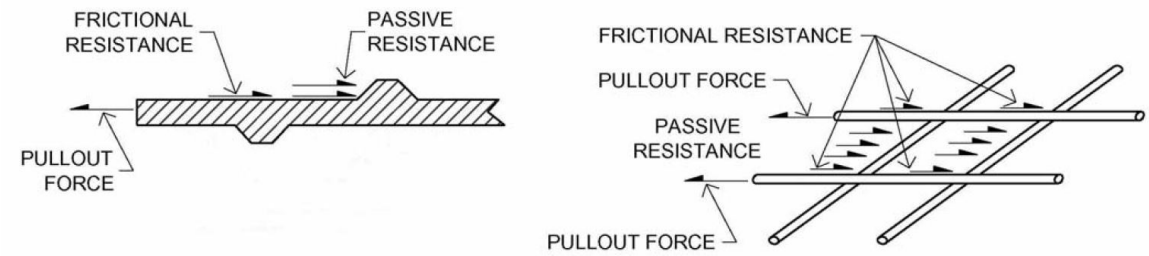

Figure 2.1 Load transfer between soil and reinforcement (from Berg et al. 2009).

2.1.2 In-Service Performance

Geosynthetic-reinforced soil (GRS) bridge abutments are becoming widely used in transportation infrastructure and provide many advantages over traditional pile-supported designs, including lower cost, faster and easier construction, and smoother transition between the bridge and approach roadway. Lee and Wu (2004) reviewed several case studies of in-service GRS bridge abutments (Won et al. 1996; Abu-Hejleh et al. 2000, 2001, 2002), and reported generally satisfactory performance in terms of lateral facing displacements and bridge seat settlements under service load conditions.

Won et al. (1996) reported field monitoring results of a 9.5 m-high GRS bridge abutment consisted of four terraced segmental block GRS walls in New South Wales, Australia. The backfill material was a fine sand compacted to at least 95% relative compaction according to the standard Proctor compaction effort. The GRS bridge abutment had 17 layers of geogrid with vertical spacings of 0.4 m or 0.6 m at different elevations. The maximum bridge seat settlement was 80 mm, and the maximum lateral facing displacements for the lowest-tiered wall were 10 mm at the end of construction and 26 mm under traffic loads. The maximum geogrid strain was 1.6%, which occurred in the lowest tier of the wall.

Abu-Hejleh et al. (2000, 2001, 2002) reported results from a comprehensive field monitoring study on the GRS bridge abutments at either ends of the bridge supporting the Founders/Meadows Parkway Bridge across Interstate 25 in Castle Rock, Colorado. The bridge has two spans, with each having a length of 34.5 m and a width of 34.5 m, as shown in Figure 2.2. The GRS bridge abutments consist of lower and upper GRS walls over

bedrock foundation, and the cross-sectional view is shown in Figure 2.3. The geogrid reinforcement had a vertical spacing of 0.4 m. The backfill soil was composed of gravel (35.0%), sand (54.4%), and fines (10.6%). The maximum lateral facing displacement was 12 mm after construction of the lower wall. The maximum incremental lateral facing displacement was 10 mm and the bridge seat settlement was 12 mm due to the construction of bridge structures and approach roadway. The post-construction deformations for the GRS bridge abutments after opening to traffic were small, with a maximum lateral facing displacement of 5 mm and bridge seat settlement of 10 mm.

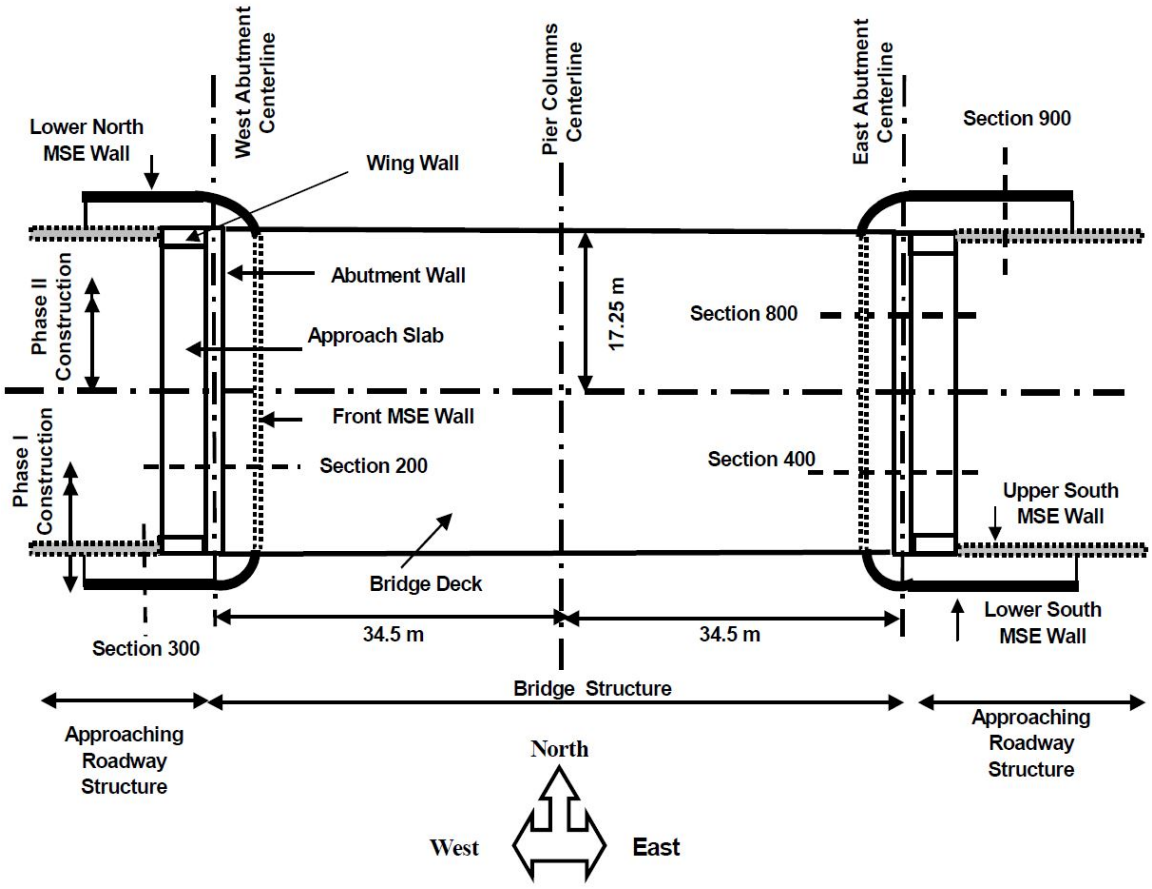

Figure 2.2 Top view of the Founders/Meadows Parkway Bridge (from Abu-Hejleh et al. 2000).

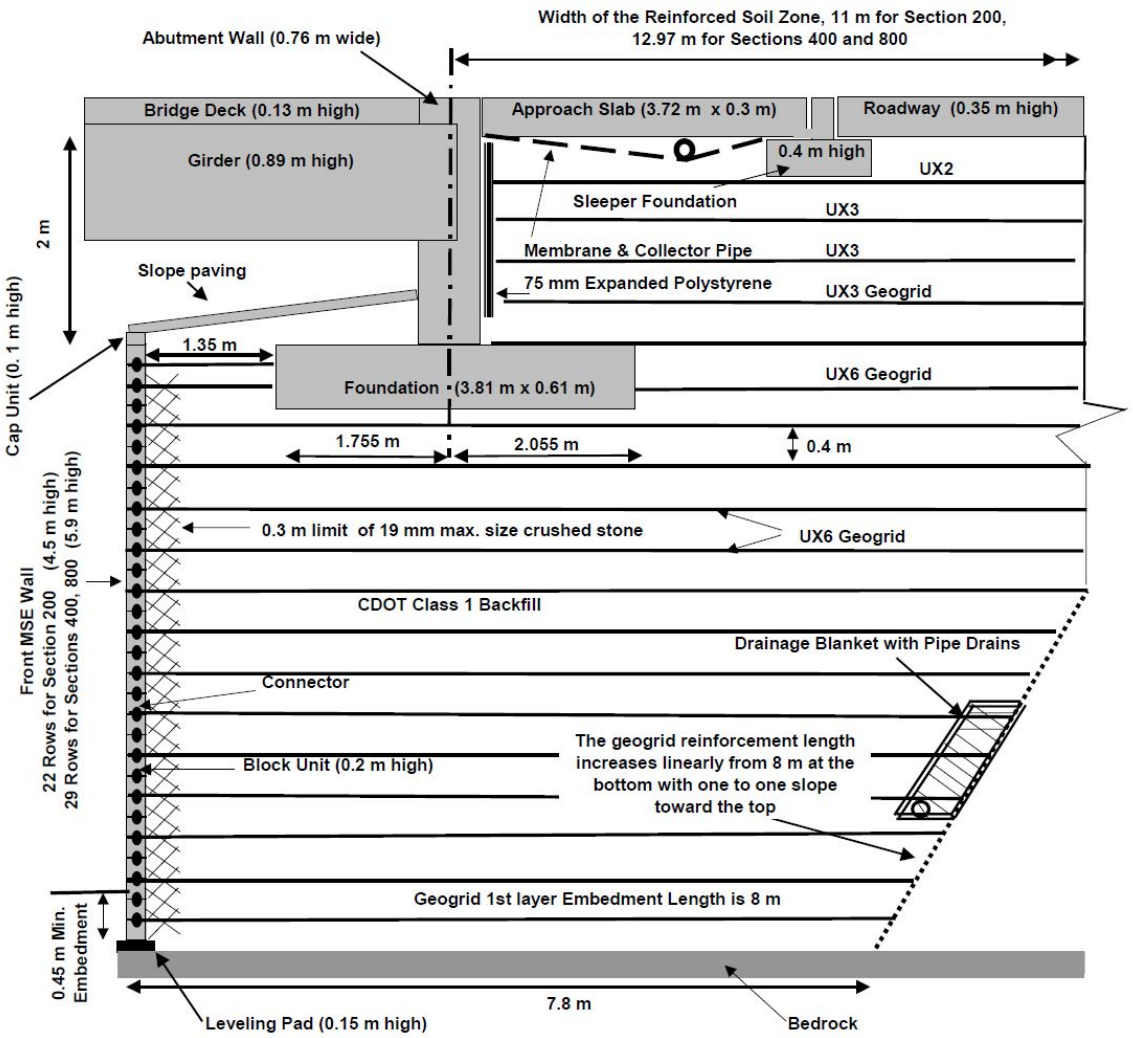

Figure 2.3 Cross-sectional view of the east GRS bridge abutment for the Founders/Meadows Parkway Bridge (from Abu-Hejleh et al. 2000).

Adams et al. (2007, 2008, 2011b) reported the monitoring results from the first geosynthetic reinforced soil-integrated bridge system (GRS-IBS) abutment constructed for the Bowman Road Bridge in Ohio. The GRS abutment compression was 14.3 mm under an average applied vertical stress of 124 kPa, and the post-construction settlement was small. Adams et al. (2011a) also reported excellent performance for five in-service GRS-IBS abutments with regard to bridge settlement, abutment compression, and differential settlement.

2.1.3 Post-Earthquake Observations

GRS retaining walls have been widely used in seismically active regions over the world. Post-earthquake observations on the field performance have indicated that the GRS retaining walls in general had better performance than conventional retaining walls under seismic loading due to the ductility and flexibility of this type of structures.

The performance characteristics of several GRS retaining walls under the 1989 Loma Prieta Earthquake were reported by Collin et al. (1992). Visual inspection indicated that the GRS retaining walls investigated experienced almost no distress after earthquake shaking. One of the GRS retaining walls that was originally designed for a maximum horizontal acceleration of 0.1*g* had good performance when subjected to shaking with a maximum acceleration of 0.4*g*.

Sandri (1997) evaluated the performance of GRS retaining walls that experienced shaking during the 1994 Northridge earthquake and observed no distress. However, cantilever walls located near the GRS retaining walls showed significant cracking. Tatsuoka et al. (1997) evaluated GRS retaining walls in Japan after the 1995 Kobe earthquake. GRS retaining walls with full-height rigid facing panel were found to perform well and suffered only slight damages, while the gravity and cantilever reinforced concrete walls had moderate to serious damages. This confirms that the GRS retaining walls may have better seismic performance than conventional retaining walls due to their ductility.

Ling et al. (2001) conducted post-earthquake investigations after the 1999 Chi-Chi earthquake, and reported that several GRS retaining walls with modular block facing suffered moderate to serious damages, including large cracks on the backfill surface behind

the wall facing, large horizontal displacements of the wall facing, and collapse of the wall. Reasons for these damages mainly included low quality backfill soil, inadequate global stability analysis, large reinforcement vertical spacing, and insufficient connection strength.

Yen et al. (2011) conducted post-earthquake reconnaissance for the 2010 Maule Earthquake, and found that a GRS bridge abutment, as shown in Figure 2.4, exhibited no signs of lateral or vertical movements after shaking. However, the bridge suffered minor damage that may have resulted from the severe bridge skew angle.

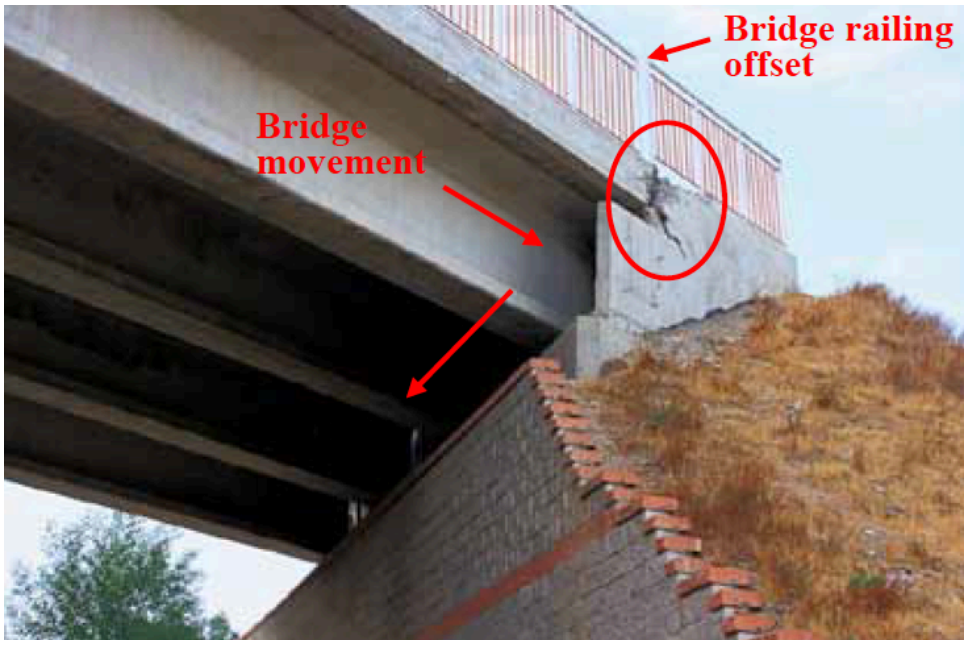

Figure 2.4 GRS bridge abutment at Estribo Francisco Mostazal (from Yen et al. 2011).

2.2 Experimental Studies

2.2.1 Laboratory Model Tests

The geotechnical research group at the Royal Military College (RMC) of Canada conducted a testing program to investigate the behavior of full-scale GRS retaining wall model tests that started in 1987. Issues that were investigated include the behavior of GRS retaining walls during construction, under working stresses, and under surcharge stresses approaching failure. The GRS wall models were 3.6 m-high and 3.4 m-wide, and the backfill soil extended approximately 6 m from the facing, as shown in Figure 2.5. The backfill soil was a uniform size rounded sand with a peak plane strain friction angle of 44°. The reinforcements included biaxial polypropylene (PP) geogrid, polyester (PET) geogrid, and welded wire mesh. Bathurst et al. (2000) investigated the effects of reinforcement stiffness, reinforcement spacing, and wall facing type on the performance of GRS walls. Four GRS wall models were constructed and loaded up to the surcharge stress of 115 kPa. Results indicate that lateral facing displacements can be reduced by increasing reinforcement stiffness or decreasing vertical reinforcement spacing. The toe of the GRS walls was found to carry a significant portion of the total horizontal earth forces. Bathurst (2006) and Bathurst et al. (2006, 2009) reported results for another series of 11 full-scale GRS wall models to investigate the effects of reinforcement type, reinforcement stiffness, reinforcement spacing, backfill compaction effort, wall facing stiffness and batter. Results indicated that peak loads in the reinforcement for a wrapped-face wall were about 3.5 times larger than those for modular block face wall at the end of construction, and increased

about 2 times under the surcharge stress of 80 kPa. The modular block facing acted as a structural element that reduced lateral facing displacements and reinforcement strains. For the GRS walls with modular block facing and incremental panel facing, connection loads were the largest in the reinforcement at the end of construction. Results also indicated that the effect of compaction effort was as important as reinforcement stiffness at the end of construction. However, the effect became attenuated as the surcharge stress increased, and the effect was almost erased at the surcharge stress of 30 kPa.

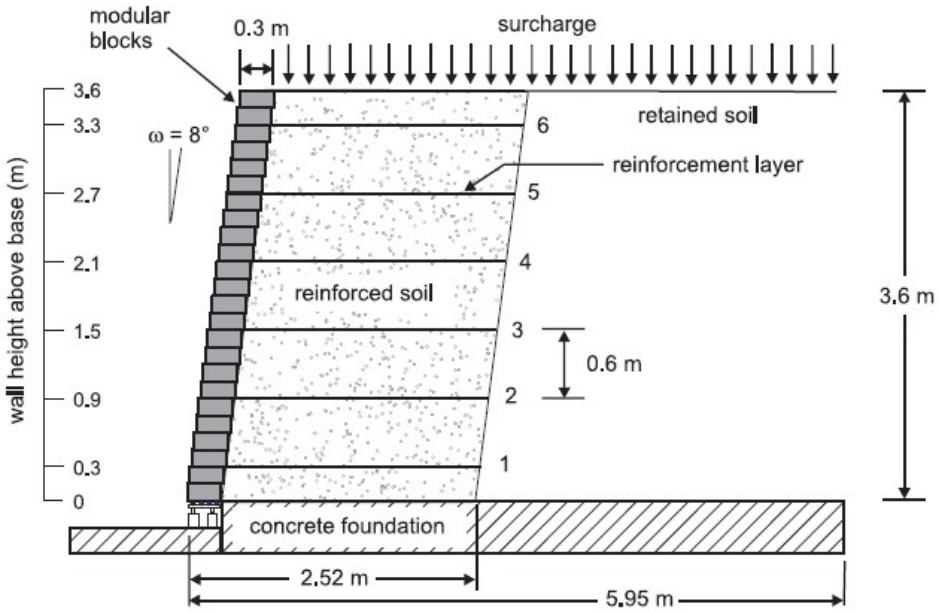

Figure 2.5 Typical cross-section of GRS retaining wall (from Bathurst et al. 2006).

Ehrlich et al. (2012), Ehrlich and Mirmoradi (2013), Mirmoradi et al. (2016), and Mirmoradi and Ehrlich (2016) conducted a series of physical model tests to investigate the effects of compaction effort, facing stiffness, and toe resistance on the behavior of GRS walls. The 1.5 m-high model wall was subjected to a surcharge stress of 100 kPa to simulate

the bottom potion of a 7 m-high prototype GRS wall. The backfill soil was a well-graded sand, and the reinforcement was a PET geogrid. The summation of mobilized tensile forces along the reinforcement layers for the GRS wall with heavy compaction at the end of construction were much larger than for the wall with light compaction. However, the difference decreased with increasing surcharge stress, and the summation of tensile forces were approximately the same at the surcharge stress of 100 kPa. For the restrained toe condition, the facing stiffness had an important effect on the reinforcement tensile forces. The mobilized tensile forces were also affected by the properties of the interface between the facing column and foundations soil. A higher toe restraint resulted in greater toe load and lower reinforcement tensile forces, and smaller lateral facing displacements.

2.2.2 Field Loading Tests

Experimental studies, including field and laboratory loading tests, have been conducted for large-scale GRS piers and abutments and generally indicated satisfactory performance under service load conditions and relatively large load capacity (Adams 1997; Gotteland et al. 1997; Ketchart and Wu 1997; Wu et al. 2001, 2006a; Nicks et al. 2013a, 2016; Adams et al. 2014; Iwamoto et al. 2015). Lee and Wu (2004) reviewed the results of several large-scale loading tests and suggested that the bearing capacity can be high for closely spaced reinforcement and well graded and well compacted backfill soil.

Gotteland et al. (1997) conducted full-scale loading tests to investigate the failure behavior of GRS walls as bridge support structures. The tested model consisted of two GRS wall sections with one reinforced using woven geotextile and the other one using nonwoven geotextile. The backfill material was a fine sand with a friction angle of 30° and cohesion of 2 kPa, and was compacted to the maximum dry density of standard Proctor. The intermediate reinforcement in the woven geotextile reinforced soil wall was shorter than in that in the nonwoven geotextile reinforced soil wall. Loading was applied on top of each GRS wall through a foundation slab. The applied loads at failure were 140 kN/m with a settlement of 36 mm for the nonwoven geotextile reinforced soil wall and 123 kN/m with a settlement of 33 mm for the woven geotextile reinforced soil wall.

Adams (1997) reported full-scale loading tests on a 5.4 m-high bridge pier at the Turner-Fairbank Highway Research Center in McLean, Virginia. The GRS pier was reinforced using woven geotextile at a vertical spacing of 0.2 m. The backfill material was a well-graded gravel and was compacted to 95% of the maximum dry density. The GRS

pier had a settlement of 13 mm and maximum lateral facing displacement of 6 mm at the intermediate height of 3.0 m under a surcharge stress of 200 kPa, which indicated the satisfactory performance of GRS pier under service load conditions. At the full height, the pier settlements were 25 mm and 70 mm under vertical stresses of 415 kPa and 900 kPa, respectively.

Ketchart and Wu (1997) conducted full-scale loading tests on two GRS piers and one GRS abutment, called the Havana Yard GRS bridge piers and abutment. The outer pier and abutment were 7.6 m high and the center pier was 7.3 m high. Each structure was reinforced using woven geotextile at a vertical spacing of 0.2 m. The backfill was a "road base" material with 13% of fines. The applied vertical stresses are 232 kPa and 130 kPa on the outer pier and abutment, respectively. Measured settlements were 36.6 mm for the pier and 27.1 mm for the abutment, corresponding to vertical strains of 0.35% and 0.48%, respectively.

Wu et al. (2001) conducted loading tests on two GRS bridge abutments that support a 36 m span steel arch bridge in Black Hawk, Colorado. In each abutment, two square footings were placed on top of the lower wall and one strip footing was constructed on the upper wall. The GRS bridge abutments were reinforced using woven geotextile at a vertical spacing of 0.3 m. The backfill material was an on-site soil with 12% of fines and had a friction angle of 31.3° and cohesion of 34.3 kPa. Four square footings were preloaded to a vertical stress of 245 kPa, and then reloaded to the design stress of 150 kPa. Results indicated that settlements of four square footings under the design stress could be reduced by a factor of 1.5 to 6 by the preloading to a vertical stress of 245 kPa.

Wu et al. (2006a) reported results for the NCHRP full-scale loading tests conducted at the Turner-Fairbank Highway Research Center in McLean, Virginia. The abutment model was 4.65 m high and had two sections with a back-to-back configuration. A non-plastic silty sand with a friction angle of 37.3° and a cohesion of 20 kPa was used as the backfill material. The GRS bridge abutment had both primary and secondary reinforcement (three layers at the top). Two woven geotextile reinforcements, one with an ultimate strength of 70 kN/m and the other one with an ultimate strength of 21 kN/m, were used for the two sections, respectively. At the maximum allowable vertical stress of 200 kPa, the abutment compressions were 40 mm and 72 mm, respectively. The two GRS bridge abutments failed at applied vertical stresses of 814 kPa and 414 kPa, respectively, and the corresponding abutment compressions are 163 mm and 175 mm.

A series of performance tests on 2 m-high GRS mini-piers have been conducted to investigate the effects of various factor on the behavior of GRS composite (Nicks et al. 2013a, 2016; Adams et al. 2014; Iwamoto et al. 2015). Results indicated that reinforcement spacing and strength have the most important effects on the ultimate capacity. Bearing bed reinforcements are effective on increasing the ultimate bearing capacity, but cannot reduce deformations for service load conditions. Also, increasing levels of backfill compaction and use of well graded backfill materials can increase the stiffness of a GRS composite pier.

2.2.3 Dynamic Centrifuge Tests

Sakaguchi (1996) conducted dynamic centrifuge tests to simulate a 4.5 m high GRS wall. Three geotextile reinforcements with different maximum tensile strength and reinforcement length were used. Results indicated that lateral facing displacements generally decreased with increasing reinforcement length, and the optimal reinforcement length was between 2/3 H and H. Maximum reinforcement tensile strength had little effect on the seismic response of GRS walls, as the tensile forces developed during seismic events were well below the tensile strengths.

Takemura and Takahashi (2003) conducted centrifuge tests to investigate the effects of reinforcement length, vertical reinforcement spacing, and backfill dry density on the dynamic response of GRS walls. The prototype wall was 7.5 m high and was subjected to sinusoidal excitation. Results showed that the wall specimen with lower backfill dry density experienced larger horizontal displacements and larger reinforcement tensile strains.

Siddharthan et al. (2004) carried out centrifuge tests on bar mat-reinforced soil retaining walls subjected to step waves and earthquake ground motions. Test results showed that the maximum lateral facing displacement typically occurred at the mid-height of the walls, and the walls with longer reinforcement had less deformations.

Nova-Roessig and Sitar (2006) conducted a series of centrifuge modeling tests on GRS slopes and walls using geosynthetic and metal grids reinforcements. Results showed that amplification occurred when the maximum acceleration of input motion is smaller than 0.4*g*-0.5*g*, whereas attenuation occurred for stronger input motions. Nova-Roessig and

Sitar (2006) suggested that the amplification and attenuation effects be considered in the seismic design of reinforced soil structures.

Liu et al. (2010) conducted dynamic centrifuge tests on three GRS walls with modular block facing. Two walls were subjected to the Kobe earthquake ground motion with the peak ground acceleration (PGA) scaled to 0.24*g*, and the other was excited using a sinusoidal wave with a PGA of 0.114*g*. Accelerations were amplified considerably in both the reinforced and retained zones under modest seismic shaking. Liu et al. (2010) suggested that the acceleration amplification be considered in the seismic design.

2.2.4 1*g* Shaking Table Tests

1*g* shaking table testing technique has been used to investigate the dynamic response of reinforced soil structures since the 1970s. However, due to the limitation of size and capacity of typical shaking tables, most of the tests were conducted for reduced-scale model, in which soil and reinforcement properties need to be properly scaled. The similitude relationships between the reduced-scale model and prototype structure have been proposed by Iai (1989), Sugimoto et al. (1994), and Telekes et al. (1994). Early studies focused on metallic reinforced soil walls till the late 1980s, and a number of tests started to investigate the seismic performance of GRS walls since the 1990s, mainly focusing on GRS walls with rigid facing and wrapped-face, and then GRS walls with modular block facing gained more popularity. Several full-scale shake table tests have also been conducted for this types of walls, which provided more valuable results (Ling et al. 2005a, 2012; Fox et al. 2015).

Richardson and Lee (1975) pioneered the use of shaking table tests on a series of 300 mm-high reduced-scale soil walls reinforced with aluminum strips subjected to sinusoidal motions to investigate the failure modes. Results indicated that strips pullout with ductile behavior is more desirable than strip breakage that causes sudden collapse. This study was followed by a 6 m-high full-scale steel reinforced soil wall subjected to both forced vibrations and blast excitations, and results showed reinforced soil walls could withstand severe shaking even designed for static criteria (Richardson et al. 1977).

Wolfe et al. (1978) carried out a series of shaking table tests on 610 mm-high reinforced soil walls subjected to horizontal, vertical, and combined horizontal and vertical

excitations. Similar responses were observed for excitations in horizontal direction only and both directions, thus the effect of vertical component could be ignored in the design.

Chida et al. (1982) carried out a series of shaking table tests on 4.4 m-high steel reinforced soil walls and found that the average peak horizontal acceleration in the soil behind the walls was equal to the PGA for ground motion frequencies less than 3 Hz.

Nagel and Elms (1985) tested seven 320 mm-high walls reinforced using wide satin ribbon at the University of Canterbury, and observed that all walls remained vertical during failure except for the bottom panel. Results indicated that reinforcement density and length affected the failure surface geometry. This study was followed by shake table tests for six 1 m-high reinforced soil walls by Fairless (1989), which showed that the seismic shaking cause dramatic increases in tensile forces for the reinforcing strips and permanent outward displacements when the ground acceleration exceeds a yield acceleration.

A number of shake table tests have been conducted for GRS walls with various facing conditions since the late 1980s (Koga et al. 1988; Koga and Washida 1992; Sakaguchi et al. 1992; Murata et al. 1994; Budhu and Halloum 1994; Sakaguchi 1996; Koseki et al. 1998; Matsuo et al. 1998). Murata et al. (1994) tested 2.5 m-high GRS walls with gabion and rigid concrete panel facings subjected to both sinusoidal and scaled earthquake motions. Results indicated that acceleration amplification was negligible up to the mid-height of the wall, and then increased to about 1.5 at the top, and the sinusoidal motion resulted in greater deformations than scaled earthquake motions. Sakaguchi (1996) performed shaking table tests to compare the dynamic responses of a 1.5 m-high wrapped-face GRS wall and three unreinforced conventional type retaining walls. The GRS wall failed at a much higher acceleration than the other unreinforced walls, but experienced

larger deformations under smaller accelerations. Koseki et al. (1998) conducted shaking table tests on 500 mm-high GRS walls with rigid facing and conventional type retaining walls. The model walls were subjected to a sinusoidal excitation at a frequency of 5 Hz and showed a primary failure mode of overturning with tilting of wall facing after shaking. Results also indicated that increasing reinforcement length for top layers could increase the resistance against the overturning failure. Matsuo et al. (1998) conducted shaking table tests on six 1.0 m- to 1.4 m-high GRS walls to investigate the effects of various factors on the dynamic response, and found that increasing reinforcement length is the most effective means to reduce lateral facing displacements, and the wall with continuous rigid facing experienced larger lateral displacements than the wall with segmental facing panels.

Ramakrishnan et al. (1998) tested two GRS walls with wrapped-face and modular block facing, respectively, and observed that the modular block facing wall can sustain two times the critical acceleration than the wrapped-face wall. An analytical method was also developed to calculate the critical acceleration.

El-Emam and Bathurst (2004; 2005; 2007) performed a series of shaking table tests on reduced-scale reinforced soil walls with a full-height rigid facing panel to investigate the effects of toe boundary conditions, facing conditions, reinforcement layout, and input motion on dynamic response. Fourteen 1/6 scale walls with a full-height rigid facing panel were subjected to stepped-amplitude sinusoidal loading. The model walls were 1 m-high and the backfill soil zone was 2.4 m long, as shown in Figure 2.6. Excitations were applied in 0.05*g* increments with a duration of 5 seconds and continued until excessive wall deformations occurred. The backfill soil had a peak friction angle of 51° and a dilation angle of 15°. Experimental results showed that facing lateral displacements could be

reduced by using smaller facing panel mass, inclined facing panels, longer reinforcement, stiffer reinforcement, and smaller reinforcement vertical spacing. Reinforcement load was the largest near the facing connections both at the end of construction and during shaking. The summation of reinforcement connection loads generally decreased with increasing facing mass, greater horizontal toe restraint and greater facing inclination angle. A restrained toe with a stiff facing panel was found to carry a significant portion of total horizontal earth force for both static and dynamic conditions.

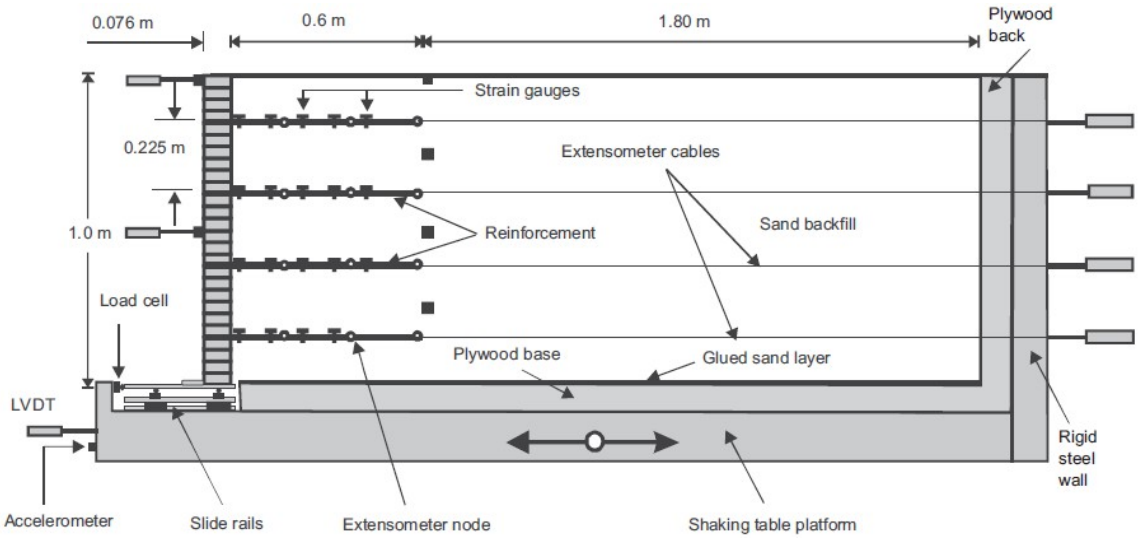

Figure 2.6 Cross-section view and instrumentation layout for reduced-scale reinforced soil model walls (from El-Emam and Bathurst 2005).

Ling et al. (2005a) conducted full-scale shaking table tests on three GRS walls with modular block facing for the Kobe earthquake ground motion. The walls were 2.8 m-high and had a 0.2 m-thick foundation soil, as show in Figure 2.7. Walls 1 and 2 were subjected to horizontal shaking only, whereas Wall 3 was subjected to both horizontal and vertical shaking. For the first excitation, the ground motion record was scaled to a PGA of 0.4*g*,

and to PGA of 0.8*g* for the second excitation. The backfill and foundation soil was a fine sand with medium relative density and a friction angle of 38°. Experimental results showed that the GRS walls experienced negligible deformation under moderate earthquake loading (PGA = 0.4*g*) and performed well under strong earthquake loading with a PGA of 0.8*g*. Ling et al. (2005a) found that using longer reinforcement for the top layer and smaller reinforcement vertical spacing could improve the seismic performance. Vertical acceleration did not have a major effect on wall deformations, but increased vertical stresses at foundation level and reinforcement loads. Ling et al. (2012) performed another set of shaking table tests on GRS walls constructed using a silty sand backfill soil with 43.3% fines content. The backfill and foundation soil had a friction angle of 39° and apparent cohesion of 40 kPa. These walls were subjected to both horizontal and vertical components of the Kobe earthquake motion. Comparing experimental results with previous tests results (Ling et al. 2005a), Ling et al. (2012) found that GRS walls constructed using low-quality backfill soil had better seismic performance than otherwise identical walls with sandy backfill with respect to wall deformations, dynamic earth pressures and reinforcement forces. Ling et al. (2012) suggested that the good seismic performance was due to the apparent cohesion of the fine-grained soils. However, the use of apparent cohesion in the design is cautioned, as this cohesion value could vary significantly due to environmental changes during the service life of GRS walls.

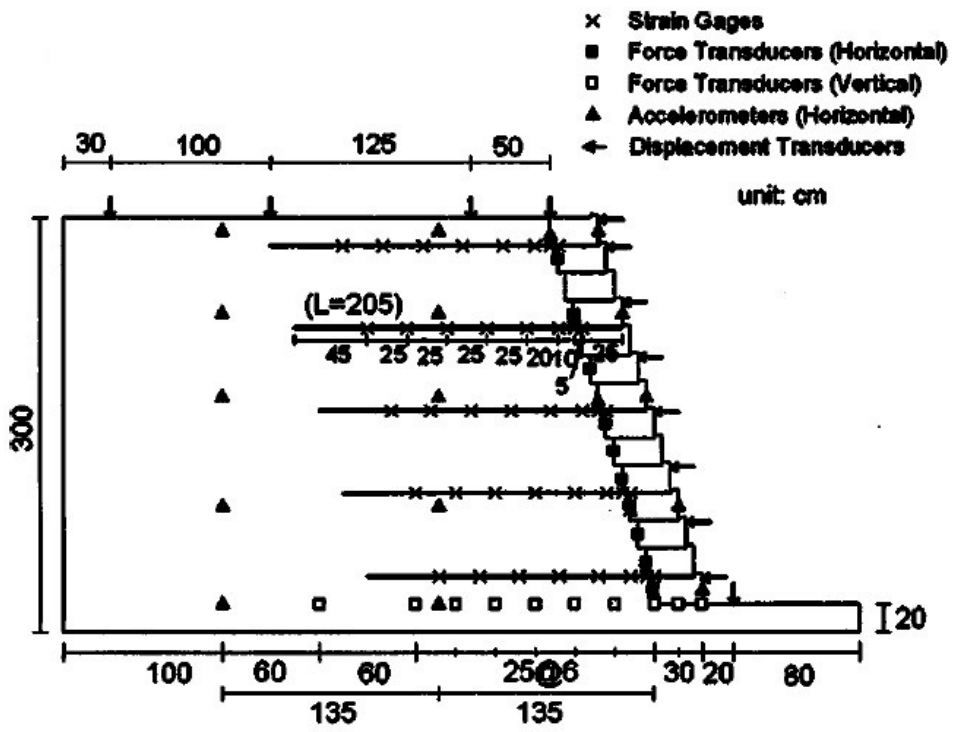

Figure 2.7 Cross-section view and instrumentation layout for Wall 1 in full-scale shaking table tests (from Ling et al. 2005a).

Latha and Krishna (2008) studied the influence of backfill soil relative density on the seismic response of GRS walls with wrapped-face and full-height rigid facing panel. A total of 24 walls were subjected to sinusoidal excitations. Lateral facing displacements for walls with wrapped facing were generally much larger than walls with a full-height rigid facing panel. The effects of backfill soil relative density were pronounced only at low relative densities and higher base excitations. Krishna and Latha (2009) also investigated the effects of reinforcement properties on seismic performance of GRS walls with a full-height rigid facing. Reinforcement layers, even with low tensile strength, were very effective on reducing lateral facing displacements compared with measured displacements of unreinforced walls. However, acceleration amplification within the backfill was not much influenced by reinforcement properties. Latha and Santhanakumar (2015) also

conducted shake table tests for a series of 600 mm-high GRS walls with rigid facing and modular block facing, and concluded that increasing backfill soil relatively density has important effects on reducing lateral facing displacements and settlements for walls with both rigid facing and modular block facing.

Guler and Enunlu (2009) performed shaking table tests for two half-scale 2 m-high GRS walls with modular block facing and different reinforcement lengths. For the model wall with shorter reinforcement, lateral facing displacements and dynamic tensile forces in reinforcement were larger, and a shallower internal failure surface was observed than the other wall with longer reinforcement. Guler and Selek (2014) reported a series of eight reduced-scale shaking table tests to investigate the effect of various factors, including PGA, reinforcement length and spacing, model scale, and treatment of top two facing blocks, on the seismic performance of GRS walls. The similitude relationships proposed by Iai (1989) were followed in this series of tests. Results indicated that accelerations were not affected by model size, but displacements for prototype structure increased with decreasing model size. Lateral facing displacements were not significantly affected by reinforcement length and spacing, which might be attributed to the relatively high reinforcement stiffness and apparent cohesion for the backfill soil.

Helwany et al. (2012) conducted large-scale shaking table tests on a GRS bridge abutment at the U.S. Army Engineering Research and Development Center – Construction Engineering Research Laboratory (ERDC-CERL) using the Triaxial Earthquake and Shock Simulator (TESS). The GRS bridge abutment model had a total height of 3.6 m, including a 3.2 m-high lower wall and 0.4 m-high upper wall. The test setup and cross-sectional view are shown in Figure 2.8 and Figure 2.9, respectively. The abutment was reinforced using a

woven geotextile with a vertical spacing of 0.2 m. The backfill soil was poorly-graded gravel with sand and clay, and had a friction angle of 44°. The bridge superstructure had a total weight of 445 kN and yielded an average vertical stress of 111 kPa on the abutment. In the shaking table tests, the GRS bridge abutment model was subjected a series of horizontal sinusoidal motions with increasing amplitude in the longitudinal direction. The first test was performed using a sinusoidal motion at a frequency of 1.5 Hz with an amplitude of 0.15*g* for 20 seconds. Four additional tests were conducted at a frequency of 3 Hz with amplitudes of 0.3*g*, 0.45*g*, 0.67*g*, and 1.0*g*. No damage was observed until the acceleration reached 0.67*g*, and no significant distress occurred for accelerations up to 1*g*. The incremental bridge seat settlement was approximately 50 mm when the acceleration increased from 0.67*g* to 1.0*g*. In general, the GRS bridge abutment remained functional under sinusoidal motion with horizontal accelerations up to 1.0*g*.

Figure 2.8 Shaking table test setup for GRS bridge abutment (from Helwany et al. 2012).

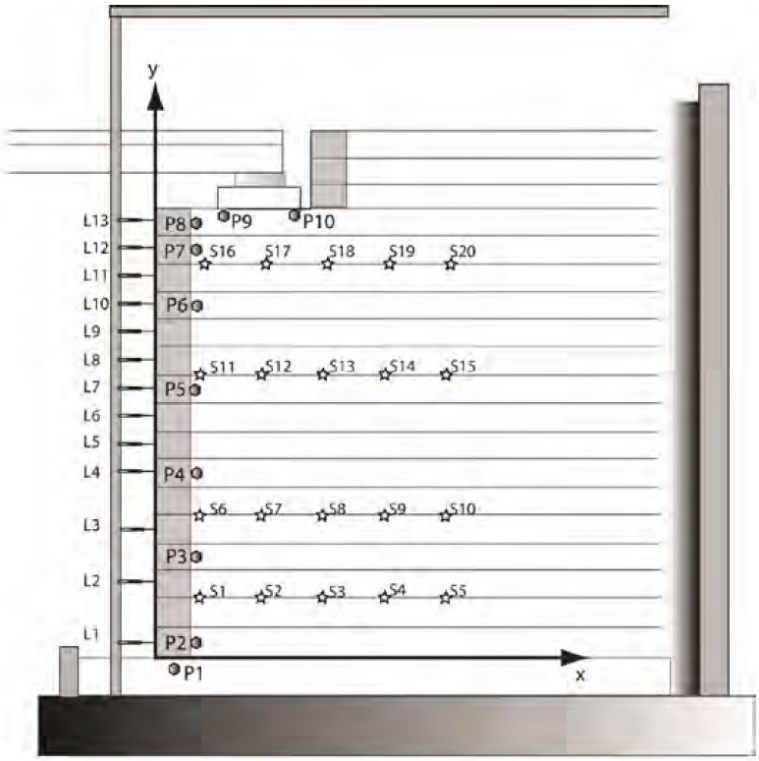

Figure 2.9 Cross-sectional view and instrumentation layout for GRS bridge abutment model (from Helwany et al. 2012).

2.3 Numerical Studies

2.3.1 Static Loading

2.3.1.1 GRS Retaining Walls

Bathurst et al. (1992) and Karpurapu and Bathurst (1995) simulated two full-scale GRS walls with incremental panel facing and full height panel facing using the finite element program GEOFEM. A modified hyperbolic model that included dilation was used to simulate the backfill soil, and the reinforcement was simulated with a nonlinear load-strain model using uniaxial elements. Zero thickness joint elements with Mohr-Coulomb failure criterion were used to simulate the interfaces between soil and reinforcement, and between soil and facing panels. Triaxial tests and direct shear tests were conducted to determine parameters for the modified Duncan-Chang model. Constant creep load tests were carried out to obtain the isochronous load-strain-time relationships for the reinforcement, and interface shear tests were conducted to determine shear stiffness of various interfaces. Simulation results, including lateral facing displacements and reinforcement strains at the end of construction and under uniform surcharge loading, were compared with experimental results, and showed good agreement for both working stress and collapse conditions. It is important to consider the soil dilation to accurately simulate the performance of GRS walls because soil dilation have an important effect on transferring load from reinforcement to soils during shearing. Lateral facing displacements and reinforcement strains could be over-predicted by a factor of two if soil dilation was not

accounted for. The simulated failure surface was also in good agreement with experimental observed failure surface and the failure surface predicted using Rankine earth pressure theory.

Ho and Rowe (1996), and Rowe and Ho (1997, 1998) carried out parametric studies on GRS walls with continuous facing panels using the finite element program AFENA. In these studies, the effects of reinforcement properties, soil properties, interface friction angles, wall facing rigidity, and wall height were investigated. The backfill soil was modeled as an elasto-plastic material with the Mohr-Coulomb failure criterion and non-associated flow rule. The reinforcement was modeled using linearly elastic bar elements with negligible compressive strength. Soil-reinforcement, soil-facing panel, and soil-foundation interfaces were modeled using joint elements with the Mohr-Coulomb failure criterion and zero dilation. Simulation results indicated that reinforcement stiffness and backfill soil friction angle have the most significant effects on the lateral facing displacements, whereas the interface friction angles, soil Young's modulus, and facing rigidity are less important. For a reinforcement length to wall height ratio (L/H) greater than 0.7, the effect of reinforcement length on the lateral facing displacements and reinforcement strains was very small, while the effect could be significant for L/H less than 0.7. The maximum reinforcement load increases with increasing reinforcement stiffness density, decreasing backfill soil friction angle, decreasing soil-facing interface friction angle, and decreasing facing rigidity.

Helwany et al. (1999) verified finite element model using measured results from the Denver Test Wall using the finite element program DACSAR. In this study, the backfill soil was simulated using a nonlinear elastic hyperbolic model, and the model parameters

were calibrated from triaxial tests. The timber facing and geotextile reinforcement were modeled using linearly elastic beam elements and truss elements, respectively. Simulated lateral facing displacements and reinforcement strains were in reasonable agreement with measured results. A parametric study was conducted using the validated numerical model to investigate the effects of various factors on the behavior of GRS wall under a uniform surcharge stress of 35 kPa. Results indicated that the backfill soil type was the most important factor that affected the performance of GRS walls. Reinforcement stiffness was also important when the backfill soil stiffness and strength were low. Design charts were developed for selecting appropriate backfill soil type and reinforcement stiffness to satisfy the performance requirements (e.g. maximum lateral facing displacement, maximum reinforcement strain, and/or average factor of safety) for the design of GRS walls.

Ling et al. (2000) used the finite element program M-CANDE to reproduce results of a full-scale GRS retaining wall model test at the Public Works Research Institute (referred to as PWRI Wall). The PWRI Wall was 6 m-high and 5 m-wide, and was reinforced using primary geogrid (3.5 m-long) and secondary geogrid (1.0 m-long). In this study, both the backfill soil and geosynthetic reinforcement were modeled using the hyperbolic model, and the model parameters were calibrated using results from triaxial tests for the backfill soil and tensile tests for the reinforcement. The block-block interface and soil-block interfaces were simulated using interface elements, and the interface friction angles and tensile strengths were determined from interface direct shear tests. Simulated results, including lateral facing displacements, lateral and vertical stresses, and reinforcement strains during construction were compared with measured results, and showed satisfactory agreement. Ling and Leshchinsky (2003) carried out a parametric

study using the validated model to investigate the effects of various design parameters on the behavior of GRS walls under working stress conditions. Results indicated that lateral facing displacements and maximum reinforcement tensile forces increased with increasing reinforcement vertical spacing. Lateral facing displacements decreased with increasing reinforcement stiffness, whereas the maximum tensile forces were the largest for the stiffest reinforcement. For block-block interface friction angles greater than 20°, the variations for wall displacements and maximum reinforcement strains were negligible. Ling (2003) also compared simplistic and sophisticated finite element analyses for GRS walls. Both the backfill soil and geosynthetic reinforcement were characterized using hyperbolic model in the simplistic analysis, whereas in the sophisticated analysis, the backfill soil was modeled using a generalized plasticity model and the geogrid was simulated using a bounding surface model. Results for wall facing displacements, lateral and vertical stresses, and reinforcement strains from simplistic and sophisticated analyses were in good agreement, and both provided a reasonable match with measured results from a full-scale model test.

Lee (2000) validated a FLAC model with monitored results from several instrumented full-scale GRS walls. A parametric study was carried out to investigate the influences of soil properties, reinforcement properties, toe restraint, and facing type on the performance of GRS retaining walls. Results indicated that the backfill soil strength properties and global reinforcement spacing have the most significant effects on the facing displacements and reinforcement strains. Toe restraint (embedded toe condition) could reduce the maximum facing displacement and reinforcement tensile forces. For GRS walls constructed using good quality backfill soil and with large reinforcement vertical spacing, secondary reinforcement was effective on improving the performance. A structural facing

system such as modular blocks and concrete panels could increase the stability, and reduce wall deformations and reinforcement strains, especially for GRS walls with large reinforcement spacing.

Leshchinsky and Vulova (2001) investigated the effects of reinforcement spacing on the failure mechanisms of GRS walls using FLAC. The backfill soil was modeled using the Duncan-Chang hyperbolic stress-strain relationship prior to failure and the Mohr-Coulomb failure criterion. The frictional connection between the reinforcement and facing blocks was simulated using beam elements and interface elements. Four modes of failure were observed, including external (direct sliding and toppling), deep seated (bearing capacity), compound, and connection, based on the development of plastic zones. Deep seated failure occurred for the cases with closely-spaced reinforcement and weak foundation soil. Connection failures were observed for all cases with reinforcement spacing equal to or greater than 0.6 m. Leshchinsky and Vulova (2001) suggested that reinforcement spacing plays an important role in the behavior of GRS walls and significantly affects the potential failure mode.

Hatami and Bathurst (2005a; b) validated a FLAC model using measured results from full-scale model tests on GRS walls at the end of construction. The backfill soil was modeled as a nonlinear elastic-plastic material with the Duncan-Chang hyperbolic relationship, Mohr-Coulomb failure criterion and non-associated flow rule. The reinforcement was also simulated using a hyperbolic model, and was assumed to be rigidly connected to the facing blocks using beam elements. In this study, the backfill soil compaction during construction were simulated using a temporarily-applied surcharge stress of 8 kPa after placement of each lift, and was removed before the placement of the

next soil lift. Simulated results, including toe loads, vertical foundation pressures, facing displacements, connection loads, and reinforcement strains were compared with measured results, and yielded good agreement. The influence of soil constitutive model on the wall performance was also investigated. Simulation results for a linearly elastic-perfectly plastic soil model showed good agreement with regarding to facing displacements and toe loads, but lesser agreement for reinforcement strain distributions. Hatami and Bathurst (2005c) and Bathurst and Hatami (2006a) investigated the effects of various design parameters on the behavior of GRS walls at the end of construction using FLAC. Results showed that, as the wall height increased, the maximum lateral facing displacement increased. For a granular soil, a value of cohesion as low as 10 kPa can significantly reduce lateral facing displacements and can also influence the facing displacement pattern and reinforcement strain distribution. Hatami and Bathurst (2006) and Bathurst and Hatami (2006b) further validated the FLAC model for GRS retaining walls under surcharge loading using measured results from instrumented full-scale model tests. Bathurst et al. (2008) and Huang et al. (2010) conducted numerical simulations to investigate the effects of toe restraint conditions on the performance of GRS walls using the validated FLAC model. Results indicated that displacements at the bottom of the wall and reinforcement loads increased as the toe stiffness decreased. Huang et al. (2009) also investigated the effect of soil constitutive model on the behavior of GRS walls using FLAC. The investigated soil constitutive models included linearly elastic plastic Mohr-Coulomb model, modified Duncan-Chang hyperbolic model, and Lade's single hardening model. Simulated results for three constitutive models were evaluated by comparing with measured results at the end of construction and under surcharge loading conditions. Huang et al. (2009) concluded

that the simple Mohr-Coulomb model is better suited for GRS walls that are at incipient failure conditions than for working stress conditions. The Lade's model can simulate the shear dilatancy and strain softening behavior of soil during shearing; however, this model requires many parameters that lack physical meaning. On the other hand, the modified Duncan-Chang model can reasonably predict the response of GRS walls under work stress conditions, and the model parameters can be determined from conventional triaxial tests. Damians et al. (2014) investigate the effects of foundation compressibility and reinforcement stiffness on the behavior of reinforced soil walls using FLAC. Results indicated that facing displacements, connection loads, and reinforcement strains all increase, as foundation stiffness decreases, and the influence of reinforcement stiffness is greater than foundation stiffness for reinforced soil walls under working stress conditions. Yu et al. (2016) conducted a benchmark study to validate a numerical model using well-documented data for two instrumented GRS walls. This study described the detailed modeling procedures for GRS walls with high-quality data, including calibration of model parameters for backfill soil and geosynthetic reinforcement, and selection of constitutive models for backfill soil.

Guler et al. (2007) conducted a numerical investigation on the failure mechanisms of GRS walls using the strength reduction method. The finite element model in PLAXIS was first validated using data reported by Hatami and Bathurst (2005a, 2006) for three full-scale GRS walls, in which the backfill soil was simulated using hardening soil model and the geogrid was modeled using elastic element. A parametric study was carried out to investigate the effects of reinforcement length, reinforcement vertical spacing, and backfill

soil type on the failure mechanism. Results indicated that sliding is the primary failure mode for GRS walls using both granular and cohesive backfill soil.

Mirmoradi and Ehrlich (2015, 2017) conducted a series of numerical studies to investigate the combined effects of toe condition, facing stiffness, backfill compaction, reinforcement stiffness, and wall height on the behavior of GRS walls under working stress conditions. The finite element model using PLAXIS was validated using data reported by Hatami and Bathurst (2005a, 2006) for a full-scale GRS wall. Results indicated that toe condition has an important effect on the reinforcement tensile force at the bottom section of the wall. For fixed toe conditions, as facing stiffness increase, horizontal toe load increases and reinforcement tensile forces decrease. For GRS walls with greater reinforcement stiffness, the reinforcement forces are larger and the horizontal toe load is smaller. Also, the combined effects of different factors on the reinforcement tensile force distributions are limited to 4 m above the foundation level.

2.3.1.2 GRS Bridge Abutments

Numerical modeling studies have been conducted to investigate the static behavior of GRS bridge abutments. Skinner and Rowe (2005) conducted finite element analyses to investigate the behavior of GRS bridge abutments constructed on a yielding clay foundation. Zevgolis and Bourdeau (2007) studied the deformation behavior of GRS bridge abutments with different foundation soil conditions using the finite element program PLAXIS. Some numerical models have been validated using results from field monitoring and/or field loading tests, which provide more convincing insights on the behavior of GRS

bridge abutments (Helwany et al. 2003, 2007; Wu et al. 2006a, b; Fakharian and Attar 2007; Ambauen et al. 2015).

Helwany et al. (2003) performed finite element analyses using the program DACSAR. The numerical model was validated using measurements for the Founders/Meadows GRS bridge abutment. The backfill soil was simulated as a nonlinear elastic material using the Duncan-Chang hyperbolic relationship, and the geosynthetic reinforcement was simulated as a linearly elastic material and was assumed to be perfectly bonded to backfill soils. Using the same abutment configuration, a parametric study was conducted to investigate the effects of foundation soil conditions on the behavior of GRS bridge abutments. Results showed that a loose sand foundation yielded much larger bridge footing settlements and lateral facing displacements than a dense sand foundation. Differential settlements between the bridge and approach embankment were acceptable for sand and medium-to-stiff clay foundation soils.

Wu et al. (2006a, 2006b) conducted a series of finite element analyses to investigate the effects of bridge seat type, bridge seat width, backfill soil stiffness and strength, reinforcement spacing, and foundation stiffness on the load-bearing capacity of GRS bridge abutments. The allowable bearing pressures were determined based on a limiting displacement criterion or a limiting shear strain criterion. Results indicated that reinforcement spacing is the most important factor that influences the load-bearing capacity of a GRS bridge abutment. Based on the simulation results, design procedures were developed to determine the allowable bearing pressures considering footing type, reinforcement spacing, and soil conditions.

Helwany et al. (2007) performed finite element analysis for large-scale loading tests of the National Cooperative Highway Research Program (NCHRP) GRS bridge abutment (Wu et al. 2006a). The soil behavior was simulated using a cap plasticity model and the geosynthetic reinforcement was modeled using an elastic-plastic model. Simulated lateral facing displacements and bridge footing settlements were in close agreement with measurements. A corresponding parametric study indicated that soil friction angle, reinforcement spacing, and reinforcement stiffness are important factors that influence the behavior of GRS bridge abutments.

Fakharian and Attar (2007) also conducted an investigation of the Founders/Meadows bridge abutment using finite difference analysis. The backfill soil was modeled as Mohr-Coulomb with the Duncan-Chang hyperbolic relationship to account for nonlinear behavior. Simulated results were in generally satisfactory agreement with field measurements, including facing displacements, bridge footing settlements, earth pressures, and reinforcement strains.

Leshchinsky (2014) and Xie and Leshchinsky (2015) performed a series of parametric studies using limit analysis to investigate the optimal reinforcement design and failure mechanism of GRS bridge abutments. Results indicated that more closely spaced reinforcement in the upper part of a GRS wall can efficiently increase the ultimate bearing capacity, and also showed a curved failure surface between the heel of bridge footing and the toe of GRS bridge abutment for a footing setback distance of less than 1.35 m.

Ambauen et al. (2015) validated a finite element model using results from full-scale GRS walls under surcharge loading (Hatami and Bathurst 2006). A parametric study was conducted to investigate the effects of reinforcement type, reinforcement spacing, bridge

footing location, bridge footing dimensions, and toe restraint conditions on the lateral earth pressure distributions, wall facing displacements, and reinforcement strains for service load conditions. Results indicate that close reinforcement vertical spacing resulted in increases of lateral earth pressures, but decreases of wall facing displacement, bridge footing settlements, and reinforcement strains.

2.3.2 Dynamic Loading

2.3.2.1 GRS Retaining Walls

Segrestion and Bastick (1988) validated a dynamic finite element model in the program SUPERFLUSH with measured results from a shaking table test on a steel strip reinforced soil wall (Chida et al. 1982). Yogendrakumar et al. (1991) studied the seismic response of 6 m-high retaining walls reinforced with steel strips using the program TARA-3. Yogendrakumar and Bathurst (1992) and Bachus et al. (1993) conducted dynamic finite element modeling of reinforced soil walls subjected to blast loading using the programs RESBLAST and DYNA3D, respectively. Yogendrakumar et al. (1992) compared the dynamic response of reinforced soil walls under blast loading using both equivalent linear approach and nonlinear incremental approach, and found that the nonlinear incremental approach yielded better predictions when compared with measured results from a field test.

Cai and Bathurst (1995) conducted dynamic finite element modeling of GRS retaining walls with modular block facing using TARA-3. The cyclic shear behavior of backfill soil was modeled using a hyperbolic stress-strain relationship with Masing hysteretic rules for unloading and reloading. The reinforcement was modeled using a similar hysteretic model to capture the measured response of cyclic tensile tests on unconfined geogrid specimens. Slip elements were used to simulate the interactions between different components. The scaled El-Centro earthquake record with a PGA of 0.25*g* was applied to the base of the model. Relative displacements and shear forces between blocks were greatest at the reinforcement elevations and shear capacity was exceeded at some locations. Cai and Bathurst (1995) concluded that the block-block

interface properties are important for seismic design of GRS walls. Furthermore, predicted tensile forces in the reinforcement were smaller than calculated using the pseudo-static approach, which implied that the pseudo-static approach is conservative for the seismic design of GRS walls with modular block facing.

Bathurst and Hatami (1998, 1999) investigated the effect of different design parameters on the dynamic response of GRS walls with a rigid full-height facing panel using FLAC. The dynamic response of GRS walls was most sensitive to toe boundary condition (i.e., fixed toe vs. sliding toe). Both the facing displacements at the top and the relative displacement with respect to the toe were smaller for a wall with a sliding toe condition than with a fixed toe. Facing displacements decreased with increasing reinforcement stiffness and reinforcement length, but the effect was relatively small for a ratio of reinforcement length to wall height (L/H) greater than 0.7. Hatami and Bathurst (2000a) studied the effects of different structural design parameters on the fundamental frequency of GRS walls and concluded that fundamental frequency can be estimated with reasonable accuracy using a one-dimensional solution based on linear elastic theory. Results also showed that the fundamental frequency was not significantly affected by reinforcement stiffness, reinforcement length, toe restraint conditions and backfill soil friction angle, but was dependent on ground motion intensity and the width-to-height ratio (W/H) of the backfill. Hatami and Bathurst (2000b) simulated the dynamic response of GRS walls with modular block facing subjected to different ground motions. Facing displacements and reinforcement forces for GRS walls subjected to a single frequency harmonic motion were larger than the responses of walls subjected to actual earthquake ground motions with comparable predominant frequencies. The low-frequency ground

motions with high intensity could result in significant structural responses for short-period GRS walls.

Helwany et al. (2001) validated a finite element model in the program DYNA3D using measured results from a small-scale shaking table test on a 0.9 m-high GRS wall with modular block facing. Nonlinear hysteretic behavior of the backfill soil under cyclic loading was simulated using the Ramberg-Osgood model with parameters determined from laboratory tests. The geotextile was modeled as a linearly elastic material. Helwany and McCallen (2001) investigated the influence of facing block connection on the static and dynamic behavior of GRS walls using the validated model. At the end of construction, the wall facing blocks with pin connections had smaller lateral facing displacements than without pin connections, while the facing blocks with pin connections experienced larger dynamic facing displacements. The smaller dynamic facing displacements for the wall without pin connections were due to smaller lateral earth pressures behind the wall facing, as the blocks without pin connections permitted more relative sliding between the blocks.

Ling et al. (2004) validated a finite element model for both static and dynamic analyses using a modified version of Diana-Swandyne II. A generalized plasticity model which accounted for the stress-dependent stiffness, strength and dilatancy, and cyclic hardening behavior, was used for the backfill soil. A bounding surface model was used to simulate the cyclic behavior of uniaxial geogrid. The interactions between different components were simulated using interface elements. The dynamic finite element model was validated using measured results from dynamic centrifuge tests. In these tests, the GRS walls were subjected to 20 cycles of sinusoidal excitation with a frequency of 2 Hz and acceleration amplitude of 0.2*g*. Simulated accelerations, facing displacements, crest

settlement, and maximum tensile forces in the geogrid showed good agreement with measured results. Ling et al. (2005b) conducted a parametric study using the validated finite element model to investigate effects of soil and reinforcement properties, reinforcement length and spacing, and block interaction properties on the performance of GRS walls at the end of construction and under earthquake loading. Lateral facing displacements and crest settlement were mainly influenced by soil cyclic behavior, reinforcement layout, and earthquake motions. The effects of reinforcement vertical spacing on facing displacements, reinforcement forces, and lateral earth pressures were more significant than the reinforcement length.

El-Emam et al. (2004) and Fakharian and Attar (2007) validated FLAC models using measured results from reduced-scale shaking table tests on GRS walls with a rigid full-height facing panel conducted at RMC (El-Emam and Bathurst 2004, 2005, 2007).

Above numerical model validations have been based on either reduced-scale shaking table tests or dynamic centrifuge tests, both of which have disadvantages such as model size effects, stress level effects, and boundary condition effects. The large-scale shaking table tests on 2.8 m-high GRS walls with modular block facing conducted by Ling et al. (2005a) have provided valuable data for validation of dynamic numerical models (Ling et al. 2010; Lee et al. 2010; Guler et al. 2012; Ren et al. 2016). Ling et al. (2010) validated a dynamic finite element model using experimental results and improved the soil and geosynthetic models (Ling 2003; Ling et al. 2005b). The unified general plasticity model for soil was improved by considering the effect of soil density, and the S-shaped load-strain relationship was accounted for to simulate the cyclic behavior of geogrid. Lee et al. (2010) also simulated the large-scale shaking table tests using the finite element

program LS-DYNA. The backfill soil was simulated using a geological cap model and the geogrid reinforcement was simulated using a plastic-kinematic model with a bilinear stress-strain curve. Lee and Chang (2012) conducted a parametric study using the validated program to investigate the effects of different design parameters, including wall height, wall batter angle, backfill soil friction angle, reinforcement spacing, and reinforcement stiffness, on the seismic performance of GRS walls. Results showed that GRS walls become less stable with a decreasing batter angle (e.g., more near vertical) for the wall facing and a close reinforcement vertical spacing of 0.2 m is effective on reducing wall deformations and reinforcement forces. Maximum tension line is close to the wall facing, which indicates that connection strength is important for the seismic design for internal stability.

2.3.2.2 GRS Bridge Abutments

Helwany et al. (2012) validated a 3-D ABAQUS finite element model using measured results from the full-scale shaking table tests on the GRS bridge abutment. The backfill soil was simulated using a cyclic model with isotropic/kinematic hardening and the geotextile was modeled using membrane elements. Interface elements that allow sliding and separation were also placed between blocks and reinforcement, between soil and reinforcement, and between blocks and soil. Parametric studies were conducted to investigate the influences of various design parameters, including backfill soil friction angle, reinforcement stiffness, reinforcement spacing, bridge height, bridge span, and earthquake ground motion, on the seismic performance of GRS bridge abutments.

Simulation results indicated that GRS bridge abutments would generally experience small seat settlements (less than 5 cm) but relatively large facing lateral displacements (up to 20 cm) for strong earthquake motions.

Chapter 3

Numerical Simulation of GRS Bridge Abutments under Static Loading

3.1 Introduction

Extensive numerical studies have been conducted on the behavior of GRS retaining walls for static loading conditions; however, significantly less work has been conducted for GRS bridge abutments. Helwany et al. (2003) performed finite element analysis for the Founders/Meadows GRS bridge abutment and showed that simulated reinforcement strains and vertical earth pressure distributions at the end of construction were in general agreement with field measurements; however, vertical pressures directly under the bridge seat were not in agreement. Using the same abutment configuration, a corresponding parametric study indicated that lateral facing displacements, bridge seat settlements, and differential settlements between the bridge and approach embankment were acceptable for

sand and medium-to-stiff clay foundation soils. Fakharian and Attar (2007) also conducted an investigation of the Founders/Meadows GRS bridge abutment using finite difference analysis. The backfill soil was modeled as Mohr-Coulomb with the Duncan-Chang hyperbolic relationship to account for nonlinear behavior. Simulated results were in generally satisfactory agreement with field measurements, including abutment displacements, earth pressures, and reinforcement strains. Helwany et al. (2007) performed finite element analysis using a soil cap model for large-scale loading tests of the National Cooperative Highway Research Program (NCHRP) GRS bridge abutment (Wu et al. 2006a) and found that simulated lateral facing displacements and bridge seat settlements were in close agreement with measurements. A corresponding parametric study indicated that soil friction angle, reinforcement spacing, and reinforcement stiffness have important effects on the performance of GRS bridge abutments. Zheng et al. (2014, 2015a) conducted finite difference analysis for GRS bridge abutments and reported maximum values of lateral facing displacement and bridge seat settlement that, depending on soil modulus and cohesion, ranged from 15 mm to 38 mm for a design-level applied vertical stress of 200 kPa. In each of the above numerical investigations, bridge loads were simulated by applying an equivalent vertical stress on the bridge seat; however, the effect of horizontal restraint from the bridge structure was neglected.

This chapter presents a numerical investigation of the performance of GRS bridge abutments under static loading conditions and with realistic conditions for system geometry and applied loads. The response of the Founders/Meadows GRS bridge abutment during construction and service is first considered and numerical results are compared to field measurements. A parametric study for a single-span full bridge system, including two GRS

bridge abutments and associated horizontal restraining effects from the bridge structure, was then conducted to investigate the effects of various factors on the performance of GRS bridge abutments. Results from this investigation provide insights with regard to numerical modeling of GRS bridge abutments and performance of these structures for highway applications.

3.2 Model Validation

3.2.1 Founders/Meadows GRS Bridge Abutment

The Founders/Meadows Parkway Bridge was constructed by the Colorado Department of Transportation in Castle Rock, Colorado, in 1999, and includes GRS bridge abutments to support the bridge and approach roadway (Abu-Hejleh et al. 2000, 2001). A cross section for the instrumented Section 800 of the east abutment is shown in Figure 3.1. The abutment consists of lower and upper walls over a sandstone bedrock foundation. The lower GRS wall has modular block facing with geogrid reinforcement attached using mechanical connectors. The upper wall is a cast-in-place concrete structure that consists of the abutment wall and bridge seat. Behind the upper wall is a GRS fill. Bridge loads are transmitted to the lower reinforced soil mass through the abutment wall and bridge seat. The bridge girders and deck were cast monolithically with the abutment wall to form an integral structure. The bridge and abutment system was constructed in six stages: Stage 1: lower GRS wall; Stage 2: bridge seat and abutment wall; Stage 3: bridge girders; Stage 4: upper GRS fill; Stage 5: bridge deck; and Stage 6: approach slab and roadway (Figure 3.1). Stage 7 refers to in-service performance after the bridge was open to traffic for 12 months. Table 3.1 provides the estimated average vertical stress at the contact between bridge seat and backfill soil for each construction stage. The backfill soil is composed of gravel (35.0%), sand (54.4%), and fines (10.6%), and is classified as SW-SM according to the Unified Soil Classification System (USCS). The geogrid length is 8.0 m at the bottom and increases linearly with elevation according to a 1V:1H slope. Geogrid layers were placed

at a vertical spacing of 0.4 m for both the lower GRS wall and upper GRS fill. Instrumentation for Section 800 is also shown in Figure 3.1. Location line A is close to the lower wall facing, lines B and C are located along the centerline and at the back edge of the bridge seat, respectively, and line D is located behind the bridge seat. Additional description and instrumentation details are provided by Abu-Hejleh et al. (2000, 2001).

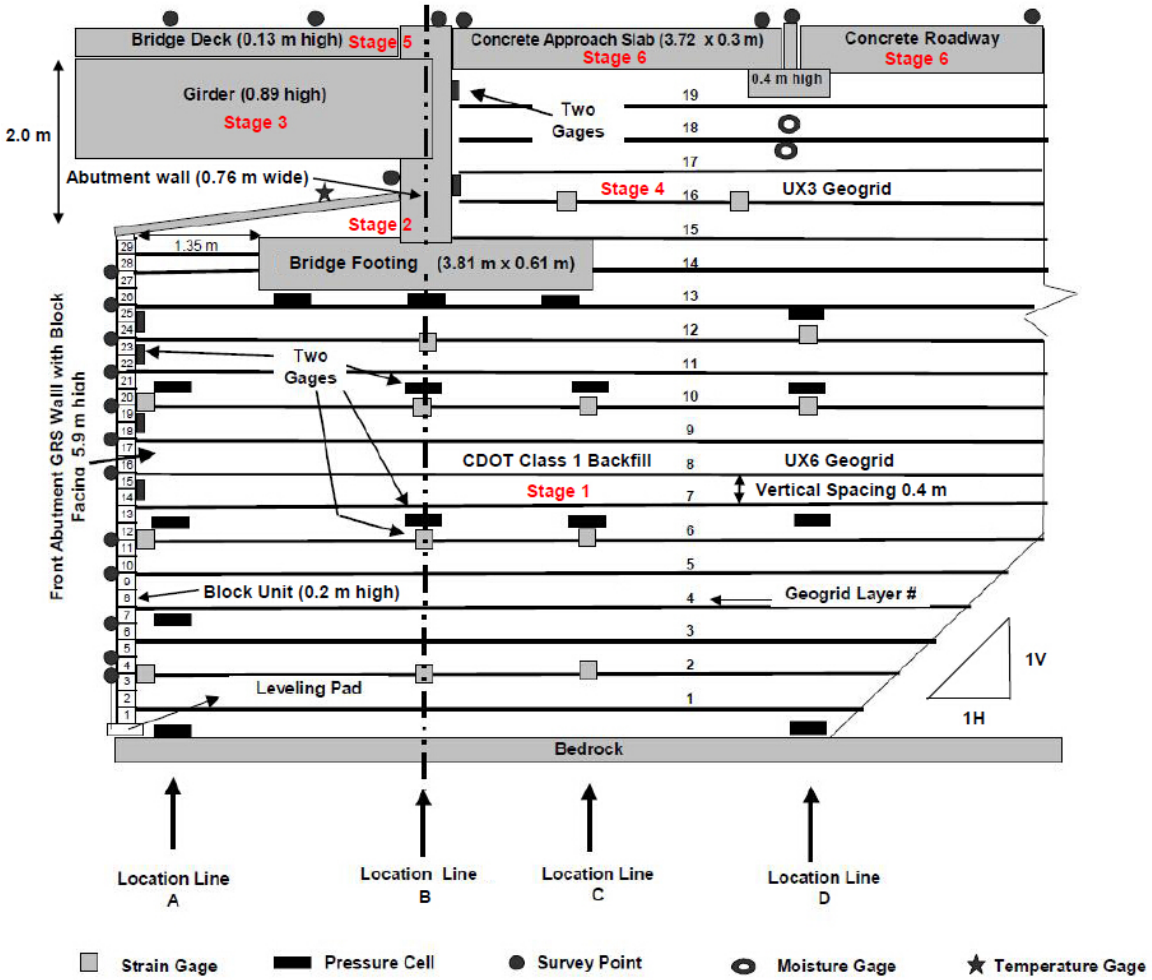

Figure 3.1 Instrumented Section 800 for the Founders/Meadows east bridge abutment (adapted from Abu-Hejleh et al. 2002).

Table 3.1 Estimated average vertical stress under bridge seat (data from Abu-Hejleh et al. 2001).

Construction stage	Vertical stress (kPa)
1	0
2	22
3	64
4	84
5	101
6	115
7	150

3.2.2 Numerical Model

The two-dimensional finite difference program *FLAC Version 7.0* (Itasca Consulting Group Inc. 2011) was used to simulate the performance of the Founders/Meadows east bridge abutment during construction and service. *FLAC* is applicable for plane strain conditions, which represents a simplification for this three-dimensional structure.

3.2.2.1 Model Geometry

The finite difference grid and boundary conditions for the Founders/Meadows east bridge abutment model are shown in Figure 3.2. The abutment has a total height H = 8 m, consisting of a 6 m-high lower GRS wall and 2 m-high upper abutment wall, and rests on a 6 m-deep stiff foundation layer. Lateral boundaries are located at 32 m (4H) behind and 8 m (H) in front of the lower wall, and are fixed in the horizontal direction and free to move in the vertical direction. The bottom boundary is fixed in both horizontal and vertical directions. Considering the monolithic construction of the abutment wall with the bridge girders and deck, horizontal movement and rotation of the abutment wall are fixed due to restraint from the bridge structure.

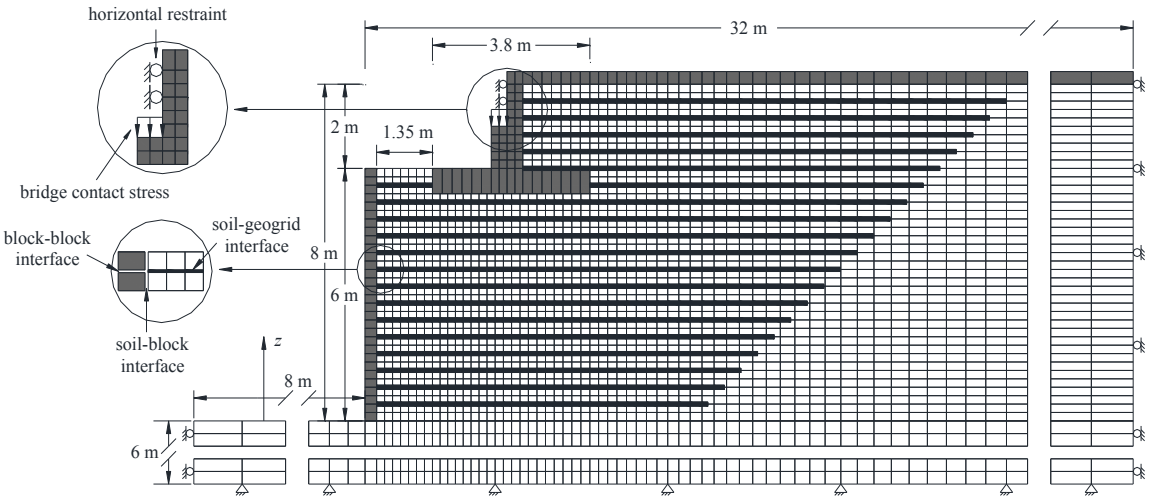

Figure 3.2 Finite difference grid and boundary conditions for the Founders/Meadows east bridge abutment model.

3.2.2.2 Material Models and Properties

The concrete facing blocks, bridge seat, abutment wall, approach slab, and roadway were modeled as linearly elastic materials with modulus E = 20 GPa and Poisson's ratio v = 0.2. Backfill soil was modeled as an elastic-plastic material with Mohr-Coulomb failure criterion and nonassociated flow rule, and the Duncan-Chang hyperbolic relationship (Duncan et al. 1980). This approach accounts for nonlinear and dilatant behavior, and has been used successfully to simulate the static response of GRS walls and abutments (Hatami and Bathurst 2005a, 2006; Fakharian and Attar 2007). Expressions for tangent elastic modulus E_t, bulk modulus B, and tangent Poisson's ratio v_t for the backfill soil are (Duncan et al. 1980),

$$E_t = \left[1 - \frac{R_f(1-\sin\phi')(\sigma_1' - \sigma_3')}{2c'\cos\phi' + 2\sigma_3'\sin\phi'}\right]^2 Kp_a\left(\frac{\sigma_3'}{p_a}\right)^n \tag{3.1}$$

$$B = K_b p_a \left(\frac{\sigma_3'}{p_a}\right)^m \tag{3.2}$$

$$\nu_t = \frac{1}{2} - \frac{E_t}{6B} \tag{3.3}$$

where σ_1' and σ_3' = major and minor principal effective stresses, ϕ' = friction angle, c' = cohesion, R_f = failure ratio, K = elastic modulus number, K_b = bulk modulus number, m and n = modulus exponents, and p_a = atmospheric pressure. Equations (3.1), (3.2), and (3.3) were implemented into FLAC using FISH subroutines to update stress-dependent moduli during the course of each simulation.

Backfill soil parameters were calibrated using data from large-scale triaxial tests conducted on specimens compacted at field moisture content (Abu-Hejleh et al. 2000). Figure 3.3 shows a comparison between the measured and simulated results. The nonlinear stress-strain behavior is accurately captured by the hyperbolic model, especially leading up to peak shear strength. A dilation angle ψ = 6.0° was determined by fitting the measured data. Simulated response for soil dilation is in close agreement for effective confining stress σ_3' = 138 kPa and 207 kPa; however, the simulations underestimate measured dilation for σ_3' = 69 kPa. The average unit weight for backfill soil γ = 22.1 kN/m^3. A summary of parameters for the Founders/Meadows (FM) backfill soil is provided in Table 3.2. The foundation soil was modeled as a stiff soil layer using Mohr-Coulomb with E = 150 MPa, ν = 0.2, c' = 0, and ϕ' = 35°.

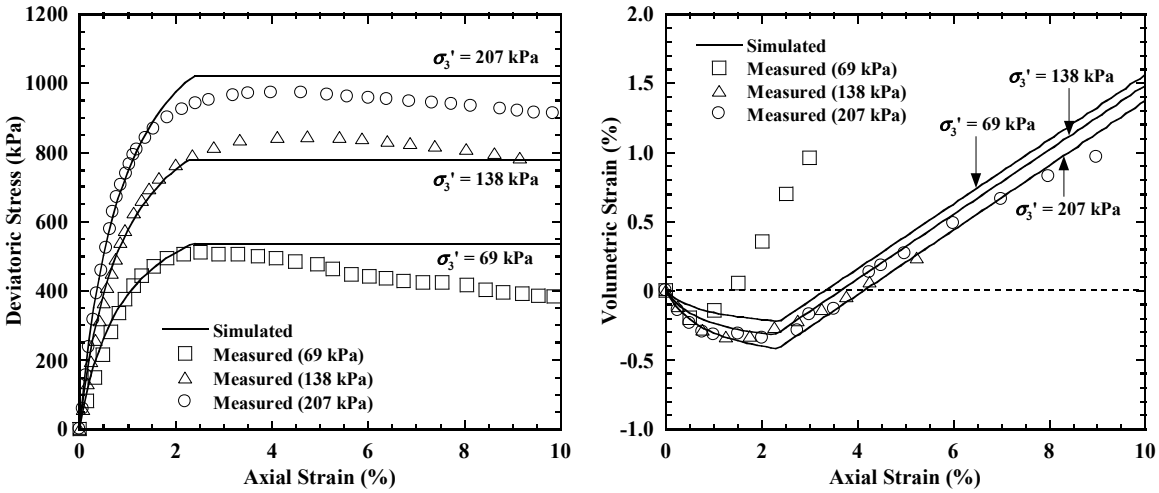

(a) (b)

Figure 3.3 Comparison of measured and simulated triaxial test results: (a) deviatoric stress vs. axial strain; (b) volumetric strain vs. axial strain (measured data from Abu-Hejleh et al. 2000).

Table 3.2 Parameters for backfill soils used in numerical simulations.

Soil type	γ (kN/m^3)	K	n	R_f	K_b	m	p_a (kPa)	c' (kPa)	ϕ' (°)	ψ (°)
FM[1]	22.1	1000	0.6	0.72	800	0	100	69.8	39.5	6.0
DC[2] (RC = 90%)	21.2	200	0.4	0.7	50	0.2	100	0	33.0	0
DC (RC = 95%)	22.0	300	0.4	0.7	75	0.2	100	0	36.0	3.8
DC (RC = 100%)	22.8	450	0.4	0.7	125	0.2	100	0	39.0	7.5
DC (RC = 105%)	23.6	600	0.4	0.7	175	0.2	100	0	42.0	11.3

[1] FM: Founders/Meadows backfill soil (Abu-Hejleh et al. 2000)
[2] DC: Duncan-Chang sand (Duncan et al. 1980)

Geogrid reinforcement was modeled using linearly elastic-plastic cable elements. For the lower GRS wall, these elements have tensile stiffness J = 2000 kN/m and tensile yield strength T_y = 157.3 kN/m, and are rigidly connected to the facing blocks. Corresponding values for the upper GRS fill are J = 1000 kN/m and T_y = 64.2 kN/m. The

soil-geogrid interfaces had friction angle = 35.6° ($0.9\phi'$) and zero cohesion. Following the results of direct shear tests conducted by Ling et al. (2010), soil-concrete and concrete-concrete interfaces were modeled using interface elements with friction angles = 27.7° ($0.7\phi'$) and 35°, respectively.

3.2.2.3 Modeling Procedures

The abutment construction sequence was reproduced for the numerical simulations. For stage 1, the lower GRS wall was constructed in lifts to the elevation of the bridge seat (z = 5.4 m). The thickness of each lift was equal to the height of one facing block (0.2 m). Similar to many previous studies (Ling et al. 2000, 2003; Helwany et al. 2003, 2007), the soil compaction process was not simulated during construction in this study. For stage 2, the bridge seat and abutment wall were placed on the reinforced soil mass, and the remaining lifts for the lower GRS wall were constructed to z = 6.0 m. A large tensile strength was assigned to concrete-concrete interfaces between the top three facing blocks to simulate the effect of grouting for these blocks. In stages 3 and 5, loads from the bridge girders and bridge deck were simulated by applying vertical stress increments of 420 kPa and 170 kPa, respectively, on the abutment wall at the bridge contact (length = 0.38 m), as shown in Figure 3.2. These values yield the average vertical stress increments under the bridge seat given in Table 3.1. In stage 4, backfill soil and reinforcement for the upper GRS fill were constructed using successive lifts. In stage 6, the concrete approach slab and roadway were placed on the upper GRS fill. Finally, for stage 7, traffic loads on the bridge deck, approach slab, and roadway were simulated using a uniform vertical stress of 13.2

kPa, which is equivalent to a surcharge of 0.6 m-high backfill soil as suggested by FHWA design guidelines (Berg et al. 2009). Gravity loads were applied to the model after placement of each soil lift and after each stage of construction.

3.2.3 Comparison of Results

3.2.3.1 Displacements

Measured and simulated values for incremental maximum lateral facing displacement and incremental bridge seat settlement, corresponding to construction stages 1, 2-6, and 7, are presented in Table 3.3. Field measurements were reported by Abu-Hejleh et al. (2000, 2001). Simulations were conducted for the bridge seat and abutment wall with horizontal restraint (HR), as shown in Figure 3.2, and no horizontal restraint (NHR), which allowed free displacement and rotation. Table 3.3 indicates that measured and simulated values are in good agreement throughout the construction process, and that horizontal restraint from the bridge structure reduces lateral facing displacements and bridge seat settlements. Figure 3.4 presents measured and simulated profiles of incremental lateral facing displacement for the lower GRS wall for construction stages 2-6. The HR profile is in good agreement with field measurements, whereas the NHR profile overestimates the maximum displacement by approximately 40%. This suggests that consideration of the horizontal restraining effect of the bridge structure can be important for numerical modeling of GRS bridge abutments. Subsequent simulated results for the Founders/Meadows GRS bridge abutment include this effect. Detailed simulation results for NHR were reported by Zheng et al. (2015b). Simulated displacements for both HR and NHR were smaller than measured values for stage 7. This is attributed to the equivalent static surcharge used to simulate traffic loading, as vehicular impact load also applies on the bridge.

Table 3.3 Incremental displacements for the Founders/Meadows GRS bridge abutment.

	Lower wall construction (Stage 1)	Bridge/approach construction (Stages 2-6)	Traffic loading (Stage 7)
	Incremental maximum lateral facing displacement (mm)		
Measured	12	10	5
Simulated HR	n/a*	9	3
Simulated NHR	11	14	4
	Incremental bridge seat settlement (mm)		
Measured	n/a	12	10
Simulated HR	n/a	13	5
Simulated NHR	n/a	14	7

* not applicable

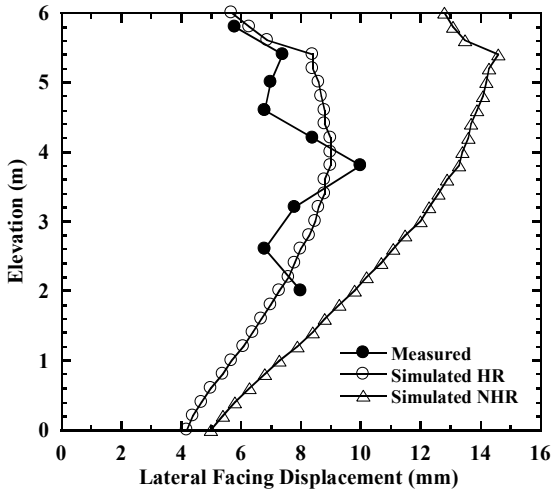

Figure 3.4 Profiles of incremental lateral facing displacement for lower GRS wall for construction stages 2-6.

3.2.3.2 Earth Pressures

Figure 3.5 presents measured and simulated earth pressures during construction. Lateral earth pressures behind the lower wall facing at $z = 4.5$ m are shown in Figure 3.5(a). Simulated values are in good agreement with field measurements. Measured pressures decreased slightly when bridge deck was placed (stage 5), whereas the simulated results show little variation after placement of the bridge girders (stage 3). Vertical earth pressures for location lines A and B (Figure 3.1) at $z = 4.0$ m are shown in Figure 3.5(b) and indicate similar agreement. Earth pressures for line B correspond to the centerline of the bridge seat and increased throughout the construction process. Simulated values for location lines C and D at $z = 4.0$ m and lines A-D at $z = 2.4$ m (not shown) also display good agreement with field measurements.

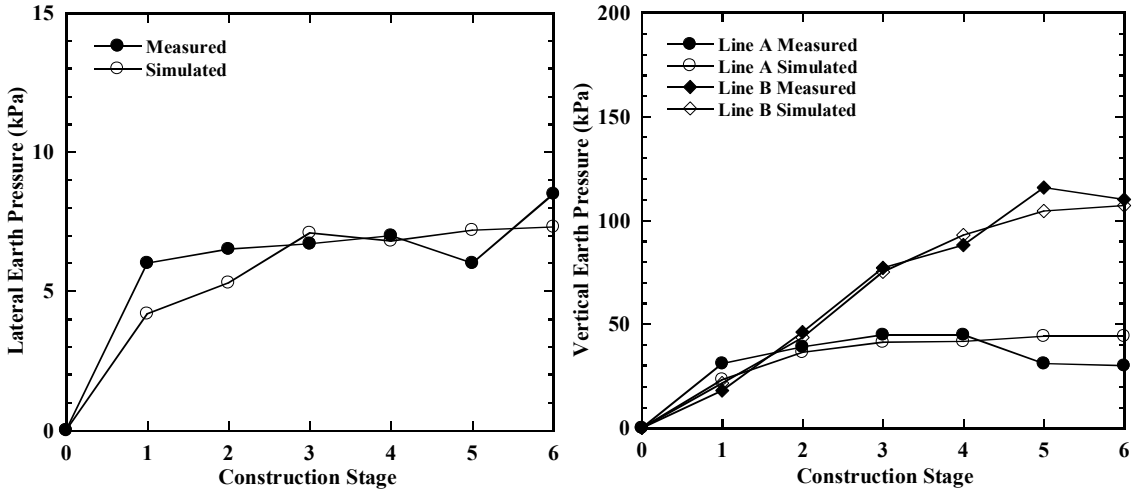

(a) (b)

Figure 3.5 Earth pressures: (a) lateral earth pressures behind lower wall facing at $z = 4.5$ m; (b) vertical earth pressures for location lines A and B at $z = 4.0$ m.

3.2.3.3 Reinforcement Tensile Strains and Forces

Measured and simulated tensile strains in geogrid layer 6 (z = 2.4 m) and geogrid layer 10 (z = 4.0 m) at locations lines A, B, and C are presented in Figure 3.6 and show similar trends; however, there are some discrepancies in magnitude. Shown in Figure 3.6(a), simulated tensile strain is approximately 0.1% less than the measured value for geogrid layer 6 at line A for stage 1. This discrepancy may have resulted from erroneous initial readings during construction (Abu-Hejleh et al. 2001). After stage 1, measured and simulated strain increments at line A are in close agreement. Measured and simulated strains for geogrid layer 6 at line B are in reasonable agreement and show a relatively large amount of strain during stage 1, followed by slower increases during stages 2 through 6. Strains likewise increase at location line C for the simulated results, whereas field measurements are essentially constant after stage 1. Figure 3.6(b) indicates similar behavior for geogrid layer 10, in which measured and simulated strain increments are in reasonable agreement after stage 1. One exception is measured strains at line A, which show a sharp reduction at stage 5. This is consistent with a decrease of measured lateral and vertical earth pressures at the same stage, as discussed by Abu-Hejleh et al. (2001). Measured and simulated strains at different locations along geogrid layers 6 and 10 at stage 6 are presented in Figure 3.7 and show reasonable agreement.

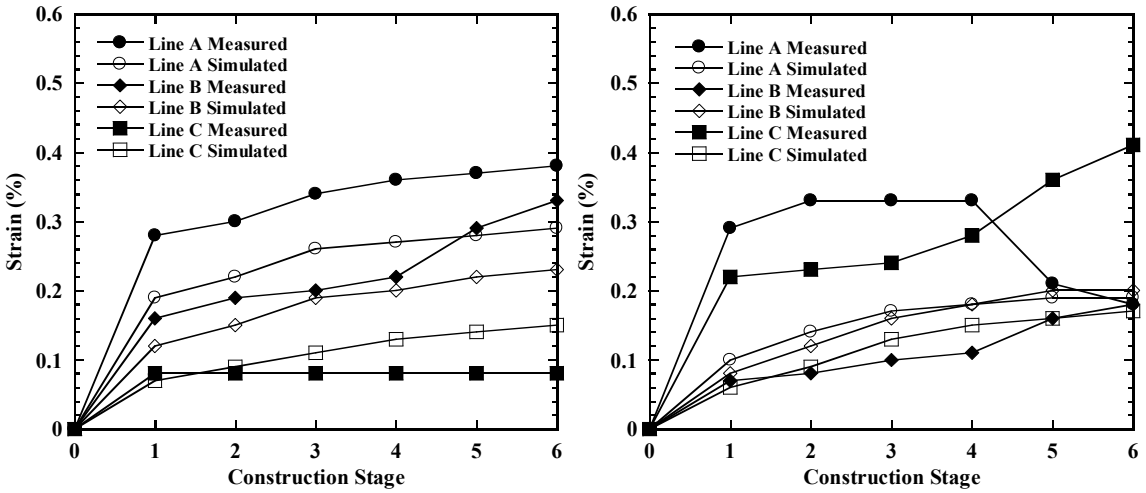

Figure 3.6 Reinforcement tensile strains: (a) geogrid layer 6 (z = 2.4 m); (b) geogrid layer 10 (z = 4.0 m).

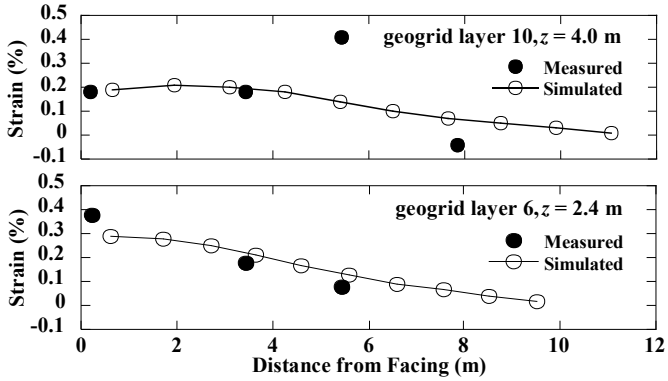

Figure 3.7 Reinforcement tensile strains at stage 6 (end of construction).

Table 3.4 presents estimated, measured, and simulated values of maximum and connection tensile forces in geogrid layers 6 and 10 at stage 6 (end of construction). Estimated and measured values were reported by Abu-Hejleh et al. (2001), and the estimated values were calculated using the AASHTO (1996) design procedures. The numerical simulations underestimate maximum tensile forces in geogrid layers 6 and 10. Estimated maximum tensile forces are much larger than measured and simulated values,

which indicates that the AASHTO design procedure is conservative for these conditions. Measured and simulated tensile forces at the geogrid connections are in reasonable agreement for layers 6 and 10.

Table 3.4 Reinforcement tensile forces at stage 6.

Geogrid layer	Maximum tensile force (kN/m)			Connection tensile force (kN/m)		
	Estimated	Measured	Simulated	Estimated	Measured	Simulated
6	16.5	7.7	5.7	16.5	7.7	5.7
10	14.3	8.2	4.1	14.3	3.6	3.8

3.3 Parametric Study

Using similar modeling methods, a parametric study was conducted to investigate the general performance of GRS bridge abutments under static loading conditions. Each simulation was conducted for a single-span full bridge system, including the bridge, two GRS bridge abutments, and foundation soil. The variables investigated were bridge contact friction coefficient, backfill soil relative compaction, backfill soil cohesion, reinforcement spacing, reinforcement length, reinforcement stiffness, and bridge load. A baseline case is first described and was used as a point of departure for the remaining simulations. For each series of simulations, only the variable of interest was changed while the other variables were held constant and equal to values for the baseline case.

3.3.1 Baseline Case

3.3.1.1 Numerical Model

Model geometry for the baseline case is shown in Figure 3.8. A single-span bridge has length L_b = 45 m and symmetrical GRS bridge abutments at both ends. Each GRS bridge abutment consists of a lower GRS wall with modular block facing, bridge seat, upper GRS fill, and approach roadway. The lower GRS walls have height h = 5.0 m and are composed of 25 modular block facing elements (0.3 m length × 0.2 m height). The bridge seat is an L-shaped structure, which is similar to footings used for GRS bridge abutments in previous studies (Wu et al. 2006a, 2006b; Helwany et al. 2007; Berg et al. 2009; Vennapusa et al. 2012). Each concrete bridge seat has a thickness of 0.4 m and rests on top of the backfill for the lower GRS wall with a 0.2 m setback from the facing. As such, the clearance height for the bridge is 5.4 m, which satisfies the FHWA minimum requirement of 4.9 m for interstate highways (Stein and Neuman 2007). Assuming a bridge span-to-depth ratio $R_{sd} = L_b/D = 20$, the depth of the bridge structure D = 2.25 m. The upper GRS fill lies behind the vertical stem of the L-shaped seat and has wrapped facing. The height of the upper GRS fill and approach roadway = 2.65 m (D + 0.4 m), which gives a total height H = 7.65 m. To minimize the influence of boundaries on system response, the foundation soil has a depth of 15.3 m (2H) and lateral boundaries are located at 30.6 m (4H) behind the lower wall on each side. Lateral boundaries are fixed in the horizontal direction and free to move in the vertical direction, whereas the bottom boundary is fixed in both horizontal and vertical directions.

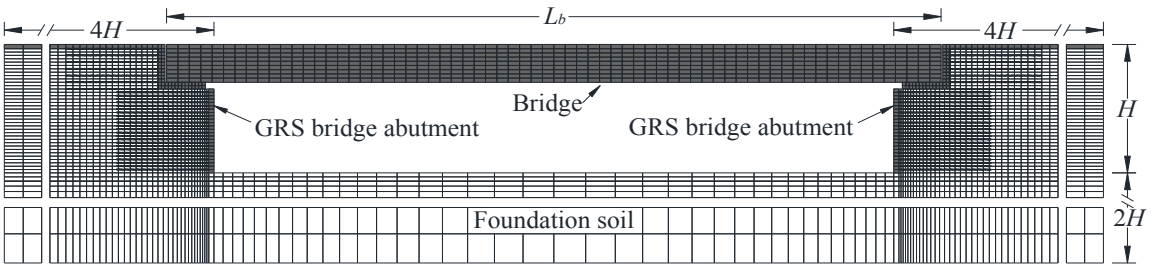

(a)

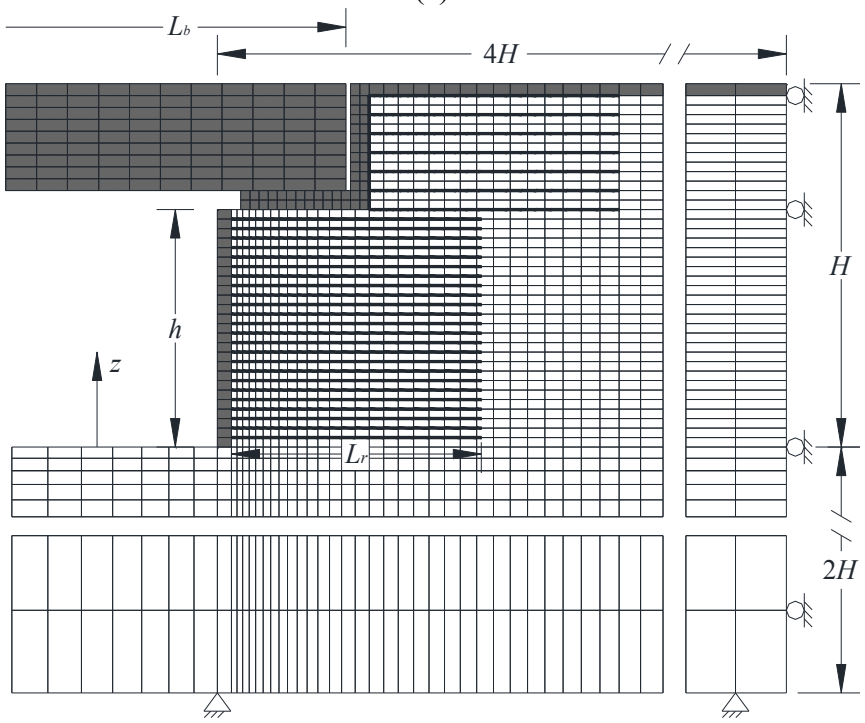

(b)

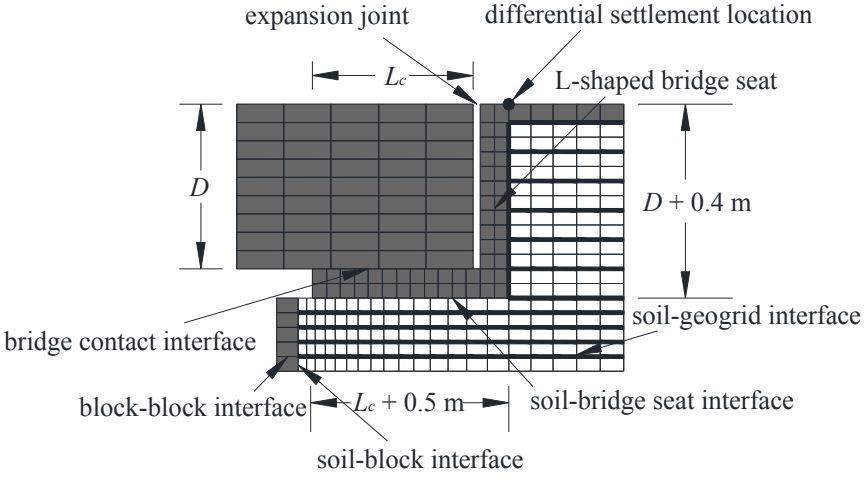

(c)

Figure 3.8 Geometry for baseline case model: (a) bridge system; (b) GRS bridge abutment; (c) connection between bridge and GRS bridge abutment.

A longitudinal slice of the bridge with unit width was modeled as a solid block ($L_b \times D \times 1$) composed of elastic elements having equivalent unit weight γ_{eq} = 5.88 kN/m^3, which yields the intended total weight. The bridge rests on the L-shaped seats with contact length $L_c = D$ = 2.25 m, and has a 100 mm-wide expansion joint on each end. Bridge contact interfaces between the bridge and seats were simulated using interface elements with friction coefficient μ = 0.4, which provides a horizontal restraining force on each abutment. The bridge load on each seat = $LD\gamma_{eq}$ = 298 kN/m, and the corresponding average applied vertical stress = 132 kPa. Since the bottom surface length of the seat (L_c + 0.5 m) is greater than the bridge contact length (L_c), the average vertical stress on the backfill soil is 108 kPa, which is similar to the estimated value of 115 kPa for the Founders/Meadows bridge abutment (Abu-Hejleh et al. 2000, 2001).

The backfill soil was modeled as an SW/SP material with relative compaction (RC) = 95%. Parameters are summarized in Table 3.2 and correspond to Mohr-Coulomb with a Duncan-Chang hyperbolic relationship. Dilation angle ψ was estimated as (Bolton 1986)

$$\phi' = \phi'_{cv} + 0.8\psi \tag{3.4}$$

where ϕ_{cv}' = constant volume friction angle. A value of ϕ_{cv}' = 33° was assumed and corresponds to quartz sand. The foundation soil was modeled as dense sand using Mohr-Coulomb with E = 50 MPa, v = 0.3, c' = 0, ϕ' = 42°, and ψ = 11.3°. The geogrid reinforcement has length L_r = 5.35 m (0.7H) for the lower GRS wall and upper GRS fill. Vertical spacing of the reinforcement S_v = 0.2 m for the lower GRS wall and 0.4 m for the upper GRS fill. The reinforcement was modeled using cable elements with J = 1000 kN/m

and T_y = 100 kN/m. Interface friction angle = 32.4° (0.9ϕ') for soil-geogrid interfaces and 25.2° (0.7ϕ') for soil-concrete interfaces.

3.3.1.2 Simulation Results

The performance of GRS bridge abutment is evaluated in terms of lateral facing displacements for the lower wall, bridge seat and foundation soil settlements, backfill soil vertical compression (i.e., difference between bridge seat and foundation soil settlements), and differential settlement between the bridge seat and approach roadway. Bridge seat settlement is taken as an average over the base of the seat and foundation soil settlement is taken as settlement of the lowermost wall facing block. The location for differential settlement is indicated in Figure 3.8(c). For the baseline case, the maximum lateral facing displacement is 37.0 mm and occurs at elevation z = 2.6 m above the bottom of the wall. Bridge seat settlement due to subsequent construction after seat placement is 68.4 mm. The corresponding foundation soil settlement, also after bridge seat placement, is 14.8 mm. Thus, vertical compression of the backfill soil for the lower wall is 53.6 mm. This corresponds to 1.1%h, which slightly exceeds the criterion of 1%h for GRS bridge abutments suggested by Wu et al. (2006a). Relatively high soil compression occurs for the baseline case because backfill soil parameters represent conservative values for stiffness and strength (Duncan et al. 1980). The differential settlement between the bridge seat and approach roadway is 8.2 mm.

3.3.2 Effect of Bridge Contact Friction Coefficient

To investigate the first variable for the parametric study, numerical simulations were conducted for bridge contact friction coefficient μ = 0, 0.2, 0.4, and 0.6. A value of 0 provides no horizontal restraining force from the bridge structure, 0.2 is conservative, 0.4 is typical for a bearing pad, and 0.6 is typical for a concrete-concrete interface. Figure 3.9 presents the simulation results. Slip occurred on the bridge contact interface for μ = 0 and 0.2, whereas no slip occurred for μ = 0.4 and 0.6. Lateral facing displacements are presented in Figure 3.9(a) and indicate essentially the same profiles for the no-slip condition ($\mu \geq 0.4$). Displacements are larger for μ = 0.2 and significantly larger for μ = 0. Maximum lateral facing displacement for the frictionless interface (μ = 0) is 67.7 mm, which is almost twice the value for the baseline case (μ = 0.4). High friction at the bridge contact interface reduces lateral facing displacements because the friction provides restraint against outward movement of the abutment. The profiles also indicate that the location of maximum lateral facing displacement moves lower with increasing friction coefficient. Settlements and backfill compression are presented in Figure 3.9(b) and show modest decreases with increasing bridge contact friction coefficient, with essentially constant values for the no-slip condition. Bridge seat settlement decreases from 77.1 mm to 68.4 mm, and backfill compression decreases from 57.9 mm to 53.6 mm. Foundation soil settlement is much lower and ranges from 14.5 mm to 19.5 mm. Differential settlement is also small and decreases from 14.5 mm for μ = 0 to approximately 8 mm for $\mu \geq 0.2$. The numerical results in Figure 3.9 are consistent with those for the Founders/Meadows bridge

abutment and indicate that abutment deformations are smaller when the horizontal restraining force from the bridge structure is included in the analysis.

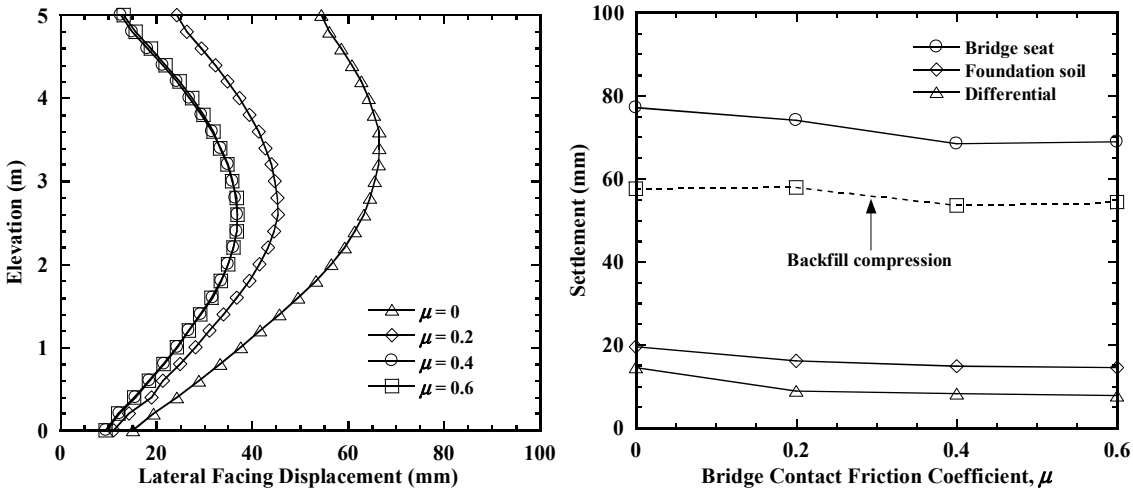

(a) (b)

Figure 3.9 Effect of bridge contact friction coefficient: (a) lateral facing displacements; (b) settlements and backfill compression.

3.3.3 Effect of Backfill Soil Relative Compaction

Numerical simulations were conducted for four backfill soils consisting of cohesionless sand with relative compaction (RC) = 90%, 95%, 100%, and 105%. Soil parameters were taken from triaxial test results reported by Duncan et al. (1980) and are summarized in Table 3.2. Dilation angles were calculated using Equation (3.4) with $\phi_{cv}' = 33°$. Figure 3.10 shows simulated triaxial test results for $\sigma_3' = 50$ kPa and indicates that soil strength, modulus, and dilation increase with relative compaction. Lateral facing displacements are presented in Figure 3.11(a) and show significant decrease with increasing relative compaction of the backfill soil. Maximum lateral facing displacement ranges from 47.7 mm at RC = 90% to 20.8 mm at RC = 105%, and occurs at mid-height for each case. Settlements and backfill soil compression are presented in Figure 3.11(b). Similar to the lateral facing displacement profiles, bridge seat settlement and backfill compression are significantly affected by the relative compaction. As RC increases from 90% to 105%, bridge seat settlement decreases from 83.7 mm to 41.9 mm and backfill compression decreases from 67.7 mm to 31.6 mm. Foundation and differential settlements both vary in a narrow range and decrease slightly with increasing relative compaction. Figure 3.11 suggests that abutment deformations can be reduced significantly with increased relative compaction of the backfill soil.

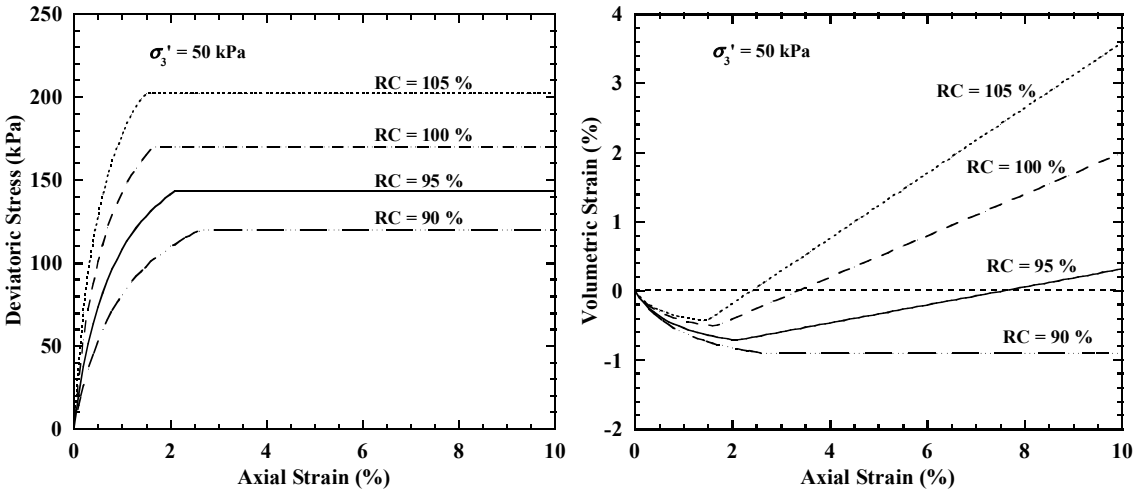

(a) (b)

Figure 3.10 Simulated triaxial test results for backfill soils with different relative compaction: (a) deviatoric stress vs. axial strain; (b) volumetric strain vs. axial strain.

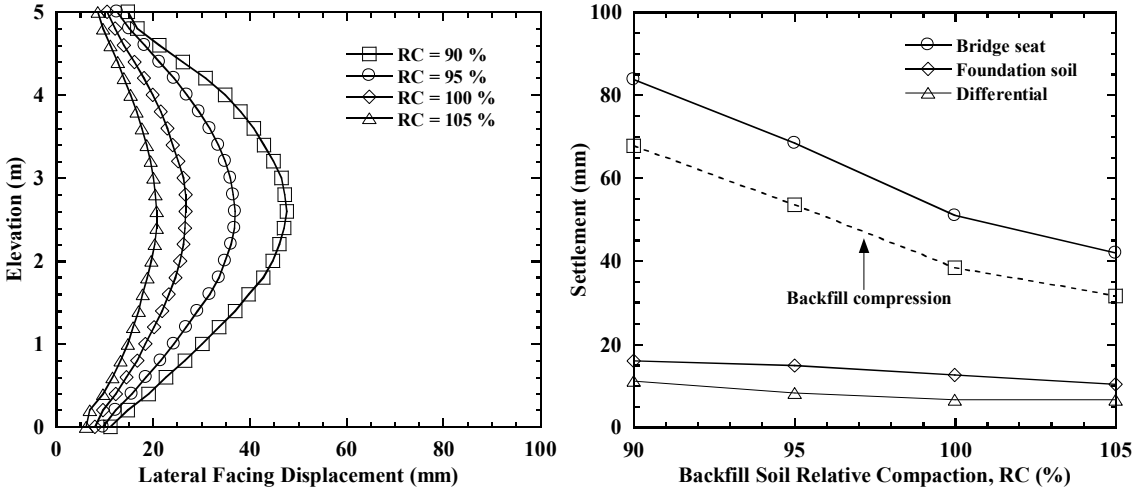

(a) (b)

Figure 3.11 Effect of backfill soil relative compaction: (a) lateral facing displacements; (b) settlements and backfill compression.

3.3.4 Effect of Backfill Soil Cohesion

Figure 3.12(a) shows lateral facing displacements for backfill soil with c = 0, 25 kPa, 50 kPa, and 75 kPa. Backfill soil cohesion has an important effect on lateral facing displacements, as maximum displacement decreases by almost 75% when cohesion increases from 0 to 75 kPa. Settlements and backfill soil compression, shown in Figure 3.12(b), are nearly independent of cohesion. Bridge seat settlement is approximately 67 mm and differential settlement is approximately 9 mm. The results indicate that backfill soil cohesion can have an important effect on lateral facing displacements but is unlikely to be significant with regard to bridge seat settlement. In many case, however, zero cohesion is assumed for design to be conservative.

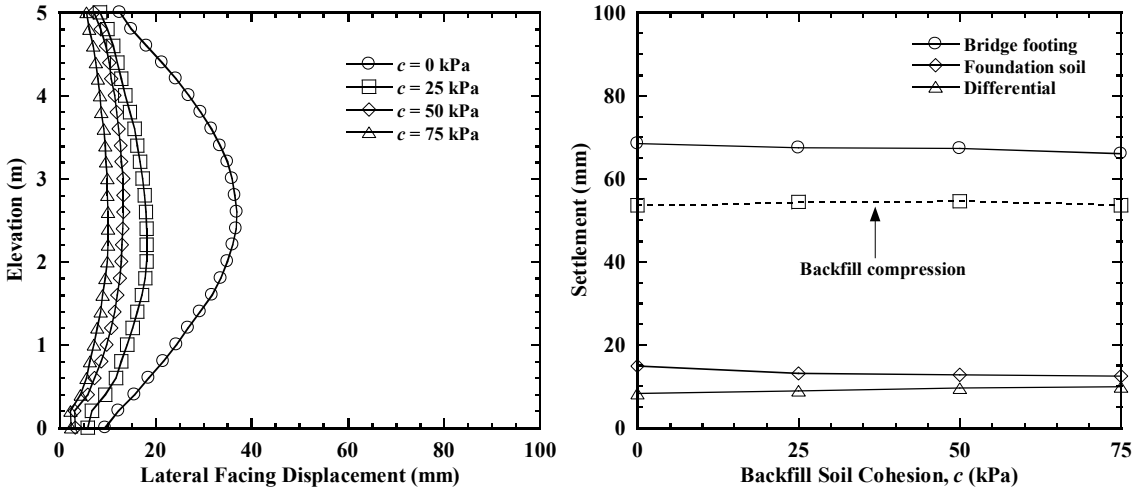

(a) (b)

Figure 3.12 Effect of backfill soil cohesion: (a) lateral facing displacements; (b) settlements and backfill compression.

3.3.5 Effect of Reinforcement Spacing

Numerical simulations were conducted for vertical reinforcement spacing S_v = 0.2 m, 0.4 m, and 0.6 m for the lower GRS wall. The NCHRP default design value is 0.2 m and the maximum allowable value is 0.4 m for GRS bridge abutments with flexible facing (Wu et al. 2006a). Figure 3.13 indicates that lateral facing displacements and bridge seat settlements are significantly affected by reinforcement spacing. With increasing S_v, maximum lateral facing displacement increases from 37.0 mm to 69.2 mm and bridge seat settlement increases almost linearly from 68.4 to 96.7 mm. Corresponding values of backfill compression increase from 53.6 mm to 80.7 mm. Foundation and differential settlements are both low values and nearly independent of reinforcement spacing.

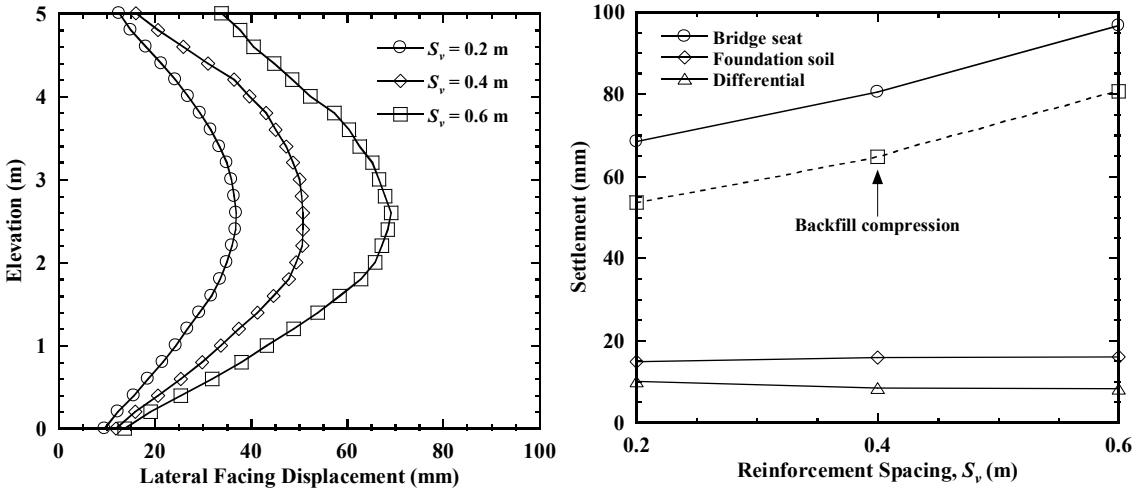

(a) (b)

Figure 3.13 Effect of reinforcement spacing: (a) lateral facing displacements; (b) settlements and backfill compression.

3.3.6 Effect of Reinforcement Length

Numerical simulations were conducted for reinforcement length L_r = 0.5H, 0.7H, 0.9H, and 1.1H for both the lower GRS wall and upper GRS fill. Figure 3.14(a) indicates that the effect of reinforcement length on lateral facing displacements is minimal, especially for $L_r \geq 0.7H$. A small increase of 9% for the maximum lateral facing displacement is observed when reinforcement length decreases from 0.7H to 0.5H. In general, maximum lateral facing displacement varies within a narrow range of 34.6 mm to 40.2 mm and decreases slightly with increasing reinforcement length. Settlements and backfill soil compression, shown in Figure 3.14(b), also are nearly constant. These results indicate that, for the conditions investigated, increasing reinforcement length beyond the industry default value of $L_r = 0.7H$ is unlikely to significantly improve the performance of GRS bridge abutments under static loading.

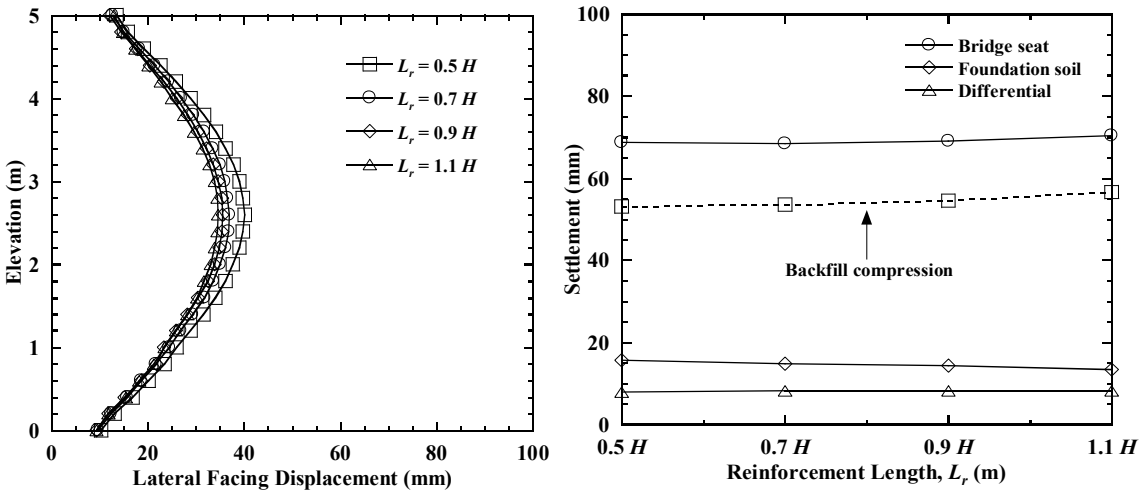

(a) (b)

Figure 3.14 Effect of reinforcement length: (a) lateral facing displacements; (b) settlements and backfill compression.

3.3.7 Effect of Reinforcement Stiffness

Figure 3.15(a) presents lateral facing displacement profiles for reinforcement stiffness J = 500 kN/m, 1000 kN/m, 1500 kN/m, and 2000 kN/m. Lateral facing displacements decrease with increasing stiffness, with the maximum value decreasing from 48.6 mm for J = 500 kN/m to 27.2 mm for J = 2000 kN/m. In Figure 3.15(b), corresponding bridge seat settlement and backfill soil compression show similar trends and decrease from 81.2 mm to 64.2 mm and 66.4 mm to 49.8 mm, respectively. This effect becomes less significant with increasing stiffness, especially for $J \geq$ 1500 kN/m. Foundation and differential settlements are both low values and nearly independent of reinforcement stiffness.

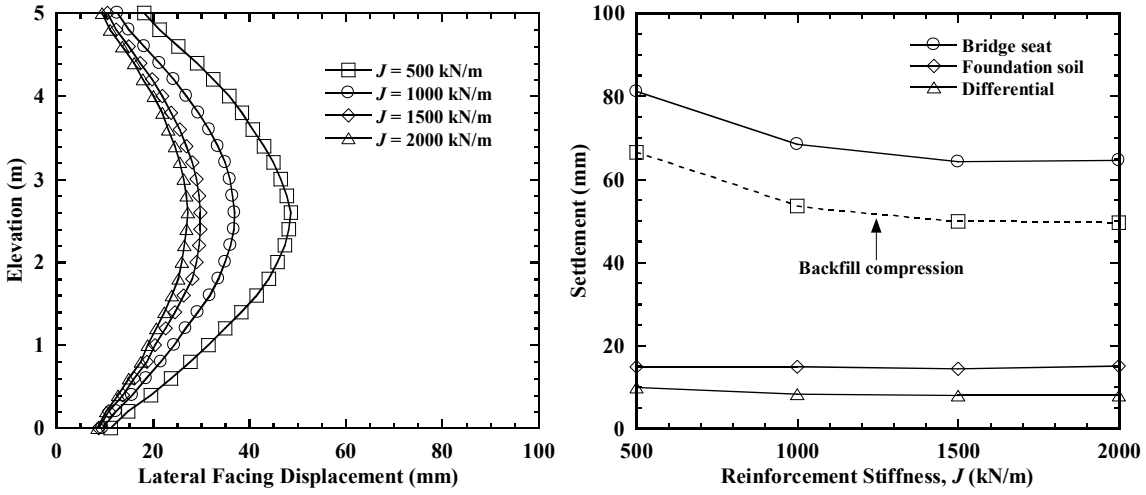

(a) (b)

Figure 3.15 Effect of reinforcement stiffness: (a) lateral facing displacements; (b) settlements and backfill compression.

3.3.8 Effect of Bridge Load

Numerical simulations were conducted for varying total bridge weight corresponding to bridge span L_b = 25 m, 35 m, 45 m, and 55 m. Following the baseline case with R_{sd} = 20, L_c = D, and γ_{eq} = 5.88 kN/m^3, the resulting applied vertical loads per unit width on each abutment F_v = 92 kN/m, 180 kN/m, 298 kN/m, and 446 kN/m, and the corresponding applied vertical stresses on the bridge seats are 74 kPa, 103 kPa, 132 kPa, and 162 kPa, respectively. Figure 3.16 indicates that lateral facing displacements and bridge seat settlements are significantly affected by bridge load. As F_v increases from 92 kN/m to 446 kN/m, the maximum lateral facing displacement increases from 28.7 mm to 41.2 mm and bridge seat settlement increases almost linearly from 37.0 mm to 87.1 mm. Corresponding values of backfill soil compression display a similar trend and increase from 30.5 mm to 69.0 mm. Foundation settlement varies from 6.5 mm to 18.1 mm and also increases with increasing load. Differential settlement between the bridge seat and approach roadway is generally small (≤ 8.3 mm) and decreases slightly with increasing bridge load due to the increase of upper GRS fill height with increasing bridge length and load.

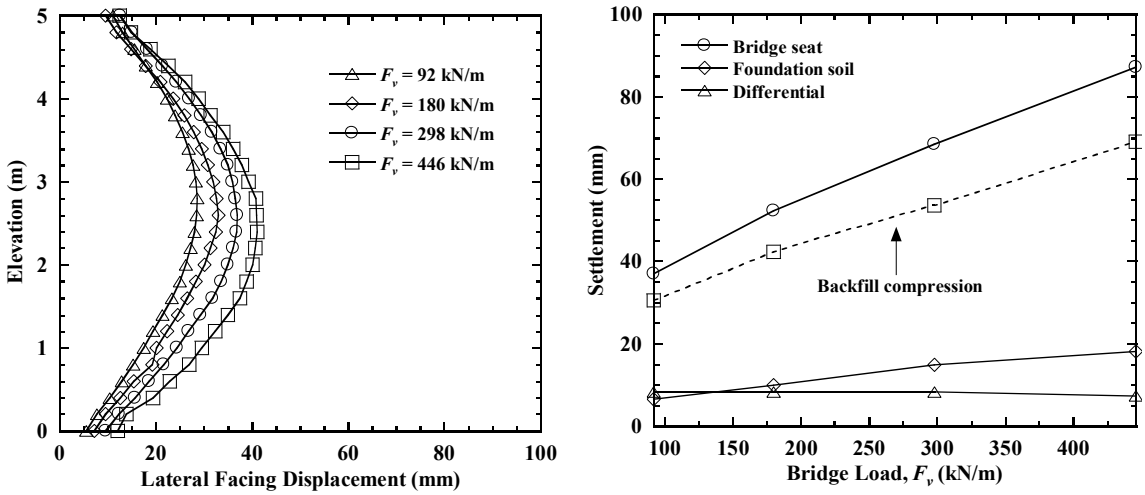

(a) (b)

Figure 3.16 Effect of bridge load: (a) lateral facing displacements; (b) settlements and backfill compression.

3.4 Acknowledgements

The text below is reproduced verbatim as it appears in the acknowledgments section per the UCSD Office of Graduate Studies Formatting Requirements.

Chapter 3 of this dissertation is based on materials published by the Journal of Geotechnical and Geoenvironmental Engineering titled “Numerical Investigation of Geosynthetic-Reinforced Soil Bridge Abutments under Static Loading” with authors, Yewei Zheng and Patrick J. Fox (2016). The dissertation author is the first author of this paper.

Chapter 4

Numerical Simulation of the GRS-IBS under Static Loading

4.1 Introduction

In recent years, geosynthetic reinforced soil (GRS) retaining walls have been used as bridge abutments with loads applied directly to the top of the reinforced soil mass. The Federal Highway Administration (FHWA) has refined this concept and developed a specific bridge abutment design, called the Geosynthetic Reinforced Soil-Integrated Bridge System (GRS-IBS), to meet demands for the next generation of small to medium single span bridges in the United States (Adams et al. 2011a, 2011b). This technology has many advantages over conventional pile-supported designs, including lower cost, faster and easier construction, and smoother transition between the bridge and approach roadway. These advantages have brought attention to the concept and genuine interest has developed

to promote and use this technology (Adams et al. 2007, 2008; Kost et al. 2014; Talebi et al. 2014).

The GRS-IBS design consists of three main components: reinforced soil foundation, GRS abutment, and integrated approach. Figure 4.1 shows a typical cross-section. A reinforced soil foundation is placed at the toe of a cut slope and increases bearing capacity for the GRS abutment. The GRS abutment is constructed using well compacted backfill soil and closely spaced geosynthetic reinforcement to provide support for the bridge. The bridge seat is a thin layer consisting of wrapped-face GRS fill. Bearing bed reinforcement layers are incorporated into the abutment underneath the bridge seat to provide additional support for the bridge load. Concrete bridge structures are placed directly on the bridge seat, whereas steel bridge structures are placed on a concrete pad. The approach roadway consists of a wrapped-face GRS fill that is integrated with the bridge (i.e., no joint) to create a smooth transition and minimize differential settlement. These features distinguish the GRS-IBS design from more general GRS abutment configurations.

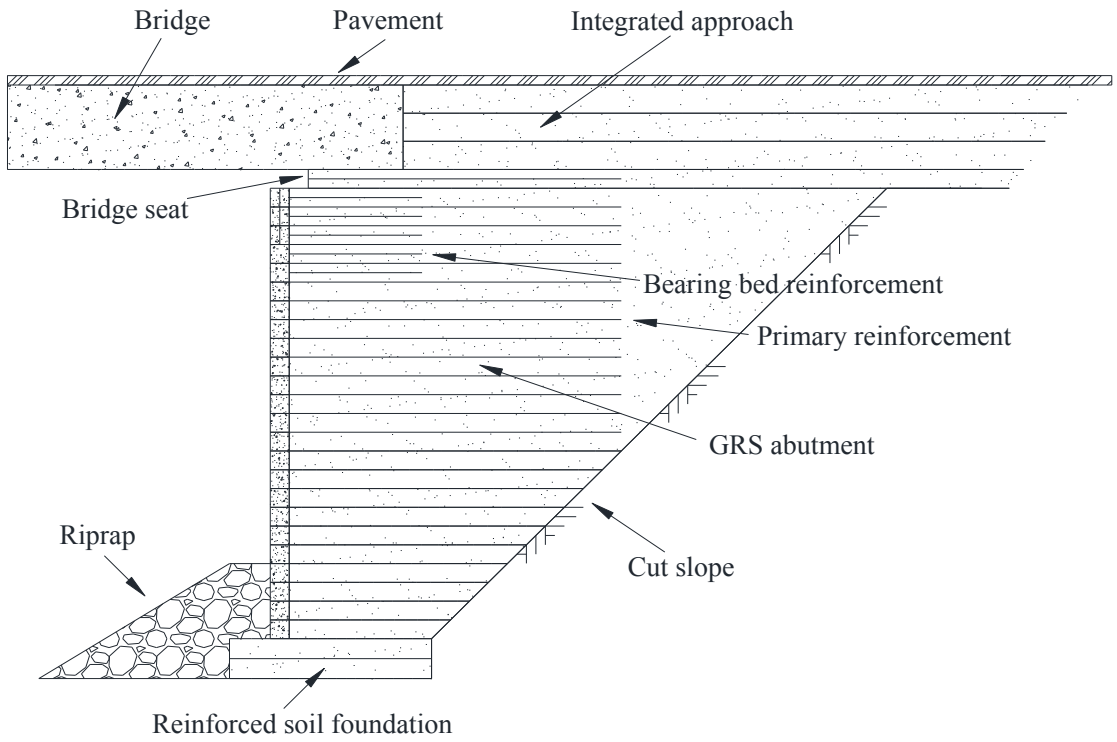

Figure 4.1 Typical cross-section of bridge abutment for GRS-IBS (adapted from Adams et al. 2011b).

GRS abutments, in general, are subjected to much larger surcharge loads than conventional GRS walls and, as such, allowable bearing pressure and resulting deformations are important issues for design. Wu et al. (2006a, 2006b) developed procedures to determine allowable bearing pressure considering bridge seat type, reinforcement spacing, and backfill soil condition. FHWA provides both analytical and empirical design methods to predict the ultimate bearing capacity for GRS abutments, with the corresponding allowable bearing pressure calculated using a factor of safety (Adams et al. 2011a, 2011b). The FHWA analytical design method is based on the soil-geosynthetic composite load capacity and accounts for backfill soil friction angle and maximum aggregate size, and reinforcement spacing and tensile strength (Wu and Pham 2013; Wu et

al. 2013). The FHWA empirical design method is based on an experimentally-determined vertical stress-strain relationship that is obtained from performance tests (i.e., GRS mini-pier loading tests) conducted using project-specific geosynthetic reinforcement and backfill soil. The FHWA guidelines specify an ultimate bearing capacity at 5% vertical strain and a maximum allowable bearing pressure of 200 kPa for GRS abutments (Berg et al. 2009; Adams et al. 2011b).

Lee and Wu (2004) reviewed several case studies of in-service GRS abutments (Won et al. 1996; Wu et al. 2001; Abu-Hejleh et al. 2002), and reported satisfactory performance under service loading conditions. Numerical modeling investigations have been conducted for GRS abutments under static loading (Helwany et al. 2003, 2007; Wu et al. 2006a, 2006b; Fakharian and Attar 2007; Zheng et al. 2014, 2015a, 2015b; Zheng and Fox 2016a). Results from these investigations show relatively small lateral facing displacements and bridge seat settlements for design-level stresses. Corresponding parametric studies indicate that relative compaction of backfill soil, reinforcement spacing, reinforcement stiffness, and bridge load have significant effects on the performance of GRS abutments (Helwany et al. 2007; Zheng and Fox 2016a). Zheng and Fox (2016a) simulated a full bridge system with two GRS abutments and found that horizontal restraining forces from the bridge structure have an important influence on abutment deformations. Based on these results, Zheng and Fox (2016a) recommended that numerical modeling work should be conducted for full bridge systems, rather than single abutments individually, to account for this effect. The above studies have focused on general GRS abutments; however, much less work has been conducted for the specific conditions of GRS-IBS. Adams et al. (2011a) reported excellent performance for five in-service GRS-IBS abutments with regard to

bridge settlement, abutment compression, and differential settlement. These findings confirm that GRS-IBS may offer significant advantages under certain conditions and detailed investigations are needed to better understand system performance.

This chapter presents a numerical investigation of the performance of GRS-IBS with realistic conditions for system geometry, backfill soil, geosynthetic reinforcement, and applied loads. Simulation results, including lateral facing displacements, settlements, lateral and vertical earth pressures, and reinforcement tensile strains and forces, are presented for various stages of construction and under traffic loads. A parametric study then is presented to illustrate the effects of various factors on the performance of GRS-IBS at end of construction. Results from this investigation provide insights with regard to practical use of the GRS-IBS design.

4.2 Baseline Case

4.2.1 Numerical Model

The two-dimensional finite difference program *FLAC Version 7.0* (Itasca Consulting Group 2011) was used for the current investigation. Zheng and Fox (2016a) successfully developed a similar FLAC model to simulate the performance of the Founders/Meadows GRS bridge abutment (Abu-Hejleh et al. 2000, 2001) for static loading conditions. Simulation results, including lateral facing displacements, bridge seat settlements, lateral and vertical earth pressures, and reinforcement tensile strains and forces, were in good agreement with field measurements at various stages of construction. Based on these results, Zheng and Fox (2016a) concluded that this type of numerical model has the capability to simulate the performance of GRS abutments under static loading. *FLAC* is applicable for plane strain conditions, which represents a simplification for these three-dimensional structures.

4.2.1.1 Model Configuration

The GRS-IBS numerical model is based, in general, on the design of the first bridge to use this technology, the Bowman Road Bridge located in Defiance County, Ohio (Adams et al. 2011b), and satisfies all design requirements for GRS-IBS. Figure 4.2(a) shows the model configuration. A single-span bridge has length L_b = 24 m and symmetrical structures on both ends. Each end structure consists of a reinforced soil foundation, GRS abutment,

and integrated approach, and is constructed on a 1V:1H cut slope in native foundation soil. Figure 4.2(b) shows the finite difference grid and boundary conditions for the right-hand side of the model. Assuming a bridge span-to-depth ratio $R_{sd} = L_b/D = 24$, the depth of the bridge structure D = 1.0 m, including a concrete box beam with a depth of 0.9 m and overlying pavement with a thickness of 0.1 m. The integrated approach consists of three lifts of wrapped-face GRS fill behind the bridge. The GRS abutment has a total height H = 5 m, including the bridge seat and GRS wall. The bridge seat has bearing length $b = D$ = 1.0 m for the bridge and setback distance a_b = 0.2 m from the facing. The clear distance between the top of facing and bottom of bridge structure d_e is equal to the bridge seat thickness of 0.2 m. The GRS wall is 4.8 m high and has 24 concrete masonry unit (CMU) facing blocks (0.2 m in length × 0.2 m in height). The base length for the GRS abutment B_a = 1.5 m (= $0.3H$), and thus the total base length, including facing block, B_{total} = 1.7 m (= B_a + 0.2 m). The reinforced soil foundation has length B_f = 2.13 m (= $1.25B_{total}$) and depth D_f = 0.43 m (= $0.25B_{total}$). To minimize the influence of boundary conditions on system response, the foundation soil has a depth of 10 m (= $2H$) and lateral boundaries are located at 20 m (= $4H$) behind the GRS wall facing on each side. Lateral boundaries are fixed in the horizontal direction and free to move in the vertical direction, whereas the bottom boundary is fixed in both horizontal and vertical directions.

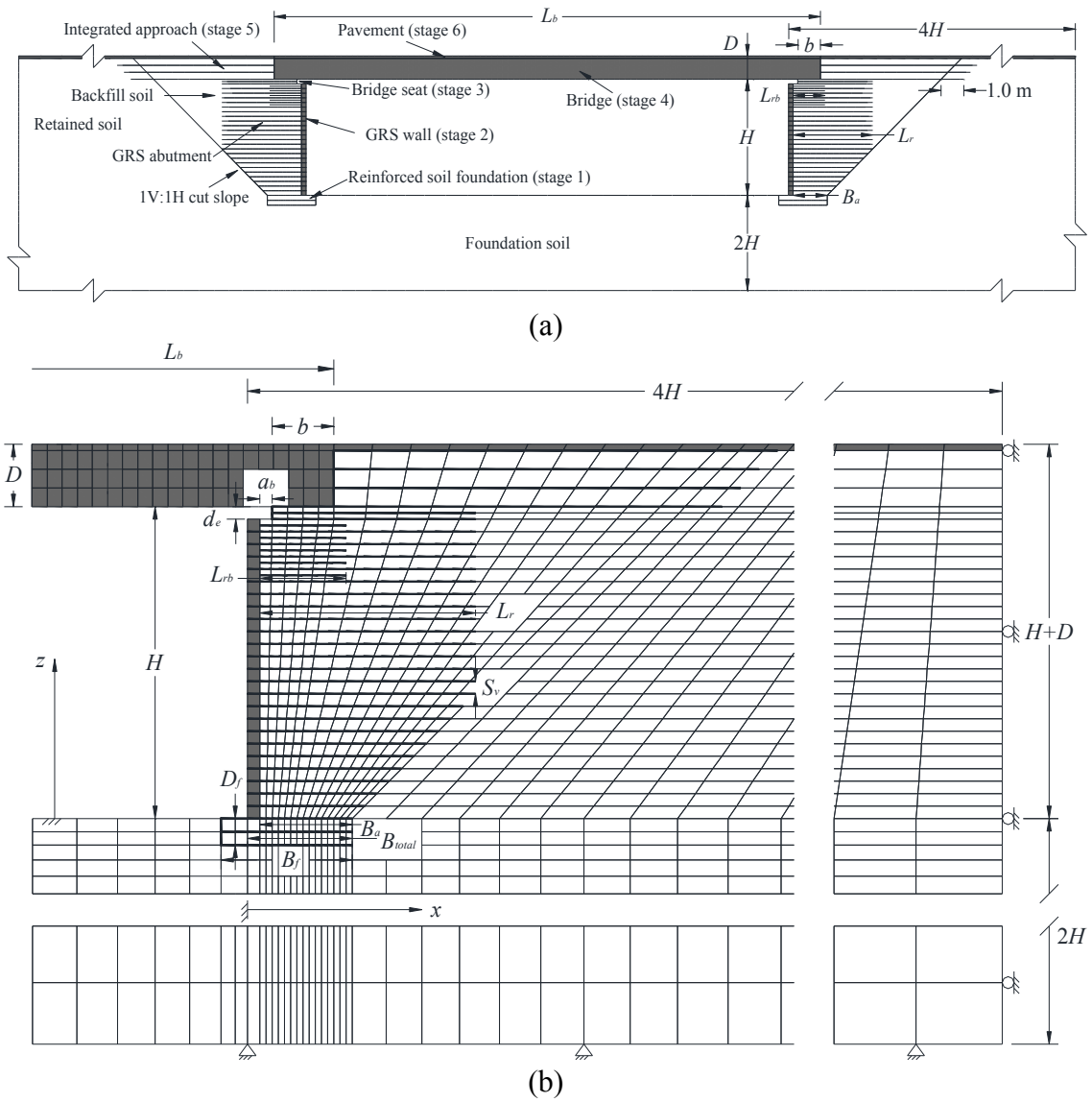

Figure 4.2 GRS-IBS numerical model: (a) configuration; (b) finite difference grid and boundary conditions for right-hand side.

4.2.1.2 Soils

An open-graded soil described by Gebrenegus et al. (2015) was specified as backfill soil for the GRS-IBS model because of the relative ease of construction and favorable drainage characteristics for this material, as recommended by FHWA (Adams et al. 2011b).

The soil is classified as AASHTO No. 8 according to the American Association of State Highway and Transportation Officials (AASHTO) M 43 specification, and as GP, poorly graded gravel, according to the Unified Soil Classification System (USCS). This soil has maximum and minimum dry unit weights γ_{max} = 17.8 kN/m^3 and γ_{min} = 15.5 kN/m^3, respectively, and a maximum aggregate size D_{max} = 12.7 mm (Gebrenegus et al. 2015). The backfill soil was modeled as a nonlinear elastic-plastic material with Mohr-Coulomb failure criterion, nonassociated flow rule, and the Duncan-Chang hyperbolic relationship (Duncan et al. 1980). This approach accounts for nonlinear behavior and has been used successfully to simulate the static response of GRS walls and abutments (Hatami and Bathurst 2005a, 2006; Fakharian and Attar 2007; Zheng and Fox 2016a). The tangent elastic modulus E_t, unloading-reloading modulus E_{ur}, bulk modulus B, and tangent Poisson's ratio v_t are expressed as (Duncan et al. 1980)

$$E_t = \left[1 - \frac{R_f(1-\sin\phi')(\sigma_1' - \sigma_3')}{2c'\cos\phi' + 2\sigma_3'\sin\phi'}\right]^2 Kp_a\left(\frac{\sigma_3'}{p_a}\right)^n \tag{4.1}$$

$$E_{ur} = K_{ur}p_a\left(\frac{\sigma_3'}{p_a}\right)^n \tag{4.2}$$

$$B = K_b p_a\left(\frac{\sigma_3'}{p_a}\right)^m \tag{4.3}$$

$$v_t = \frac{1}{2} - \frac{E_t}{6B} \tag{4.4}$$

where σ_1' and σ_3' = major and minor principal effective stresses; ϕ' = friction angle; c' = cohesion; R_f = failure ratio; K = elastic modulus number; n = elastic modulus exponent; p_a = atmospheric pressure; K_{ur} = unloading-reloading modulus number; K_b = bulk modulus

number; m = bulk modulus exponent; and v_t is limited to a range of 0 to 0.49. Equations (4.1), (4.2), (4.3), and (4.4) were implemented into FLAC using FISH subroutines to update the stress-dependent soil moduli during the course of each simulation.

Backfill soil parameters were calibrated using data from large-size consolidated-drained (CD) triaxial tests conducted by Gebrenegus et al. (2015). The specimens were compacted at a relative density of 95% with a unit weight γ = 17.7 kN/m^3, which satisfies the field compaction requirement for GRS-IBS. A series of single element triaxial tests were simulated for axisymmetric condition. Figure 4.3 shows a comparison between measured and simulated results. Nonlinear stress-strain behavior is accurately captured by the hyperbolic model, especially leading up to peak shear strength. The simulated response for soil dilation is also in reasonable agreement with measured data using a back-calculated dilation angle ψ = 13.0°. The foundation and retained soil is classified as SM-SC according to the USCS, and characterized using triaxial test results reported by Duncan et al. (1980). A summary of properties for the backfill soil, and foundation and retained soil, are provided in Table 4.1.

The effect of backfill soil compaction during construction was simulated by applying a temporary uniform surcharge stress of 8 kPa to the top surface of each soil lift for the reinforced soil foundation, GRS abutment, and integrated approach. Hatami and Bathurst (2006) and Guler et al. (2007) used this method and obtained good agreement between measured and simulated results for full-scale GRS walls. The surcharge stress produces additional compression beyond that resulting from soil self-weight alone and increases the yield stress. The unloading path for surcharge removal and reloading path for

subsequent lifts follow a stiffer response, as shown in Figure 4.3(a), with a higher modulus value that depends on the minor principal stress.

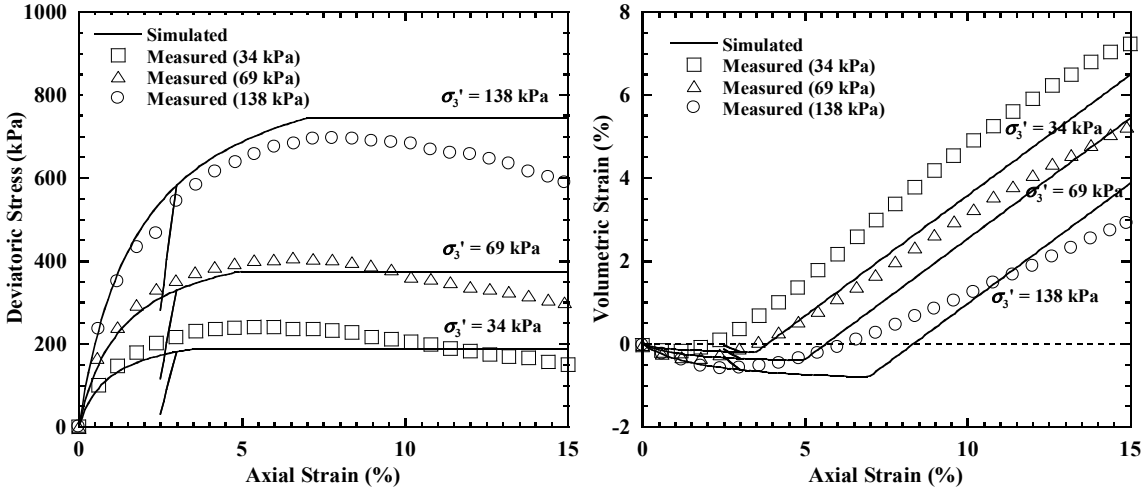

(a) (b)

Figure 4.3 Comparison of measured and simulated triaxial test results: (a) deviatoric stress vs. axial strain; (b) volumetric strain vs. axial strain (measured data from Gebrenegus et al. 2015).

Table 4.1 Soil properties for numerical simulations.

Soil	γ (kN/m^3)	K	K_{ur}	n	R_f	K_b	m	p_a (kPa)	c' (kPa)	ϕ' (°)	ψ (°)
Backfill soil	17.7	429	515	0.5	0.79	306	0	101.3	0	46.7	13.0
Foundation and retained soil	21.2	400	480	0.6	0.7	200	0.5	101.3	23.9	33.0	0

4.2.1.3 Structural Components

A longitudinal slice of the bridge with unit width was modeled as a solid block ($L_b \times D \times 1$) composed of elastic elements having equivalent unit weight γ_{eq} = 10.33 kN/m^3, elastic modulus E = 20 GPa, and Poisson's ratio v = 0.2. This equivalent unit weight

accounts for the hollow void spaces for actual bridge structures (e.g., adjacent concrete box beams or void slabs) (Adams et al. 2011b). The vertical load per unit width on each bridge seat $F_v = L_b D\gamma_{eq}/2 = 124$ kN/m and the corresponding average applied vertical stress $q_v = F_v/b = 124$ kPa, which is equal to the estimated value of 124 kPa for the Bowman Road Bridge (Adams et al. 2011b). The facing blocks and concrete pavement were modeled as elastic materials with unit weight $\gamma = 23.54$ kN/m^3, elastic modulus $E = 20$ GPa, and Poisson's ratio $v = 0.2$.

4.2.1.4 Reinforcements and Interfaces

Primary reinforcement for the GRS abutment has length $L_r = 1.5$ m ($= 0.3H$) at the base (not including facing blocks) and increases linearly with elevation (1V:1H) to $L_r = 3.5$ m ($= 0.7H$) at elevation $z = 2.0$ m, as shown in Figure 4.2(b), and vertical spacing $S_v = 0.2$ m. Five layers of secondary bearing bed reinforcement with length $L_{br} = 1.4$ m ($= b + 2a_b$) are included underneath the bridge seat. The reinforced soil foundation, bridge seat, and integrated approach consist of wrapped-face GRS fills with $S_v = 0.21$ m, 0.1 m, and 0.3 m, respectively. Reinforcement length for the integrated approach extends 1 m beyond the cut slope to reduce differential settlement between the backfill soil and cut slope.

Figure 4.4 shows reinforcement and interface details near connections between the bridge and right-side GRS abutment. Horizontal geotextiles within the backfill soil for the abutments were modeled using cable elements with tensile stiffness $J = 500$ kN/m, yield strength $T_y = 50$ kN/m, and frictional interfaces on both sides. Horizontal geotextiles between facing blocks were modeled using beam elements with zero moment of inertia

(i.e., no bending stiffness) and frictional interfaces on both sides. Reinforcement properties for the cable and beam elements are presented in Table 4.2. Bearing bed reinforcement layers are not connected to facing blocks and were also modeled using cable elements. For the wrapped-face GRS fills, the vertical face section and uppermost reinforcement layers were modeled using beam elements and the remaining reinforcement layers were modeled using cable elements. Geotextile-bridge frictional interfaces were included between the bridge, bridge seat, and integrated approach, as shown in Figure 4.4, to account for the horizontal restraining forces, which has an important effect on abutment deformations (Zheng and Fox 2016a). Vertical soil-block interfaces were also included between the facing blocks and backfill soil.

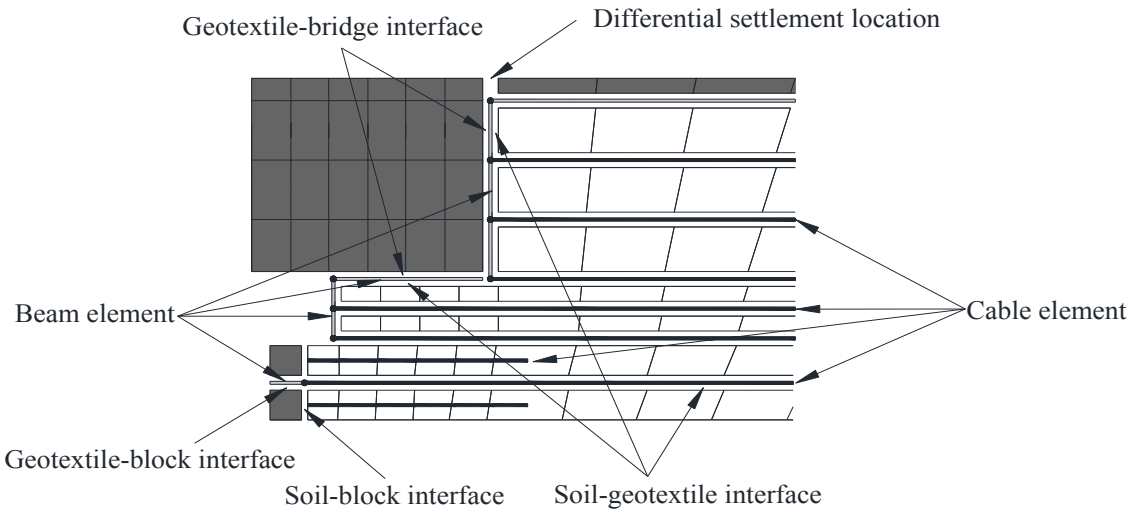

Figure 4.4 Reinforcement and interface details near connection between the bridge and right-side GRS abutment.

Table 4.2 Reinforcement properties for cable and beam elements.

Element properties	Value
Cable	
Elastic modulus, E_r	250 MPa
Cross-sectional area, A_r	0.002 m^2
Perimeter, P_r	2.004 m
Yield strength, T_y	50 kN/m
Beam	
Elastic modulus, E_r	250 MPa
Cross-sectional area, A_r	0.002 m^2
Moment of inertia, i	0 m^4

Table 4.3 presents interface properties for the numerical model. The shear strength for frictional interfaces between soil and geotextile, and block is characterized using a reduction factor RF_i defined as,

$$RF_i = \frac{\tan \delta_i}{\tan \phi'} \tag{4.5}$$

where δ_i is the interface friction angle. The lowermost facing block was placed on the reinforced soil foundation and characterized with a geotextile-block interface. Considering the embedment of wall facing at the toe (e.g., riprap as shown in Figure 4.1), a relatively high toe stiffness of 40 MPa/m was selected (Huang et al. 2010; Yu et al. 2016).

Table 4.3 Interface properties.

Interface properties	Value
Soil-geotextile[1]	
Shear stiffness, k_s	1 MN/m/m
Friction angle, δ_i	42.1°[2]
Soil-block[3]	
Normal stiffness, k_n	1,000 MPa/m
Shear stiffness, k_s	1 MPa/m
Friction angle, δ_i	34.6°[4]
Geotextile-block[3]	
Normal stiffness, k_n	100,000 MPa/m
Shear stiffness, k_s	40 MPa/m
Friction angle, δ_i	37.0°[5]
Geotextile-bridge[3]	
Normal stiffness, k_n	100,000 MPa/m
Shear stiffness, k_s	40 MPa/m
Friction angle, δ_i	35.0°[6]

[1] Included in cable element.
[2] Based on average of data (RF_i = 0.76 – 0.94 for dense sand) from Vieira et al. (2013).
[3] Simulated using interface element.
[4] Based on data (RF_i = 0.65) from Ling et al. (2010).
[5] Based on large-scale direct shear data from Nicks et al. (2013b).
[6] Based on data from Unified Facilities Guide Specifications (2008).

4.2.1.5 Construction Sequence and Traffic Loads

A typical field construction and loading sequence was used for the numerical simulations, and consisted of seven stages (Figure 4.2(a)). The initial condition corresponds to foundation soil and retained soil cut slopes (1V:1H) in equilibrium under gravitational forces. For stage 1, a reinforced soil foundation was placed at the toe of the cut slope on each side of the bridge system. For stages 2 and 3, the GRS abutments (i.e., GRS walls and bridge seats) were constructed in lifts. The thickness of each lift was equal

to the height of one facing block (0.2 m). During construction of each lift, a temporary uniform vertical surcharge stress σ_c = 8 kPa was applied to the top surface of each lift, and then removed prior to placement of the next lift to simulate backfill soil compaction. Each lift was constructed to the design height, which compensated for settlements that occurred during construction, and the soil-geotextile, soil-block, and geotextile-block interfaces were placed at the specified locations. The GRS walls were constructed to elevation z = 4.8 m and the bridge seats were placed at that level. A large tensile strength was assigned to the two interfaces between the top three facing blocks and the reinforcement was rigidly connected to the facing to model the effect of grouting for these blocks. For stage 4, the bridge was placed on the bridge seats. The integrated approaches were constructed behind the bridge for stage 5 and pavement was placed on the bridge and approach roadways for stage 6.

For stage 7, traffic loads on the bridge and approach roadway were simulated as a uniform vertical surcharge stress according to design guidelines (Berg et al. 2009; Adams et al. 2011b; AASHTO 2012). This approach represents a conservative assumption for maximum load combination and a dynamic allowance factor. A uniform surcharge of 12.7 kPa was applied to the approach roadway, which is equivalent to 0.72 m of backfill soil. Traffic load on the bridge was determined using the HL-93 LL model. Assuming the bridge contains two lanes of traffic with a total width W_b = 10 m, a uniform surcharge of 5.4 kPa was applied to the bridge span, which yielded in a vertical stress increment of 65 kPa on each bridge seat due to traffic load. Therefore, the total average vertical stress on each bridge seat is 189 kPa for stage 7, which is smaller than the maximum allowable bearing pressure of 200 kPa (Adams et al. 2011b).

4.2.2 Simulation Results

Numerical simulation results, including lateral facing displacements, settlements, lateral and vertical earth pressures, and reinforcement tensile strains and forces, are presented and discussed in the following sections. Results focus on end-of-construction conditions for the GRS walls (stage 2) and GRS-IBS (stage 6), and in-service condition for the GRS-IBS under traffic surcharge loads (stage 7). Results are presented for the right-hand side of the bridge, although both abutments have essentially equal (symmetrical) response.

The effect of numerical resolution (i.e., mesh density) was investigated for models with a total number of elements equals to 4496, 8892, and 17984. Lateral facing displacements, settlement and abutment compression are in close agreement, which indicates that the model with 4496 elements (Figure 4.2) yields good accuracy.

4.2.2.1 Lateral Facing Displacements

Figure 4.5 shows lateral facing displacement profiles for the right-hand side GRS wall. For stage 2, the maximum lateral facing displacement is 12.1 mm and occurs at elevation z = 2.2 m above the foundation soil. After construction of the bridge system (stage 6), the maximum displacement increases to 18.2 mm at z = 2.8 m, and the maximum incremental displacement is 8.3 mm at the top. Lateral facing displacements increase 8 mm for the upper one-third section of the GRS wall due to placement of the bridge. For stage

7, lateral facing displacements increase slightly (2 mm) under traffic loads, and yield a maximum value of 20.5 mm at z = 2.8 m.

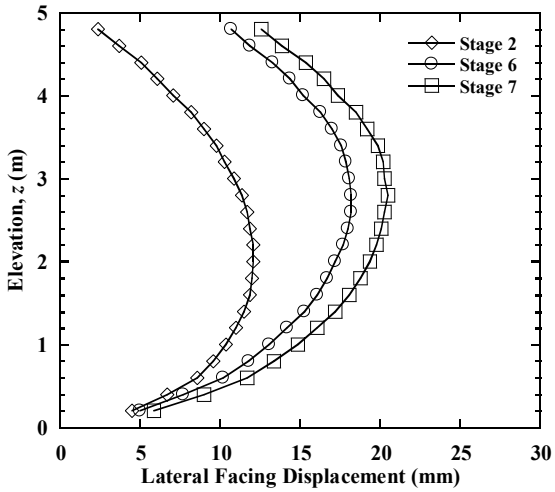

Figure 4.5 Lateral facing displacement profiles for GRS wall.

4.2.2.2 Settlements

Settlements for the GRS-IBS abutment at stages 6 and 7 are summarized in Table 4.4. The bridge seat settlement due to subsequent construction, taken as an average over the bearing length, is 25.0 mm, and the corresponding foundation soil settlement is 7.4 mm. This gives a net vertical compression of backfill soil for the GRS abutment of 17.6 mm and, based on H = 5 m, a corresponding vertical strain of 0.35%. This strain at end of construction (EOC) is within the maximum allowable criterion of 0.50% suggested by Adams et al. (2011b). Under traffic surcharge loads, the total bridge seat settlement is 37.1 mm and abutment compression increases to 24.9 mm, corresponding to a vertical strain of 0.50%.

Table 4.4 Settlements for GRS-IBS abutment.

Stage	Bridge seat settlement (mm)	Foundation soil settlement (mm)	Abutment compression (mm)	Vertical strain (%)
6	25.0	7.4	17.6	0.35
7	37.1	12.2	24.9	0.50

Although no comprehensive field instrumentation data are available in the literature for GRS-IBS abutments, Table 4.5 presents a comparison of vertical compression for the simulated GRS-IBS abutment with measured values for five case histories. The field measurements correspond to conditions after opening to traffic for several years. However, the majority of the compression occurred during construction, and the deformation due to traffic loads are relatively small (Adams et al. 2011a). Therefore, the field monitoring results are compared with simulated values obtained at the end of construction. The abutment compression of 17.6 mm and corresponding vertical strain of 0.35% for the simulated GRS-IBS abutment are in close agreement with measured values for the Bowman Road Bridge (14.3 mm and 0.28%) and within the range from 7.0 mm to 32.3 mm for all five case histories. The GRS-IBS model is based on the design of the Bowman Road Bridge, including geometry and loading conditions; however, the backfill soil and reinforcement properties are different. The geotextile reinforcement is less stiff than for the Bowman Road Bridge, which likely yields the slightly larger simulated deformation.

Table 4.5 Vertical compression for simulated GRS-IBS abutment and five case histories (data from Adams et al. 2011a).

Bridge	Average abutment height (m)	Average abutment compression (mm)	Average abutment vertical strain (%)
Vine Street	3.5	7.0	0.20
Glenburg Road	4.0	25.3	0.64
Huber Road	5.1	4.6	0.09
Bowman Road	5.1	14.3	0.28
Triffin River	5.9	32.3	0.55
Simulated (EOC)	5.0	17.6	0.35

Figure 4.6 presents settlement profiles at the transition between the bridge and approach roadway. Positive values of distance are directed away from the end of the bridge. The bridge settles slightly more than the approach roadway and differential settlement between the bridge and approach roadway (location in Figure 4.4) is minimal, and is equal to 0.2 mm for stage 6 and 2.0 mm for stage 7. The settlement profile also shows deflection of the bridge itself. In general, smooth settlement profiles at the end of construction and under traffic loads suggest minimal differential settlement between the bridge and approach roadway for this design.

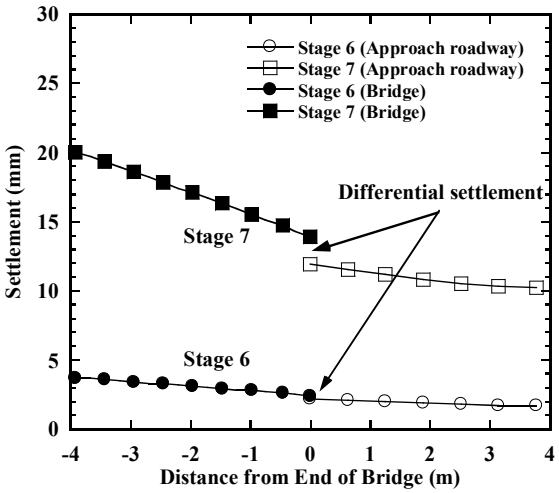

Figure 4.6 Settlement profiles for bridge and approach roadway.

4.2.2.3 Lateral Earth Pressures

Lateral earth pressures behind the GRS wall facing, as obtained from normal stresses on vertical soil-block interfaces, are shown for stages 2, 6, and 7 in Figure 4.7. For stage 2, theoretical values of Rankine active earth pressure (K_a condition) and at-rest earth pressure (K_o condition) for normally consolidated soil are also presented, where $K_a = (1 - \sin\phi')/(1 + \sin\phi')$ and $K_o = 1 - \sin\phi'$. At the end of GRS wall construction, lateral earth pressures are in close agreement with K_a values with small deviations near the top and bottom. Deviations at the top may be attributed to grouting of the top facing blocks and presence of bearing bed reinforcement. The GRS wall is a flexible structure and outward movements of facing blocks occur as a result of increased lateral earth pressures, which allow the active condition to develop. For stage 6, lateral earth pressures increase significantly, especially for the upper wall section, due to surcharge load from the bridge. Moving down from the top, lateral earth pressures increase to 17 kPa at mid-height, remain approximately constant, and then decrease near the bottom. For stage 7, lateral earth

pressures increase slightly (approximately 3 kPa) due to traffic loads. Calculated lateral stress distribution for the vertical plane behind the wall facing (x = 0.2 m) using the FHWA GRS-IBS (2011) method is also shown. This method uses Boussinesq theory to obtain additional lateral stresses due to the surcharge load from the bridge. In general, calculated lateral stresses behind wall facing are close to the simulated values, with the calculated values slightly smaller for z = 1 m to 4 m. None of the simulated lateral earth pressure profiles are in close agreement with K_o values.

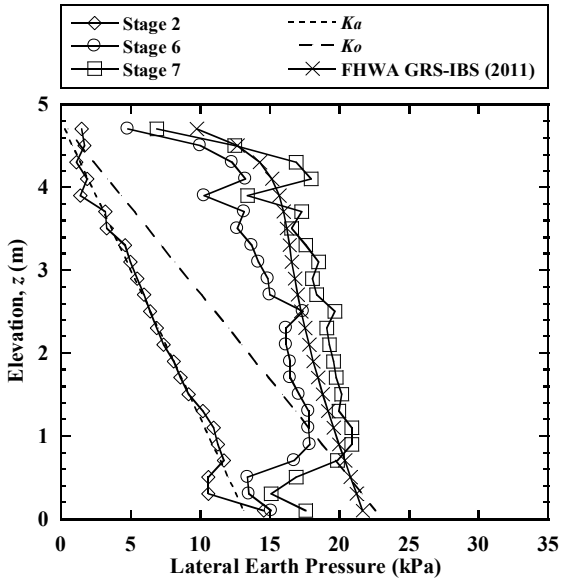

Figure 4.7 Lateral earth pressures behind GRS wall facing.

4.2.2.4 Vertical Earth Pressures

Figure 4.8(a) presents three distributions of vertical earth pressure at the foundation soil level (z = 0 m). For stage 2, vertical pressure is highest under the wall facing, which results from downdrag forces generated by relative displacement between facing blocks and backfill soil (Runser et al. 2001; Hatami and Bathurst 2005a, 2006). Vertical pressures increase significantly after construction of the bridge system (stage 6) and application of traffic loads (stage 7). Variations occur at the boundary between the reinforced and unreinforced sections of foundation soil (x = 1.7 m from facing), and are attributed to a difference in stiffness between the two materials. Vertical earth pressures at the bridge seat level (z = 4.8 m) are presented in Figure 4.8(b). At stage 6, a maximum vertical pressure of 148 kPa occurs at the toe of the bridge seat, and then decreases approximately linearly to 90 kPa at the heel. This nonuniform pressure distribution results from deflection of the bridge and asymmetric load application to the bridge seat. The simulated average vertical earth pressure on the bridge seat at end of construction is 121 kPa, which is close to the estimated value of 124 kPa in the design. After application of traffic loads, vertical pressure at the toe is 200 kPa and the average vertical pressure is 165 kPa, which is smaller than the estimated design value of 189 kPa. Behind the bridge seat, vertical pressures average to 25 kPa for stage 6 and 39 kPa for stage 7, and are approximately uniform in each case.

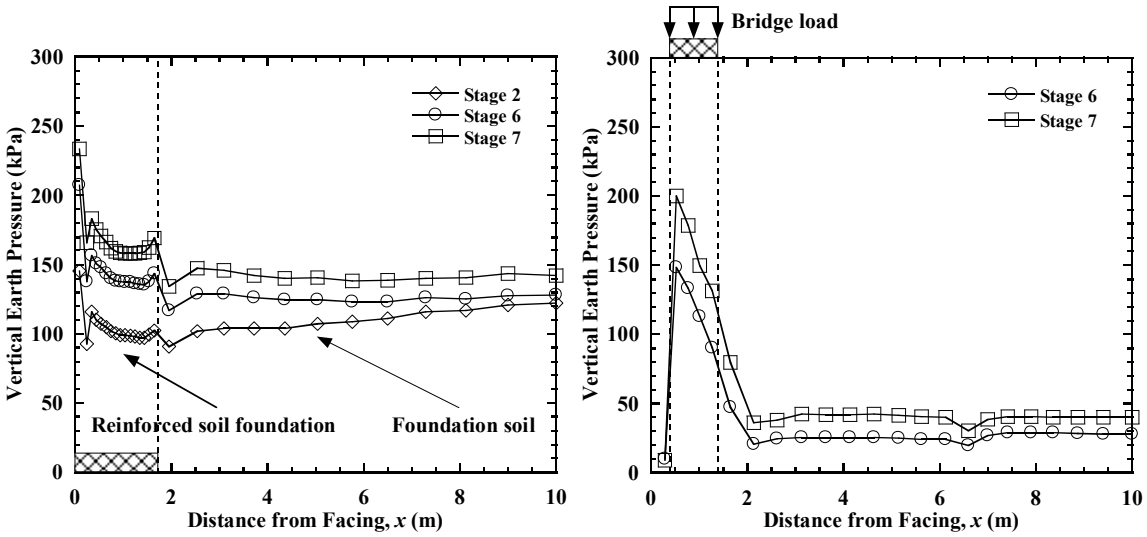

Figure 4.8 Vertical earth pressures at level of: (a) foundation soil (z = 0 m); (b) bridge seat (z = 4.8 m).

4.2.2.5 Reinforcement Strains

Distributions of tensile strain in the primary reinforcement at five elevations within the GRS abutment are presented in Figure 4.9. Prior to the application of bridge load (stage 2), the lower reinforcement layers have much larger strains than the upper layers. After construction of the bridge (stage 6), reinforcement strains under the bridge seat increase significantly, especially for upper reinforcement layers. For instance, tensile strain in layer 18 along the centerline of bridge seat increases from 0.12% to 0.51%, and tensile strain in layer 23 at the connection increases from 0.05% to 0.49%. Reinforcement strains also increase with the application of traffic loads (stage 7). For stages 6 and 7, maximum strains occur near the connection for most reinforcement layers. After the application of traffic loads (stage 7), the highest value of tensile strain is 0.78%, which is smaller than the service limit of 2% for GRS-IBS as specified by Adams et al. (2011b).

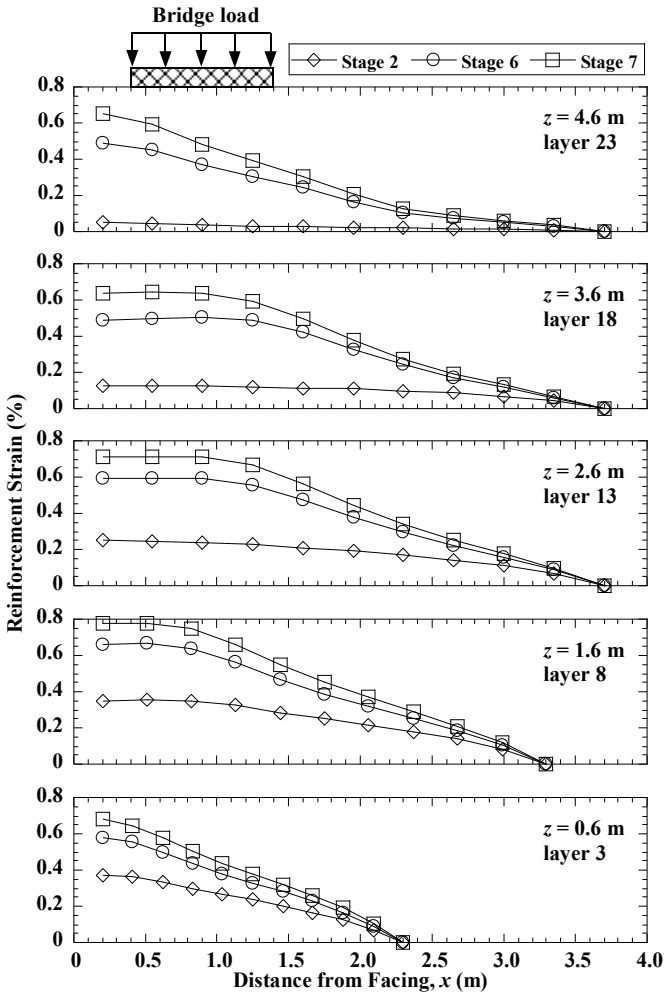

Figure 4.9 Tensile strains for primary reinforcement at five elevations within GRS abutment.

4.2.2.6 Reinforcement Forces

Values of maximum tensile force in the primary reinforcement, calculated using a constant stiffness, are presented versus elevation in Figure 4.10. For stage 2, the maximum force increases approximately linearly with depth from z = 4.2 to z = 0.8 m, and then decreases near the bottom of the wall. After construction of the bridge (stage 6) and application of traffic loads (stage 7), maximum tensile forces increase significantly,

especially for upper reinforcement layers, and show a peak value at higher elevation than for stage 2. Maximum tensile forces in the top two reinforcement layers are slightly larger than the layer below. This is attributed to grouting of the top three facing blocks and rigid reinforcement connections at these levels.

Profiles of calculated required tensile strength for the reinforcement under bridge and traffic loads (stage 7), as obtained from the FHWA GRS-IBS (2011) and AASHTO LRFD (2012) design methods, also are shown in Figure 4.10. The FHWA method is calculated using the actual backfill soil friction angle of 46.7°, while the AASHTO method is calculated for both the actual friction angle and maximum allowable friction angle of 40° in the design. Both methods predict lower values in the bearing bed zone, due to the reduced vertical reinforcement spacing of S_v = 0.1 m, and higher values below (S_v = 0.2 m). Required reinforcement strengths for the FHWA method are larger than for the AASHTO method below bearing bed zone. For the AASHTO method, the required strengths for ϕ' = 46.7° are approximately 2 kN/m smaller than for ϕ' = 40°; however, the maximum friction angle of 40° is used in the design because a higher friction angle might lead to underestimation of reinforcement forces (AASHTO 2012). The simulated maximum tensile force is 3.9 kN/m and occurs at z = 1.4 m, which is smaller than the calculated required maximum strengths of 6.9 kN/m and 11.0 kN/m at the bottom using the AASHTO (ϕ' = 40°) and FHWA methods, respectively. Figure 4.10 indicates that the FHWA GRS-IBS method is more conservative than the AASHTO LRFD method with regard to required tensile strength for the reinforcement, especially below the bearing bed reinforcement zone.

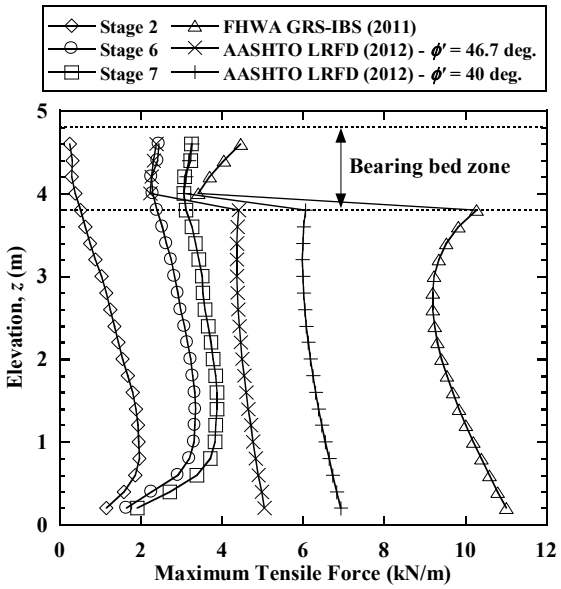

Figure 4.10 Maximum tensile forces for primary reinforcement in GRS abutment.

4.3 Parametric Study

A parametric study was conducted to investigate general performance of the GRS-IBS under static loading. Using the above numerical model and conditions at end of construction (stage 6) as a baseline case, variables for the study were backfill soil compaction, reinforcement length, reinforcement stiffness, bearing bed reinforcement, bridge seat setback distance, bridge load, and abutment height. For each series of simulations, only the variable of interest was changed and the other variables were held constant and equal to values for the baseline case. The performance of GRS-IBS at end of construction is evaluated in terms of lateral facing displacements for GRS wall, bridge seat and foundation soil settlements, abutment vertical compression, and differential settlement between the bridge and approach roadway.

4.3.1 Effect of Backfill Soil Compaction

Recent studies have indicated that level of compaction for backfill soil can have important effects on the performance of GRS walls (Bathurst et al. 2009; Ehrlich et al. 2012; Mirmoradi and Ehrlich 2014). Numerical simulations were conducted for compaction stress (i.e., temporarily-applied uniform surcharge stress) σ_c = 0, 8, and 16 kPa, where σ_c = 0 kPa represents soil lifts placed with self-weight and no additional compaction effort, and σ_c = 8 and 16 kPa represent light and heavy compactors, respectively. Figure 4.11(a) shows that lateral facing displacements increase with increasing compaction stress, and the effect becomes more significant as compaction stress increases. The maximum lateral facing displacement increases from 17.1 to 18.2 to 21.8 mm when conditions change from no compaction to a lightweight compactor and then to a heavyweight compactor. Values of settlement and abutment compression, shown in Figure 4.11(b), decrease significantly with increasing compaction stress. Bridge seat settlement decreases from 29.3 to 21.0 mm when compaction stress increases from 0 to 16 kPa, and corresponding abutment compression decreases from 20.4 (0.41%H) to 15.4 mm (0.31%H). A greater compaction stress produces larger settlement for each lift during construction; however, this settlement is compensated by subsequent lift placement. The greater compaction stress also results in a larger yield stress, thus produces less settlements upon reloading. In general, increasing the level of compaction for backfill soil can effectively reduce bridge seat settlement and abutment compression, but also produce larger lateral facing displacements.

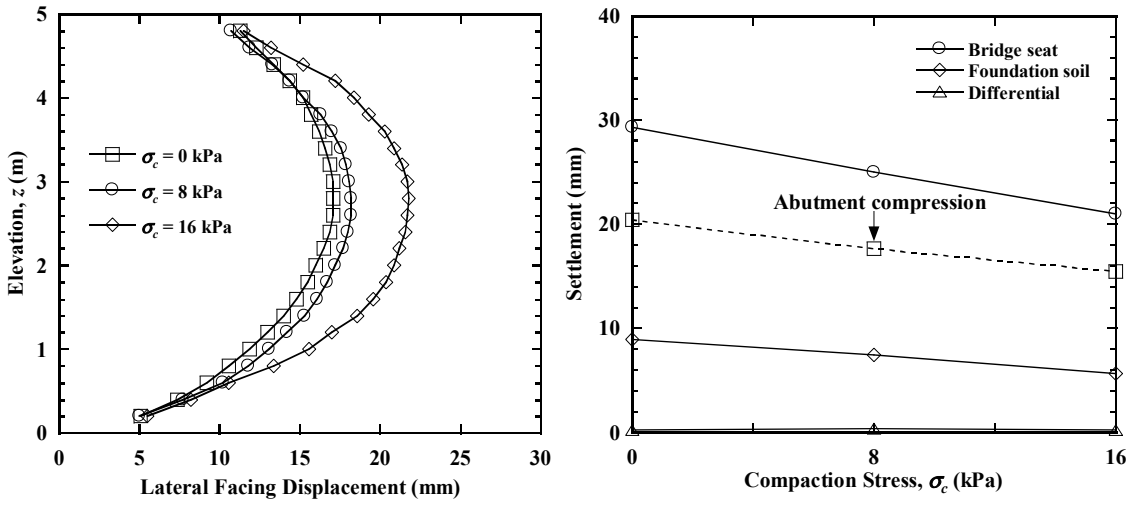

(a) (b)

Figure 4.11 Effect of backfill soil compaction: (a) lateral facing displacements; (b) settlements and abutment compression.

4.3.2 Effect of Reinforcement Length

Figure 4.12(a) presents lateral facing displacements for maximum primary reinforcement length L_r = 0.5H, 0.7H, 0.9H, and 1.1H in the GRS abutments. Reinforcement length has minimal effect on lateral facing displacements, especially for L_r ≥ 0.7H. For instance, the maximum lateral facing displacement of 18.7 mm for L_r = 0.5H is only slightly larger than for the baseline case (18.2 mm). Settlements and abutment compression are presented in Figure 4.12(b) and also are essentially independent of reinforcement length. Figure 4.12 indicates that, for the conditions studied, increasing reinforcement length beyond the default design value of L_r = 0.7H is unlikely to improve the performance of GRS-IBS under static loading.

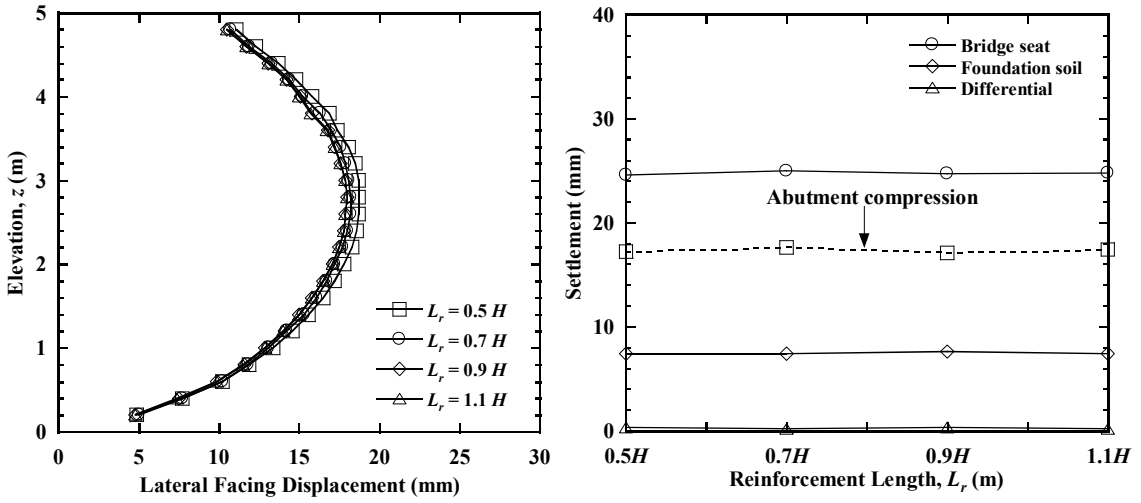

(a) (b)

Figure 4.12 Effect of reinforcement length: (a) lateral facing displacements; (b) settlements and abutment compression.

4.3.3 Effect of Reinforcement Stiffness

Simulations were conducted for primary and bearing bed reinforcement stiffness J = 250, 500, 750, and 1000 kN/m, which encompasses typical values for geotextiles (Boyle et al. 1996). Figure 4.13 shows that lateral facing displacements and bridge seat settlement decrease with increasing stiffness. As reinforcement stiffness increases from J = 250 to 1000 kN/m, the maximum lateral facing displacement decreases from 27.0 to 13.6 mm, and bridge seat settlement decreases from 30.5 to 21.2 mm. Corresponding values for abutment vertical compression decrease from 23.1 mm (0.46%H) to 14.0 (0.28%H). Differential settlements between the bridge and approach roadway are nearly constant (0.2 mm) for different values of reinforcement stiffness. In general, the effect of increasing reinforcement stiffness becomes less significant with higher stiffness values.

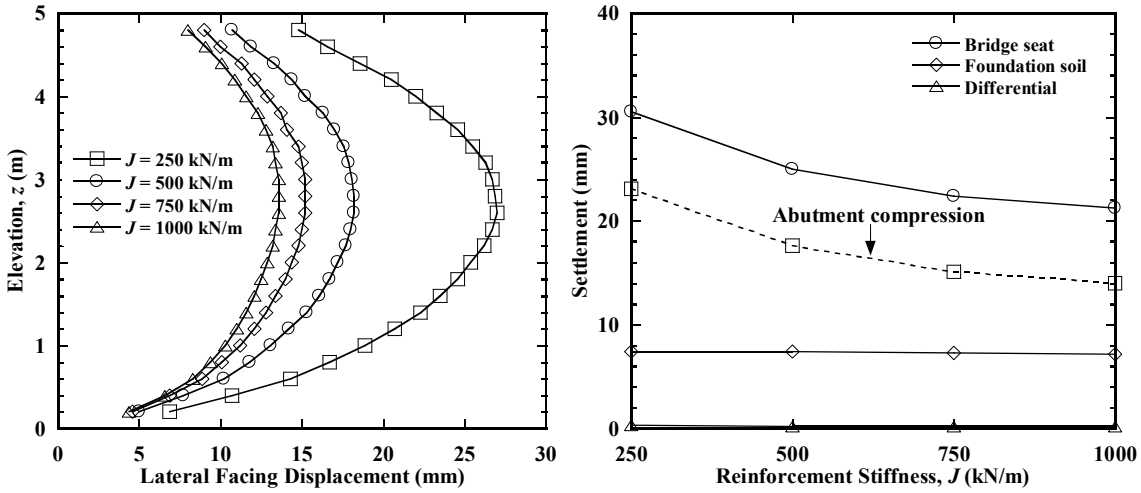

(a) (b)

Figure 4.13 Effect of reinforcement stiffness: (a) lateral facing displacements; (b) settlements and abutment compression.

4.3.4 Effect of Bearing Bed Reinforcement

Simulations were conducted for bearing bed reinforcement layer number n_{br} = 0, 5, 10, and 15, where n_{br} = 0 indicates no bearing bed reinforcement and n_{br} = 15 indicates 15 layers of bearing bed reinforcement placed underneath the bridge seat between elevations z = 1.8 and 4.8 m. The length of bearing bed reinforcement was held constant at L_{br} = 1.4 m. Figure 4.14(a) shows that lateral facing displacements decrease slightly when bearing bed reinforcement is included. For instance, in the zone between the 11th and 15th bearing bed reinforcement layers, lateral facing displacements for n_{br} = 15 are smaller than for the other cases. As bearing bed reinforcement increases from n_{br} = 0 to 15, the maximum lateral facing displacement decreases from 18.2 mm to 16.3 mm. In contrast, values of settlement and abutment compression are nearly equal for all n_{br}. The simulation results are consistent with observations from large-scale loading tests on GRS mini piers, which indicate that bearing bed reinforcement can reduce lateral facing displacements but is unlikely to reduce settlement under typical design-level applied vertical stress conditions (≤ 200 kPa) (Nicks et al. 2013a). The effect of bearing bed reinforcement in Figure 4.14(a) is less significant than results reported by Nicks et al. (2013a) because the bridge structure in the current study imposes horizontal friction forces on the bridge seat that act to reduce outward movement of the GRS abutment. This effect was not included in the experiments conducted by Nicks et al. (2013a).

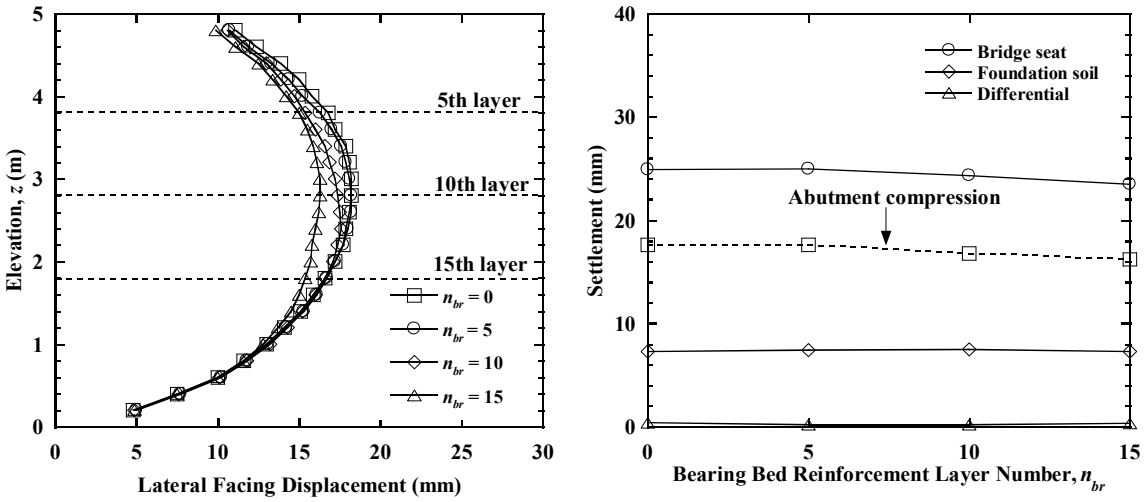

(a) (b)

Figure 4.14 Effect of bearing bed reinforcement: (a) lateral facing displacements; (b) settlements and abutment compression.

4.3.5 Effect of Bridge Seat Setback Distance

Figure 4.15(a) presents lateral facing displacements for bridge seat setback distance a_b = 0, 0.2, 0.6, and 1.0 m. The maximum lateral facing displacements are slightly larger for greater setback values; however, corresponding lateral facing displacements at the top of the GRS wall show the opposite trend. This is consistent with the expectation that the bridge load produces higher lateral earth pressure at the top of GRS wall as the setback distance decreases. Figure 4.15(b) indicates that bridge seat setback distance has a small effect on settlements and abutment compression. As setback distance increases from a_b = 0 to 1.0 m, bridge seat settlement decreases from 26.5 mm to 21.6 mm, and the corresponding abutment compression decreases from 18.8 (0.38%H) to 15.9 mm (0.32% H).

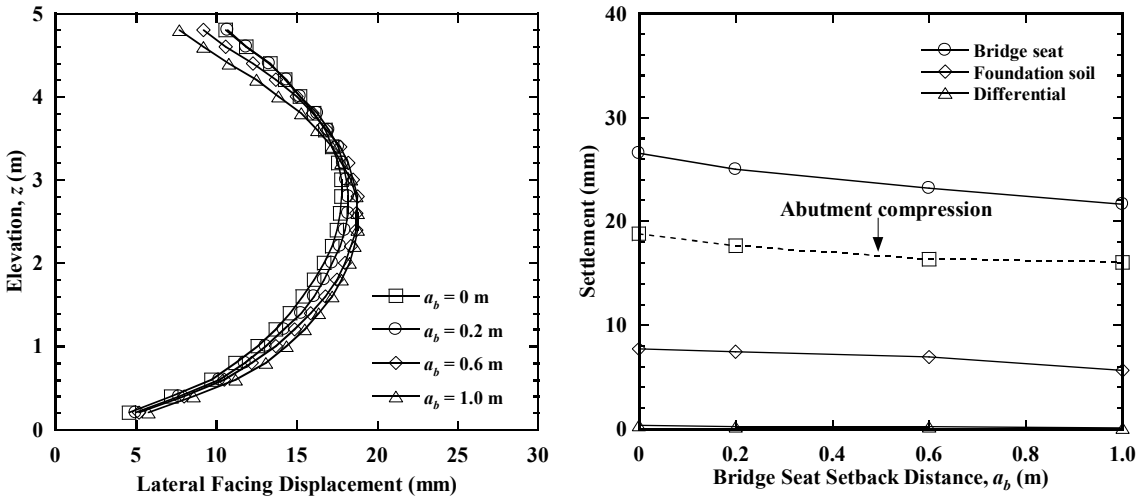

(a) (b)

Figure 4.15 Effect of bridge seat setback distance: (a) lateral facing displacements; (b) settlements and abutment compression.

4.3.6 Effect of Bridge Load

Simulations were conducted for varying bridge weight corresponding to span L_b = 16, 24, 32, and 40 m. Following the baseline case model with R_{sd} = 24, $b = D$, and γ_{eq} = 10.33 kN/m^3, the resulting bridge load per unit width on each GRS abutment F_v = 55, 124, 220, and 344 kN/m, and the corresponding average applied vertical stress q_v = 83, 124, 165, and 207 kPa, respectively. Lateral facing displacements are shown in Figure 4.16(a) and display similar trends in each case. Maximum values occur near mid-height, range from 14.7 to 26.2 mm, and increase with increasing bridge load. Settlements and abutment compression, presented in Figure 4.16(b), also increase significantly with increasing bridge load. As the applied load increases from 55 to 344 kN/m, bridge seat settlement increases from 12.4 mm to 53.6 mm, and the corresponding abutment compression increases from 9.1 mm (0.18%H) to 33.6 mm (0.67%H). The abutment compression of 0.67%H under F_v = 344 kN/m exceeds the recommended vertical strain limit of 0.5% H for GRS-IBS (Adams et al. 2011b). Specification of reinforcement with higher stiffness can reduce abutment deformations for high bridge load conditions (Figure 4.13). Differential settlements between the bridge and approach roadway are small (≤ 0.8 mm), and increase slightly with increasing bridge load.

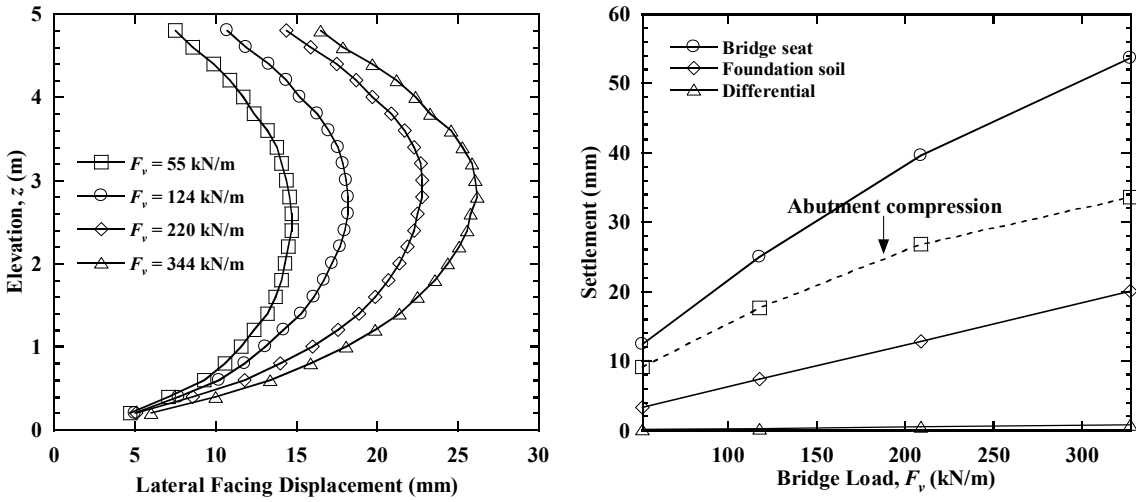

(a) (b)

Figure 4.16 Effect of bridge load: (a) lateral facing displacements; (b) settlements and abutment compression.

4.3.7 Effect of Abutment Height

Simulations were conducted for GRS abutments with height H = 3, 5, 7, and 9 m. Figure 4.17 indicates that abutment height has a significant effect on system performance. Profiles of lateral facing displacement are presented in Figure 4.17(a) and show similar trends, with maximum values occurring near mid-height in each case. Maximum lateral facing displacements increase significantly from 10.8 mm for H = 3 m to 38.2 mm for H = 9 m. Figure 4.17(b) shows that corresponding values of bridge seat settlement increase from 19.7 mm to 28.5 mm, and foundation soil settlement increase from 6.6 mm to 7.8 mm. Values for abutment compression display a similar trend and increase from 13.1 mm (0.44%H) to 20.7 mm (0.23%H). However, the average vertical strain decreases from 0.44% for H = 3 m to 0.23% for H = 9 m, which results from higher average stress conditions, and larger soil stiffness, for the taller abutments. Differential settlements between the bridge and approach roadway are small ($\leq$ 0.3 mm) for all simulated conditions.

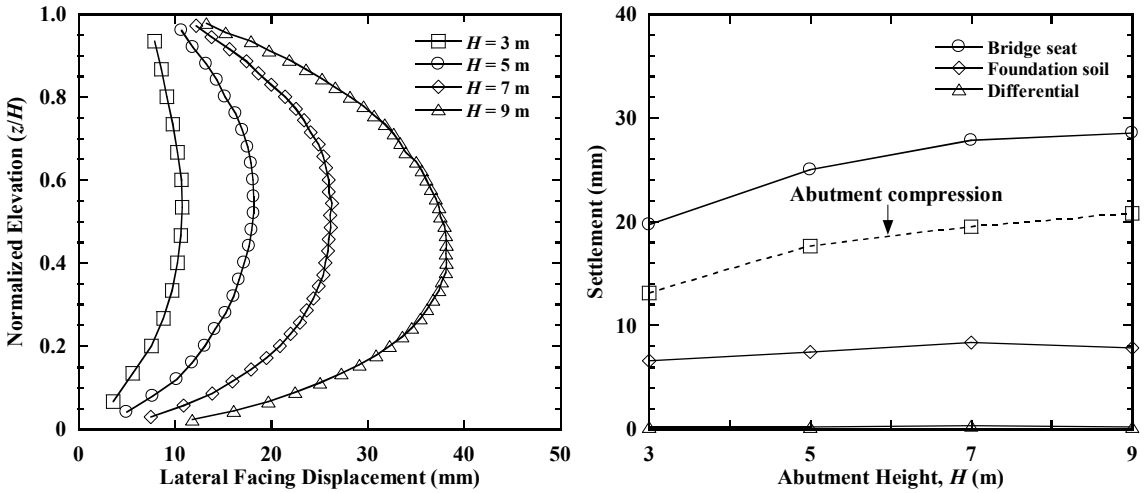

(a) (b)

Figure 4.17 Effect of abutment height: (a) lateral facing displacements; (b) settlements and abutment compression.

4.4 Acknowledgements

The text below is reproduced verbatim as it appears in the acknowledgments section per the UCSD Office of Graduate Studies Formatting Requirements.

Chapter 4 of this dissertation is based on materials published by the Journal of Geotechnical and Geoenvironmental Engineering titled “Numerical Investigation of the Geosynthetic Reinforced Soil-Integrated Bridge System under Static Loading” with authors, Yewei Zheng and Patrick J. Fox (2017). The dissertation author is the first author of this paper.

Chapter 5

Numerical Simulation of Load-Deformation and Failure Behavior of GRS Bridge Abutments

5.1 Introduction

Numerical studies have been conducted for geosynthetic-reinforced soil (GRS) bridge abutments under service loading conditions (Helwany et al. 2003, 2007; Zheng et al. 2014, 2015a; Ambauen et al. 2015; Zheng and Fox 2016a, 2017). These studies have considered perfectly plastic soil and linearly elastic reinforcement, and indicated that GRS bridge abutments generally have relatively small lateral facing displacements and abutment compressions for the service limit state. Numerical modeling work on the deformation behavior and bearing capacity of GRS bridge abutments corresponding to the strength limit

state, including large deformations up to failure, is more limited and has also assumed perfectly plastic soil and linearly elastic geosynthetic reinforcement (Wu et al. 2006a, 2006b). Based on other related research findings (e.g., Walters et al. 2002; Hatami and Bathurst 2006; Liu and Ling 2012; Yang et al. 2012; Zheng and Fox 2016b), strain softening of backfill soil and nonlinear response of geosynthetic reinforcement would be expected to have important effects on the behavior of GRS bridge abutments under high load conditions. Such an investigation, including failure behavior, would represent an important contribution to the literature.

Deformations, including lateral facing displacements and abutment compression, are important considerations in the design of GRS bridge abutments for the service limit state, whereas the bearing capacity is important for the strength limit state. The Federal Highway Administration (FHWA) provides analytical and empirical methods for the design of GRS bridge abutments for both limit states (Adams et al. 2011a, 2011b). The FHWA analytical method for ultimate bearing capacity is based on the soil-geosynthetic composite load capacity and accounts for friction angle and maximum aggregate size of the backfill soil, and spacing and ultimate tensile strength of the reinforcement (Wu and Pham 2013; Wu et al. 2013). The allowable vertical stress for the service limit state is 10% of the calculated ultimate bearing capacity (Nicks et al. 2013a, 2016). The FHWA empirical method is based on an experimentally-determined vertical stress-strain relationship that is obtained from performance tests (i.e., GRS mini-pier loading tests) conducted using project-specific soil and geosynthetic reinforcement (Adams et al. 2011a, 2011b). The FHWA guidelines specify an allowable vertical stress at 0.5% vertical strain or a maximum allowable stress of 200 kPa for the service limit state, and an ultimate

bearing capacity at 5% vertical strain for the strength limit state (Berg et al. 2009; Adams et al. 2011a, 2011b).

This chapter presents a numerical investigation of load-deformation and failure behavior for GRS bridge abutments. Simulations were performed to investigate the effects of strain softening soil and nonlinear reinforcement behavior on abutment deformations. A parametric study then was conducted to investigate the effects of various reinforcement, backfill soil, and abutment geometry parameters. Discussion is included on the effects of various parameters on the failure mechanism of GRS bridge abutments. Results from this investigation provide insights regarding the design of GRS bridge abutments for the service limit state and strength limit state.

5.2 Baseline Case

5.2.1 Numerical Model

The two-dimensional finite difference program *FLAC Version 7.0* (Itasca Consulting Group 2011) was used for the current investigation. Zheng and Fox (2016a) successfully developed a similar FLAC model to simulate the performance of the Founders/Meadows GRS bridge abutment (Abu-Hejleh et al. 2000, 2001) for service loading conditions. Simulation results, including lateral facing displacements, bridge seat settlements, lateral and vertical earth pressures, and reinforcement tensile strains and forces, were in good agreement with field measurements at various stages of construction. Based on these results, Zheng and Fox (2016a) concluded that this type of numerical model has the capability to simulate the performance of GRS bridge abutments for service loading conditions. In the current study, the model is enhanced by incorporating strain softening behavior for the backfill soil and rate-dependent behavior for the geosynthetic reinforcement to simulate the load-deformation behavior of GRS bridge abutments up to failure condition. *FLAC* is applicable for plane strain conditions, which represents a simplification for these three-dimensional structures.

5.2.1.1 Model Geometry

The finite difference grid and boundary conditions for the GRS bridge abutment model are shown in Figure 5.1. This model represents a single-span bridge system with a span L_b = 30 m and symmetrical structures on both ends. Each end structure consists of a lower GRS wall (i.e., GRS bridge abutment), bridge seat, upper GRS fill, and approach roadway. Only the right-hand side of the bridge system was simulated due to symmetry. The GRS bridge abutment has a height h = 5 m and 25 modular facing blocks with dimensions of 0.3 m × 0.2 m (length × height). An L-shaped bridge seat with a thickness of 0.4 m rests on top of the GRS bridge abutment and has a setback distance a_b = 0.2 m from the wall facing. The clear distance between the top of facing and bottom of bridge structure d_e is equal to the bridge seat thickness of 0.4 m. The clearance height for the bridge structure is 5.4 m, which satisfies the FHWA minimum requirement of 4.9 m for interstate highways (Stein and Neuman 2007). The bridge seat has a contact length L_c = 1.0 m for the bridge structure and a length L_f = 1.5 m on the bottom surface. There is a 100 mm-wide expansion joint between the bridge structure and seat. Assuming a bridge span-to-depth ratio $R_{sd} = L_b/D$ = 20, the depth of the bridge structure D = 1.5 m. A 1.8 m-high upper GRS fill lies behind the seat and has a 0.1 m-thick concrete roadway on top. The reinforcement has a uniform length L_r = 3.5 m (0.7h) and vertical spacing S_v = 0.2 m for both the GRS bridge abutment and upper GRS fill.

To minimize the influence of boundary conditions on system response, the foundation soil has a depth of 10 m (2h) and the rear boundary is located at 20 m (4h) behind the wall facing. Lateral boundaries are fixed in the horizontal direction and free to

move in the vertical direction, whereas the bottom boundary is fixed in both horizontal and vertical directions.

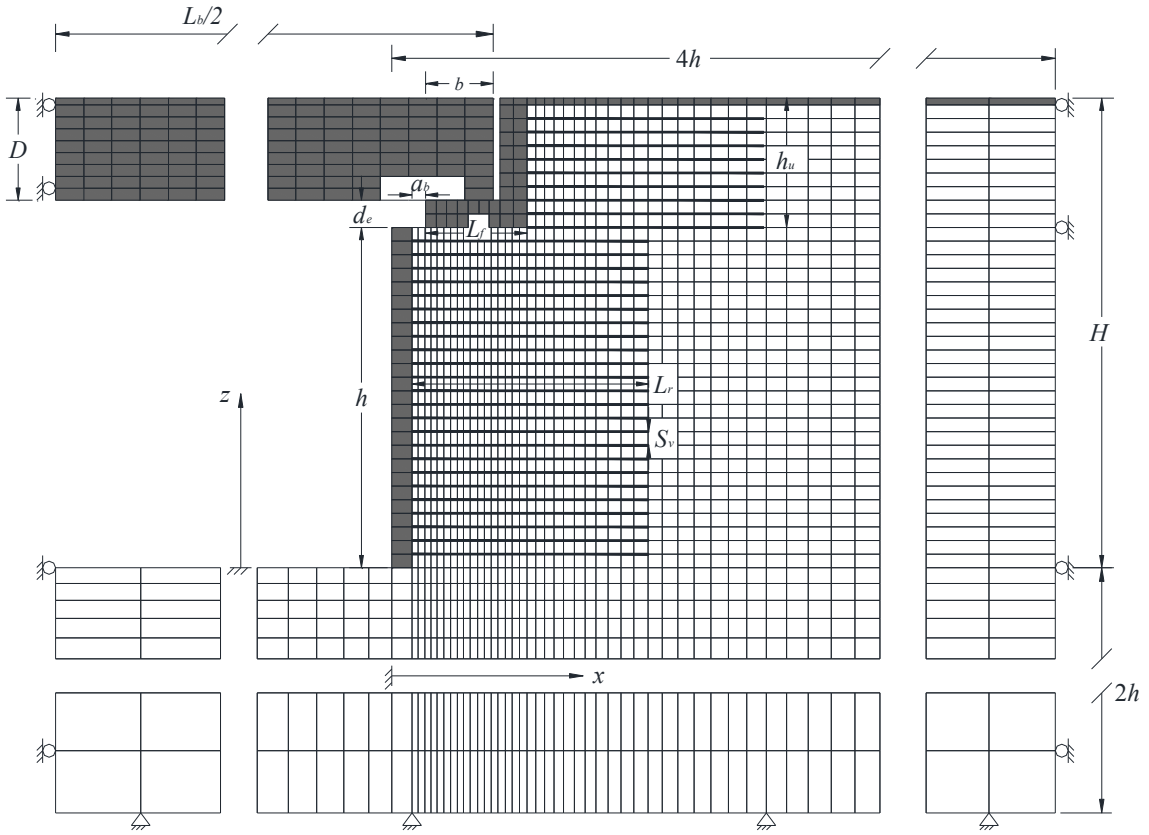

Figure 5.1 Finite difference grid and boundary conditions for GRS bridge abutment model.

5.2.1.2 Soils

Zheng and Fox (2016a) successfully simulated the static response of GRS bridge abutments for the service limit state using a nonlinear elastic-plastic model with the Duncan-Chang hyperbolic relationship (Duncan et al. 1980) and Mohr-Coulomb failure criterion. In the current investigation, the model is enhanced to incorporate strain softening behavior of soil at larger strain levels (e.g., > 5%) to simulate the response of GRS bridge

abutments at the strength limit state. In this model, the tangent elastic modulus E_t, unloading-reloading modulus E_{ur}, bulk modulus B, and tangent Poisson's ratio v_t are expressed as follows (Duncan et al. 1980)

$$E_t = \left[1 - \frac{R_f(1-\sin\phi')(\sigma_1' - \sigma_3')}{2c'\cos\phi' + 2\sigma_3'\sin\phi'}\right]^2 Kp_a\left(\frac{\sigma_3'}{p_a}\right)^n \tag{5.1}$$

$$E_{ur} = K_{ur}p_a\left(\frac{\sigma_3'}{p_a}\right)^n \tag{5.2}$$

$$B = K_b p_a\left(\frac{\sigma_3'}{p_a}\right)^m \tag{5.3}$$

$$v_t = \frac{1}{2} - \frac{E_t}{6B} \tag{5.4}$$

where σ_1' and σ_3' = major and minor principal effective stresses; ϕ' = friction angle; c' = cohesion; R_f = failure ratio; K = elastic modulus number; n = elastic modulus exponent; p_a = atmospheric pressure; K_{ur} = unloading-reloading modulus number; K_b = bulk modulus number; m = bulk modulus exponent; and v_t is limited to a range of 0 to 0.49. Equations (5.1), (5.2), (5.3), and (5.4) were implemented into *FLAC* using FISH subroutines to update the stress-dependent soil moduli during the course of each simulation. To account for strain softening behavior, the friction angle and dilation angle are defined as piece-wise linear functions of plastic shear strain, which can be calibrated using triaxial test data. The friction angle and dilation angle are interpolated according to the defined functions and are updated at each timestep.

Properties for the backfill soil of the GRS bridge abutment were based on a well-graded angular sand with maximum particle size d_{max} = 9.5 mm. Consolidated-drained (CD)

triaxial tests were conducted on sand specimens at five levels of effective confining stress. The specimens were compacted at a relative density of 80% with unit weight γ = 17.3 kN/m^3. Triaxial tests were numerically simulated for axisymmetric loading, and soil parameters were calibrated using the experimental results. The resulting functions for friction angle and dilation angle are shown in Figure 5.2. Post-peak evolution of friction angle and dilation angle are based on cumulative values of plastic shear strain ε_p, which begins to accrue once a soil element reaches the Mohr-Coulomb failure criterion. The soil responds with peak values of friction angle and dilation angle of $\phi_p' = 46°$ and $\psi_p = 17°$, respectively, up to a plastic shear strain $\varepsilon_p = 4\%$. At this point, both angles experience a linear decrease in magnitude to $\varepsilon_p = 15\%$ and are constant thereafter. The constant volume (i.e., steady state) values of friction angle and dilation angle are $\phi_{cv}' = 43°$ and $\psi_{cv} = 0°$, respectively. Using these parameters, a comparison of measured and simulated triaxial test results is shown in Figure 5.3. The nonlinear stress-strain behavior before peak strength and post-peak strain softening behavior are characterized with reasonable accuracy using this approach. The simulated response for decreasing dilation with increasing strain is also in reasonable agreement with the measured data.

The foundation soil was specified as a dense silty sandy gravel and simulated using a linearly elastic-perfectly plastic model with the Mohr-Coulomb failure criterion. A firm foundation soil was used for all simulations so that the response of the GRS bridge abutments would not be affected by foundation stiffness. A summary of properties for the backfill soil and foundation soil is provided in Table 5.1.

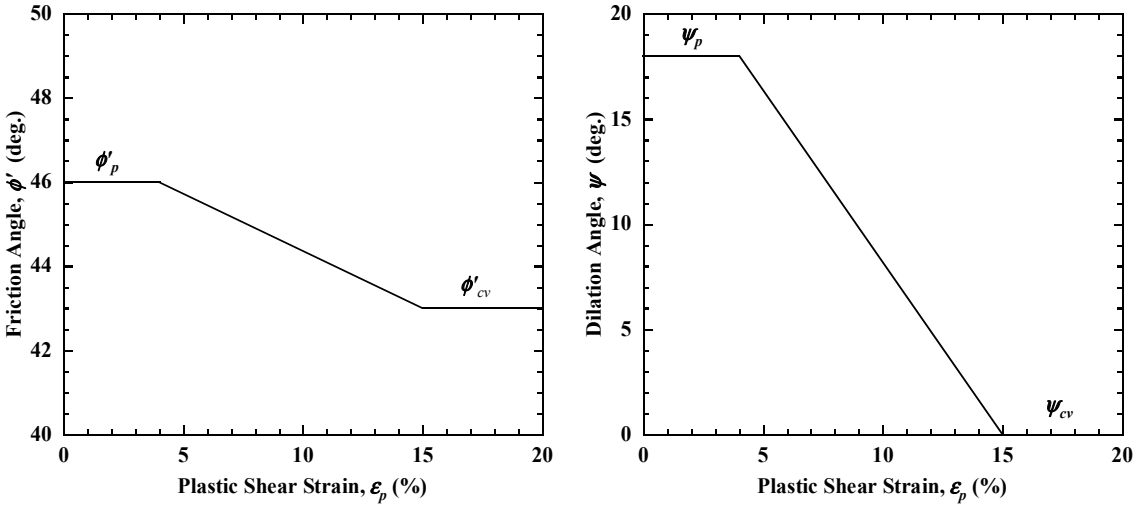

(a) (b)

Figure 5.2 Variation of soil parameters with plastic shear strain: (a) friction angle; (b) dilation angle

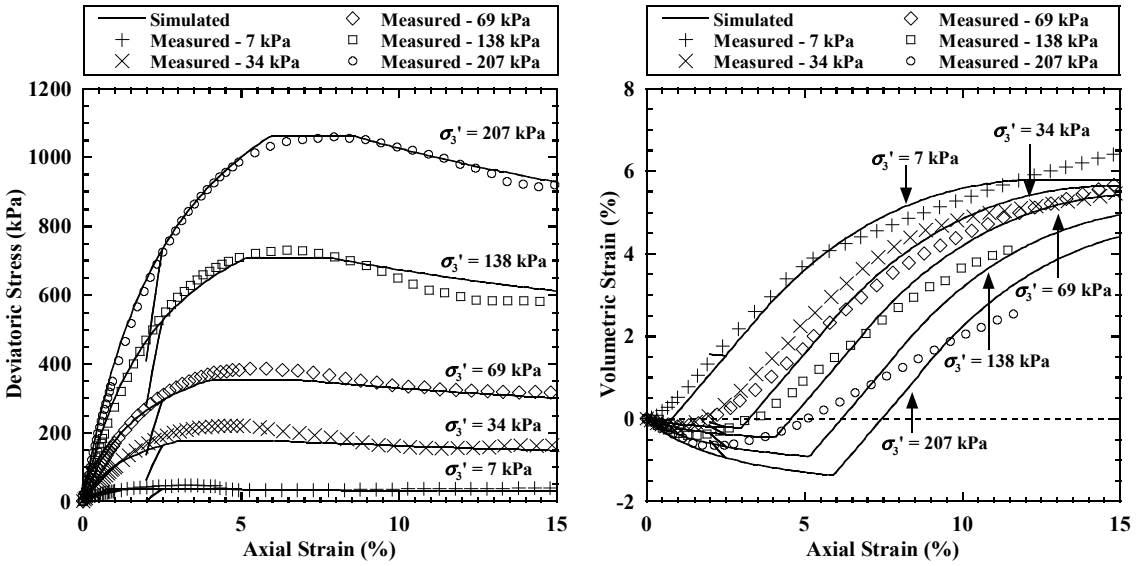

(a) (b)

Figure 5.3 Comparison of measured and simulated triaxial test results: (a) deviatoric stress vs. axial strain; (b) volumetric strain vs. axial strain.

Table 5.1 Soil properties.

Property	Value
Backfill soil	
Unit weight, γ (kN/m^3)	17.3
Elastic modulus number, K	334
Unloading-reloading elastic modulus number, K_{ur}	401
Elastic modulus exponent, n	0.66
Failure ratio, R_f	0.67
Bulk modulus number, B	254
Bulk modulus exponent, m	0
Atmospheric pressure, p_a (kPa)	101.3
Cohesion, c' (kPa)	0
Peak friction angle, ϕ_p' (°)	46
Constant volume friction angle, ϕ_{cv}' (°)	43
Peak dilation angle, ψ_p (°)	18
Constant volume dilation angle, ψ_{cv} (°)	0
Foundation soil[1]	
Unit weight, γ (kN/m^3)	21.7
Elastic modulus, E (MPa)	80
Poisson's ratio, v	0.3
Cohesion, c' (kPa)	2.0
Friction angle, ϕ' (°)	54
Dilation angle, ψ (°)	14

[1] from Yu et al. (2016).

5.2.1.3 Reinforcements

A typical high density polyethylene (HDPE) uniaxial geogrid was specified for the GRS bridge abutment and characterized using the hyperbolic load-strain-time model proposed by Allen and Bathurst (2014a, 2014b) for rate-dependent behavior. Detailed information on this model is provided by Yu et al. (2016). Tensile force is calculated as the product of a strain-dependent and time-dependent secant stiffness $J_s(\varepsilon,t)$ and axial strain ε, as follows:

$$T(\varepsilon,t) = J_s(\varepsilon,t) \times \varepsilon \tag{5.5}$$

where

$$J_s(\varepsilon,t) = \frac{1}{\frac{1}{J_0(t)} + \chi(t)\varepsilon} \tag{5.6}$$

and $J_0(t)$ = initial tangent stiffness, $\chi(t)$ = empirical fitting parameter, and t = time. Tangent stiffness of the reinforcement is calculated as:

$$J_t(\varepsilon,t) = \frac{1}{J_0(t)[\frac{1}{J_0(t)} + \chi(t)\varepsilon]^2} \tag{5.7}$$

Yu et al. (2016) found that the stiffness values are not significantly affected by practical times of interest. As such, a typical end-of-construction (EOC) time t = 3600 hours was assumed for the current simulations.

Tensile behavior of the HDPE geogrid (Geogrid-2), shown in Figure 5.4, indicates that initial stiffness J_0 = 596 kN/m and tensile stiffness decreases with increasing strain. The geogrid reinforcement was simulated using cable elements and rigidly connected to

the facing blocks. In *FLAC*, the actual input parameter of elastic modulus was calculated as

$$E_r = J_t(\varepsilon, t) / t_r \tag{5.8}$$

where t_r is the thickness of geogrid. During construction and loading stages of the numerical simulations, the elastic modulus of each cable element was updated according to Equations (5.7) and (5.8) with t = 3600 hours. A summary of reinforcement parameters for Geogrid-2 is provided in Table 5.2. Geogrid-1 and Geogrid-3 are discussed later for the parametric study.

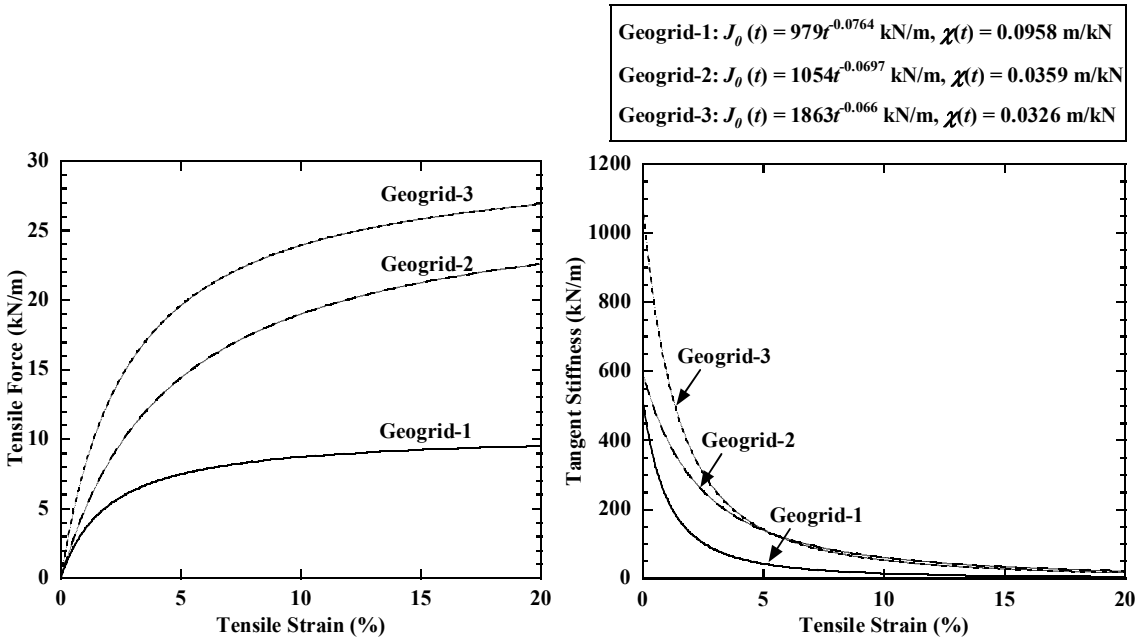

(a) (b)

Figure 5.4 Tensile behavior of HDPE geogrids at t = 3600 hours: (a) tensile force-strain relationship; (b) tangent stiffness (parameters from Yu et al. (2016)).

Table 5.2 Reinforcement properties.

Property	Geogrid-1	Geogrid-2	Geogrid-3
Elastic modulus, E_r	Variable[a]	Variable[a]	Variable[a]
Cross-sectional area, A_r	0.002 m^2	0.002 m^2	0.002 m^2
Thickness, t_r	0.002 m	0.002 m	0.002 m
Perimeter, P_r	2.004 m	2.004 m	2.004 m
Tensile strength @5% strain, $T_{5\%}$[b]	27 kN/m	31 kN/m	52 kN/m
Ultimate tensile strength, T_{ult}[b]	58 kN/m	70 kN/m	114 kN/m

[a] Calculated based on parameters reported by Yu et al. (2016).
[b] Provided by manufacturer.

5.2.1.4 Structural Components

The concrete modular facing blocks, bridge seat, and roadway were modeled as linearly elastic materials with unit weight $\gamma = 23.5$ kN/m^3, elastic modulus $E = 20$ GPa, and Poisson's ratio $v = 0.2$. The bridge structure with unit width was modeled as a solid block ($L_b \times D \times 1$) composed of elastic elements with elastic modulus $E = 20$ GPa, and Poisson's ratio $v = 0.2$. The unit weight of the bridge structure γ_b was changed to produce different values of applied vertical stress on the GRS bridge abutment during the loading stage of the numerical simulations. The vertical load per unit width on the GRS bridge abutment was $F_v = L_b D \gamma_b / 2$, and the corresponding applied average vertical stress on the bottom surface of the bridge seat was $q_v = F_v / L_f$.

5.2.1.5 Interfaces

Table 5.3 presents the interface properties for the numerical model. Shear strengths for the various interfaces between soil, geogrid, block, and bridge seat account for frictional sliding and are characterized using a reduction factor RF_i defined as follows:

$$RF_i = \frac{\tan \delta_i}{\tan \phi'} \tag{5.9}$$

where δ_i is the interface friction angle. Considering the typical embedment of wall facing at the toe in the field, a relatively high toe stiffness of 40 MPa/m was selected for the interface between the lowermost facing block and foundation soil (Huang et al. 2010; Yu et al. 2016). The frictional interface between the bridge structure and seat produces a lateral restraining force on the top of the GRS bridge abutment, which has an important effect on abutment deformations (Zheng and Fox 2016a).

Table 5.3 Interface properties.

Property	Soil-geogrid[1]	Soil-block/bridge seat[2]	Block-block[2]	Bridge-bridge seat[2]
Normal stiffness, k_n	-	1,000 MPa/m	100,000 MPa/m	100,000 MPa/m
Shear stiffness, k_s	1 MN/m/m	1 MPa/m	40 MPa/m	40 MPa/m
Friction angle, δ_i	41.4°[3]	33.9°[4]	36.0°[5]	21.8°[6]
Cohesion, c_i'	0	0	58 kPa[5]	0

[1] Included in cable element.
[2] Simulated using interface element.
[3] Based on average of data (RF_i = 0.85) from Vieira et al. (2013).
[4] Based on data (RF_i = 0.65) from Ling et al. (2010).
[5] Based on Yu et al. (2016).
[6] Based on a friction coefficient of 0.4 for bearing pads from Caltrans (1994).

5.2.1.6 Modeling Procedures

For each numerical simulation, the GRS bridge abutment model first was constructed in stages and then loaded to failure. The initial condition corresponds to the equilibrium state of foundation soil under gravitational forces. The GRS bridge abutment was constructed in lifts on top of the foundation. Each lift consisted of one layer of soil, one facing block, and one layer of geogrid reinforcement, with the necessary interfaces included between components. Following the work of Hatami and Bathurst (2006), Guler et al. (2007), Zheng and Fox (2017), and Zheng et al. (2017), a temporary uniform vertical surcharge stress of 8 kPa was applied to the top surface of each soil lift, and then removed prior to placement of the next lift to simulate backfill soil compaction. The bridge seat then was placed on the GRS bridge abutment, the upper GRS fill was constructed in lifts behind the seat, and the approach roadway was placed on the GRS fill. For the loading stage, the initial unit weight of the bridge structure was chosen to produce an initial applied average vertical stress of q_v = 50 kPa on the GRS bridge abutment, and then during the subsequent loading stage the unit weight of bridge structure was increased to produce failure for the GRS bridge abutment. For each construction and loading stage, the numerical model was resolved to an equilibrium condition. Abutment failure was assumed to occur if *FLAC* could not converge to equilibrium or the abutment reached a vertical strain of 10%.

5.2.2 Simulation Results

A baseline case is defined by the above modeling conditions and parameters. Simulations were also performed for two additional cases to investigate the effects of soil strain softening behavior and nonlinear behavior of geosynthetic reinforcement on the load-deformation response of the GRS bridge abutment. The first additional case assumes perfectly plastic soil (PPS) with constant friction angle and dilation angle ($\phi' = 46°$ and $\psi = 18°$) and nonlinear reinforcement (as in baseline case), and the second additional case assumes linearly elastic reinforcement (LER) with constant stiffness corresponding to a secant stiffness at 5% tensile strain $J_{5\%} = 620$ kN/m, and nonlinear strain softening soil (as in baseline case).

Figure 5.5(a) presents lateral facing displacement profiles for all three cases and two levels of applied vertical stress $q_v = 400$ kPa and 800 kPa. At $q_v = 400$ kPa, a maximum lateral facing displacement of 60.6 mm occurs near the top of the wall at elevation $z = 4.2$ m above the foundation soil for the baseline case. Lateral facing displacements for the baseline and PPS cases are in close agreement, and are larger than those for the LER case. At $q_v = 800$ kPa, lateral facing displacements increase significantly and the trends are similar and more exaggerated. The baseline case yields the largest facing displacements, with a maximum value of 148.4 mm at $z = 4.0$ m. Maximum lateral facing displacements for the PPS and LER cases are 138.0 mm and 75.0 mm, respectively. Corresponding profiles of maximum reinforcement tensile force are presented in Figure 5.5(b). At $q_v = 400$ kPa, the maximum tensile force (13.9 kN/m) occurs at $z = 4.8$ m for the baseline case with an associated reinforcement strain of 4.7%. The factor of safety (FS) against

reinforcement rupture, based on the ultimate strength of 70 kN/m (Table 5.2), is equal to 5.0. For the PPS and LER cases, maximum tensile forces are 13.7 kN/m and 16.1 kN/m, and factors of safety are 5.1 and 4.3, respectively. The maximum tensile forces for the baseline and PPS cases are in close agreement, and are slightly smaller than for the LER case. At q_v = 800 kPa, maximum tensile forces increase and the trends are similar. However, the maximum tensile forces for the LER case are much larger than for the baseline and PPS cases near the top of the wall. The maximum tensile force of 21.3 kN/m occurs at z = 4.6 m for the baseline case with a corresponding reinforcement strain of 14.4% and yields FS = 3.3. Maximum tensile forces are 21.0 kN/m and 33.6 kN/m for the PPS and LER cases, respectively, and the corresponding FS values are equal to 3.3 and 2.1.

Figure 5.5 also shows that, for the LER case, lateral facing displacements are significantly less whereas maximum tensile forces are significantly larger for q_v = 800 kPa, which suggests that the geosynthetic constitutive model has a significant effect on the results. At higher applied stress conditions, the maximum tensile forces for the baseline case are slightly larger than for the PPS case because the soil gets softer and, as a result, the reinforcement picks up more load. As strain increases, the tensile forces increase significantly for the linearly reinforcement, whereas the forces increase more slowly for the two other cases with nonlinear reinforcement because the reinforcement stiffness decreases significantly with increasing strain (Figure 5.4). This contributed to the smaller lateral facing displacements and larger reinforcement tensile forces for the LER case.

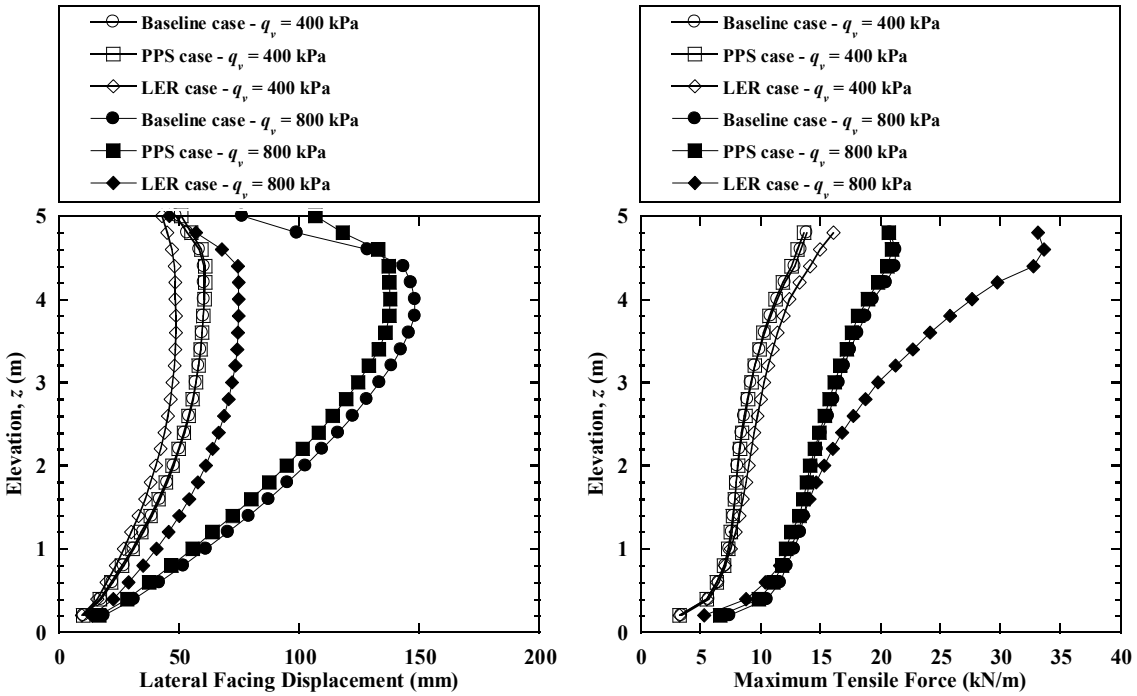

Figure 5.5 Simulation results for q_v = 400 kPa and 800 kPa: (a) lateral facing displacement; (b) maximum reinforcement tensile force.

Figure 5.6 presents plots of maximum lateral facing displacement, average abutment compression, and corresponding average abutment vertical strain (ε_v) vs. applied vertical stress (q_v) for the three simulation cases. Abutment compression is defined as the difference between average downward displacement of the bridge seat and average downward displacement of the foundation soil. Values of maximum lateral facing displacement $\Delta_{h,200}$ and average abutment compression $\Delta_{v,200}$ at q_v = 200 kPa for the service limit state, along with the applied vertical stresses at ε_v = 0.5% ($q_{0.5\%}$) and 5% ($q_{0.5\%}$), are presented in Table 5.4. At q_v = 200 kPa, $\Delta_{h,200}$ = 38.0 mm and $\Delta_{v,200}$ = 33.6 mm for baseline and PPS cases, and $\Delta_{h,200}$ = 35.2 mm and $\Delta_{v,200}$ = 31.3 mm for LER case. At the service limit state, the $q_{0.5\%}$ value of 127 kPa for LER case is slightly larger than for the baseline and PPS cases (118 kPa). This indicates that the effect of reinforcement nonlinear behavior

is relatively small at the service limit state. According to FHWA guidelines (Nicks et al. 2013a, 2016), the bearing capacity for the service limit state $q_{0.5\%}$ is 10% of the ultimate bearing capacity q_{ult}, and is calculated as (Wu and Pham 2013; Wu et al. 2013)

$$q_{0.5\%} = 10\% q_{ult} = 10\%[0.7^{\frac{S_v}{6d_{max}}}(\frac{T_{ult}}{S_v})]K_{pr} \tag{5.10}$$

where K_{pr} is the Rankine passive earth pressure coefficient and T_{ult} is the ultimate tensile strength of reinforcement. Using Equation (5.10), the calculated value of $q_{0.5\%}$ is 61 kPa for the baseline case, which is approximately one-half of the numerically simulated value of 118 kPa. Similar conservative results for Equation (5.10) were also reported by Nicks et al. (2016) for GRS mini-pier loading tests using a well-graded soil. At the strength limit state ($\varepsilon_v = 5\%$), a numerical simulation with the perfectly plastic soil model yielded a higher bearing capacity by 14% than the baseline case, and the linearly elastic reinforcement model yielded a higher bearing capacity by 75%.

Table 5.4 Deformations and vertical stresses for service and strength limit states.

	Service limit			Strength limit
	$\Delta_{h,200}$ (mm)	$\Delta_{v,200}$ (mm)	$q_{0.5\%}$ (kPa)	$q_{5\%}$ (kPa)
Baseline	38.0	33.6	118	917
Perfectly plastic soil	38.0	33.6	118	1043
Linearly elastic reinforcement	35.2	31.3	127	1600

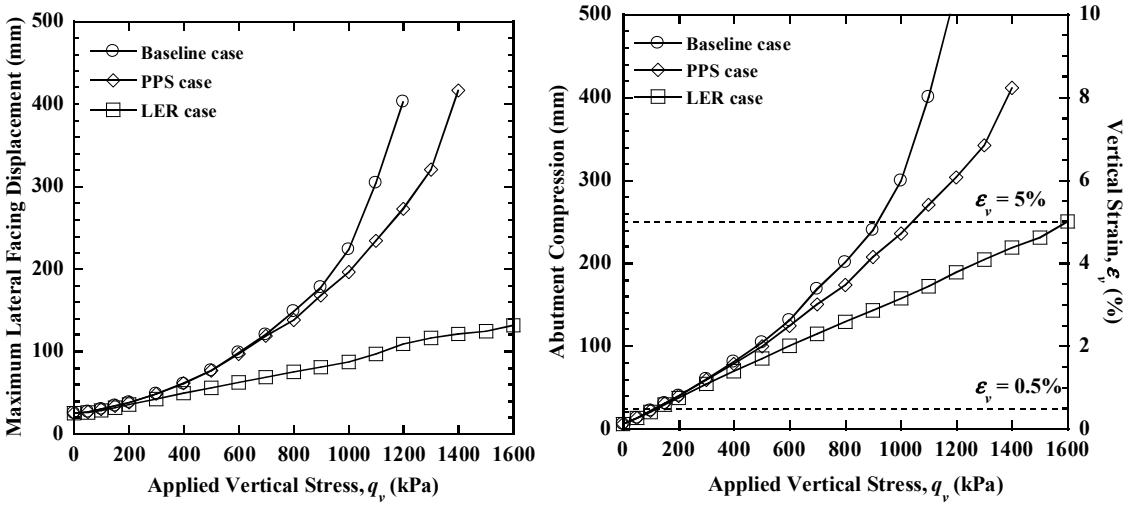

(a) (b)

Figure 5.6 Simulation results: (a) maximum lateral facing displacement; (b) abutment compression and vertical strain.

In general, Figure 5.6 indicates that the baseline and PPS cases display nonlinear responses, whereas the LER case yields a nearly linear response for both lateral facing displacement and abutment compression deformations. Deformations are essentially equal for the baseline and PPS cases for $q_v \leq 600$ kPa because the soil has not reached a strain softening condition. Beyond 600 kPa, the baseline case shows a softer response than for the PPS case. Deformations for the LER case are close to the baseline case for $q_v \leq 200$ kPa, and then deviate substantially with increasing applied vertical stress. This suggests that, for the conditions considered, a linearly elastic reinforcement model can capture the deformation behavior of GRS bridge abutments for service loads, but not for larger applied loads approaching failure. However, the selection of a single stiffness value for the reinforcement is challenging. In the current study, the $J_{5\%}$ value gives good accuracy for $q_v \leq 200$ kPa. However, a nonlinear reinforcement model is needed to capture deformation behavior for larger applied stresses.

5.3 Parametric Study

A parametric study was conducted to investigate the effects of various reinforcement and backfill soil, and abutment geometry parameters on the load-deformation behavior of GRS bridge abutments. The variables are reinforcement spacing, reinforcement stiffness, reinforcement length, secondary reinforcement, soil cohesion, soil friction angle, soil dilation angle, bridge seat setback distance, bridge seat length, and abutment height. For each series of simulations, only the variable of interest was changed and the other variables were held constant and equal to values for the baseline case. Results for deformations and vertical stresses for the service and strength limit states are summarized in Table 5.5.

Table 5.5 Deformations and vertical stresses for service and strength limit states.

		Service limit			Strength limit
		$\Delta_{h,200}$ (mm)	$\Delta_{v,200}$ (mm)	$q_{0.5\%}$ (kPa)	$q_{5\%}$ (kPa)
Reinforcement spacing	0.2 m	38.0	33.6	118	917
	0.4 m	60.5	48.0	82	519
	0.6 m	93.6	70.2	65	364
Reinforcement stiffness	Geogrid-1	47.6	41.5	104	500
	Geogrid-2	38.0	33.6	118	917
	Geogrid-3	30.7	28.8	143	1121
Reinforcement length	0.3*h*	65.4	46.8	101	523
	0.5*h*	40.3	34.5	115	898
	0.7*h*	38.0	33.6	118	917
	0.9*h*	37.5	33.5	119	925
	1.1*h*	37.5	33.5	119	948
No. of secondary reinforcement	0	38.0	33.6	118	917
	5	37.0	32.7	123	1007
	10	35.0	31.6	127	1117
	15	34.0	30.9	131	1232
Backfill soil cohesion	0 kPa	38.0	33.6	118	917
	10 kPa	33.6	31.5	127	975
	20 kPa	32.8	31.0	128	1037
	30 kPa	32.5	30.2	128	1091
Backfill soil friction angle	38°	51.4	40.7	99	682
	42°	43.7	36.9	108	805
	46°	38.0	33.6	118	917
	50°	34.3	31.2	127	1059
Backfill soil dilation angle	6°	39.4	39.7	105	777
	12°	38.7	36.0	113	852
	18°	38.0	33.6	118	917
	24°	38.0	32.3	123	968
Bridge seat setback distance	0.2 m	38.0	33.6	118	917
	0.6 m	40.0	32.5	131	962
	1.0 m	39.1	30.8	146	1040
	1.4 m	38.5	28.2	157	1127
Bridge seat length	1.0 m	35.4	29.0	127	983
	1.5 m	38.0	33.6	118	917
	2.0 m	40.9	37.7	115	907
	2.5 m	42.3	38.5	115	980
Abutment height	3.0 m	26.7	23.9	143	926
	5.0 m	38.0	33.6	118	917
	7.0 m	49.2	39.9	137	1008
	9.0 m	60.6	43.1	158	1049

5.3.1 Effect of Reinforcement Spacing

Numerical simulations were conducted for reinforcement vertical spacing S_v = 0.2 m, 0.4 m, and 0.6 m. Figure 5.7 indicates that deformations of GRS bridge abutments increase significantly with increasing reinforcement spacing. For instance, $\Delta_{h,200}$ increases significantly from 38.0 mm to 93.6 mm when S_v increases from 0.2 m to 0.6 m, and $\Delta_{v,200}$ also increases from 33.6 mm to 70.2 mm. At the service limit state, a value of $q_{0.5\%}$ = 118 kPa for S_v = 0.2 m is nearly twice that for S_v = 0.6 m (65 kPa). At the strength limit state, $q_{5\%}$ decreases significantly from 917 kPa to 519 kPa to 364 kPa when S_v increases from 0.2 m to 0.4 m to 0.6 m.

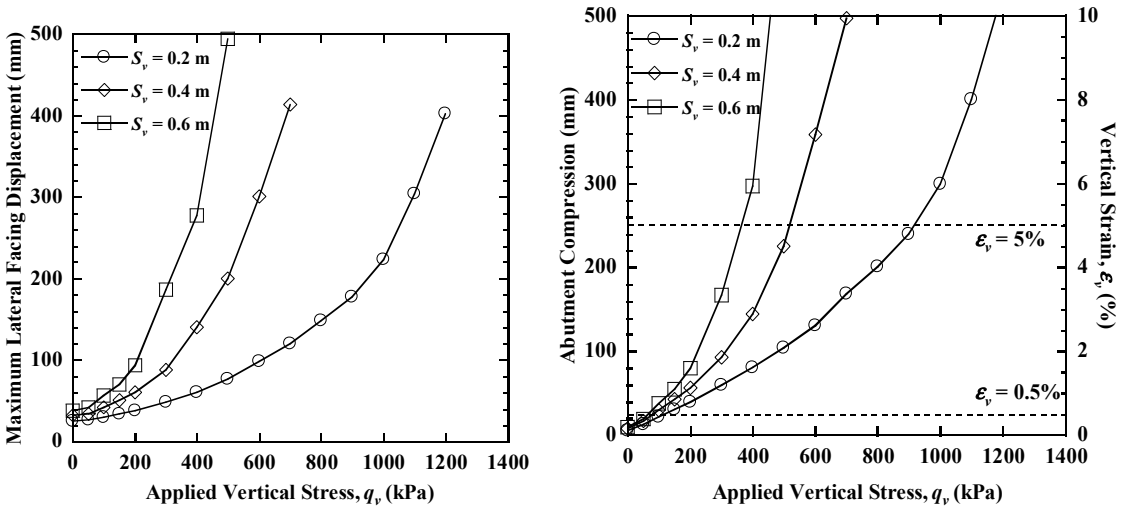

(a) (b)

Figure 5.7 Effect of reinforcement spacing: (a) maximum lateral facing displacement; (b) abutment compression and vertical strain.

5.3.2 Effect of Reinforcement Stiffness

Simulations were conducted for three geogrids, Geogrid-1, Geogrid-2 (baseline), and Geogrid-3, as originally described by Yu et al. (2016). The material properties are provided in Table 5.2 and tensile responses are shown in Figure 5.4. As shown in Figure 5.8, the maximum lateral facing displacement and abutment compression decrease significantly with increasing reinforcement stiffness. At q_v = 200 kPa, $\Delta_{h,200}$ decreases from 47.6 mm to 30.7 mm and $\Delta_{v,200}$ decreases from 41.5 mm to 28.8 mm when reinforcement changes from Geogrid-1 to Geogrid-3. As reinforcement stiffness increases, $q_{0.5\%}$ increases from 104 kPa to 143 kPa and $q_{5\%}$ increases significantly from 500 kPa to 1121 kPa.

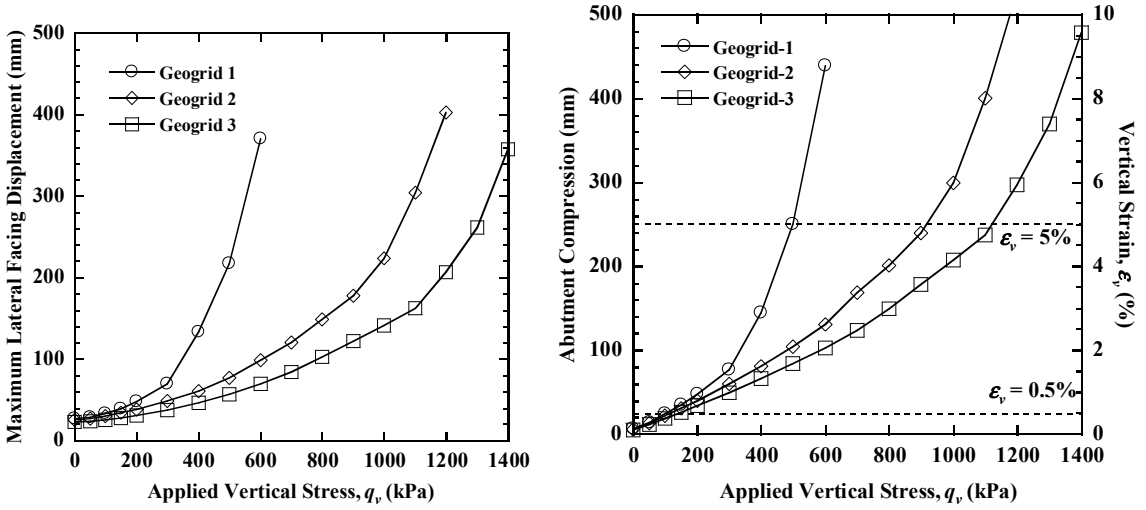

(a) (b)

Figure 5.8 Effect of reinforcement stiffness: (a) maximum lateral facing displacement; (b) abutment compression and vertical strain.

5.3.3 Effect of Reinforcement Length

Figure 5.9 presents results for L_r = 0.3h, 0.5h, 0.7h, 0.9h, and 1.1h, and indicates that deformations only decrease slightly with increasing reinforcement length for $L_r \geq 0.5h$, which is consistent with the findings of Zheng and Fox (2016a) for the service limit state. Numerical simulation results also indicated that reinforcement elongation, rather than reinforcement pullout, is the predominant failure mode for internal instability. At the strength limit state, $q_{5\%}$ increases from 898 kPa to 948 kPa when L_r increases from 0.5h to 1.1h. For L_r = 0.3h (= 1.5 m), the deformations are much larger than the other cases and failure occurs at a lower applied vertical stress. In this case, the reinforcement did not extend beyond the failure surface, which at the top of the wall intersects the heel of the bridge seat (distance from wall facing x = 1.7 m).

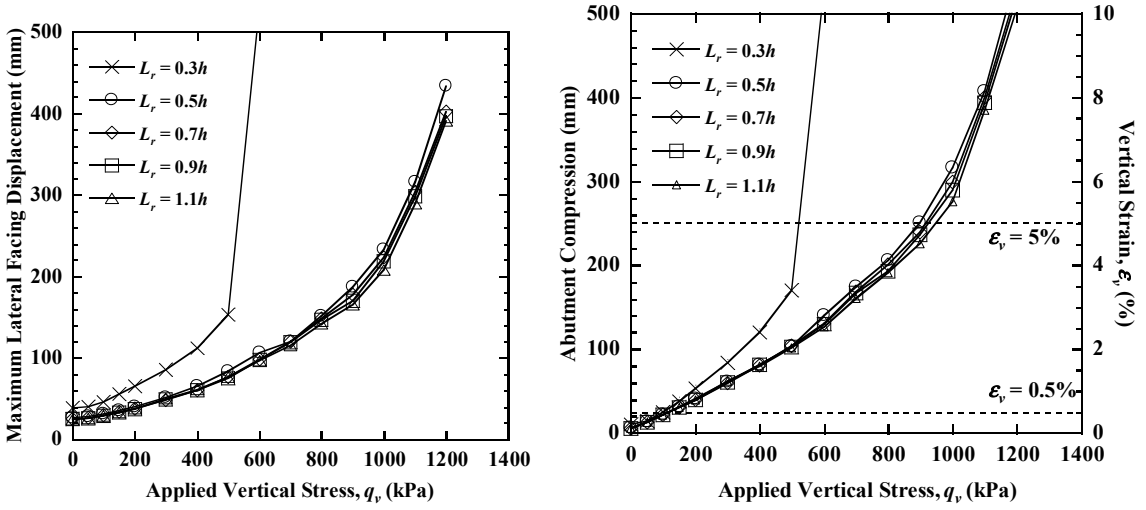

(a) (b)

Figure 5.9 Effect of reinforcement length: (a) maximum lateral facing displacement; (b) abutment compression and vertical strain.

5.3.4 Effect of Secondary Reinforcement

Secondary reinforcement layers are included below the bridge seat to provide additional support for the GRS-IBS design (Adams et al. 2011b). In the current study, numerical simulations were conducted for secondary reinforcement layer number n_{sr} = 0, 5, 10, and 15, where n_{sr} = 0 indicates no secondary reinforcement and n_{sr} = 15 represents 15 layers of secondary reinforcement between elevations z = 2.0 m and 5.0 m. The secondary reinforcement layers had a length of $L_f + 2a_b$ (= 1.9 m) and were not connected to the facing blocks (Adams et al. 2011b). Figure 5.10 indicates that when n_{sr} increases from 0 to 15, the deformations are only slightly reduced for $q_v \leq 200$ kPa. At higher stress levels, abutment deformations are significantly lower for increasing secondary reinforcement layers. At the strength limit state, $q_{5\%}$ increases from 917 kPa for n_{sr} = 0 to 1232 kPa for n_{sr} = 15. The results are consistent with results from large-scale loading tests on GRS mini-piers that show secondary reinforcement is unlikely to reduce abutment compression for design-level stresses but can increase the ultimate bearing capacity (Nicks et al. 2013a).

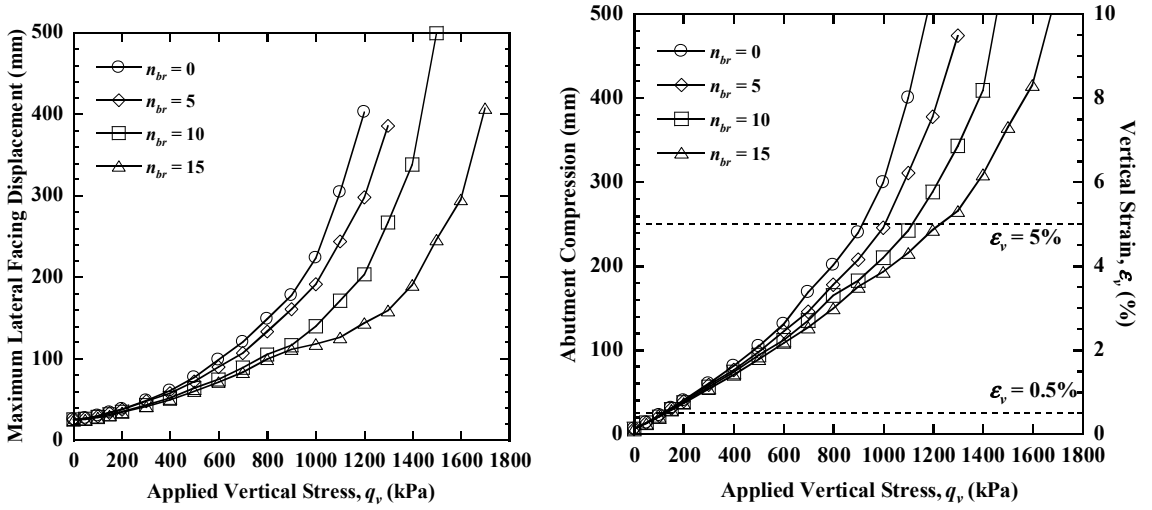

(a) (b)

Figure 5.10 Effect of secondary reinforcement: (a) maximum lateral facing displacement; (b) abutment compression and vertical strain.

5.3.5 Effect of Backfill Soil Cohesion

Figure 5.11 presents results for c = 0, 10 kPa, 20 kPa, and 30 kPa. The effect of increasing soil cohesion on abutment deformations is relatively small for $q_v \leq 200$ kPa, but becomes more significant as q_v increases beyond 200 kPa. As cohesion increases from 0 to 30 kPa, $q_{0.5\%}$ increases slightly from 118 kPa to 128 kPa and $q_{5\%}$ increases from 917 kPa to 1091 kPa.

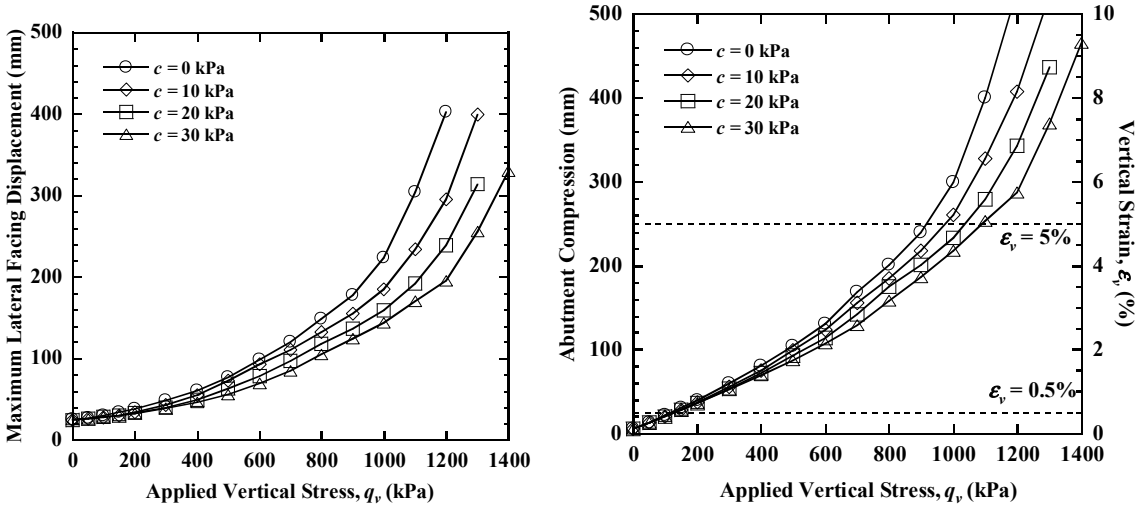

(a) (b)

Figure 5.11 Effect of backfill soil cohesion: (a) maximum lateral facing displacement; (b) abutment compression and vertical strain.

5.3.6 Effect of Backfill Soil Friction Angle

Simulations were conducted for ϕ_p' = 38°, 42°, 46°, and 52°, with corresponding ϕ_{cv}' = 35°, 39°, 43°, and 49°, respectively. Figure 5.12 indicates that friction angle has a significant effect on the deformations, for both the service and strength limit states. For instance, $\Delta_{h,200}$ decreases from 51.4 mm to 34.3 mm when ϕ_p' increases from 38° to 52°, and $\Delta_{v,200}$ also decreases from 40.7 mm to 31.2 mm. As ϕ_p' increases from 38° to 52°, $q_{0.5\%}$ increases from 99 kPa to 127 kPa at the service limit state and $q_{5\%}$ increases significantly from 682 kPa to 1059 kPa at the strength limit state.

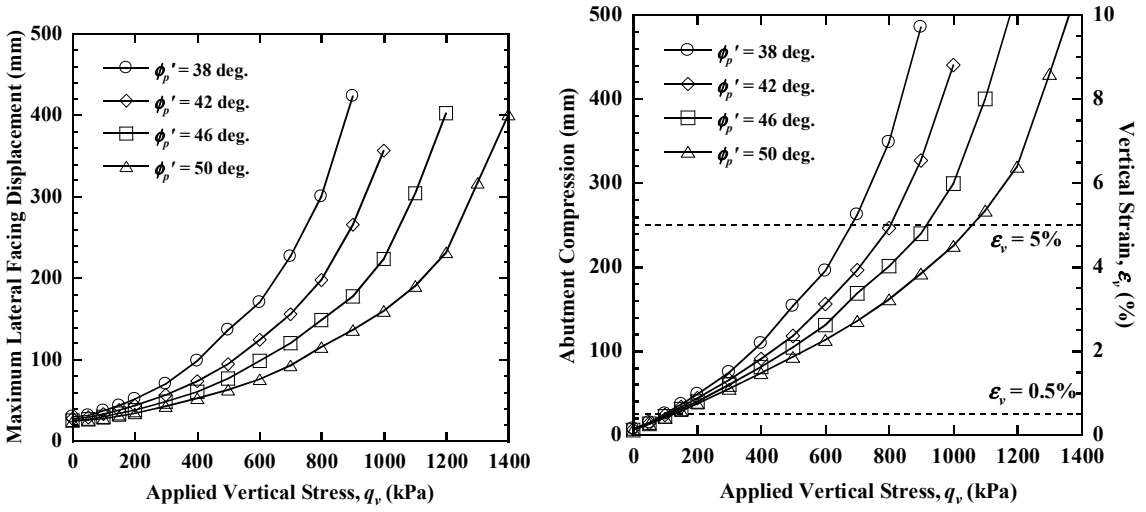

(a) (b)

Figure 5.12 Effect of backfill soil friction angle: (a) maximum lateral facing displacement; (b) abutment compression and vertical strain.

5.3.7 Effect of Backfill Soil Dilation Angle

Figure 5.13 presents results for ψ_p = 6°, 12°, 18°, and 24°. In general, the maximum lateral facing displacements are not significantly affected by dilation angle, whereas abutment compression decreases with increasing ψ_p, especially at higher stress levels. At the strength limit state, $q_{5\%}$ increases from 777 kPa to 968 kPa when ψ_p increases from 6° to 24°.

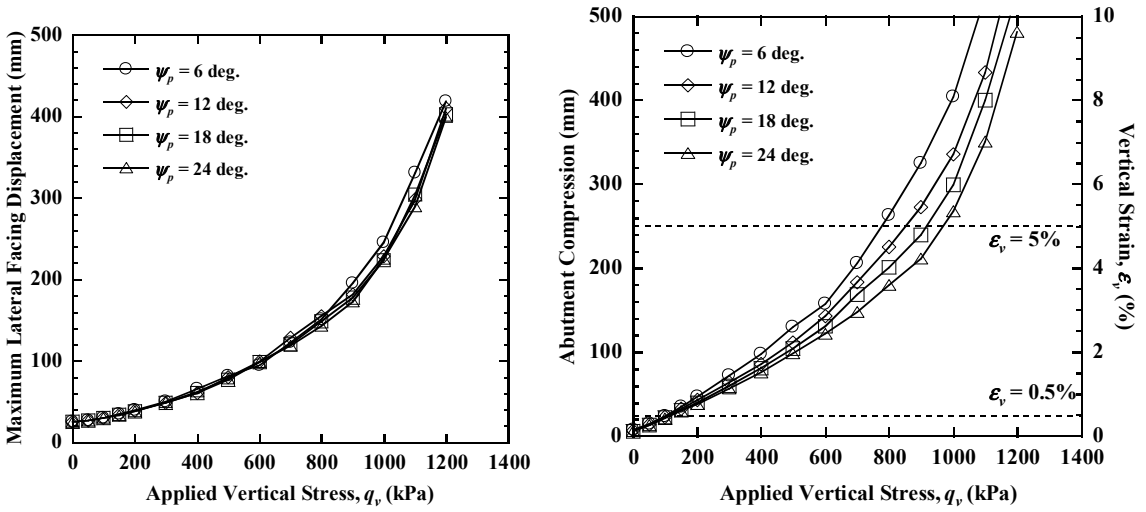

(a) (b)

Figure 5.13 Effect of backfill soil dilation angle: (a) maximum lateral facing displacement; (b) abutment compression and vertical strain.

5.3.8 Effect of Bridge Seat Setback Distance

Figure 5.14(a) presents maximum lateral facing displacements for a_b = 0.2 m, 0.6 m, 1.0 m, and 1.4 m, and indicates that bridge seat setback has little effect for $q_v \leq 600$ kPa, whereas the maximum displacement decreases with increasing a_b beyond 600 kPa. Similar to lateral facing displacements, Figure 5.14(b) shows that abutment compression also decreases slightly as a_b increases from 0.2 m to 1.4 m, and $q_{5\%}$ increases from 917 kPa to 1127 kPa. In general, bridge seat setback shows a relatively small effect on abutment deformations for service loading conditions; therefore, a smaller setback distance may be preferred in the field to shorten the bridge structure, which can reduce the bridge load and project cost.

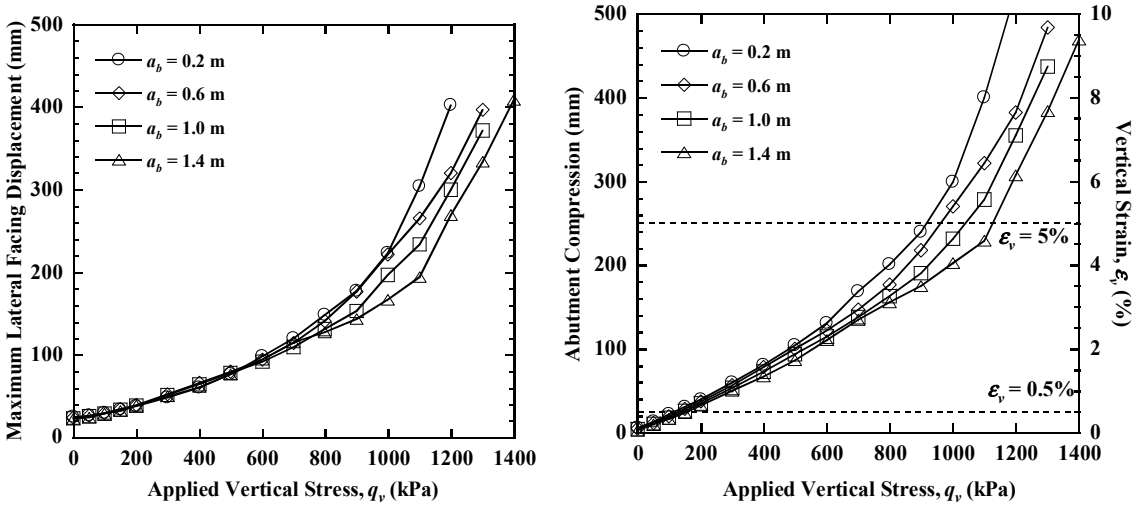

(a) (b)

Figure 5.14 Effect of bridge seat setback distance: (a) maximum lateral facing displacement; (b) abutment compression and vertical strain.

5.3.9 Effect of Bridge Seat Length

Deformations for L_f= 1.0 m, 1.5 m, 2.0 m, and 2.5 m are presented in Figure 5.15. The maximum lateral facing displacement and abutment compression increase moderately with increasing L_f. $q_{5\%}$ decreases from 983 kPa to 917 kPa to 907 kPa when L_f increases from 1.0 m to 1.5 m to 2.0 m. However, for L_f = 2.5 m, the maximum lateral facing displacement curve is similar to L_f= 1.5 m and the abutment compression curve is close to values for L_f= 1.0 m. Similar to bridge seat setback, the bridge seat length has little effect on abutment deformations under service loading conditions.

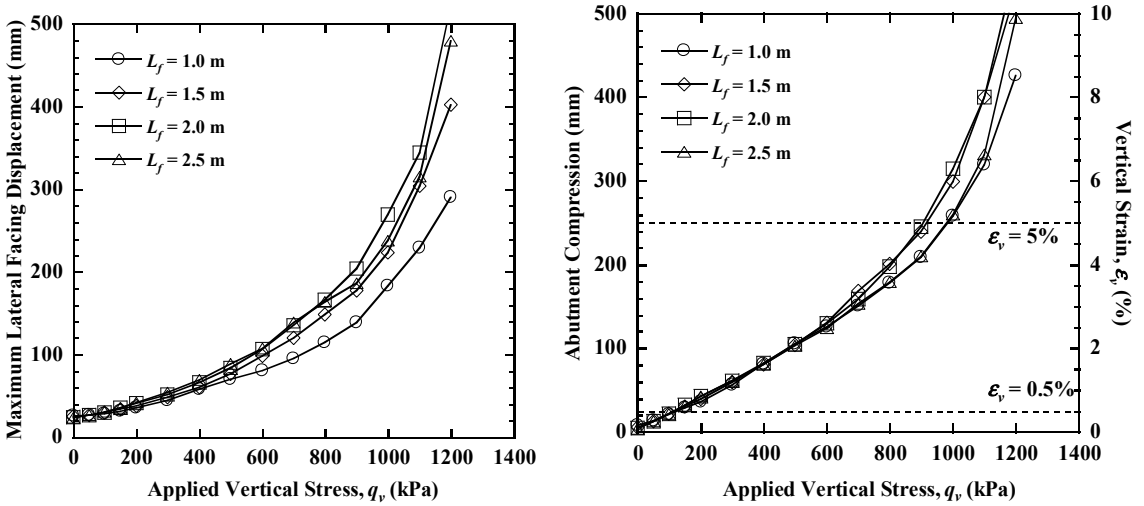

(a) (b)

Figure 5.15 Effect of bridge seat length: (a) maximum lateral facing displacement; (b) abutment compression and vertical strain.

5.3.10 Effect of Abutment Height

Numerical simulations were conducted for GRS bridge abutments with height h = 3 m, 5 m, 7 m, and 9 m. Figure 5.16(a) and (b) show that maximum lateral facing displacement and abutment compression increase with increasing abutment height. At q_v = 200 kPa, $\Delta_{h,200}$ increases from 26.7 mm to 60.6 mm and $\Delta_{v,200}$ increases from 23.9 mm to 43.1 mm when h increases from 3 m to 9 m. The vertical stress-strain relationships normalized by abutment height, shown in Figure 5.16(c), indicate that vertical strain decreases as h increases from 3 m to 9 m for the same applied vertical stress, which indicates that a taller abutment has a stiffer response. This is attributed to the higher average effective stress conditions and larger soil stiffness for taller abutments. These results further suggest that, all else being equal, laboratory or field tests conducted on reduced-scale physical models may yield conservative load-deformation relationships for the design of GRS bridge abutments.

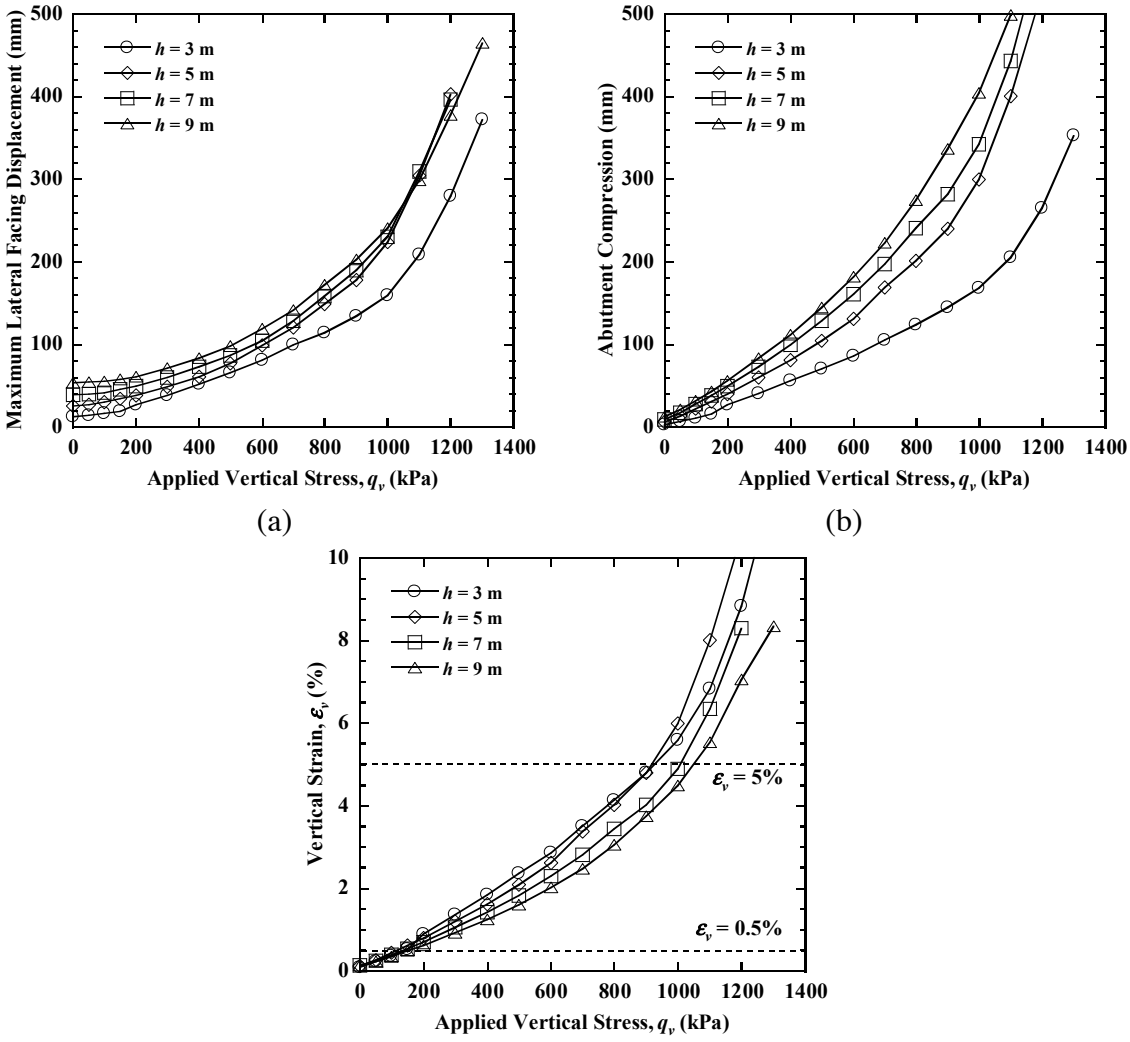

Figure 5.16 Effect of abutment height: (a) maximum lateral facing displacement; (b) abutment compression; (c) vertical strain.

5.4 Failure Mechanisms

The explicit Lagrangian calculation method and mixed-discretization zoning technique used in *FLAC* are well suited to characterize plastic deformations, strain localization, and collapse behavior, and can be used to assess failure of GRS bridge abutments under high load application. The failure surface develops as shear strains increase during the loading stage. Contours of shear strain magnitude for the baseline case at the service limit state and strength limit state are shown in Figure 5.17. At the service limit ($\varepsilon_v = 0.5\%$), shear strains are generally small, as shown in Figure 5.17(a). Shear strains are concentrated at the heel of the bridge seat and indicate a potential failure surface that moves from the heel to the toe of the GRS bridge abutment. At the strength limit ($\varepsilon_v = 5\%$), the GRS bridge abutment is approaching failure as manifested by the formation of continuous large shear strain zones, as shown in Figure 5.17(b). The failure mechanism is a combination of punching shear failure of the bridge seat and internal instability of the GRS bridge abutment, with the internal failure of abutment as the predominant mode. The internal failure surface is indicated by a large shear strain zone that moves nearly vertically downward from the heel of the bridge seat to approximately the mid-height of the abutment, and then to the toe of GRS bridge abutment. A similar failure surface shape was identified by Leshchinsky (2014) using limit analysis.

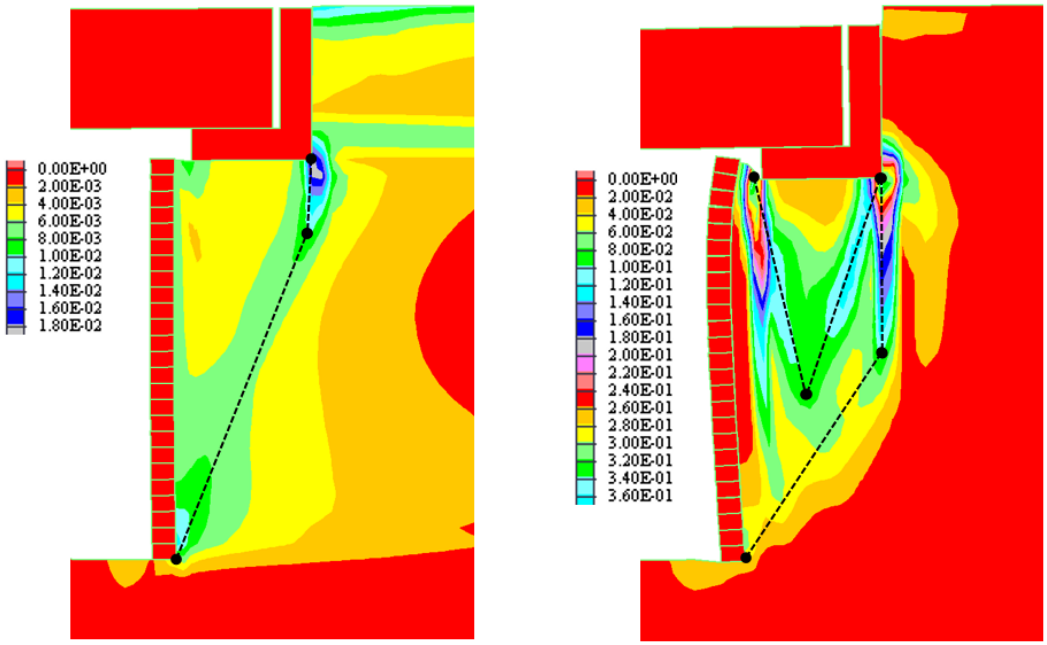

(a) (b)

Figure 5.17 Contours of shear strain magnitude for baseline case: (a) service limit state (ε_v = 0.5%); (b) strength limit state (ε_v = 5%). Note: color scales are different for these plots.

Similar to Figure 5.17(b), a bilinear failure surface was determined for each simulation of the parametric study at the strength limit state based on contours of shear strain magnitude. These simplified diagrams are presented together for comparison in Figure 5.18. In general, the geometry of these surfaces show close similarity over a wide range of simulated conditions, with some exceptions. The failure surface always occurs at the heel of bridge seat as seat location and size change, and moves down to the mid-height of the GRS bridge abutment. Failure surfaces show essentially no effect from changing vertical reinforcement spacing in Figure 5.18(a), and similar close agreement from changing geogrid stiffness and length in Figure 5.18(b) and (c), respectively. Figure 5.18(d) indicates that the intersection point of the bilinear surface moves downward with an increasing the number of layers of secondary reinforcement below the bridge seat, as might

be expected. Figure 5.18(e)–(g) indicate that soil cohesion, friction angle, and dilation angle have essentially no effect on failure surface geometry. Figure 5.18(h)–(j) show that parameters for abutment geometry have important effects. Figure 5.18(h) indicates that increasing the bridge seat setback distance changes the slope of the upper line of the bilinear failure surface but, interestingly, has no effect on the lower line and intersection point. Figure 5.18(i) indicates that increasing the bridge seat length changes the geometry for both sections of the failure surface but the vertical elevation of the intersection point remains consistent. Finally, abutment heights of 5 m, 7 m, and 9 m indicate the same relative geometry (i.e., when plotted as h/z); however, the lower height of 3 m shows a clearly a different geometry, similar to failure surfaces for abutments with larger a_b and L_f values.

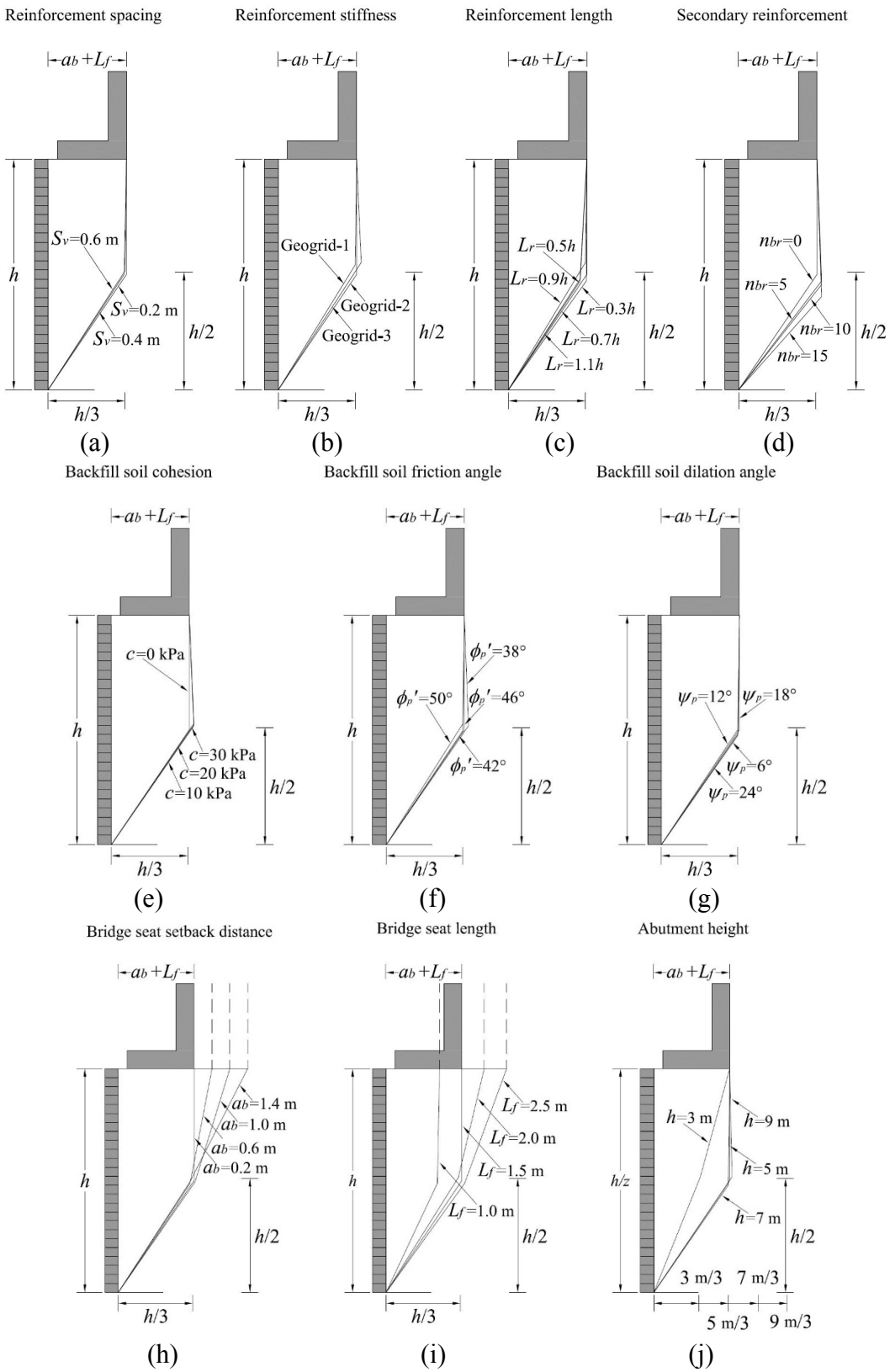

Figure 5.18 Bilinear failure surfaces for parametric study.

Based on the trends in Figure 5.18, a general bilinear failure surface is proposed and illustrated in Figure 5.19 for GRS bridge abutments under conditions similar to those investigated in the current study. The failure surface starts at the heel of the bridge seat, and moves downward to the mid-height (h/2). The intersection point (i.e., intersection of the upper and lower lines) of the bilinear surface is controlled by geometry. For $a_b + L_f \leq h/3$, the upper line moves vertically downward to the mid-height. For $a_b + L_f > h/3$, the upper line moves vertically downward to the mid-height and also horizontally toward the wall facing to position $x = h/3$. The lower line of the failure surface then moves linearly from the intersection point at mid-height to the toe of the GRS bridge abutment.

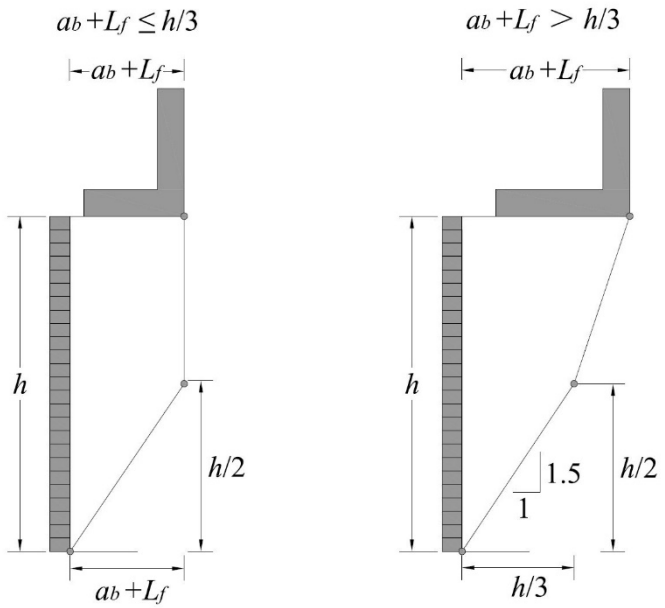

Figure 5.19 Proposed bilinear failure surface for GRS bridge abutment.

5.5 Acknowledgements

The text below is reproduced verbatim as it appears in the acknowledgments section per the UCSD Office of Graduate Studies Formatting Requirements.

Chapter 5 of this dissertation is based on materials from a manuscript under review for publication by the Journal of Geotechnical and Geoenvironmental Engineering titled "Numerical Simulation of Load-Deformation and Failure Behavior of Geosynthetic-Reinforced Soil Bridge Abutments" with authors, Yewei Zheng, Patrick J. Fox, and John S. McCartney (2017). The dissertation author is the first author of this paper.

Chapter 6

Shaking Table Testing Program

6.1 Introduction

A total of six shaking table tests on reinforced soil bridge abutments were performed using the indoor shaking table at the University of California, San Diego (UCSD) Powell Structural Laboratory. The shaking table has areal footprint dimensions of 5 m × 3 m and a maximum payload capacity of 356 kN. The table slides horizontally in one direction on two stationary shafts and is driven by a servo-hydraulic actuator with a static capacity of 490 kN, dynamic capacity of 405 kN, and maximum stroke of ± 150 mm. The shaking table was refurbished prior to this study to increase the fidelity of dynamic motion (Trautner et al. 2017).

Details of the shaking table testing program performed as part of this study are summarized in Table 6.1. The testing program consists of five tests where the direction of shaking is in the longitudinal direction of the bridge beam, referred to as longitudinal

shaking tests (Tests 1-5), and one test where the direction of shaking is perpendicular to the bridge beam, referred to as a transverse shaking test (Test 6). The longitudinal shaking tests include a baseline configuration (Test 1) and a parametric study to investigate the effects of bridge stress magnitude (Test 2), reinforcement spacing (Test 3), reinforcement stiffness (Test 4), and steel reinforcement (Test 5) on the seismic response of reinforced soil bridge abutments. The transverse shaking test (Test 6) has a similar configuration to Test 1 except that the input motions are applied in the transverse direction and the length of the abutment was reduced to fit on the table. This dissertation focuses on the tests on geosynthetic reinforced soil (GRS) bridge abutments (Tests 1, 2, 3, 4, and 6), but the results from Test 5 can be found in (McCartney et al. 2018).

Table 6.1 Shaking table test plan.

Test	Variable	Bridge Stress (kPa)	Reinforcement Spacing (m)	Reinforcement Stiffness (kN/m)	Shaking Direction
1	Baseline Case	66	0.15	380	Longitudinal
2	Bridge Stress	43	0.15	380	Longitudinal
3	Reinforcement Spacing	66	0.30	380	Longitudinal
4	Reinforcement Stiffness	66	0.15	190	Longitudinal
5	Steel Reinforcement	66	0.15	4800	Longitudinal
6	Shaking Direction	66	0.15	380	Transverse

6.2 Similitude Relationships

Considering the size and payload capacity of the indoor shaking table at UCSD, reduced-scale model tests were conducted with a length scaling factor of $\lambda = 2$. The length scaling factor is defined as the ratio of prototype length to model length, so a value of $\lambda = 2$ denotes a half-scale model test. A GRS bridge abutment with a total height of 5.4 m and a typical bridge beam clearance height of 4.5 m (Stein and Neuman 2007) was selected as the prototype structure. Therefore, half-scale GRS bridge abutment models with a total height of 2.7 m and a bridge beam clearance height of 2.25 m were constructed and tested on the shaking table.

The similitude relationships proposed by Iai (1989) have been widely used for 1g shaking table tests on geotechnical engineering structures, including tests on GRS walls (El-Emam and Bathurst 2004, 2005, 2007; Guler and Enunlu 2009; Sabermahani et al. 2009; Guler and Selek 2014; Latha and Santhanakumar 2015; Panah et al. 2015). Iai (1989) hypothesized that the moduli of materials in the model should be reduced so that the reduced-scale model will have a similar stress-strain response under lower stress conditions as the full-scale prototype structure. The theoretical scaling factors for the similitude relationships from Iai (1989) are summarized in Table 6.2. Model geometry, geosynthetic reinforcement stiffness, backfill soil modulus, bridge stress, and frequencies of the earthquake motions were scaled accordingly for $\lambda = 2$ using the factors given in Table 6.2.

Table 6.2 Similitude relationships for 1*g* shaking table testing (Iai 1989).

Variable	Theoretical scaling factor	Scaling factor for $\lambda = 2$
Length	λ	2
Material density	1	1
Strain	1	1
Mass	λ^3	8
Acceleration	1	1
Velocity	$\lambda^{1/2}$	1.414
Stress	λ	2
Modulus	λ	2
Stiffness	λ^2	4
Force	λ^3	8
Time	$\lambda^{1/2}$	1.414
Frequency	$\lambda^{-1/2}$	0.707

6.3 Material Properties

6.3.1 Backfill Soil

6.3.1.1 Geotechnical Characterization

The backfill soil used in this study was a manufactured sand obtained from *West Coast Sand & Gravel, Inc*. A sieve analysis was performed to characterize the particle size distribution of the backfill soil, as shown in Figure 6.1. The backfill soil has a coefficient of uniformity C_u = 6.1, coefficient of curvature C_z = 1.0, and is classified as a well-graded sand (SW) according to the USCS (Unified Soil Classification System). After application of the similitude relationships (λ = 2) in Table 6.1, the mean particle size D_{50} of 0.85 mm corresponds to a prototype value of 1.7 mm, which still falls within the sand-size range. The sand has a fines content of 2.5% (i.e., percent passing No. 200 sieve). This well-graded sand satisfies the backfill material requirements for GRS-IBS abutments (Adams et al. 2011b).

The measured maximum and minimum dry unit weights are $\gamma_{d,max}$ = 18.7 kN/m^3 and $\gamma_{d,min}$ = 13.8 kN/m^3 according to ASTM D4253 and D4254, respectively, and the corresponding minimum and maximum void ratios are e_{min} = 0.371 and e_{max} = 0.853 with measured a specific gravity of G_s = 2.61 according to ASTM D854.

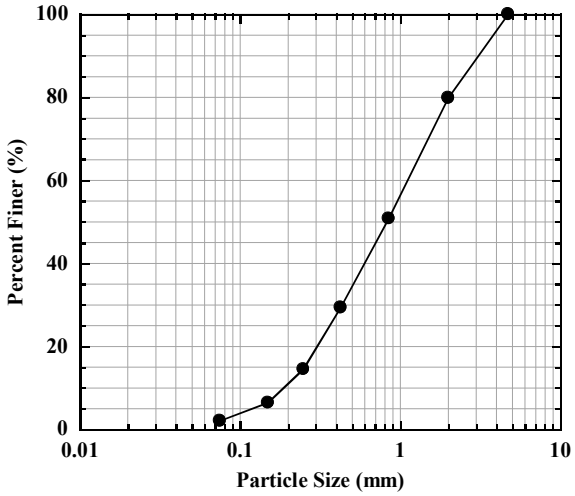

Figure 6.1 Particle size distribution curve.

6.3.1.2 Compaction Behavior

A standard Proctor compaction test was performed according to ASTM D698 to define the compaction curve for the backfill soil. Inspection of the standard Proctor compaction curve shown in Figure 6.2 indicates that compaction water content does not have a significant effect on dry unit weight for this sand (i.e., the curve is essentially flat).

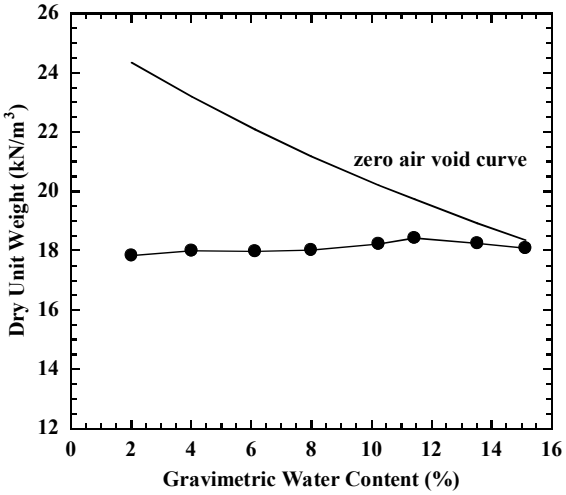

Figure 6.2 Standard Proctor compaction curve.

6.3.1.3 Selection of Target Compaction Conditions

For this sand, a relative density of 85% corresponds to a relative compaction of 96% with respect to the maximum standard Proctor dry unit weight of 18.4 kN/m^3, which is within the typical range of backfill soil compaction requirements for prototype GRS bridge abutments. A triaxial test was conducted for a dry sand specimen compacted at a relative density D_r = 85% under an effective confining stress of σ_3' = 69 kPa to represent the average stress-strain response of the backfill in the prototype structure. To meet the similitude relationships for backfill soil modulus, a series of drained triaxial compression tests were performed for specimens compacted at various relative densities under an effective confining stress of σ_3' = 34 kPa to find the target relative density for the backfill soil in the half-scale model shaking table tests.

Test results for the deviatoric stress versus axial strain for these different triaxial tests are shown in Figure 6.3. As expected, the secant modulus and peak shear strength increase with increasing relative density. The principal stress ratios are shown in Figure 6.5, which represent the mobilization of friction during shear. Although the shapes of the principal stress ratio curves are the same as the deviatoric stress curves, evaluation of the principal stress ratio curves are normalized to account for the effects of the different confining stresses representative of the model and prototype GRS bridge abutments considered in this analysis. The principal stress ratio curve for the specimen with D_r = 85% and σ_3' = 69 kPa is similar to the curve for the specimen with D_r = 70% and σ_3' = 34 kPa. This indicates that a reduced-scale model (under lower effective confining stresses) with backfill soil compacted at D_r = 70% will have the same response as a prototype structure

with backfill soil compacted at D_r = 85%. The secant moduli at different levels of axial strain are plotted in Figure 6.5. Theoretical soil secant moduli for σ_3' = 34 kPa are calculated based on the measured moduli for D_r = 85% and σ_3' = 69 kPa divided by the scaling factor of 2. Results confirm that a relative density of 70% yields similar secant moduli to the theoretical values for different levels of axial strain. The analyses shown in Figure 6.4 and Figure 6.5 confirm that the backfill soil in the GRS bridge abutment models should be compacted at a relative density of 70%.

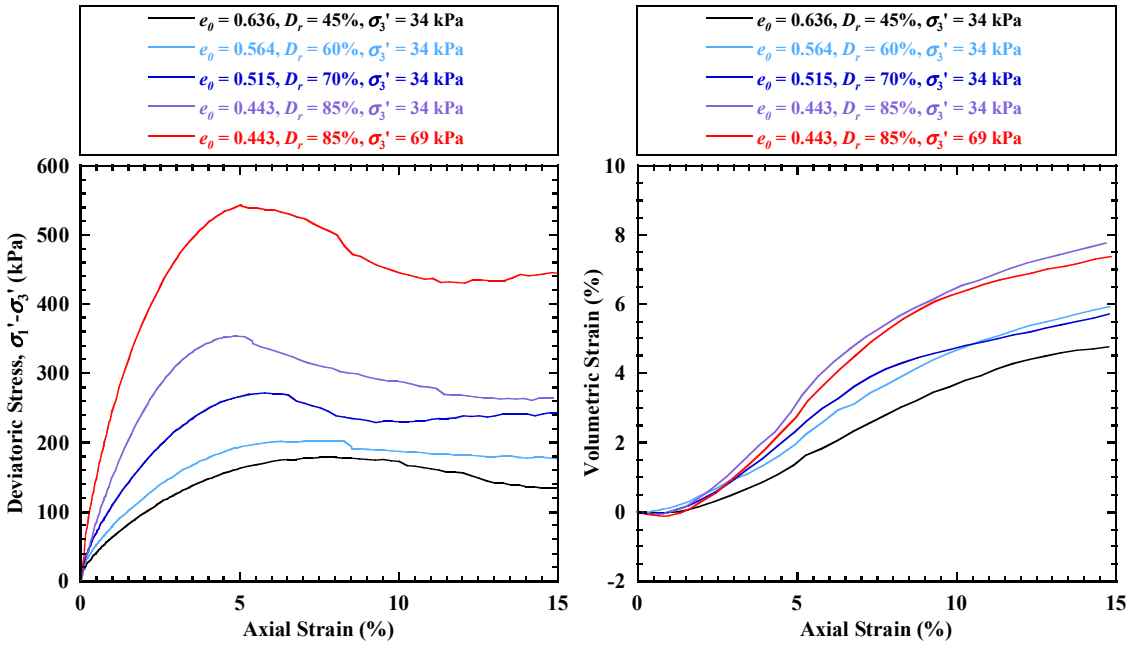

(a) (b)

Figure 6.3 Drained triaxial compression test results: (a) deviatoric stress vs. axial strain; (b) volumetric strain vs. axial strain.

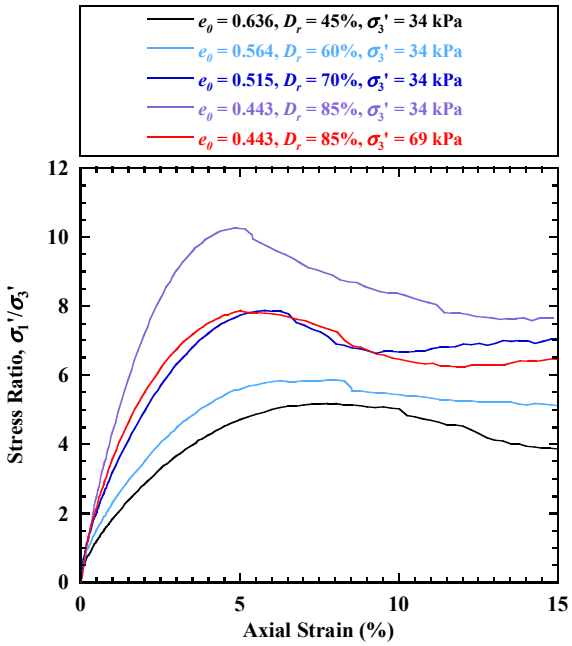

Figure 6.4 Principal stress ratio vs. axial strain.

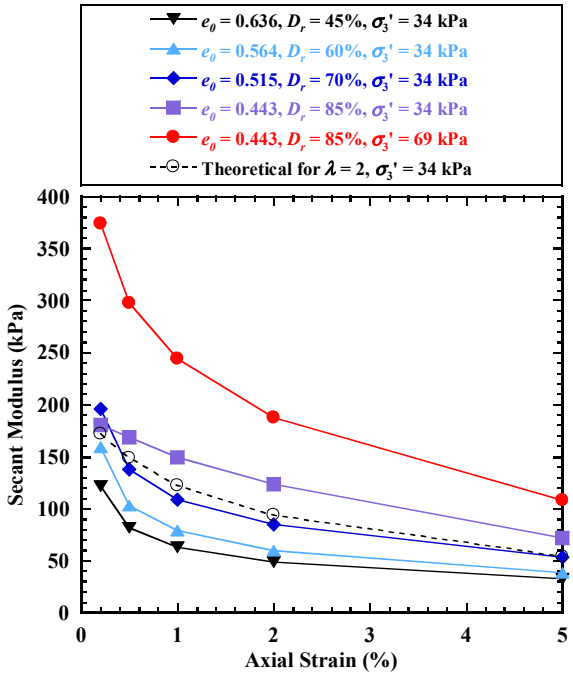

Figure 6.5 Secant moduli at different levels of axial strain.

Several trial experiments were performed on the backfill soil compacted with a vibrating plate compactor. It was found that a relative density of 70% could be attained repeatedly. The sand was compacted at gravimetric water content w_c = 5%, which was selected for the convenience of construction as it was difficult to maintain dry sand conditions in the laboratory. The impact of the non-zero gravimetric water content on the shear strength of the sand will be discussed later. The selected target compaction conditions for construction of the half-scale GRS bridge abutment models are shown in Figure 6.6.

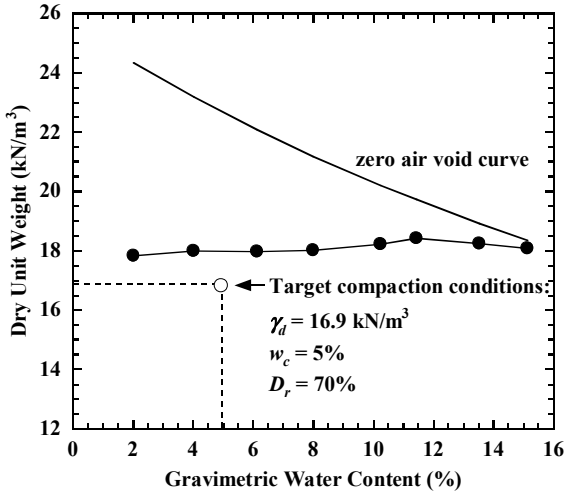

Figure 6.6 Target compaction conditions.

6.3.1.4 Shear Strength

Since the specimen is relatively narrow in the transverse direction due to the constraint of the UCSD shaking table dimensions, the stress state in the backfill soil is expected to be closer to triaxial compression conditions than plane strain compression conditions. A series of consolidated-drained (CD) triaxial compression tests were performed on dry sand specimens compacted at the target relative density of D_r = 70% to

measure the shear strength and volume change behavior. The specimens were compacted within a latex membrane held in place by a split-wall compaction mold. After compaction, a vacuum was applied to the soil specimen, and the split mold was removed. The sand specimens had a diameter of 71.1 mm and height of 142.2 mm. Different levels of confining stress were applied to the different specimens prior to shearing at a constant axial strain rate of 1.0%/min. The volume change was recorded during drained shearing through monitoring of the volume of cell fluid. The triaxial test setup with a typical sand specimen is shown in Figure 6.7.

Figure 6.7 Consolidated drained triaxial compression test setup.

The results from three triaxial compression tests performed at effective confining stresses of 14, 34, and 69 kPa are shown in Figure 6.8. These mean effective stresses

encompass the stress range expected in the half-scale GRS bridge abutment models. The sand was observed to show a clear peak value representative of dense conditions, and showed dilation after an initial contraction. A dilation angle of $\psi = 13.0°$ was determined for the volumetric strains ranging from the axial strain at the point of maximum contraction to an axial strain of 5%. A linear Mohr-Coulomb failure envelope was fitted to the data as shown in Figure 6.9, and a peak friction angle of $\phi_p' = 51.3°$ and zero cohesion were calculated for the dry backfill sand with $D_r = 70\%$.

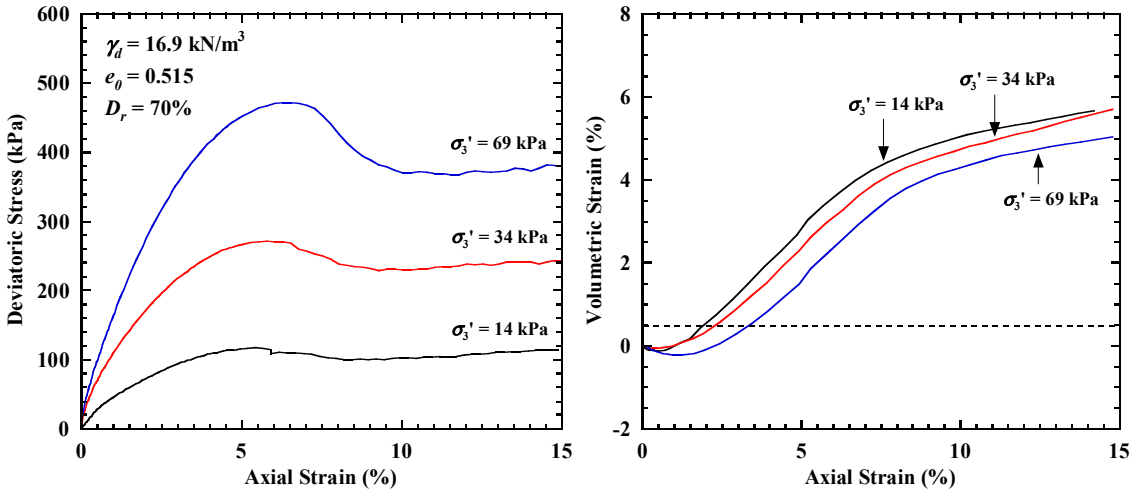

(a) (b)

Figure 6.8 Triaxial test results: (a) deviatoric stress vs. axial strain; (b) volumetric strain vs. axial strain.

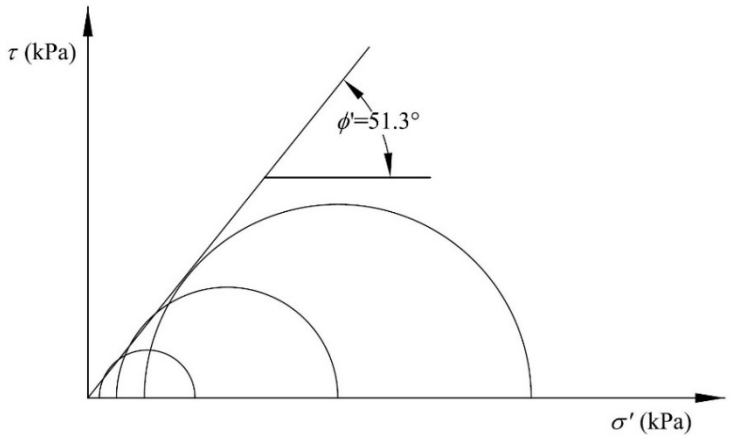

Figure 6.9 Mohr-Coulomb failure envelope.

6.3.1.5 Soil Water Retention Curve (SWRC)

A hanging column test was performed on a sand specimen with D_r = 70% to measure the soil water retention curve (SWRC) for both drying and wetting paths. Results are shown in Figure 6.10. The SWRC data was fitted using the model of van Genuchten (1980):

$$\theta = \theta_r + (\theta_{\max} - \theta_r)[1 + (\alpha_{vG}\psi_s)^{N_{vG}}]^{-(1-\frac{1}{N_{vG}})} \tag{6.1}$$

where θ is the volumetric water content (volume of water/total volume of soil in percent), ψ_s is the matric suction, θ_{max} is the volumetric water content at zero matric suction for either path, θ_r is the residual saturation, and α_{vG} and N_{vG} are the van Genuchten (1980) SWRC model parameters.

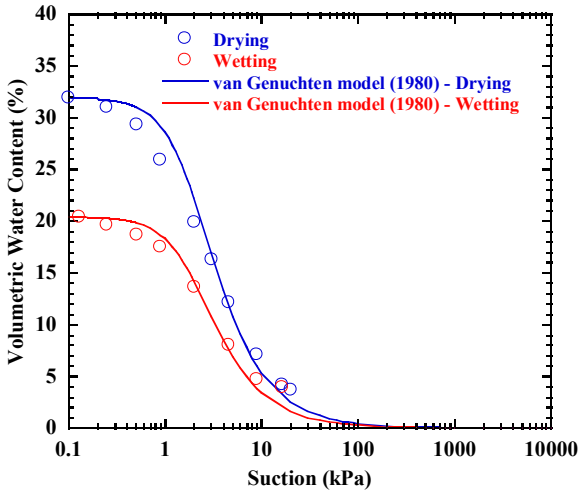

Figure 6.10 Wetting- and drying-path soil-water retention curve data with fitted relationship.

A summary of the backfill soil properties are presented in Table 6.3.

Table 6.3 Backfill soil properties.

Property	Value
Specific gravity, G_s	2.61
Coefficient of uniformity, C_u	6.1
Coefficient of curvature, C_z	1.0
Maximum void ratio, e_{max}	0.853
Minimum void ratio, e_{min}	0.371
Peak friction angle, ϕ_p' (°)	51.3
Dilation angle, ψ (°)	13.0
van Genuchten (1980) SWRC model parameter, α_{vG} (kPa^{-1})	0.5
van Genuchten (1980) SWRC model parameter, N_{vG}	2.1
Drying curve volumetric water content at zero suction, θ_d (m^3/m^3)	0.32
Wetting curve volumetric water content at zero suction, θ_w (m^3/m^3)	0.20
Residual volumetric water content, θ_r (m^3/m^3)	0.00

6.3.2 Geogrid Reinforcement

The geosynthetic reinforcement is a uniaxial high density polyethylene (HDPE) geogrid (Tensar LH800). The aperture size is 120 mm by 25 mm. A series of single rib tensile tests were conducted according to ASTM D6637 to evaluate the stiffness and strength of the geogrid. The single rib geogrid specimen in the machine direction has four junctions (three apertures) with a length of 360 mm, and was loaded at a strain rate of 10%/min. The tensile test setup is shown in Figure 6.11.

Figure 6.11 Single rib tensile test setup.

Tensile tests were first performed for three specimens at a strain rate of 10%/min. The load-strain curves in Figure 6.12 show consistent results and indicate the repeatability of tests. The geogrid has secant stiffness at 5% strain $J_{5\%}$ = 380 kN/m and ultimate strength T_{ult} = 38 kN/m in the machine direction. Using the similitude relationships in Table 6.2,

the tensile stiffness of this geogrid yields a value of 1520 kN/m for the prototype geogrid, which is in the typical range for field structures. A tensile test was conducted for the geogrid in the cross-machine direction, and results are shown in Figure 6.13. The geogrid has $J_{5\%}$ = 80 kN/m and T_{ult} = 4 kN/m in the cross-machine direction, which are much lower than for the machine direction.

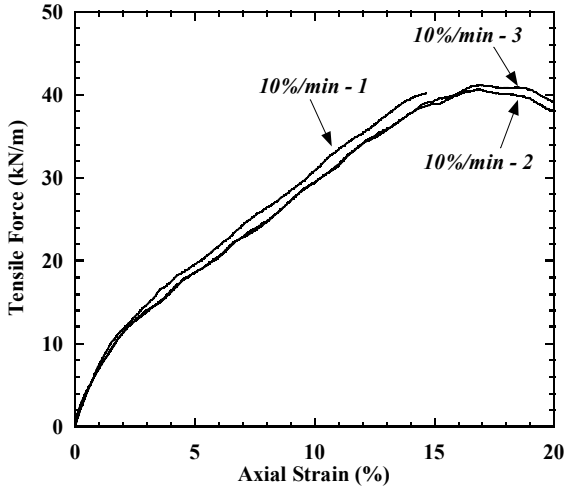

Figure 6.12 Load-strain curves at strain rate 10%/min.

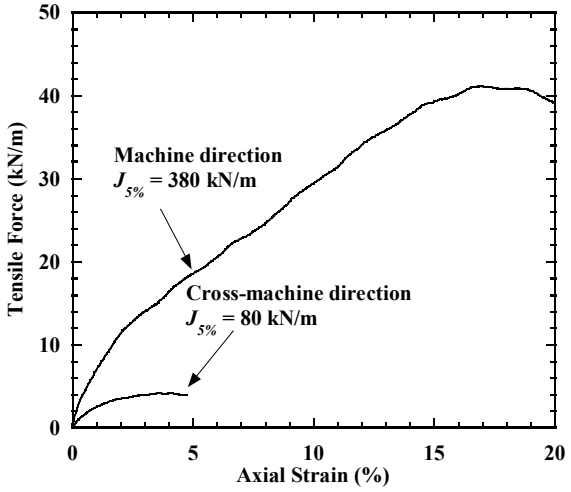

Figure 6.13 Load-strain curves for machine direction and cross-machine direction.

Tensile tests were also conducted at strain rates of 1, 5, 10, 50, and 100%/min to investigate the effect of strain rate. Results, as shown in Figure 6.14, indicate that tensile stiffness and strength increase with increasing strain rate. Secant stiffness at 1% and 5% axial strains for different strain rates are plotted in Figure 6.15. When strain rate increase from 1 to 100%/min, the secant stiffness increases from 400 to 1000 kN/m for 1% axial strain and increases from 220 to 580 kN/m for 5% axial strain.

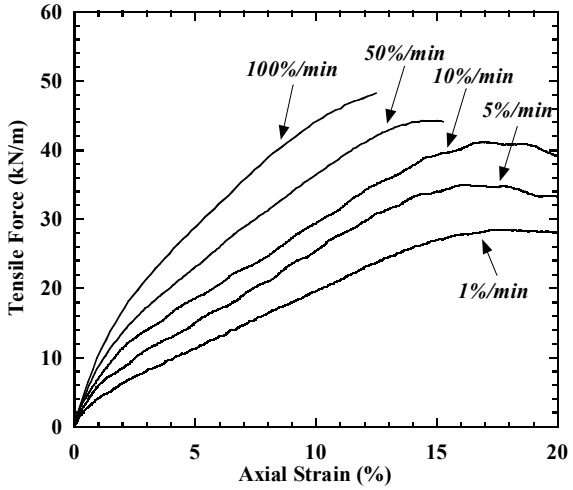

Figure 6.14 Effect of loading rate on load-strain curves.

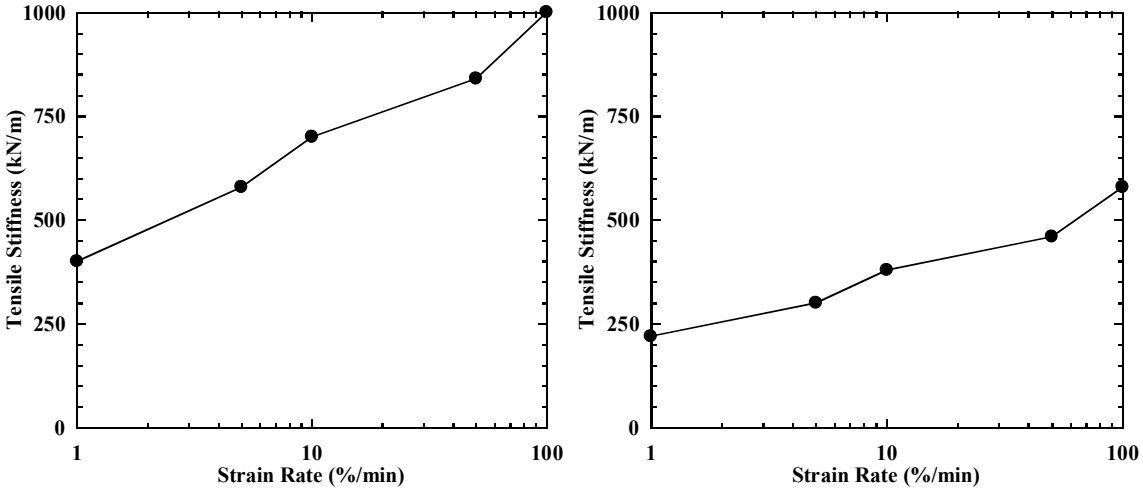

Figure 6.15 Effect of strain rate on secant stiffness: (a) 1% strain; (b) 5% strain.

6.3.3 Facing Elements

Facing elements for GRS bridge abutments vary depending on the desired aesthetics and contractor approach. The two main facing elements used in practice are modular block facings and precast concrete panels, and reinforcement-facing connections also change with the type of facing. This project used a modulus block facing in the GRS bridge abutment models to give more flexibility in scaling and in the mode of reinforcement-wall connections. To meet the similitude relationships in Table 6.2, concrete modular facing blocks from Keystone, Inc., with dimensions of 0.3 m × 0.25 m × 0.15 m (length × width × height) were selected. Geogrid reinforcement layer was sandwiched between blocks with fiberglass pins through the geogrid apertures for block alignment.

6.4 Test Configuration

6.4.1 Longitudinal Test

The shaking table test configuration of the bridge system for longitudinal test is shown in Figure 6.16. The bridge beam has dimensions of 6.4 m × 0.9 m × 0.45 m (length × width × height), and is placed on a bridge seat that rests on the GRS bridge abutment at one end and on a concrete support wall that rests on a sliding platform at the other end. The bottom of the concrete support wall is rigidly connected to the shaking table using steel beams and experiences the same motion as the table. The bridge beam represents a longitudinal slice of a prototype bridge superstructure whose length was selected to accommodate the available laboratory space. Elastomeric bearing pads (model NEOSORB, Voss Engineering, Inc.) with plan dimensions of 0.45 m × 0.9 m, thickness of 25 mm, and elastic modulus of 3.6 MPa were placed under both ends of the bridge beam. The seismic joint (i.e., gap) between the bridge beam and vertical back wall of the bridge seat is 25 mm wide. During shaking, the bridge beam interacts with the GRS bridge abutment and support wall through friction developed on the bearing pads and potentially contacts (i.e., impacts) with the back wall of the bridge seat. The clear distance between the top of the wall facing and bottom of the bridge beam is 0.15 m.

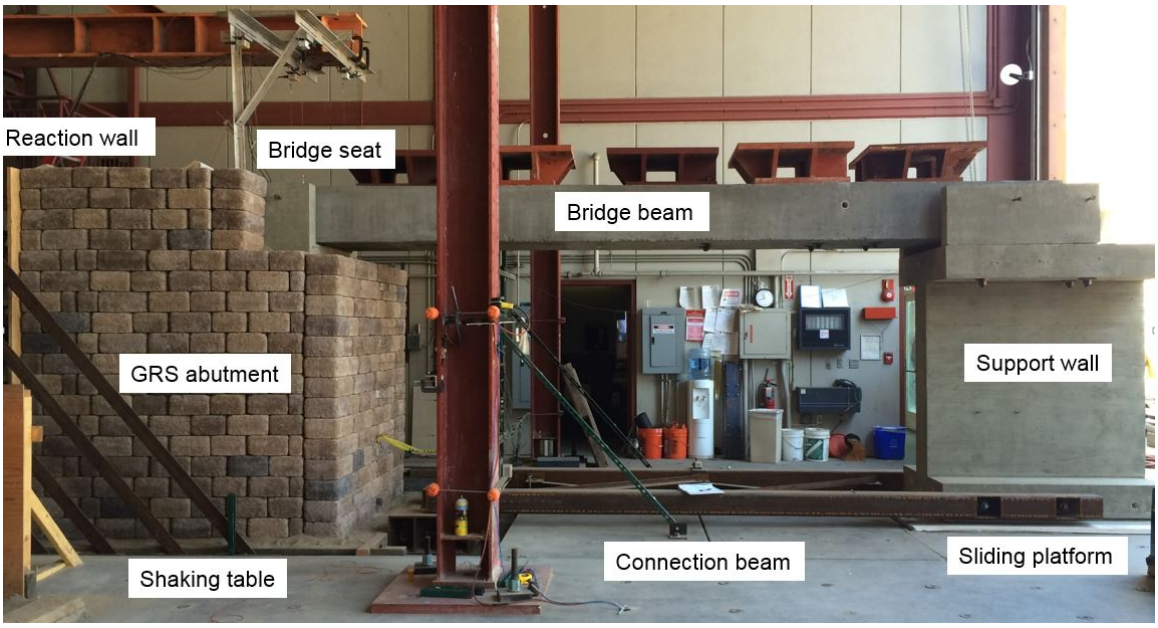

Figure 6.16 Shaking table test configuration of bridge system for longitudinal test.

The self-weight of the concrete bridge beam is 65 kN, and additional dead weights (steel plates) of 33 kN are evenly distributed and rigidly attached to the beam to produce the desired total bridge weight (98 kN) while keeping the mass center of the beam relatively low to minimize rocking. The total weight of the beam and dead weights produces an average vertical stress of 121 kPa on top of the bridge seat. The bridge seat has a self-weight of 7 kN and a bottom surface with plan dimensions of 0.65 m × 1.3 m. The average vertical stress on the backfill soil from the bridge seat is 66 kPa, which corresponds to a prototype vertical stress of 132 kPa and is in the typical range for GRS bridge abutments in the field (Adams et al. 2011b). For Test 2, only the bridge beam was placed (i.e., no additional dead weight), so the average vertical stress on the abutment is 43 kPa, corresponding to a vertical stress of 86 kPa for prototype structure.

The GRS bridge abutment has modular block facing on three sides, including a front wall facing perpendicular to the longitudinal direction and two side wall facings

perpendicular to the transverse direction. The back of the GRS bridge abutment is supported by a rigid reaction wall consisting of a steel frame with plywood face. The reaction wall was designed to be sufficiently stiff to provide at-rest conditions during construction and experience minimal deflections during shaking. Although the reaction wall moves in phase with the shaking table and thus does not reproduce the deformation boundary condition of a retained soil mass in the field, this simple configuration can be readily incorporated into numerical simulations for calibration purposes. To reduce effects of the reaction wall on the abutment response, the length of the retained soil zone was maximized within the geometry and payload constraints of the table. The total weight of the entire bridge system is 450 kN.

The GRS bridge abutment model has a total height of 2.7 m, consisting of a 2.1 m-high lower GRS wall and a 0.6 m-high upper wall, resting on a 0.15 m-thick foundation soil layer placed directly on the shaking table. A top view diagram is shown in Figure 6.17(a) and cross-sectional view diagrams in the longitudinal and transverse directions are shown in Figure 6.17(b) and (c), respectively. The abutment has plan dimensions of 2.35 m × 2.1 m, including wall facing blocks. The bridge seat rests on top of the backfill soil for the lower GRS wall and has a setback distance of 0.15 m from each of the three wall facings. The lower GRS wall was constructed in fourteen 0.15 m-thick soil lifts. Each lift includes reinforcement layers in the longitudinal direction (i.e., direction of shaking), and the transverse direction. The longitudinal reinforcement layers are frictionally connected to the front wall facing and extend 1.47 m into the backfill soil. The transverse reinforcement layers are frictionally connected to each side wall facing and extend 0.8 m into the backfill soil, and meet (but are not connected) at the center. The transverse reinforcement layers

and side wall facing blocks are offset by 25 mm vertically from the longitudinal reinforcement layers and front wall facing blocks. Although longitudinal and transverse reinforcement layers are in close proximity vertically, the maximum particle size of the backfill soil is sufficiently small to permit typical soil-reinforcement interaction. The length of the retained soil zone between the reinforced soil zone and reaction wall is 0.63 m. Transverse reinforcement layers support the side walls in the retained soil zone and are not connected to transverse reinforcements in the reinforced soil zone.

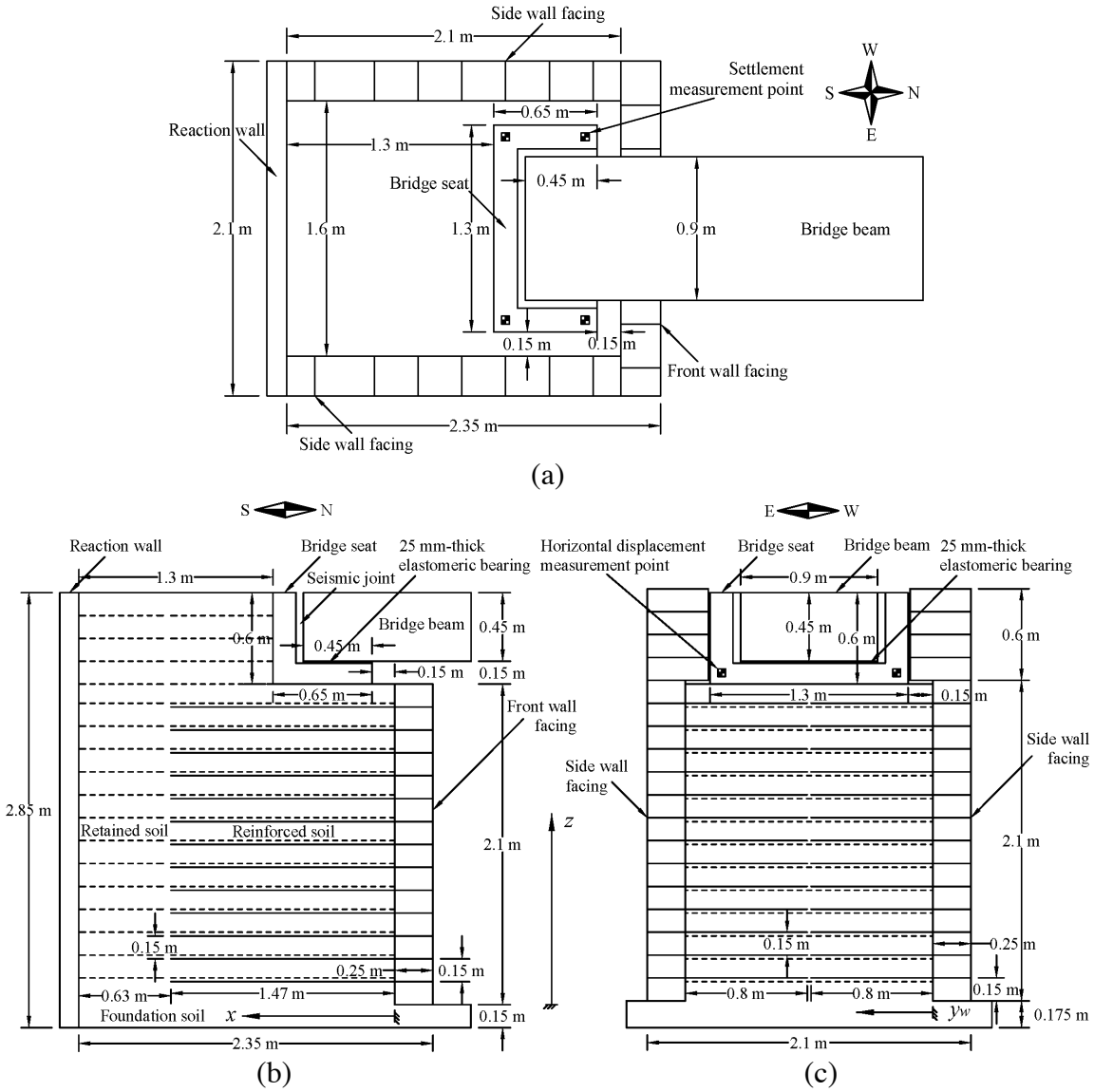

Figure 6.17 GRS bridge abutment model for longitudinal test: (a) top view; (b) longitudinal cross-sectional view; (c) transverse cross-sectional view. Note: dashed lines indicate reinforcement layers perpendicular to diagram.

The support wall for the other end of the bridge beam rests on a sliding platform, as shown in Figure 6.18. Based on the low friction boundary concept developed by Fox et al. (1997, 2006), this platform consists of 273 rolling stainless steel balls (diameter = 19 mm) sandwiched between two stainless steel plates (thickness = 6 mm). The steel balls are placed inside a plastic guide plate (thickness = 13 mm) with 273 oversized holes (diameter

= 25 mm) to keep the balls orderly during shaking tests. A 13 mm-thick rubber sheet is placed between the sliding platform and the support wall to reduce stress concentrations on the sliding platform. The base of the support wall is connected to the shaking table using steel beams to transmit table motions and ensure that the entire system is shaken uniformly.

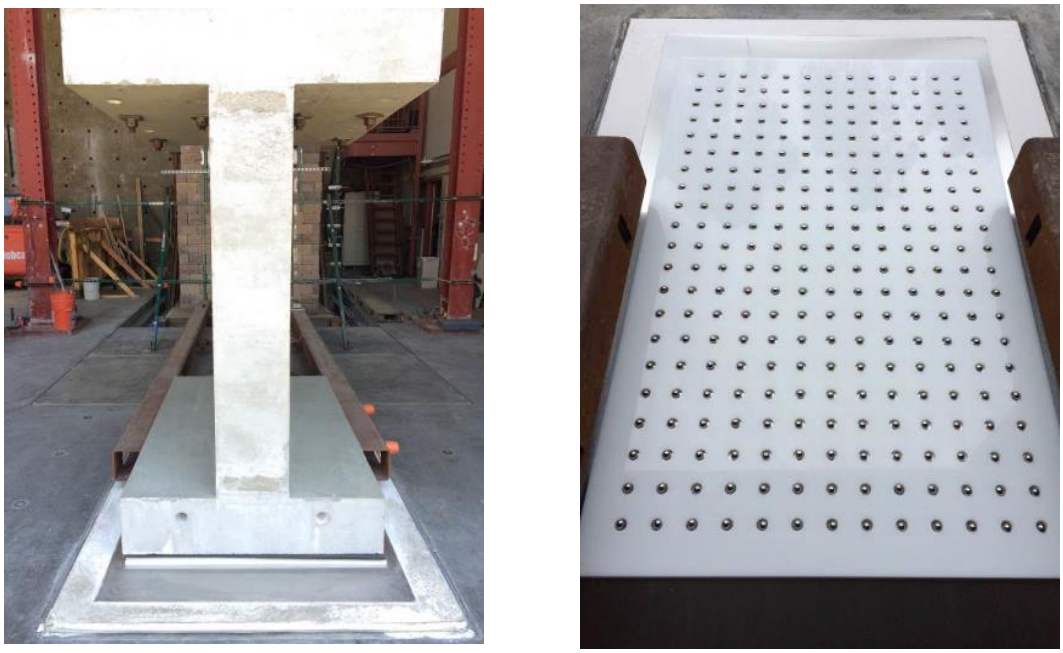

(a) (b)

Figure 6.18 Bridge support wall: (a) end view; (b) low friction sliding platform.

6.4.2 Transverse Test

The shaking table test configuration of the bridge system for transverse test is similar to longitudinal test except that the specimen was rotated 90 degree so that the shaking motions can be applied in the transverse direction, as shown in Figure 6.19. Braces were welded to the connection beams to increase the stiffness in the transverse direction. The retained soil zone of the GRS bridge abutment was removed to accommodate the available table space. The dimensions for the GRS bridge abutment model for transverse test is shown in Figure 6.20. The dimensions are essentially the same as longitudinal test except that the abutment specimen for transverse test has plan dimensions of 1.72 m × 2.1 m with no retained soil zone.

Figure 6.19 Shaking table test configuration for bridge system for transverse test.

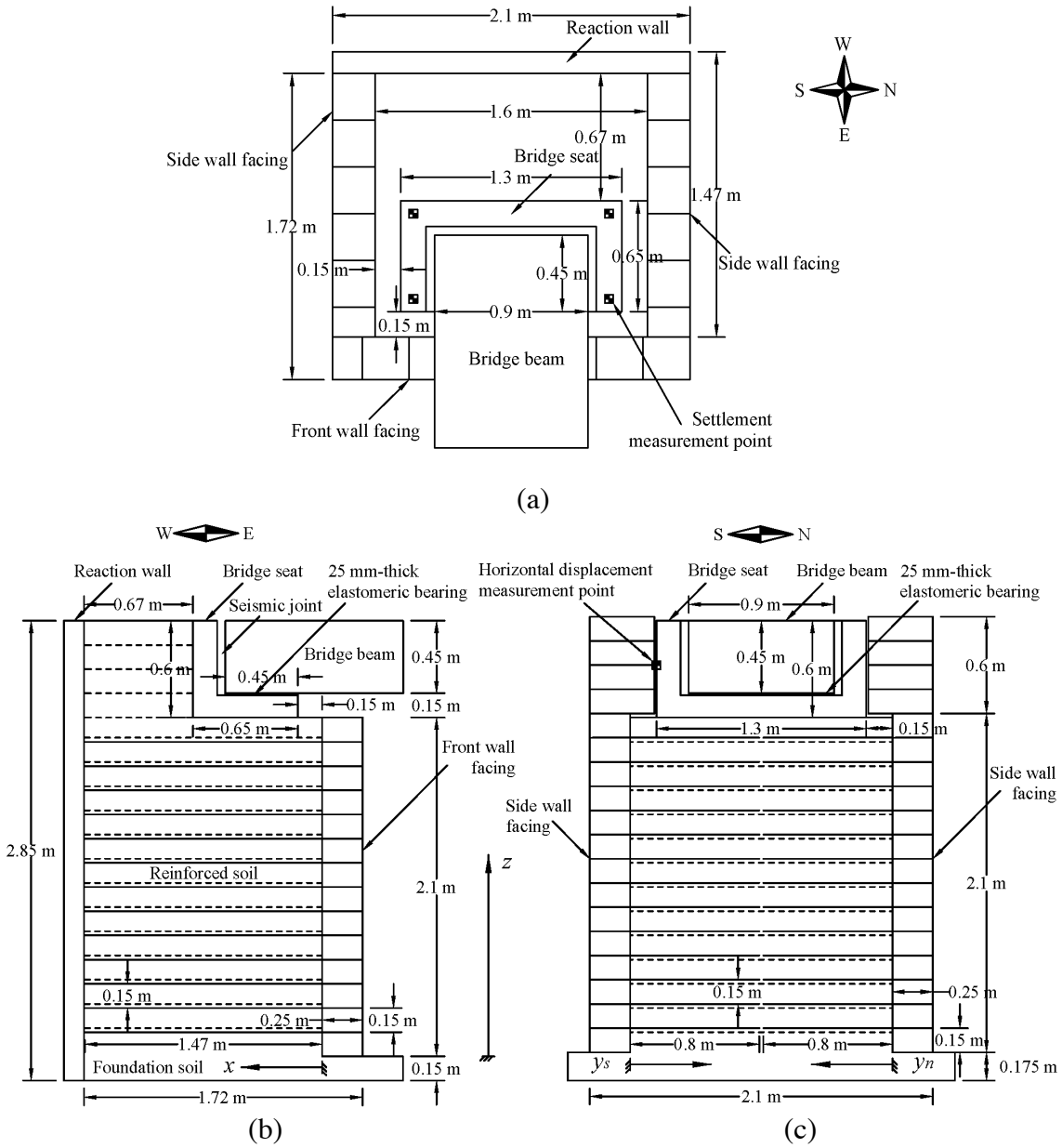

Figure 6.20 GRS bridge abutment model for transverse test: (a) top view; (b) longitudinal cross-sectional view; (c) transverse cross-sectional view. Note: dashed lines indicate reinforcement layers perpendicular to diagram.

6.5 Instrumentation

6.5.1 Sensors

Specimen data was collected using an automatic data acquisition system with 160 channels and a simultaneous sampling rate of 256 Hz during shaking. Figure 6.21 shows sensors for the shaking table tests, including string potentiometers (Model P-5A/15A/25A/30A/40A Rayelco, PATRIOT Sensors and Controls Corp.), linear potentiometers (Model 606, BEI sensors), total pressure cells (Model SPT-3K/6K, AFB Engineered Test System), load cells (Model 1220BF-50K, Interface Inc.), accelerometers (Model CXL02LF1, Crossbow), and geogrid strain gauges (KFG-2-120-C1-11, Kyowa Americas, Inc.).

Horizontal displacements for the wall facing blocks at different elevations, bridge seat, reaction wall, bridge beam, and support wall in the shaking direction were measured using string potentiometers, and horizontal displacements of the wall facing blocks perpendicular to the shaking direction were measured using linear potentiometers. String potentiometers were used to measure settlements at the four corners of the bridge seat. String potentiometers were mounted on rigid reference frames apart from the shaking table and had sufficient tension to measure dynamic motions for the frequency band of the test. The string potentiometer measurements were corrected using measured horizontal displacements of the shaking table in the longitudinal direction to yield relative displacements with respect to the table. Earth pressure cells were seated into 38 mm-thick PVC plates with plan dimensions of 127 mm × 203 mm for horizontal orientation and 203

mm × 203 mm for vertical orientation. The PVC plates provide a flush surface to improve measurements of vertical and horizontal total stresses. Two load cells were embedded in the south end of the bridge beam to measure potential contact forces between the bridge beam and bridge seat during shaking. Accelerometers were attached on the wall facing and placed within the reinforced and retained soil zones, and attached on the structures to measure horizontal accelerations in the longitudinal direction. Geogrid tensile strains were measured using strain gauges mounted in pairs at the mid-point of longitudinal ribs, with one gauge on top and the other on bottom to correct for rib bending (Bathurst et al. 2002). Considering that strain gauge measurements may be affected by attachment technique and non-uniform stiffness along a rib (Bathurst et al. 2002), tensile tests were conducted to obtain a correction factor (CF), defined as the ratio of global strain to gauge strain. Calibration results for loading rates of 1%/min, 10%/min, and 100%/min are shown in Figure 6.22. The data indicate that CF has an average value of 1.1 and is not significantly affected by loading rate. All measured geogrid strains were corrected using this CF value. Within the GRS bridge abutment specimen, strains were measured at 4 points along each of 5 geogrid layers.

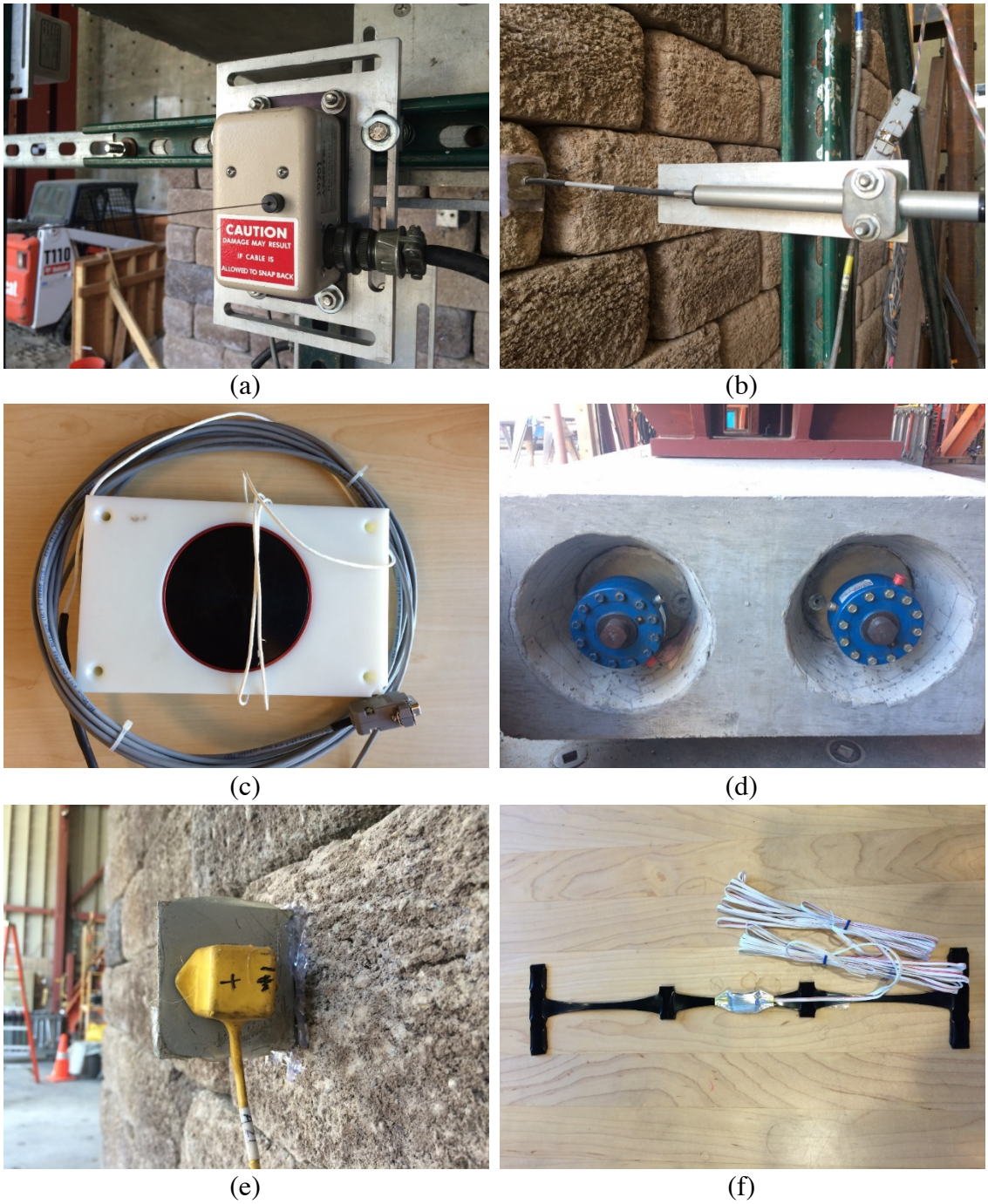

(a) (b)

(c) (d)

(e) (f)

Figure 6.21 Sensors: (a) string potentiometer; (b) linear potentiometer; (c) pressure cell, (d) load cell; (e) accelerometer; (f) geogrid strain gauge.

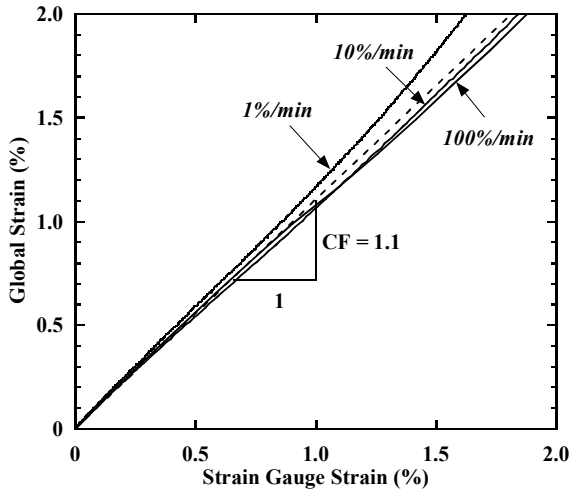

Figure 6.22 Calibration relationship for strain gauge measurements.

6.5.2 Longitudinal Test

Instrumented sections for longitudinal tests are shown in Figure 6.23, including a longitudinal centerline section L1, longitudinal off-centerline section L2, and transverse section T1. The detailed instrumentation for each section are shown in Figure 6.24. The longitudinal centerline section L1 has extensive instrumentation to investigate the seismic response of GRS bridge abutment in the longitudinal direction. The longitudinal off-centerline section L2 has an offset of 0.45 m west from L1, and measurements are used to evaluate the plane strain assumptions in current design guidelines. Transverse section T1 has distance of 0.48 m from the front wall facing, and measurements are used to evaluate the 3D effects on the response of GRS bridge abutment subjected to longitudinal shaking.

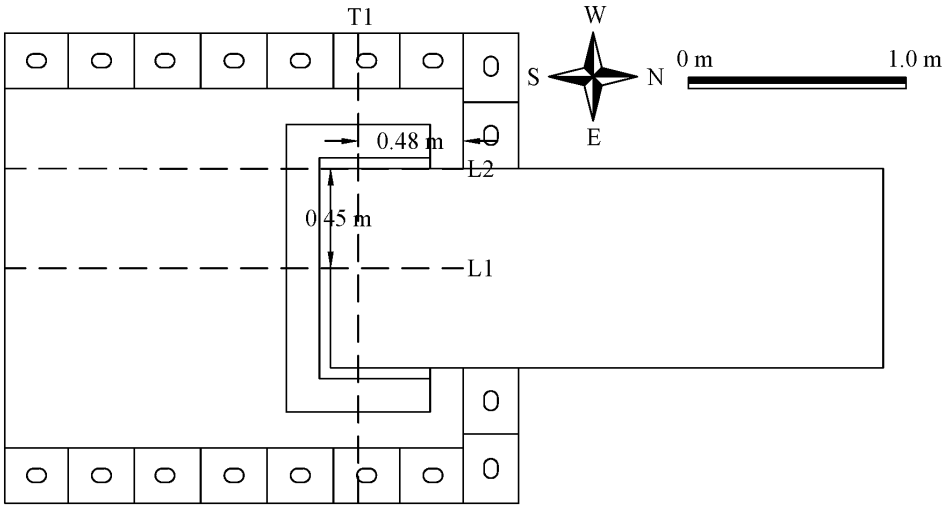

Figure 6.23 Instrumented sections for longitudinal test (shaking direction from North to South).

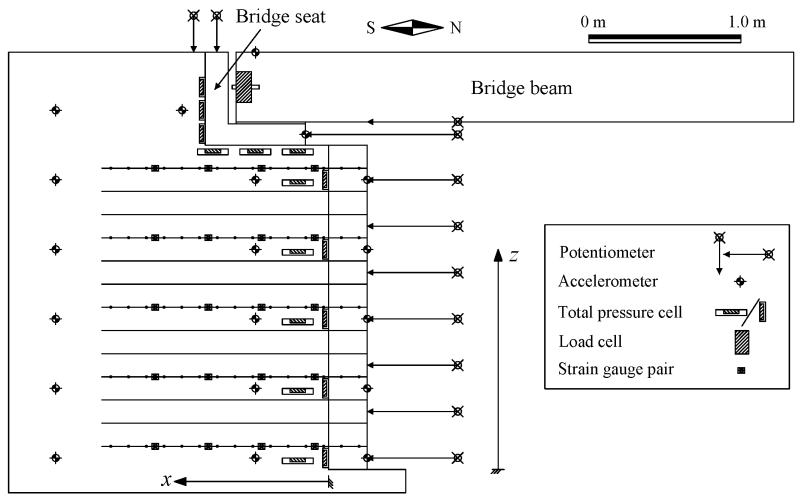

(a)

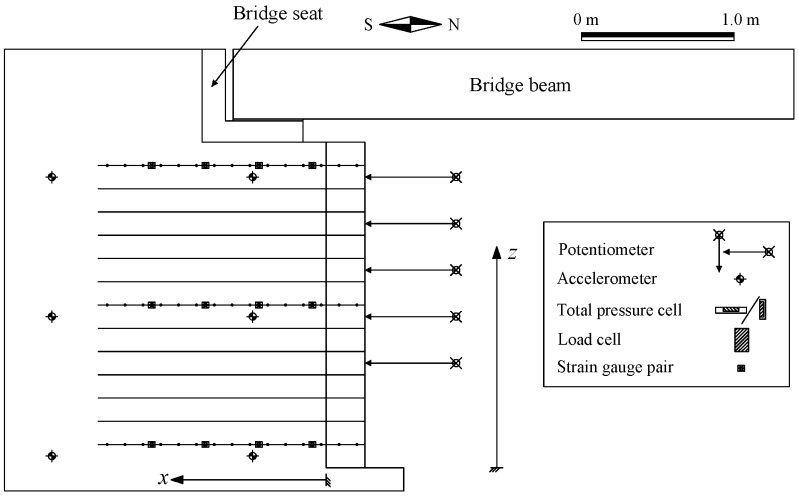

(b)

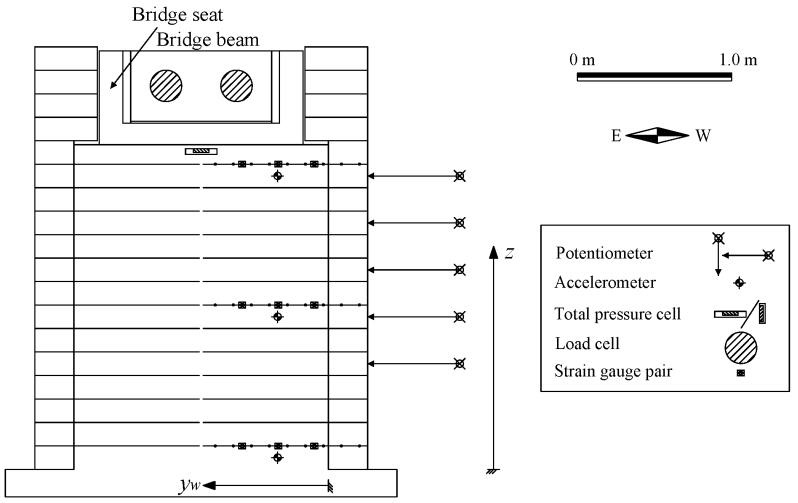

(c)

Figure 6.24 Instrumentation for longitudinal test: (a) L1; (b) L2; (c) T1.

6.5.3 Transverse Test

Instrumented sections for longitudinal tests are shown in Figure 6.25, including a transverse section T1 under the bridge seat, transverse section T2 behind bridge seat, and longitudinal centerline section L1. The detailed instrumentation for each section are shown in Figure 6.26. The transverse section T1 has extensive instrumentation to investigate the seismic response of GRS bridge abutment in the transverse direction. Measurements for longitudinal centerline section L1 are used to evaluate the 3D effects on the response of GRS bridge abutment subjected to transverse shaking.

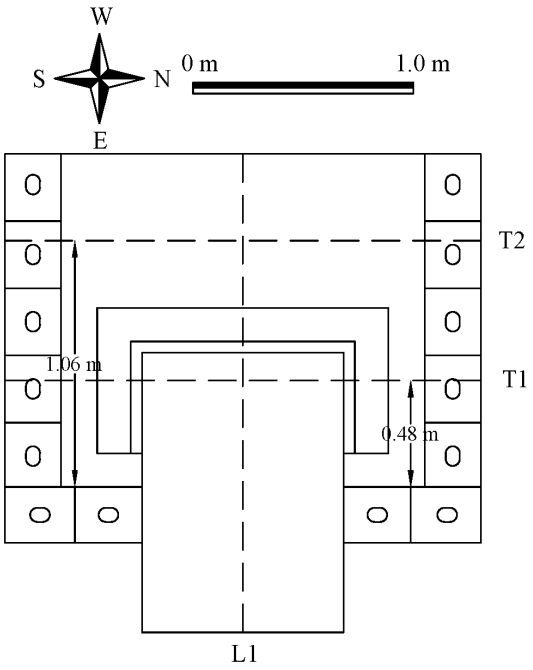

Figure 6.25 Instrumented sections for transverse test (shaking direction from North to South).

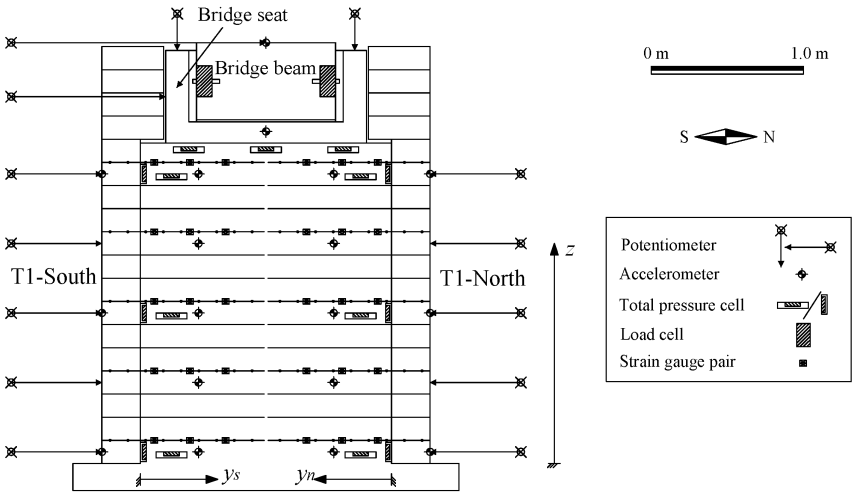

(a)

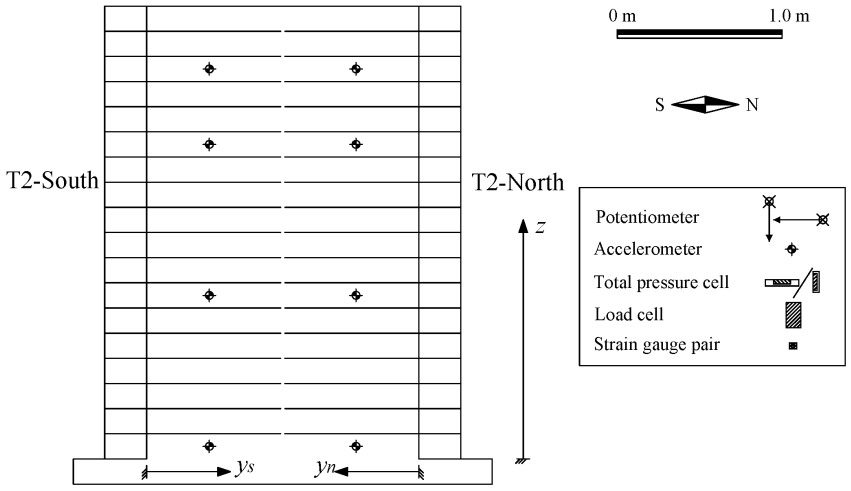

(b)

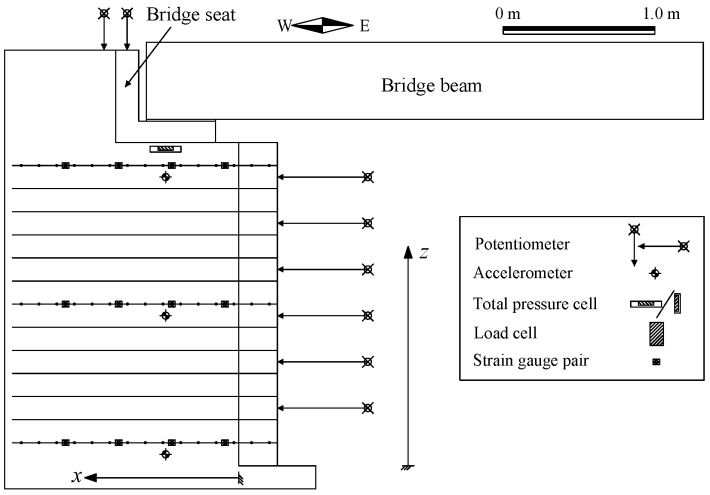

(c)

Figure 6.26 Instrumentation for transverse test: (a) T1; (b) T2; (c) L1.

6.6 Construction

A 0.15 m-thick foundation sand layer was first placed within the edge containment of the shaking table and at a higher relative density (D_r = 85%) than the backfill sand to provide a firm base for the GRS bridge abutment. The table surface has transverse shear fins to transfer motion to the foundation layer with minimal slippage. The first course of facing blocks was placed and leveled on the foundation layer, with the side wall blocks offset vertically by 25 mm from the front wall blocks. This offset was needed to avoid direct contact between longitudinal and transverse geogrid layers and maintain interaction with the backfill soil. Although not used in actual GRS bridge abutments, this technique was necessary for the current study due to width constraints of the shaking table. As a result of the 25 mm offset, the side wall and front wall facing blocks could not be interlocked in a typical masonry pattern at the corners.

Longitudinal and transverse reinforcement layers were placed horizontally within the backfill soil from the block contact interfaces and are shown in Figure 6.27(a) and (b), respectively. The transverse reinforcement would not be expected to significantly affect abutment behavior in the longitudinal direction because geogrid stiffness in the cross-machine direction is much lower than in the machine direction (Figure 6.13); however, the effect of transverse reinforcement should still be included when using results from this test for numerical model validation. During construction, geogrid layers were placed between the blocks for over 80% of the block-to-block contact surface and the blocks were aligned using fiberglass pins. Although typically grouted together in the field (Helwany et al. 2012),

the upper course of blocks remained ungrouted for this test. After construction of the lower GRS wall, the bridge seat was placed on top of the backfill soil for the lower wall and the 0.6 m-high upper wall was constructed in four lifts with only transverse reinforcement layers. Finally, the concrete bridge beam with additional dead weights was placed on the bridge seat and support wall. A bridge beam is typically placed prior to construction of upper wall in the field; however, the beam was added last in the current study for convenience.

(a) (b)

Figure 6.27 Construction of GRS bridge abutment: (a) longitudinal reinforcement layer; (b) transverse reinforcement layer.

During construction of each soil lift, backfill sand was compacted with a target gravimetric water content of $w_c = 5\%$ and target relative density $D_r = 70\%$ using a vibratory plate compactor. Random soil samples were collected for each lift during construction to measure the actual gravimetric water content. The measured gravimetric water content profiles are shown in Figure 6.28 and indicates values ranging from 3.3% to 9.1%.

Considering that the compaction curve is relatively flat for this sand, the variation in water content is unlikely to significantly affect compacted dry unit weight.

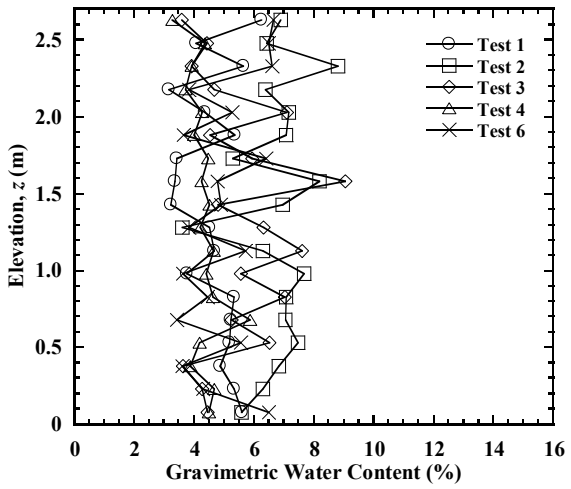

Figure 6.28 Gravimetric water content profiles.

The gravimetric water content profiles can be combined with the SWRC to estimate the apparent cohesion c_a using the suction stress concept of Lu et al. (2010):

$$c_a = \sigma^s \tan\phi' = S_e \psi_s \tan\phi' \tag{6.2}$$

where σ^s = suction stress, ψ_s = matric suction, and S_e = effective saturation, defined as:

$$S_e = \frac{\theta - \theta_r}{\theta_{\max} - \theta_r} \tag{6.3}$$

Matric suction values interpreted from the SWRC range from 3 to 10 kPa, as shown in Figure 6.29, and yield the calculated profiles of apparent cohesion for drying and wetting conditions in Figure 6.30. Apparent cohesion is essentially uniform at approximately 2 kPa for both conditions. Apparent cohesion can have an important effect on the ultimate state of GRS walls (Vahedifard et al. 2014, 2015), and unsaturated conditions can have a significant effect on the stiffness of sand (Khosravi et al. 2010).

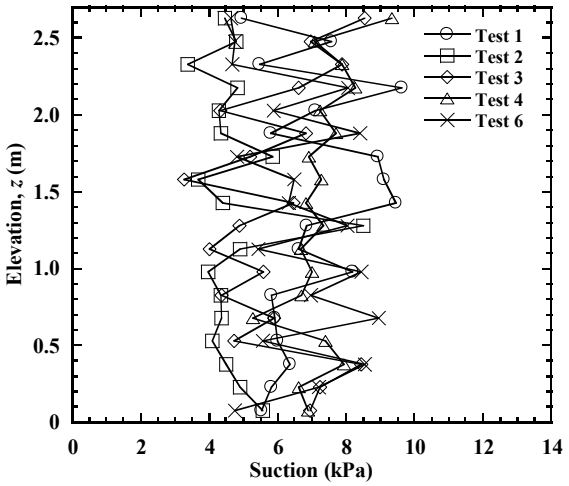

Figure 6.29 Calculated suction profiles.

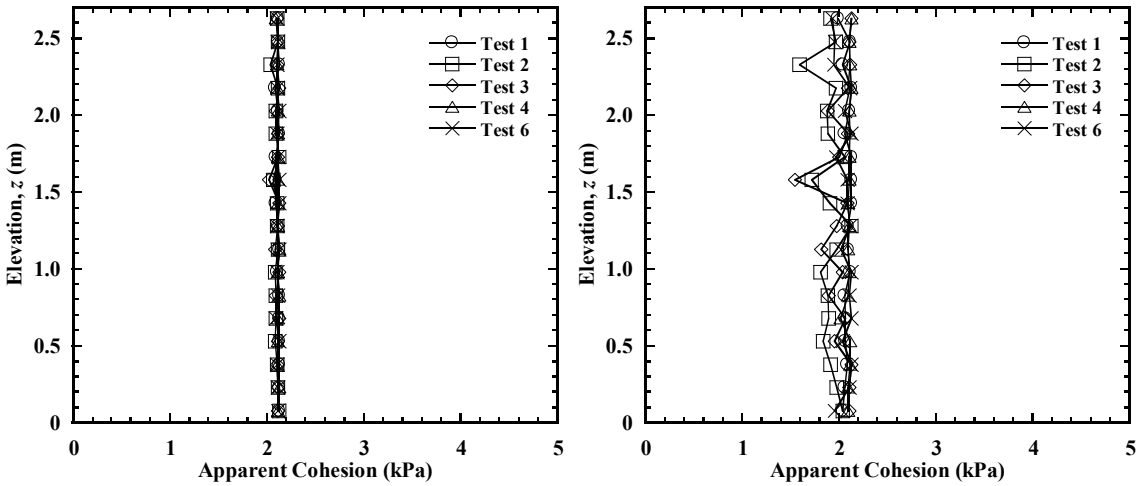

(a) (b)

Figure 6.30 Calculated apparent cohesion profiles: (a) drying condition; (b) wetting condition.

Sand cone tests were performed at selected elevations after compaction of the lift to measure actual dry unit weight, and results for all specimens are shown in Figure 6.31. The actual dry unit weight ranges from 16.0 to 17.8 kN/m^3, and the corresponding relative density ranges from 54% to 86%. Due to the variability in the unit weight values interpreted from the sand cone tests, it is assumed that the achieved dry unit weight values in the

shaking table experiments are consistent enough for direct comparison with each other. A summary of average gravimetric water content, dry unit weight, and relative density for each specimen is presented in Table 6.4.

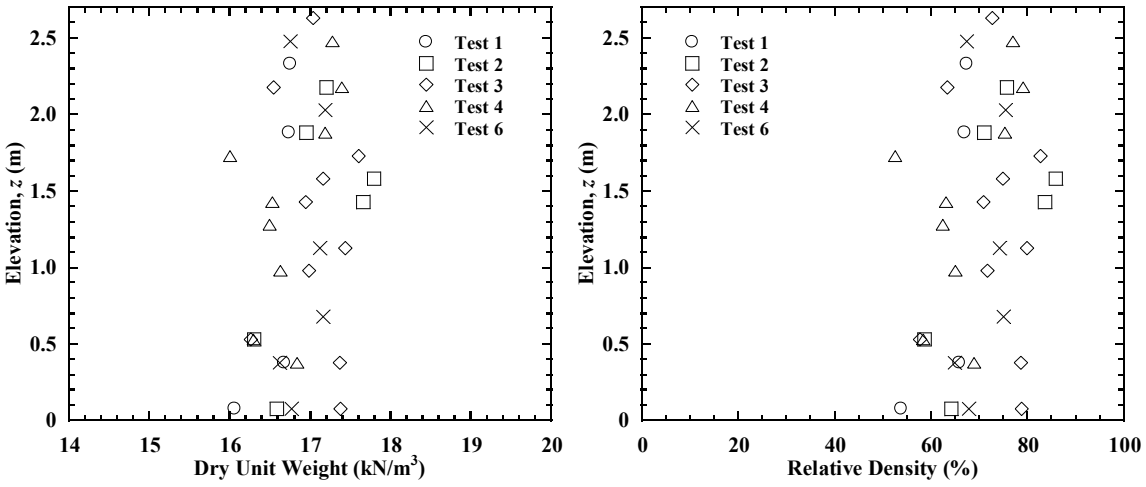

Figure 6.31 Sand cone results: (a) dry unit weight; (b) relative density.

Table 6.4 Average gravimetric water content, dry unit weight, and relative density for each test.

Test	Average gravimetric water content (%)	Average dry unit weight (kN/m^3)	Average relative density (%)
1	4.7	16.6	64
2	6.7	17.1	73
3	5.5	17.1	73
4	4.3	16.7	67
6	5.0	16.9	71

6.7 Input Motions

A series of motions, including white noise, earthquake, and sinusoidal motions, were applied to the GRS bridge abutment system. The shaking table was operated in acceleration-control mode for white noise motions and displacement-control mode for earthquake and sinusoidal motions. A summary of the input motions for shaking table testing is presented in Table 6.5.

Table 6.5 Input motions for shaking table.

Shaking event	Motion	Model-scale duration (s)	Peak ground acceleration (g)	Peak ground displacement (mm)
1	White Noise	120.0	0.10	2.7
2	1940 Imperial Valley	28.3	0.31	65.2
3	White Noise	120.0	0.10	2.7
4	2010 Maule	100.4	0.40	108.0
5	White Noise	120.0	0.10	2.7
6	1994 Northridge[1]	28.3	0.58	88.7
7	White Noise	120.0	0.10	2.7
8	Sin @ 0.5 Hz	40.0	0.05	50.0
9	Sin @ 1 Hz	40.0	0.10	25.0
10	Sin @ 2 Hz	40.0	0.20	12.5
11	Sin @ 5 Hz	40.0	0.25	2.5
12	White Noise	120.0	0.10	2.7

[1] The Northridge motion was applied after sinusoidal motions for Test 1.

White noise motions were used to characterize natural frequencies of the bridge system, and identify any changes in system response (i.e., modulus and damping) due to strains incurred from previous shaking. The nominal white noise motion has a peak acceleration of 0.1*g*, a root-mean-square (RMS) acceleration of 0.025*g*, and frequency content ranging from 0.1 to 50 Hz, as shown in Figure 6.32.

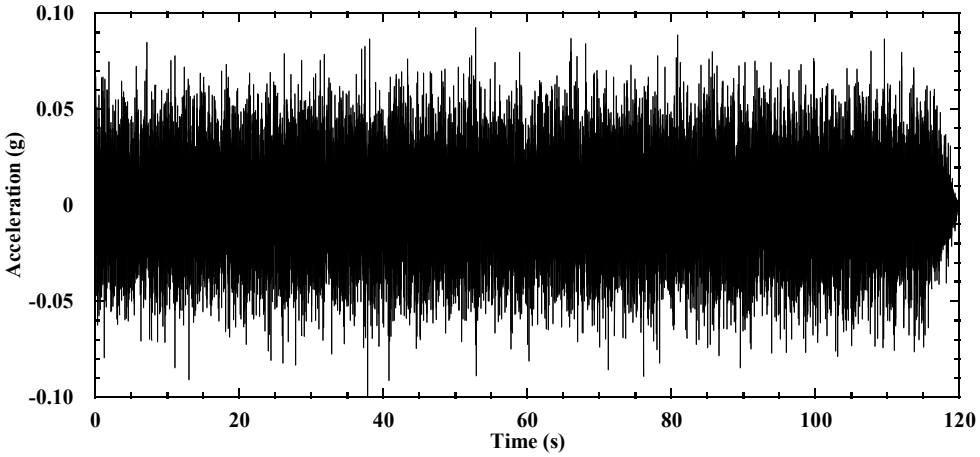

Figure 6.32 White noise motion.

Shaking tests were conducted using earthquake motions scaled from the strike-slip 1940 Imperial Valley earthquake (El Centro station), the subduction zone 2010 Maule earthquake (Concepcion station), and the strike-slip 1994 Northridge earthquake (Newhall station) records. Acceleration and displacement time histories for the original Imperial Valley record are shown in Figure 6.33, and indicate a peak ground acceleration (PGA) of 0.31*g* and peak ground displacement (PGD) of 130.4 mm. To obtain the input acceleration time history for the shaking test, also shown in Figure 6.33(a), acceleration amplitudes of the original record were not scaled and frequencies were scaled (increased) by a factor of $\sqrt{2}$ (Table 6.2). The scaled displacement time history is shown in Figure 6.33(b) and was

obtained by double integration of the scaled acceleration. The displacement motion indicates PGD = 65.2 mm, which is one-half of the PGD for the original record. Scaled input motions for the Maule and Northridge earthquake records were obtained similarly, and yield PGA = 0.40*g* and PGD = 108.0 mm for the Maule motion and PGA = 0.58*g* and PGD = 88.7 mm for the Northridge motion, as shown in Figure 6.34 and Figure 6.35, respectively. The time increment is 0.00707 s for the scaled Imperial Valley and Northridge motions, and is 0.00354 s for the Maule motion.

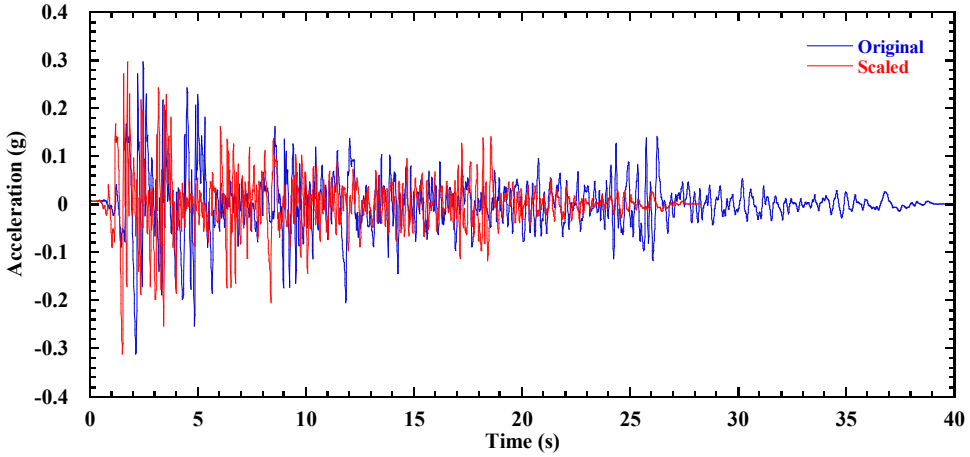

(a)

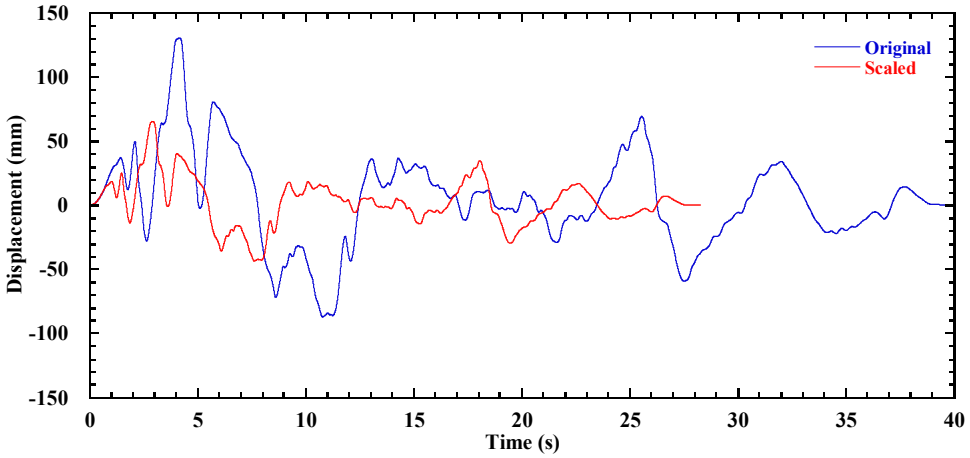

(b)

Figure 6.33 Original records and scaled motions for the 1940 Imperial Valley earthquake (El Centro station): (a) acceleration time history; (b) displacement time history.

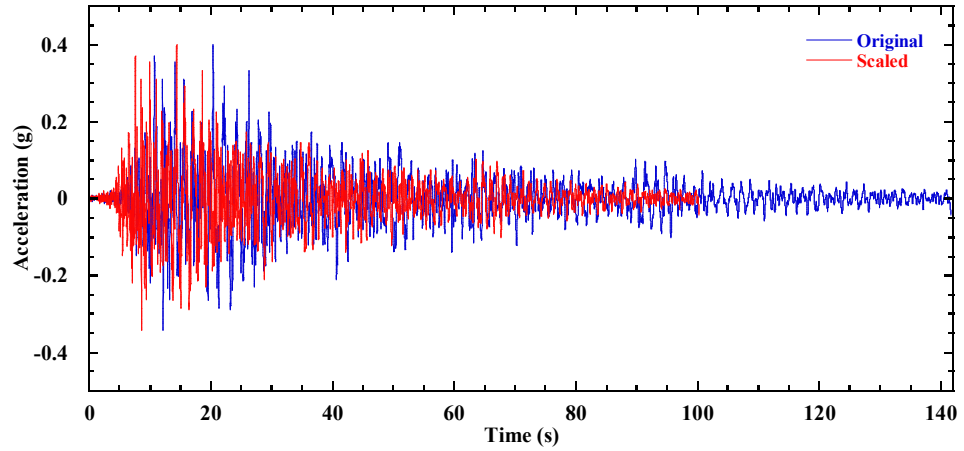

(a)

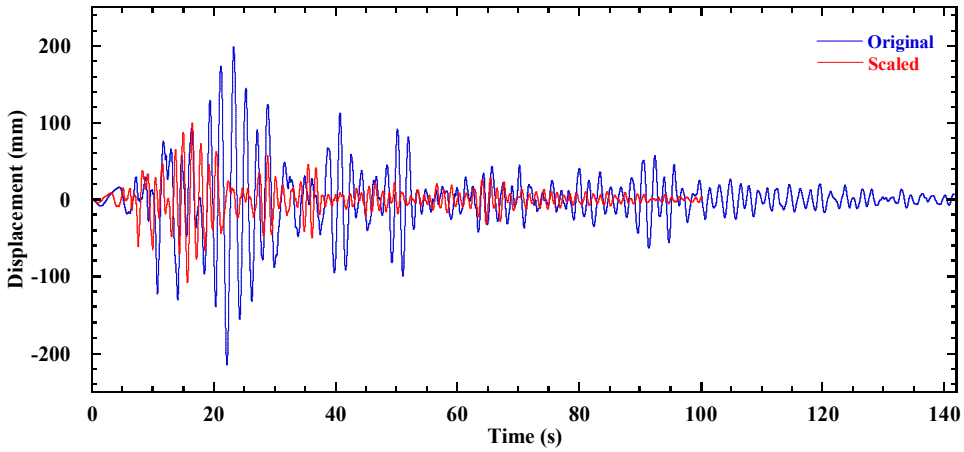

(b)

Figure 6.34 Original records and scaled motions for the 2010 Maule earthquake (Concepcion station): (a) acceleration time history; (b) displacement time history.

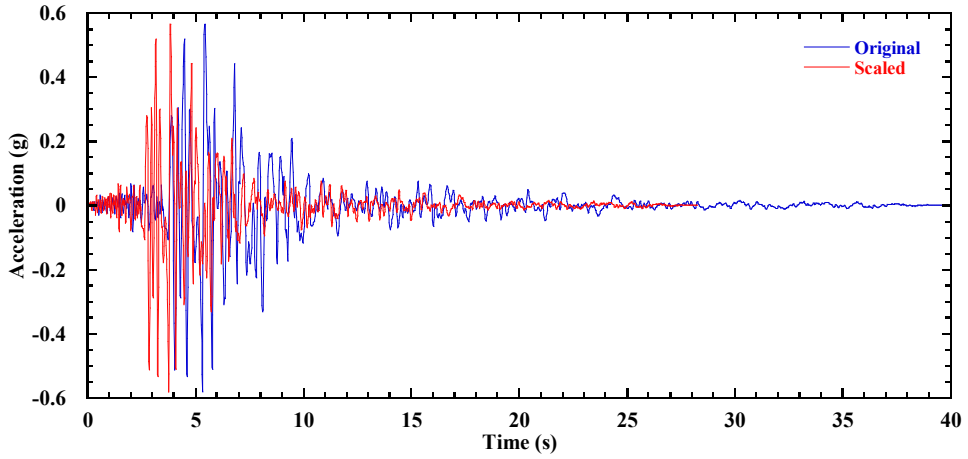

(a)

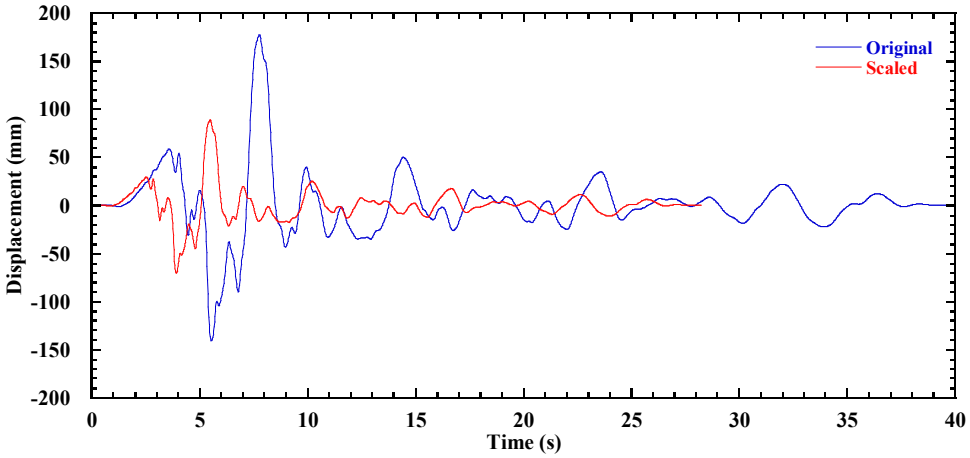

(b)

Figure 6.35 Original records and scaled motions for the 1994 Northridge earthquake (Newhall station): (a) acceleration time history; (b) displacement time history.

Sinusoidal motions with frequencies of 0.5, 1.0, 2.0, 5.0 Hz were also applied to the GRS bridge abutment systems after the earthquake motions. Example displacement time history for the sinusoidal motions is shown in Figure 6.36.

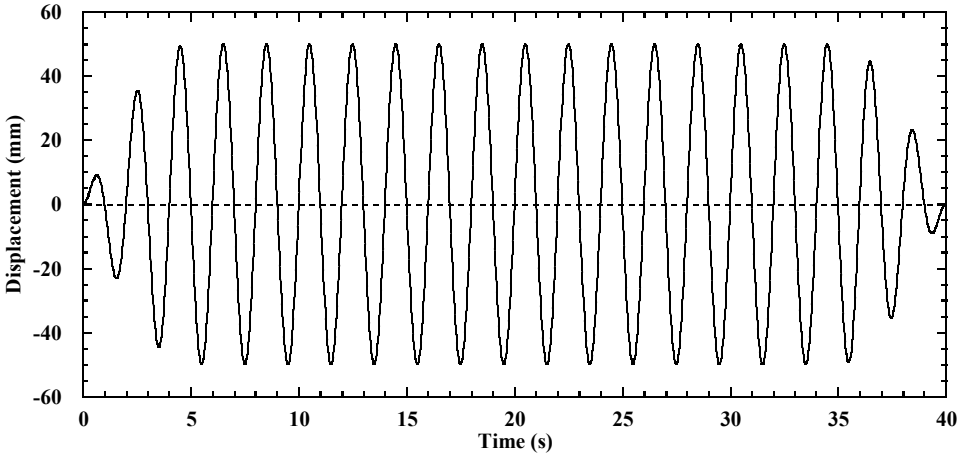

(a)

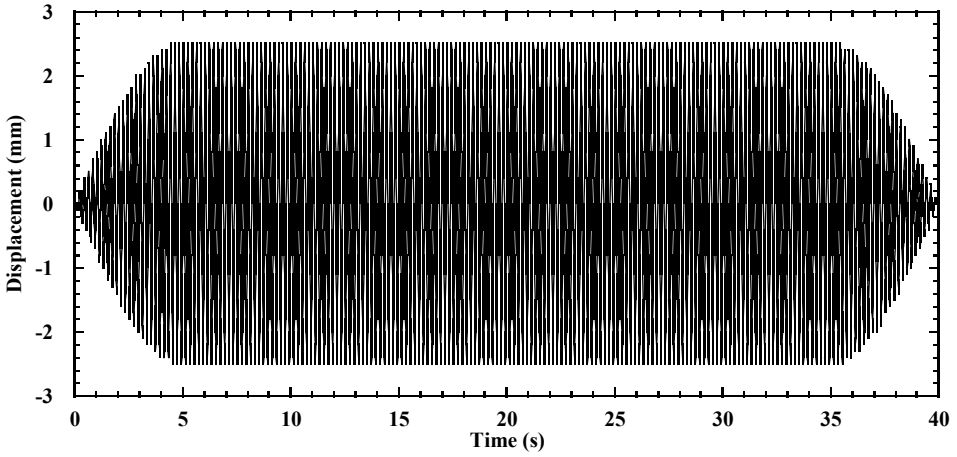

(b)

Figure 6.36 Displacement time history for sinusoidal motion: (a) 0.5 Hz; (b) 5.0 Hz.

6.8 Acknowledgements

The text below is reproduced verbatim as it appears in the acknowledgments section per the UCSD Office of Graduate Studies Formatting Requirements.

Chapter 6 of this dissertation is partially based on materials from a manuscript under review for publication by the Geotechnical Testing Journal titled “Shaking Table Test of a Half-Scale Geosynthetic Reinforced Soil Bridge Abutment” with authors, Yewei Zheng, Andrew C. Sander, Wenyong Rong, Patrick J. Fox, P. Benson Shing, and John S. McCartney (2017). The dissertation author is the first author of this paper.

Chapter 7

Longitudinal Test Results and Analysis

7.1 Introduction

This chapter presents results and analysis for the longitudinal tests on the GRS bridge abutments (Tests 1-4). In addition to the characterization tests for the system identification and testing system performance, results are presented in this chapter including facing displacements, bridge seat and bridge beam displacements, acceleration responses, lateral and vertical stresses, reinforcement strains, and contact forces between the bridge seat and bridge beam during a series of shaking events in the longitudinal direction. Detailed results including time histories for Test 1 (baseline case) are presented and discussed to describe the general behavior of GRS bridge abutments, and synthesis results from different tests are compared and discussed to investigate the effects of different design parameters. More detailed results on the other tests can be found in McCartney et al. (2018).

When processing the data, the string potentiometer measurements for horizontal displacements of the front wall facing, bridge seat, and bridge beam were corrected using measured horizontal displacements of the shaking table in the direction of shaking to yield relative displacements with respect to the table. In the direction of shaking, horizontal displacements and accelerations toward the north direction (Figure 6.17) are defined as positive. In the direction perpendicular to shaking, outward displacements of the side wall facings are defined as positive. Consistent with geotechnical sign conventions, downward vertical settlements are defined as positive. For static loading (construction stages), Stage 1 involved construction of the lower GRS wall, Stage 2 involved construction of the bridge seat and upper GRS wall, and Stage 3 involved placement of the bridge beam atop the GRS bridge abutment. All presented results are in model-scale, and results should be adjusted using the similitude relationships in Table 6.2 to obtain corresponding values for prototype structures.

7.2 System Identification

System identification tests were conducted using the white noise motions at different stages of the shaking program. The first such test was conducted on the reaction wall itself prior to construction of the GRS bridge abutment. Amplitudes of the horizontal acceleration transfer functions (i.e., output divided by input in frequency domain) of the reaction wall with respect to the shaking table are shown in Figure 7.1(a). The reaction wall has a fundamental frequency of 37.5 Hz, which is well above the operating frequency band of the shaking table and fundamental frequency of the GRS bridge abutment. Therefore, the reaction wall is not expected to resonate during shaking and should move essentially in phase with the shaking table.

White noise tests also were conducted on the GRS bridge abutment system before and after each earthquake motion to detect changes in fundamental frequency due to softening of the backfill soil. Amplitudes of the horizontal acceleration transfer functions for the bridge beam and bridge seat with respect to the shaking table in the longitudinal direction for the initial white noise test (Shaking event 1) are shown in Figure 7.1(b). The results indicate fundamental frequencies of 5.5 Hz and 11.9 Hz for the bridge beam and bridge seat, respectively. Amplitudes of the horizontal acceleration transfer functions for the GRS bridge abutment (measured at $x = 0.48$ m, $z = 1.875$ m) with respect to the shaking table for white noise tests before and after the earthquake motions are shown in Figure 7.1(c). The GRS bridge abutment has the same fundamental frequency as the bridge seat (11.9 Hz) before the Imperial Valley motion. The corresponding fundamental frequency

for the prototype GRS bridge abutment is 8.4 Hz according to the scaling factors in Table 6.2. After the Imperial Valley motion, the fundamental frequency of the abutment decreased from 11.9 to 11.3 Hz, and then decreased further to 10.9 Hz after the Maule motion. These decreases are attributed to shear modulus reduction of the backfill soil associated with shear strain development during successive shaking events.

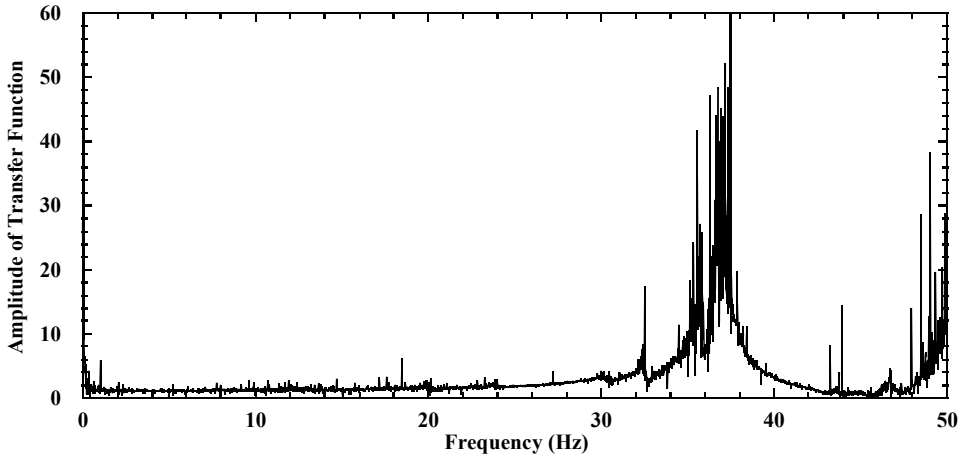

(a)

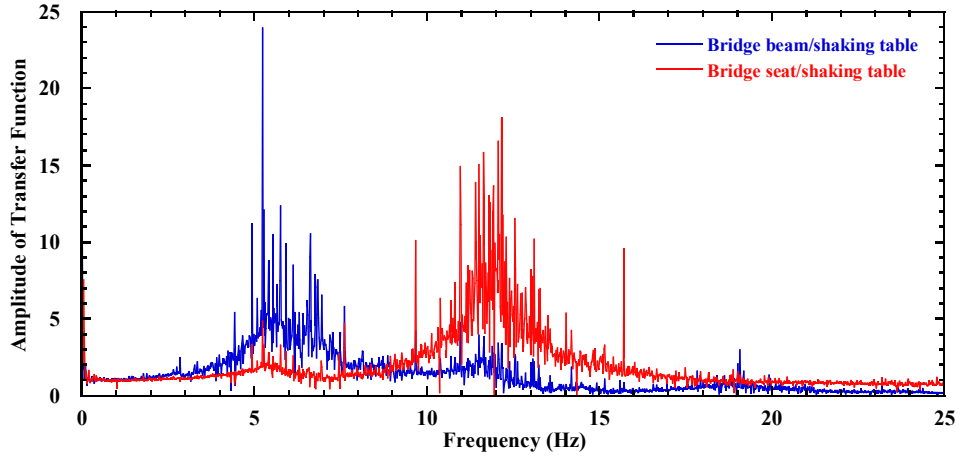

(b)

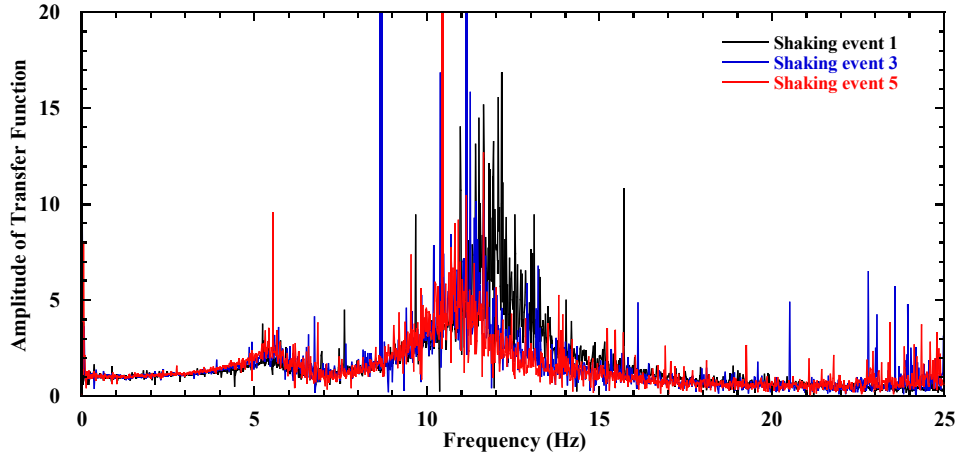

(c)

Figure 7.1 Horizontal acceleration transfer function amplitudes for white noise tests in Test 1: (a) reaction wall only; (b) bridge seat and bridge beam for the initial white noise motion; (c) GRS bridge abutment before and after the first two earthquake motions.

7.3 Testing System Performance

The characterization of the testing system performance is critical for the longitudinal test because the configuration of the bridge system with one end (i.e., support wall) moving on a sliding platform off the shaking table is unique and has not been evaluated in a previous shaking table experiment. The approach used in this study permits a unique evaluation of the GRS bridge abutment response in a longitudinal configuration.

The performance of the testing system (i.e., the shaking table and the connected support wall resting on the sliding platform) was evaluated based on the measured displacement and acceleration responses in the direction of shaking. The testing system responses for the Imperial Valley, Maule, and Northridge motions in Test 1 are shown in Figure 7.2, Figure 7.3, and Figure 7.4, respectively, and a summary of the target and measured peak responses of the shaking table for the three earthquake motions is presented in Table 7.1.

Table 7.1 Shaking table response for earthquake motions in Test 1.

Shaking event	Earthquake motion	Model-scale duration (s)	Target PGA (*g*)	Actual PGA (*g*)	Target PGD (mm)	Actual PGD (mm)
2	Imperial Valley	28.3	0.31	0.42	65.2	65.2
4	Maule	100.4	0.40	0.58	108.0	108.0
11	Northridge	28.3	0.58	1.09	88.7	88.6

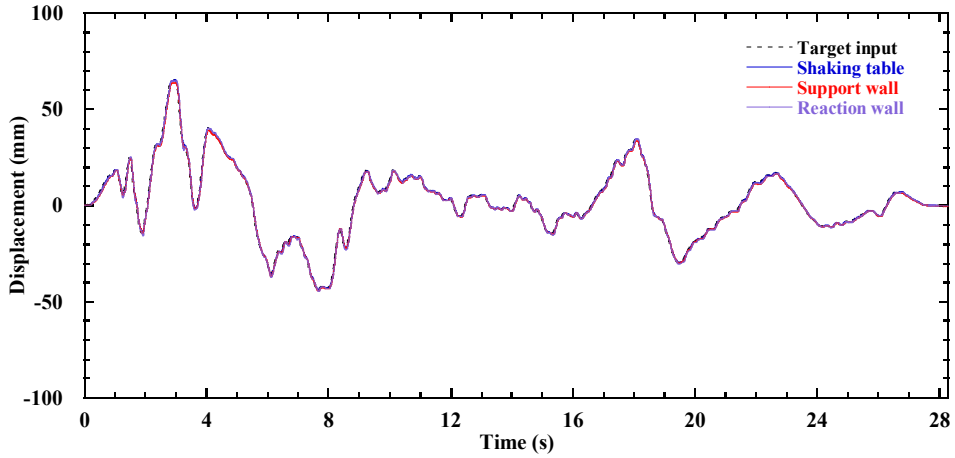

(a)

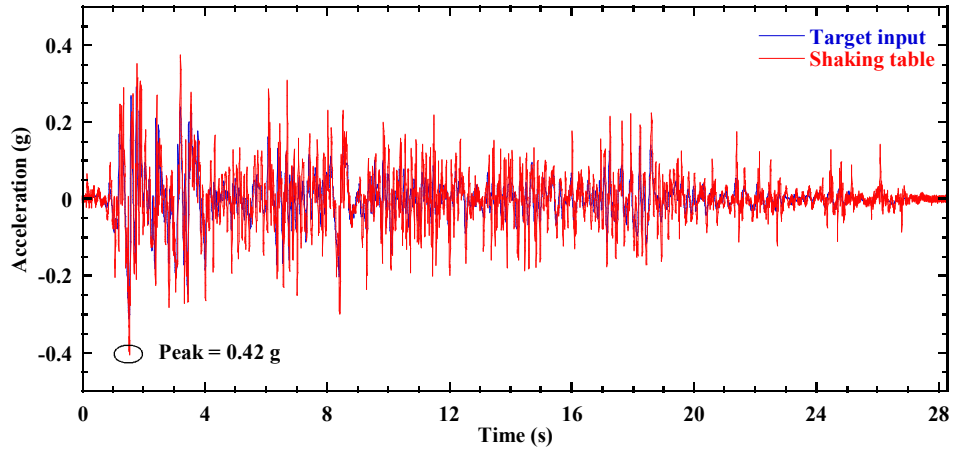

(b)

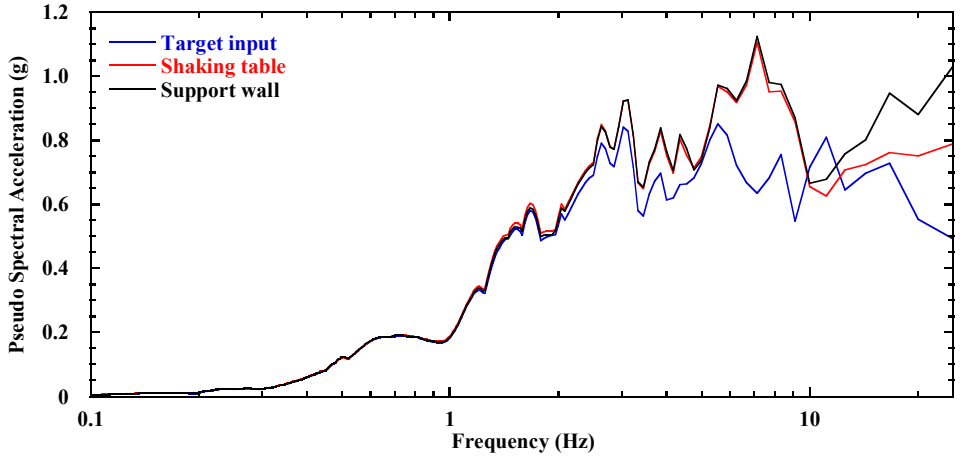

(c)

Figure 7.2 Testing system response for the Imperial Valley motion in Test 1: (a) displacement time history; (b) acceleration time history; (c) response spectra (5% damping).

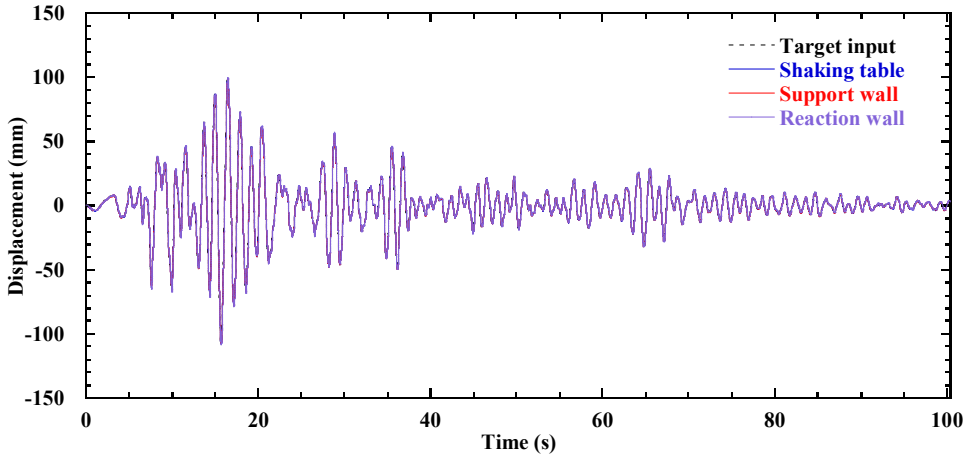

(a)

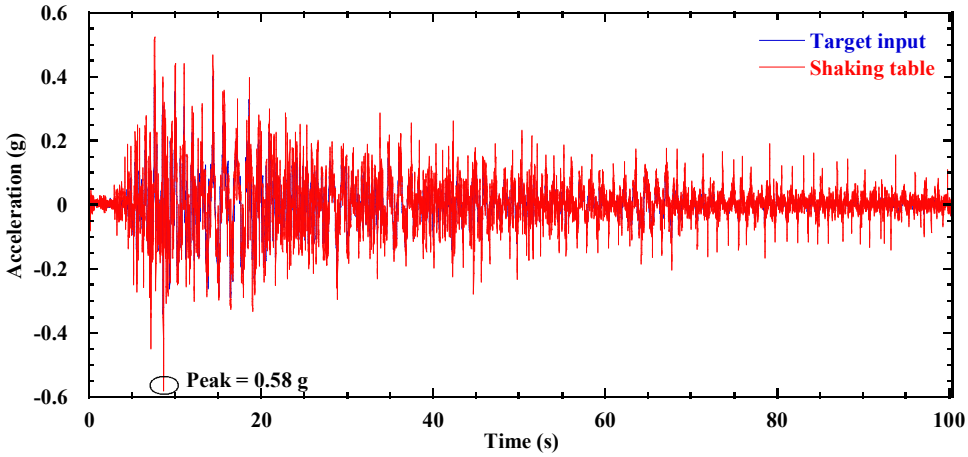

(b)

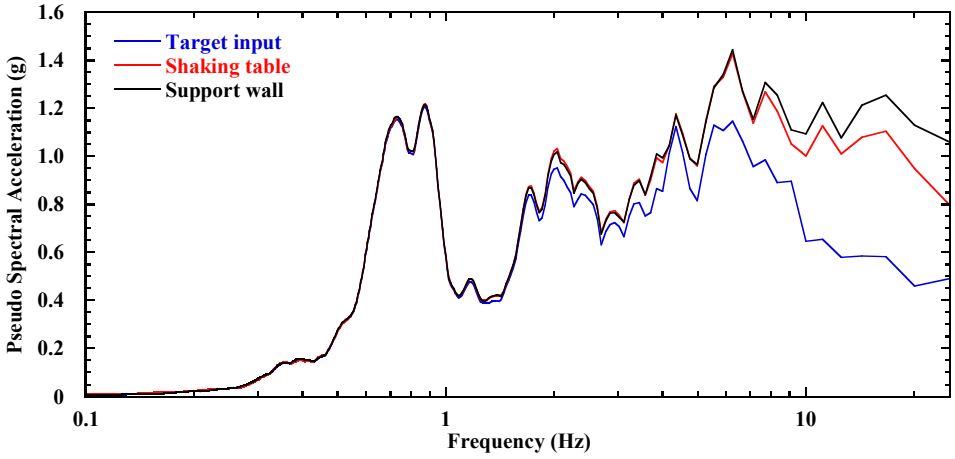

(c)

Figure 7.3 Testing system response for the Maule motion in Test 1: (a) displacement time history; (b) acceleration time history; (c) response spectra (5% damping).

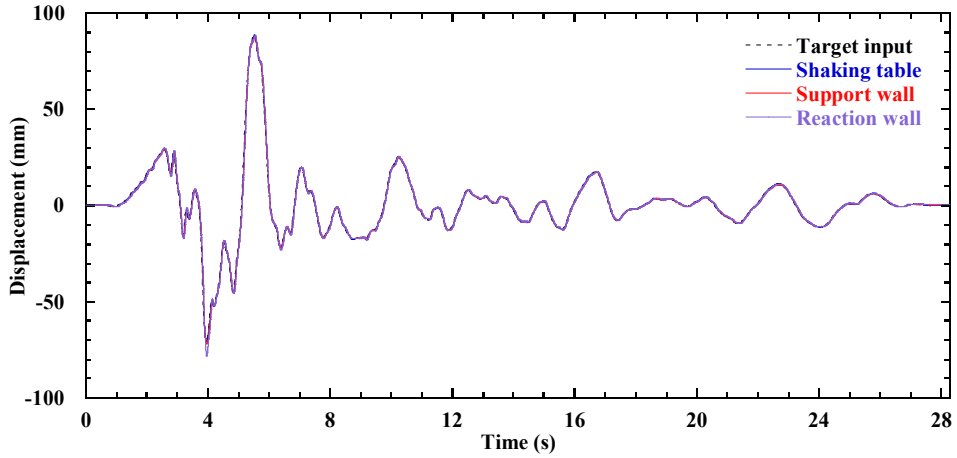

(a)

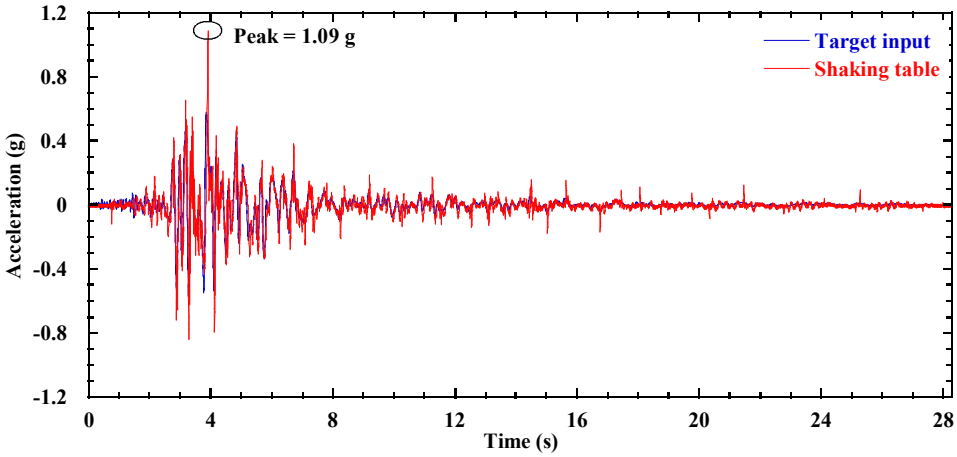

(b)

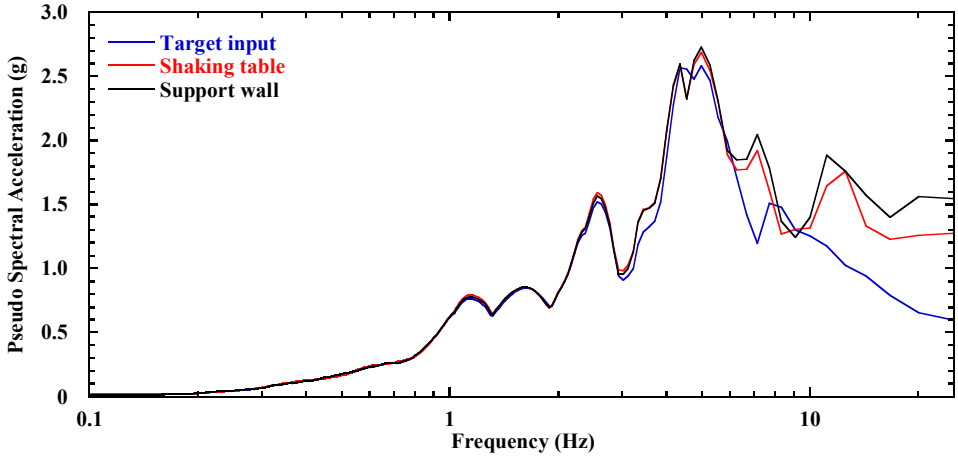

(c)

Figure 7.4 Testing system response for the Northridge motion in Test 1: (a) displacement time history; (b) acceleration time history; (c) response spectra (5% damping).

The measured displacement time histories of the shaking table, reaction wall, and support wall are essentially in identical agreement with the target input for all three earthquake motions. This indicates that (1) the shaking table performed well in displacement-control mode for earthquake motions; (2) the reaction wall is sufficiently stiff and moved essentially in phase with the shaking table; and (3) the steel connection beams and sliding platform successfully transmitted table motions to the base of the support wall.

The measured acceleration time history for the shaking table, generally matches well with the target input accelerations, but shows larger peak accelerations. For instance, the measured peak acceleration of the shaking table for the Imperial Valley motion is 0.42*g* at 1.6 s, which is larger than the target value of 0.31*g*. The shaking table was refurbished prior to this study to increase the fidelity of dynamic motion. After repair of the shaking table, overshooting of peak accelerations was still observed, but the overshooting was much smaller than before repair, which indicates that the performance of the table has been improved (Trautner et al. 2017). The overshooting is likely due to the inertia of the table itself and also affected by the structures on the table.

The pseudo-spectral accelerations of the shaking table and target motion are in good agreement for frequencies less than 10 Hz for all three motions, which indicates that the shaking table adequately reproduced the salient characteristics of the target input motions. The actual pseudo-spectral acceleration at the fundamental frequency of 11.9 Hz for the GRS bridge abutment is slightly larger than the target value for all three motions. In general, results show that the shaking table followed the target input motion, and the support wall moved in phase with the shaking table.

7.4 Facing Displacements

7.4.1 Static Loading

Facing displacements were measured for the longitudinal centerline and off-centerline sections (referred to as L1 and L2 as labeled in Figure 6.23) and the transverse section T1 (referred to as T1). Facing displacement profiles for the three instrumented sections after the three stages of construction are shown in Figure 7.5, and the maximum values of facing displacement profiles are presented in Table 7.2.

For Stage 1, facing displacement profiles for the longitudinal sections L1 and L2 are similar, and have maximum displacements of 2.3 mm and 2.0 mm, respectively, both at an elevation z = 0.675 m above the foundation soil level. Transverse section T1 has smaller facing displacements with a maximum value of 1.2 mm at the mid-height of the wall. Although the shapes of facing displacement profile for the longitudinal and transverse sections are different, the magnitudes of the facing displacements are small and it is difficult to identify a consistent shape to reflect construction effects. For Stage 2, facing displacements increased slightly due to construction of the bridge seat and upper wall. For Stage 3, the upper half section of the wall increased 0.8 mm for all three sections. The maximum displacement for L1 is 3.2 mm at z = 1.575 m, and the maximum value for T1 is 2.2 mm at z = 1.275 m. In general, the longitudinal sections L1 and L2 had similar facing displacement profiles for construction stages, and the transverse section T1 showed smaller displacements.

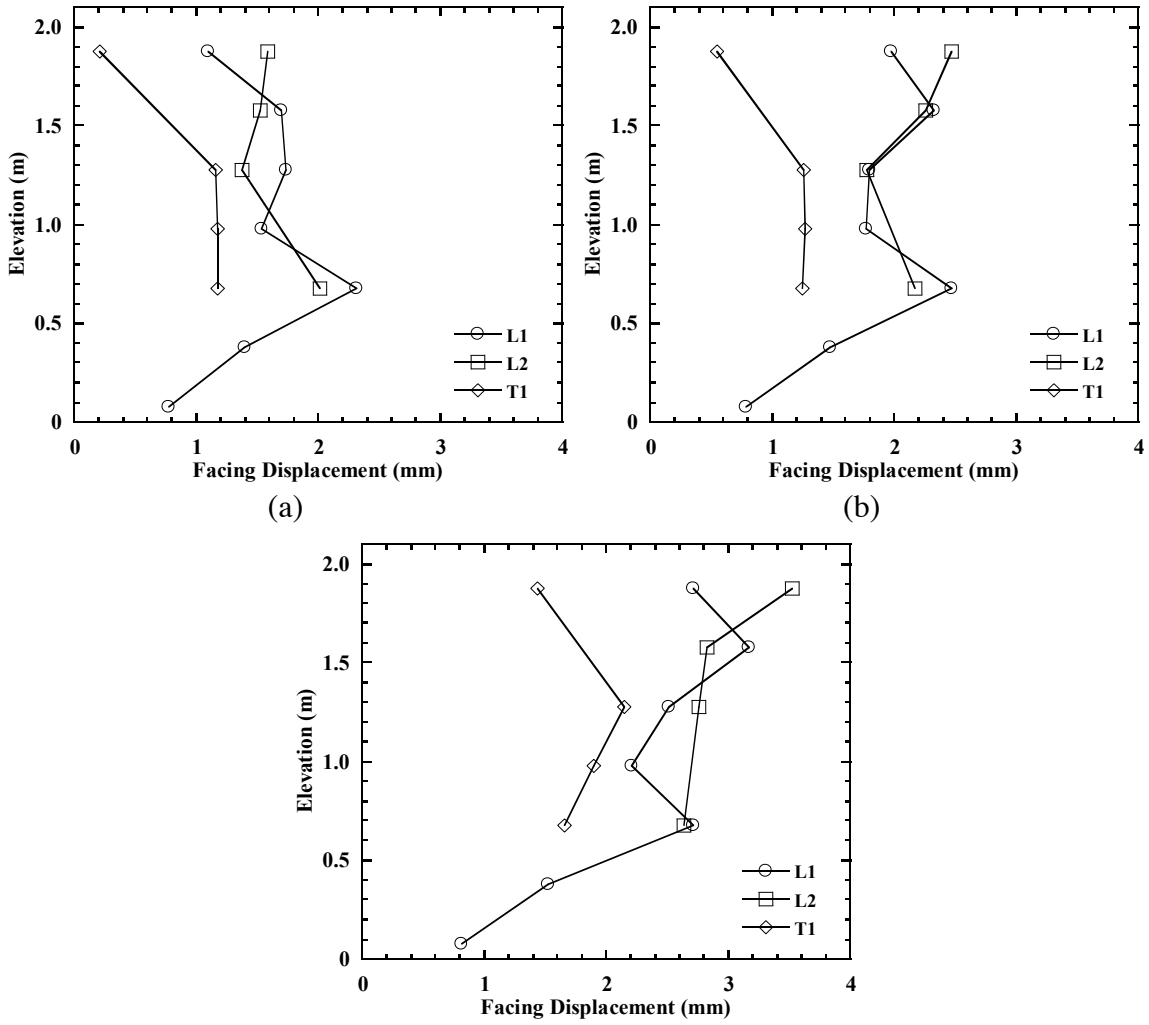

Figure 7.5 Facing displacement profiles for construction stages in Test 1: (a) Stage 1; (b) Stage 2; (c) Stage 3.

Table 7.2 Maximum facing displacements for construction stages in Test 1 (model-scale).

Construction stage	Maximum displacement (mm) for L1	Maximum displacement (mm) for L2	Maximum displacement (mm) for T1
Stage 1	2.3	2.0	1.2
Stage 2	2.5	2.5	1.3
Stage 3	3.2	3.5	2.2

Facing displacement profiles for different tests (Tests 1-4) after Stages 1 and 3 are shown in Figure 7.6 and Figure 7.7, respectively, and the maximum values of the facing displacement profiles are presented in Table 7.3. For Stage 1, facing displacements of the longitudinal section L1 are the largest for Test 4 with a maximum value of 4.7 mm at z = 0.975 m, and the facing displacement profiles for Test 3 also show slightly larger facing displacements than Tests 1 and 2 with a maximum displacement of 2.7 mm at the same elevation. For the transverse section T1, facing displacements for Tests 2, 3, and 4 are similar and are larger than for Test 1. For Stage 1, Test 1 had similar facing displacements with Test 2 for L1, but smaller displacements for T1, which may be attributed to greater compaction near the side wall facings for Test 2 during construction, as the specimens for Tests 1 and 2 have the same configuration at this stage.

For Stage 3, the facing displacements for L1 in Tests 3 and 4 are larger than Tests 1 and 2, with maximum values of 5.0 mm and 6.0 mm, respectively, which indicate that the reinforcement stiffness and spacing have important effects on the facing displacements. Test 1 has larger facing displacements than Test 2 for the upper section of the wall due to the greater bridge load in Test 1. For instance, the maximum facing displacement of 3.2 mm for L1 in Test 1 at z = 1.575 m is greater than 2.4 mm at the same elevation for Test 2. Larger facing displacements for T1 are observed in Tests 3 and 4, as shown in Figure 7.7(b), similar to the observations for L1 in these tests. Facing displacements for T1 in Test 2 are larger than Test 1, which is consistent with the observation for Stage 1.

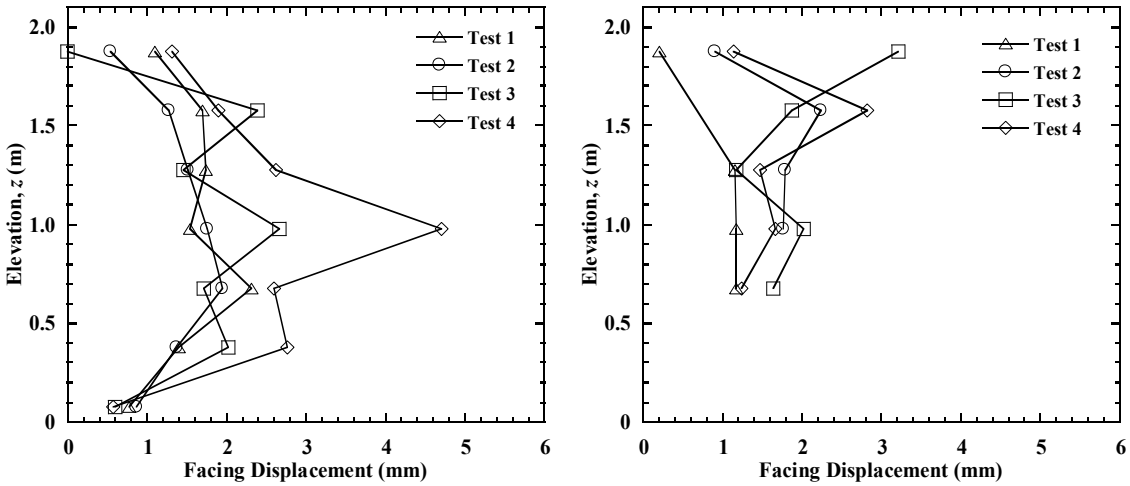

Figure 7.6 Facing displacement profiles for Stage 1 in Tests 1 to 4: (a) L1; (b) T1.

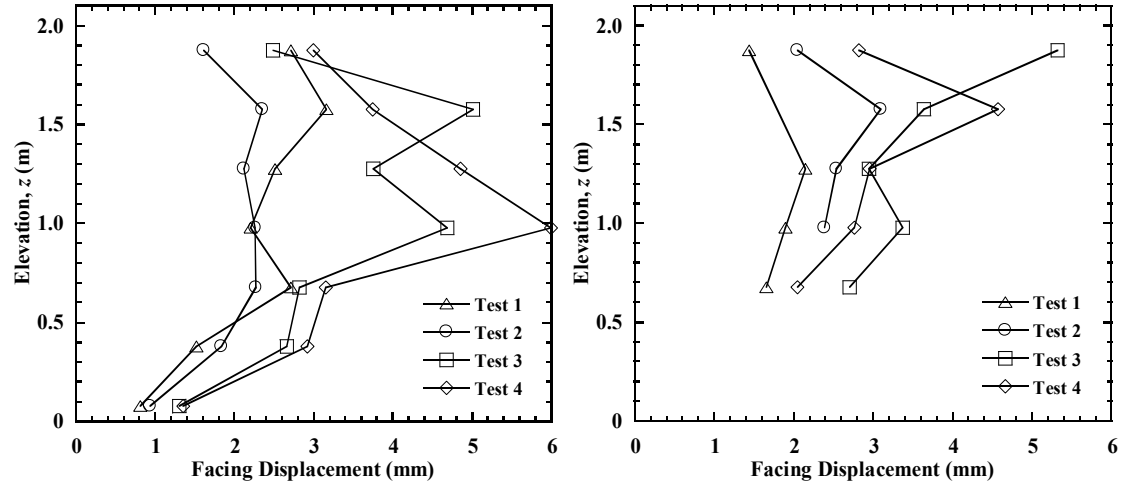

Figure 7.7 Facing displacement profiles for Stage 3 in Tests 1 to 4: (a) L1; (b) T1.

Table 7.3 Maximum facing displacements for construction stages in Tests 1 to 4 (model-scale).

Construction stage	Maximum displacement (mm) in Test 1		Maximum displacement (mm) in Test 2		Maximum displacement (mm) in Test 3		Maximum displacement (mm) in Test 4	
	L1	T1	L1	T1	L1	T1	L1	T1
Stage 1	2.3	1.2	2.0	2.2	2.7	3.2	4.7	2.8
Stage 2	2.5	1.3	2.2	2.7	3.2	4.2	5.0	3.5
Stage 3	3.2	2.2	2.4	3.1	5.0	5.3	6.0	4.6

Facing displacements for Stages 1 and 2 might be subjected to the influences of construction technique (e.g., backfill soil compaction and facing block alignment) to some extent. In order to better understand the effects of different design parameters for static loading conditions, the incremental facing displacements due to placement of bridge beam (from Stages 2 to 3) for L1 and T1 are plotted in Figure 7.8.

For the longitudinal section L1, Test 3 has the largest incremental facing displacements with a maximum value of 2.0 mm at z = 1.575 m, and the incremental facing displacement is 1.5 mm for Test 4 at the same elevation. Tests 1 and 2 have similar incremental facing displacements for the lower section of the wall, but the incremental facing displacements of the upper section in Test 1 are slightly larger than Test 2, as expected. Similar to the incremental facing displacement profiles for L1, Test 3 has the largest incremental facing displacements for T1. However, the facing displacement profiles for Tests 1 and 4 are similar. The incremental facing displacements of T1 for Test 1 are larger than Test 2, though the cumulative facing displacements are smaller at the end of construction (Figure 7.7).

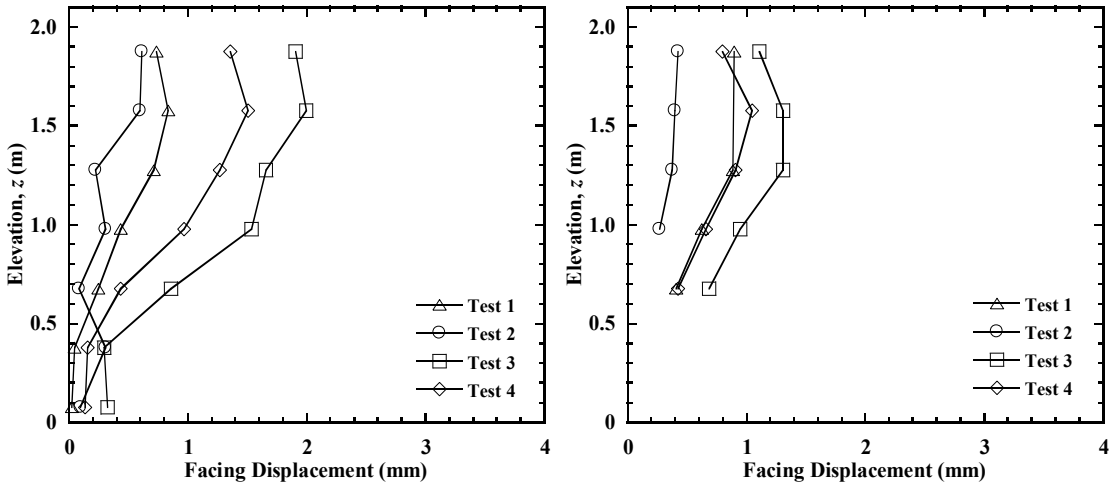

Figure 7.8 Incremental facing displacement profiles due to bridge load placement (from Stages 2 to 3) in Tests 1 to 4: (a) L1; (b) T1.

Results in this section indicate that the reinforcement spacing and stiffness have important effects on the facing displacements of GRS bridge abutments for static loading conditions. Facing displacements increase with increasing reinforcement spacing and decreased reinforcement stiffness. Greater bridge load also induces larger facing displacements for the upper section of the wall in both the longitudinal and transverse directions.

7.4.2 Dynamic Loading

Time histories of incremental facing displacements for the longitudinal sections L1 and L2 during the Imperial Valley, Maule, and Northridge motions in Test 1 are shown in Figure 7.9, Figure 7.10, and Figure 7.11, respectively. Time histories of incremental facing displacements for the transverse section T1 during the three earthquake motions are shown in Figure 7.12, Figure 7.13, and Figure 7.14. The incremental facing displacements are relative to the initial horizontal displacements before each shaking event, and were corrected using the measured horizontal displacements of the shaking table to yield relative facing displacements with respect to the shaking table. For brevity, the relative facing displacements are referred to as facing displacements in this chapter. As mentioned, positive values represent outward facing displacements, and negative values represent inward facing displacements.

Maximum (i.e., during shaking) and residual (i.e., after shaking) facing displacements at the top of the wall are generally larger than at the bottom. For instance, during the Imperial Valley motion, the maximum dynamic facing displacement for L1 at elevation z = 1.875 m is 3.7 mm (t = 1.6 s) and the residual facing displacement is 0.9 mm. For z = 0.075 m, the bottom of the wall had dynamic facing displacements of ±1 mm. In general, the magnitudes of dynamic facing displacements for L1 and L2 are similar during shaking, and most of the dynamic facing displacements were recovered after shaking.

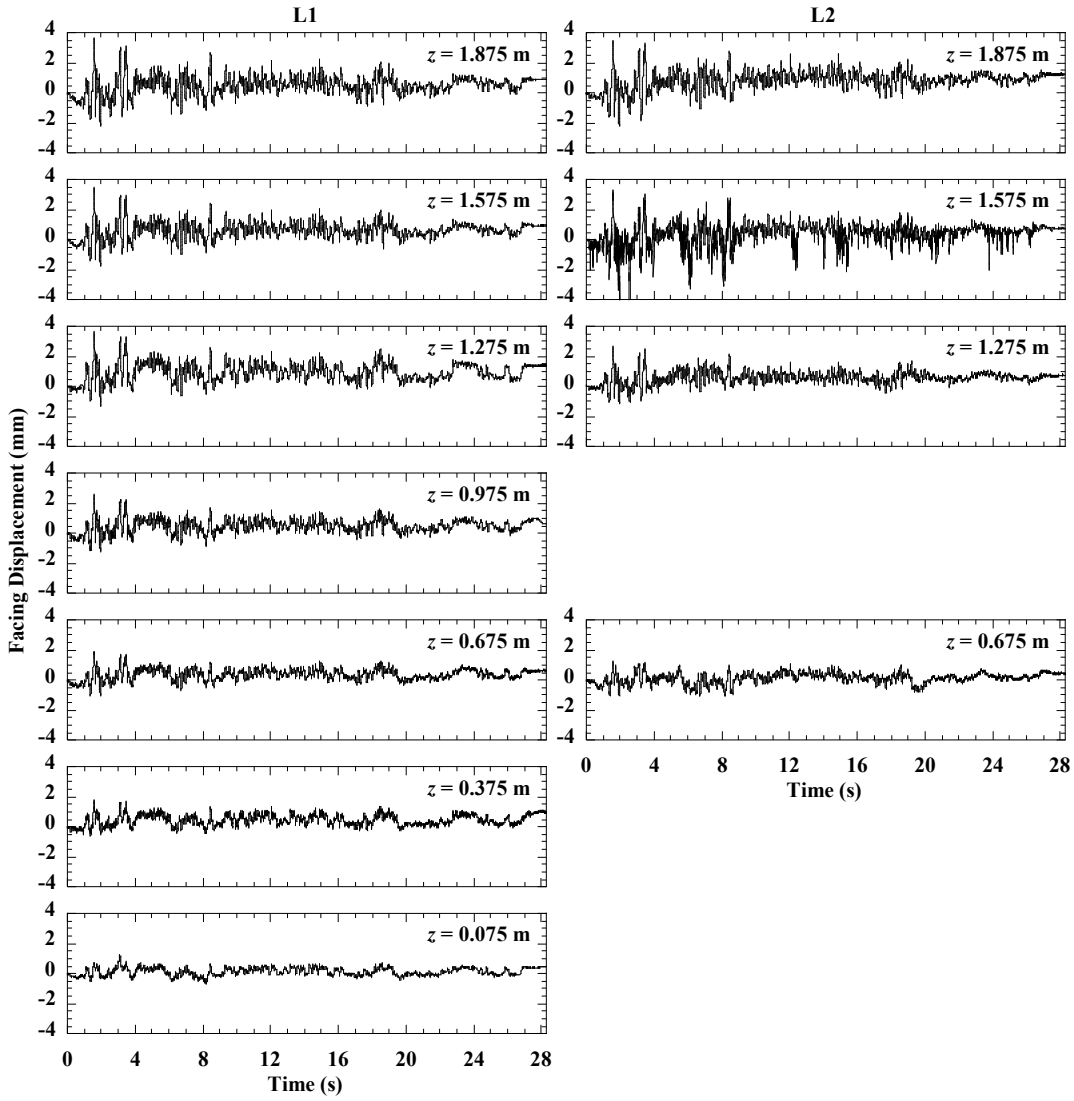

Figure 7.9 Time histories of incremental facing displacement for L1 and L2 during the Imperial Valley motion in Test 1.

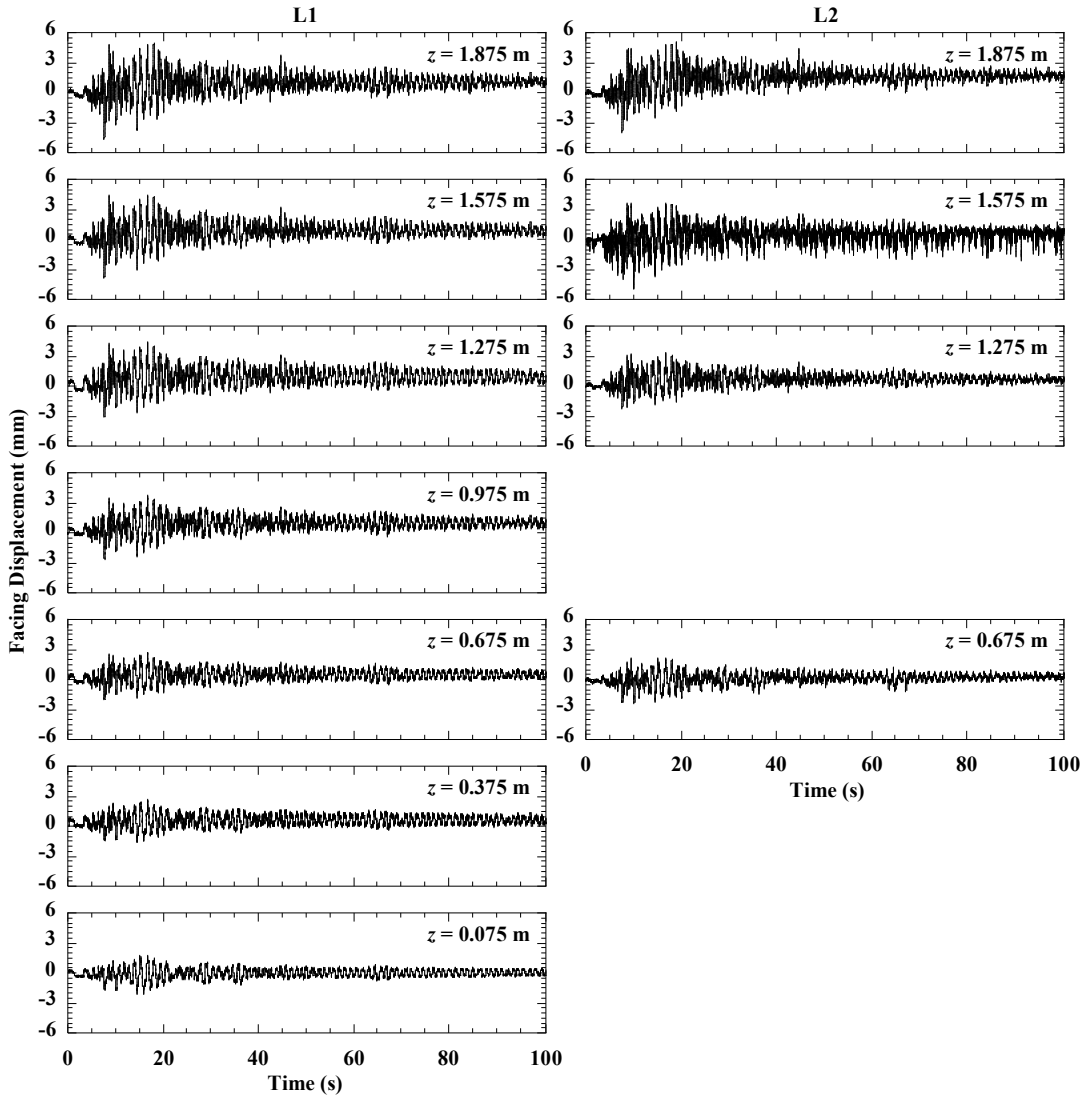

Figure 7.10 Time histories of incremental facing displacement for L1 and L2 during the Maule motion in Test 1.

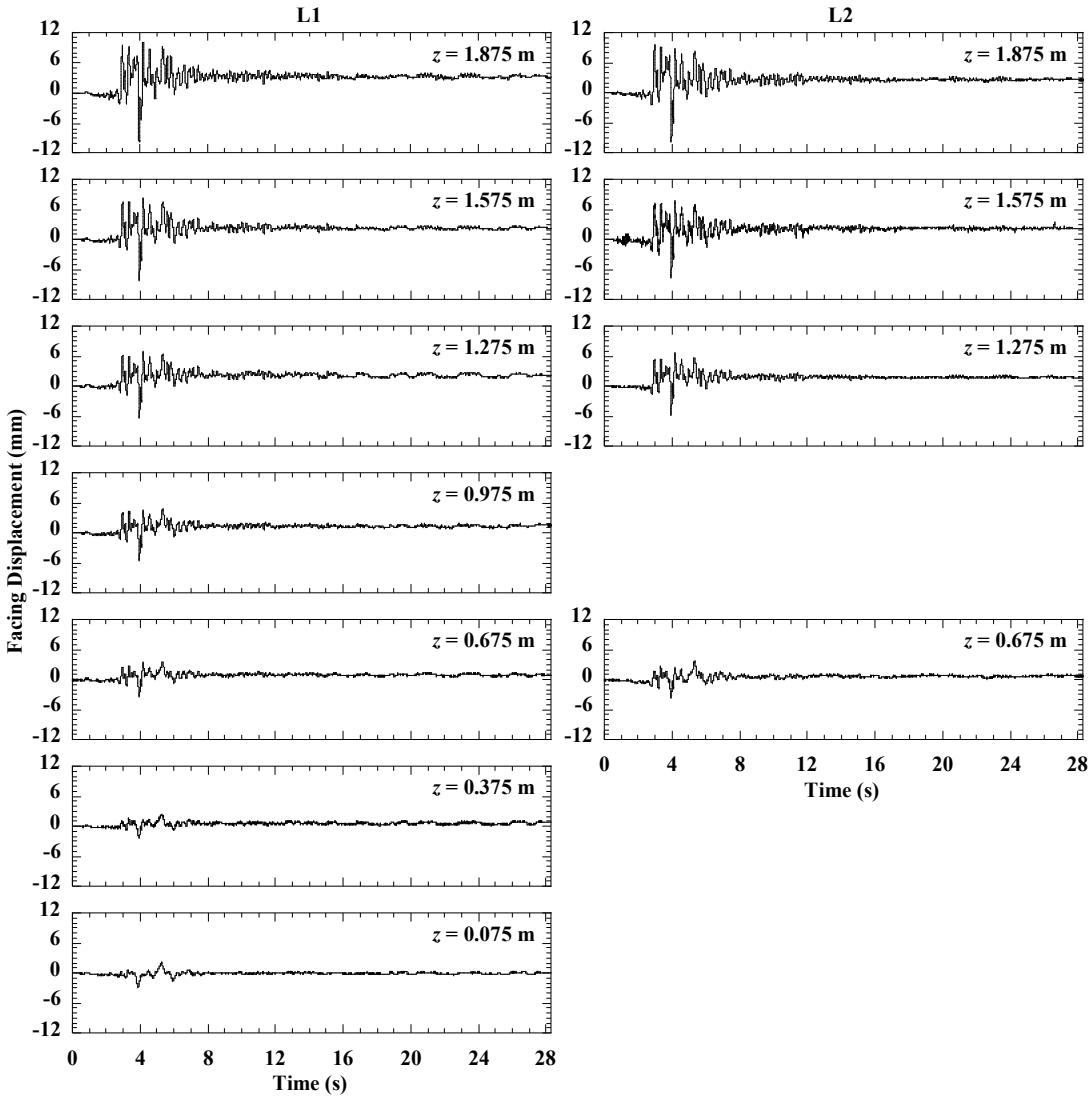

Figure 7.11 Time histories of incremental facing displacement for L1 and L2 during the Northridge motion in Test 1.

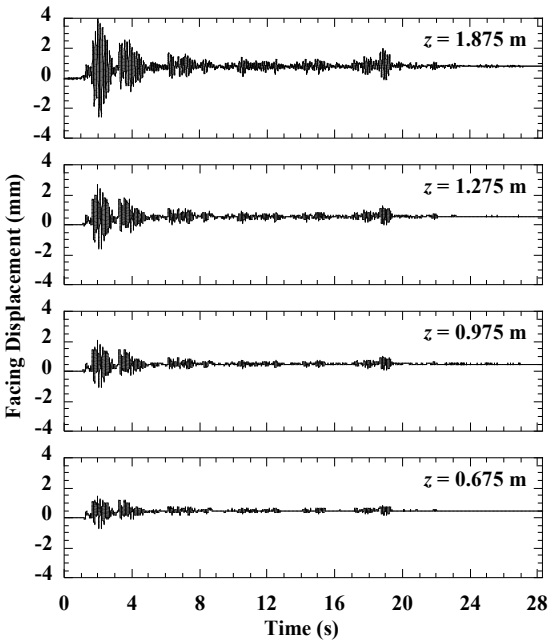

Figure 7.12 Time histories of incremental facing displacement for T1 during the Imperial Valley motion in Test 1.

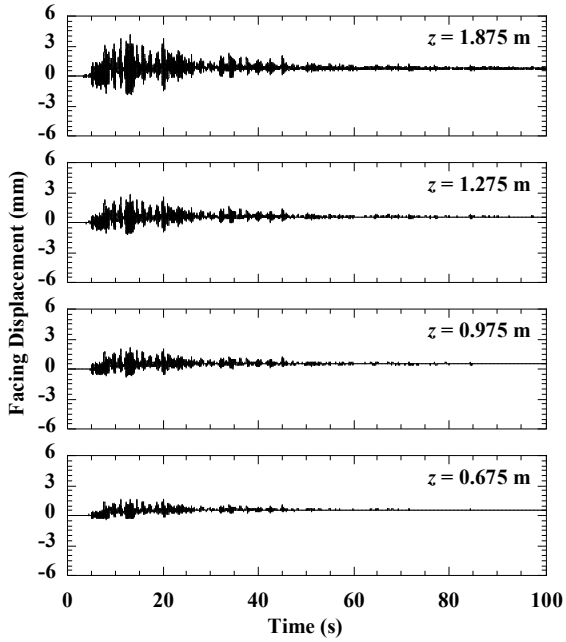

Figure 7.13 Time histories of incremental facing displacement for T1 during the Maule motion in Test 1.

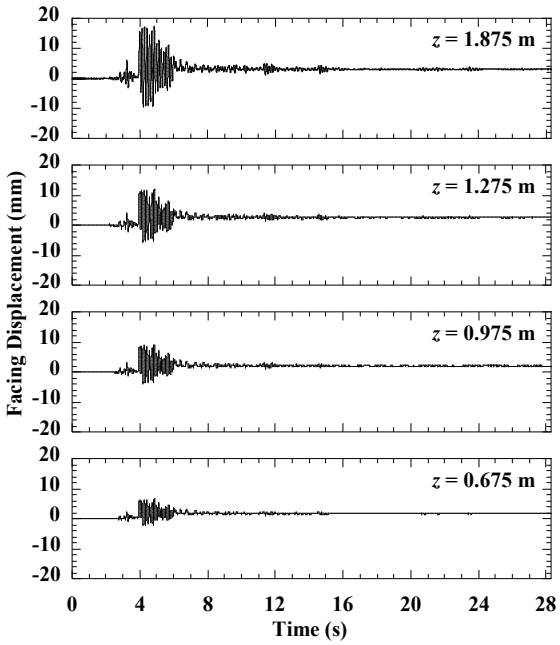

Figure 7.14 Time histories of incremental facing displacement for T1 during the Northridge motion in Test 1.

Profiles of incremental maximum and residual facing displacements of the three instrumented sections for each earthquake motion are shown in Figure 7.15, and maximum values of the incremental facing displacement profiles are presented in Table 7.4. The maximum facing displacement profiles correspond to the specific times associated with maximum incremental outward facing displacement measurements.

For the Imperial Valley motion, the maximum outward displacements of the front wall for L1 are slightly larger than for L2, with maximum values of 3.7 mm and 3.5 mm, respectively, both at the top of the wall. These facing displacement profiles for L1 and L2 correspond to the specific times associated with maximum facing displacement measurements of L1 (i.e., t = 1.59 s for the Imperial Valley motion). The maximum outward displacement profile of the west side wall facing (t = 1.98 s) for the transverse direction T1 has a similar trend to the longitudinal sections L1 and L2, with an

approximately linear increase with increasing elevation with a maximum value of 4.0 mm at the top of the wall. Residual facing displacements for three sections are also similar, and range from 0.4 to 1.4 mm and generally increase toward the top of the wall. Visual comparison of the maximum and residual facing displacement profiles clearly indicates that dynamic facing displacements are largely recovered after shaking, especially for the upper section of the wall. Figure 7.15 also indicates that shaking in the longitudinal direction induced facing displacements in the transverse direction for the side walls, which is attributed to a Poisson effect associated with bridge seat settlement which will be discussed in the next section. Figure 7.15(b) shows that the magnitudes of both the maximum and residual facing displacements for the Maule motion are similar to the Imperial Valley motion. However, the maximum facing displacements for the Northridge motion are much larger than for the other two motions. Maximum facing displacements increase almost nearly with increasing elevation for all sections. The longitudinal sections L1 and L2 have similar maximum displacement profiles with maximum values of 10.1 mm and 8.9 mm at the top of the wall, whereas the transverse section T1 has much larger facing displacements with a maximum value of 17.4 mm at the same elevation. The residual facing displacements are similar for the three sections, and also increase with elevation and range from 0.1 mm to 3.2 mm.

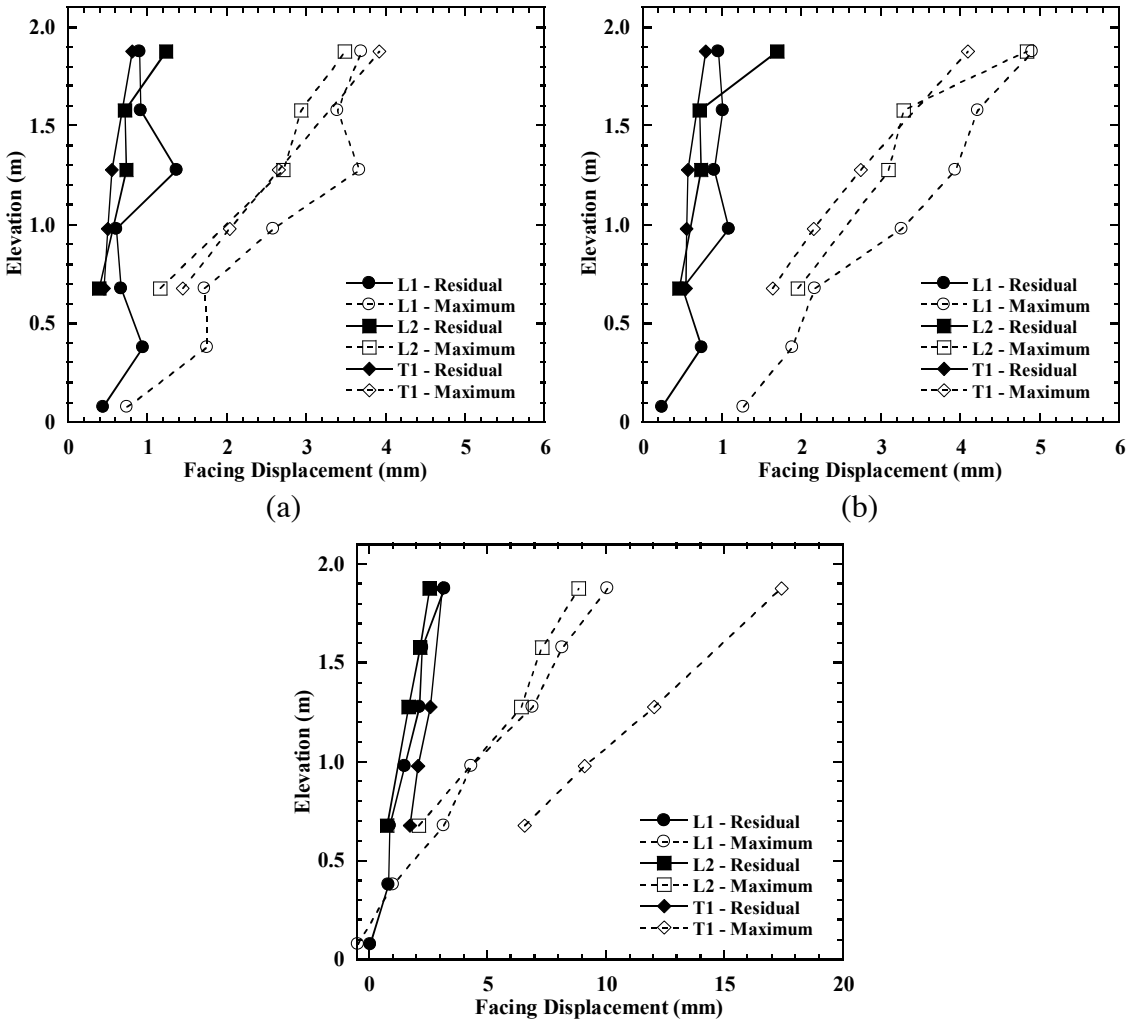

Figure 7.15 Incremental facing displacement profiles in Test 1: (a) Imperial Valley motion; (b) Maule motion; (c) Northridge motion.

Table 7.4 Maximum incremental facing displacements for earthquake motions in Test 1 (model-scale).

Earthquake motion	Maximum displacement (mm) for L1		Maximum displacement (mm) for L2		Maximum displacement (mm) for T1	
	Maximum	Residual	Maximum	Residual	Maximum	Residual
Imperial Valley	3.7	1.4	3.5	1.2	3.9	0.8
Maule	4.9	1.1	4.8	1.7	4.1	0.8
Northridge	10.1	3.2	8.9	2.6	17.4	3.1

Time histories of incremental facing displacements for L1 at selected elevations during the Imperial Valley motion in Tests 1 to 4 are shown in Figure 7.16. For the longitudinal section L1, the dynamic and residual facing displacements at the top of the wall for Tests 3 and 4 are larger than for Tests 1 and 2.

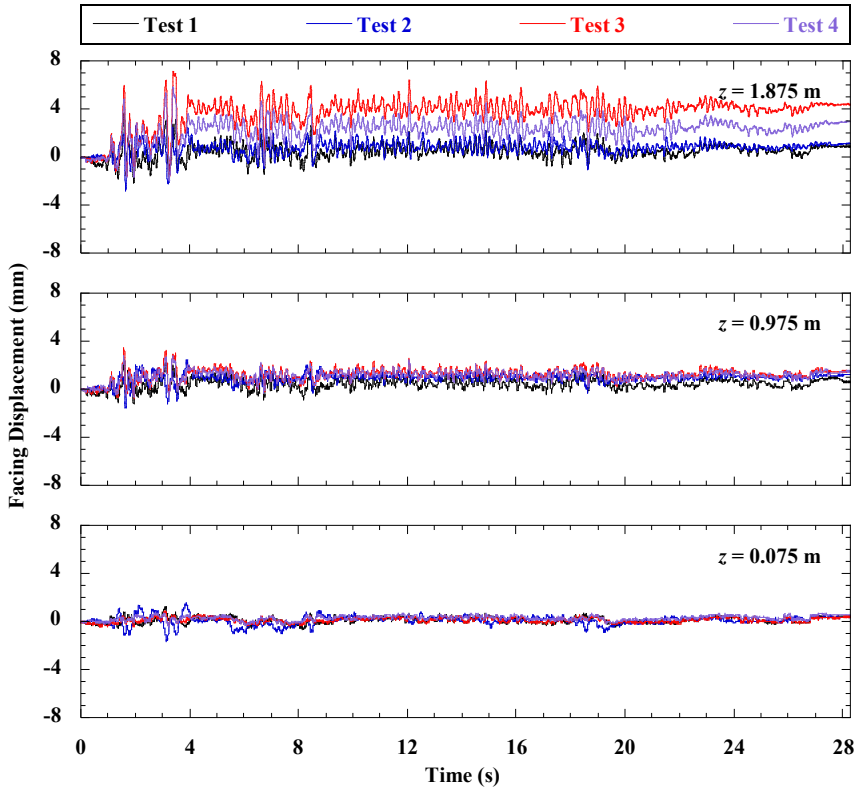

Figure 7.16 Time histories of incremental facing displacement for L1 during the Imperial Valley motion in Tests 1 to 4.

Incremental residual facing displacement profiles for the Imperial Valley, Maule, and Northridge motions in Tests 1 to 4 are shown in Figure 7.17, Figure 7.18, and Figure 7.19, respectively. For instance, for the Imperial Valley motion, facing displacements for L1 are the largest in Test 4 (increased reinforcement spacing) with a maximum value of 4.4 mm at the top of the wall. Test 3 (reduced reinforcement stiffness) has similar facing

displacements to Test 4 for the lower section of the wall, but smaller facing displacements for the upper section with a maximum value of 3.0 mm at the top of the wall. Tests 1 and 2 have smaller reinforcement vertical spacing and larger reinforcement stiffness than Tests 3 and 4, also have smaller facing displacements under dynamic loading. In contrast to the facing displacements under static loading, Test 1 (baseline case) has smaller facing displacements than Test 2 (reduced bridge load) under dynamic loading, which is attributed to the larger backfill soil stiffness under greater bridge load for Test 1. Similar trends for facing displacements of L2 are also observed in Figure 7.17(b), but the magnitudes of facing displacements are slightly smaller than L1. For instance, the maximum facing displacement of 3.2 mm for L2 at the top of the wall in Test 3 is smaller than the maximum value of 4.4 mm at the same elevation for L1. For the facing displacements of T1, Test 3 also has the largest facing displacements with a maximum value of 2.3 mm at the top of the wall, and Test 4 shows a similar trend with Test 3, but with smaller facing displacements. Facing displacements for Tests 1 and 2 are similar and range from 0.5 mm to 0.8 mm. Facing displacements for the Maule motion are similar to the Imperial Valley motion with similar trends, while the Northridge motion has larger facing displacements. For the Northridge motion, Test 1 experienced larger facing displacements than Test 2, which is different from the other two motions. This is attributed to the softer behavior of the GRS bridge abutment in Test 1 before shaking because the Northridge motion was applied after the sinusoidal motions for Test 1.

In general, the reinforcement spacing and stiffness show the most significant effects on facing displacements under dynamic loading. Facing displacements increase significantly with increased reinforcement spacing and reduced reinforcement stiffness. In

contrast to static loading, facing displacements are smaller for greater bridge loads under dynamic loading, which is attributed to the greater backfill soil stiffness under the confining stress associated with the greater bridge load.

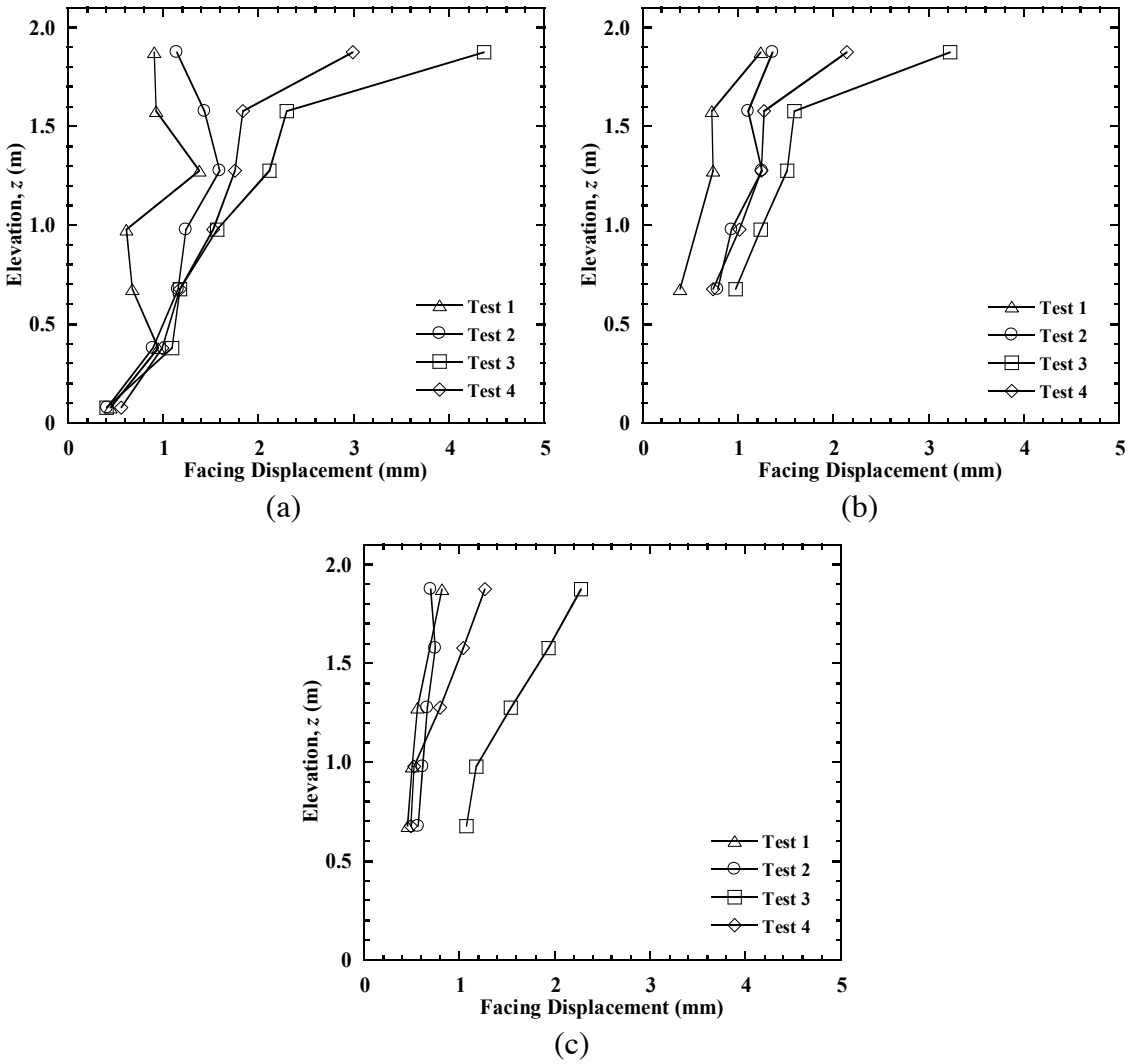

Figure 7.17 Incremental residual facing displacement profiles for the Imperial Valley motion in Tests 1 to 4: (a) L1; (b) L2; (c) T1.

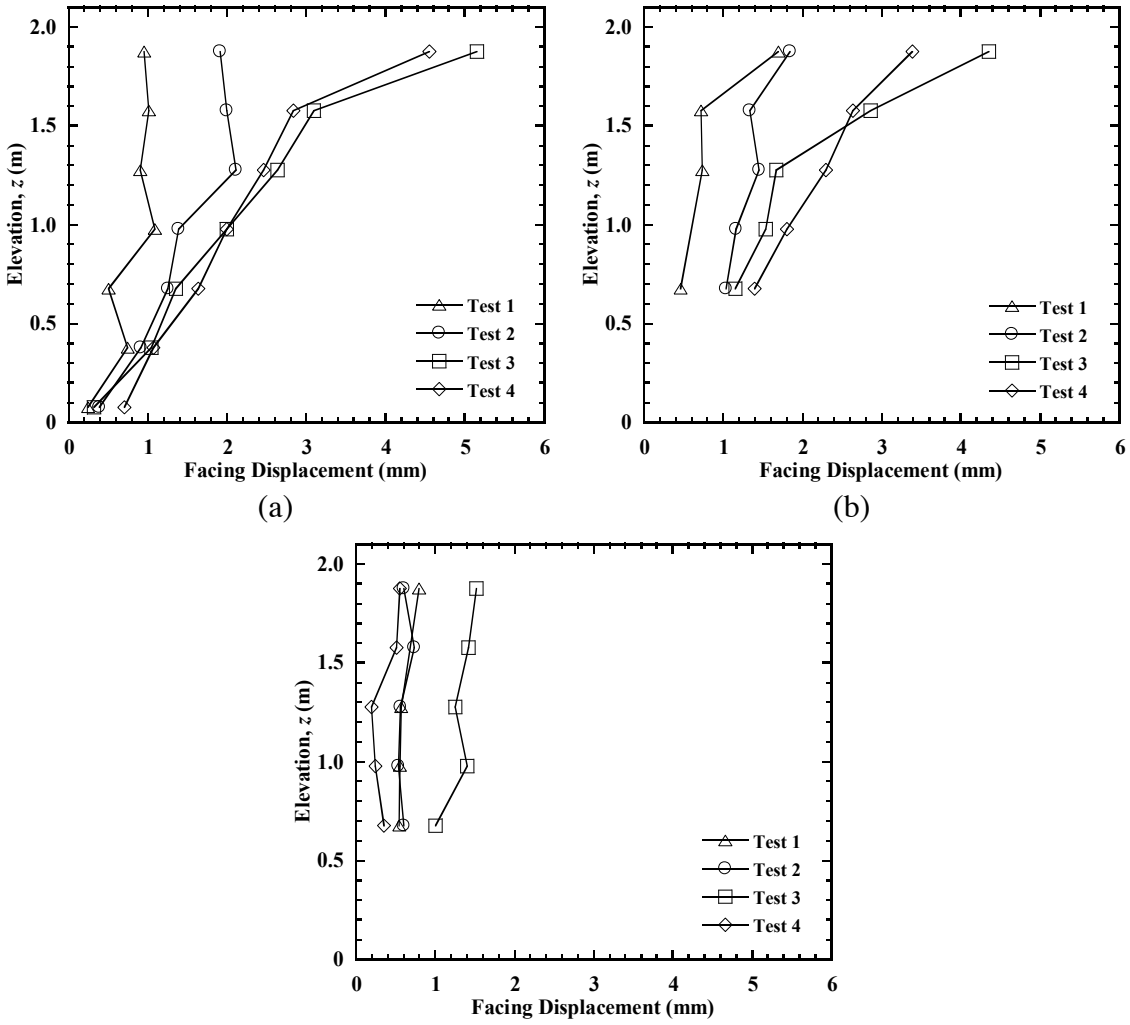

Figure 7.18 Incremental residual facing displacement profiles for the Maule motion in Tests 1 to 4: (a) L1; (b) L2; (c) T1.

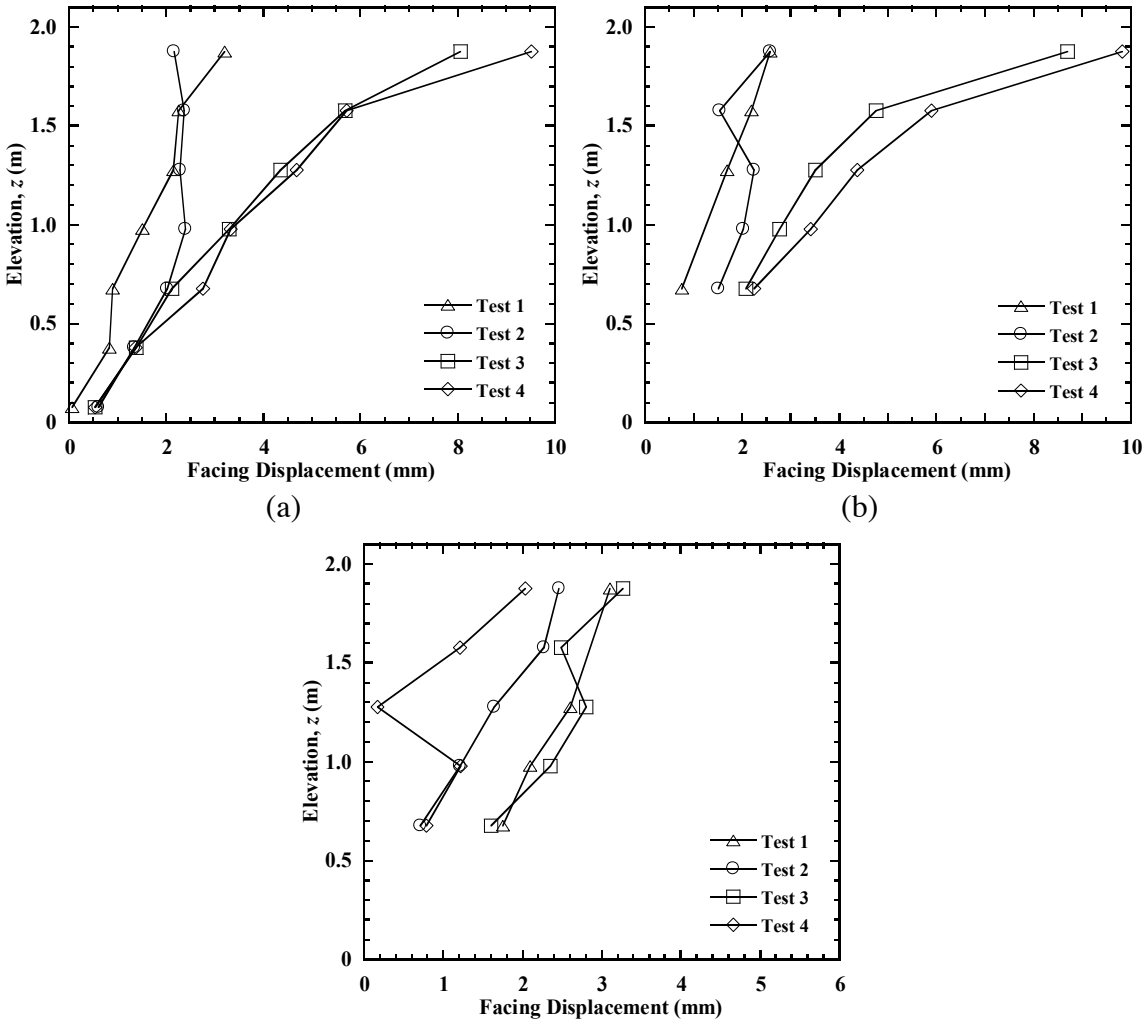

Figure 7.19 Incremental residual facing displacement profiles for the Northridge motion in Tests 1 to 4: (a) L1; (b) L2; (c) T1.

Table 7.5 Maximum incremental residual facing displacements for earthquake motions in Tests 1 to 4 (model-scale).

Earthquake motion	Maximum displacement (mm) in Test 1		Maximum displacement (mm) in Test 2		Maximum displacement (mm) in Test 3		Maximum displacement (mm) in Test 4	
	L1	T1	L1	T1	L1	T1	L1	T1
Imperial Valley	1.4	0.8	1.6	0.8	4.4	2.3	3.0	1.3
Maule	1.1	0.8	2.1	0.7	5.2	1.5	4.6	0.6
Northridge	3.2	3.1	2.4	2.5	8.1	3.3	9.5	2.0

7.5 Bridge Seat and Bridge Beam Displacements

7.5.1 Bridge Seat Settlements

7.5.1.1 Static Loading

Settlements of the bridge seat were measured under static and dynamic loading at the four locations shown in Figure 6.16. One of the string potentiometers on the southeast (SE) side of the bridge seat was not working for Stage 3 (placement of the bridge beam) but was replaced before application of the earthquake motions. Settlement time histories of bridge seat corner measurements and average values for Stage 3 are shown in Figure 7.20. The settlements due to application of the bridge beam were relatively instantaneous and did not vary significantly over time, indicating negligible creep. The settlement on the west side of the bridge seat (NW and SW) is 3.1 mm, while the settlement on the east (NE) is 0.7 mm. This indicates a slight tilting of the bridge seat toward the west side after placement of the bridge seat. The average bridge seat settlement is 2.3 mm after construction for 92 hours. The small fluctuations in the measured settlements over time observed in Figure 7.20 may have occurred due to temperature changes in the laboratory.

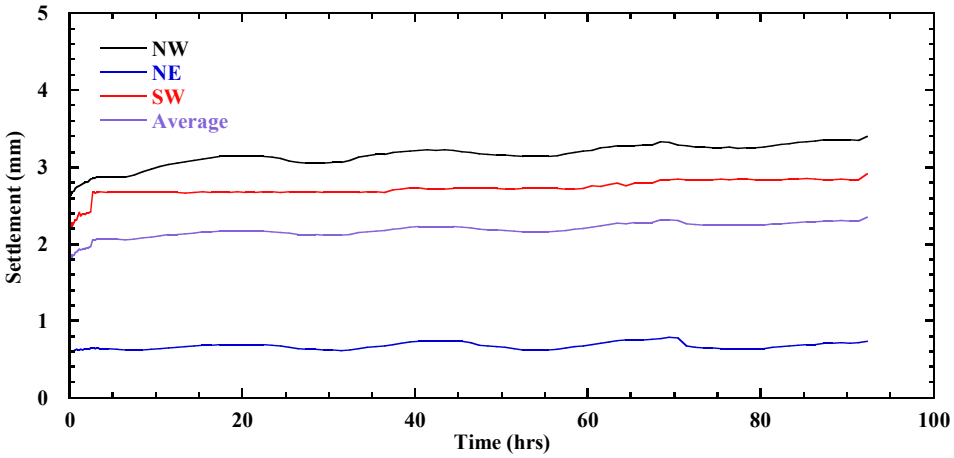

Figure 7.20 Time histories of bridge seat settlements for Stage 3 in Test 1.

The average bridge seat settlements due to placement of bridge beam for different tests are presented in Table 7.6. Test 3 (increased reinforcement spacing) has the largest bridge seat settlement of 3.5 mm, whereas Test 2 (reduced bridge load) has the smallest settlement of 1.5 mm. Settlements for Tests 1 (baseline) and 4 (reduced reinforcement stiffness) are similar, with values of 2.3 mm and 2.4 mm, respectively. Results indicate that reinforcement spacing has the most significant effect on bridge seat settlement under static loading and reinforcement stiffness shows a relatively small effect for the conditions investigated. As expected, greater bridge load results in larger settlement under static loading.

Table 7.6 Average bridge seat settlement for Stage 3 in Tests 1 to 4.

Construction stage	Average settlement (mm) in Test 1	Average settlement (mm) in Test 2	Average settlement (mm) in Test 3	Average settlement (mm) in Test 4
Stage 3	2.3	1.5	3.5	2.4

7.5.1.2 Dynamic Loading

Time histories of incremental bridge seat corner settlement for the four string potentiometers during application of the earthquake motions in Test 1 are shown in Figure 7.21, and the average incremental bridge seat settlements are shown in Figure 7.22. During the Imperial Valley motion, the maximum value is 3.1 mm and the minimum value is -0.1 mm (i.e., uplift). The average residual settlement is 1.4 mm, which corresponds to a vertical strain of 0.07% for the 2.1 m-high lower GRS wall. Average incremental bridge seat settlements for each earthquake motion in Test 1 are summarized in Table 7.7. For the Maule motion, the bridge seat had maximum dynamic settlement of 7.0 mm and residual settlement of 1.4 mm. Maximum dynamic settlement for the Northridge motion is 7.0 mm, and the residual value is 2.2 mm (0.1% vertical strain), which corresponds to 4.4 mm at prototype scale. At t = 3.98 s during the Northridge motion, the north side of the bridge seat (NW and NE) had a positive settlement of 1.7 mm, whereas the south side (SW and SE) had a negative settlement (i.e., uplift) of 1.9 mm, which indicated rocking of the bridge seat in the N-S direction (i.e., the direction of shaking). The residual settlement on the west side (NW and SW) is larger than the east side (NE and SE), which indicated that the bridge seat tilted further toward the west after shaking.

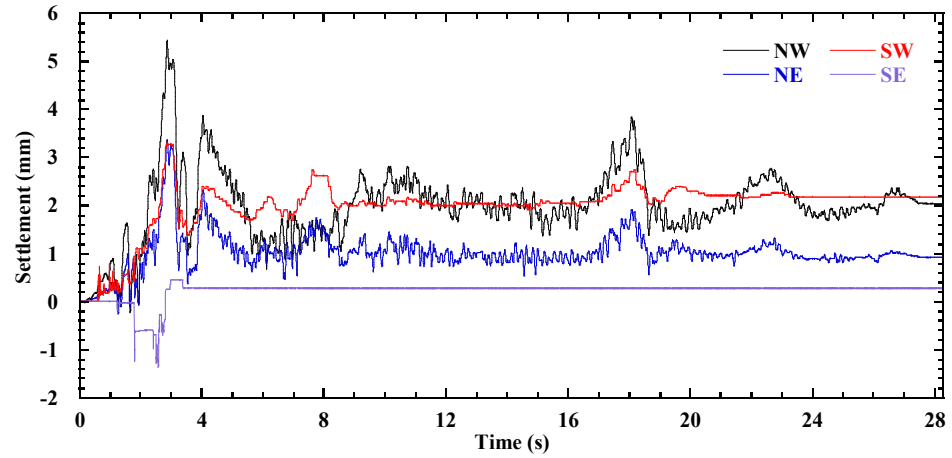

(a)

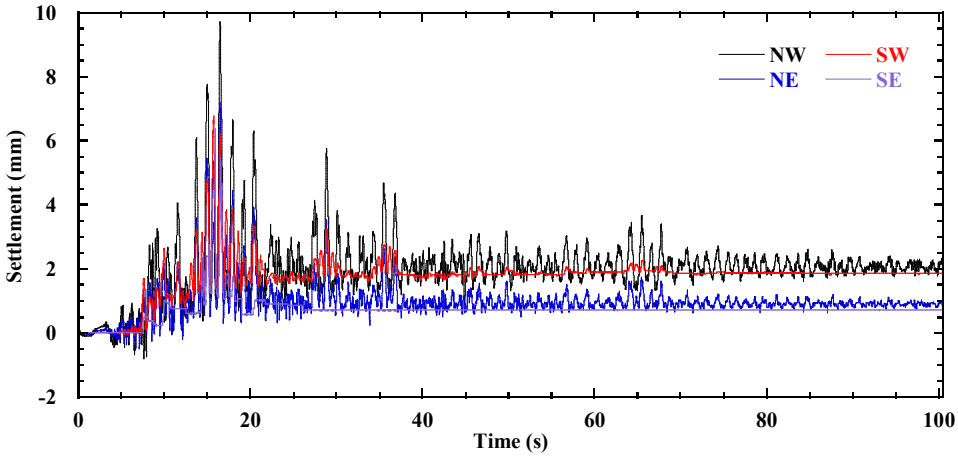

(b)

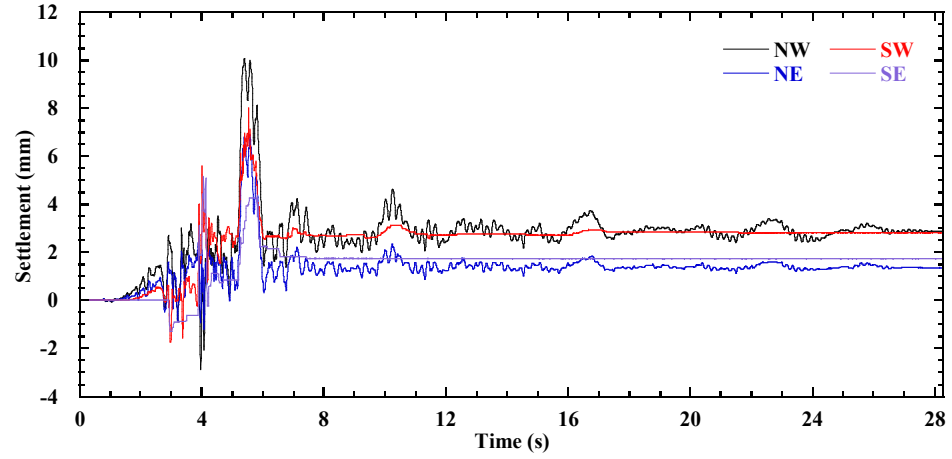

(c)

Figure 7.21 Time histories of incremental bridge seat corner settlements in Test 1: (a) Imperial Valley motion; (b) Maule motion; (c) Northridge motion.

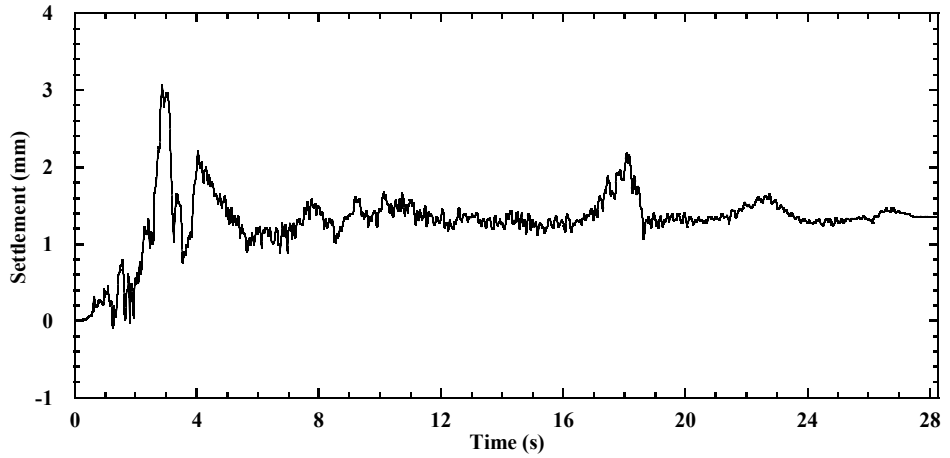

(a)

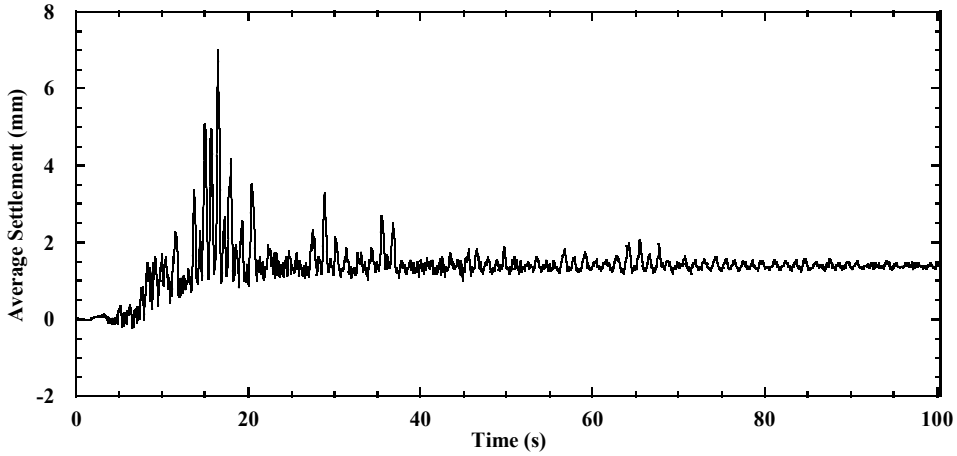

(b)

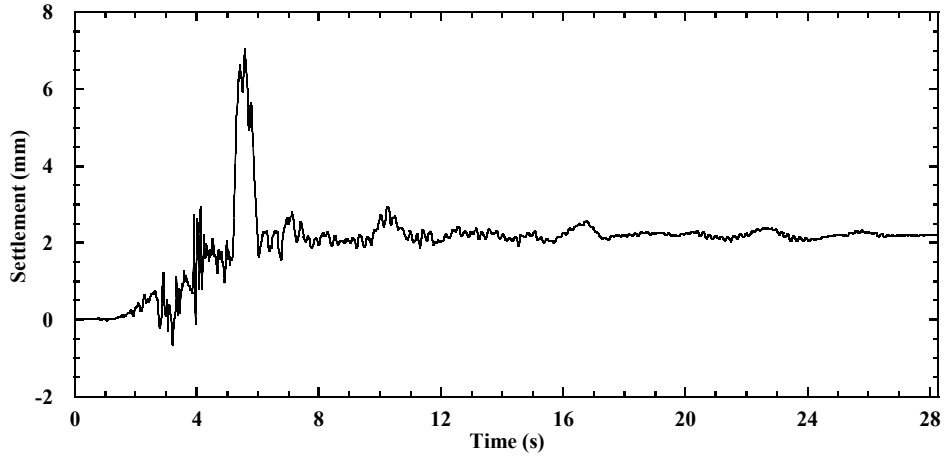

(c)

Figure 7.22 Time histories of average incremental bridge seat settlements in Test 1: (a) Imperial Valley motion; (b) Maule motion; (c) Northridge motion.

Table 7.7 Average incremental bridge seat settlements in Test 1.

Earthquake motion	Maximum dynamic settlement (mm)	Minimum dynamic settlement (mm)	Residual settlement (mm)
Imperial Valley	3.1	-0.1	1.4
Maule	7.0	-0.2	1.4
Northridge	7.0	-0.7	2.2

Time histories of average incremental bridge seat settlement during the Imperial Valley, Maule, Northridge motions for different tests are shown in Figure 7.23. For instance, during the Maule motion, Test 3 has the largest dynamic settlements of 10.3 mm, and the maximum dynamic settlements for Tests 1, 2, and 4 are similar and range from 7.0 mm to 7.8 mm. The minimum dynamic settlements are small for all tests. Test 3 has the largest residual settlement of 5.6 mm, which corresponds to a vertical strain of 0.27%, whereas Test 1 has the smallest residual settlement of 1.4 mm. The residual settlements are 3.0 mm and 3.8 mm for Tests 2 and 4, respectively.

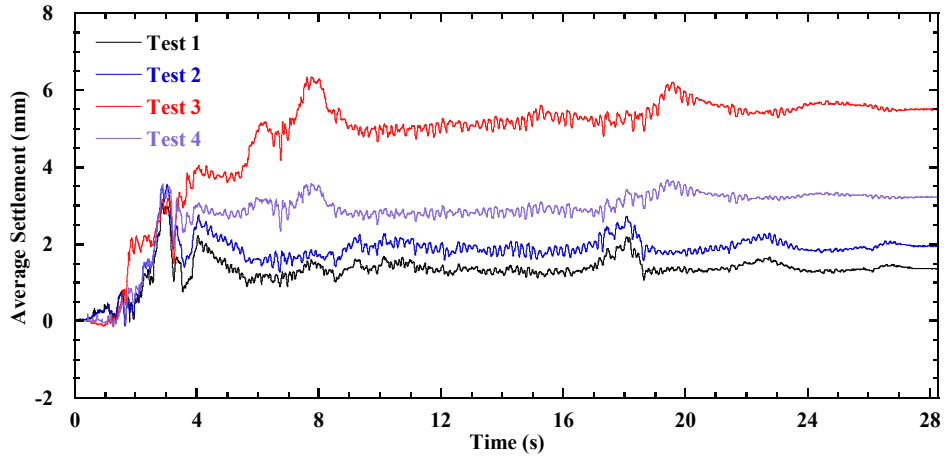

(a)

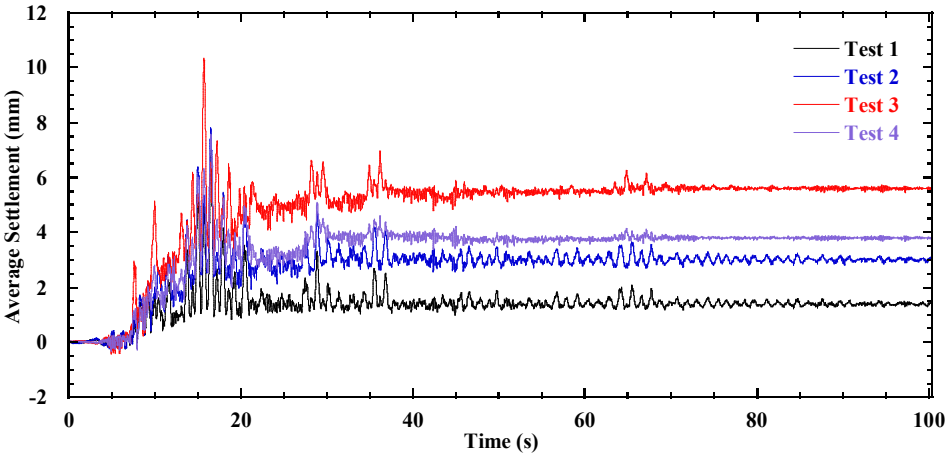

(b)

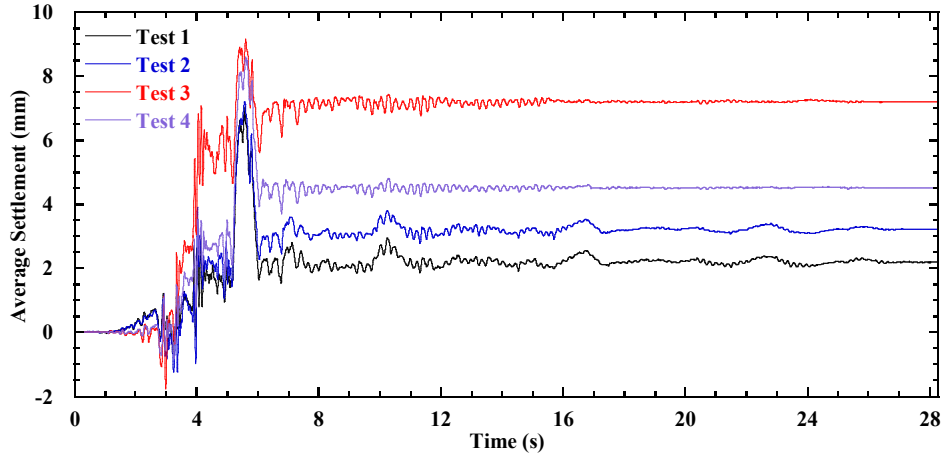

(c)

Figure 7.23 Time histories of average incremental bridge seat settlements in Tests 1 to 4: (a) Imperial Valley motion; (b) Maule motion; (c) Northridge motion.

Average incremental and total residual bridge seat settlements for different testing stages in Tests 1 to 4 are shown in Figure 7.24 and the incremental values are presented in Table 7.8. Test 3 (increased reinforcement spacing) has the largest bridge seat settlements for all testing stages, which indicate that reinforcement spacing has the most significant effect for both static and dynamic loading conditions. The incremental residual settlement is 7.2 mm for the Northridge motion, which corresponds to a vertical strain of 0.34%. Test 4 (reduced reinforcement stiffness) also shows larger bridge seat settlements than Test 1 (baseline case) for all testing stages, and this indicates that reinforcement stiffness also has an important effect, especially for dynamic loading condition. Therefore, reducing reinforcement vertical spacing and increasing reinforcement stiffness can effectively reduce bridge seat settlements for both static and dynamic loading conditions. Test 2 (reduced bridge load) has smaller bridge seat settlements than Test 1 under static loading, but larger settlements under dynamic loading. The greater bridge load for Test 1 yielded larger a backfill soil stiffness, and thus resulted in smaller bridge seat settlements under dynamic loading, which are also consistent with the facing displacements.

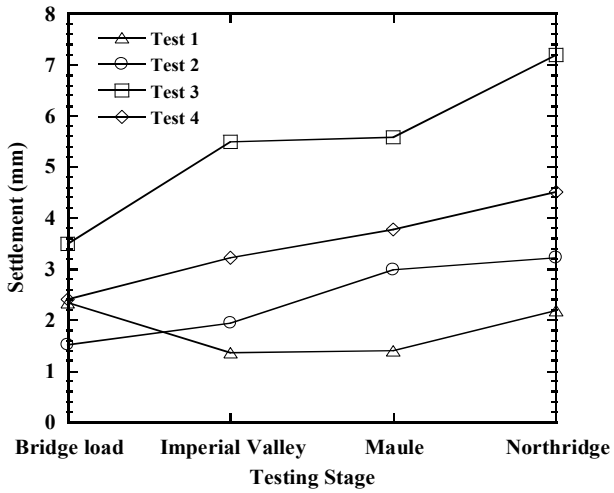

(a)

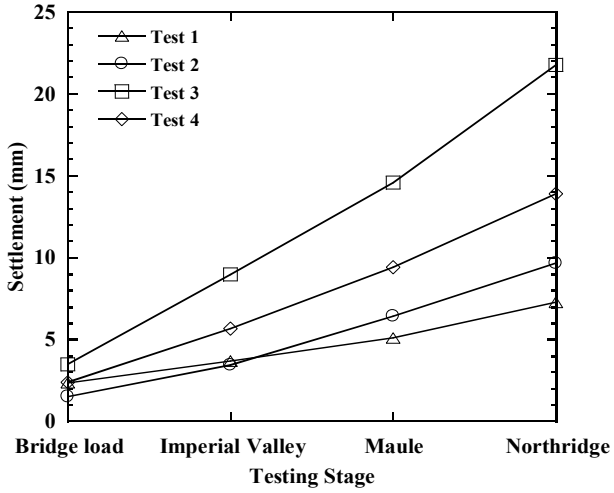

(b)

Figure 7.24 Average bridge seat settlement for different testing stages: (a) incremental settlement; (b) total settlement.

Table 7.8 Average incremental residual bridge seat settlements (model-scale).

Earthquake motion	Average settlement (mm) in Test 1	Average settlement (mm) in Test 2	Average settlement (mm) in Test 3	Average settlement (mm) in Test 4
Imperial Valley	1.4	1.9	5.5	3.2
Maule	1.4	3.0	5.6	3.8
Northridge	2.2[1]	3.2	7.2	4.5

[1] The Northridge motion was applied after the sinusoidal motions for Test 1.

The settlement of backfill soil surface behind the bridge seat for the upper wall was also measured in Tests 2, 3, and 4, as shown in Figure 6.24(c). For Test 2, the incremental backfill soil settlements are generally larger than the average bridge seat settlements (Table 7.8) for the same motion. For instance, the residual backfill soil settlement is 2.8 mm for the Imperial Valley motion, and the average bridge seat settlement is 1.9 mm, yielding a differential settlement of 0.9 mm. The differential settlements for the Maule and Northridge motions are much larger and reached 12.3 mm and 5.2 mm, respectively. For Test 3, the incremental average bridge seat settlements are larger than backfill soil settlements, and the differential settlements range from 1.9 mm to 3.8 mm for the three motions. In general, the differential settlements under dynamic loading are relatively small for the conditions investigated, and this type of differential settlement can be easily mitigated after earthquakes.

Table 7.9 Incremental backfill soil settlements and differential settlements in Tests 2 to 4 (model-scale).

Earthquake motion	Settlement (mm) in Test 2		Settlement (mm) in Test 3		Settlement (mm) in Test 4	
	Soil	Differential	Soil	Differential	Soil	Differential
Imperial Valley	2.8	0.9	2.5	3.0	1.9	1.3
Maule	15.3	12.3	3.7	1.9	5.8	2.0
Northridge	8.4	5.2	3.4	3.8	1.3	3.2

7.5.2 Bridge Seat and Bridge Beam Horizontal Displacements

Horizontal displacements in the longitudinal direction for the bridge seat and bridge beam were measured at the locations shown in Figure 6.16, time histories of incremental horizontal displacement for the earthquake motions in Test 1 are shown in Figure 7.25. Displacements at the east and west sides of the bridge seat are similar with respect to both trend and magnitude for all three motions. This indicates essentially uniform translational movement of the bridge seat in the longitudinal direction during shaking. The bridge beam experienced larger horizontal displacements than the bridge seat during shaking, which indicated sliding of the bridge beam with respect to the bridge seat. The horizontal displacements for the bridge seat and bridge beam are highly dependent on the characteristics of the earthquake motions.

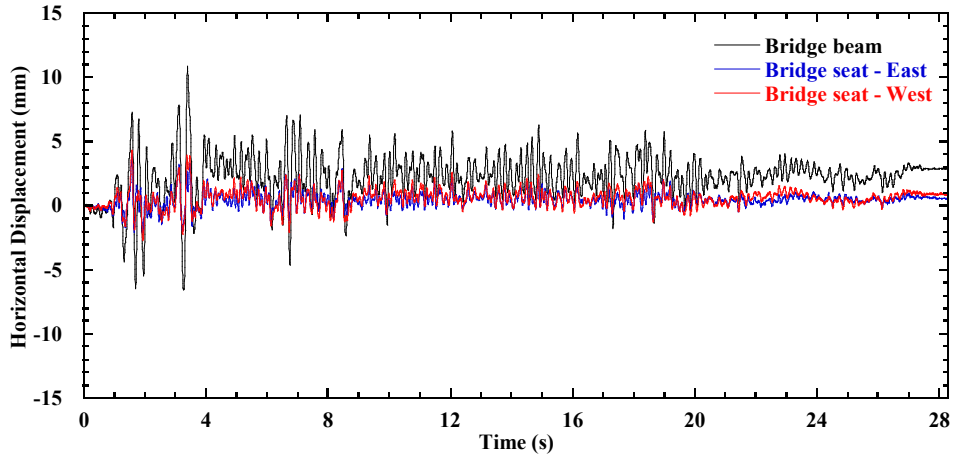

(a)

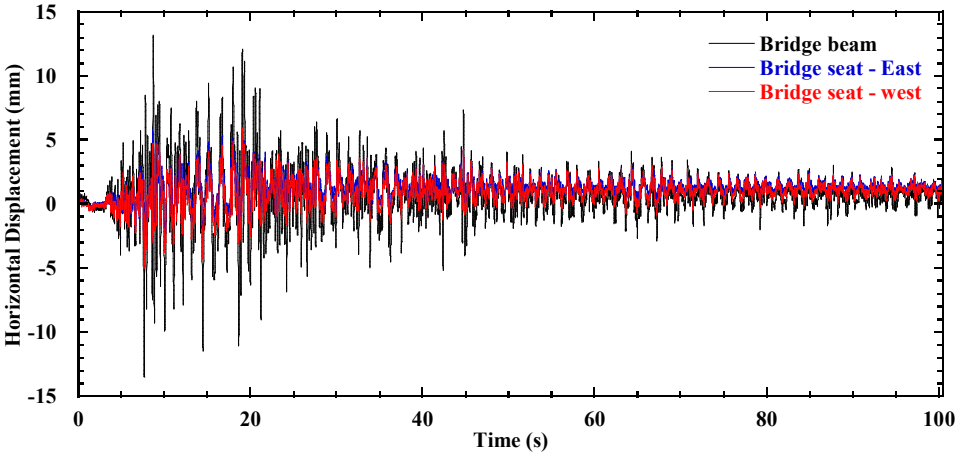

(b)

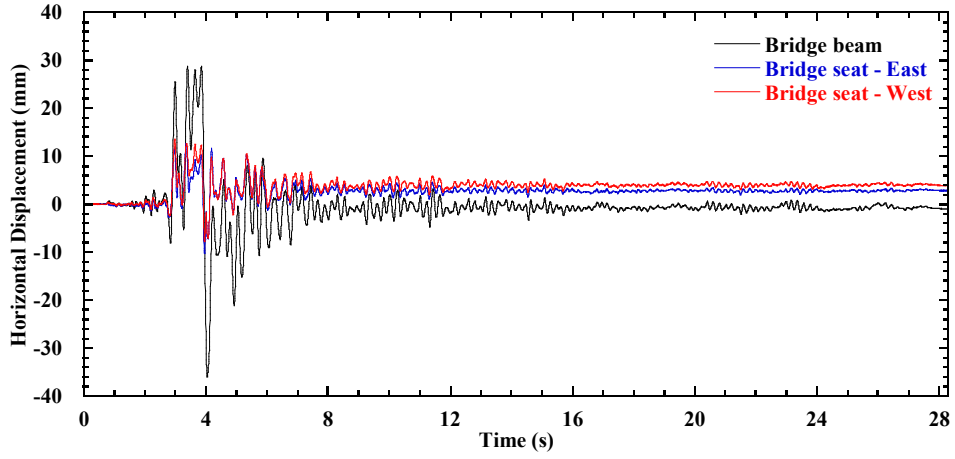

(c)

Figure 7.25 Time histories of incremental horizontal displacement for bridge seat and bridge beam in Test 1: (a) Imperial Valley motion; (b) Maule motion; (c) Northridge motion.

Time histories of incremental horizontal displacement for the bridge seat relative to the top of GRS bridge abutment (measurements taken at the facing block z = 1.875 m for L1) and bridge beam relative to the bridge seat are shown in Figure 7.26. For the Imperial Valley and Maule motions, the bridge seat had relatively small magnitudes of horizontal displacement on the GRS bridge abutment, which indicates that the bridge seat essentially moved together with the GRS bridge abutment during shaking. The bridge beam had residual relative horizontal displacements of 2.2 mm and -0.1 mm with respect to the bridge seat for the two motions, respectively. For the Northridge motion, the bridge beam experienced significant sliding with respect to the bridge seat during shaking. The maximum and minimum dynamic relative horizontal displacements are 20.6 mm and -30.0 mm, respectively, and the residual horizontal displacement is -4.3 mm. Final inspection revealed significant slide marks on both sides of the elastomeric bearing pad, which suggests that relative displacements between the bridge beam and bridge seat occurred primarily as a result of sliding on the pad and not shear deformation of the pad itself. The width of the seismic joint is also associated with the relative horizontal displacement of the bridge beam with respect to the bridge seat and will be discussed in Section 7.10.

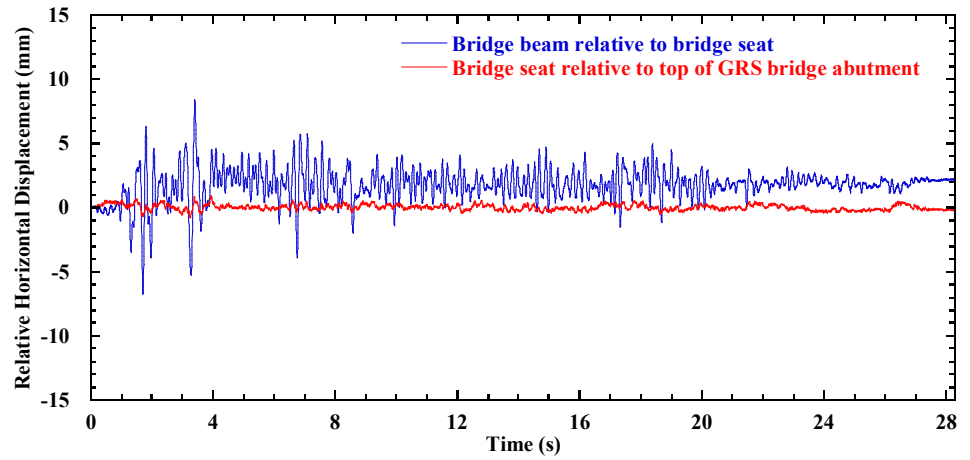

(a)

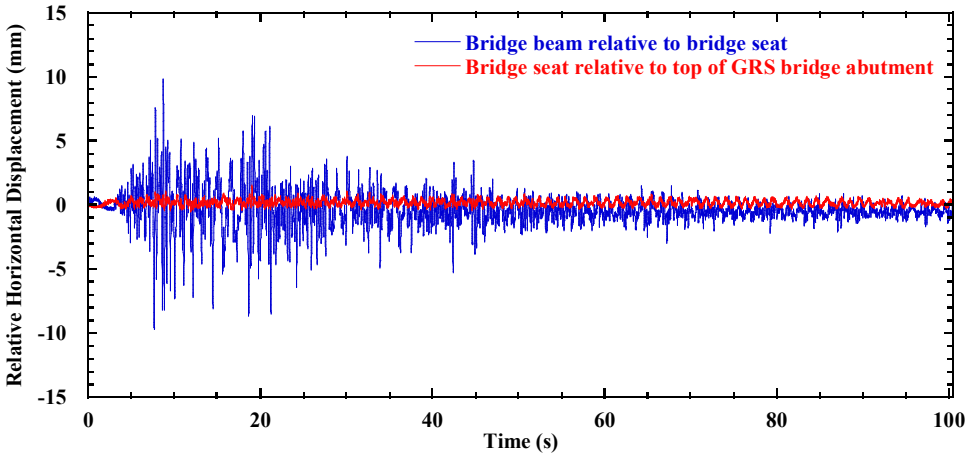

(b)

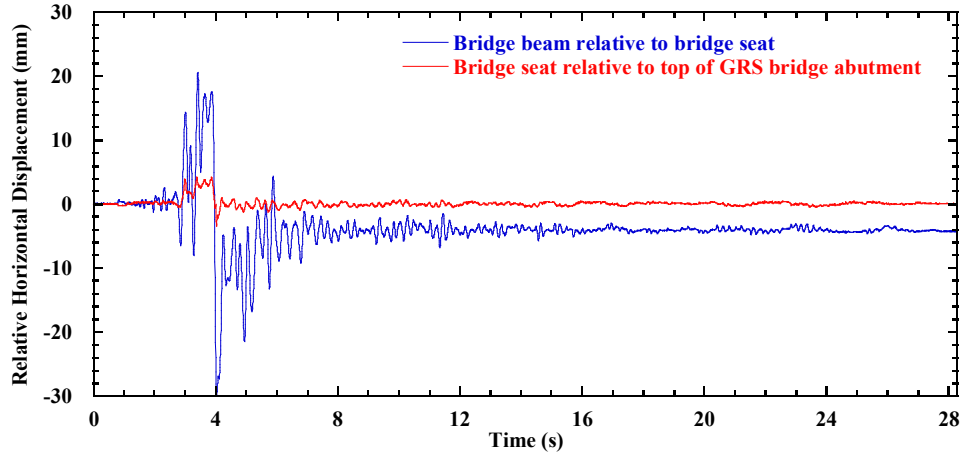

(c)

Figure 7.26 Time histories of incremental relative horizontal displacement for bridge seat and bridge beam in Test 1: (a) Imperial Valley motion; (b) Maule motion; (c) Northridge motion.

7.6 Acceleration Responses

7.6.1 Structures

In the seismic design of GRS bridge abutments, the bridge seat is typically treated as a gravity retaining wall for external stability evaluation. However, there is no guidance on the selection of acceleration for the bridge seat in the current design guidelines. The acceleration response of bridge beam also is important in the design, as the inertial forces are transferred to the bridge seat through frictions on the bearings and potential contact forces on the backwall of the bridge seat.

Time histories of horizontal acceleration in the longitudinal direction for the bridge seat and bridge beam for earthquake motions in Test 1 are shown in Figure 7.27. For the Imperial Valley motion, the bridge seat had a peak acceleration of 0.63g, while the bridge beam had a smaller peak acceleration of 0.53g, and the peak accelerations are 0.66g and 0.63g, respectively, for the Maule motion. For the Northridge motion, the peak accelerations are much larger than the other two motions, and the peak accelerations are 1.81g and 1.52g for the bridge seat and bridge beam, respectively.

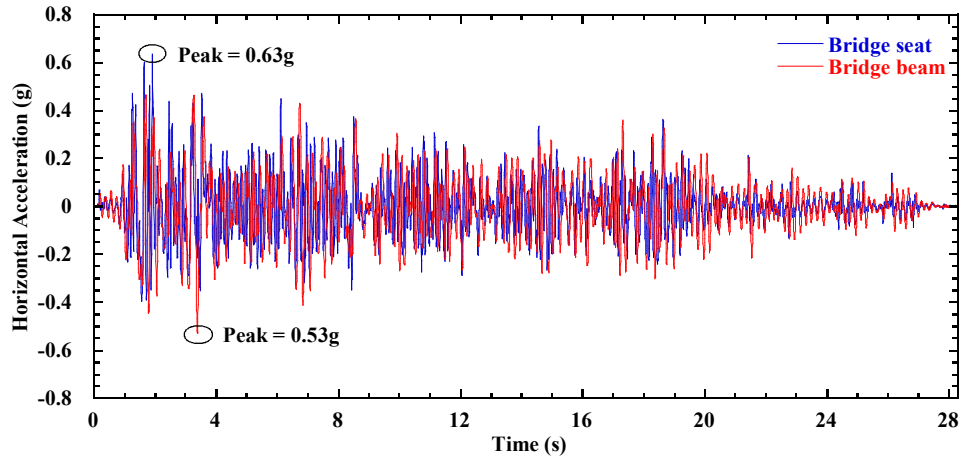

(a)

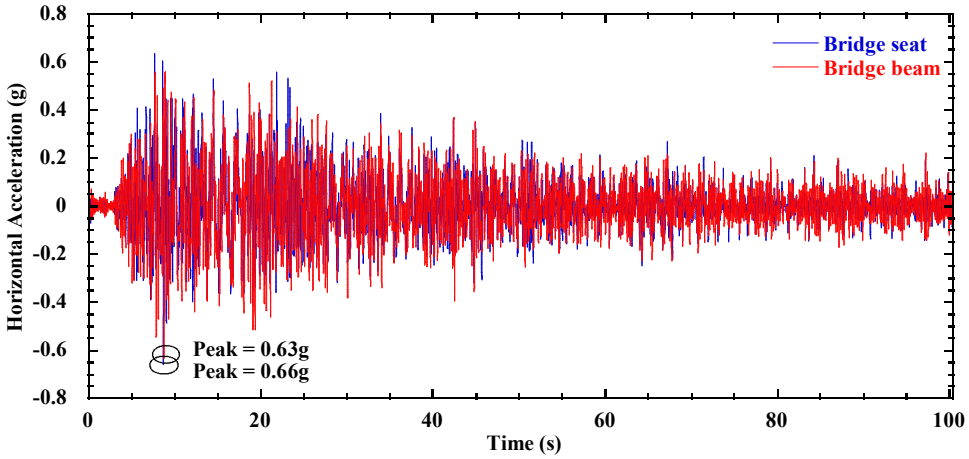

(b)

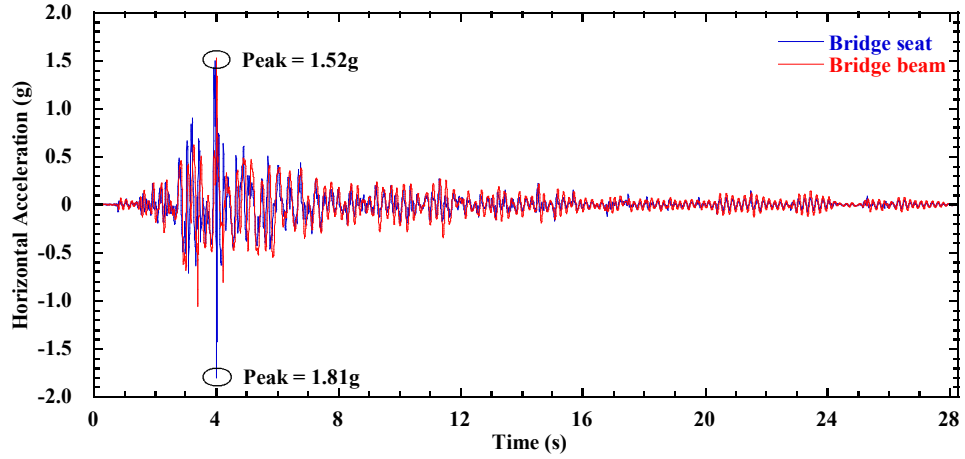

(c)

Figure 7.27 Time histories of horizontal acceleration for bridge seat and bridge beam in Test 1: (a) Imperial Valley motion; (b) Maule motion; (c) Northridge motion.

The root-mean-square (RMS) method can be used to mitigate the effects of high frequency noise and also characterize the amplitude and frequency content of a measured response (Kramer 1996; El-Emam and Bathurst 2005). The calculated ratios for the bridge seat and bridge beam RMS accelerations in Tests 1 to 4 normalized by the shaking table RMS acceleration are presented in Table 7.10. In Test 1, for the Imperial Valley motion, the bridge beam has an acceleration amplification ratio of 1.80, and is greater than the ratio of 1.60 for the bridge seat. For the Maule motion, the ratios decrease to 1.73 and 1.38 for the bridge beam and bridge seat, respectively. In general, the RMS acceleration ratios for the bridge beam are larger than the bridge seat.

For the Imperial Valley motion, the bridge seat in Tests 1 and 2 has larger acceleration ratios than in Tests 3 and 4. The acceleration ratio for the bridge beam is the largest for Test 2, which is likely due to the smaller bridge load. The acceleration ratio for the bridge beam in Test 1 is smaller than in Tests 3 and 4. The trend of acceleration ratios for the bridge beam is the same for the Maule motion. However, the bridge seat has the smallest acceleration ratio in Test 1, while the acceleration ratios are similar in Tests 2, 3, and 4.

Table 7.10 RMS acceleration ratios for bridge seat and bridge beam in Tests 1 to 4 (model-scale).

Earthquake motion	Acceleration ratio for Test 1		Acceleration ratio for Test 2		Acceleration ratio for Test 3		Acceleration ratio for Test 4	
	Seat	Beam	Seat	Beam	Seat	Beam	Seat	Beam
Imperial Valley	1.60	1.80	1.58	2.29	1.51	2.01	1.52	2.00
Maule	1.38	1.73	1.46	2.02	1.44	1.81	1.48	1.82
Northridge	1.45	1.58	1.55	1.64	1.45	1.51	1.48	1.50

7.6.2 Abutment

Horizontal acceleration were measured for wall facing, reinforced soil zone (measured at x = 0.48 m), and retained soil zone (measured at x = 1.77 m) for the longitudinal sections L1 and L2. Time histories of horizontal accelerations in the reinforced soil zone and retained soil zone for L1 during the Imperial Valley, Maule, and Northridge motions in Test 1 are shown in Figure 7.28, Figure 7.29, and Figure 7.30, respectively. For the Imperial Valley motion, data show that horizontal accelerations in the backfill soil increase with elevation for both L1 and L2, and indicate the acceleration amplification toward the top of the lower GRS wall. Similar acceleration amplification trend is also observed for both L1 and L2 during the Maule and Northridge motions. In general, the magnitudes of horizontal acceleration at the same elevations for L1 and L2 are similar.

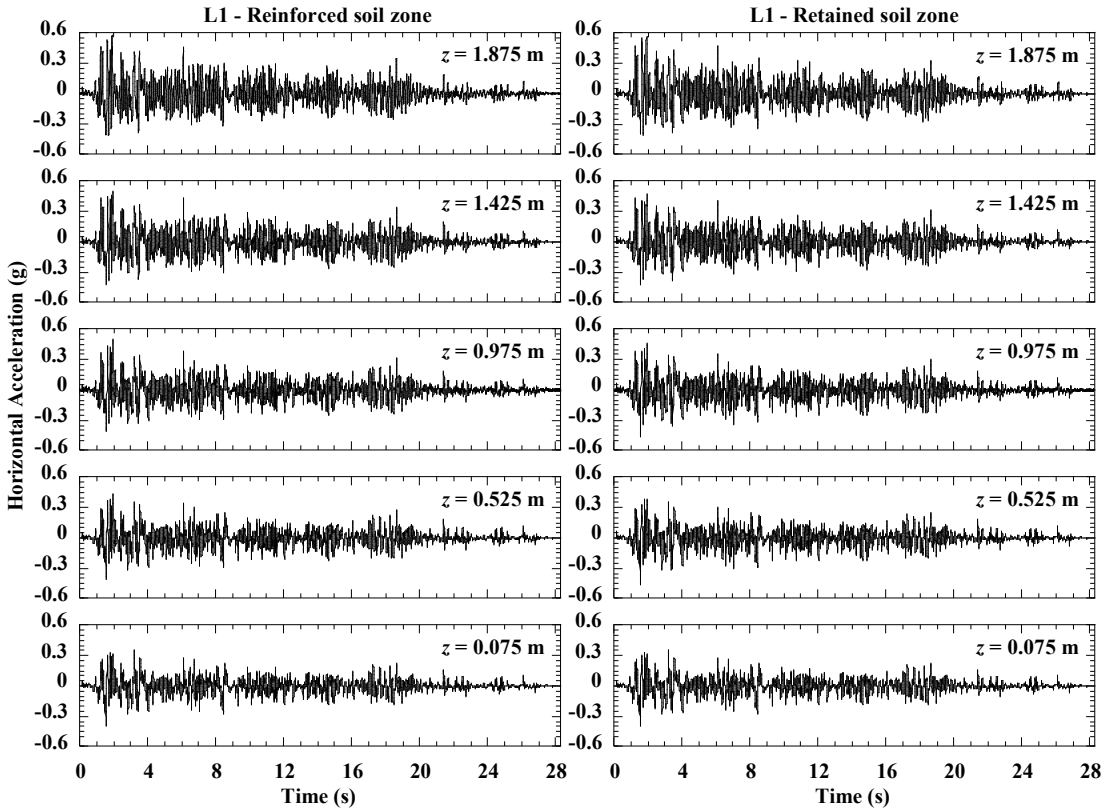

Figure 7.28 Time histories of horizontal acceleration for L1 during the Imperial Valley motion in Test 1.

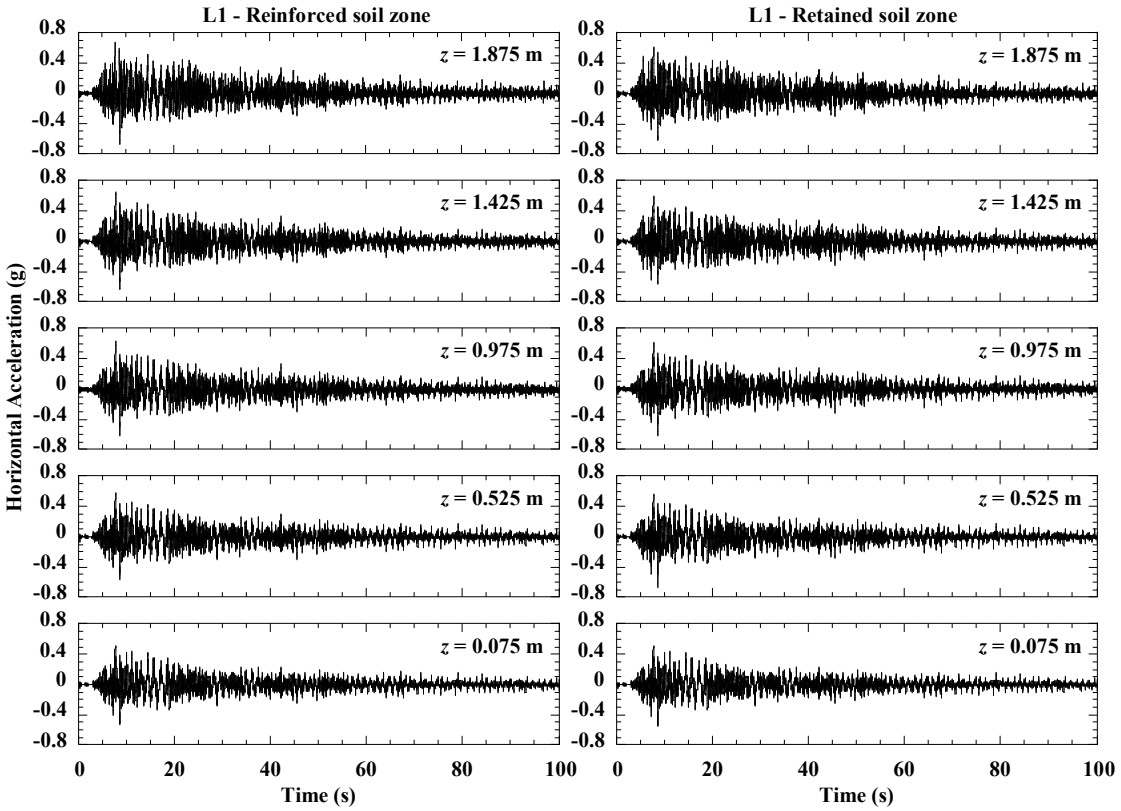

Figure 7.29 Time histories of horizontal acceleration for L1 during the Maule motion in Test 1.

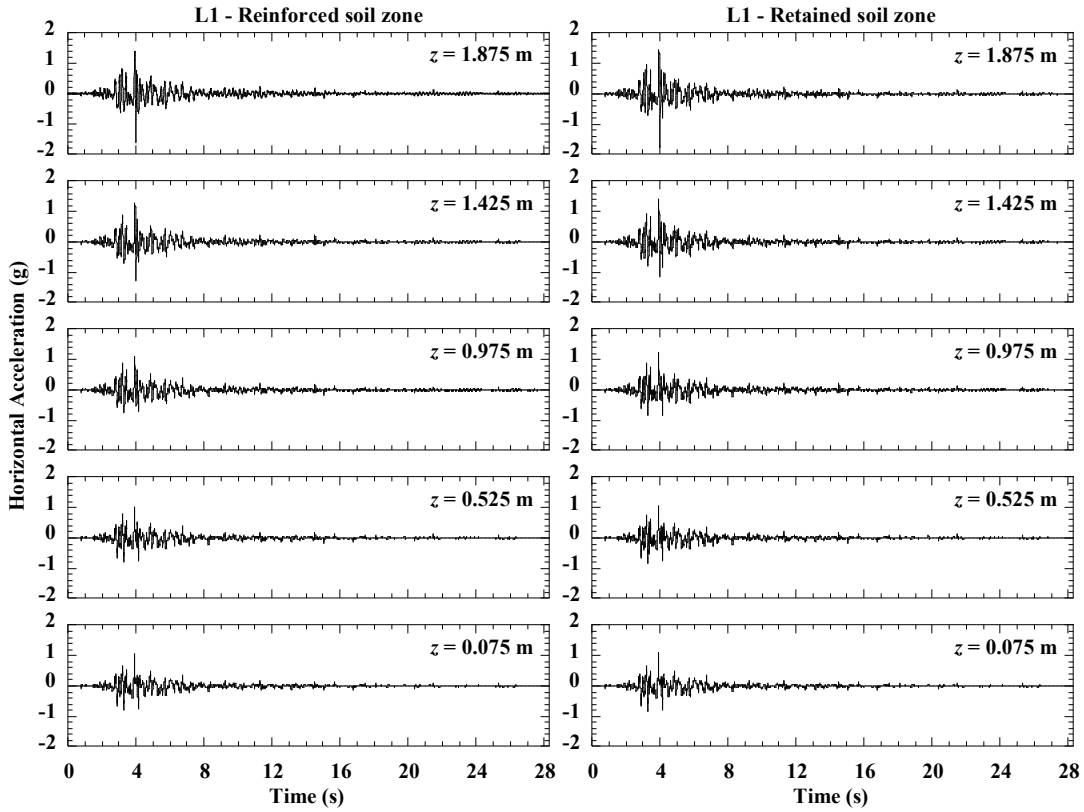

Figure 7.30 Time histories of horizontal acceleration for L1 during the Northridge motion in Test 1.

Figure 7.31 shows the RMS acceleration ratio profiles of L1 for earthquake motions in Test 1, where the RMS acceleration at each location is normalized by the actual shaking table RMS acceleration. For the Imperial Valley motion, acceleration ratio increases essentially linearly with elevation for all three sections and again indicates increasing amplification toward the top of the wall. Maximum acceleration ratios were measured at the top of the wall (z = 1.875 m), and are equal to 1.56, 1.57, and 1.59 for the retained soil zone, reinforced soil zone, and front wall facing, respectively. Similar trends are also observed for the Maule and the Northridge motions, but the acceleration ratios are smaller. For instance, the acceleration ratios at the top in the reinforced soil zone are 1.34 and 1.39 for the Maule and the Northridge motions, respectively, which are smaller than the value of 1.57 for the Imperial Valley motion. In general, for all three earthquake motions, the acceleration amplification ratios increase slightly from the retained soil zone to reinforced soil zone to wall facing. The decreasing amplification behavior as shaking proceeded may be due to the softening of the soil (i.e., shear modulus reduction) under successive earthquake motions. However, further investigations are needed to confirm this using numerical simulations.

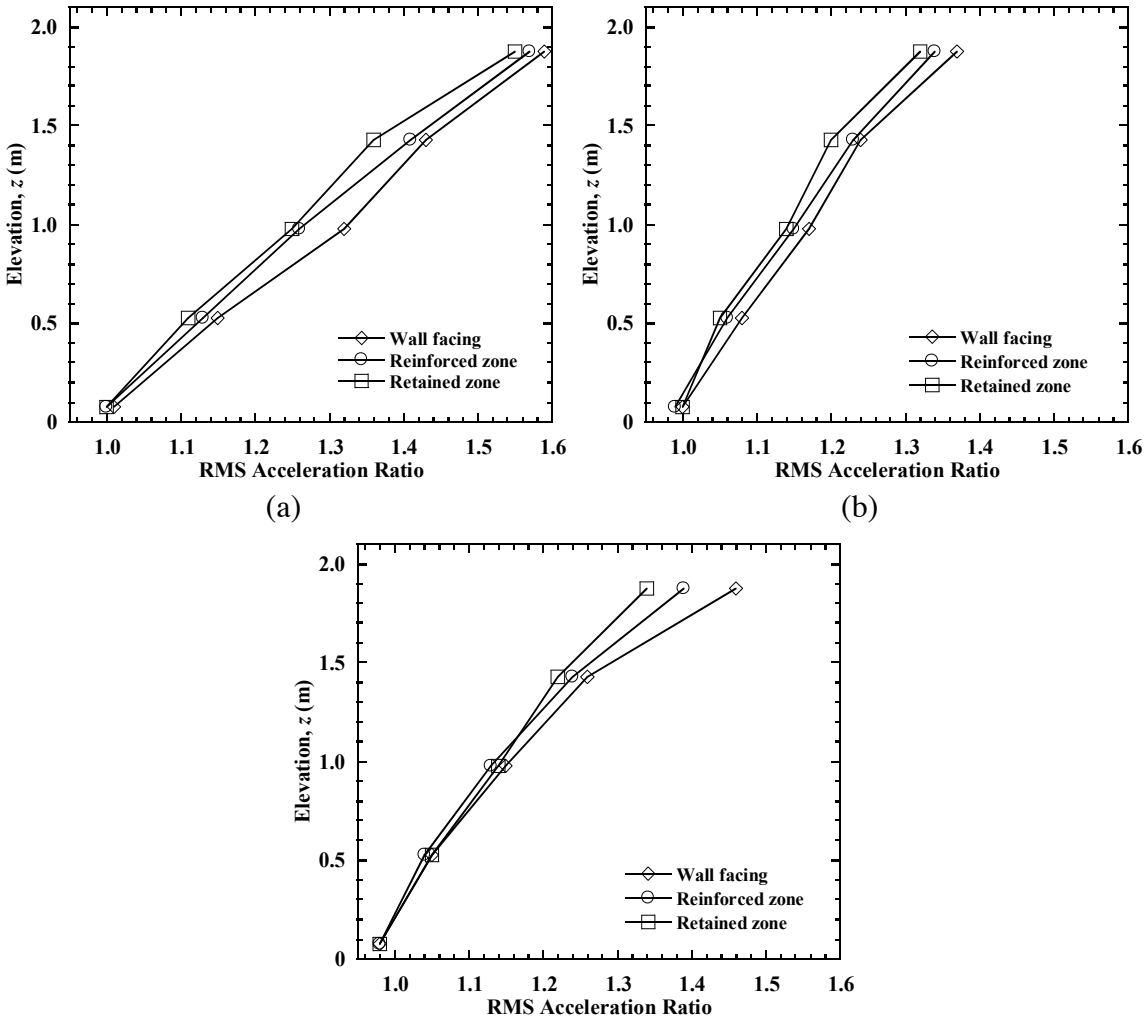

Figure 7.31 RMS acceleration ratio profiles for L1 in Test 1: (a) Imperial Valley motion; (b) Maule motion; (c) Northridge motion.

RMS acceleration ratio profiles for L1 and L2 in Test 1 are shown in Figure 7.32. For the reinforced soil zone, the acceleration ratios for L1 and L2 are similar for the lower section, whereas the acceleration ratios for L1 are larger than L2 for the upper section. The acceleration ratio at the top of L1 has an acceleration ratio of 1.57 for the Imperial Valley motion, which is larger than the value of 1.47 at the same elevation for L2. For the retained soil zone, the acceleration profiles for L1 and L2 are similar.

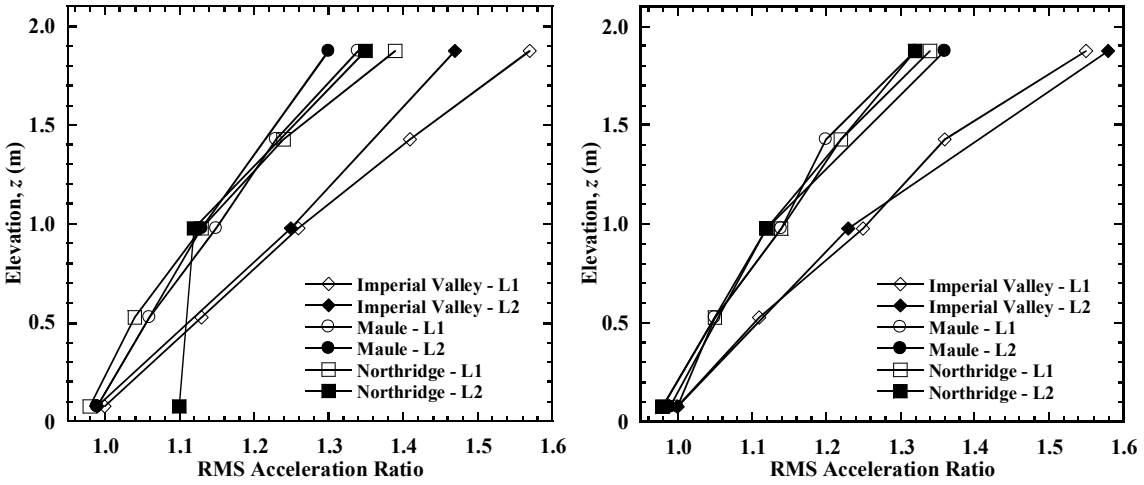

Figure 7.32 RMS acceleration ratio profiles for L1 and L2 in Test 1: (a) reinforced soil zone; (b) retained soil zone.

Time histories of the horizontal accelerations at selected elevations in the reinforced soil zone and retained soil zone for L1 during the Imperial Valley motion in Tests 1 to 4 are shown in Figure 7.33 and Figure 7.34, respectively. Time histories of the horizontal acceleration show similar trend at the same elevations in both the reinforced and retained soil zones for Tests 1 to 4, and also show the acceleration amplification toward the top of the wall.

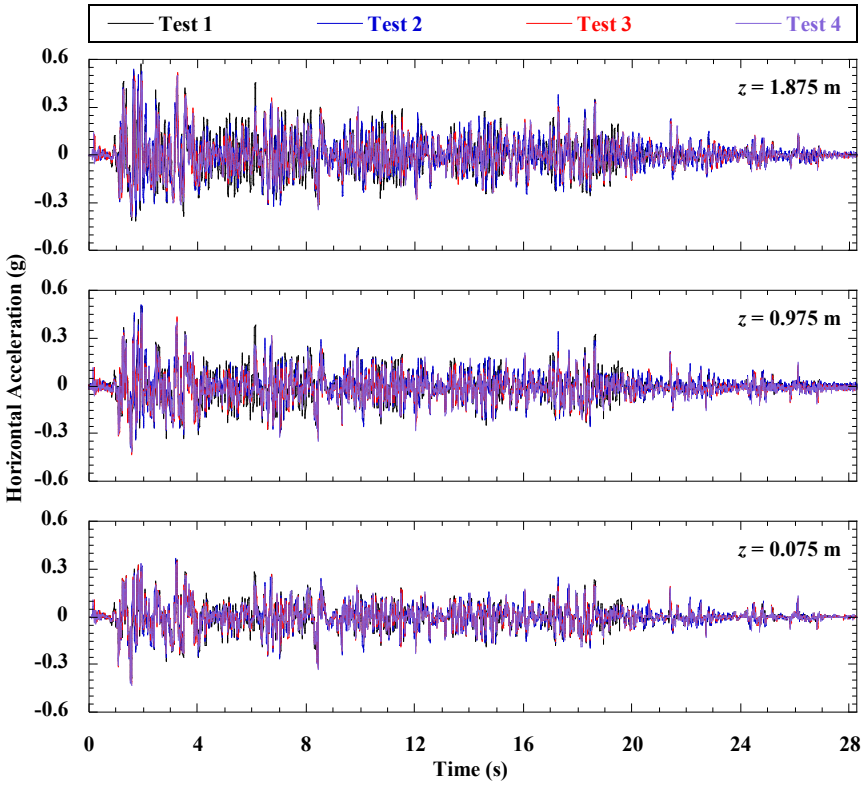

Figure 7.33 Time histories of horizontal acceleration for reinforced soil zone during the Imperial Valley motion in Tests 1 to 4.

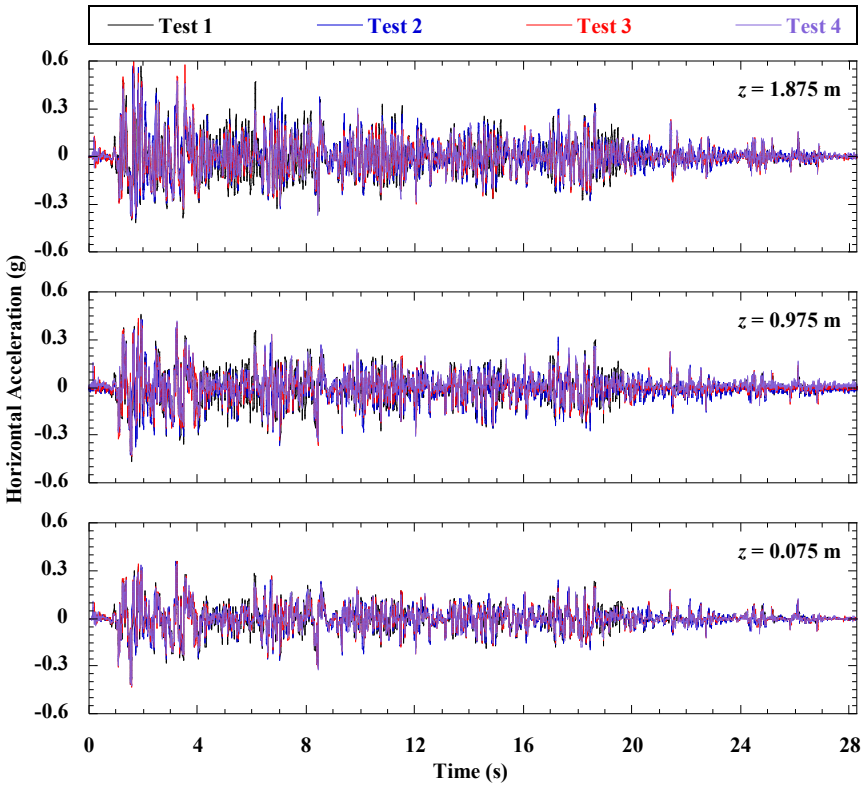

Figure 7.34 Time histories of horizontal acceleration for retained soil zone during the Imperial Valley motion in Tests 1 to 4.

Acceleration ratio profiles for L1 in the reinforced soil zone and retained soil zone in Tests 1 to 4 for the Imperial Valley, Maule, and Northridge motions, are shown in Figure 7.35, Figure 7.36, and Figure 7.37, respectively. For the Imperial Valley motion, Test 1 has the largest acceleration ratios for both the reinforced and retained soil zones. Accelerations ratios for Test 2 are smaller than Test 1, which indicate that the acceleration amplification increases with increasing bridge load for the GRS bridge abutments. Acceleration ratios for Tests 3 and 4 are similar in both the reinforced and retained soil zones, and are much smaller than Test 1. This indicates that acceleration ratios increase with decreasing reinforcement spacing and increasing reinforcement stiffness. Similar trends are also

observed for the Maule and Northridge motions, but acceleration ratios for Test 3 are smaller than for Test 4.

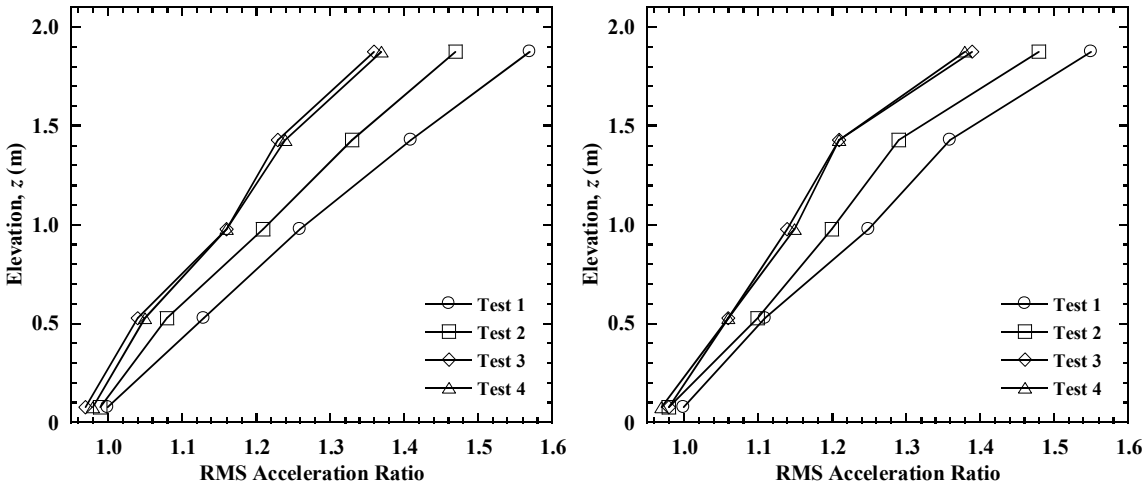

Figure 7.35 RMS acceleration ratio profiles of L1 for the Imperial Valley motion: (a) reinforced soil zone; (b) retained soil zone.

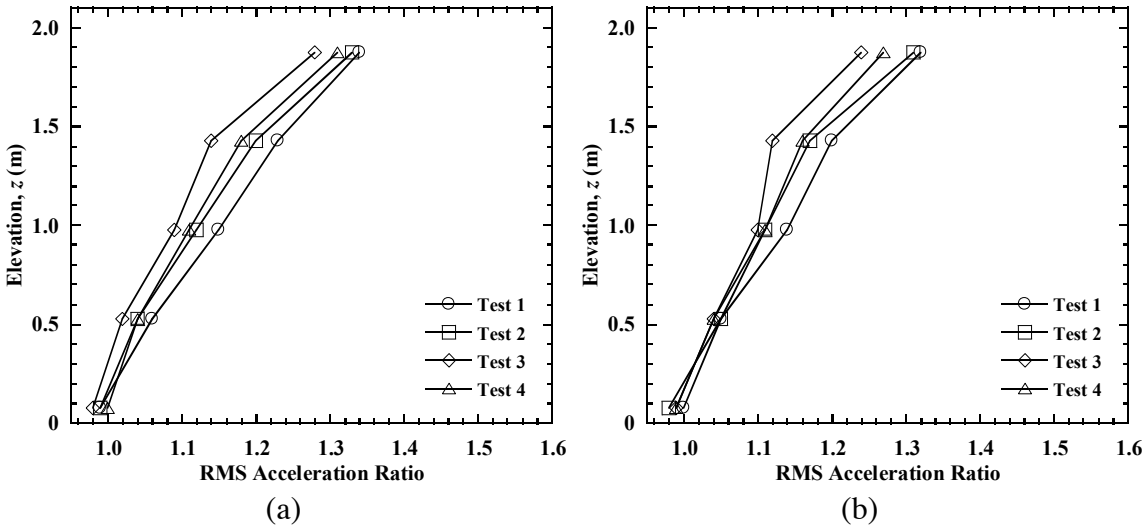

Figure 7.36 RMS acceleration ratio profiles of L1 for the Maule motion: (a) reinforced soil zone; (b) retained soil zone.

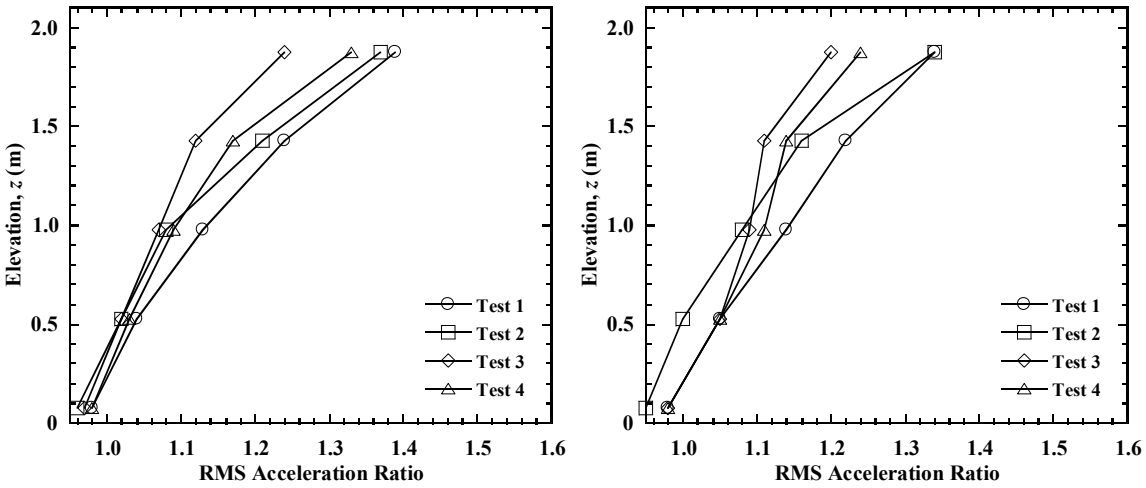

Figure 7.37 RMS acceleration ratio profiles of L1 for the Northridge motion: (a) reinforced soil zone; (b) retained soil zone.

7.7 Vertical Stresses

7.7.1 Static Loading

Vertical stresses were measured behind the wall facing for the longitudinal centerline section L1, and the measured vertical stress profiles for construction stages in Test 1 are shown in Figure 7.38(a). The measured vertical stresses generally increase with decreasing elevation (i.e., increasing depth) for Stage 1, and the vertical stress increased slightly due to construction of the bridge seat and upper wall for Stage 2. For Stage 3, the vertical stresses for the lower half section increased approximately 10 kPa, whereas the upper half section increased significantly, especially at the top of the wall. For instance, the vertical stress at an elevation of z = 1.875 m increased from 16.2 kPa to 70.1 kPa due to placement of bridge beam (from Stages 2 to 3).

Calculated vertical stress profiles for Stages 1 and 3 using the AASHTO method (2012) are shown in Figure 7.38(b), where the values for Stage 1 represent the self-weight of backfill soil and the values for Stage 3 were calculated using the 2:1 vertical stress distribution assumption for flexible walls to obtain the stress increments due to bridge load. For Stage 1, the measured vertical stresses are close to the calculated self-weight values near the top of the wall, but show smaller values toward the bottom, which is attributed to the soil arching effects within the backfill soil. For Stage 3, the measured vertical stress of 70.1 kPa at z = 1.875 m is greater than the calculated value of 54.2 kPa using the AASHTO method, whereas the measured vertical stresses for the lower section are much smaller than the calculated values.

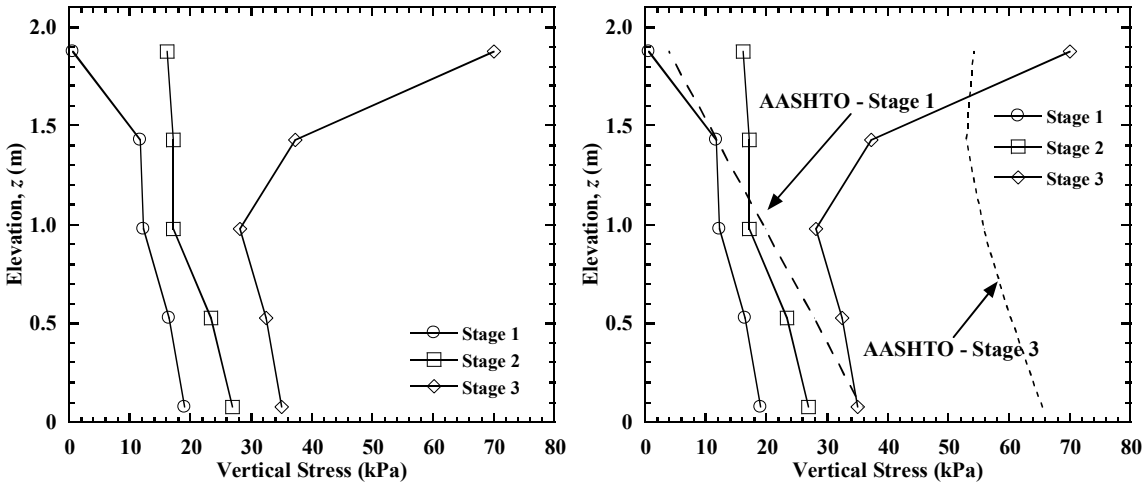

Figure 7.38 Vertical stress profiles behind wall facing for construction stages in Test 1: (a) measurements; (b) analysis.

Measured vertical stress profiles for Stages 1 and 3 in Tests 1 to 4 are shown in Figure 7.39. For Stage 1, the profiles are similar and show a general triangular distribution. However, the differences between the measured vertical stresses and calculated self-weight values generally increase with decreasing elevation (increasing depth). For Stage 3, measured vertical stresses in Test 1 are similar with the other tests for the lower section of the wall, but much larger vertical stresses toward the top of the wall. Although the bridge load in Test 2 is smaller than the other tests, the measured vertical stress profile is similar with the other tests. In general, the measured vertical stresses are smaller than the calculated values except the vertical stress at the top of the wall in Test 1.

The incremental vertical stresses from Stages 1 to 3 for Tests 1 to 4 are shown in Figure 7.40. Profiles of incremental vertical stress in Tests 2, 3, and 4 show a more or less uniform distribution, while the incremental vertical stresses in Test 1 show a much larger

value at z = 1.875 m. In general, the measured incremental vertical stresses are much smaller than the calculated incremental values.

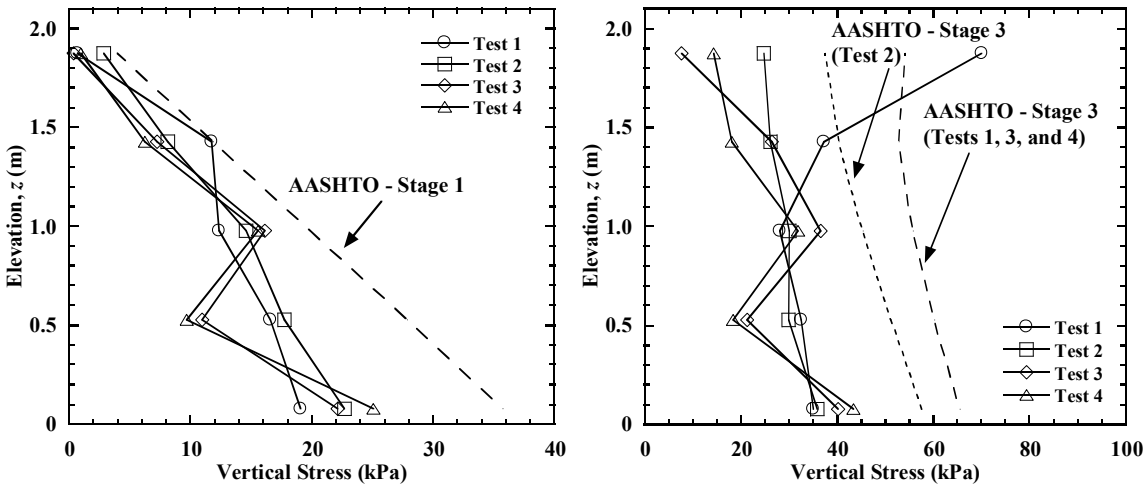

Figure 7.39 Vertical stress profiles behind wall facing for construction stages in Tests 1 to 4: (a) Stage 1; (b) Stage 3.

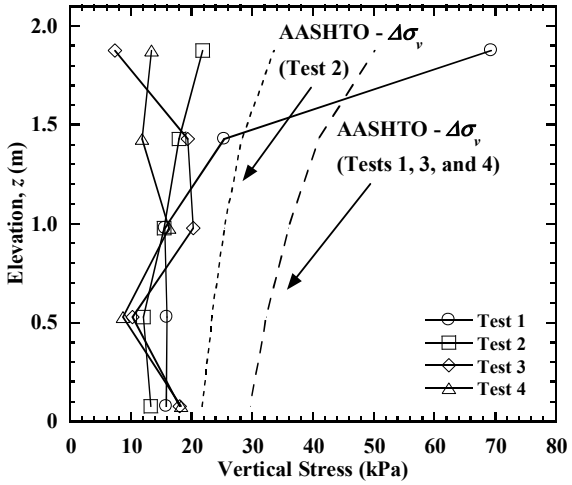

Figure 7.40 Incremental vertical stress profiles behind wall facing from Stages 1 to 3 in Tests 1 to 4.

7.7.2 Dynamic Loading

Time histories of vertical stress behind the wall facing for L1 during the Imperial Valley, Maule, and Northridge motions in Test 1 are shown in Figure 7.41, Figure 7.42, and Figure 7.43, respectively. For all three motions, the dynamic vertical stresses at the top of the wall (z = 1.875 m) are much larger than the lower section. The maximum dynamic vertical stress reached 103.9 kPa, 114.3 kPa, and 117.4 kPa at the top of the wall for the Imperial Valley, Maule, and Northridge motions, respectively. For the Northridge motion, the dynamic vertical stresses varied significantly during shaking, and reached the maximum values at t = 3.34 s and the minimum values at t = 3.98 s.

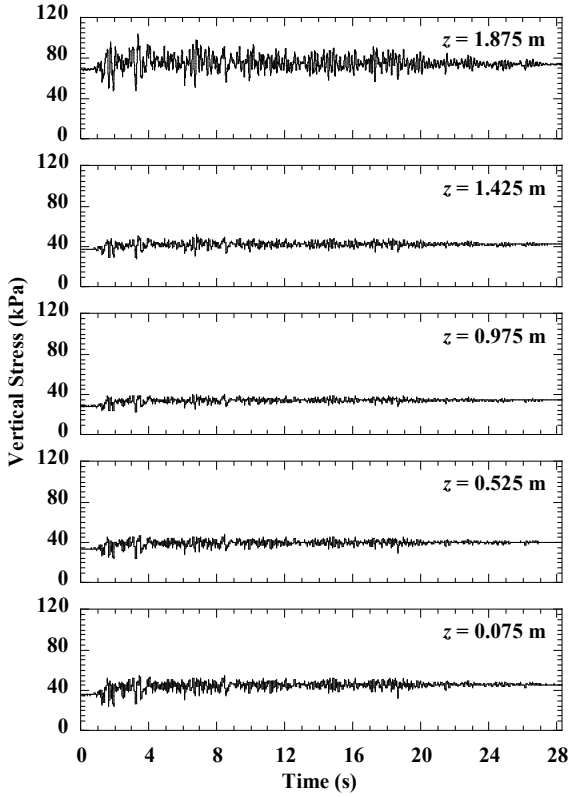

Figure 7.41 Time histories of vertical stress behind wall facing during the Imperial Valley motion in Test 1.

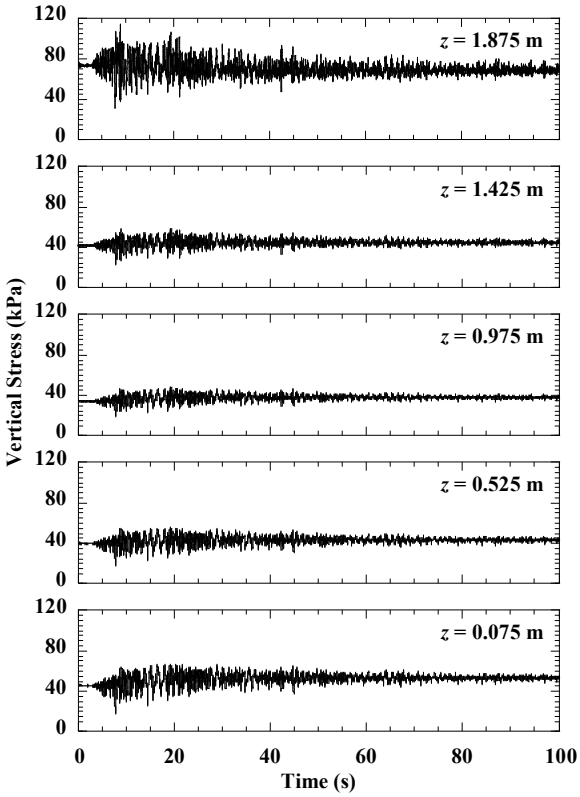

Figure 7.42 Time histories of vertical stress behind wall facing during the Maule motion in Test 1.

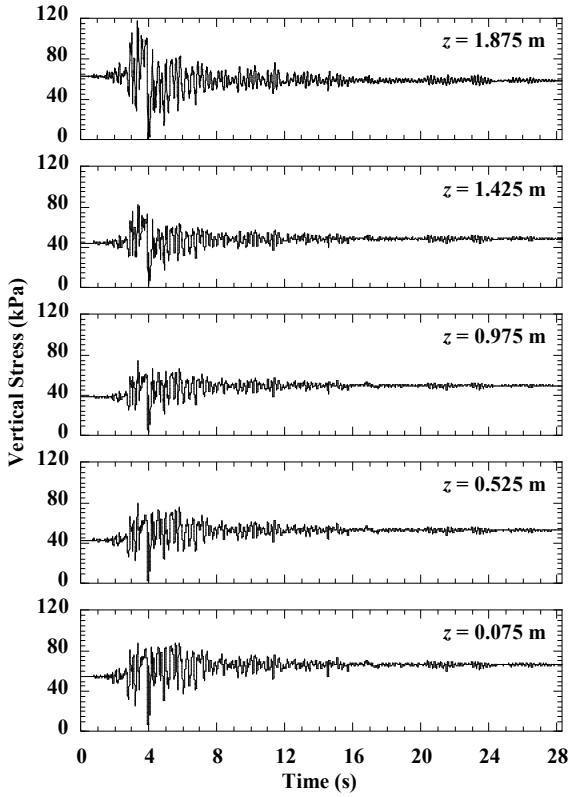

Figure 7.43 Time histories of vertical stress behind wall facing during the Northridge motion in Test 1.

Profiles of the initial (before shaking), maximum (during shaking), and residual (after shaking) vertical stresses in Test 1 are shown in Figure 7.44. For the Imperial Valley motion, the maximum vertical stress is 103.9 kPa at the top of the wall, but recovered to 73.8 kPa after shaking. The change of vertical stress during shaking is mainly due to rocking of the bridge seat. The residual vertical stresses increased slightly as compared to initial values after shaking. Similar observations are also observed for the Maule motion. For the Northridge motion, the maximum vertical stresses during shaking are much larger than the initial values due to strong shaking. The residual vertical stress profile becomes similar to the calculated vertical stress profile under static loading, which might be attributed to the change of arching chains within the backfill soil during shaking.

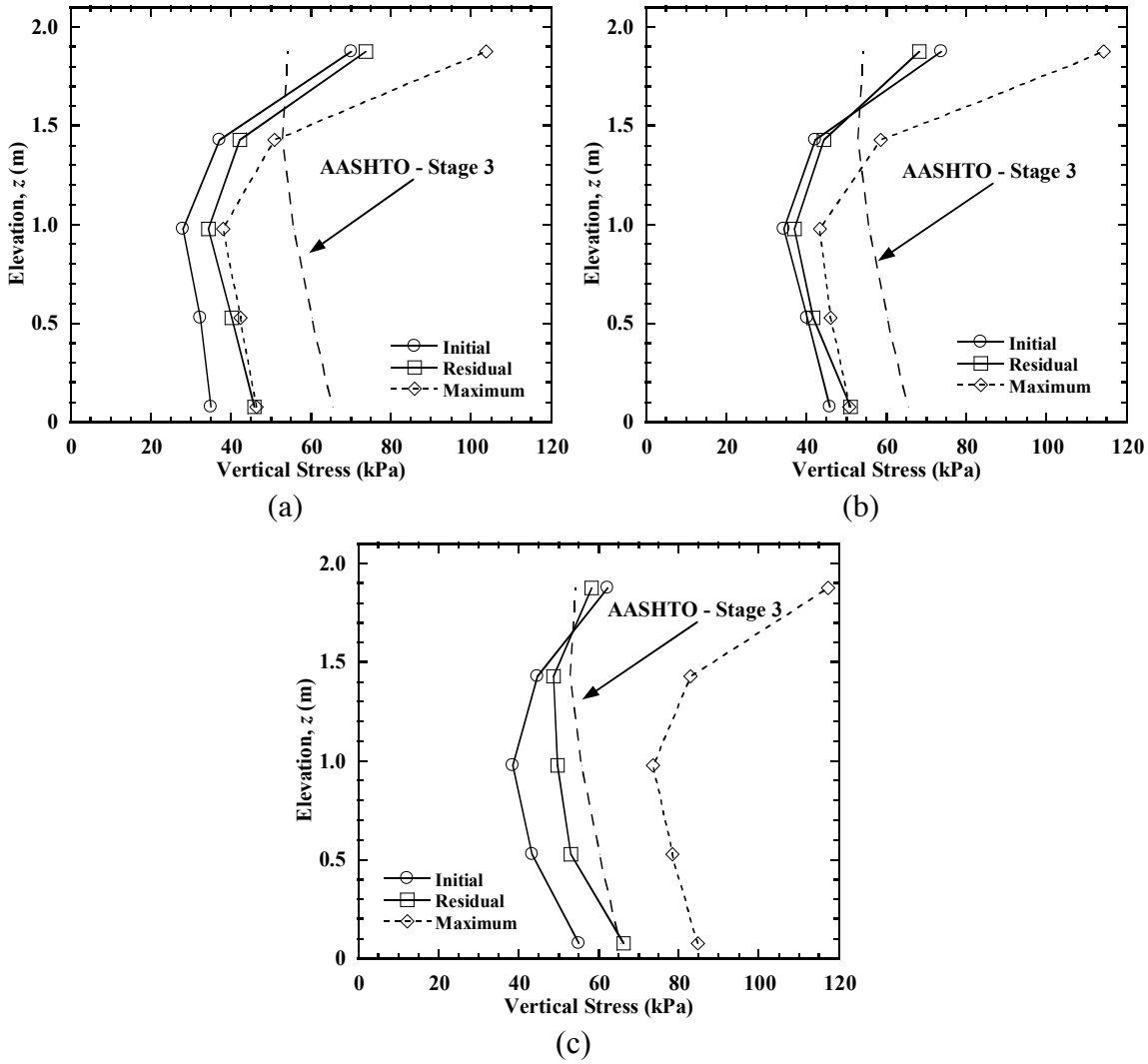

Figure 7.44 Vertical stress profiles behind wall facing in Test 1: (a) Imperial Valley motion; (b) Maule motion; (c) Northridge motion.

Time histories of the total and incremental vertical stresses at selected elevations during the Imperial Valley motion in Tests 1 to 4 are shown in Figure 7.45 and Figure 7.46, respectively. At the top of the wall (z = 1.875 m), the dynamic vertical stresses are the largest for Test 1. Much smaller values were observed for Tests 3 and 4. At the mid-height of the wall (z = 0.975 m), the dynamic vertical stresses are similar for all four tests. However, the dynamic vertical stresses for Tests 3 and 4 are larger than Tests 1 and 2 at

the bottom of the wall (z = 0.075 m). Similar trends for different longitudinal tests are also observed for the incremental vertical stresses as shown in Figure 7.46.

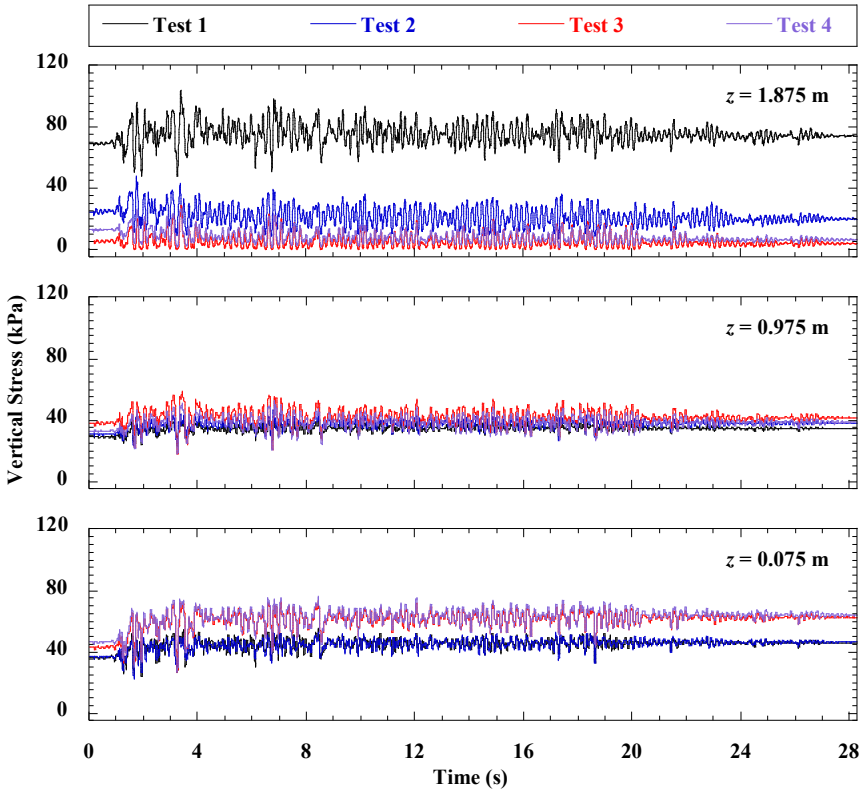

Figure 7.45 Time histories of vertical stress behind wall facing during the Imperial Valley motion in Tests 1 to 4.

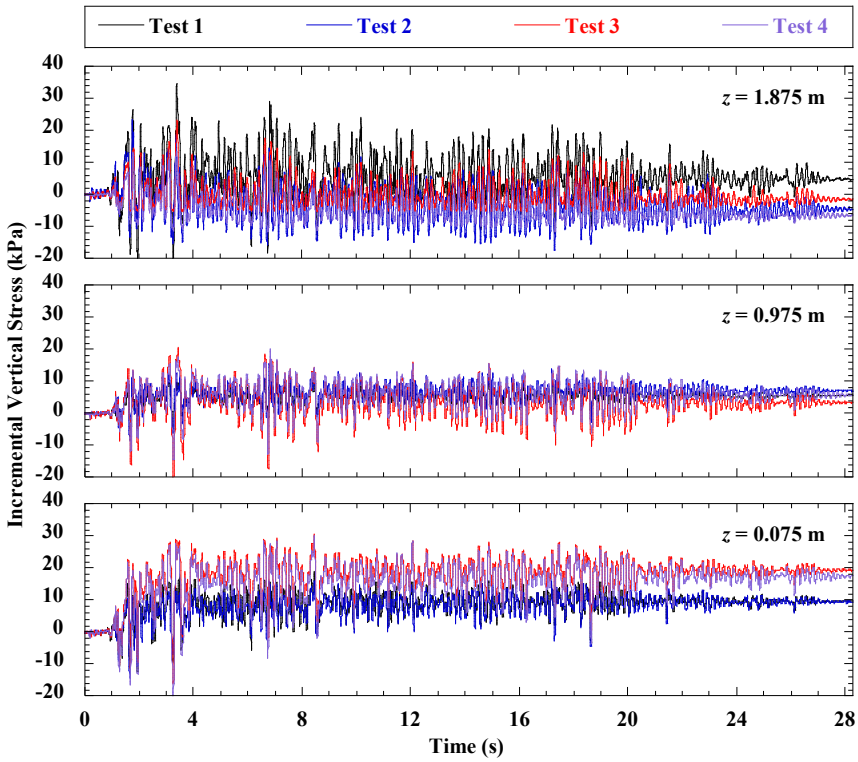

Figure 7.46 Time histories of incremental vertical stress behind wall facing during the Imperial Valley motion in Tests 1 to 4.

The vertical stress profiles for the Imperial Valley, Maule, and Northridge motions in Tests 1 to 4 are shown in Figure 7.47, Figure 7.48, and Figure 7.49, respectively. For the Imperial Valley motion, maximum dynamic vertical stress profiles show the maximum value at the top of the wall for Test 1, while at the bottom of the wall with a triangular distribution for Tests 2, 3, and 4. Similar distributions are also observed for the incremental maximum stresses shown in Figure 7.47(b). The residual vertical stress profiles also show consistent shapes with the maximum vertical stress profiles, and the measured vertical stresses are generally smaller than calculated values under static loading. For the Maule motion, the incremental maximum stresses show a more or less uniform distribution for Test 3 with an incremental vertical stress of approximately 25 kPa, and the residual vertical

stresses are closer to the calculated values. For the Northridge motion, the incremental maximum vertical stresses are much larger than for the other two motions due to the strong shaking. The residual vertical stress profile for Test 1 is similar to the calculated vertical stress profile, while the residual vertical stresses for Tests 2, 3, and 4 increase almost linearly with decreasing elevation (increasing depth) with smaller values than the calculated values at the top of the wall and larger values at the bottom of the wall.

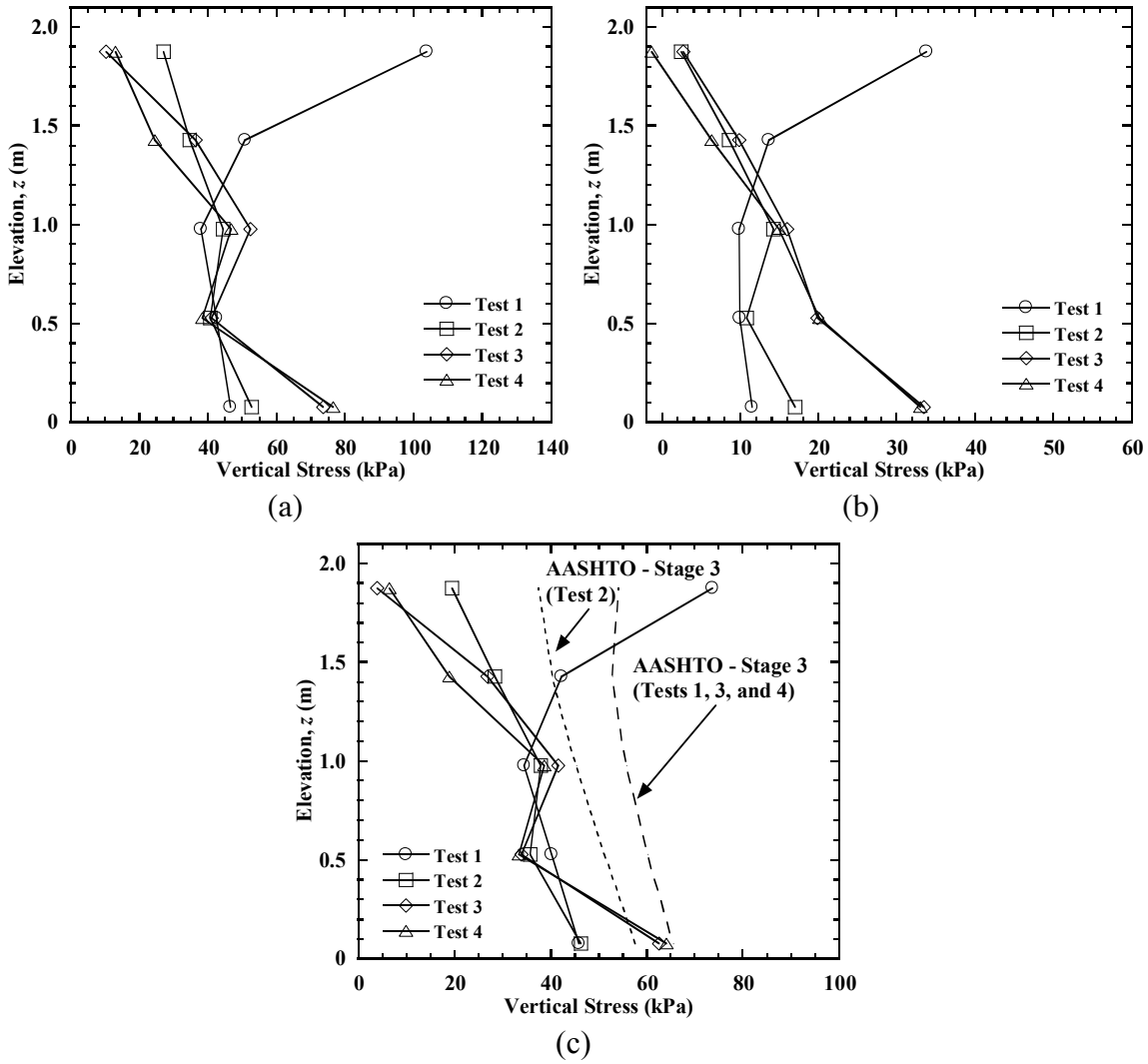

Figure 7.47 Vertical stress profiles behind wall facing for the Imperial Valley motion: (a) maximum vertical stress; (b) incremental maximum stress; (c) residual vertical stress.

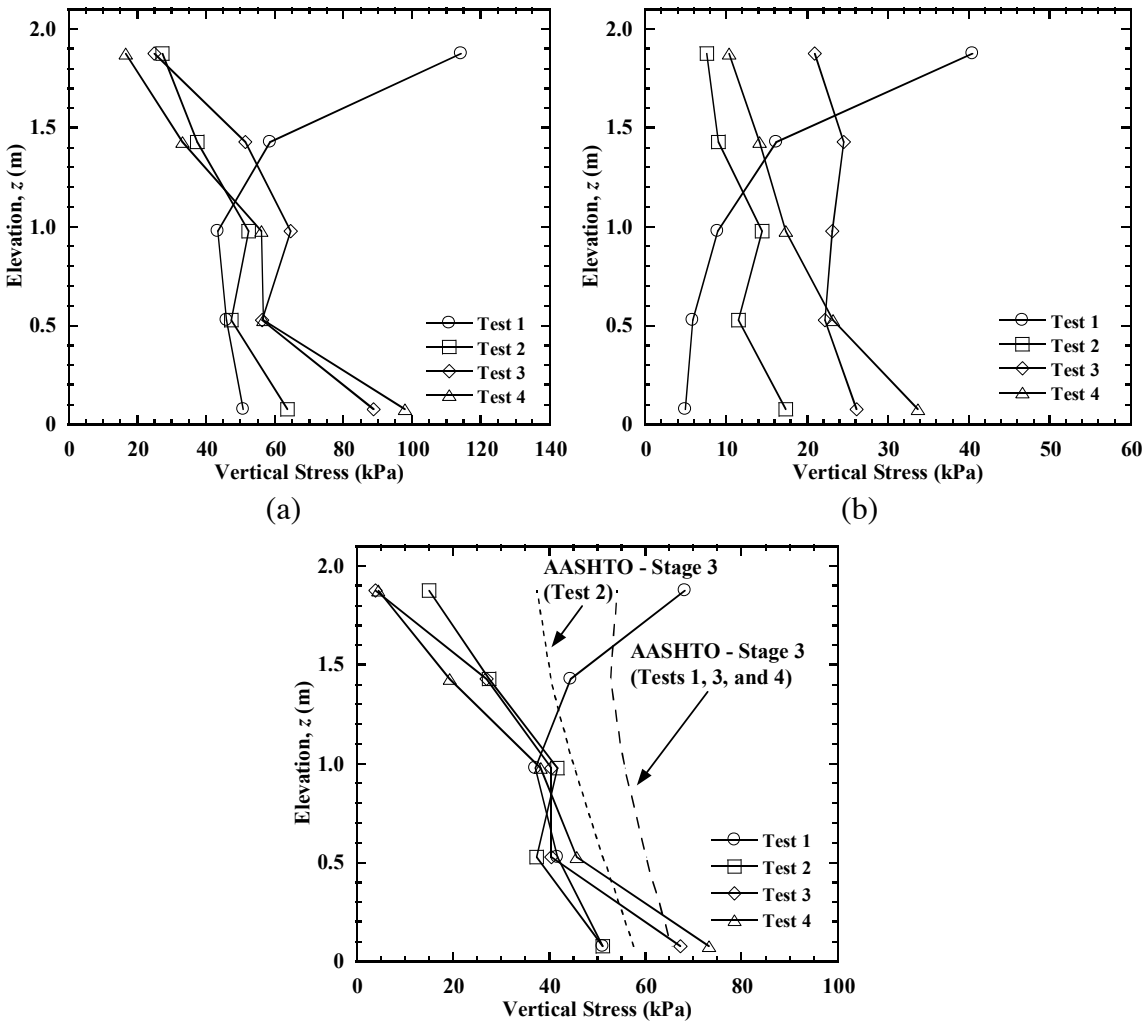

Figure 7.48 Vertical stress profiles behind wall facing for the Maule motion: (a) maximum vertical stress; (b) incremental maximum stress; (c) residual vertical stress.

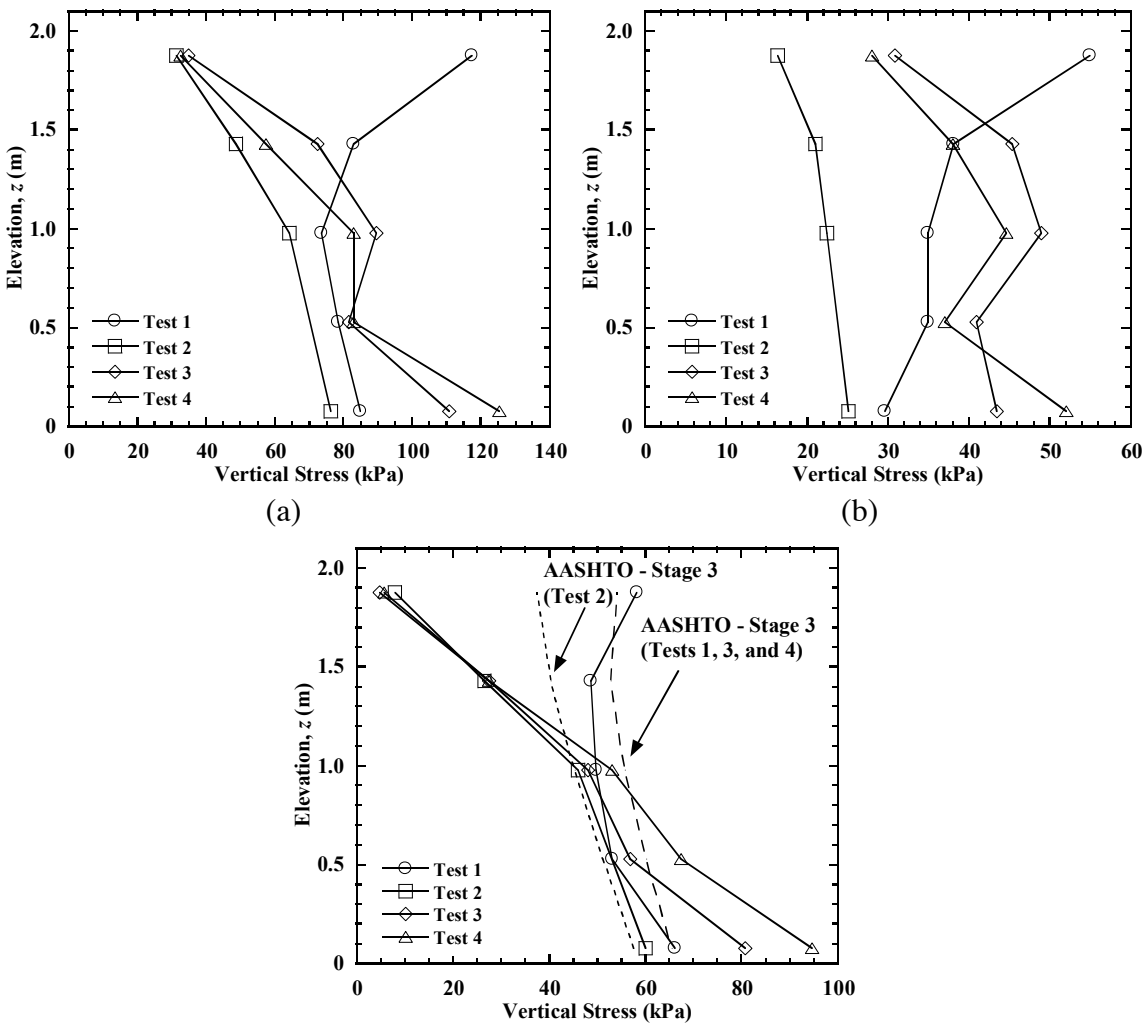

Figure 7.49 Vertical stress profiles behind wall facing for the Northridge motion: (a) maximum vertical stress; (b) incremental maximum stress; (c) residual vertical stress.

7.8 Lateral Stresses

7.8.1 Static Loading

Lateral stresses behind the wall facing were measured for the longitudinal section L1, and the profiles for construction stages in Test 1 are shown in Figure 7.50(a). For Stage 1, the lateral stresses generally increase with decreasing elevation (increasing depth) with a minimum value of 1.2 kPa at the top of the wall and a maximum value of 3.4 kPa at the bottom. The lateral stress increased slightly due to construction of the bridge seat for Stage 2. For Stage 3, the lateral stress at the top of the wall increased from 2.0 kPa to 4.0 kPa.

The lateral stresses calculated using the AASHTO method (2012) by multiplying the active earth pressure coefficient K_a by the vertical stresses for Stages 1 and 3 are shown in Figure 7.50(b). For Stage 1, the lateral stress profile is similar to the calculated stress profile, with the measured lateral stresses larger than the calculated values at top of the wall. This is attributed to the locked-in lateral stresses due to compaction. For Stage 3, the measured lateral stresses are much smaller than the calculated values.

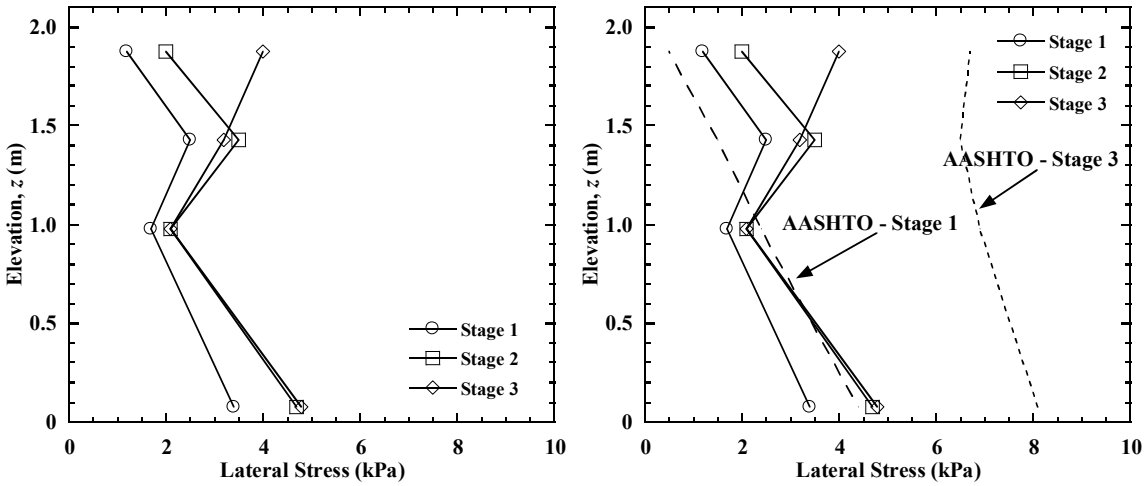

Figure 7.50 Lateral stress profiles behind wall facing for construction stages in Test 1: (a) measurements; (b) analysis.

Measured lateral stress profiles behind the wall facing for Stages 1 and 3 in Tests 1 to 4 are shown in Figure 7.51. For Stage 1, the lateral stresses are generally small with magnitude less than 5 kPa. The lateral stresses at the top of the wall are generally larger than the calculated values. Again, this is attributed to the locked-in lateral stresses due to compaction. For Stage 3, the lateral stress at the top of the wall increased due to placement of the bridge beam, which is also shown from the incremental lateral stress profiles (from Stages 1 to 3) in Figure 7.52. In general, the magnitudes of lateral stress after construction of the GRS bridge abutment are relatively small, and it is difficult to identify a consistent shape from the lateral stress profiles between different longitudinal tests.

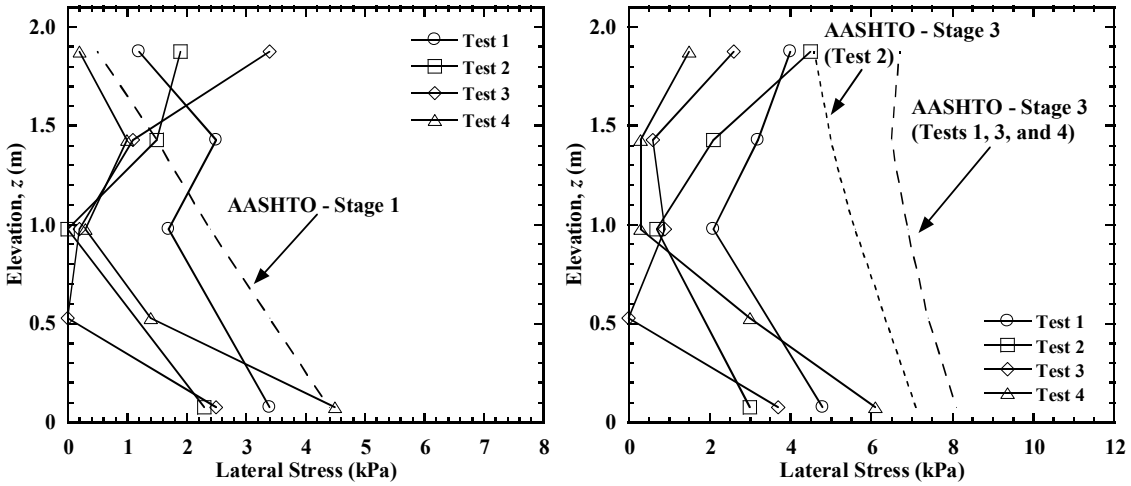

(a) (b)

Figure 7.51 Lateral stress profiles behind wall facing for construction stages in Tests 1 to 4: (a) Stage 1; (b) Stage 3.

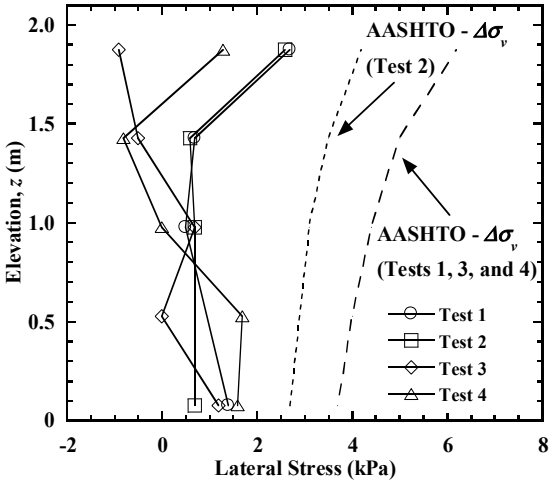

Figure 7.52 Incremental lateral stress profiles behind wall facing from Stages 1 to 3 in Tests 1 to 4.

7.8.2 Dynamic Loading

Time histories of lateral stress for the longitudinal section L1 during the Imperial Valley, Maule, and Northridge motions in Test 1 are shown in Figure 7.53, Figure 7.54, and Figure 7.55, respectively. Similar to the vertical stresses, the dynamic lateral stress at the top of the wall (z = 1.875 m) are generally larger than the lower section for all three motions. The dynamic lateral stresses for the upper section of the wall (z = 1.425 m and 1.875 m) were essentially all recovered after shaking, while the residual vertical stresses for the lower section of the wall (z = 0.075 m and 0.975 m) increased slightly.

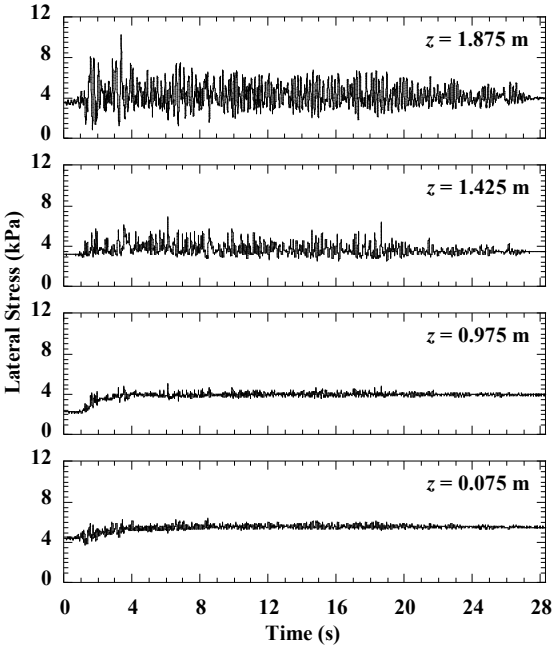

Figure 7.53 Time histories of lateral stress behind wall facing during the Imperial Valley motion in Test 1.

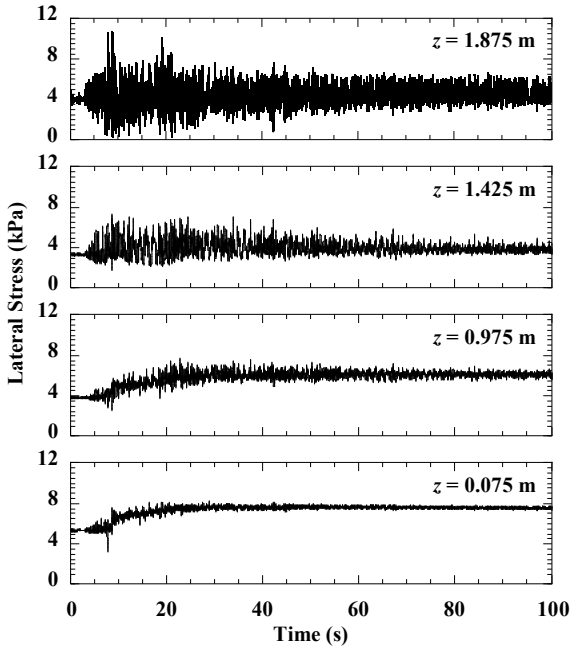

Figure 7.54 Time histories of lateral stress behind wall facing during the Maule motion in Test 1.

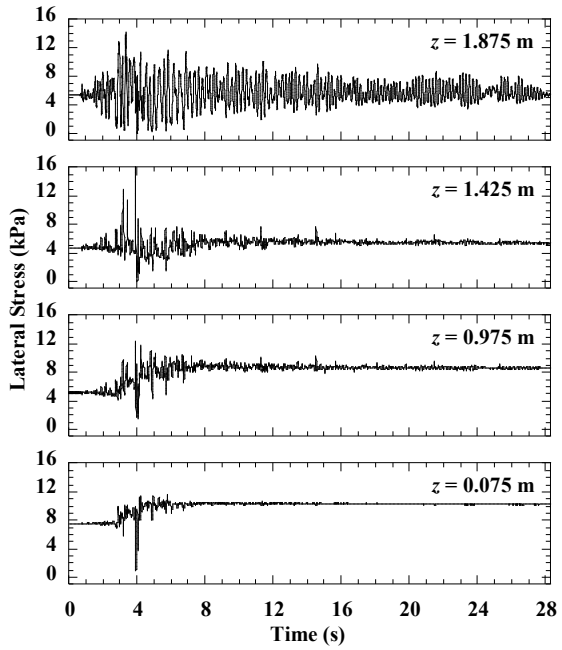

Figure 7.55 Time histories of lateral stress behind wall facing during the Northridge motion in Test 1.

Profiles of the initial (before shaking), maximum (during shaking), and residual (after shaking) lateral stresses in Test 1 are shown in Figure 7.56. The maximum dynamic lateral stress occurred at the top of the wall for the Imperial Valley and Maule motions, and reached 10.2 kPa and 10.7 kPa, respectively. After shaking, the dynamic lateral stresses were almost all recovered. For the Northridge motion, the maximum dynamic lateral stresses increased significantly as compared to the initial lateral stresses due to the strong shaking, and the maximum lateral stress is 16.7 kPa at z = 1.425 m. The residual lateral stress profile becomes similar to the calculated lateral stress profile under static loading. The dynamic lateral stresses are a result of both the inertial forces of the backfill soil due to shaking and the dynamic vertical stresses associated with rocking of the bridge seat.

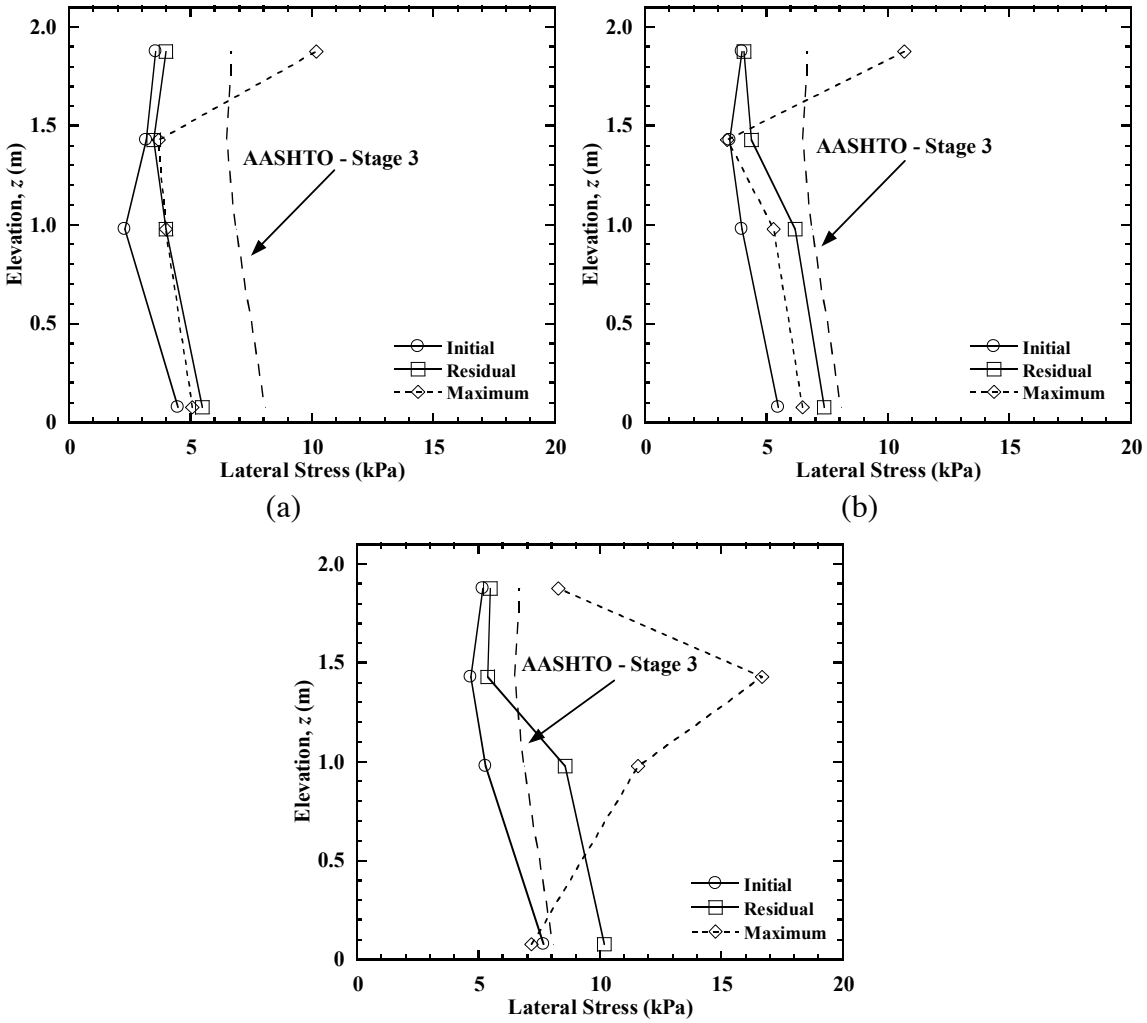

Figure 7.56 Lateral stress profiles behind wall facing in Test 1: (a) Imperial Valley motion; (b) Maule motion; (c) Northridge motion.

Time histories of the total and incremental lateral stresses at selected elevations during the Imperial Valley motion in Tests 1 to 4 are shown in Figure 7.57 and Figure 7.58. At the top of the wall (z = 1.875 m), the magnitudes of incremental dynamic lateral stress are the largest for Test 2, while the dynamic lateral stress are relatively small and even decreased slightly for Test 3. The incremental dynamic lateral stresses for Test 4 are relatively large both at the mid-height (z = 0.975 m) and bottom of the wall (z = 0.075 m).

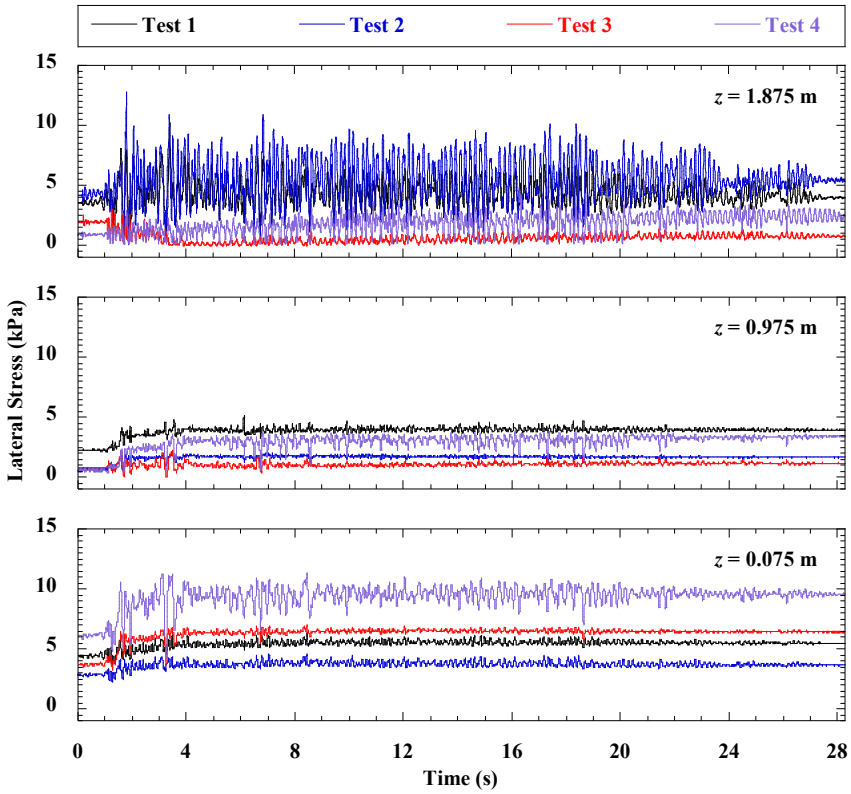

Figure 7.57 Time histories of lateral stress behind wall facing during the Imperial Valley motion in Tests 1 to 4.

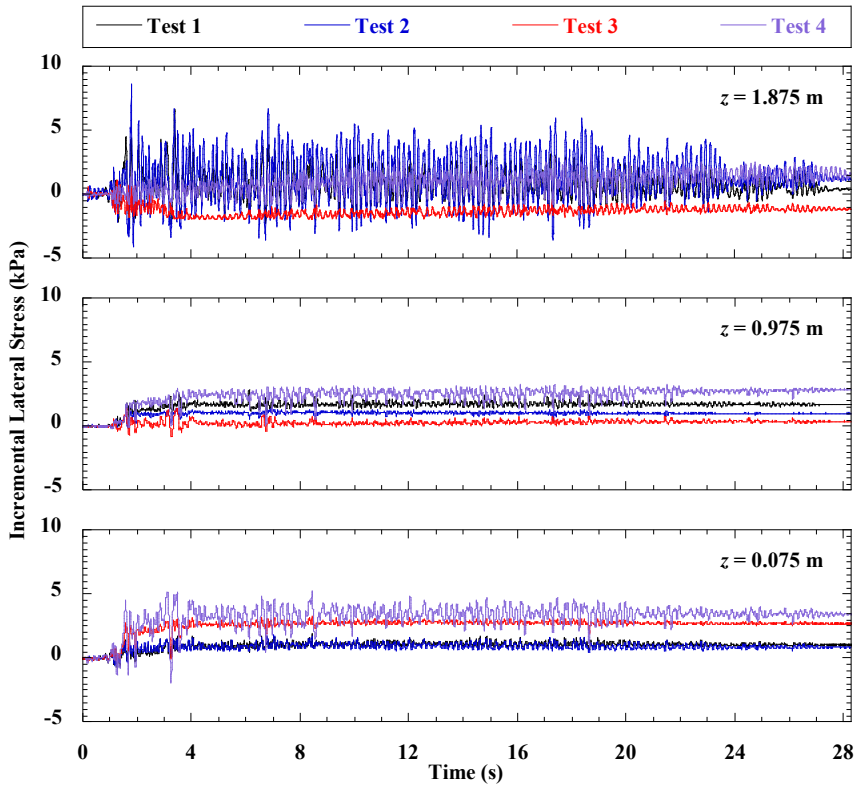

Figure 7.58 Time histories of incremental lateral stress behind wall facing during the Imperial Valley motion in Tests 1 to 4.

The lateral stress profiles in different longitudinal tests for the Imperial Valley, Maule, and Northridge motions are shown in Figure 7.59, Figure 7.60, and Figure 7.61, respectively. For the Imperial Valley motion, maximum dynamic lateral stress profiles show maximum values at the top for Tests 1 and 2, while at the bottom of the wall for Tests 3 and 4. The incremental maximum lateral stress profiles show a triangular distribution for Tests 3 and 4. The residual lateral stresses at the top of the wall for Tests 1 and 2 after shaking are 4.0 kPa and 5.3 kPa, respectively. The measured lateral stresses are generally smaller than calculated values under static loading. For the Maule motion, the incremental maximum lateral stresses are the largest for Test 3, and also show large incremental lateral stresses for Tests 1 and 2. After shaking, the residual lateral stresses become closer to the

calculated values under static loading. For the Northridge motion, the incremental maximum lateral stresses are much larger than the other two motions due to the strong shaking. The incremental maximum dynamic lateral stress is 13.9 kPa at the top of the wall for Test 2 and is 8.8 kPa at the bottom of the wall for Test 4. The residual lateral stresses for Tests 1, 3, and 4 are generally larger than the calculated values.

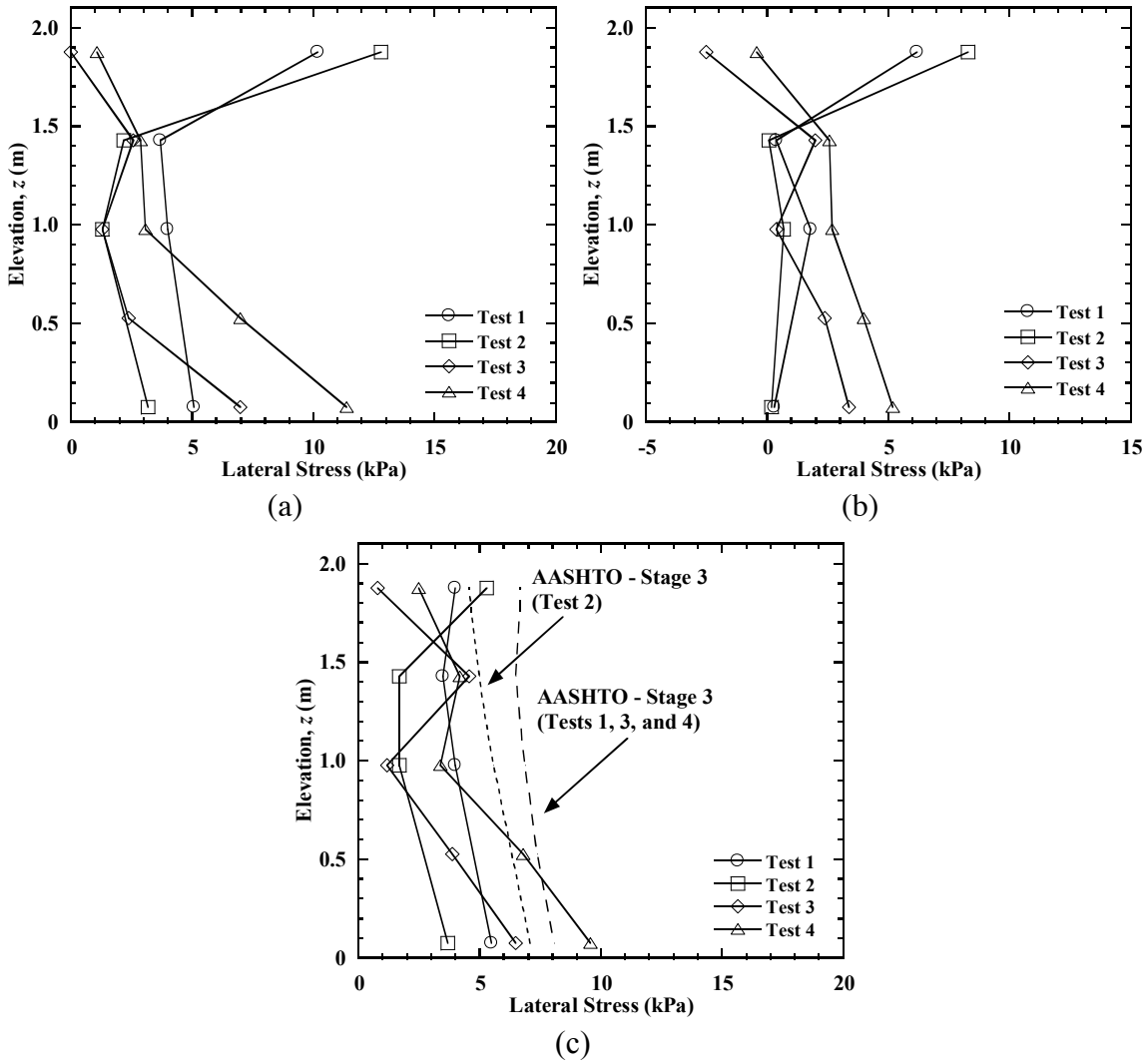

Figure 7.59 Lateral stress profiles behind wall facing for the Imperial Valley motion: (a) maximum lateral stress; (b) incremental maximum lateral stress; (c) residual lateral stress.

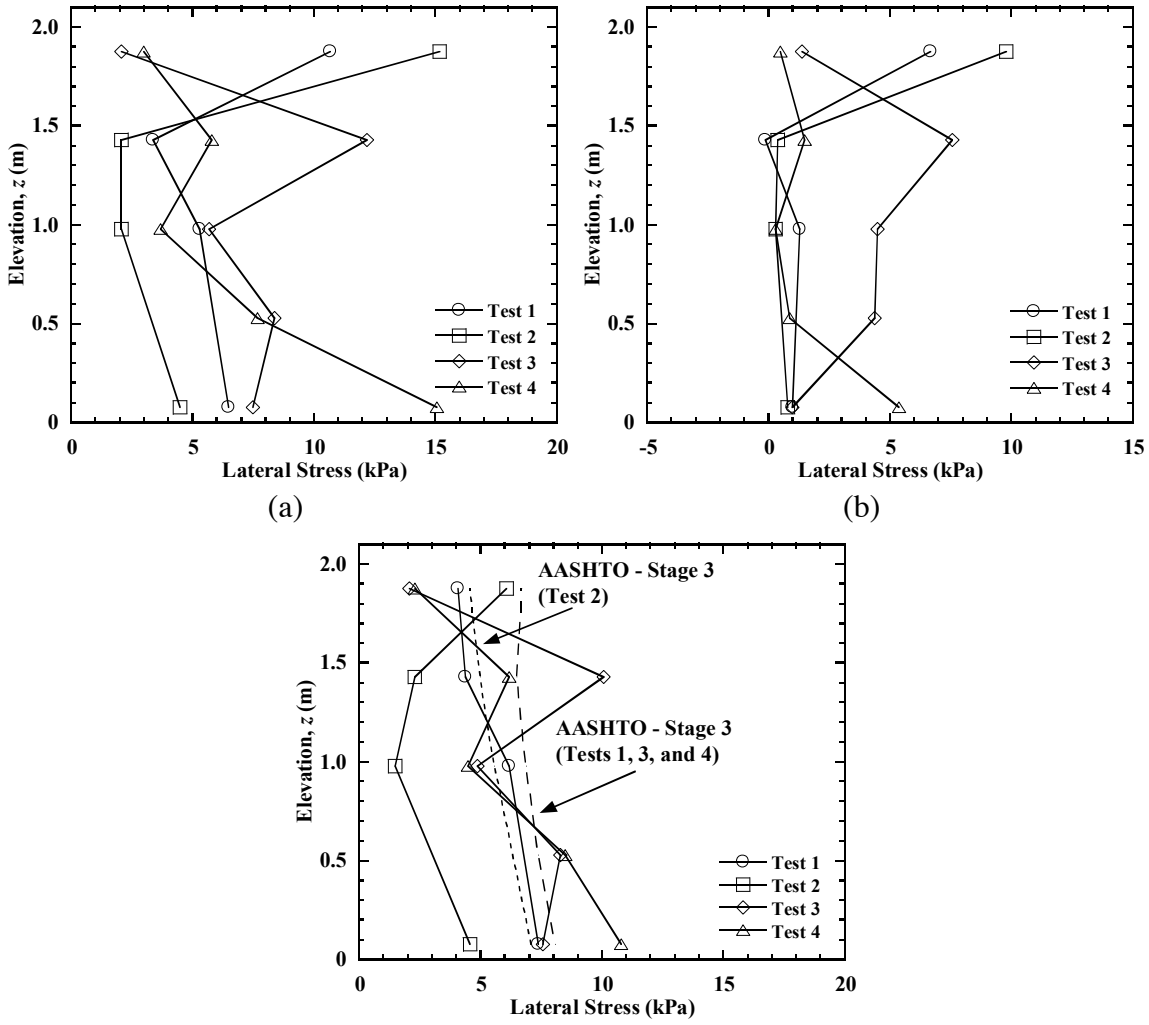

Figure 7.60 Lateral stress profiles behind wall facing for the Maule motion: (a) maximum lateral stress; (b) incremental maximum lateral stress; (c) residual lateral stress.

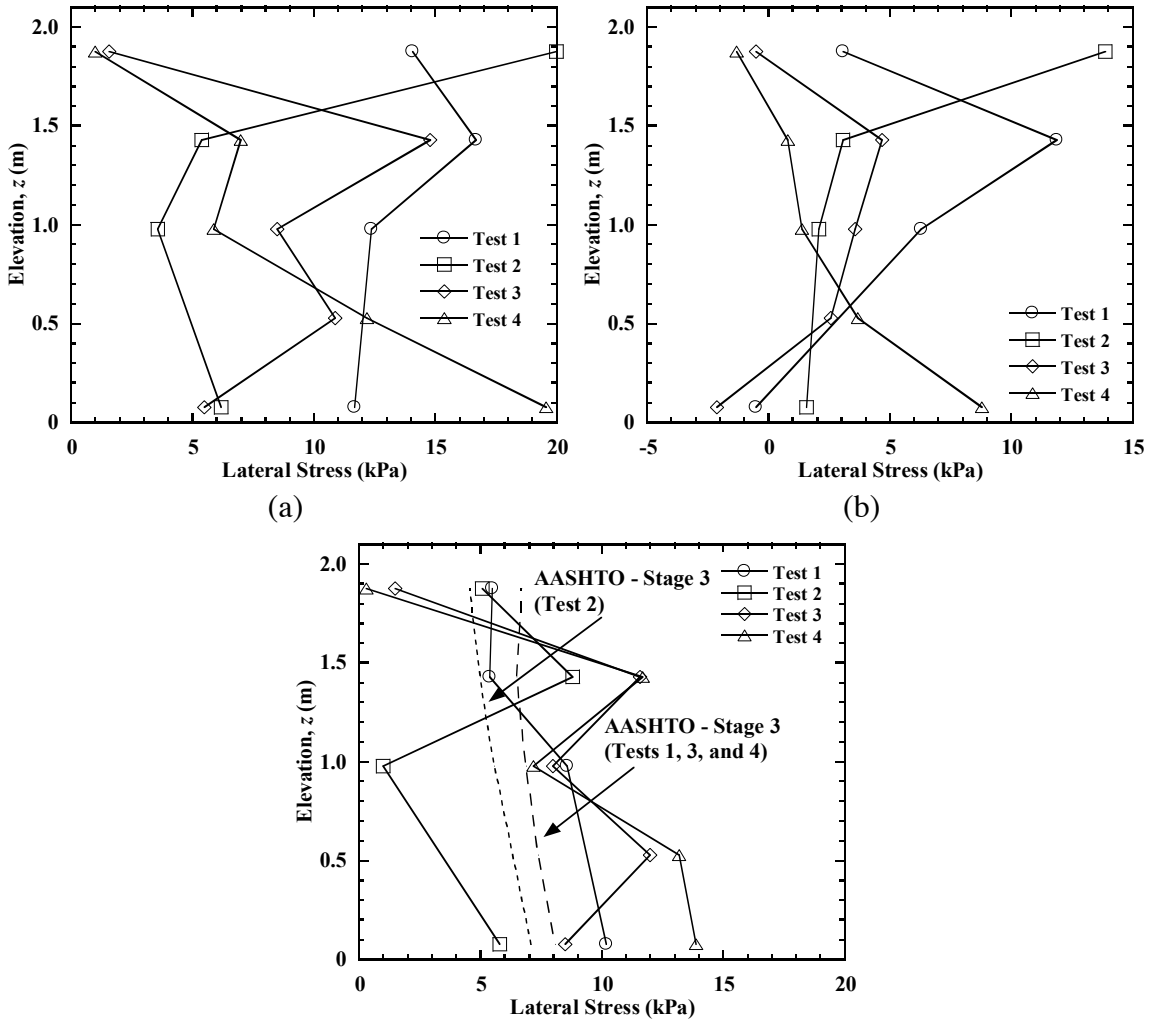

Figure 7.61 Lateral stress profiles behind wall facing for the Northridge motion: (a) maximum lateral stress; (b) incremental maximum lateral stress; (c) residual lateral stress.

7.9 Reinforcement Strains

7.9.1 Static Loading

Reinforcement strain distributions in the longitudinal sections L1 and L2 for construction stages in Test 1 are shown in Figure 7.62. Each measurement represents the average value from a pair of top and bottom gauges, and zero strain at the free end of each reinforcement layer is also plotted.

For Stage 1, the reinforcement strain distributions in L1 show maximum strains near the connections (at distance x = 0.1 m from the front wall facing) for layers 1, 4, and 7, and under the bridge seat (x = 0.8 m) for layer 10. The reinforcement strains in layer 13 are relatively small and do not show a clear maximum value. For Stage 2, reinforcement strains near the connections and under the bridge seat increased slightly due to construction of the bridge seat and upper wall. The reinforcement strains in L2 generally show similar distributions to L1 with respect to both magnitude and trend for Stages 1 and 2. For Stage 3, reinforcement strains in L1 had greater increases near the connections for layers 1, 4, and 7, and under the bridge seat for layers 10 and 13 due to placement of the bridge beam. The reinforcement strains in layers 1 and 7 for L1 show similar magnitudes of strain to L2. However, the reinforcement strains in layer 13 under the bridge seat for L2 had much larger increase than L1. The reinforcement strain at x = 0.45 m in layer 13 is 0.15% for L2, which is much larger than the value of 0.05% for L1. This is attributed to tilting of the bridge seat toward the west side for Stage 3 as shown in Figure 7.20.

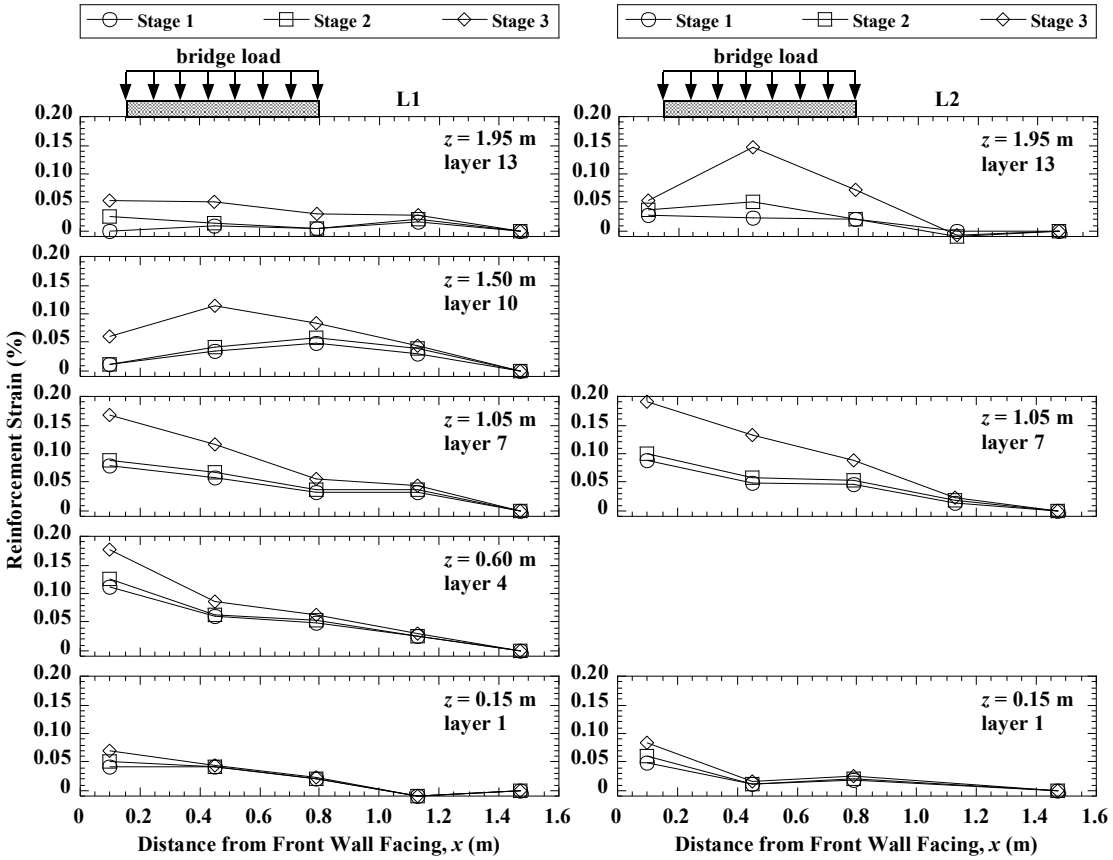

Figure 7.62 Reinforcement strain distributions in L1 and L2 for construction stages in Test 1.

Reinforcement strain distributions in the transverse section T1 for construction stages in Test 1 are shown in Figure 7.63. For Stage 1, layers 1 and 7 show maximum strains near the connections, and layer 13 shows relatively small strains. For Stage 2, construction of the bridge seat resulted in greater increases in layer 13 both near the connection and under the bridge seat. For Stage 3, the placement of bridge beam caused significant increases of reinforcement strain in layers 7 and 13. The reinforcement strain at y_w = 0.33 m from the west side wall facing reached 0.14%, which is similar to the strain value of 0.15% at the same elevation for the longitudinal section L2 (also on the west side).

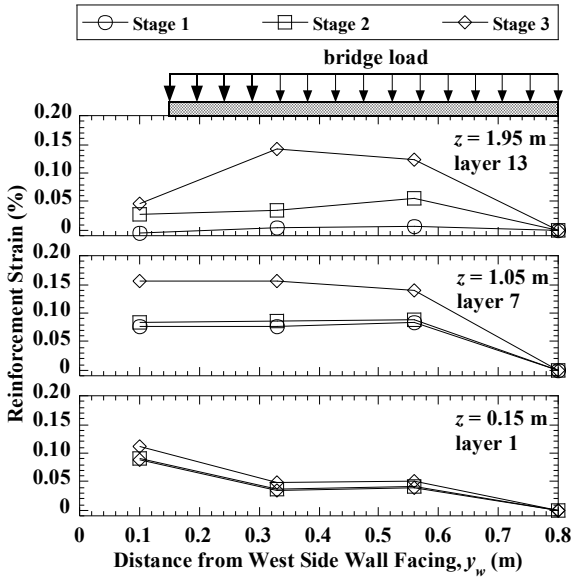

Figure 7.63 Reinforcement strain distributions in T1 for construction stages in Test 1.

Reinforcement strain distributions in the longitudinal sections L1 and L2 for Stages 1 and 3 in Tests 1 to 4 are shown in Figure 7.64 and Figure 7.65, respectively. For the longitudinal off-centerline section L2, reinforcement strains were measured only for layer 7 in Test 3. For Stage 1, the magnitudes of reinforcement strain in L1 are relatively small and show generally similar values. The reinforcement strains at x = 0.45 m in layer 1 for L2 in Test 4 shows much larger value than the other tests, which may be due to over compaction for this layer in Test 4. For Stage 3, the reinforcement strains in L1 and L2 in Tests 3 and 4 are the larger than in Tests 1 and 2.

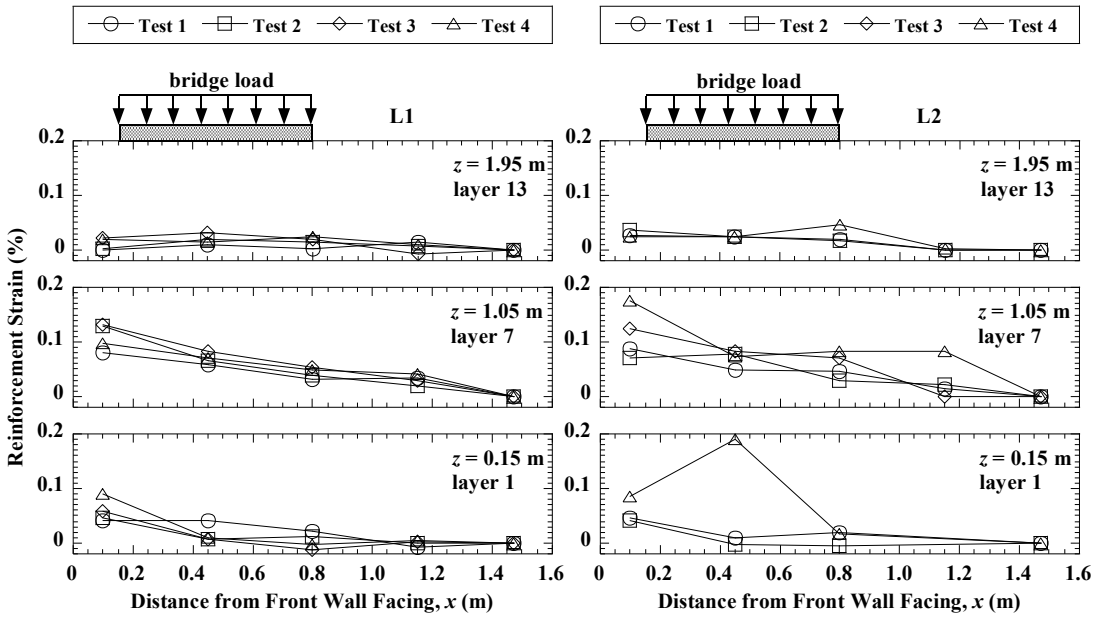

Figure 7.64 Reinforcement strain distributions in L1 and L2 for Stage 1 in Tests 1 to 4.

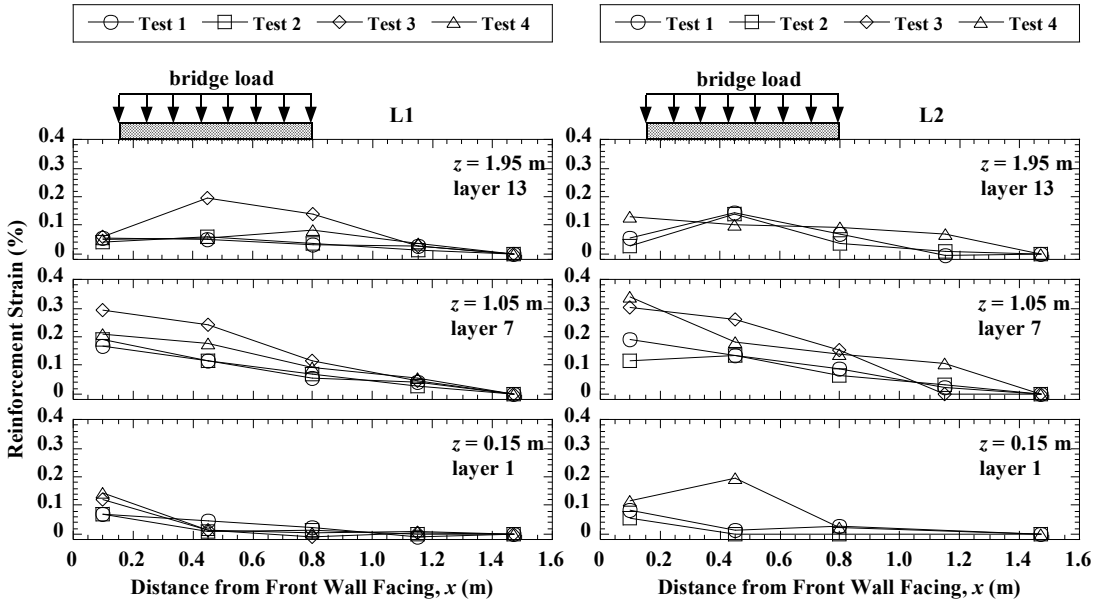

Figure 7.65 Reinforcement strain distributions in L1 and L2 for Stage 3 in Tests 1 to 4.

The incremental reinforcement strain distributions due to placement of the bridge beam (from Stages 2 to 3) in L1 and L2 are shown in Figure 7.76. Results for L1 and L2 show that the incremental strains in Test 3 are larger than the other tests for all layers shown, especially for layers 7 and 13, which indicates that reinforcement spacing has the most significant effect. The incremental strains in Test 4 also have larger strain values than Tests 1 and 2 for both L1 and L2. This indicates that reinforcement stiffness also have important effects on the reinforcement strains. As expected, for both L1 and L2, the incremental strains in Test 1 with greater bridge load are larger than the incremental strains in Test 2.

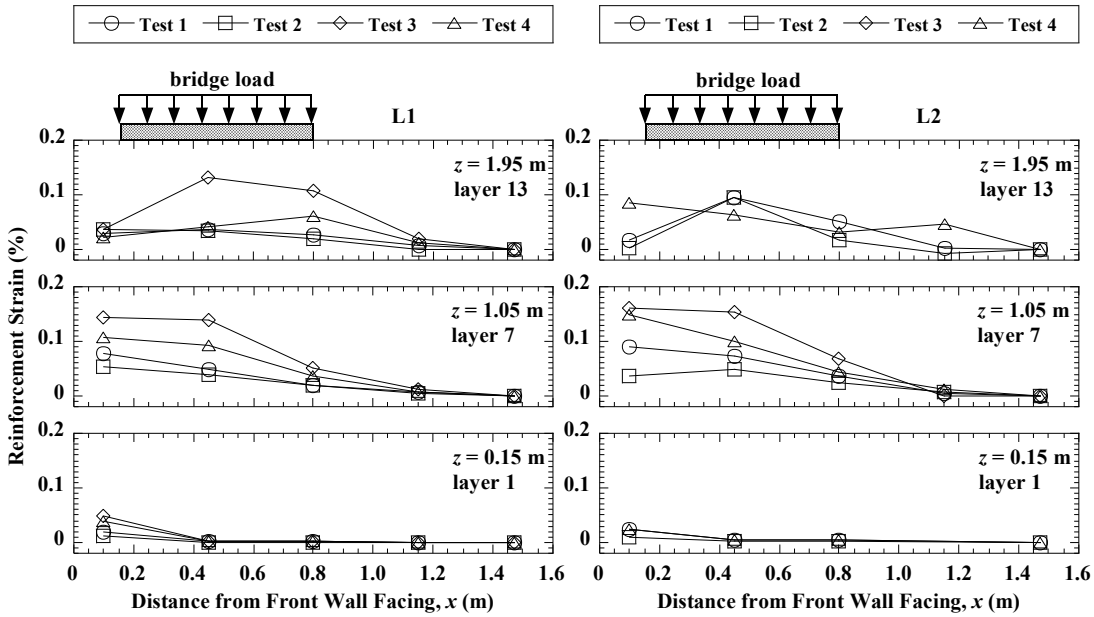

Figure 7.66 Incremental reinforcement strain distributions in L1 and L2 due to bridge beam placement (from Stages 2 to 3) in Tests 1 to 4.

Reinforcement strain distributions in the transverse section T1 for Stages 1 and 3 in Tests 1 to 4 are shown in Figure 7.67 and Figure 7.68, respectively, and the incremental reinforcement strain distributions due to placement of the bridge beam (from Stages 2 to 3) are shown in Figure 7.69. In general, results are consistent with the longitudinal sections, and confirm that reinforcement spacing and stiffness have important effects on reinforcement strains under static loading.

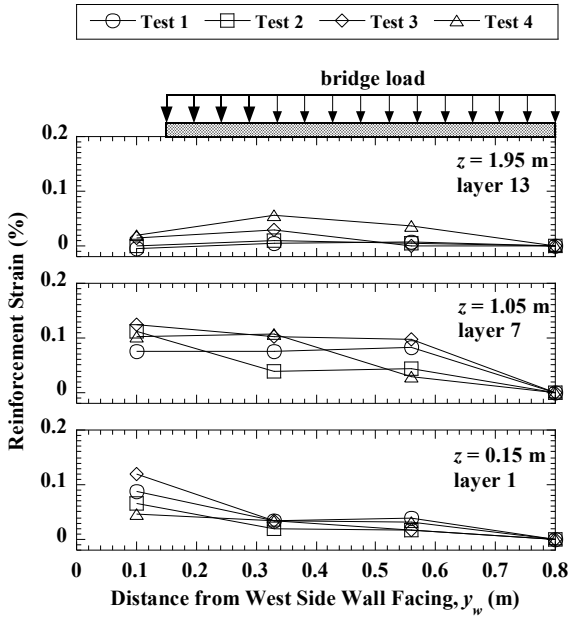

Figure 7.67 Reinforcement strain distributions in T1 for Stage 1 in Tests 1 to 4.

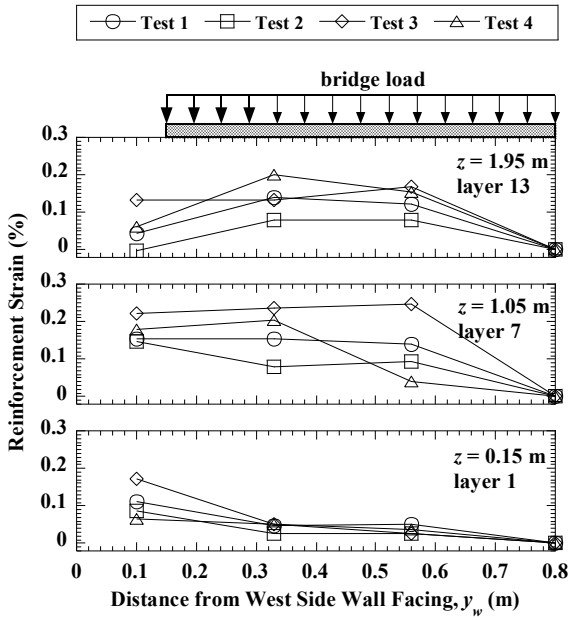

Figure 7.68 Reinforcement strain distributions in T1 for Stage 3 in Tests 1 to 4.

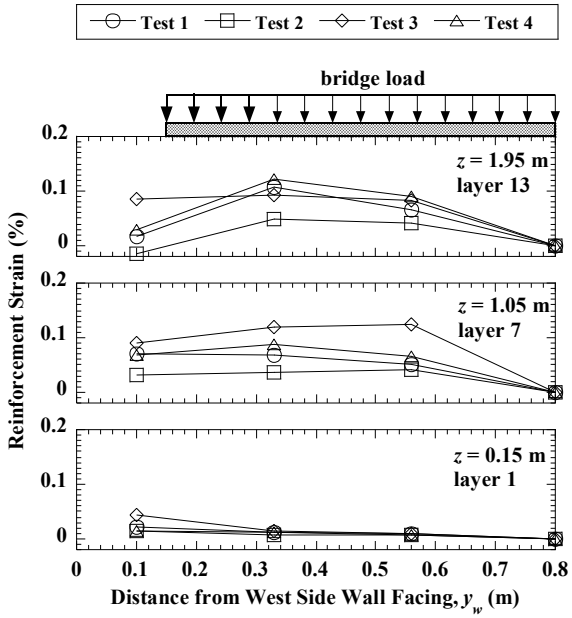

Figure 7.69 Incremental reinforcement strain distributions in T1 due to bridge beam placement (from Stages 2 to 3) in Tests 1 to 4.

7.9.2 Dynamic Loading

Time histories of strain gauge pair measurements at three elevations under the bridge seat (x = 0.45 m) in L1 during the Imperial Valley motion in Test 1 are shown in Figure 7.70. All strain values remained positive (i.e., tensile) during shaking. Measured strains for the top and bottom strain gauges are in close agreement at z = 0.075 m and z = 0.975 m, and show a similar trend but different magnitudes at z = 1.875 m. This indicates bending of the geogrid at z = 1.875 m during construction and highlights the importance of installing top and bottom gauges at each strain measurement location.

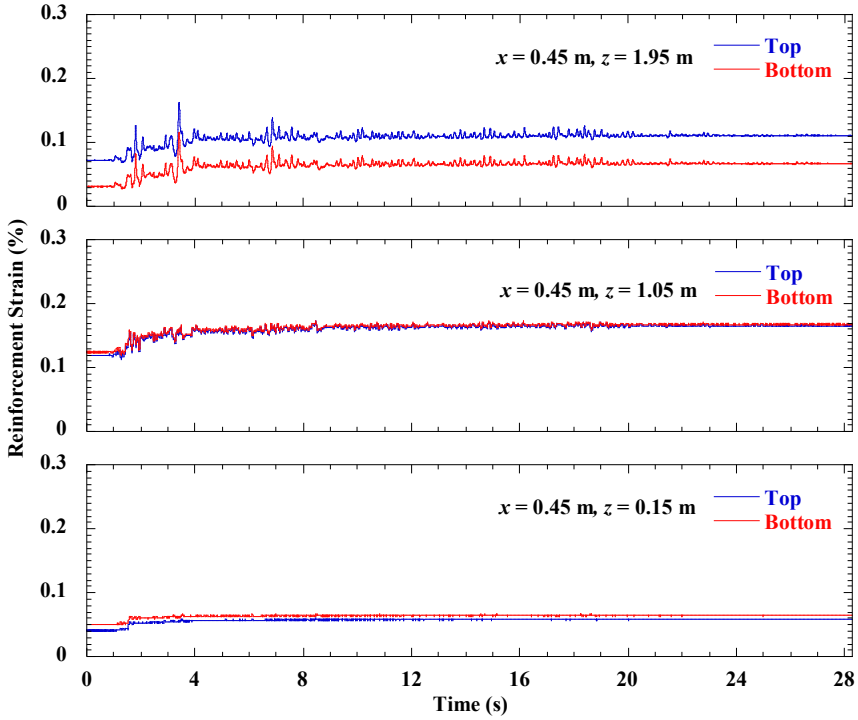

Figure 7.70 Time histories of strain gauge pair measurements in L1 during the Imperial Valley motion in Test 1.

Time histories of reinforcement strain, taken as the average time histories of each strain gauge pair, in the longitudinal sections L1 and L2 during the Imperial Valley, Maule, and Northridge motions are shown in Figure 7.71, Figure 7.72, and Figure 7.73, respectively. The dynamic reinforcement strains in L1 are relatively large near the connections for layers 1, 4, and 7, but are relatively small near the connections for layers 10 and 13. In general, the dynamic reinforcement strains in L1 and L2 are similar with respect to both magnitude and trend for layers 1 and 7, while the dynamic strains of layer 13 under the bridge seat for L2 show much larger values than L1.

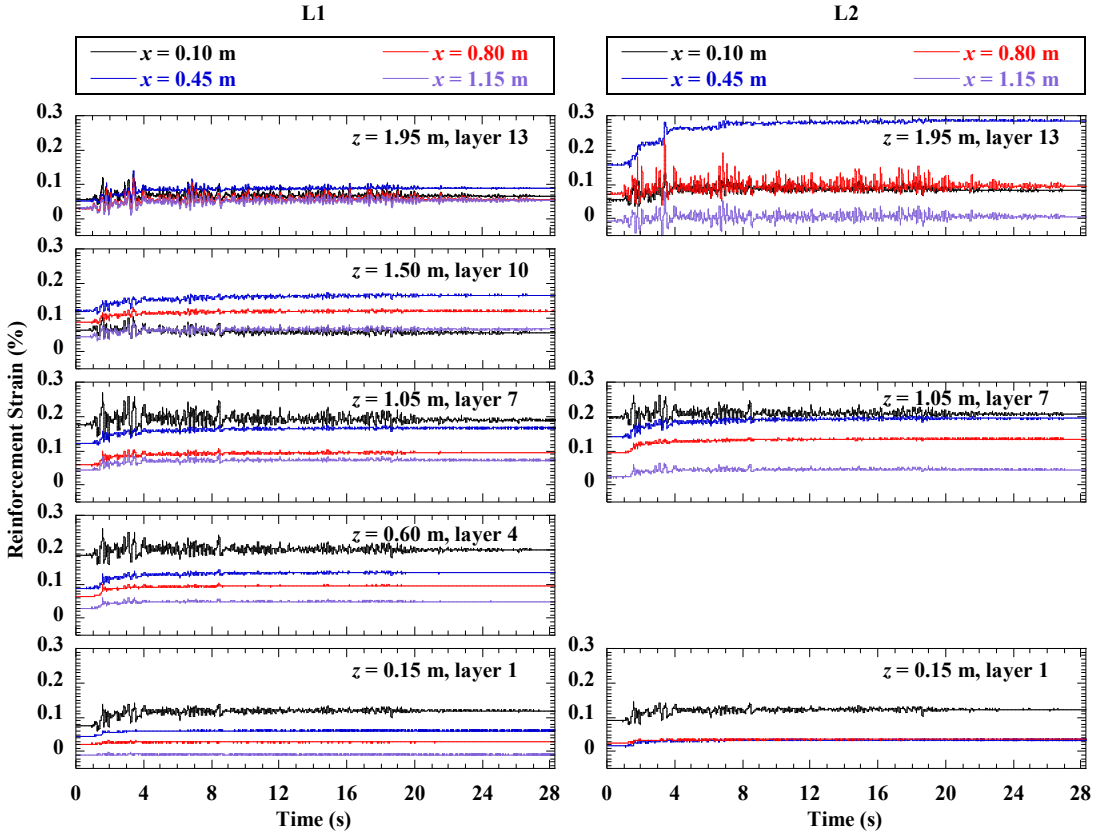

Figure 7.71 Time histories of reinforcement strain in L1 and L2 during the Imperial Valley motion in Test 1.

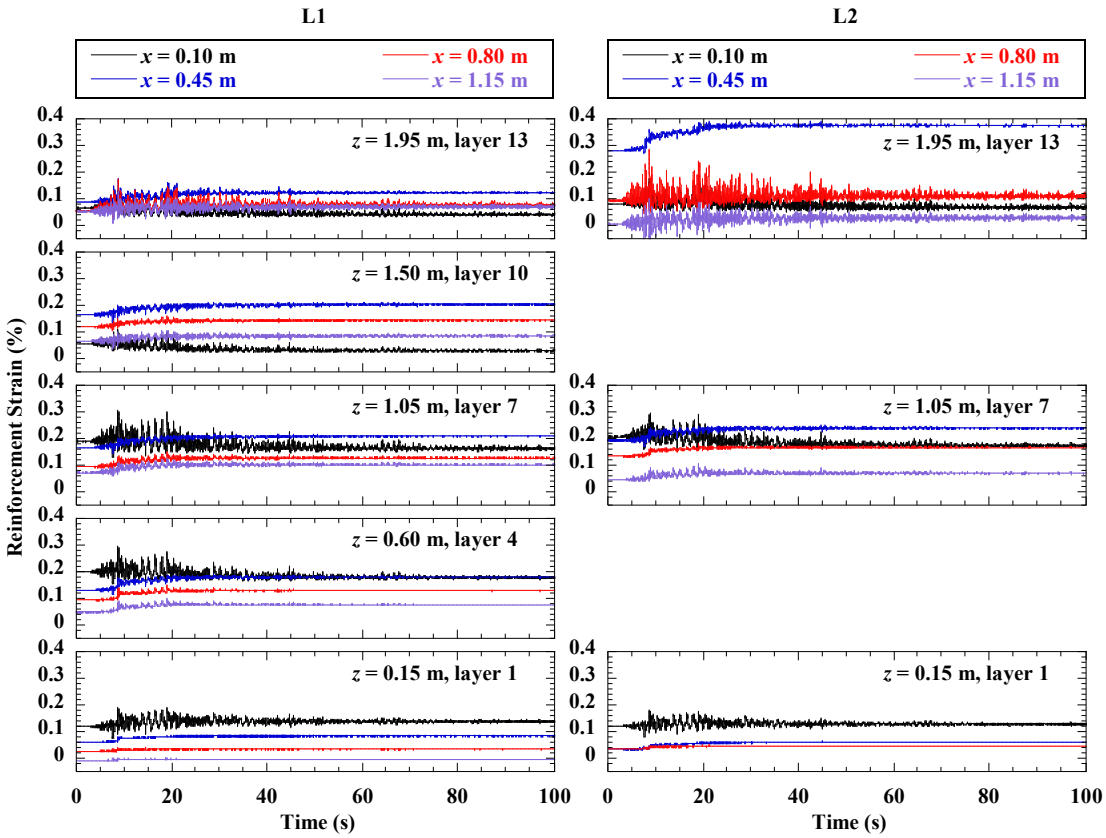

Figure 7.72 Time histories of reinforcement strain in L1 and L2 during the Maule motion in Test 1.

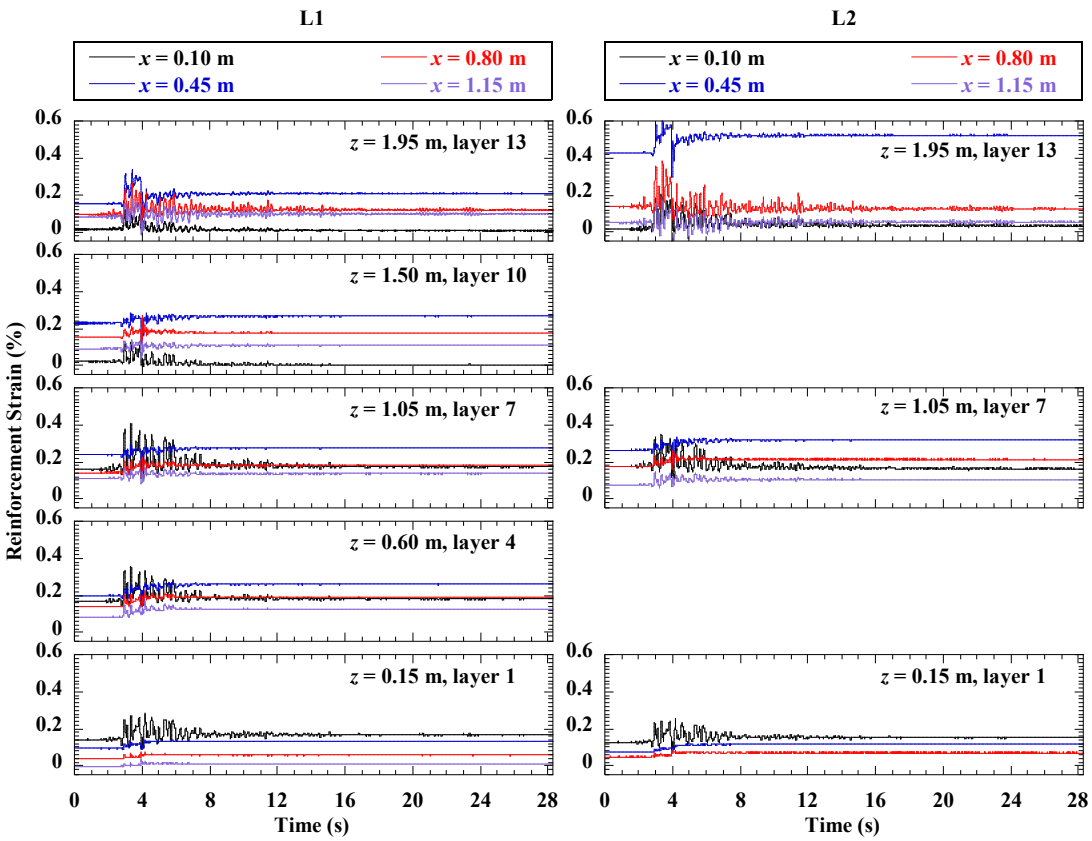

Figure 7.73 Time histories of reinforcement strain in L1 and L2 during the Northridge motion in Test 1.

Reinforcement strain distributions in L1 and L2 with the initial (before shaking), maximum (during shaking), minimum (during shaking), and residual (after shaking) values during the Imperial Valley, Maule, and Northridge motions are shown in Figure 7.74, Figure 7.75, and Figure 7.76, respectively. During the Imperial Valley motion, maximum strains in L1 are highest near the connections (x = 0.10 m) for layers 1, 4, and 7, and under the bridge seat (x = 0.45 m) for layers 10 and 13, whereas minimum strains generally are close to the initial values. The maximum dynamic strain values indicate increased strains near the connections, which is attributed to the inertial forces of the facing blocks. Except for the bottom reinforcement layer, residual strains near the connections increased only slightly as compared to the initial values and indicate that the majority of dynamic reinforcement strains were recovered. Residual strains under the bridge seat increased significantly, especially for the upper layers. The maximum and residual reinforcements strains in L2 are similar to L1 for layers 1 and 7, while are much larger than L1 for layer 13 due to tilting of the bridge seat toward the west side. The maximum dynamic strain under the bridge seat (x = 0.45 m) in layer 13 is 0.29% in L2, but is only 0.14% at the same location for L1. Similar observations are also found for the Maule and Northridge motions with larger magnitudes of maximum and residual reinforcement strains.

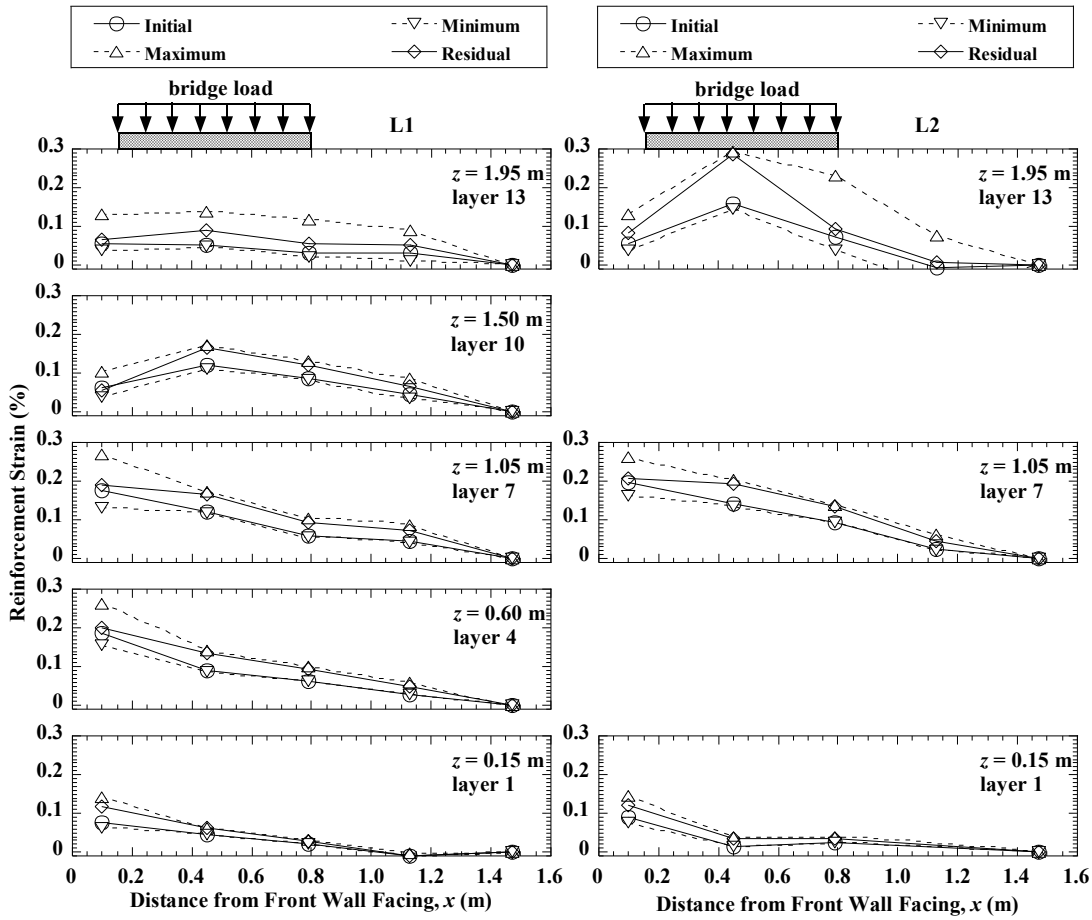

Figure 7.74 Reinforcement strain distributions in L1 and L2 during the Imperial Valley motion in Test 1.

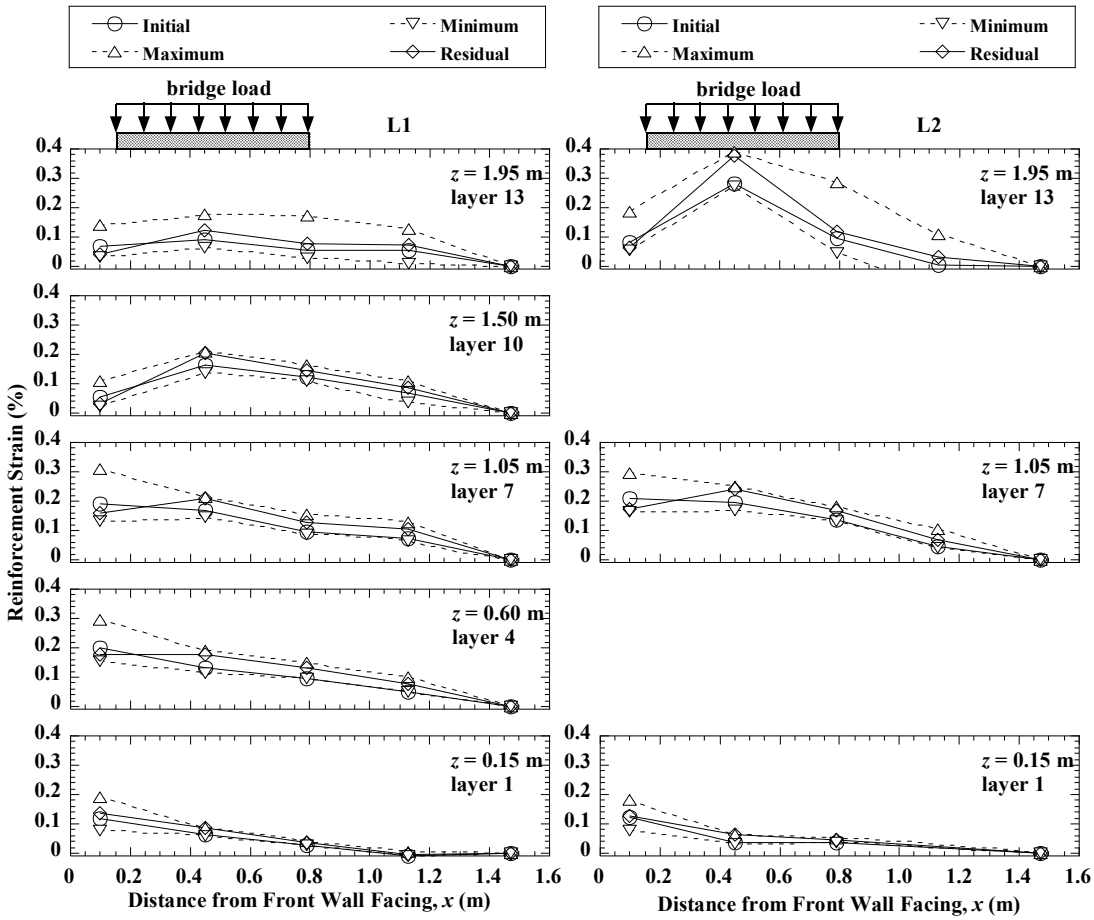

Figure 7.75 Reinforcement strain distributions in L1 and L2 during the Maule motion in Test 1.

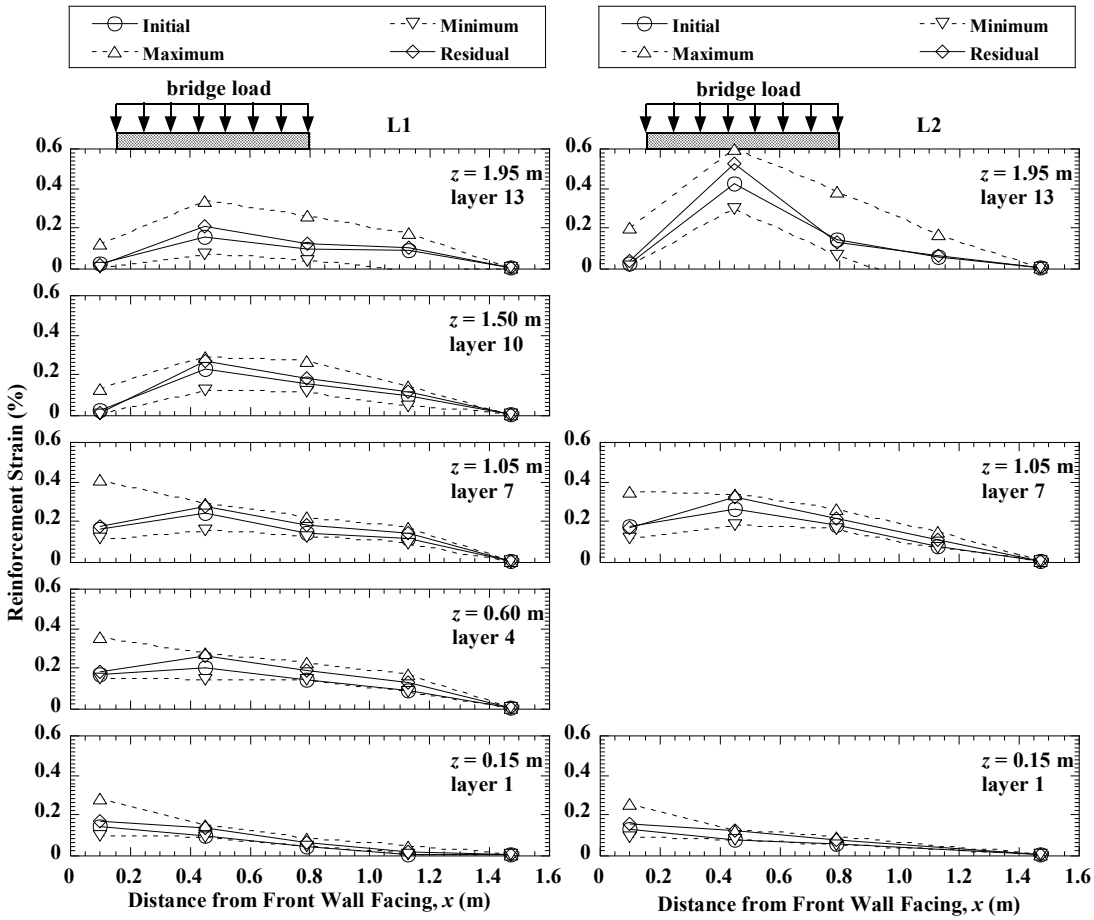

Figure 7.76 Reinforcement strain distributions in L1 and L2 during the Northridge motion in Test 1.

Time histories of reinforcement strain in the transverse section T1 during the Imperial Valley, Maule, and Northridge motions are shown in Figure 7.77, Figure 7.78, and Figure 7.79, respectively, and the reinforcement strain distributions are shown in Figure 7.80, Figure 7.81, and Figure 7.82. Similar to the longitudinal sections, the highest initial and residual strains occurred near the connections for layers 1 and 7, and under the bridge seat for layer 13. During shaking, minimum strains are close to the initial values and maximum strains are close to the residual values. Therefore, dynamic strains generally were not recovered after shaking for the reinforcement layers in the transverse direction.

Data indicate that shaking caused significant increases in strain for the transverse reinforcement, which suggests that, in addition to longitudinal reinforcement analysis, analysis of transverse reinforcement is important for seismic design.

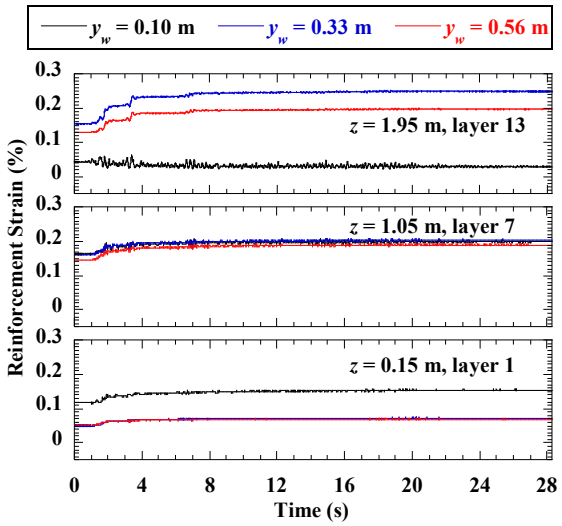

Figure 7.77 Time histories of reinforcement strain in T1 during the Imperial Valley motion in Test 1.

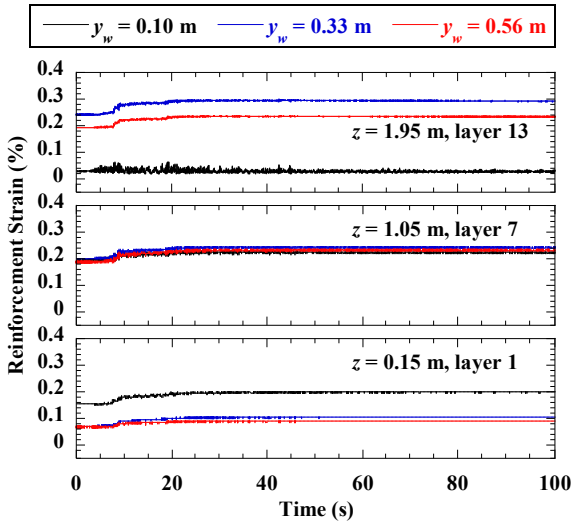

Figure 7.78 Time histories of reinforcement strain in T1 during the Maule motion in Test 1.

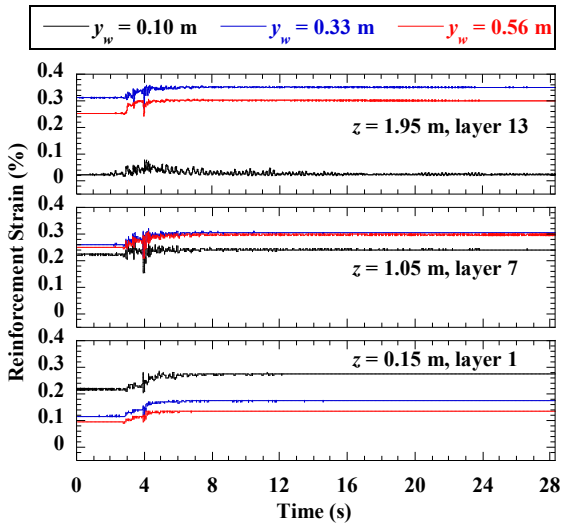

Figure 7.79 Time histories of reinforcement strain in T1 during the Northridge motion in Test 1.

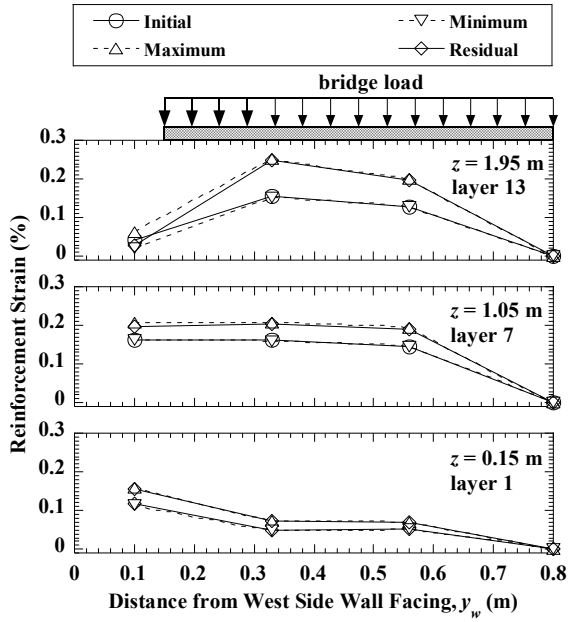

Figure 7.80 Reinforcement strain distributions in T1 during the Imperial Valley motion in Test 1.

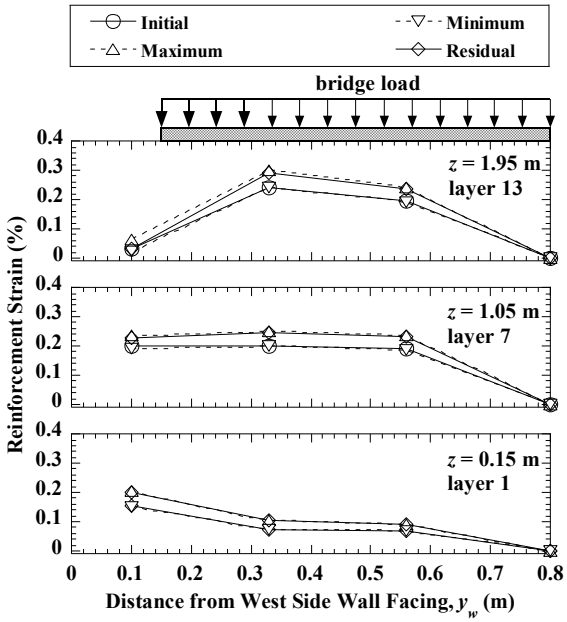

Figure 7.81 Reinforcement strain distributions in T1 during the Maule motion in Test 1.

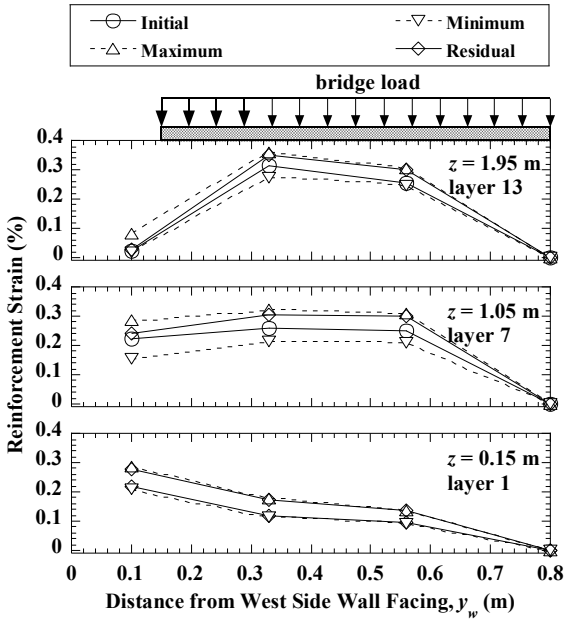

Figure 7.82 Reinforcement strain distributions in T1 during the Northridge motion in Test 1.

Residual reinforcement strain distributions in the longitudinal sections L1 and L2 are shown in Figure 7.83. The Northridge motion was applied after the sinusoidal motions in Test 1. For the longitudinal sections, the residual reinforcement strains increased significantly under the bridge seat due to successive shaking events. For instance, the reinforcement strain of 0.11% at x = 0.45 m in layer 10 for L1 at the end of construction (EOC) increased to 0.16% after the Imperial Valley motion, to 0.20% after the Maule motion, and to 0.27% after the Northridge motion. Reinforcement strain near the connections increased only for the bottom layer 1, and experienced even slight decreases for the other upper layers. This may be attributed to the loosening of backfill soil near the connections due to the inertial forces of facing blocks.

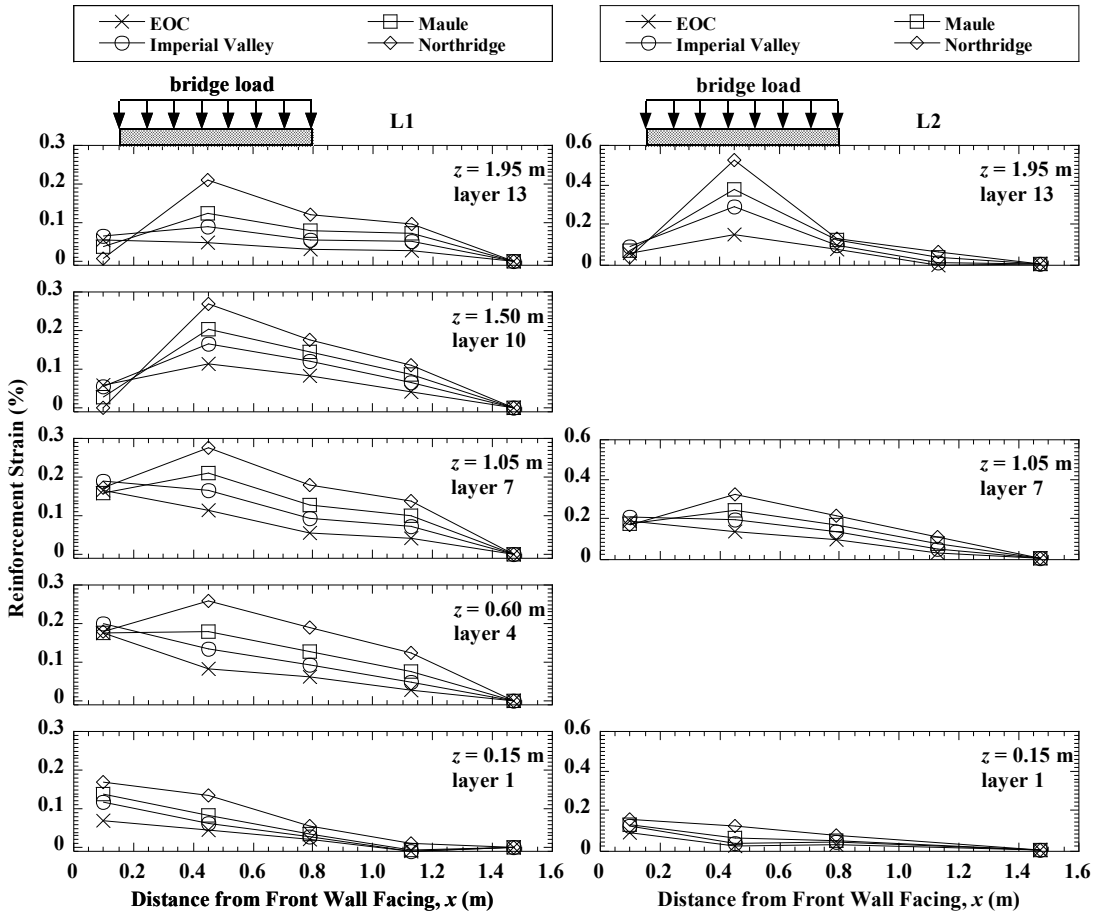

Figure 7.83 Residual reinforcement strain distributions in L1 and L2 in Test 1.

Residual reinforcement strain distributions in the transverse section T1 are shown in Figure 7.84. Results are consistent with the longitudinal sections that residual strain increased significantly under the bridge seat for upper layers (i.e., layers 7 and 13) and near the connections for lower layer (i.e., layer 1).

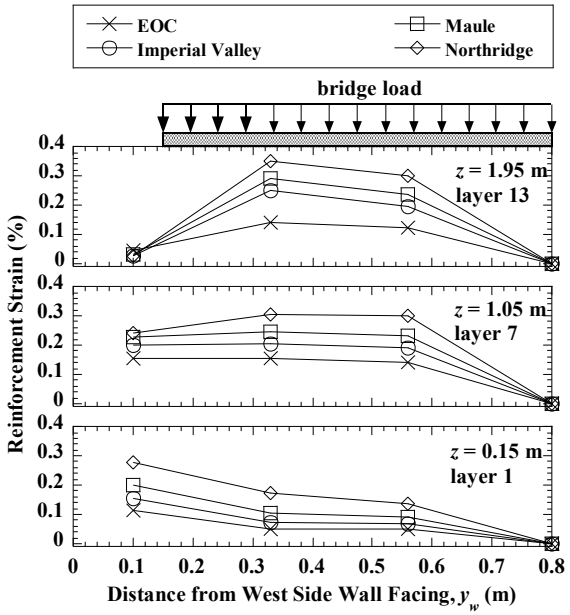

Figure 7.84 Residual reinforcement strain distributions in T1 in Test 1.

Incremental residual reinforcement strain distributions in L1 and T1 in Tests 1 to 4 for the Imperial Valley, Maule, and Northridge motions are shown in Figure 7.85, Figure 7.86, and Figure 7.87, respectively. For the Imperial Valley motion, the incremental reinforcement strains in L1 and T1 in Tests 3 and 4 are generally larger than in Tests 1 and 2. For instance, the incremental strains under the bridge seat (x = 0.45 m) in layer 13 for L1 are 0.04%, 0.07%, 0.21%, and 0.14% in Tests 1 to 4, respectively. Similar trends are also observed for the Maule and Northridge motions. Results indicate that reinforcement spacing and stiffness have important effects on the reinforcement strains under dynamic loading.

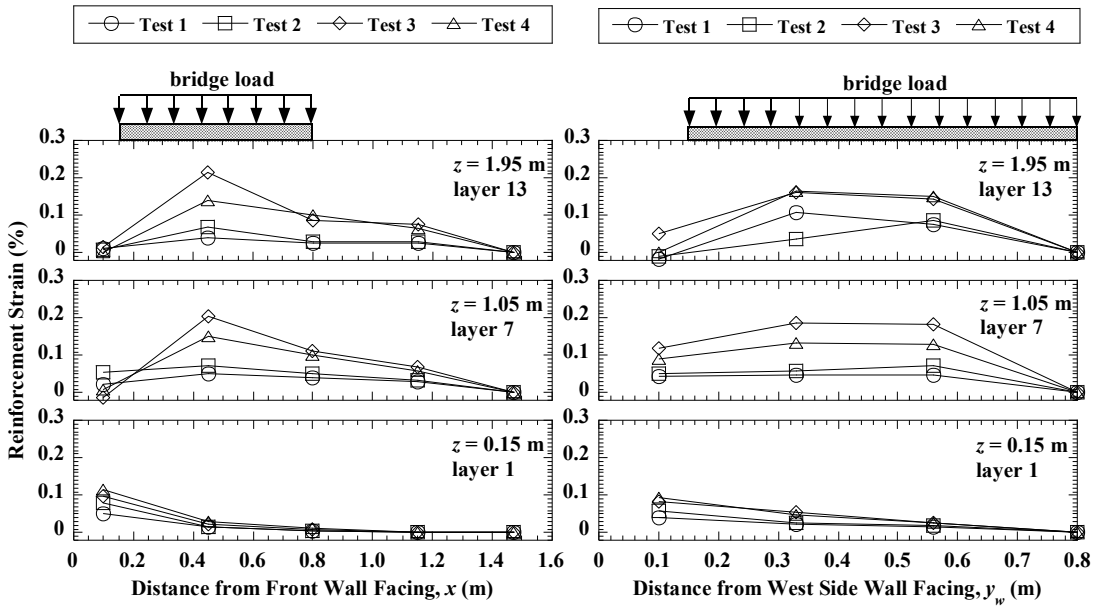

Figure 7.85 Incremental residual reinforcement strain distributions in L1 and T1 for the Imperial Valley motion in Tests 1 to 4.

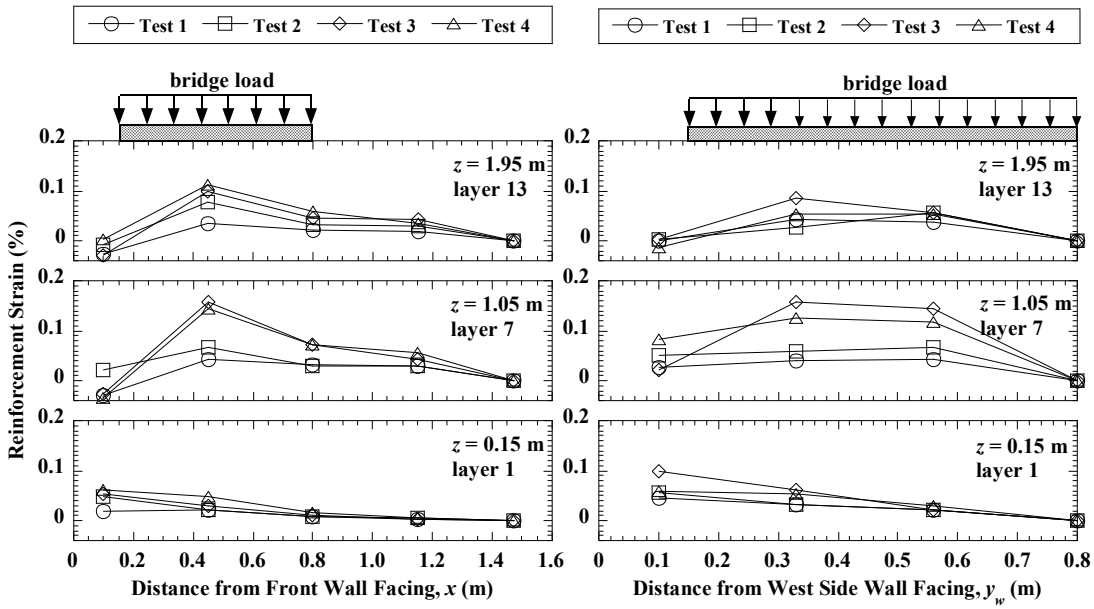

Figure 7.86 Incremental residual reinforcement strain distributions in L1 and T1 for the Maule motion in Tests 1 to 4.

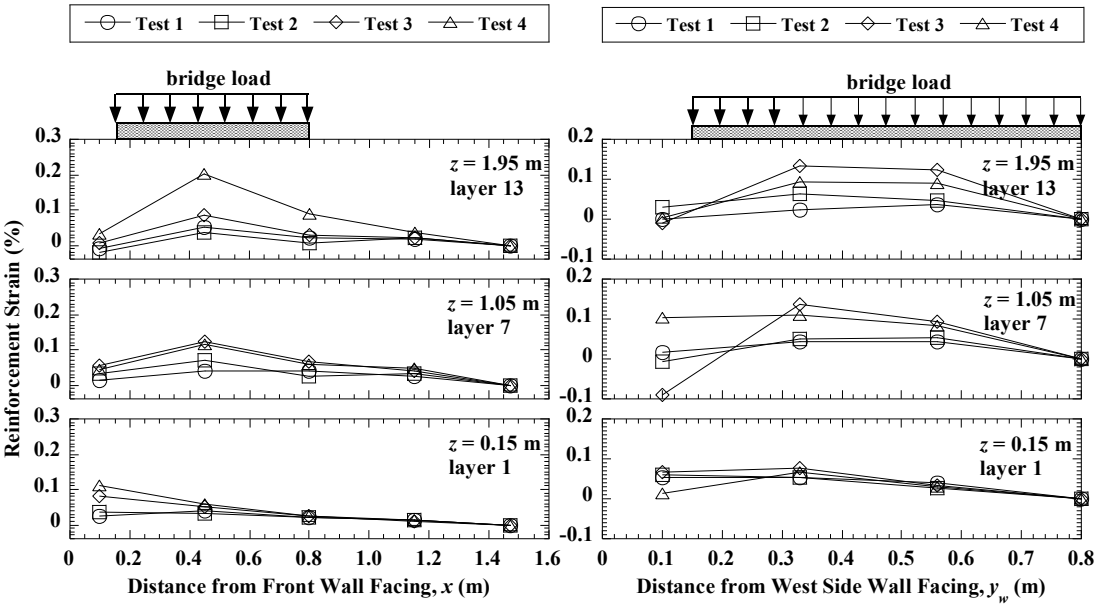

Figure 7.87 Incremental residual reinforcement strain distributions in L1 and T1 for the Northridge motion in Tests 1 to 4.

7.10 Contact Forces

The bridge beam had relative horizontal displacements with respect to the bridge seat, and thus the width of seismic joint changed during shaking. Horizontal contact forces between the bridge seat and bridge beam generate when the width of seismic joint reduces to zero. For all the longitudinal tests, the maximum and minimum dynamic relative displacements are smaller than the initial width of the seismic joint before the shaking event for the Imperial Valley and Maule motions, so joint closure and beam-seat contact did not occur during shaking, while the joint closure occurred for the Northridge motion.

Time histories of joint width for earthquake motions are shown in Figure 7.88. For the Imperial Valley motion, the initial joint width was 29.3 mm, and varied in the range of ±8 mm during shaking, and had a residual width of 31.0 mm. The joint width did not vary significantly during the Maule motion, and had a residual width of 31.4 mm. For the Northridge motion (after a series of sinusoidal motions), the initial width of the joint was 30.0 mm before shaking. During shaking, the width reached a maximum value of 47.5 mm at t = 3.88 s, and reduced to zero at t = 4.02 s as shown in Figure 7.88(c), which resulted in horizontal contact forces of 98.5 kN between the bridge seat and bridge beam, as shown in Figure 7.89. This corresponds to a contact force of 788 kN for the prototype structure. This contact force is relatively large and should be considered in the seismic design of GRS bridge abutments.

The maximum horizontal contact forces for all the longitudinal tests during the Northridge motion are presented in Table 7.11. The maximum horizontal contact force is

the smallest with a value of 68.5 kN for Test 3. There is not a consistent trend to identify the effect of different parameters on contact forces.

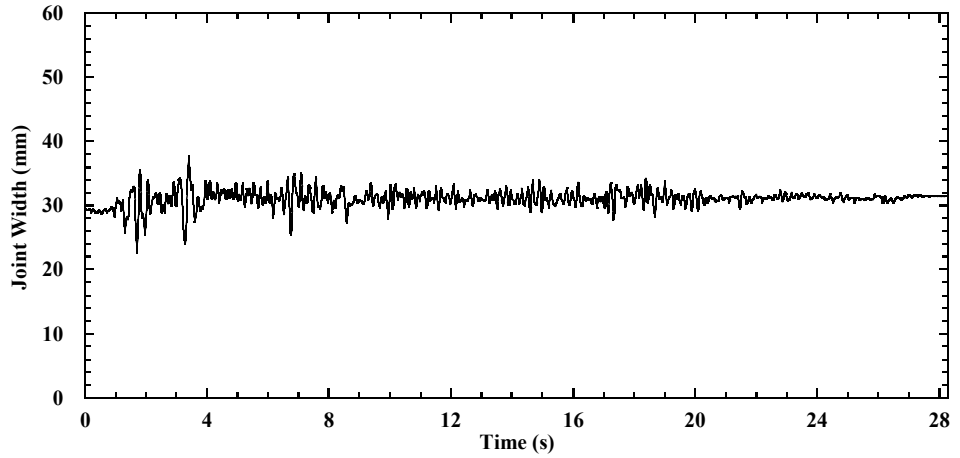

(a)

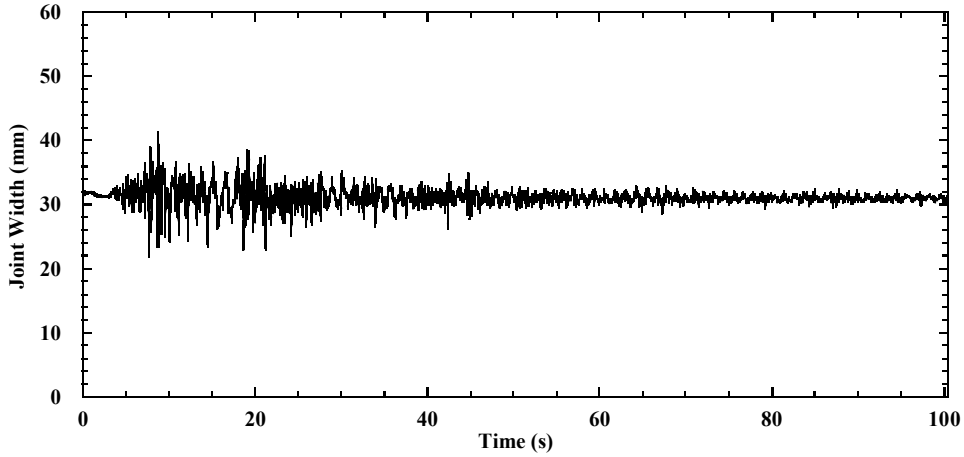

(b)

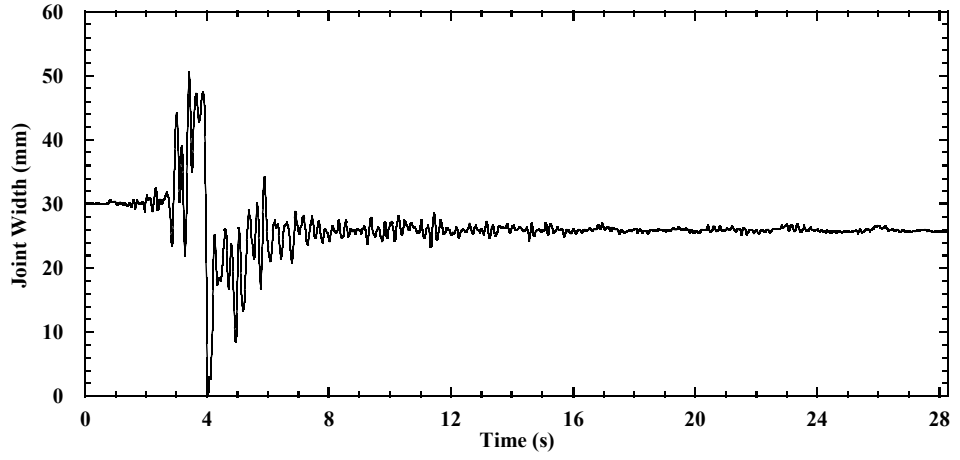

(c)

Figure 7.88 Time histories of joint width on the north side in Test 1: (a) Imperial Valley motion; (b) Maule motion; (c) Northridge motion.

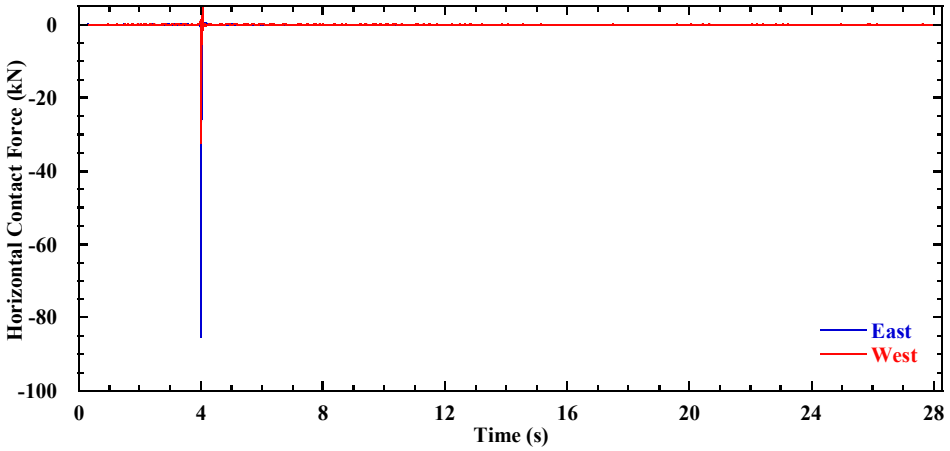

Figure 7.89 Horizontal contact forces between bridge beam and bridge seat for the Northridge motion in Test 1.

Table 7.11 Maximum contact forces for the Northridge motion.

Earthquake motion	Maximum force (kN) in Test 1	Maximum force (kN) in Test 2	Maximum force (kN) in Test 3	Maximum force (kN) in Test 4
Northridge	98.5	110.3	68.5	105.0

7.11 Acknowledgements

The text below is reproduced verbatim as it appears in the acknowledgments section per the UCSD Office of Graduate Studies Formatting Requirements.

Chapter 7 of this dissertation is based on materials from two manuscripts under preparation for publication, tentatively titled “Large-Scale Model Tests of Geosynthetic-Reinforced Soil Bridge Abutments. I: Static Loading,” and “Large-Scale Model Tests of Geosynthetic-Reinforced Soil Bridge Abutments. II: Longitudinal Shaking,” respectively, with a preliminary author list of Yewei Zheng, John S. McCartney, P. Benson Shing, and Patrick J. Fox (2017). The dissertation author is the first author of these paper.

Chapter 8

Transverse Test Results and Analysis

8.1 Introduction

This chapter presents results and analysis for the transverse test on the GRS bridge abutment in the baseline configuration (Test 6). In addition to the characterization tests on system identification and testing system performance, results are presented in this chapter including, facing displacements, bridge seat and bridge beam displacements, acceleration responses, lateral and vertical stresses, reinforcement strains, and contact forces between the bridge seat and bridge beam during a series of earthquake motions in the transverse direction.

When processing the data, the string potentiometer measurements for horizontal displacements of the side wall facings were corrected using measured horizontal displacements of the shaking table in the direction of shaking to yield relative displacements with respect to the table. Horizontal displacements and accelerations toward

the north direction (Figure 6.20) are defined as positive. In the direction of shaking, outward displacements of the side wall facings are defined as positive. In the direction perpendicular to shaking, outward displacements of the front wall facing are defined as positive. Consistent with geotechnical sign conventions, downward vertical settlements are defined as positive. For static loading (construction stages), Stage 1 involved construction of the lower GRS wall, Stage 2 involved construction of the bridge seat and upper GRS wall, and Stage 3 involved placement of the bridge beam atop the GRS bridge abutment. All presented results are in model-scale, and results should be adjusted using the similitude relationships in Table 6.2 to obtain corresponding values for prototype structures.

8.2 System Identification

System identification tests were conducted using the white noise motions before and after each of the earthquake motions to detect changes in fundamental frequencies of the bridge system in the transverse direction. Amplitudes of the horizontal acceleration transfer functions for the bridge beam, bridge seat, GRS bridge abutment (measured at y_s = 0.38 m, z = 1.875 m), and support wall with respect to the shaking table for the initial white noise motion (Shaking event 1) are shown in Figure 8.1(a). The fundamental frequency is 7.7 Hz for the bridge beam, and is 11.7 Hz for the bridge seat and GRS bridge abutment, and is 3.6 Hz for the support wall in the transverse direction. The corresponding fundamental frequency for the prototype GRS bridge abutment is 8.3 Hz according to the scaling factors in Table 6.2. Horizontal acceleration transfer functions of the GRS bridge abutment with respect to the shaking table for the white noise motions before and after each earthquake motion are shown in Figure 8.1(b), and indicates the decrease of fundamental frequency due to shear modulus reduction of the backfill soil associated with shear strain development during successive shaking events.

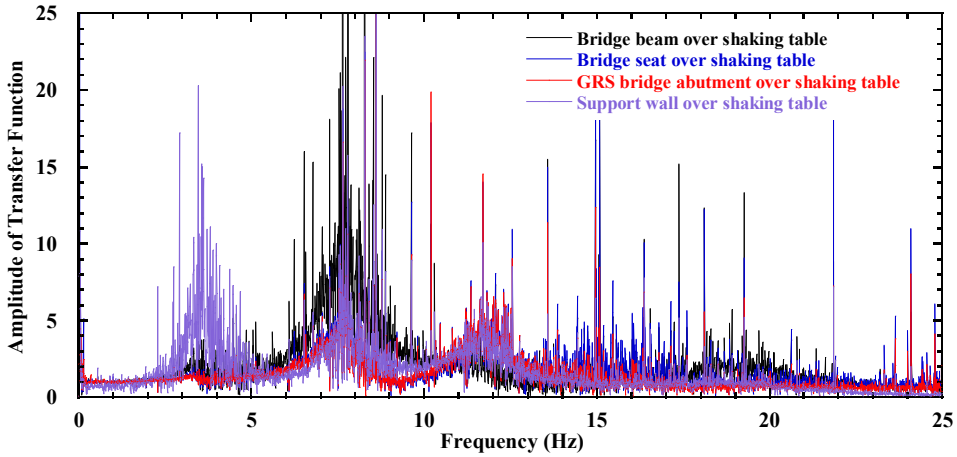

(a)

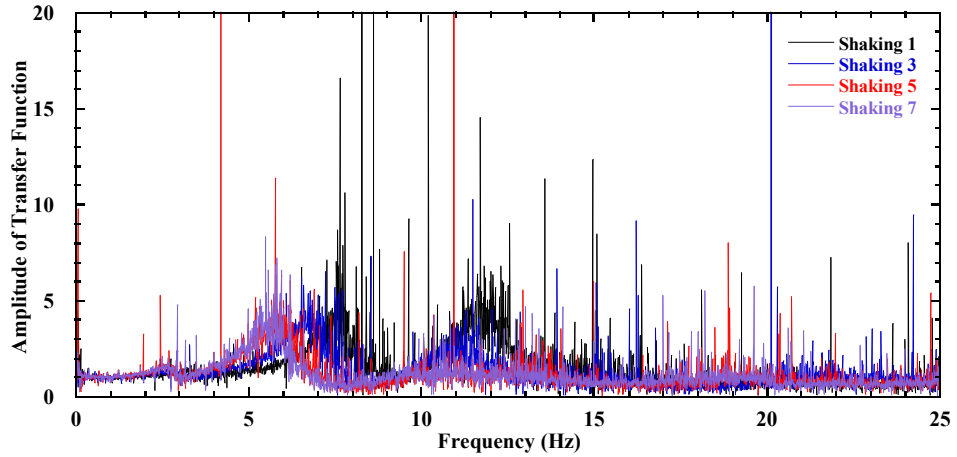

(b)

Figure 8.1 Horizontal acceleration transfer functions amplitudes for white noise tests in Test 6: (a) bridge seat, bridge beam, GRS bridge abutment, and support wall for the initial white noise test; (b) GRS bridge abutment before and after each earthquake motion.

8.3 Testing System Performance

The characterization of the testing system performance is critical for the transverse test because the configuration of the support wall connected to one side of the shaking table is unique and has not been evaluated in a previous shaking table experiment. Since the shaking table is used to drive the motion of the support wall in an unbalanced manner, rocking and cantilever type motions of the support wall are expected in the transverse test. The approach used in this study permits a unique evaluation of the GRS bridge abutment response in a transverse configuration.

The performance of the testing system (i.e., the shaking table and the connected support wall resting on the sliding platform) was evaluated based on the measured displacement and acceleration responses in the direction of shaking. The testing system responses for the Imperial Valley, Maule, and Northridge motions in Test 6 are shown in Figure 8.2, Figure 8.3, and Figure 8.4, respectively, and a summary of the target and measured peak responses of the shaking table for the three earthquake motions is presented in Table 8.1.

Table 8.1 Shaking table response for earthquake motions in Test 6.

Shaking event	Earthquake motion	Model-scale duration (s)	Target PGA (*g*)	Actual PGA (*g*)	Target PGD (mm)	Actual PGD (mm)
2	Imperial Valley	28.3	0.31	0.42	65.2	65.2
4	Maule	100.4	0.40	0.56	108.0	107.9
6	Northridge	28.3	0.58	0.86	88.7	88.6

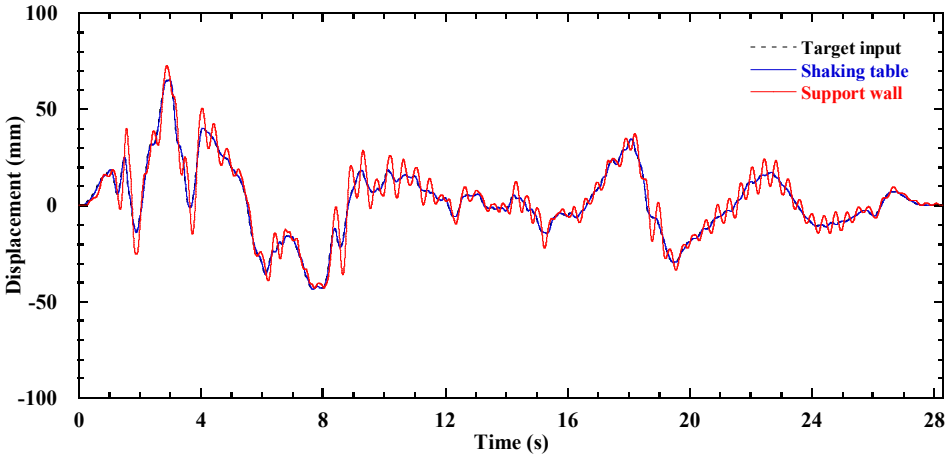

(a)

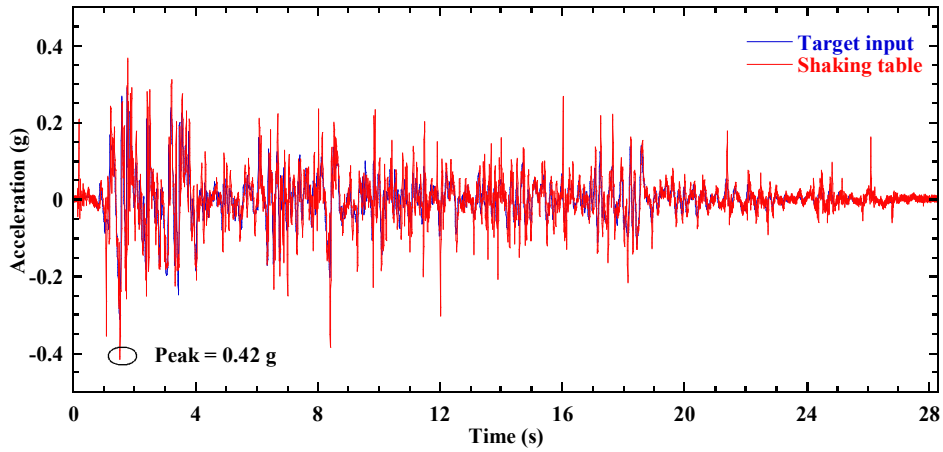

(b)

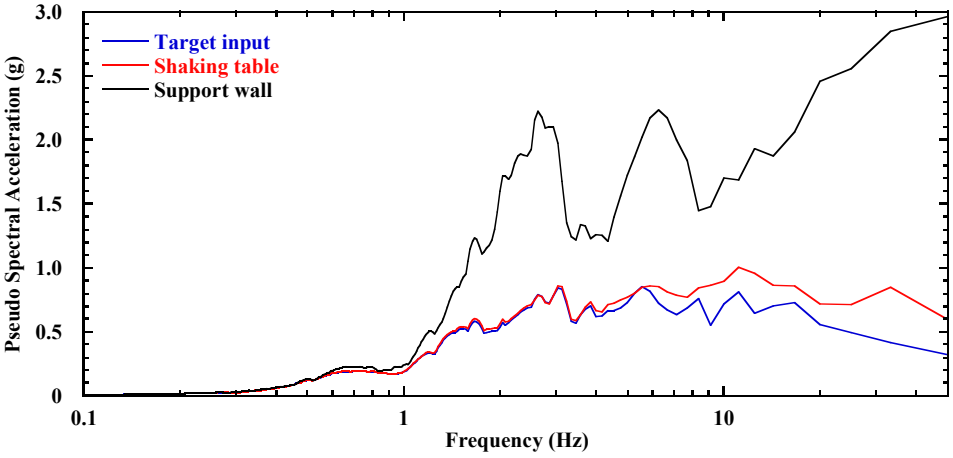

(c)

Figure 8.2 Testing system response for the Imperial Valley motion in Test 6: (a) displacement time history; (b) acceleration time history; (c) response spectra (5% damping).

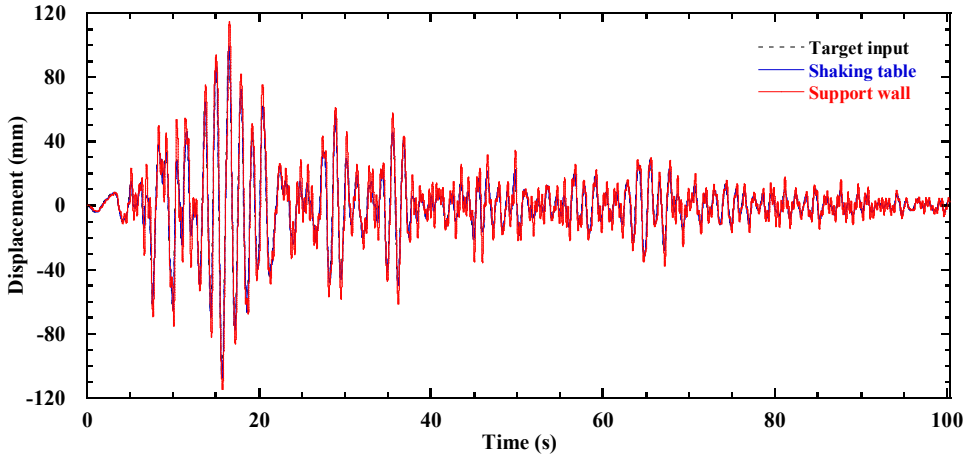

(a)

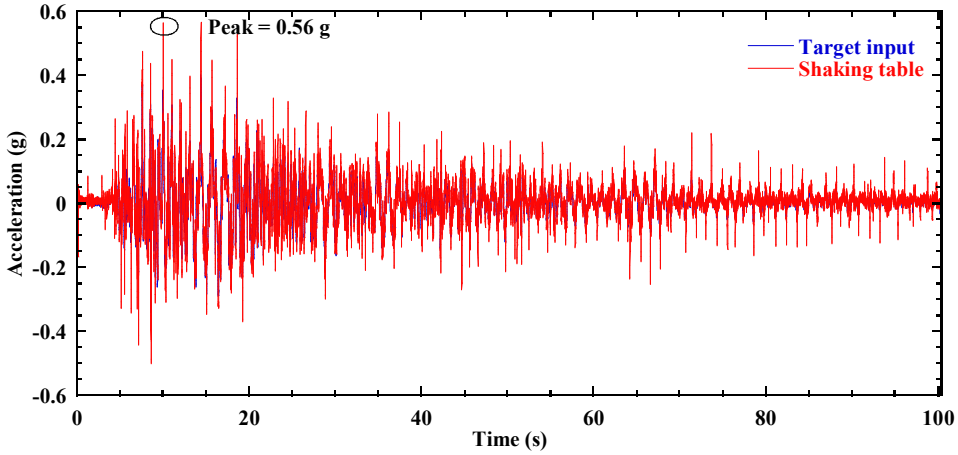

(b)

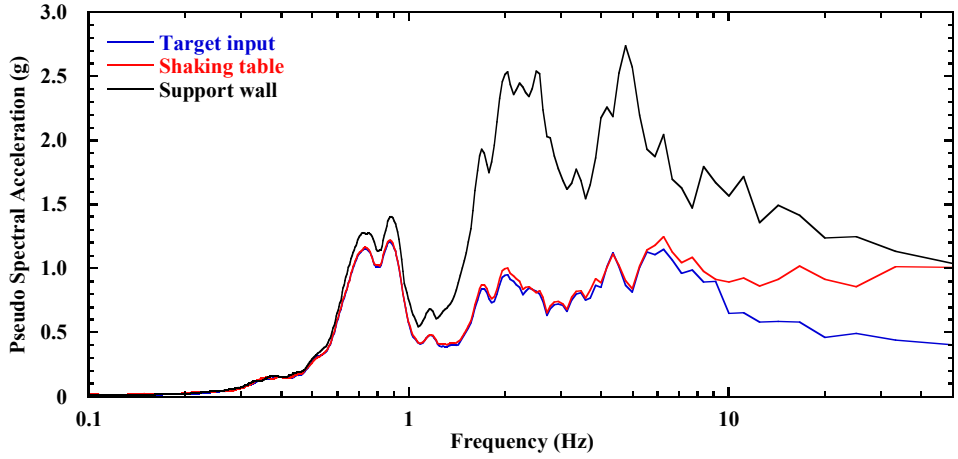

(c)

Figure 8.3 Testing system response for the Maule motion in Test 6: (a) displacement time history; (b) acceleration time history; (c) response spectra (5% damping).

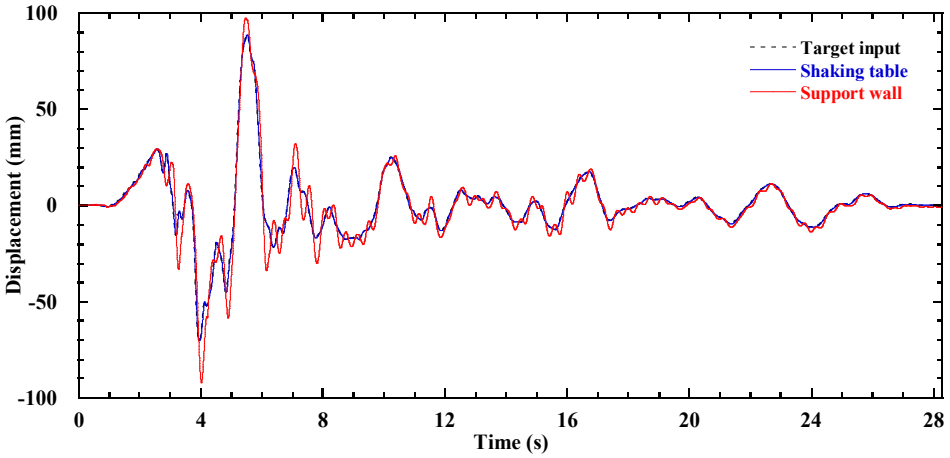

(a)

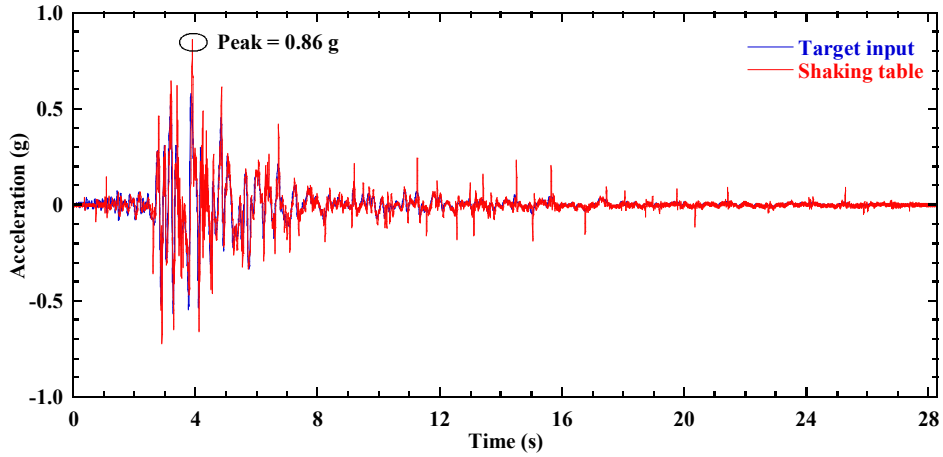

(b)

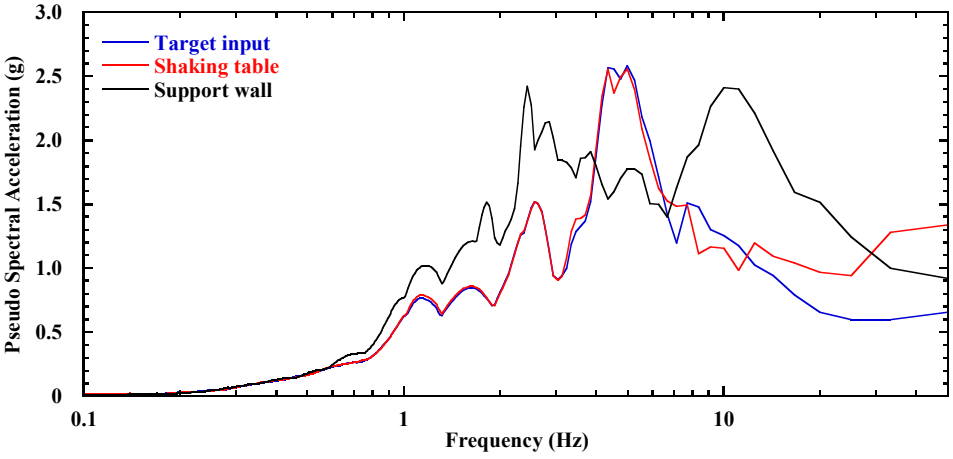

(c)

Figure 8.4 Testing system response for the Northridge motion in Test 6: (a) displacement time history; (b) acceleration time history; (c) response spectra (5% damping).

The measured displacement time histories of the shaking table are in good agreement with the target input for all three motions, whereas the displacement time histories of the support wall show larger peak values due to the inertial forces of the support wall. For the Imperial Valley motion, the displacement time history of support wall follows the general trend of the target input motion, but contains some low frequency content. This is due to the resonance of support wall during shaking, as the fundamental frequency of 3.6 Hz for the support wall is close to the predominant frequencies of the scaled Imperial Valley motion.

The measured acceleration time history of the shaking table in general matches well with the target input accelerations, but had larger peak accelerations. For instance, the measured PGA of 0.86*g* for the shaking table is larger than the target input value of 0.58*g*. The shaking table was refurbished prior to this study to increase the fidelity of dynamic motion. After repair of the shaking table, overshooting of peak accelerations was still observed, but the overshooting was much smaller than before repair, which indicates that the performance of the table has been improved (Trautner et al. 2017). The overshooting is likely due to the inertia of the table itself and is also affected by the size of the payload on the table.

The pseudo-spectral accelerations of the shaking table and target motion are in good agreement for frequencies less than 10 Hz for all three motions, which indicates that the shaking table adequately reproduced the salient characteristics of the target input motions. The actual pseudo-spectral acceleration at the fundamental frequency of 11.7 Hz for the GRS bridge abutment is slightly larger than the target value for all three motions. The pseudo-spectral accelerations for the support wall are much larger than the target values

because the fundamental frequencies of 3.6 Hz for the support wall is in the frequency range for typical earthquake motions. Although the support wall is out of phase with larger peak values, this effect was unavoidable due to the shaking in an unbalanced manner. However, the focus of this experiment is on the GRS bridge abutment, and this out of phase behavior is only expected to affect the interaction between the support wall and bridge beam on the east side of the testing system.

8.4 Facing Displacements

8.4.1 Static Loading

Facing displacements were measured on the south and north sides of the transverse section T1 (referred to as T1-South and T1-North as labeled in Figure 6.26) and the longitudinal centerline section L1 (referred to as L1). Facing displacement profiles for the three instrumented sections after the three stages of construction are shown in Figure 8.5, and the maximum values of facing displacement profiles are presented in Table 8.2.

For Stage 1, facing displacements for T1-South and T1-North are similar with maximum facing displacements of 0.8 mm and 1.1 mm, respectively, both at an elevation z = 0.975 m above the foundation soil level. The maximum facing displacement for L1 is 1.6 mm also at z = 0.975 m. Although the shapes of the longitudinal and transverse facing displacement profiles are different, the magnitudes of the facing displacements are small and it is difficult to identify a consistent shape to reflect construction effects. For Stage 2, facing displacements increased slightly due to construction of the bridge seat and upper wall. For Stage 3, the application of the bridge load caused an increase in facing displacements for all three sections, with greater increases in displacements near the top of the wall. For Stage 3, T1-South and T1-North have similar facing displacement profiles with maximum values of 1.5 mm, while the maximum facing displacement for L1 is 2.2 mm.

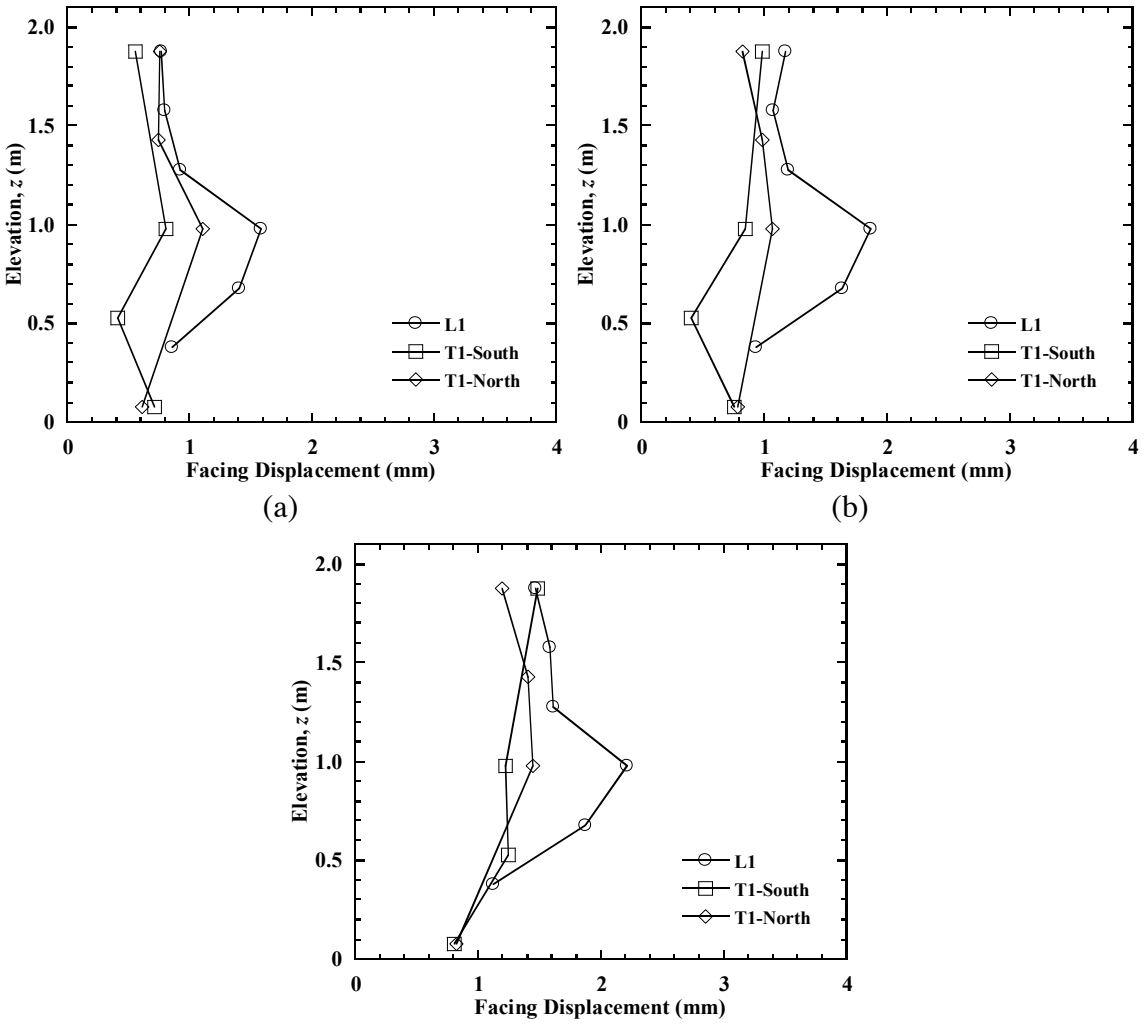

Figure 8.5 Facing displacement profiles for construction stages in Test 6: (a) Stage 1; (b) Stage 2; (c) Stage 3.

Table 8.2 Maximum facing displacements for construction stages in Test 6 (model-scale).

Construction stage	Maximum displacement (mm) for T1-South	Maximum displacement (mm) for T1-North	Maximum displacement (mm) for L1
Stage 1	0.8	1.1	1.6
Stage 2	1.0	1.1	1.9
Stage 3	1.5	1.5	2.2

8.4.2 Dynamic Loading

Time histories of incremental facing displacement for the transverse sections T1-South and T1-North during the Imperial Valley, Maule, and Northridge motions are shown in Figure 8.6, Figure 8.7, and Figure 8.8, respectively. The incremental facing displacements are relative to the initial horizontal displacements before each shaking event, and were corrected using the measured horizontal displacements of the shaking table to yield relative facing displacements with respect to the shaking table. For brevity, the relative facing displacements are referred to as facing displacements in this chapter. As mentioned, positive values represent outward facing displacements, and negative values represent inward facing displacements.

Examination of the data for T1-South and T1-North indicates that the facings on the opposite sides of the GRS bridge abutment moved in phase during shaking. Further, at any moment in time, one section had outward displacements while the other section had inward displacements. For instance, the facing displacement profiles corresponding to the specific times of maximum facing displacements for T1-South and T1-North during the Northridge motion are shown in Figure 8.9. At $t = 3.00$ s, T1-North reached the maximum outward facing displacements, whereas T1-South had inward facing displacements with similar magnitudes. A similar displacement shape is also observed at $t = 4.09$ s, when T1-South reached the maximum outward displacements. The mode shape for the transverse section (e.g., T1-South and T1-North) during shaking is similar to the first mode of the cantilever beam with displacements close to zero at the base and the maximum at the top.

After shaking, most of the dynamic facing displacements for T1-South and T1-North were recovered.

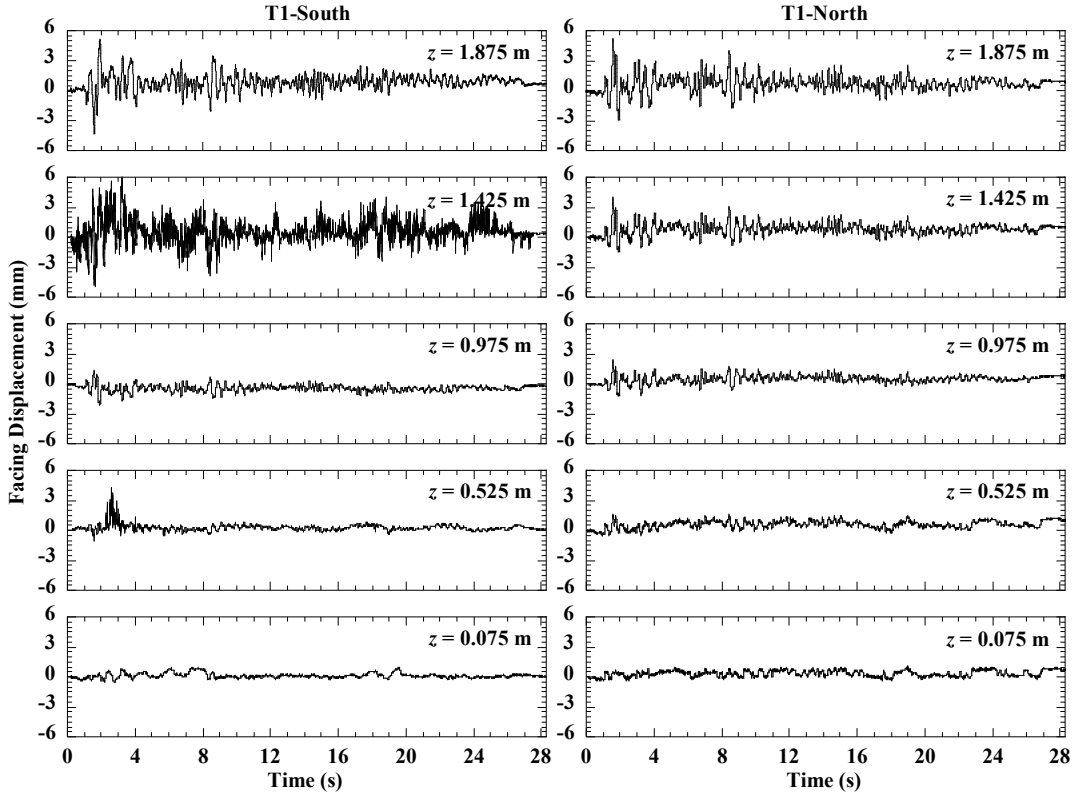

Figure 8.6 Time histories of incremental facing displacement for T1-South and T1-North during the Imperial Valley motion in Test 6.

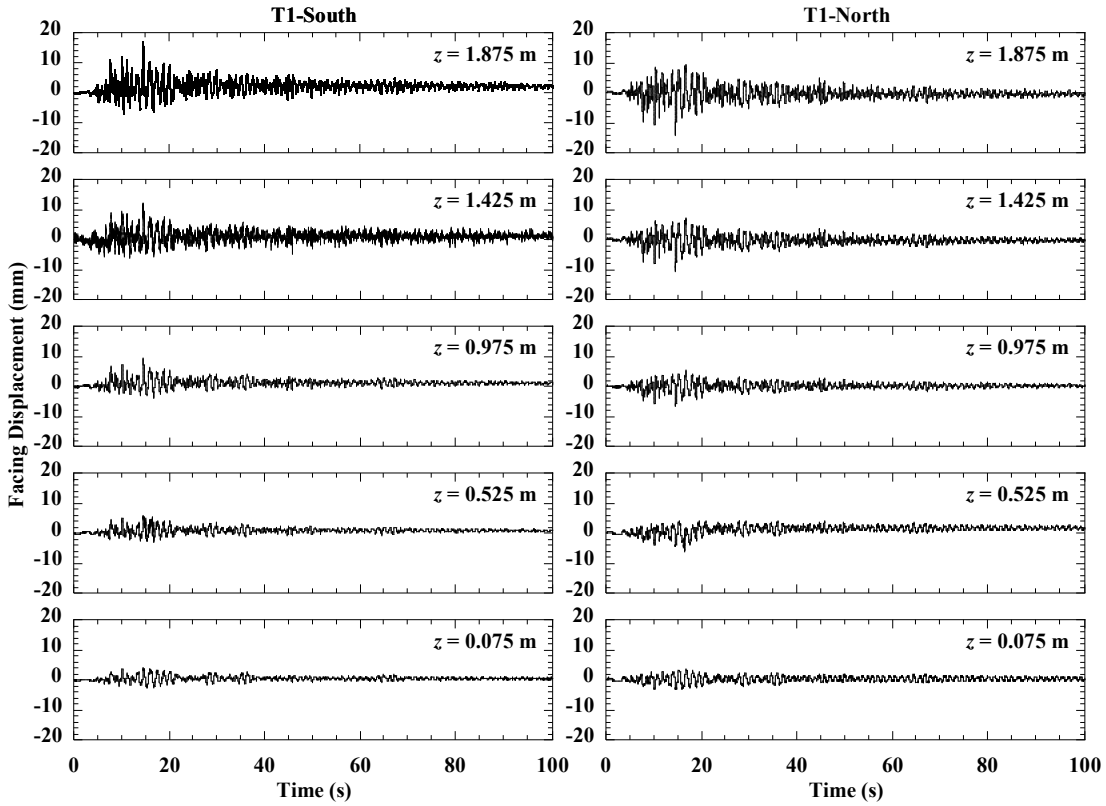

Figure 8.7 Time histories of incremental facing displacement for T1-South and T1-North during the Maule motion in Test 6.

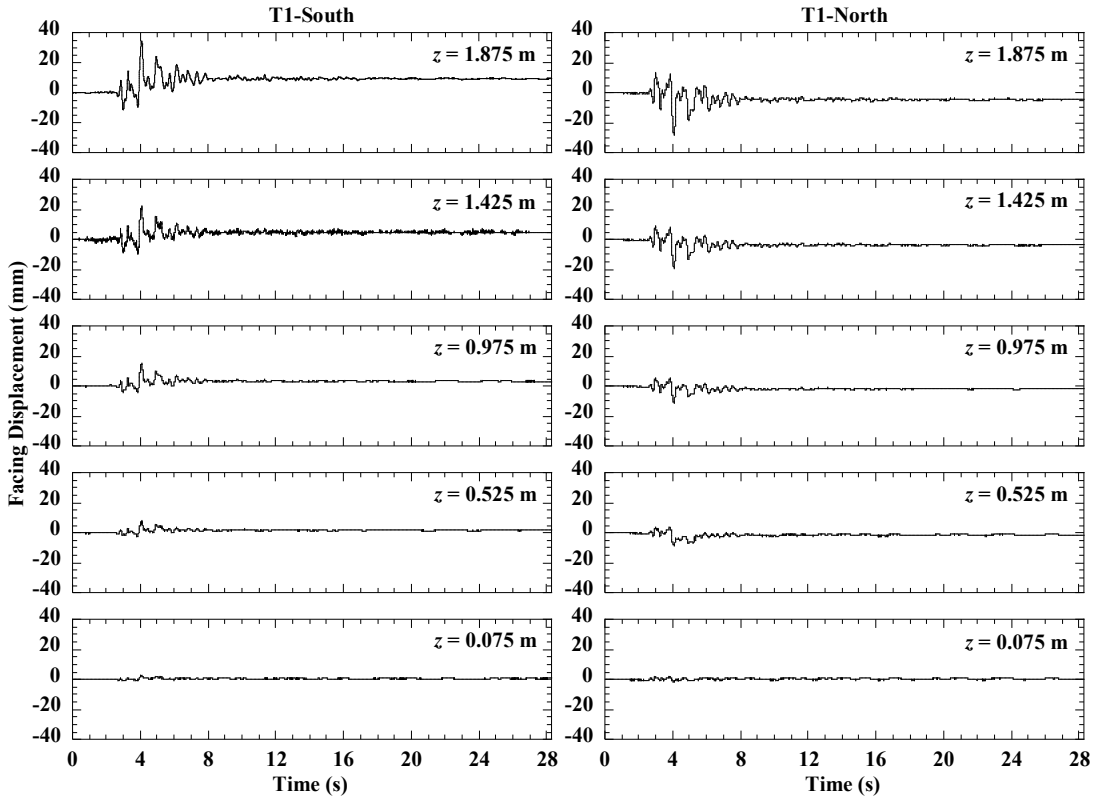

Figure 8.8 Time histories of incremental facing displacement for T1-South and T1-North during the Northridge motion in Test 6.

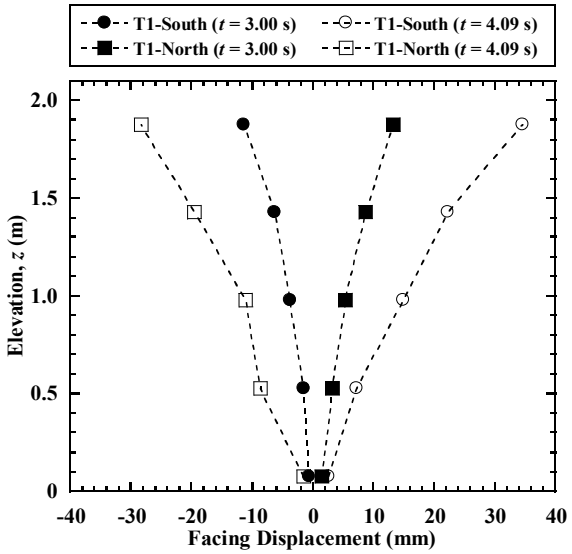

Figure 8.9 Incremental dynamic facing displacement profiles for T1-South and T1-North during the Northridge motion in Test 6.

Time histories of incremental facing displacement at selected elevations for the longitudinal section L1 during the Imperial Valley, Maule, and Northridge motions are shown in Figure 8.10, Figure 8.11, and Figure 8.12, respectively. Examination of the data indicate that shaking in the transverse direction also resulted in outward facing displacements for the longitudinal section L1. However, unlike dynamic facing displacements for T1-South and T1-North, most of the dynamic facing displacements for L1 were not recovered after shaking. Facing displacements for L1 are attributed to a Poisson's effect associated with the seismic compression of the lower GRS wall. The seismic compression of the lower GRS wall under the applied bridge load is assumed to be equal to the bridge seat settlement, which will be discussed in Section 8.5.1.

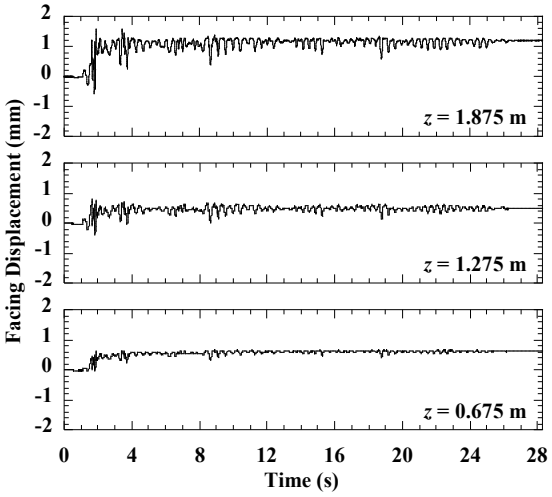

Figure 8.10 Time histories of incremental facing displacement for L1 during the Imperial Valley motion in Test 6.

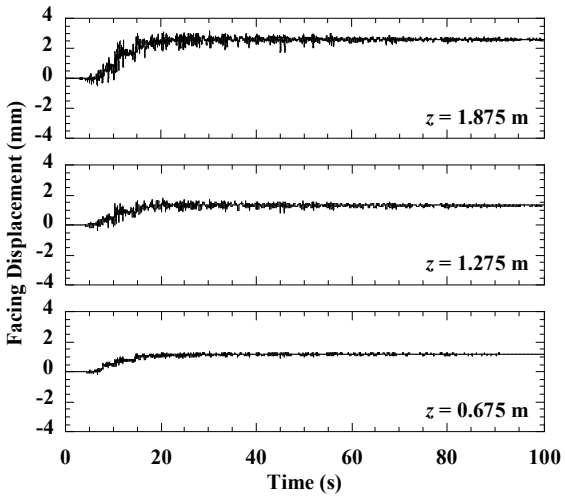

Figure 8.11 Time histories of incremental facing displacement for L1 during the Maule motion in Test 6.

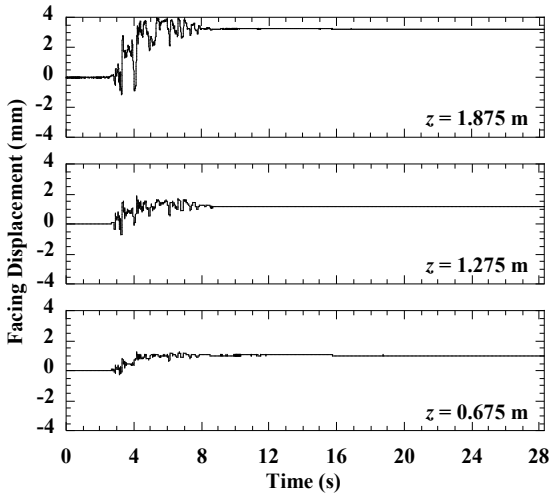

Figure 8.12 Time histories of incremental facing displacement for L1 during the Northridge motion in Test 6.

Incremental maximum and residual facing displacement profiles for different earthquake motions are shown in Figure 8.13, and maximum values of the incremental facing displacements from the profiles are presented in Table 8.3. The maximum facing displacement profiles correspond to the specific times associated with maximum incremental outward facing displacement measurements for each section.

For the Imperial Valley motion, the maximum facing displacement profiles for T1-South and T1-North are similar, with maximum values of approximately 5 mm at z = 1.875 m. After shaking, most of the dynamic facing displacements were recovered. The maximum residual facing displacements are approximately 1 mm for both sections at the top. The longitudinal section L1 has a maximum facing displacement of 1.6 mm and residual facing displacement of 1.2 mm at z = 1.875 m. For the Maule motion, T1-South had larger maximum facing displacements than T1-North, with maximum values of 17.0 mm and 9.3 mm at different times. After shaking, T1-South had an outward residual facing displacement of 2.2 mm at z = 1.875 m, whereas T1-North had an inward facing displacement of 0.4 mm at the same elevation. For the Northridge motion, facing displacements are much larger than those observed in the Imperial Valley and Maule motions. Maximum displacements at z = 1.875 m are 34.7 mm and 13.3 mm for T1-South and T1-North, respectively. The outward residual facing displacement at z = 1.875 m is 9.4 mm for T1-South, whereas T1-South has inward residual facing displacements with a maximum value of 4.6 mm at the same elevation. The maximum dynamic facing displacement for L1 is 4.0 mm at z = 1.875 m, with a residual value of 3.2 mm after shaking.

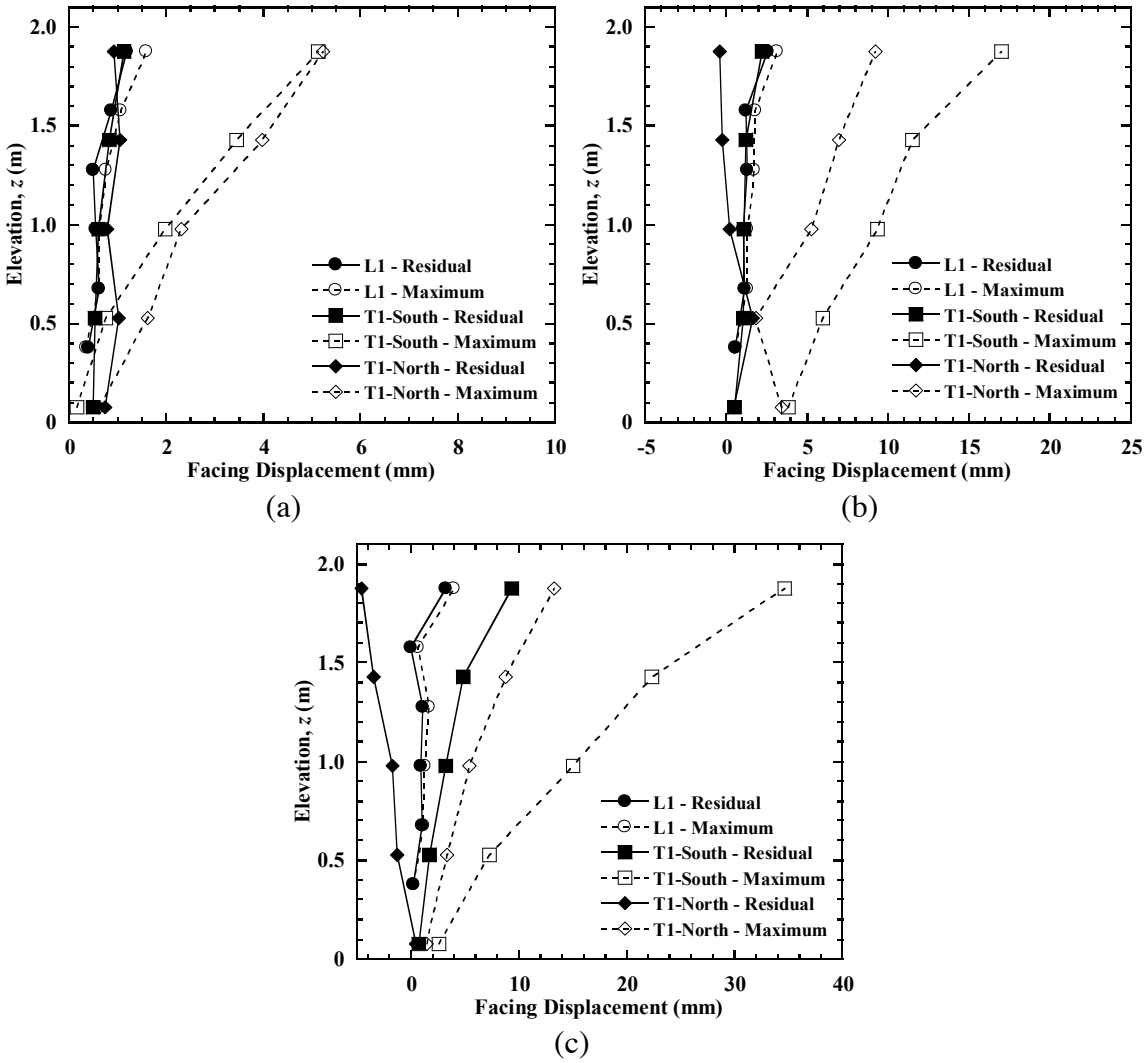

Figure 8.13 Incremental facing displacement profiles in Test 6: (a) Imperial Valley motion; (b) Maule motion; (c) Northridge motion.

Table 8.3 Maximum incremental facing displacements for earthquake motions in Test 6 (model-scale).

Earthquake motion	Maximum displacement (mm) for T1-South		Maximum displacement (mm) for T1-North		Maximum displacement (mm) for L1	
	Maximum	Residual	Maximum	Residual	Maximum	Residual
Imperial Valley	5.1	1.1	5.2	1.1	1.6	1.2
Maule	17.0	2.2	9.3	1.7	3.2	2.6
Northridge	34.7	9.4	13.1	0.5	4.0	3.2

The maximum incremental residual facing displacements for Tests 1 and 6 are presented in Table 8.4. In Test 1, facing displacements for the side wall were measured only for T1-North, but facing displacements for T1-South are supposed to be the same as T1-North, as shaking was applied in the direction perpendicular to the two symmetric transverse sections (i.e., T1-South and T1-North). Results indicate that shaking in both the longitudinal and transverse directions yielded similar maximum facing displacements for the longitudinal section L1 during all three earthquake motions, and resulted in similar maximum facing displacements for the transverse sections during the Imperial Valley and Maule motions. However, shaking in the transverse direction caused much larger maximum facing displacements for T1-South during the Northridge motion than shaking in the longitudinal direction. Facing displacements in the direction perpendicular to the direction of shaking indicate the 3D effects of 1D shaking, which is attributed to a Poisson's effect associated with the seismic compression of the lower GRS wall.

Table 8.4 Maximum incremental residual facing displacements for earthquake motions in Tests 1 and 6 (model-scale).

Earthquake motion	Maximum displacement (mm) for Test 1 (Longitudinal shaking)		Maximum displacement (mm) for Test 6 (Transverse shaking)		
	L1	T1-North	L1	T1-South	T1-North
Imperial Valley	1.4	0.8	1.2	1.1	1.1
Maule	1.1	0.8	2.6	2.2	1.7
Northridge	3.2	3.1	3.2	9.4	0.5

8.5 Bridge Seat and Bridge Beam Displacements

8.5.1 Bridge Seat Settlements

8.5.1.1 Static Loading

Settlements of the four corners of the bridge seat were measured under static and dynamic loading, as shown in Figure 6.20. One of the string potentiometers on the northwest (NW) side of the bridge seat was not working during the placement of the bridge beam but was replaced before application of the earthquake motions. Settlement time histories of bridge seat corner measurements and average values for Stage 3 are shown in Figure 8.14. The settlements due to application of the bridge beam did not occur uniformly and a sudden but small shift was observed 3 hours after the bridge beam placement. This may have been due to the arching effects that readjusted. Nonetheless, the displacements stabilized after 5 hours and did not vary significantly, indicating negligible creep. The small fluctuations in the measured settlements over time observed in Figure 8.14 may have occurred due to temperature changes in the laboratory. A slight tilting of the bridge seat toward the south side after placement of the bridge seat was observed: the settlement on the south side of the bridge seat (SW and SE) is 2 mm, while the settlement on the north side (NE) is 1 mm. The average bridge seat settlement is 1.6 mm after 94 hours from the time of the bridge beam placement.

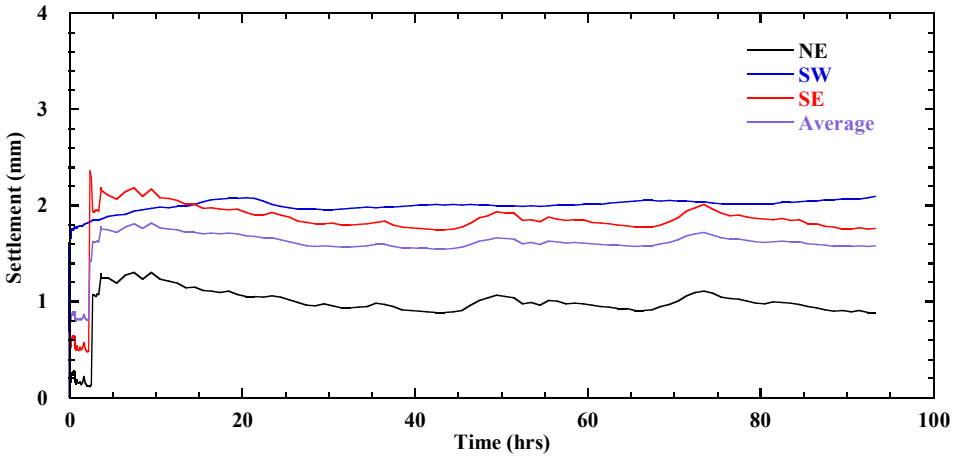

Figure 8.14 Time histories of bridge seat settlements for Stage 3 in Test 6.

8.5.1.2 Dynamic Loading

Time histories of incremental bridge seat corner settlement for the four string potentiometers during application of the earthquake motions are shown in Figure 8.15, and the average incremental bridge seat settlements are shown in Figure 8.16. For the Northridge motion, at t = 4.13 s, the south side of the bridge seat (SW and SE) had a dynamic settlement of 6.7 mm, whereas the north side (NW and NE) had a negative settlement (i.e., uplift) of 4.1 mm, which indicated rocking of the bridge seat in the N-S direction (i.e., the direction of shaking). The residual settlement on the south side (SW and SE) is larger than the north side (NW and NE), which indicated that the bridge seat tilted further toward the south after shaking. As shown in Figure 8.16(c) for the Northridge motion, the average maximum dynamic settlement is 6.1 mm and the average minimum dynamic value is -2.1 mm. The uplift is likely due to the differences in the inertial movements of the bridge beam and the GRS bridge abutment. The average residual settlement of the bridge seat is 4.7 mm, which corresponds to a vertical strain of 0.22% for

the 2.1 m-high lower GRS wall. The settlement of backfill soil surface behind the bridge seat for the upper wall was also measured, as shown in Figure 6.26(c). The incremental residual settlement for backfill soil is 5.0 mm due to strong shaking for the Northridge motion, which is greater than the average incremental bridge seat settlement of 4.7 mm, yielding an incremental differential settlement of 0.3 mm.

Average incremental bridge seat settlements and incremental backfill soil settlements for earthquake motions are summarized in Table 8.5. The maximum dynamic settlement is 3.3 mm for the Imperial Valley motion and is 9.5 mm for the Maule motion. The residual bridge seat settlements are 2.5 mm and 4.8 mm for the Imperial Valley and Maule motions, respectively, which are larger than the backfill soil settlements, yielding differential settlements of 1.2 and 1.5 mm, respectively.

Table 8.5 Average incremental bridge seat settlements and incremental backfill soil settlements for earthquake motions in Test 6 (model-scale).

Earthquake motion	Bridge seat maximum dynamic settlement (mm)	Bridge seat minimum dynamic settlement (mm)	Bridge seat residual settlement (mm)	Backfill soil residual settlement (mm)	Residual differential settlement (mm)
Imperial Valley	3.3	0	2.5	1.3	1.2
Maule	9.5	-0.1	4.8	3.3	1.5
Northridge	6.1	-2.1	4.7	5.0	0.3

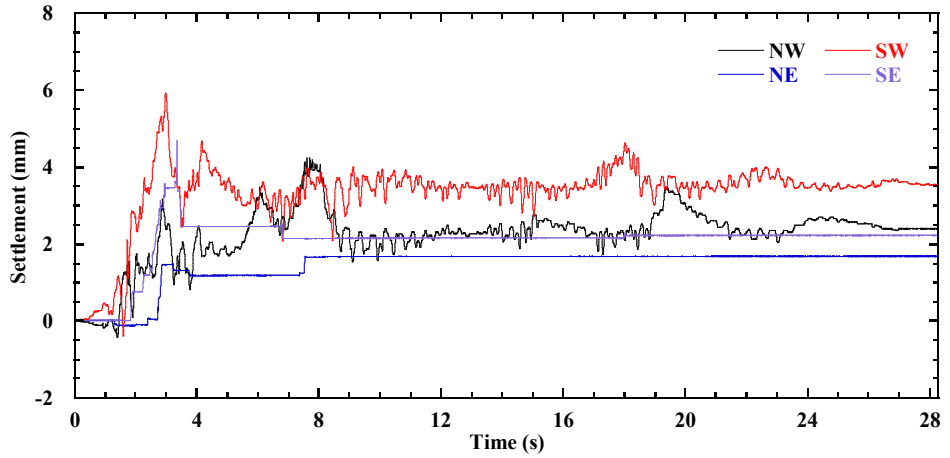

(a)

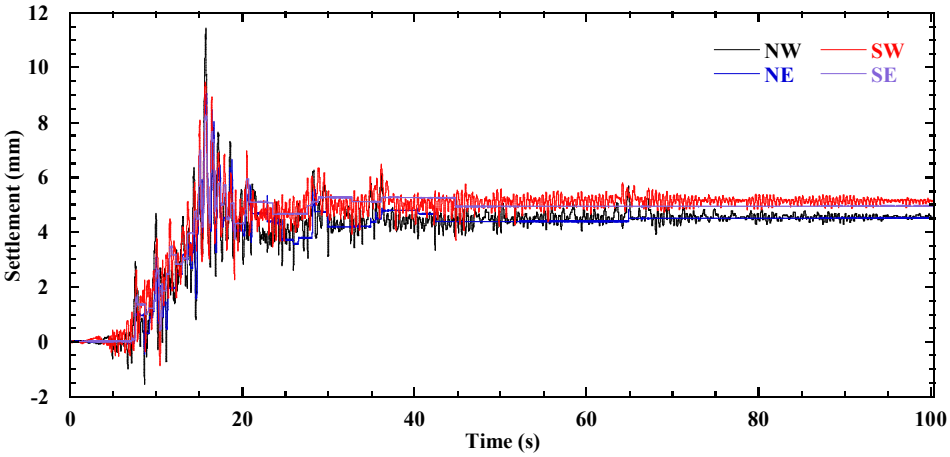

(b)

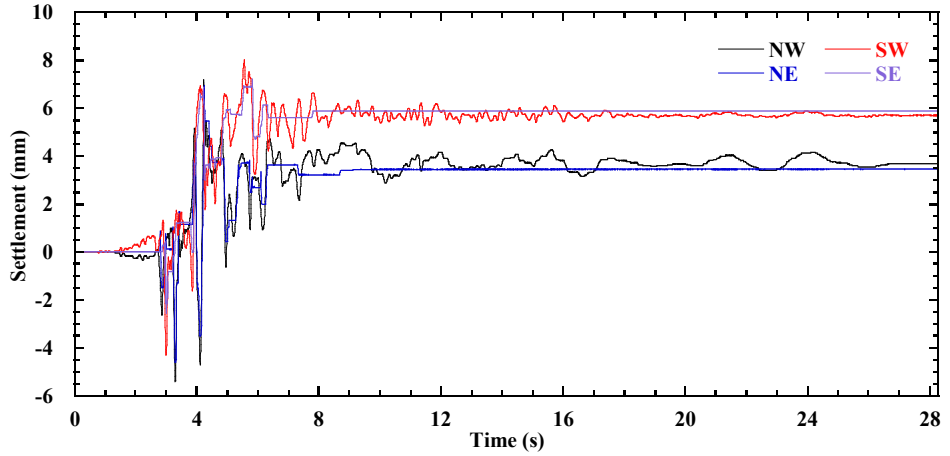

(c)

Figure 8.15 Time histories of incremental bridge seat corner settlement in Test 6: (a) Imperial Valley motion; (b) Maule motion; (c) Northridge motion.

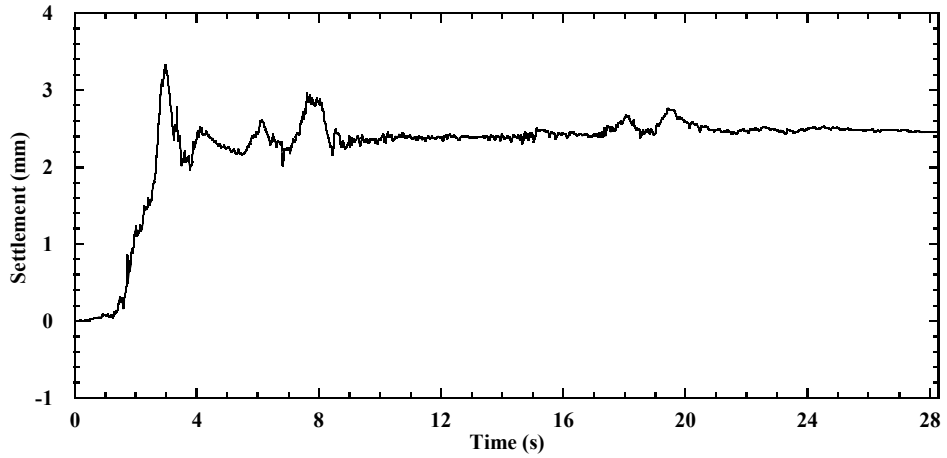

(a)

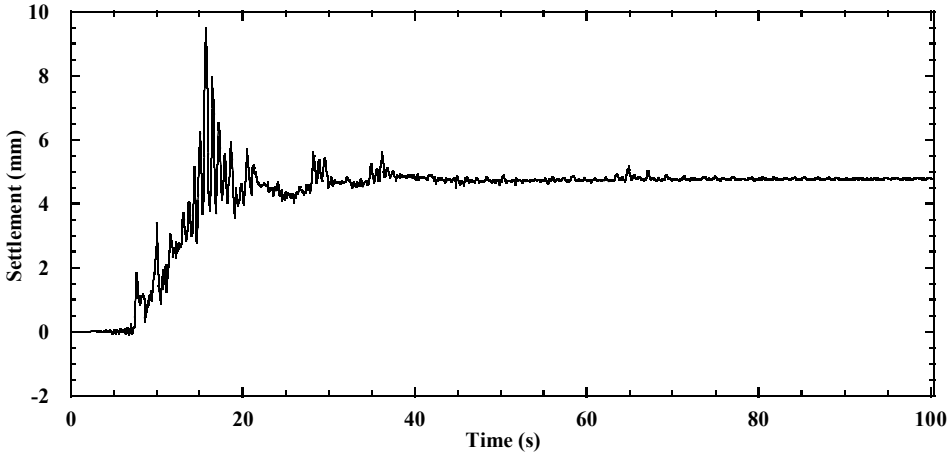

(b)

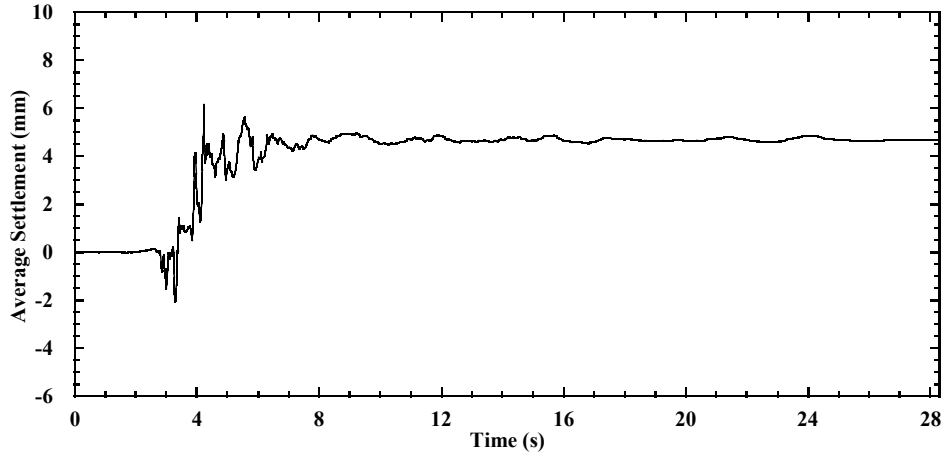

(c)

Figure 8.16 Time histories of average incremental bridge seat settlement in Test 6: (a) Imperial Valley motion; (b) Maule motion; (c) Northridge motion.

A comparison of time histories of the average incremental bridge seat settlement for earthquake motions in Tests 1 and 6 is shown in Figure 8.17, and the average incremental residual bridge seat settlements are presented in Table 8.6. The actual displacement time histories of shaking table in both tests were similar despite the difference in payloads.

For the Imperial Valley motion, the maximum dynamic settlements are similar for both tests, but the residual bridge seat settlement of 2.5 mm for Test 6 is larger than the value of 1.4 mm for Test 1. For the Maule motion, the maximum dynamic settlement and residual settlement for Test 6 are 9.5 mm and 4.8 mm, respectively, which are larger than the corresponding values of 7.0 mm and 1.4 mm for Test 1. For the Northridge motion, the maximum dynamic settlement for Test 6 is 6.1 mm, which is smaller than the value of 7.0 mm observed in Test 1. However, the residual bridge seat settlement of 4.7 mm for Test 6 is greater than the value of 2.2 mm for Test 1. In general, the average residual bridge seat settlement for Test 6 are much larger than Test 1. The larger settlement for shaking in the transverse direction is likely due to the lack of soil confinement on the two sides of the bridge seat in the transverse direction, while the backwall of the bridge seat was confined by the backfill soil for the upper GRS wall in the longitudinal direction.

Table 8.6 Average incremental residual bridge seat settlements for earthquake motions in Tests 1 and 6 (model-scale).

Earthquake motion	Average settlement (mm) for Test 1 (Longitudinal shaking)	Average settlement (mm) for Test 6 (Transverse shaking)
Imperial Valley	1.4	2.5
Maule	1.4	4.8
Northridge	2.2	4.7

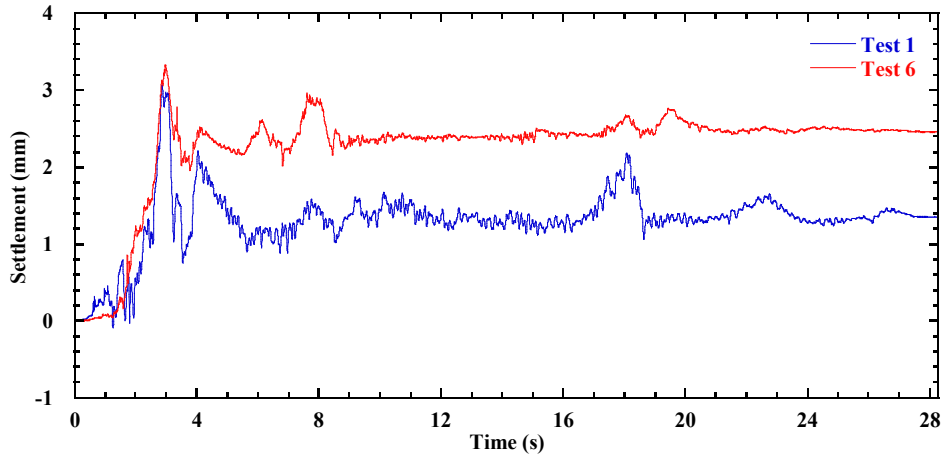

(a)

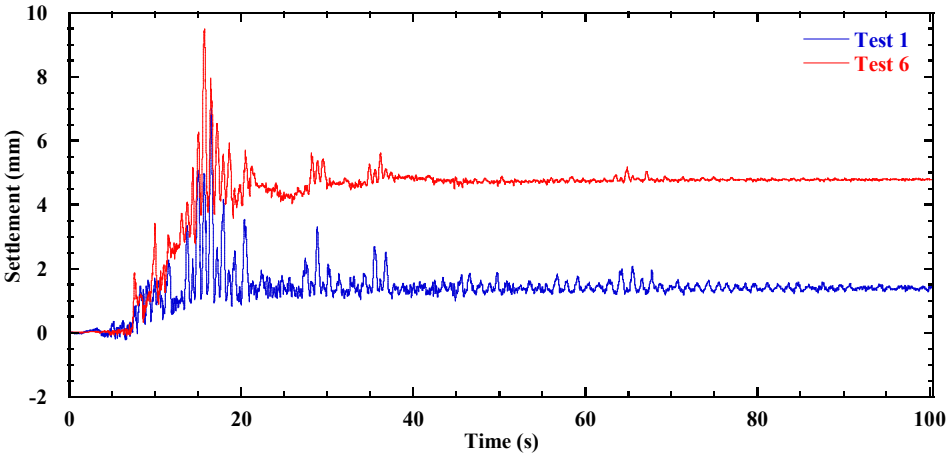

(b)

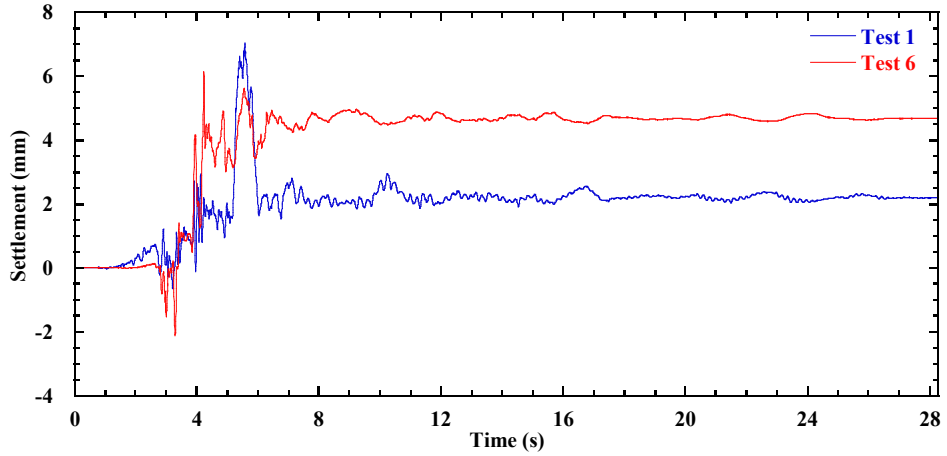

(c)

Figure 8.17 Time histories of average incremental bridge seat settlement in Tests 1 and 6: (a) Imperial Valley motion; (b) Maule motion; (c) Northridge motion.

8.5.2 Bridge Seat and Bridge Beam Horizontal Displacements

Horizontal displacements in the transverse direction for the bridge seat and bridge beam were measured at the locations shown in Figure 6.26, and time histories of incremental horizontal displacement for the earthquake motions are shown in Figure 8.18. The residual horizontal displacement for bridge seat is essentially zero for the Imperial Valley and Maule motion, but shows a permanent displacement of 17.5 mm toward the south side after the Northridge motion. The bridge beam experienced larger horizontal displacements than the bridge seat during shaking, which indicated sliding of the bridge beam with respect to the bridge seat. The horizontal displacements for the bridge seat and bridge beam are highly dependent on the characteristics of the earthquake motions.

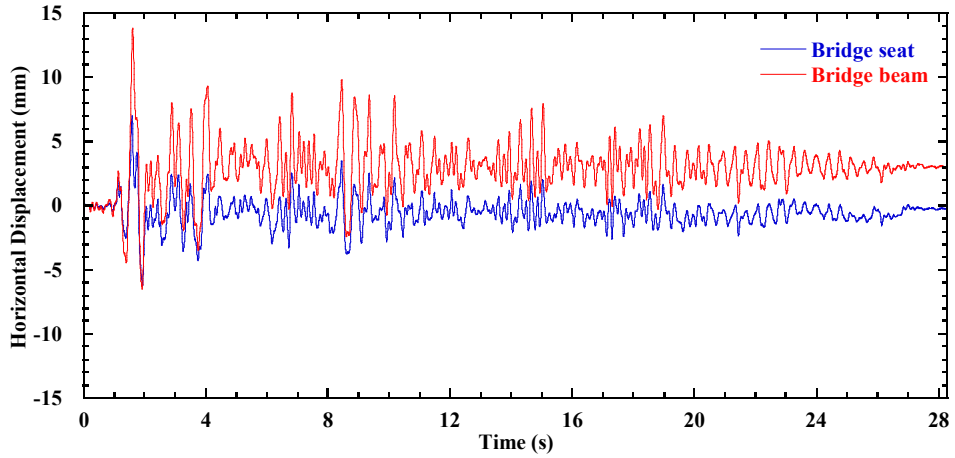

(a)

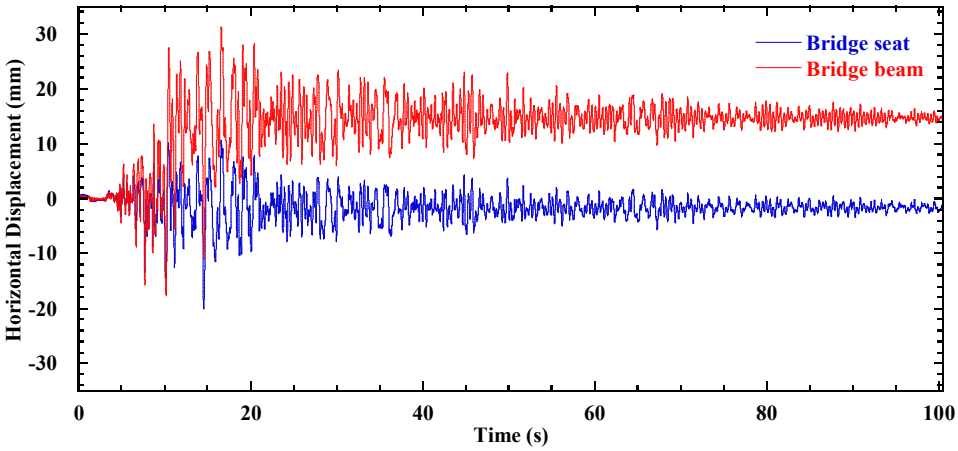

(b)

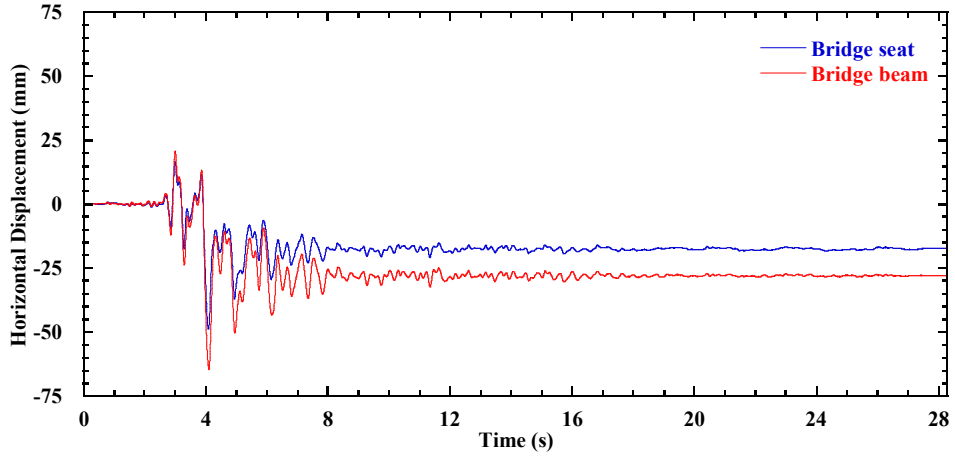

(c)

Figure 8.18 Time histories of incremental horizontal displacement for bridge seat and bridge beam in Test 6: (a) Imperial Valley motion; (b) Maule motion; (c) Northridge motion.

Time histories of incremental horizontal displacement for bridge seat relative to the top of GRS bridge abutment (i.e., measurements taken at the facing block z = 1.875 m for T1-North) and bridge beam relative to the bridge seat are shown in Figure 8.19. For the Imperial Valley motion, the bridge seat had relatively small magnitudes of horizontal displacement on the GRS bridge abutment, and the bridge beam had a residual relative horizontal displacement of 3.2 mm with respect to the bridge seat toward the north side. For the Maule motion, the bridge beam experienced a sudden sliding on the bridge seat with a horizontal displacement of approximately 20 mm at t = 10 s and had a permanent sliding distance of 16.1 mm toward the north side after shaking. For the Northridge motion, both the bridge seat and bridge beam experienced significant sliding toward the south side at t = 4 s and had residual relative horizontal displacements of 12.9 and 10.6 mm, respectively. The width of seismic joint is also associated with the relative horizontal displacement of the bridge beam with respect to the bridge seat and will be discussed in Section 8.10.

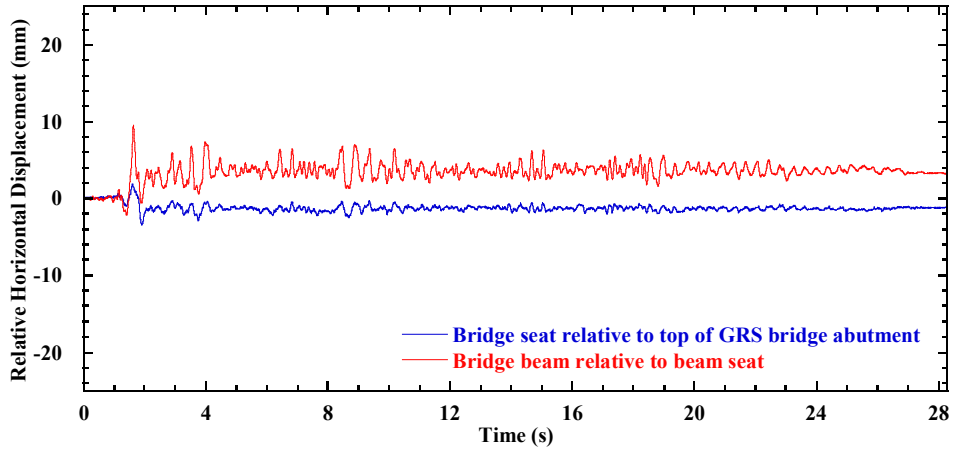

(a)

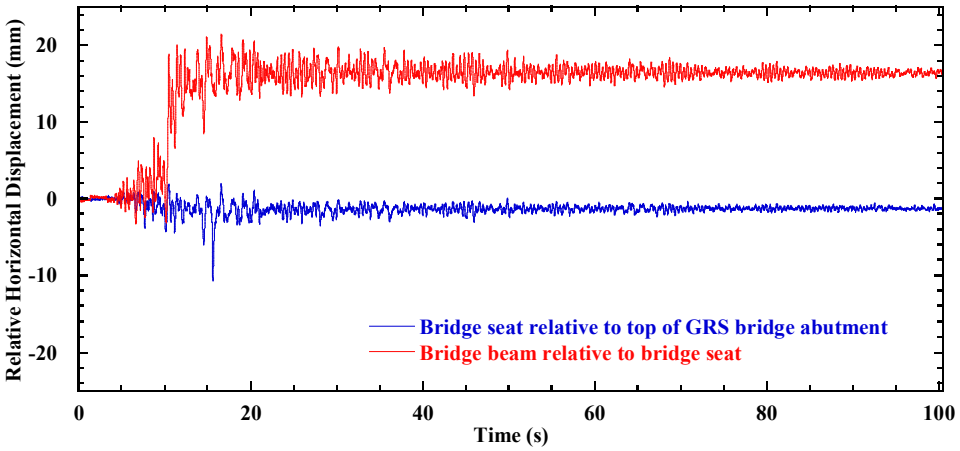

(b)

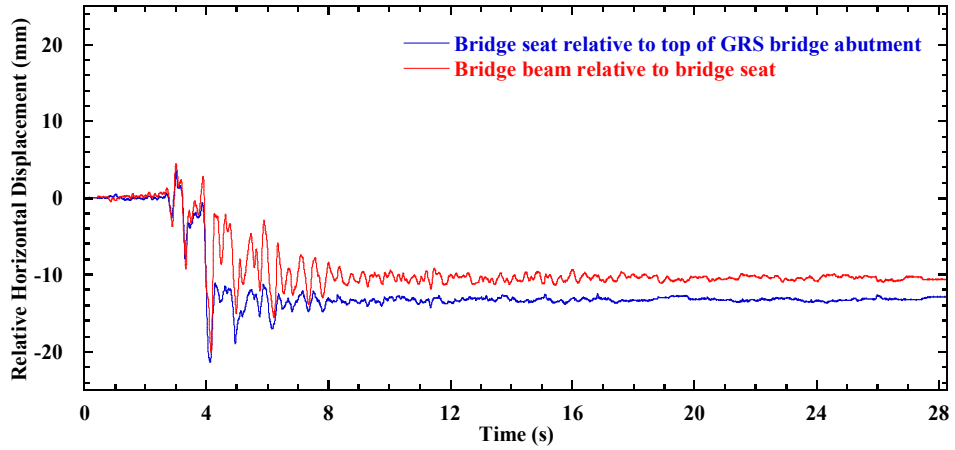

(c)

Figure 8.19 Time histories of incremental relative horizontal displacement for bridge seat and bridge beam in Test 6: (a) Imperial Valley motion; (b) Maule motion; (c) Northridge motion.

8.6 Acceleration Responses

8.6.1 Structures

Time histories of horizontal accelerations for bridge seat and bridge beam are shown in Figure 8.20. For instance, the bridge seat had a peak acceleration of 1.02*g* for the Northridge motion, and the bridge beam had a peak acceleration of 1.82*g*, which is much larger than the peak value of the shaking table (0.86*g*).

The root-mean-square (RMS) method can be used to mitigate effects of high frequency noise and also characterize amplitude and frequency content in a measured response (Kramer 1996; El-Emam and Bathurst 2005). The calculated ratios for the bridge seat and bridge beam RMS accelerations normalized by the shaking table RMS acceleration are presented in Table 8.7. For the Imperial Valley motion, the bridge beam has an acceleration amplification ratio of 1.79, and is greater than the ratio of 1.39 for the bridge seat. For the Maule motion, the ratios decrease to 1.55 and 1.27 for the bridge beam and bridge seat, respectively, and further decrease to 1.34 and 1.11 for the Northridge motion. In general, the RMS acceleration ratios for the bridge beam are larger than the bridge seat. RMS acceleration ratios for the bridge seat and bridge beam in Test 1 are also shown in Table 8.7, and indicate that the acceleration amplification ratios are larger for shaking in the longitudinal direction than in the transverse direction for the same earthquake motions.

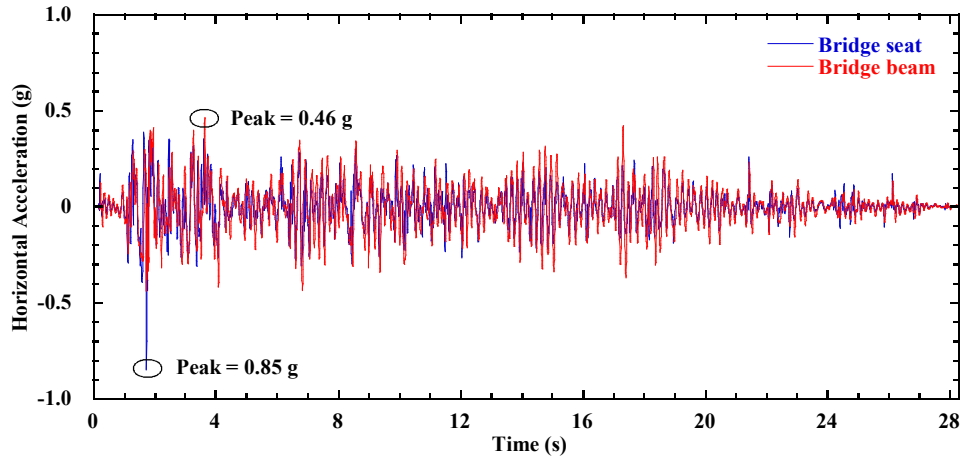

(a)

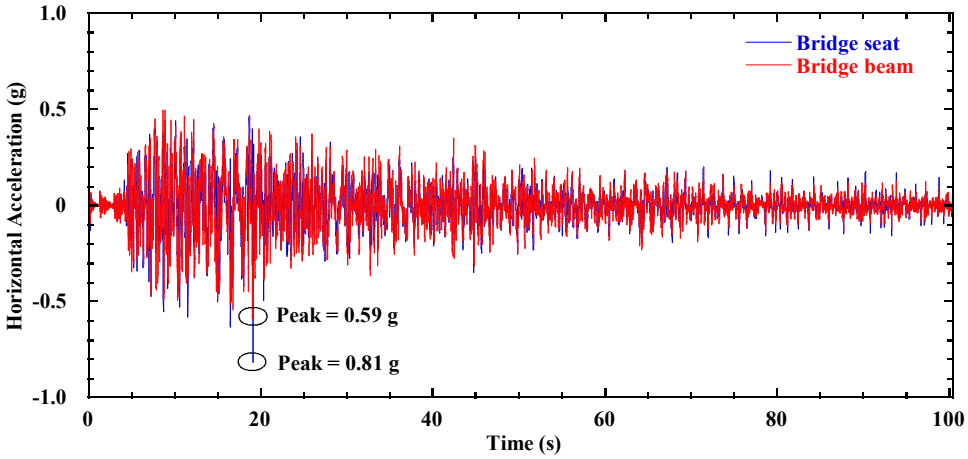

(b)

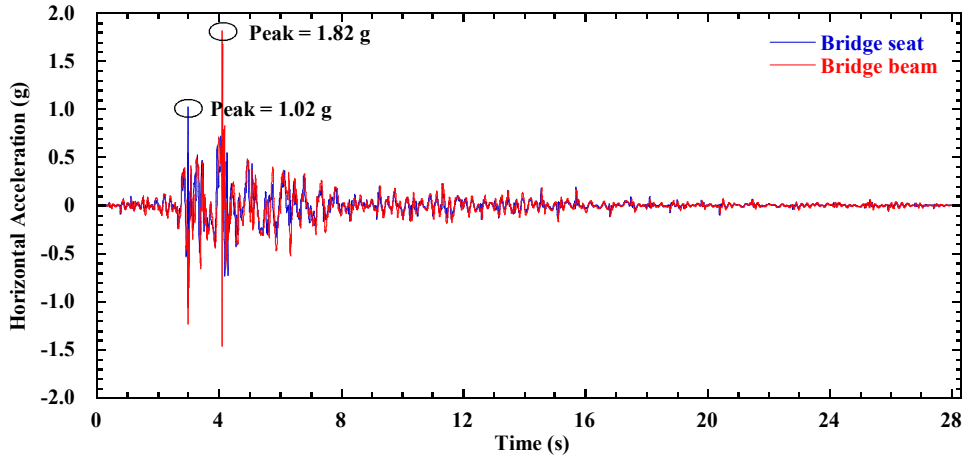

(c)

Figure 8.20 Time histories of horizontal acceleration for bridge seat and bridge beam in Test 6: (a) Imperial Valley motion; (b) Maule motion; (c) Northridge motion.

Table 8.7 RMS acceleration ratios of bridge beam and bridge seat for earthquake motions in Tests 1 and 6 (model-scale).

Earthquake motion	Acceleration ratio for Test 1		Acceleration ratio for Test 6	
	Bridge seat	Bridge beam	Bridge seat	Bridge beam
Imperial Valley	1.60	1.80	1.39	1.79
Maule	1.38	1.73	1.27	1.55
Northridge	1.45	1.58	1.11	1.34

8.6.2 Abutment

Horizontal accelerations were measured for wall facing and reinforced soil zone on the south and north sides of transverse section T1 (T1-South and T1-North). Time histories of horizontal acceleration in the reinforced soil zone for T1-South and T1-North during the Imperial Valley, Maule, and Northridge motions, are shown in Figure 8.21, Figure 8.22, and Figure 8.23, respectively. For the Imperial Valley motion, data show that horizontal accelerations in the backfill soil increase with elevation for both sections, and indicate acceleration amplification toward the top of the lower GRS wall. Similar acceleration amplification trend is also observed for both sections during the Maule motion. However, for the Northridge motion, the magnitudes of horizontal acceleration are similar for all elevations in both sections, which shows essentially no amplification with elevation. In general, the magnitudes of horizontal acceleration at the same elevations for T1-South and T1-North are similar.

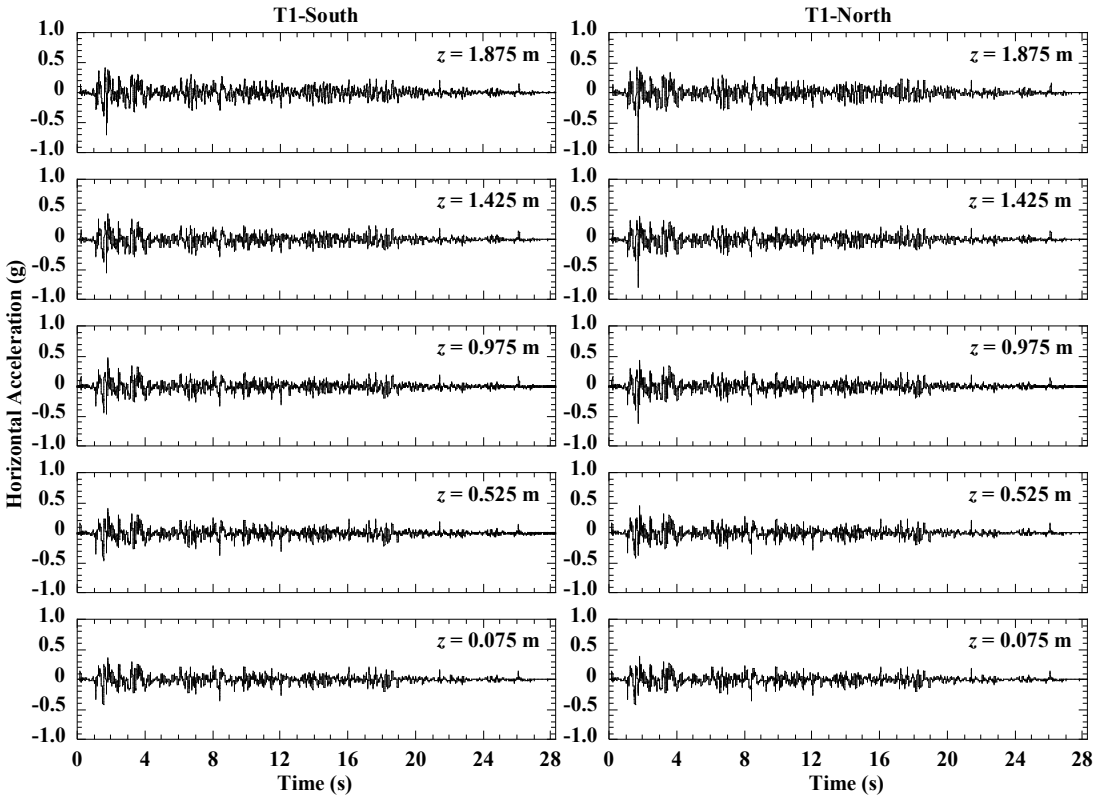

Figure 8.21 Time histories of horizontal acceleration in the reinforced soil zone for T1-South and T1-North during the Imperial Valley motion in Test 6.

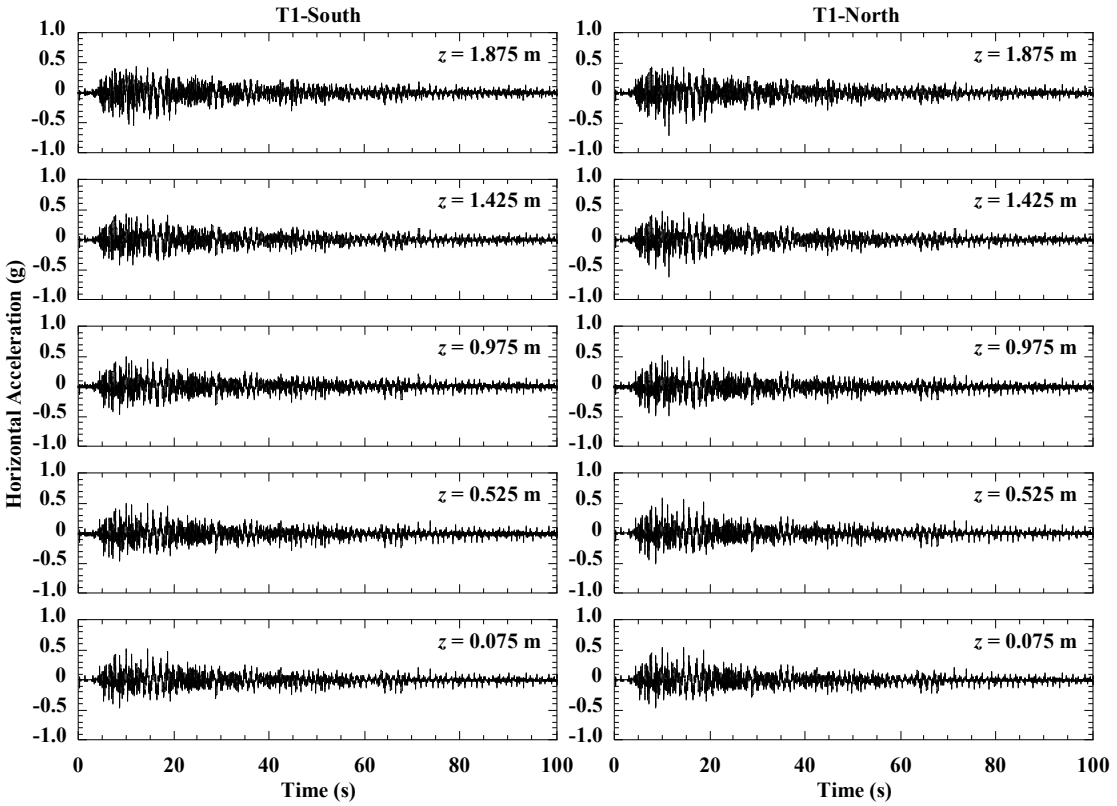

Figure 8.22 Time histories of horizontal acceleration in the reinforced soil zone for T1-South and T1-North during the Maule motion in Test 6.

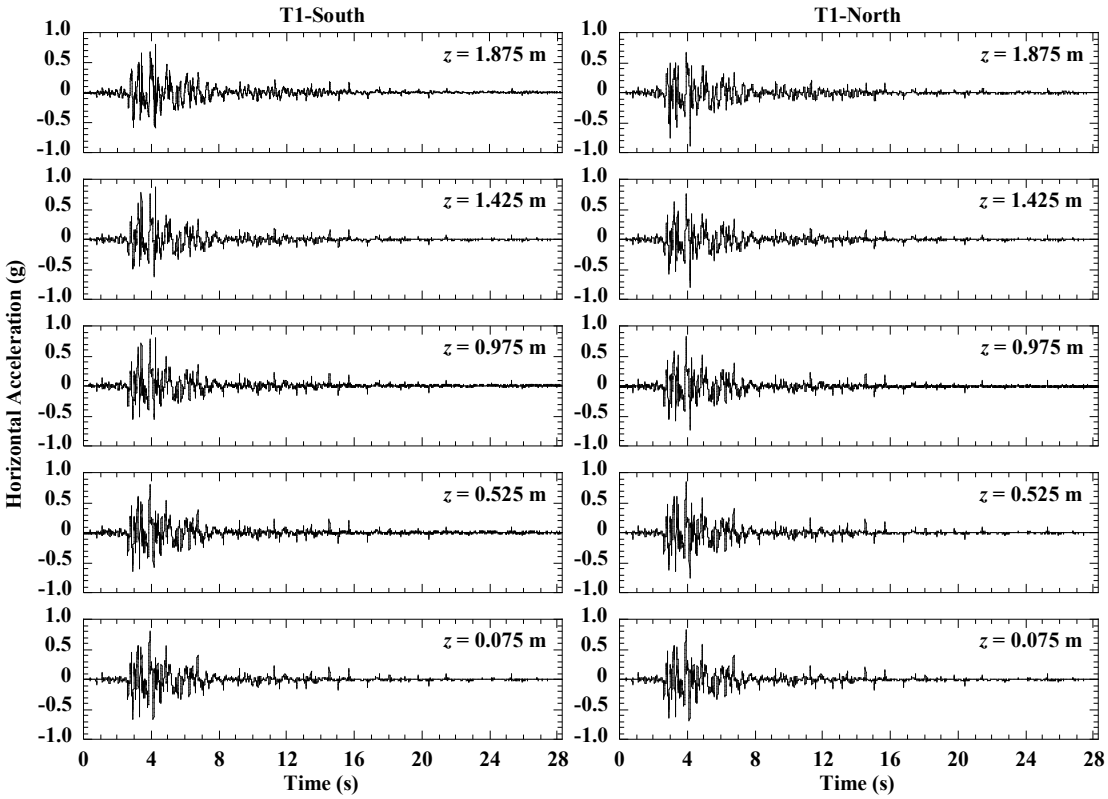

Figure 8.23 Time histories of horizontal acceleration in the reinforced soil zone for T1-South and T1-North during the Northridge motion in Test 6.

The RMS acceleration ratio profiles of wall facing and reinforced soil zone for T1-South and T1-North are shown in Figure 8.24. For the Imperial Valley motion, profiles for T1-South and T1-North in the reinforced soil zone show nonlinear increase of acceleration ratio with elevation. For instance, the acceleration ratio for T1-North increases from 0.97 at z = 0.075 m to 1.16 at z = 1.425 m, and then increases significantly to 1.32 at z = 1.875 m. Similar profiles also are observed for the Maule motion, and this indicates that accelerations amplify more toward the top. The acceleration ratios are the largest for the Imperial Valley motion, with a maximum ratio of 1.32 at the top for T1-North in the reinforced soil zone, and the maximum ratio at the same location is 1.19 for the Maule motion. However, the acceleration ratios are generally close to 1.0 for the Northridge motion, which indicates essentially no amplification with elevation. The deceasing amplification behavior as shaking proceeded may be due to the softening of the soil (i.e., shear modulus reduction) under successive earthquake motions. However, further investigations are needed to confirm this using numerical simulations. In general, acceleration ratio profiles of wall facing and reinforced soil zone are similar for T1-South and T1-North. The ratios for the wall facing are slightly larger than for the reinforced soil zone probably due to lower confinement.

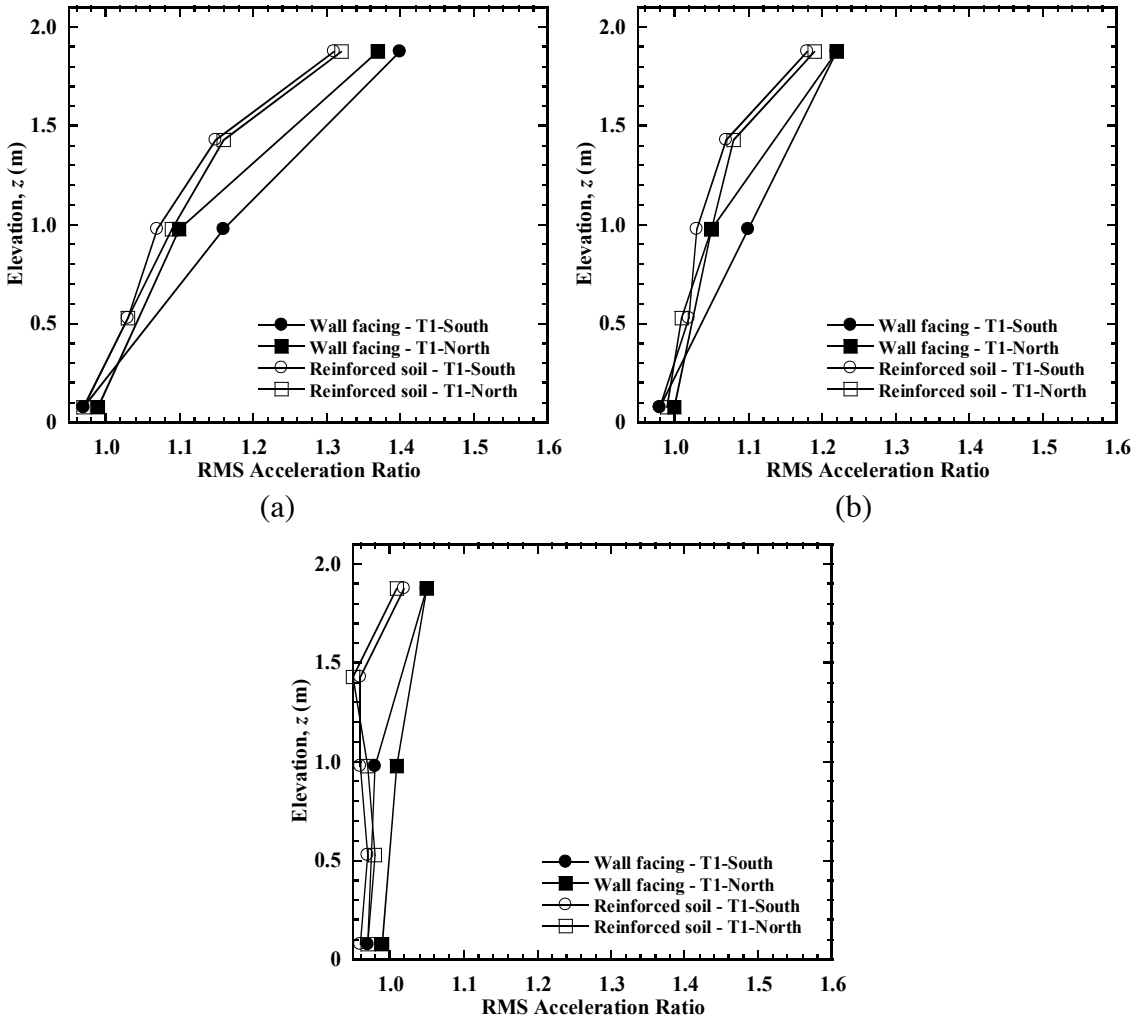

Figure 8.24 RMS acceleration ratio profiles for T1-South and T1-North in Test 6: (a) Imperial Valley motion; (b) Maule motion; (c) Northridge motion.

The RMS acceleration ratio profiles for the transverse sections T1 and T2 are shown in Figure 8.25. Transverse section T1 is under the bridge seat, while transverse section T2 is behind the bridge seat (and thus has lower vertical stresses in the backfill soil). The RMS acceleration ratio profiles for T2 also show nonlinear increase with elevation, and the acceleration ratios for the upper wall (z = 2.325 m) confirm that soil accelerations amplify more toward the top. In general, transverse section T2 has slightly larger acceleration ratios than transverse section T1 at z = 1.875 m for all three earthquake motions.

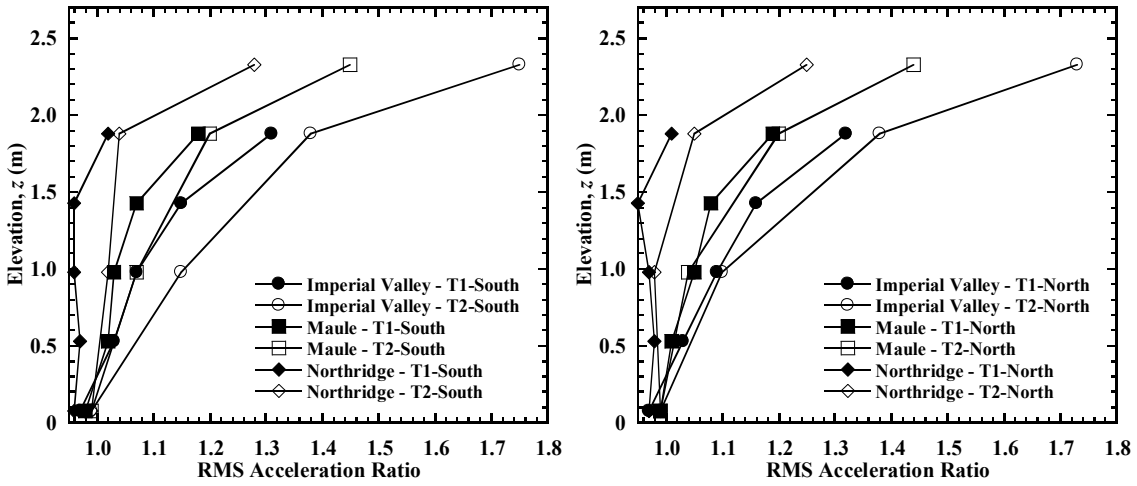

(a) (b)

Figure 8.25 RMS acceleration ratio profiles for T1 and T2 in Test 6: (a) T1-South; (b) T1-North.

8.7 Vertical Stresses

8.7.1 Static Loading

Vertical stresses behind the wall facing were measured for the south and north side of transverse section T1 (T1-South and T1-North) as shown in Figure 6.26, and measured stresses under static loading are shown in Figure 8.26(a). The vertical pressure cell at z = 0.975 m for T1-South did not work for Stages 1 and 2, but back to normal for Stage 3 due to wire contact problem. The vertical stresses for T1-South and T1-North are similar for Stage 1, and the vertical stresses increased slightly due to construction of bridge seat for Stage 2. For Stage 3, vertical stresses increased significantly at the top of the wall (z = 1.875 m), whereas there were only relatively small increases at the bottom of the wall (z = 0.075 m). Vertical stresses for T1-South increased by 21.9 kPa at the top of the wall and by 3.3 kPa at the bottom of the wall. Vertical stresses for T1-South are larger than for T1-North at the mid-height and the bottom of the wall, which might be attributed to the slight tilting of bridge seat toward the south side for Stage 3 shown in Figure 8.14.

The calculated vertical stresses profiles for Stages 1 and 3 using the AASHTO method (2012) are also shown in Figure 8.26(b). For the AASHTO method (2012), the values for Stage 1 represent self-weight of backfill soil and the values for Stage 3 were calculated using the 2:1 vertical stress distribution assumption for flexible walls to obtain the stress increments due to bridge load. For Stage 1, the vertical stress profiles for both sections are close to the calculated self-weight values at the end of the lower GRS wall construction. For Stage 3, the measured vertical stresses are smaller than calculated values

using the AASHTO method (2012) and the average vertical stress of 66 kPa under the bridge seat.

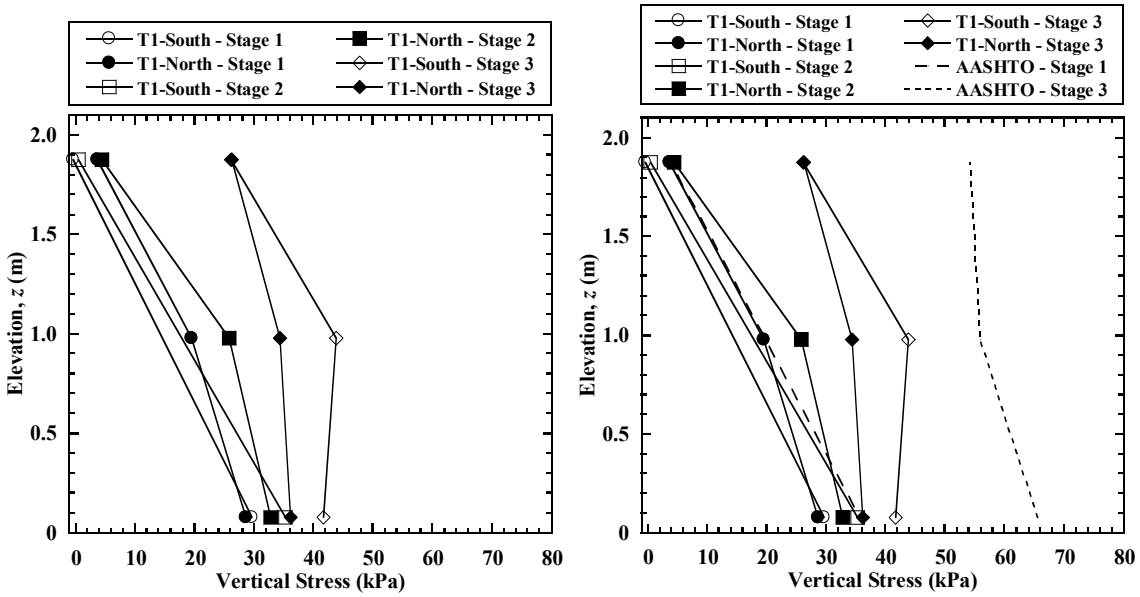

Figure 8.26 Vertical stress profiles for construction stages in Test 6: (a) measurements; (b) analysis.

8.7.2 Dynamic Loading

Time histories of vertical stress for T1-South and T1-North during the Imperial Valley, Maule, and Northridge motions are shown in Figure 8.27, Figure 8.28, and Figure 8.29, respectively. The vertical pressure cell at $z = 0.975$ m for T1-South probably had wire contact problem before $t = 7$ s, but back to normal afterward. In general, the vertical stresses at the same elevations for T1-South and T1-North had opposite spikes (i.e., stress increase vs. decrease) at any moment in time. For instance, at $t = 4.13$ s during the Northridge motion, the vertical stress at $z = 1.875$ m for T1-South reached 56.3 kPa, whereas the vertical stress at the same elevation for T1-North was 2.1 kPa. The dynamic vertical stresses correspond to stress increments of 21.5 kPa and -22.6 kPa with respect to the initial values before this shaking event for T1-South and T1-North, respectively. The results are consistent with the bridge seat settlements on the two sides at the same time shown in Figure 8.15, which confirms rocking of the bridge seat in the direction of shaking.

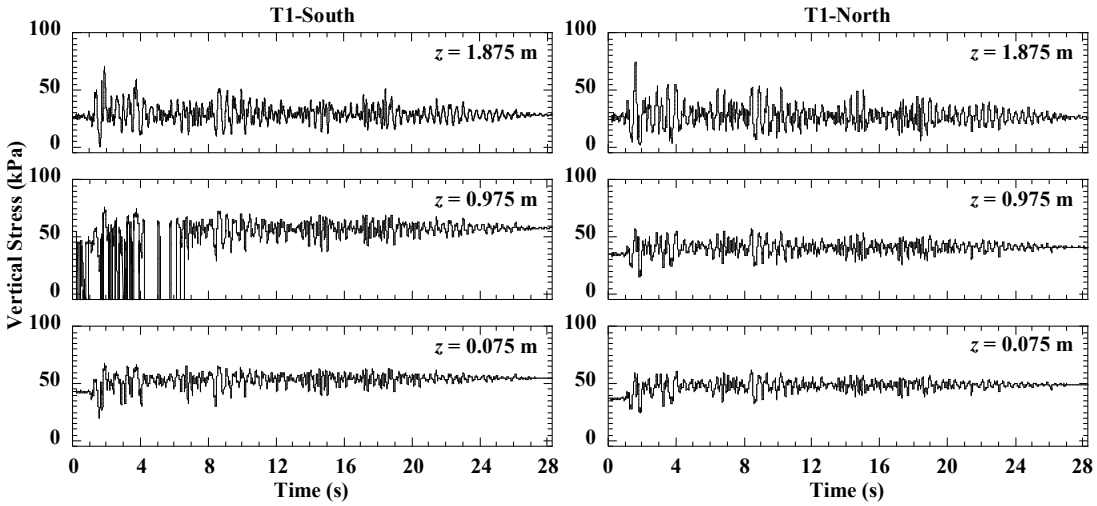

Figure 8.27 Time histories of vertical stress for T1-South and T1-North during the Imperial Valley motion in Test 6.

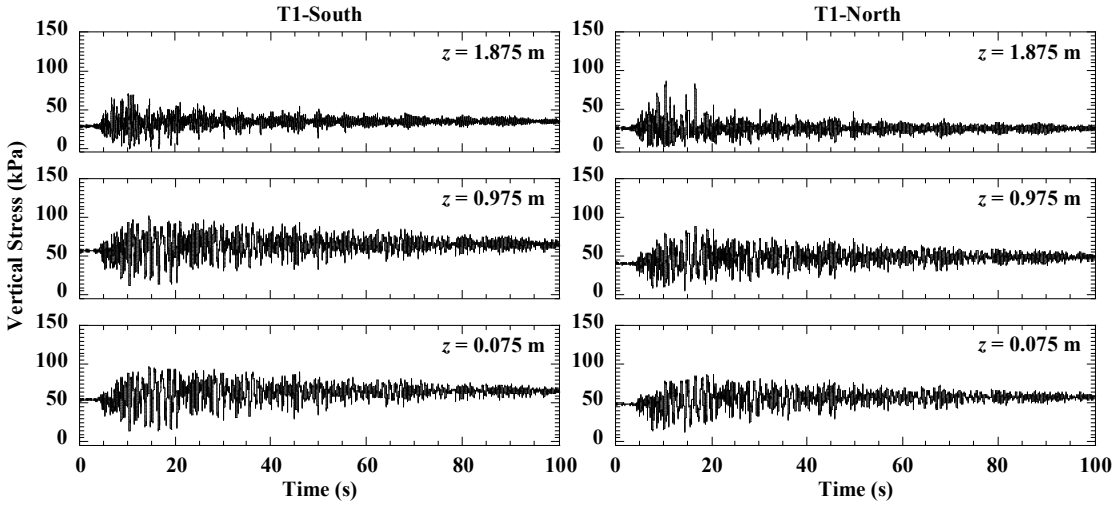

Figure 8.28 Time histories of vertical stress for T1-South and T1-North during the Maule motion in Test 6.

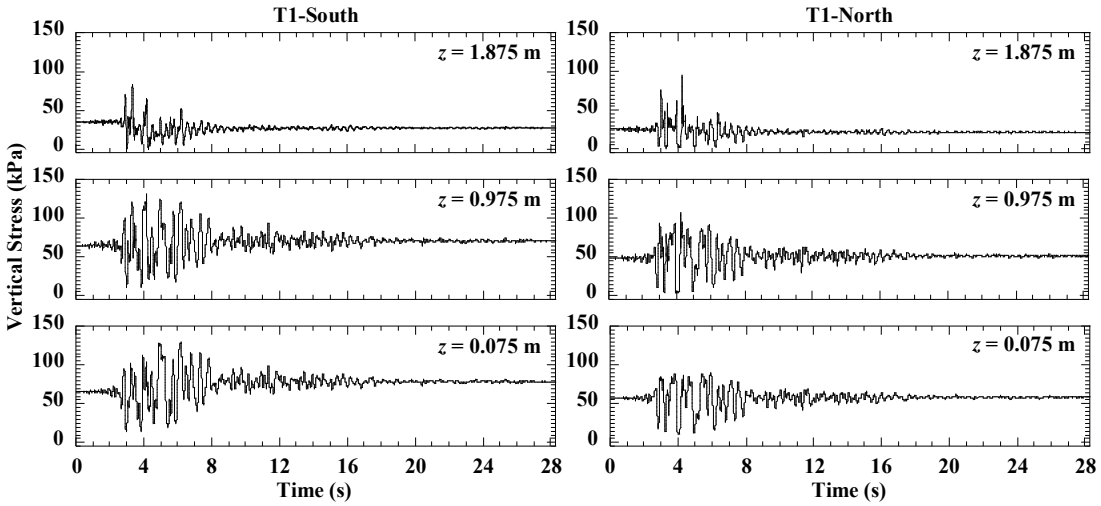

Figure 8.29 Time histories of vertical stress for T1-South and T1-North during the Northridge motion in Test 6.

Profiles for the initial (before shaking), maximum dynamic (during shaking), and residual (after shaking) vertical stresses for earthquake motions are shown in Figure 8.30. For the Imperial Valley motion, the maximum vertical stress is 76.2 kPa at the mid-height of the wall for T1-South and is 74.5 kPa at the top of the wall for T1-North. After shaking, the residual vertical stresses are larger than the initial values, which might be attributed to the change of arching chains in the backfill soil due to shaking. The maximum dynamic vertical stress at the mid-height of the wall for T1-South is 101.7 kPa during the Maule motion and is 130.9 kPa during the Northridge motion. For the Northridge motion, the residual vertical stress profiles are similar to the initial profiles, which indicates that the arching chains may have be eliminated due to shaking.

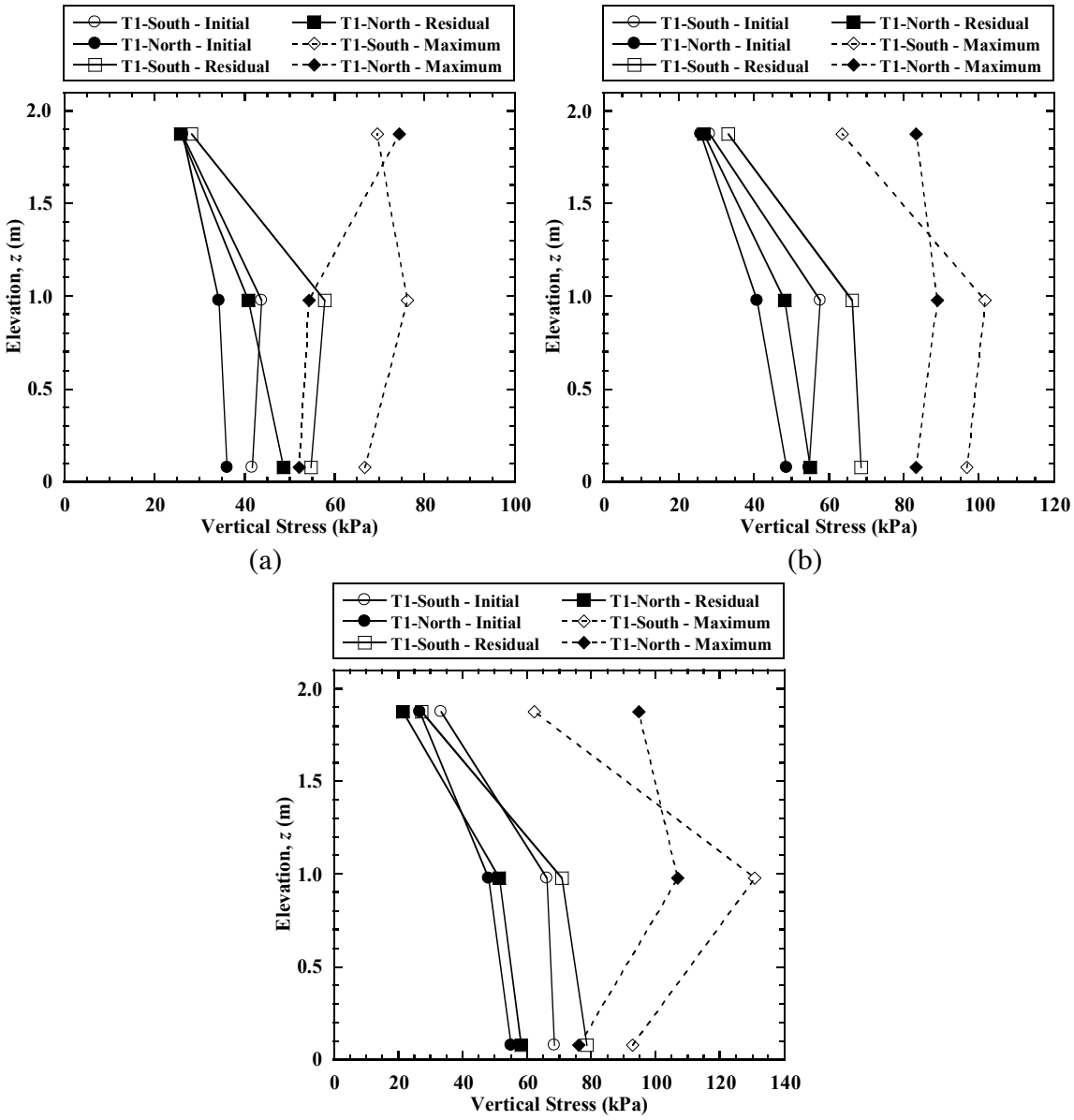

Figure 8.30 Vertical stress profiles in Test 6: (a) Imperial Valley motion; (b) Maule motion; (c) Northridge motion.

8.8 Lateral Stresses

8.8.1 Static Loading

Lateral stresses behind the wall facing were measured for the south and north side of transverse section T1 (T1-South and T1-North) as shown in Figure 6.26, and measured stresses under static loading are shown in Figure 8.31(a). For Stage 1, lateral stresses for T1-South and T1-North are similar at the top and the mid-height of the wall, but the lateral stress of 4.1 kPa at the bottom of the wall for T1-North is much larger than the value of 0.6 kPa at the same elevation for T1-South. The small lateral stress at the bottom of the wall for T1-South is attributed to the soil arching effect. Lateral stress at the top of the wall decreased slightly for both sections probably due to disturbance of construction of the bridge seat and upper wall for Stage 2, but increased due to placement of bridge beam for Stage 3.

The lateral stresses calculated using the AASHTO method (2012) by multiplying the active earth pressure coefficient K_a with the vertical stresses for Stages 1 and 3 are shown in Figure 8.31(b) and compared with the measured lateral stresses. For Stage 1, the lateral stresses of 0.9 kPa and 1.6 kPa at the top of the wall for T1-South and T1-North, respectively, are slightly larger than the K_a value of 0.5 kPa for Stage 1. This is attributed to the lock-in lateral stresses due to compaction. The lateral stress of 4.1 kPa at the bottom for T1-North is similar to the calculated value of 4.5 kPa for Stage 1. Measured lateral stresses for Stage 3 are much smaller than the calculated values using the AASHTO method (2012) for both sections.

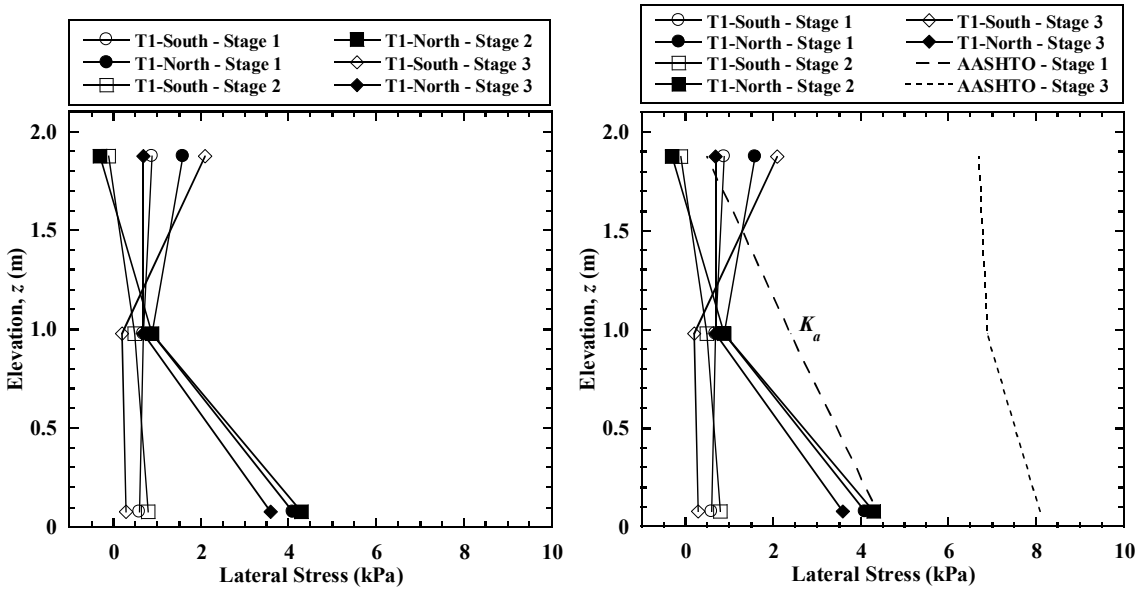

Figure 8.31 Lateral stress profiles for construction stages in Test 6: (a) measurements; (b) analysis.

8.8.2 Dynamic Loading

Time histories of lateral stress for T1-South and T1-North during the Imperial Valley, Maule, and Northridge motions are shown in Figure 8.32, Figure 8.33, and Figure 8.34, respectively. Similar to the vertical stresses, the lateral stresses at the same elevations for T1-South and T1-North had opposite spikes (i.e., stress increase vs. decrease) at any moment in time. For instance, at $t = 4.07$ s during the Northridge motion, T1-South reached the maximum lateral stresses, whereas T1-North had decreases in stress. The dynamic lateral stresses are a result of both the inertial forces of backfill soil due to shaking and the dynamic vertical stresses associated with rocking of the bridge seat.

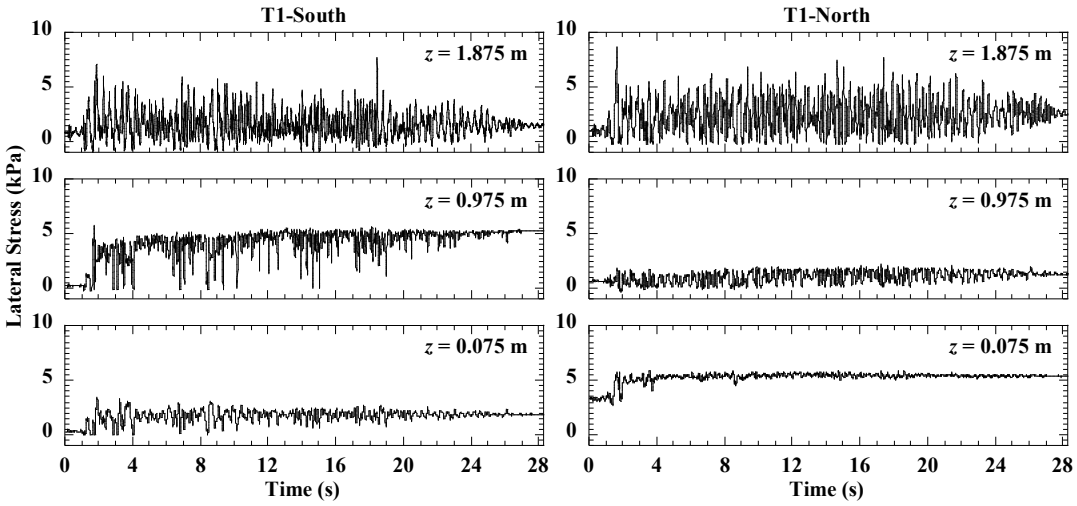

Figure 8.32 Time histories of lateral stress for T1-South and T1-North during the Imperial Valley motion in Test 6.

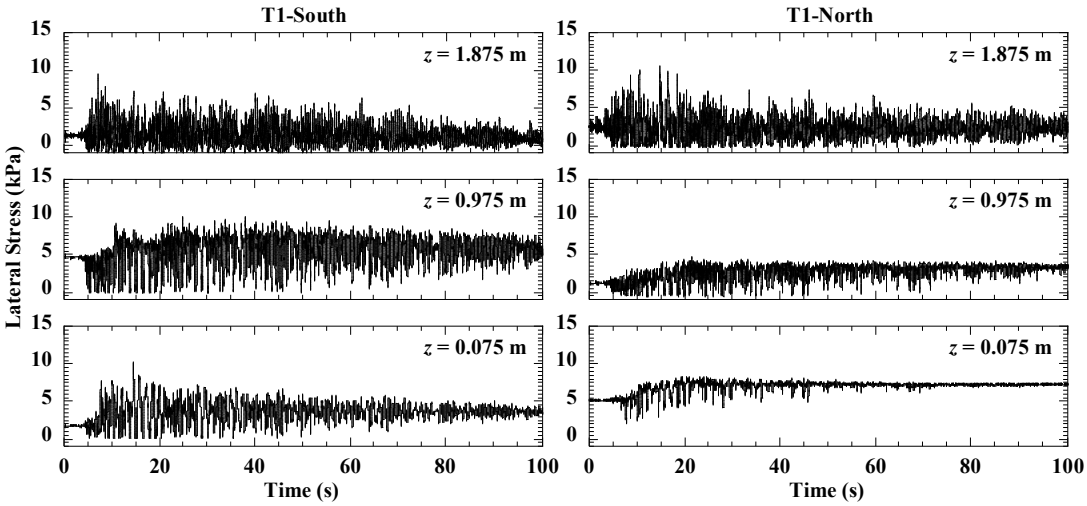

Figure 8.33 Time histories of lateral stress for T1-South and T1-North during the Maule motion in Test 6.

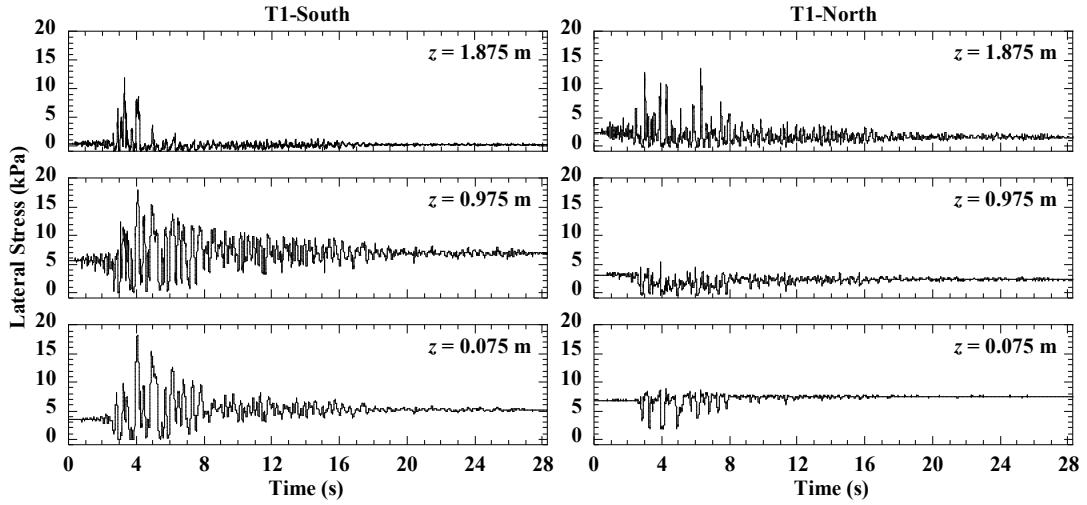

Figure 8.34 Time histories of lateral stress for T1-South and T1-North during the Northridge motion in Test 6.

Lateral stress profiles behind the wall facing for earthquake motions are shown in Figure 8.35. For the Imperial Valley motion, the maximum lateral stresses are 7.7 kPa and 8.7 kPa for T1-South and T1-North, respectively, and both occurred at the top of the wall. Similar to the vertical stress profiles, residual lateral stresses are generally larger than initial stresses. The maximum lateral stress for T1-South is 10.2 kPa at the bottom of the wall for the Maule motion and is 18.2 kPa for the Northridge motion at the same location. On the other hand, the maximum values for T1-South were observed at the top of the wall and are 10.7 kPa and 13.6 kPa for the two motions, respectively. As shaking proceeded from the Imperial Valley to the Maule to the Northridge motion, the differences between the initial and residual lateral stress profiles became smaller, and are consistent with the observations for vertical stress profiles shown in Figure 8.30.

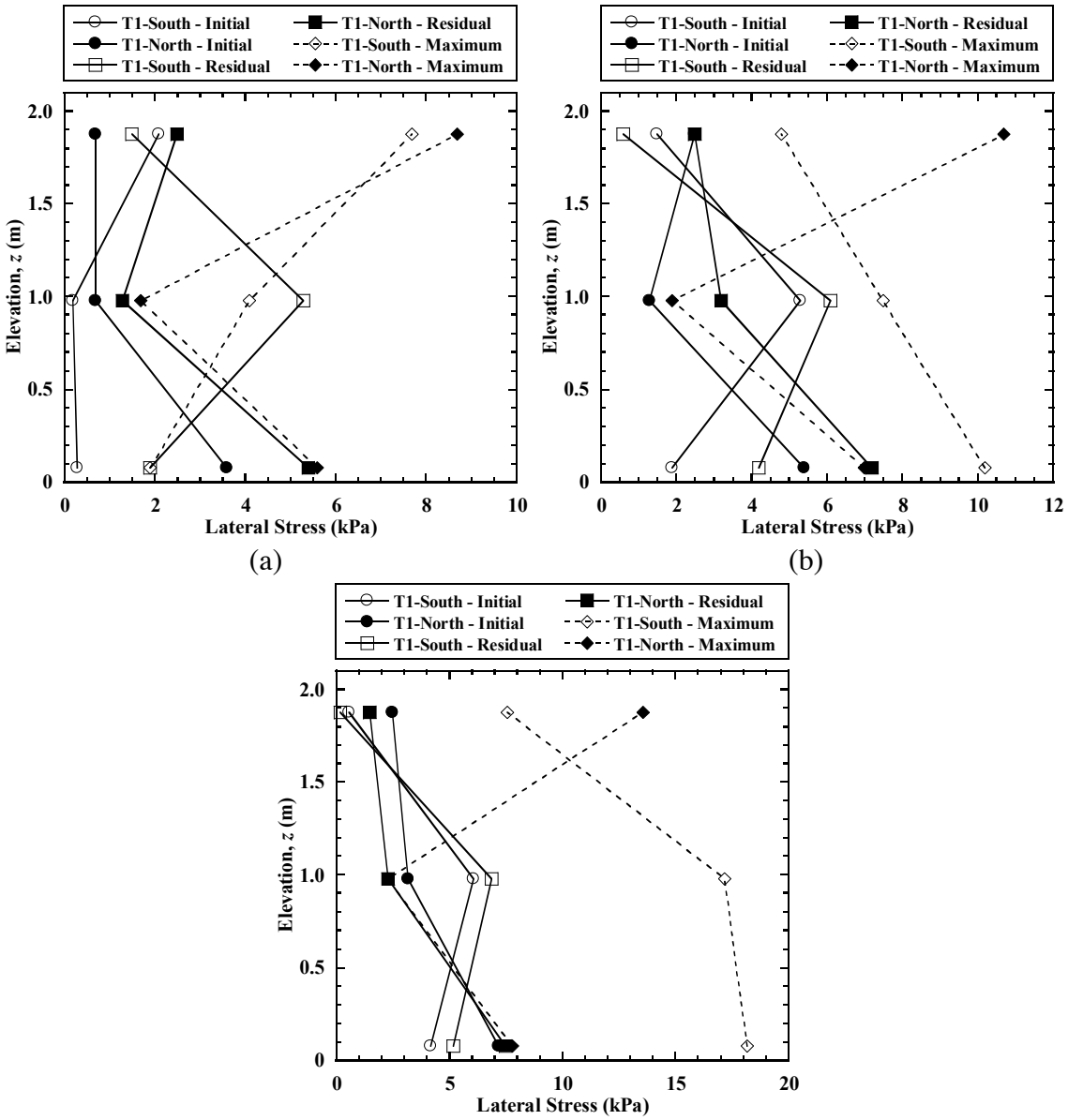

Figure 8.35 Lateral stress profiles in Test 6: (a) Imperial Valley motion; (b) Maule motion; (c) Northridge motion.

8.9 Reinforcement Strains

8.9.1 Static Loading

Reinforcement strain distributions for the geogrid layers on the south and north sides of transverse section T1 (T1-South and T1-North) for construction stages are shown in Figure 8.36. Each measurement represents the average value from a pair of top and bottom gauges, and zero strain at the free end of each reinforcement layer is also plotted.

For Stage 1, reinforcement strain distributions for T1-South and T1-North are similar, and show maximum strains at 0.1 m from each facing (near the connection) for layers 1 and 4, and at 0.33 m from each facing for layers 7 and 10. For Stage 2, reinforcement strains for layer 13 increased due to placement of bridge seat, but had little increases for the lower layers. For Stage 3, reinforcement strains increased significantly due to placement of the bridge beam, especially for the upper layers. Reinforcement strain distributions for T1-South and T1-North show similar magnitudes of strain for layers 1, 4, and 7, but significantly different magnitudes of strain for layers 10 and 13. The reinforcement strains of layers 10 and 13 under the bridge seat for T1-South are much larger than for T1-North. This is attributed to the tilting of the bridge seat toward the south side for Stage 3 as shown in Figure 8.14. The reinforcement strain at $y_s = 0.33$ m of layer 13 for T1-South reached 0.13%, which is more than twice greater than the strain value (0.06%) at $y_n = 0.33$ m for T1-North. In general, at the end of construction, maximum strain

occurred near the connections for layers 1 and 4, and at 0.33 m from each side wall facing for layers 7, 10, and 13.

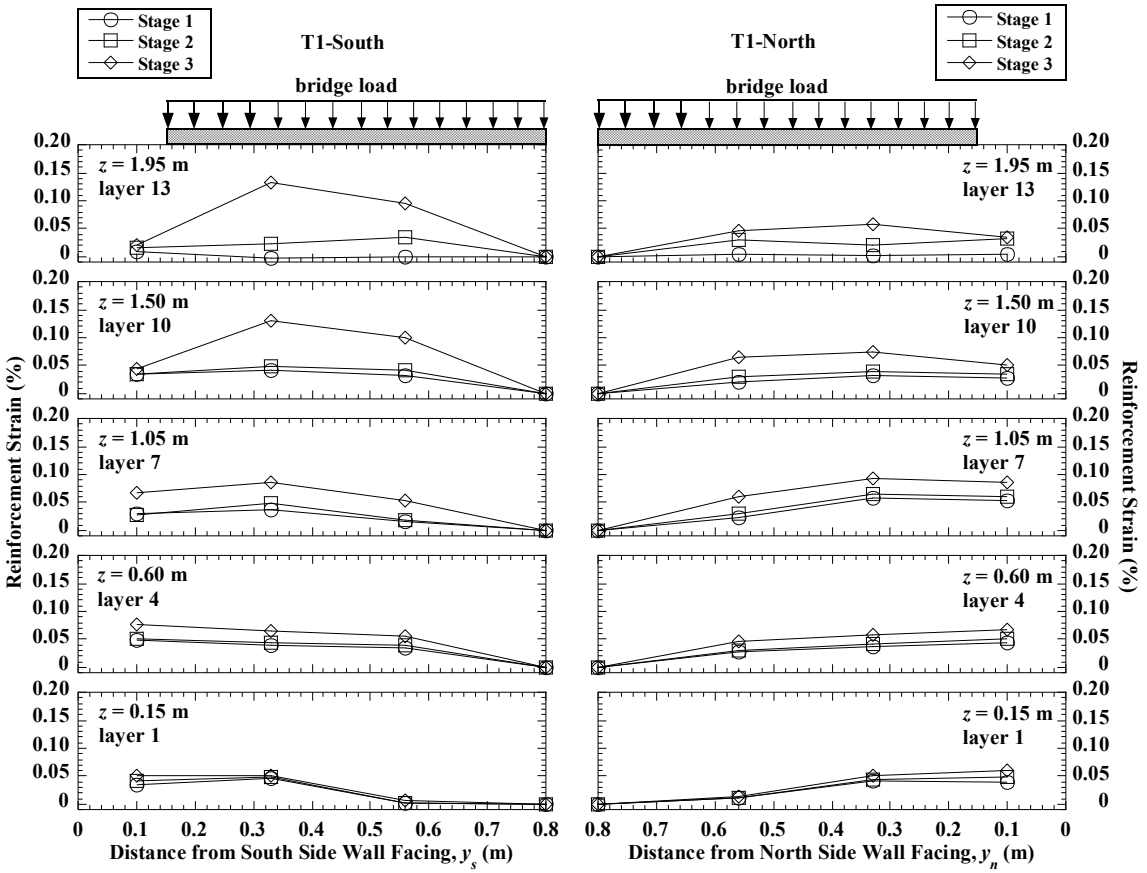

Figure 8.36 Reinforcement strain distributions of T1-South and T1-North for construction stages in Test 6.

8.9.2 Dynamic Loading

Time histories of reinforcement strain, taken as the average time histories of each strain gauge pair, for the transverse sections T1-South and T1-North during the Imperial Valley, Maule, and Northridge motions are shown in Figure 8.37, Figure 8.38, and Figure 8.39, respectively. The strain gauge pair at y_s = 0.10 m of layer 10 for T1-South was not working under dynamic loading. Similar to the facing displacements, reinforcement strains at the same elevations for T1-South and T1-North have opposite spikes (i.e., strain increase vs. decrease) at any moment in time. Reinforcement strains near the connections (i.e., y_s = 0.10 m) of layers 1, 4, and 7 for T1-South reached significant values at t = 4.09 s during the Northridge motion. Data are consistent with the dynamic maximum facing displacements (Figure 8.8) and lateral stresses (Figure 8.34) for T1-South occurred at the same time.

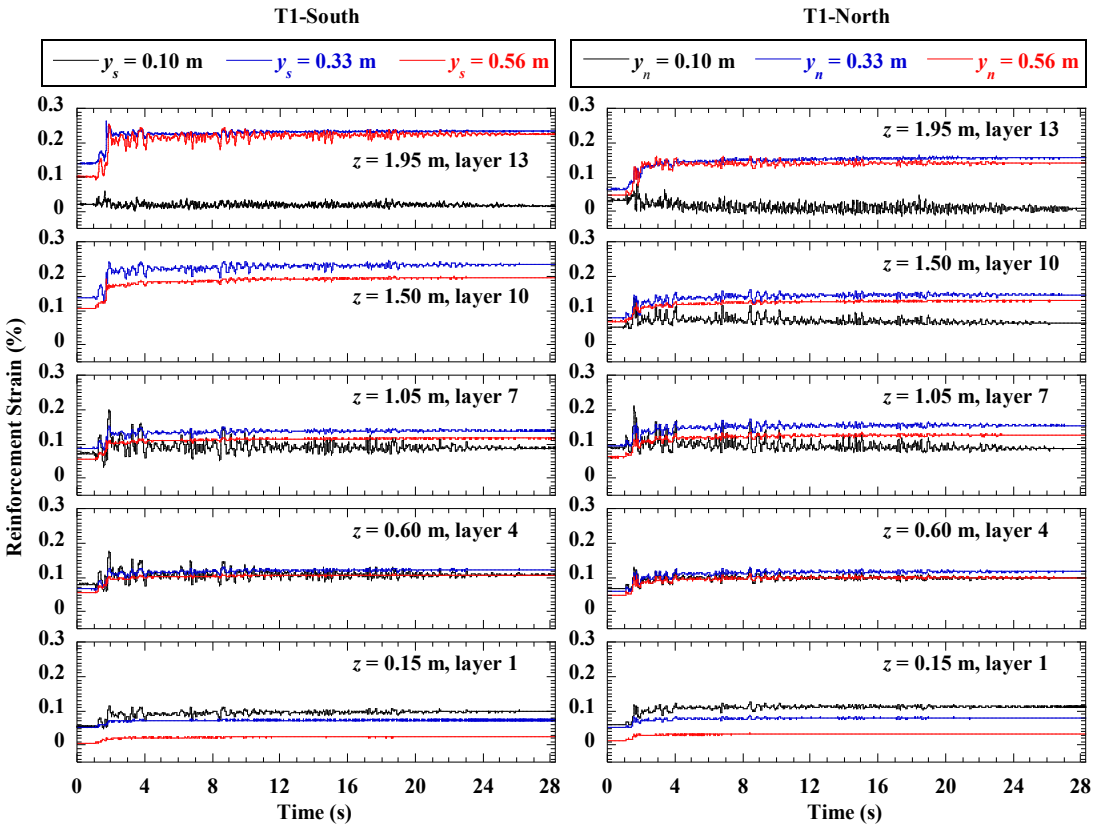

Figure 8.37 Time histories of reinforcement strain for T1-South and T1-North during the Imperial Valley motion in Test 6.

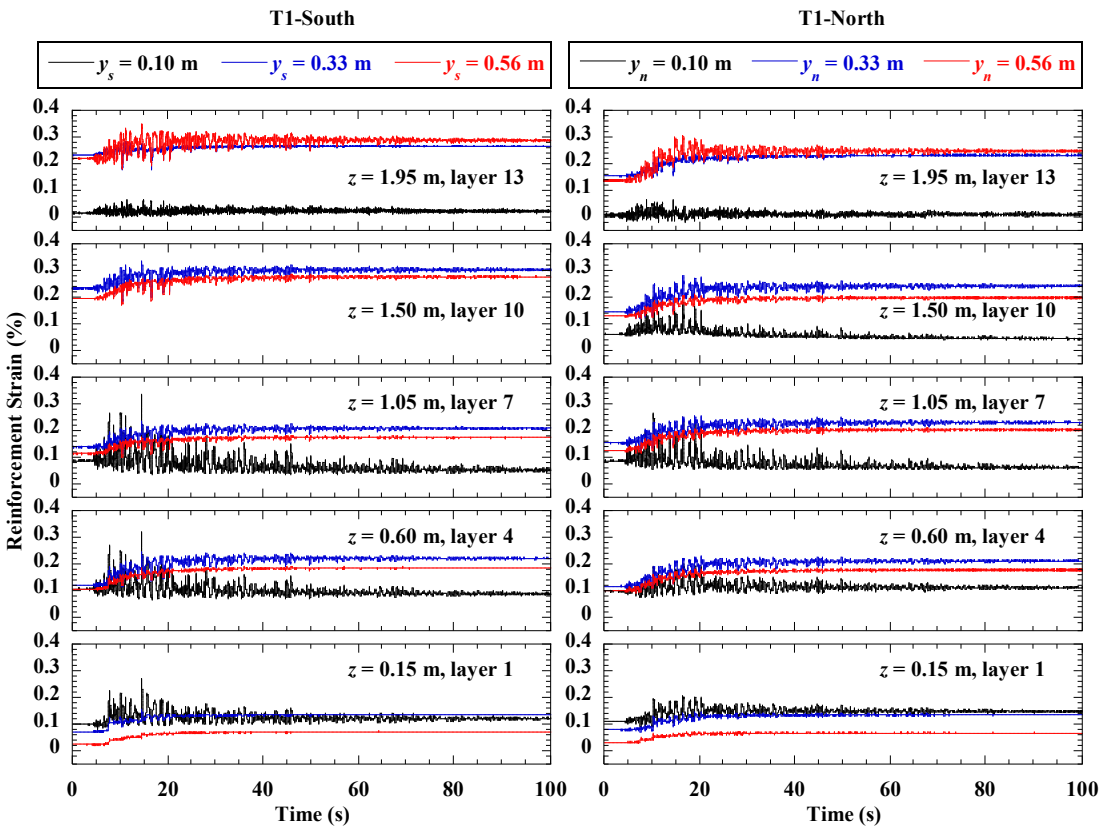

Figure 8.38 Time histories of reinforcement strain for T1-South and T1-North during the Maule motion in Test 6.

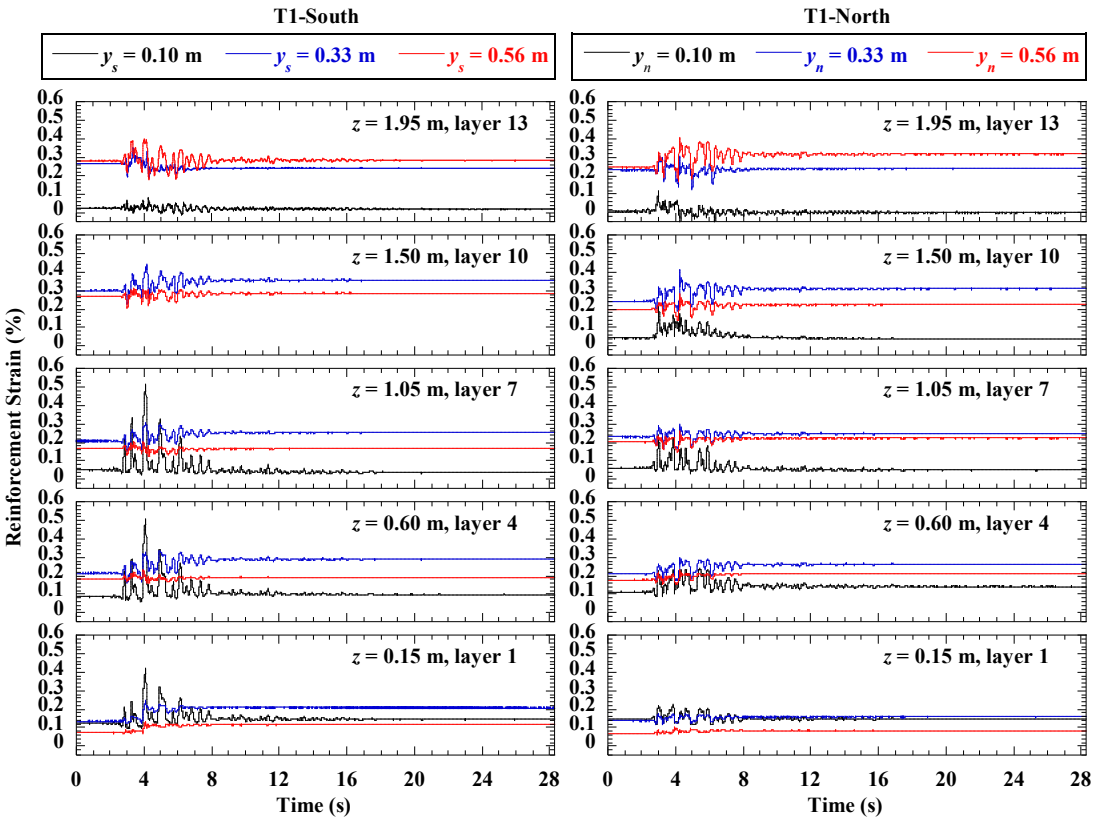

Figure 8.39 Time histories of reinforcement strain for T1-South and T1-North during the Northridge motion in Test 6.

Reinforcement strain distributions of T1-South and T1-North with the initial (before shaking), maximum (during shaking), minimum (during shaking), and residual (after shaking) values during the Imperial Valley, Maule, and Northridge motions are shown in Figure 8.40, Figure 8.41, and Figure 8.42, respectively. The reinforcement strains near the connections experienced significant increases during shaking. For instance, during the Northridge motion, the maximum strain near the connection of layer 7 for T1-South reached 0.51%, which corresponds to a dynamic strain increment of 0.47% as compared to the initial value (0.04%). However, the residual reinforcement strains near the connections for all layers are almost the same as initial values, which indicates that the dynamic

reinforcement strains were recovered after shaking. Results in Figure 8.42 indicate that reinforcement strains near the connections for the transverse sections could have significant dynamic increment during shaking. Therefore, analysis of reinforcement connection strengths for transverse section is important for seismic design.

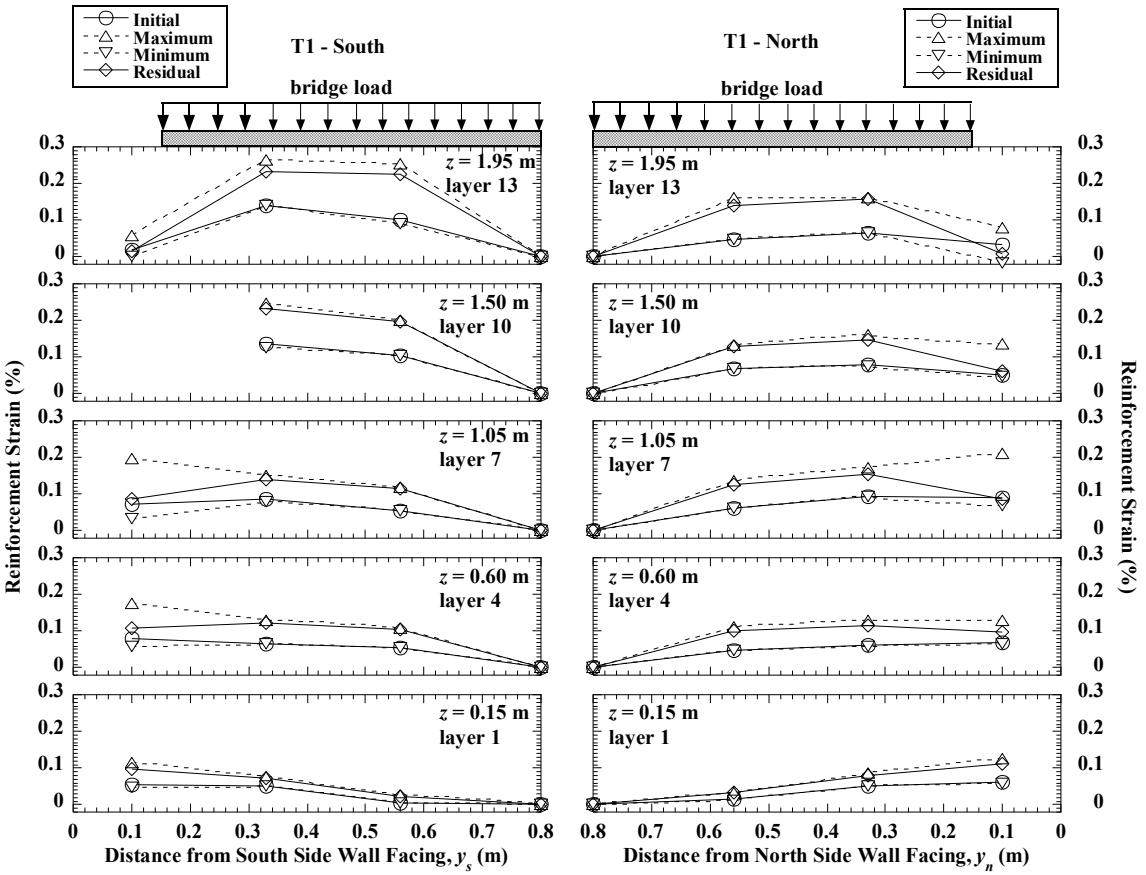

Figure 8.40 Reinforcement strain distributions for T1-South and T1-North during the Imperial Valley motion in Test 6.

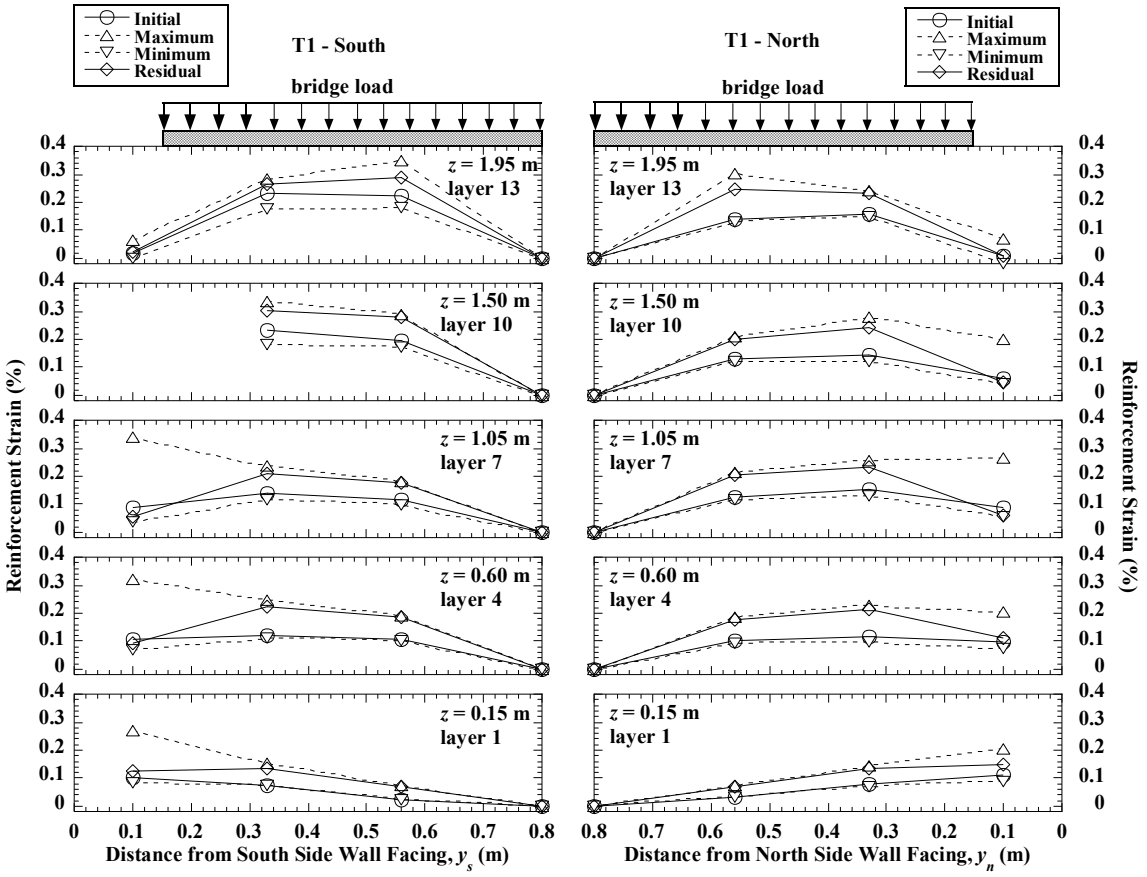

Figure 8.41 Reinforcement strain distributions for T1-South and T1-North during the Maule motion in Test 6.

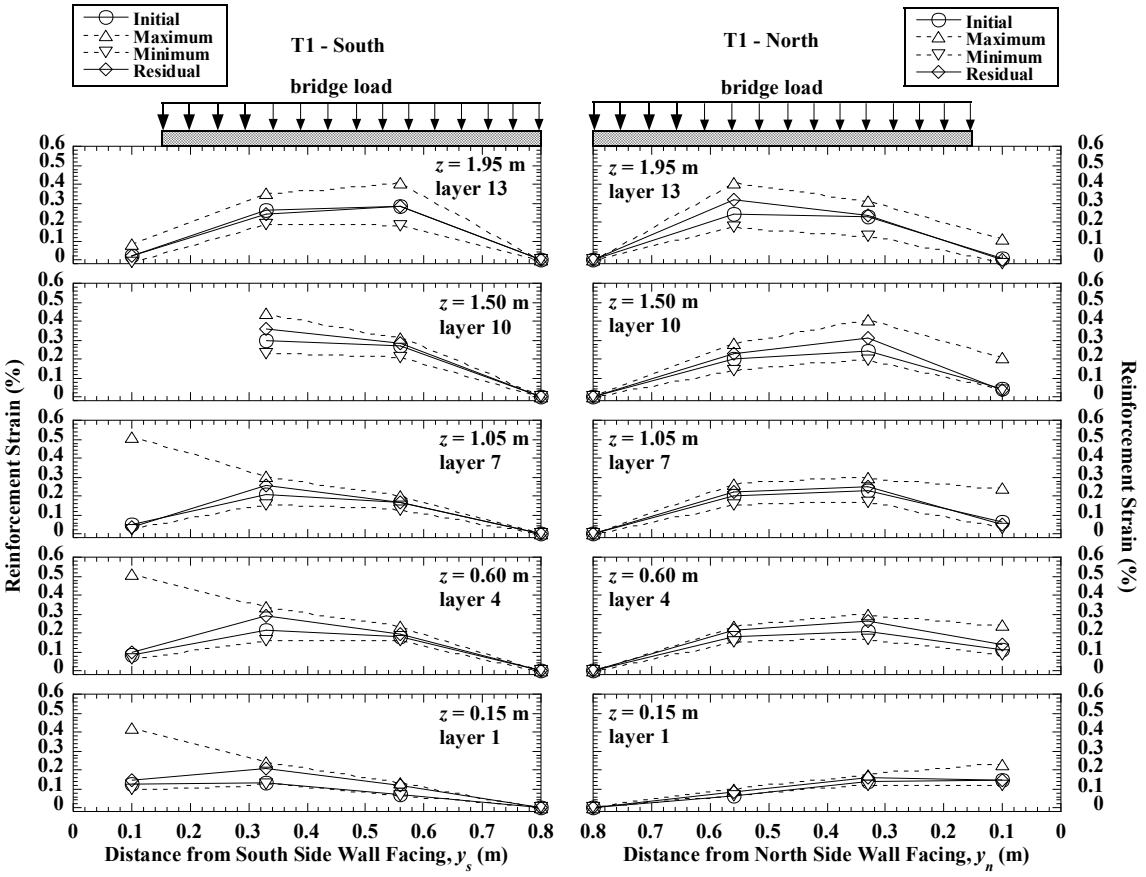

Figure 8.42 Reinforcement strain distributions for T1-South and T1-North during the Northridge motion in Test 6.

Time histories of reinforcement strain for the longitudinal section L1 during the Imperial Valley, Maule, and Northridge motions are shown in Figure 8.43, Figure 8.44, and Figure 8.45, respectively, and the reinforcement strain distributions are shown in Figure 8.46, Figure 8.47, and Figure 8.48. In general, reinforcement strains for the bottom layer experienced little change during shaking, while the mid-height and upper layers had larger dynamic strains. Most of the dynamic strains were not recovered after shaking. Results indicate that shaking in the transverse direction caused increases of strain for the

reinforcement layers in the longitudinal direction, which is consistent with the facing displacements for L1 under shaking in the transverse direction.

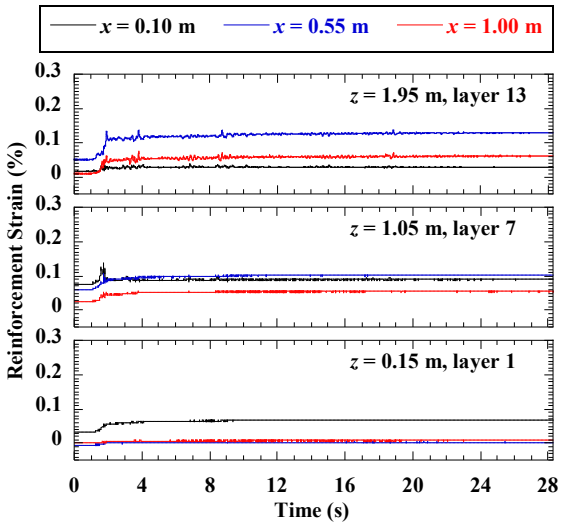

Figure 8.43 Time histories of reinforcement strain for L1 during the Imperial Valley motion in Test 6.

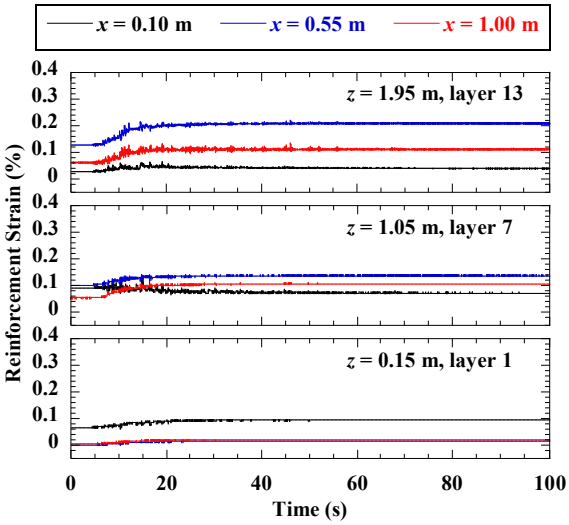

Figure 8.44 Time histories of reinforcement strain for L1 during the Maule motion in Test 6.

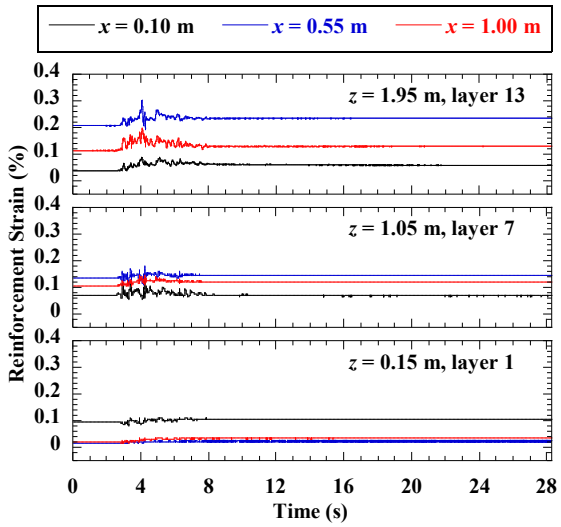

Figure 8.45 Time histories of reinforcement strain for L1 during the Northridge motion in Test 6.

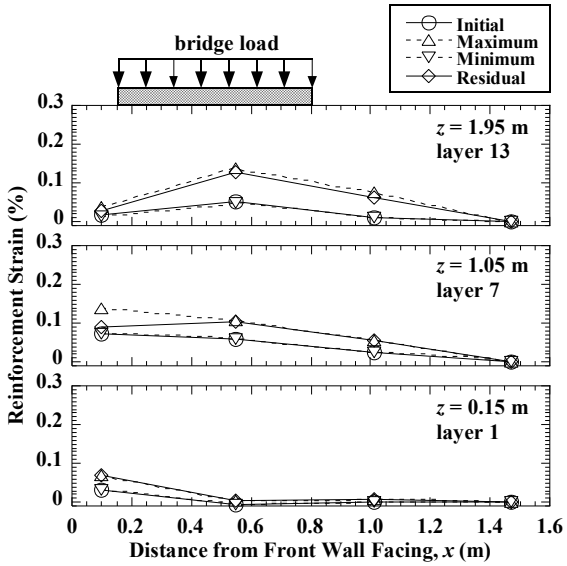

Figure 8.46 Reinforcement strain distributions for L1 during the Imperial Valley motion in Test 6.

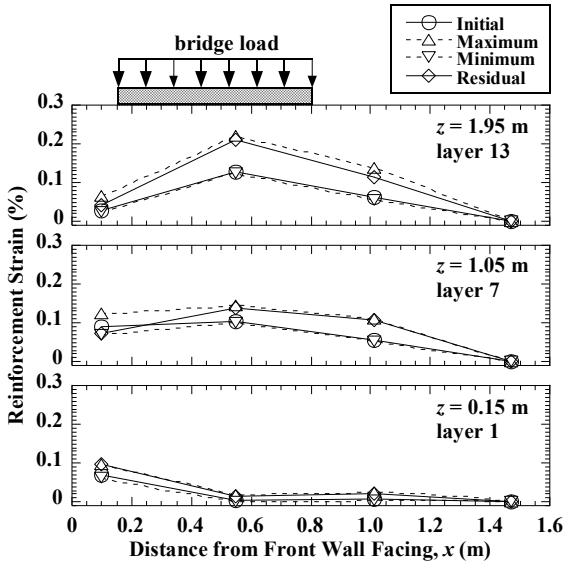

Figure 8.47 Reinforcement strain distributions for L1 during the Maule motion in Test 6.

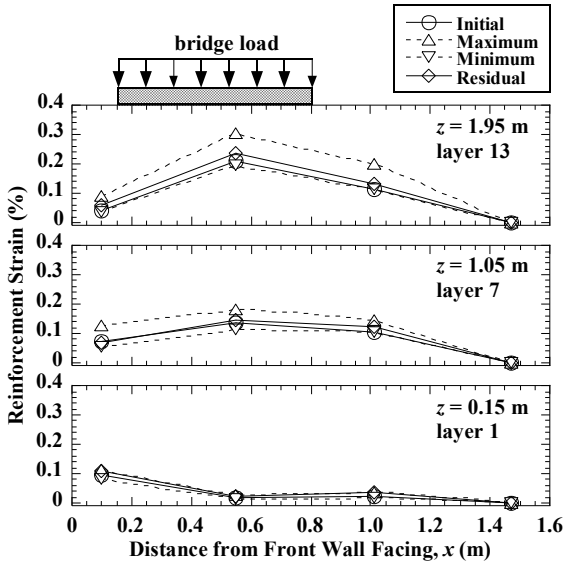

Figure 8.48 Reinforcement strain distributions for L1 during the Northridge motion in Test 6.

Residual reinforcement strain distributions for T1-South and T1-North are shown in Figure 8.49. Reinforcement strains under the bridge seat increased significantly due to successive shaking events. For instance, the reinforcement strain of 0.13% at y_s = 0.33 m

of layer 10 for T1-South at the end of construction (EOC) increased to 0.23% after the Imperial Valley motion, to 0.30% after the Maule motion, and to 0.36% after the Northridge motion. Reinforcement strains near the connections increased only for bottom layers (e.g., layer 1 for T1-South and T1-North), but not for upper layers. In general, the maximum residual strains occurred near the connection for layer 1, and under the bridge seat for other layers after earthquake motions.

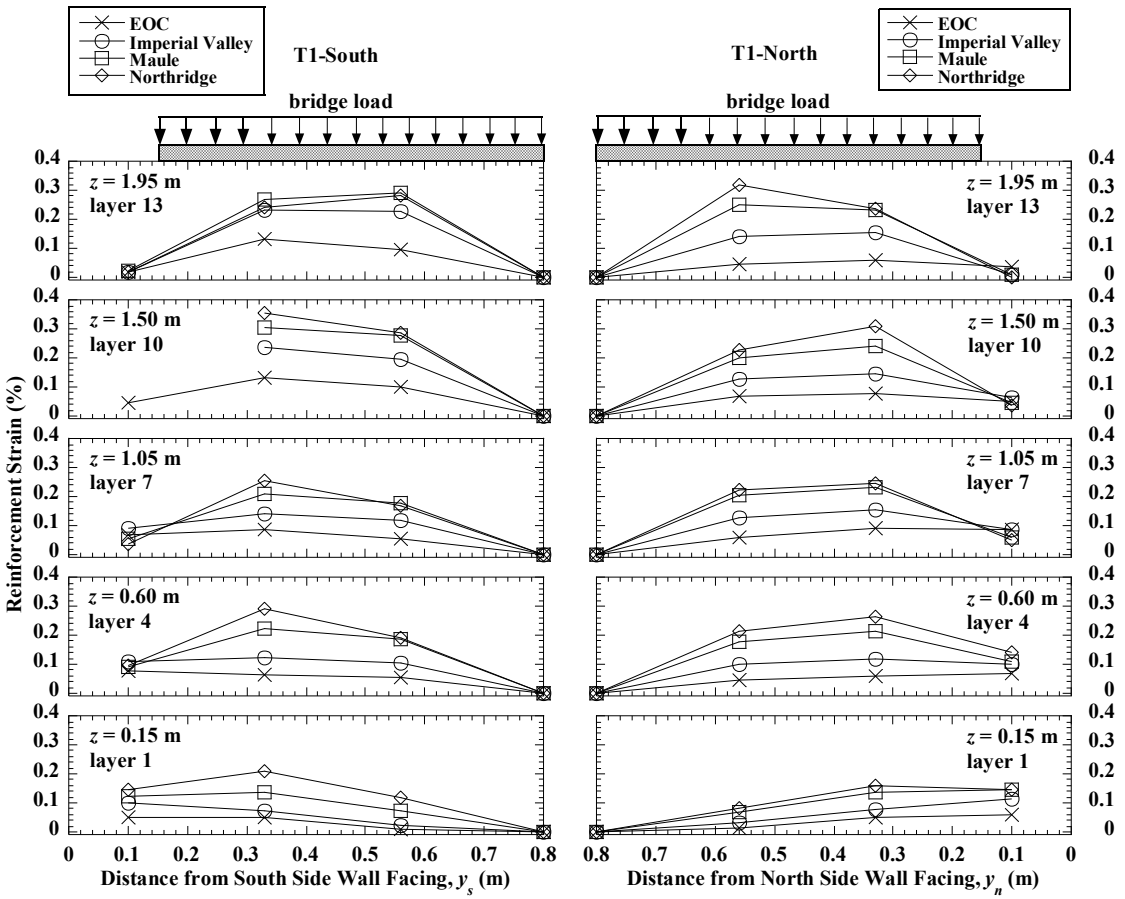

Figure 8.49 Residual reinforcement strain distributions for T1-South and T1-North in Test 6.

Residual reinforcement strain distributions for L1 are shown in Figure 8.50. Maximum strains occurred near the connection for layer 1 and under the bridge seat for layers 7 and 13 at the end of construction. Similar to T1-South and T1-North, reinforcement strains increased significantly near the connections for the bottom layer and under the bridge seat for the mid-height and upper layers after successive shaking events, but the magnitudes are generally smaller than for reinforcement layers at the same elevations for the transverse sections T1-South and T1-North.

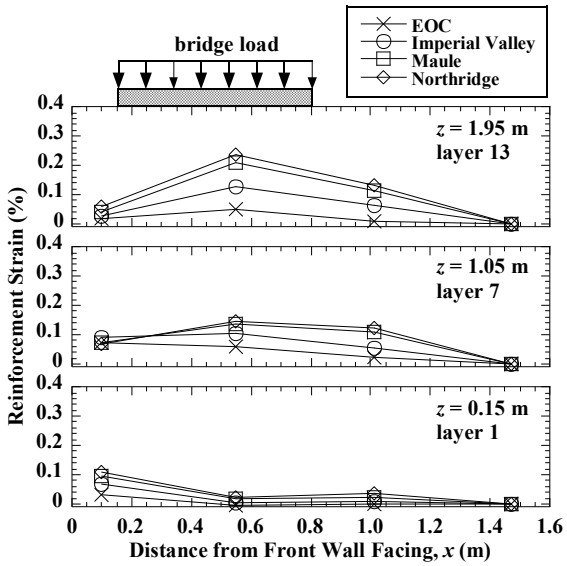

Figure 8.50 Residual reinforcement strain distributions for L1 in Test 6.

8.10 Contact Forces

The bridge beam had relative horizontal displacements with respect to the bridge seat, and thus the width of seismic joint changed during shaking. Horizontal contact forces between the bridge seat and bridge beam generate when the width of seismic joint reduces to zero. Time histories of joint width on the north side for earthquake motions are shown in Figure 8.51. The initial joint width on the north side was 24.1 mm. The total width of the two joints on the south and north sides was 50 mm, so the initial joint width on the south side was 25.9 mm. For the Imperial Valley motion, the joint width on the north side reduced to a minimum value of 14.6 mm at t = 1.64 s, and had a residual width of 20.9 mm after shaking. Joint closure was not observed for the Imperial Valley motion. For the Maule motion, the joint width on the north side reduced to zero at t = 14.91 s and generated a horizontal contact force of 5.2 kN, as shown in Figure 8.52. Joint closure on the north side occurred many times between 15 s to 50 s, and the maximum horizontal contact force was 17.4 kN at t = 16.62 s. The residual joint width was 4.9 mm after the Maule motion. For the Northridge motion, joint closure on the north side occurred only one time at t = 3.02 s and resulted in a horizontal contact force of 17.9 kN, as shown in Figure 8.52. The joint reached the maximum width of 24.7 mm at t = 4.17 s. After the Northridge motion, the joint (north side) remained open with a width of 15.1 mm, and the width of the other joint (south side) was 34.9 mm. Although the joint closure during the different earthquake motions is affected by the initial joint width at the start of each motion, and thus may

overestimate the effects of joint closure, the initial joint widths can be used in numerical simulations to properly account for these effects.

A comparison of horizontal contact forces for earthquake motions in Tests 1 and 6 is presented in Table 8.8. Joint closure was observed during the Maule motion only for Test 6, but were observed during the Northridge motion for both Tests 1 and 6. During the Northridge motion, the maximum horizontal contact force of 98.5 kN for Test 1 is much larger than the maximum value of 17.9 kN for Test 6, which indicates that shaking in the longitudinal direction resulted in greater horizontal contact forces than shaking in the transverse direction.

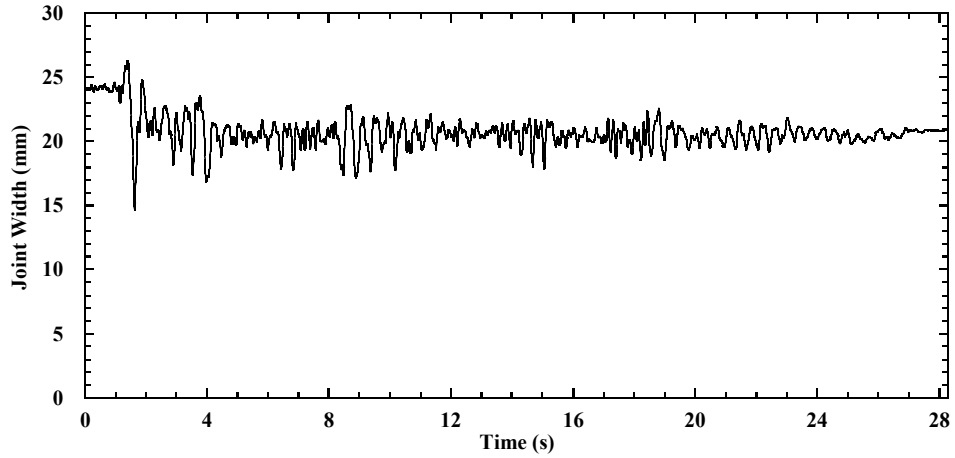

(a)

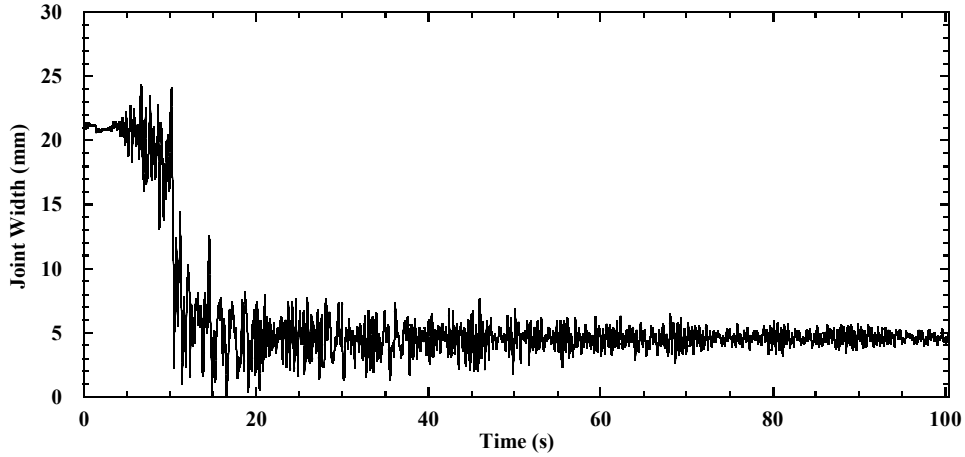

(b)

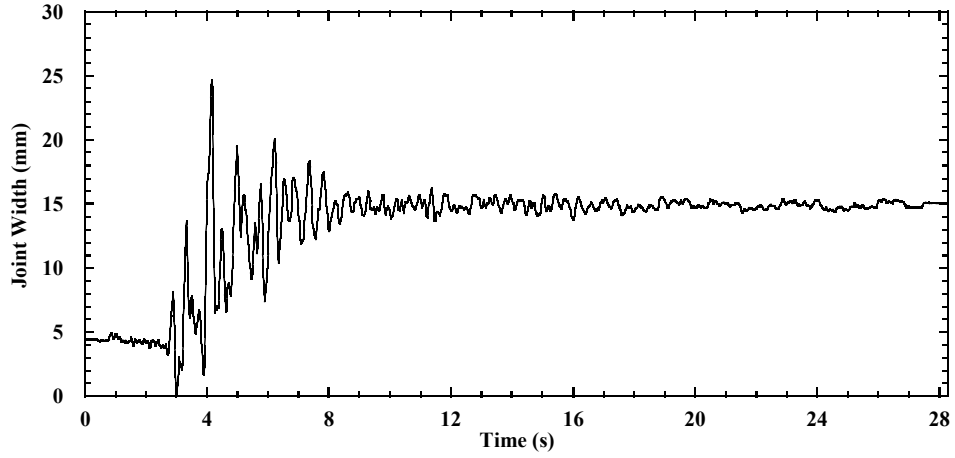

(c)

Figure 8.51 Time histories of joint width on the north side in Test 6: (a) Imperial Valley motion; (b) Maule motion; (c) Northridge motion.

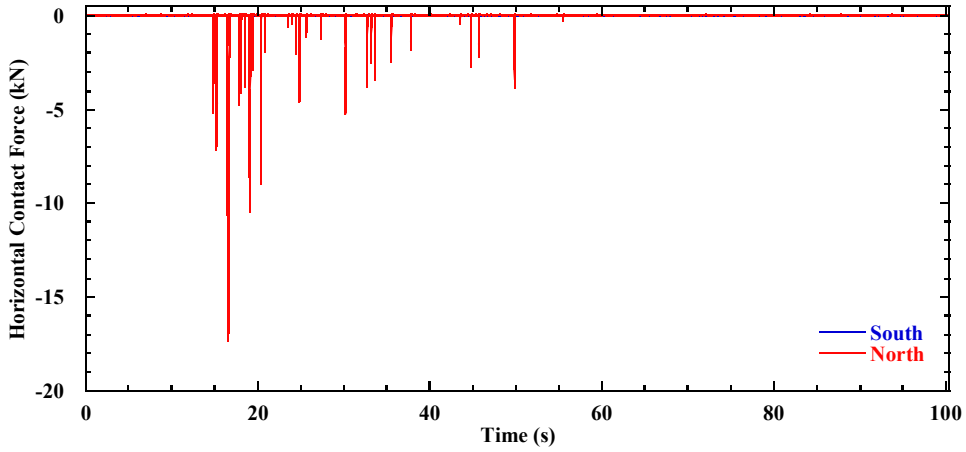

(a)

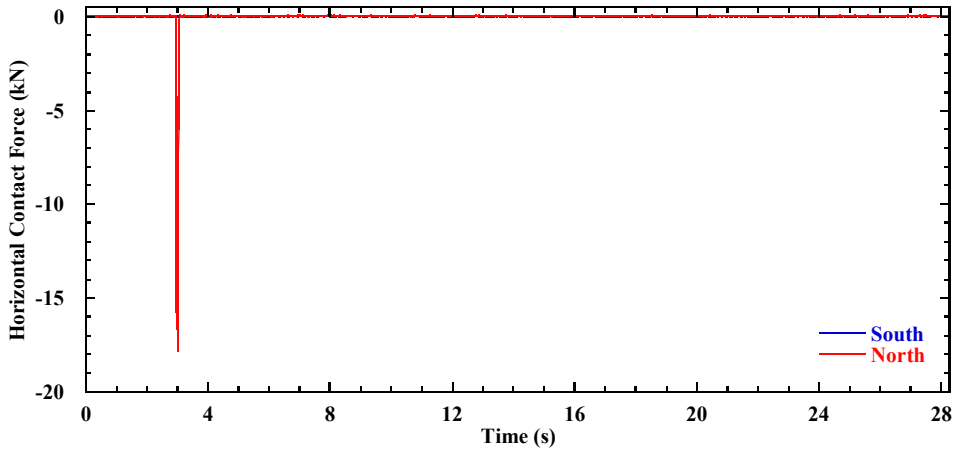

(b)

Figure 8.52 Time histories of horizontal contact forces between the bridge seat and bridge beam in Test 6: (a) Maule motion; (b) Northridge motion.

Table 8.8 Maximum horizontal contact forces in Tests 1 and 6 (model-scale).

Earthquake motion	Maximum force (kN) for Test 1 (Longitudinal shaking)	Maximum force (kN) for Test 6 (Transverse shaking)
Imperial Valley	-	-
Maule	-	17.4
Northridge	98.5[1]	17.9

[1] The Northridge motion was applied after the sinusoidal motion for Test 1.

8.11 Acknowledgements

The text below is reproduced verbatim as it appears in the acknowledgments section per the UCSD Office of Graduate Studies Formatting Requirements.

Chapter 8 of this dissertation is based on material from a manuscript under preparation for publication, tentatively titled “Large-Scale Model Tests of Geosynthetic Reinforced Soil Bridge Abutments. III: Transverse Shaking,” with a preliminary author list of Yewei Zheng, John S. McCartney, Patrick J. Fox, and P. Benson Shing (2017). The dissertation author is the first author of this paper.

Chapter 9

Conclusions and Recommendations

The following conclusions are reached as a result of: 1) the development and validation of a numerical model for GRS bridge abutments for the service limit state, including an investigation of the effects of different variables on the performance of GRS bridge abutments for service loading conditions, 2) the development of a numerical model for GRS bridge abutments for the strength limit state, including an investigation of the effects of different variables on the load-deformation and failure behavior of GRS bridge abutments up to failure condition, and 3) an experimental evaluation of the seismic response of GRS bridge abutments under an extreme event limit state (i.e., seismic loading in the longitudinal and transverse directions).

9.1 Conclusions Regarding the Service Limit State

1. Simulation results for the Founders/Meadows Parkway GRS bridge abutment, including lateral facing displacements, bridge seat settlements, lateral and vertical earth pressures, and reinforcement tensile strains and forces, were in good agreement with field measurements at various stages of construction and under service loading condition. A numerical model that considers perfectly plastic soil and linearly elastic reinforcement was found to capture the response of the GRS bridge abutments well for the service limit state.
2. The horizontal restraining forces generated by the bridge structure due to either integral construction of the bridge and abutment or frictional forces developed at the bridge/abutment contact, can have an important effect on reducing the lateral facing displacements and bridge seat settlements for GRS bridge abutments.
3. Simulation results for a geosynthetic reinforced soil-integrated bridge system (GRS-IBS) with realistic conditions for system geometry, backfill soil, geosynthetic reinforcement, and applied loads, indicated good performance at end of construction and under traffic loads. The maximum lateral facing displacement and average bridge seat settlement after construction are 18.2 mm and 25.0 mm, respectively. The corresponding abutment vertical strain (0.35%) is smaller than the maximum allowable value (0.50%) at end of construction. Differential settlement between the bridge and approach roadway is minimal. Reinforcement tensile forces increase significantly due to bridge and traffic surcharge loads,

especially for the upper reinforcement layers. A comparison between the simulated maximum reinforcement tensile forces and calculated required reinforcement strengths using current design guidelines indicates that the FHWA GRS-IBS method is more conservative than the AASHTO LRFD method.

4. Results from parametric studies indicate that reinforcement spacing, reinforcement stiffness, bridge load, and abutment height have the most significant effects on the deformations of GRS bridge abutments. Increasing the level of backfill soil compaction can effectively reduce bridge seat settlement and abutment compression, but also produces larger lateral facing displacements. Lateral facing displacements and bridge seat settlement increase with increasing bridge load and abutment height. However, the abutment vertical strain decreases with increasing abutment height due to higher stress conditions and larger soil stiffness for taller abutments. For a given level of backfill soil compaction, applied bridge load, and abutment height, simulation results indicate that, reduced reinforcement spacing and increasing reinforcement stiffness are the most effective means to reduce lateral facing displacements and bridge seat settlements. Reinforcement length and bridge seat setback distance have relatively small effects for the conditions investigated. Bearing bed reinforcement can reduce lateral facing displacements, but is unlikely to reduced bridge seat settlements under typical design-level vertical stresses.

9.2 Conclusions Regarding the Strength Limit State

1. When compared to a model with elastic-perfectly plastic soil and linearly elastic reinforcement, strain-softening behavior of backfill soil and nonlinear behavior of geogrid reinforcement have relatively small effects on the deformations of GRS bridge abutments under service loading conditions. However, these effects, especially the nonlinear behavior of reinforcement, become significant above the service limit state (ε_v = 0.5%) leading to the strength limit state (ε_v = 5%). For the condition investigated, a linearly elastic reinforcement model can capture the deformation behavior of GRS bridge abutments for service loads, but not for larger applied loads approaching failure. A nonlinear reinforcement model is needed to characterize deformation behavior of GRS bridge abutments under larger applied loads. The bearing capacity for strength limit state is slightly overestimated using a perfectly plastic soil model and is significantly overestimated using a linearly elastic reinforcement model.
2. Results from a parametric study indicates that, for the conditions simulated, reinforcement spacing, reinforcement stiffness, backfill soil friction angle, and abutment height have the most significant effects on the load-deformation behavior of GRS bridge abutments. The maximum lateral facing displacement and abutment compression decrease significantly with decreasing reinforcement spacing, increasing reinforcement stiffness and increasing backfill soil friction angle.

Reinforcement length has little effect provided that the reinforcement extends beyond the heel of bridge seat. Secondary reinforcement has a relatively small effect on the deformations under service loads, but is effective on increasing the ultimate bearing capacity of GRS bridge abutments. Backfill soil cohesion (i.e., from unsaturated conditions) has a moderate effect to reduce deformations. Increasing the backfill soil dilation angle was found to have little effect on the lateral facing displacements, but reduces the abutment compression. Bridge seat setback distance and length have relatively small effects on the deformations for service loading conditions. As the abutment height increases, the maximum lateral facing displacement and abutment compression increase, but the vertical strain decreases, which suggests that loading tests conducted on reduced-scale models may yield conservative load-deformation relationships for the design of GRS bridge abutments.

3. Reinforcement and backfill soil parameters were found to have little effect on failure surface geometry, whereas the abutment geometry parameters, including the bridge seat setback distance and length, and abutment height, were found to have important effects. The failure surface of the GRS bridge abutment manifests as a bilinear surface that starts at the heel of the bridge seat, moves vertically downward to mid-height of the GRS bridge abutment, and then linearly to the toe of the GRS bridge abutment.

9.3 Conclusions Regarding the Extreme Event Limit State

1. Experimental results indicate that the shaking table performed well in displacement-control mode for earthquake motions and the steel connection beams and sliding platform successfully transmitted table motions to the base of the support wall. Although the acceleration time history of the shaking table has larger peak acceleration values than the target input (i.e., overshooting), the pseudo-spectral accelerations of the shaking table and target motion are in good agreement for all three earthquake motions, which indicates that the shaking table adequately reproduced the salient characteristics of the target input motions.
2. For the baseline case model subjected to shaking in the longitudinal direction, the incremental maximum dynamic facing displacements during shaking increased almost linearly with elevation. However, the dynamic facing displacements were largely recovered after shaking, especially for the upper section of the wall. The maximum incremental facing displacements for the longitudinal centerline section L1 are 1.4 mm, 1.0 mm, and 3.2 mm for the Imperial Valley, Maule, and Northridge motion, respectively.
3. The average incremental residual bridge seat settlements for the baseline case are 1.4 mm for the Imperial Valley and Maule motions, and 2.2 mm for the Northridge motion, which yield incremental vertical strains of 0.07% and 0.1% for the GRS

bridge abutment. The magnitudes of residual bridge seat settlements are small and would not be expected to cause significant damages to typical bridge structures.

4. The acceleration amplification ratios, defined as the root-mean-square (RMS) acceleration at a certain location divided by the actual shaking table RMS acceleration, were observed to increase with elevation in the GRS bridge abutment. The acceleration amplification ratios increase slightly from the retained soil zone to reinforced soil zone to wall facing. The accelerations for the bridge seat and bridge beam were also observed to be amplified above the acceleration of the shaking table, and the bridge beam generally was observed to have larger amplification ratios than the bridge seat. Results indicate that the acceleration amplification ratios are different for the GRS bridge abutment, bridge seat, and bridge beam. This indicates that the assumption of a single acceleration ratio in the current design may not be appropriate.
5. Reinforcement strains for the longitudinal section were observed to increase throughout the height of the GRS bridge abutment during shaking. The location of the incremental maximum reinforcement strain was observed to be under the bridge seat in the upper reinforcement layers, but was near the facing block connections in the lower layers.
6. For shaking in the longitudinal direction, reinforcement spacing and stiffness were observed to have the greatest effects on the seismic performance of GRS bridge abutments. Facing displacements and bridge seat settlements increase significantly with increasing reinforcement spacing and decreasing reinforcement stiffness. The average incremental residual bridge seat settlement of 1.4 mm after the Imperial

Valley motion for the baseline case (reinforcement spacing S_v = 0.15 m and reinforcement stiffness $J_{5\%}$ = 380 kN/m) is smaller than the values of 5.5 mm for increased reinforcement spacing (S_v = 0.30 m and $J_{5\%}$ = 380 kN/m) and 3.2 mm for reduced reinforcement stiffness (S_v = 0.15 m and $J_{5\%}$ = 190 kN/m). Greater bridge load was observed to have larger facing displacements and bridge seat settlements for static loading conditions. However, the greater bridge load led to smaller values of lateral facing displacements and bridge seat settlements for seismic loading conditions, which is attributed to the increase in backfill soil stiffness with confining stress caused by the greater bridge load.

7. For the conditions investigated, the acceleration amplification ratios for the GRS bridge abutments were observed to increase with increasing bridge load, decreasing reinforcement spacing, and increasing reinforcement stiffness. The acceleration amplification ratio of bridge beam for reduced bridge load is larger than the other cases, which is likely due to the smaller weight of bridge beam.
8. Reinforcement strains were found to increase significantly with increasing reinforcement spacing and decreasing reinforcement stiffness. The incremental residual reinforcement strains under the bridge seat in layer 13 for the longitudinal section L1 after the Imperial Valley motion are 0.21% for increased reinforcement spacing (S_v = 0.30 m and $J_{5\%}$ = 380 kN/m) and 0.14% for reduced reinforcement stiffness (S_v = 0.15 m and $J_{5\%}$ = 190 kN/m), which are much larger than the value of 0.04% for the baseline case (S_v = 0.15 m and $J_{5\%}$ = 380 kN/m).
9. For shaking in the transverse direction, the mode shape for the transverse section during shaking is similar to the first mode of the cantilever beam with

displacements close to zero at the base and the maximum at the top. After shaking, most of the dynamic facing displacements for the transverse sections were recovered.

10. The bridge seat settlements during shaking in the transverse direction are larger than those observed during shaking in the longitudinal direction. The incremental average residual settlement for the Maule motion is 4.8 mm for shaking in the transverse direction, which is three time larger than the value of 1.4 mm for shaking in the longitudinal direction. The larger settlement for shaking in the transverse direction is likely due to the lack of soil confinement on the two sides of the bridge seat in the transverse direction, while the backwall of the bridge seat was confined by the backfill soil for the upper GRS wall in the longitudinal direction.
11. For shaking in the transverse direction, reinforcement strains near the connections with the facing blocks for the transverse sections can increase significantly, which indicates that the analysis of reinforcement-block connection strengths for the transverse section is important for seismic design.
12. Shaking in the longitudinal direction resulted in facing displacements and reinforcement strains in the transverse direction, which was attributed to a Poisson's effect associated with seismic compression of the GRS bridge abutment backfill soil under seismic loading. Similarly, shaking in the transverse direction was also found to result in lateral facing displacements and reinforcement strains in the longitudinal direction. This indicates that, in addition to the analysis of reinforcement in the direction of shaking, the analysis of reinforcement perpendicular to the direction of shaking is also important for the seismic design.

13. The width of the seismic joint was observed to vary during shaking due to sliding of the bridge beam with respect to the bridge seat (i.e., sliding on the bearing pads). Horizontal contact forces between the bridge seat and bridge beam were generated when the width of the seismic joint reduces to zero. Joint closure occurred during the Northridge motion and resulted in horizontal contact forces. The horizontal contact forces are relatively large after applying scaling factors, so they may need to be considered in the seismic design of GRS bridge abutments. However, further numerical simulations are required to understand the impact of the initial gap width for different earthquake motions.

9.4 Recommendations for Future Research

The following topics are recommended for future research:

1. More investigations are needed using 2-dimensional (2D) numerical modeling to provide guidance on the seismic design of GRS bridge abutments, including selection of design accelerations for the reinforced soil zone, retained soil zone, bridge seat, and bridge beam, maximum reinforcement tensile force line for seismic loading conditions, consideration of potential horizontal contact forces between the bridge seat and bridge beam.
2. Results of this study provide valuable experimental data that can be used for calibration of 3-dimensional (3D) numerical model of GRS bridge abutments under both static and dynamic loading. Validated numerical model can be used to investigate the effects of 3D geometry and 3D shaking on the response of GRS bridge abutments.
3. The testing program performed in this study was limited by the size and payload capacity of the UCSD Powell Structural Laboratory shaking table. However, GRS bridge abutments in the field have a much larger retained soil mass behind the reinforced soil zone, which may reduce the constraints on the deformation response of the wall in the longitudinal direction which may potentially increase wall facing displacements, bridge seat settlements, and reinforcement strains. Also, the width of the GRS bridge abutment model in this study is smaller than a proportionally-scaled GRS bridge abutment in the field, which likely changes the 3D aspects of

the dynamic response. Further, the small width of the GRS bridge abutment model investigated in this study led to an overlap of geogrid reinforcements in the transverse and longitudinal directions which may have resulted in an overall stiffer response than a scaled GRS bridge abutment in the field where such an overlap would be limited to the regions near the side walls. Additional shaking table tests on full-scale GRS bridge abutments are recommended to alleviate these effects.

4. The impact of unsaturated soil conditions on the seismic compression of the backfill soils in GRS bridge abutments is a challenging topic that requires further experimental evaluation and development of new constitutive models.

References

AASHTO. (1996). *Standard specifications for highway bridges*, 16th Edition, American Association of State Highway and Transportation Officials, Washington, D.C.

AASHTO. (2012). *AASHTO LRFD bridge design specifications*, 6th Edition, American Association of State Highway and Transportation Officials, Washington, D.C.

Abu-Hejleh, N., Outcalt, W., Wang, T., and Zornberg, J.G. (2000). "Performance of geosynthetic-reinforced walls supporting the Founders/Meadows Bridge and approaching roadway structures. Report 1: Design, materials, construction, instrumentation and preliminary results." *Report No. CDOT-DTD-R-2000-5*, Colorado DOT, Denver, CO.

Abu-Hejleh, N., Zornberg, J.G., Wang, T., McMullen, M., and Outcalt, W. (2001). "Performance of geosynthetic-reinforced walls supporting the Founders/Meadows Bridge and approaching roadway structures. Report 2: Assessment of the performance and design of the front GRS walls and recommendations for future GRS abutments." *Report No. CDOT-DTD-R-2001-12*, Colorado DOT, Denver, CO.

Abu-Hejleh, N., Zornberg, J.G., Wang, T., and Watcharamonthein, J. (2002). "Monitored displacements of unique geosynthetic-reinforced soil bridge abutments." *Geosynthetics International*, 9(1), 71-95.

Adams, M. (1997). "Performance of a prestrained geosynthetic reinforced soil bridge pier." *Mechanically Stabilized Backfill*, Balkema, Rotterdam, Netherland, 35-53.

Adams, M., Nicks, J., Stabile, T., Wu, J., Schlatter, W., and Hartmann, J. (2011a). "Geosynthetic reinforced soil integrated bridge system synthesis report." *FHWA-HRT-11-027*, U.S. DOT, Washington, D.C.

Adams, M., Nicks, J., Stabile, T., Wu, J., Schlatter, W., and Hartmann, J. (2011b). "Geosynthetic reinforced soil integrated bridge system interim implementation guide." *FHWA-HRT-11-026*, U.S. DOT, Washington, D.C.

Adams, M.T., Ooi, P.S., and Nicks, J.E. (2014). "Mini-pier testing to estimate performance of full-scale geosynthetic reinforced soil bridge abutments." *Geotechnical Testing Journal*, 37(5), 884-894.

Adams, M.T., Schlatter, W., and Stabile, T. (2007). "Geosynthetic-reinforced soil integrated abutments at the Bowman Road Bridge in Defiance County, Ohio." *Geo-Denver 2007*, ASCE, Reston, VA, USA, 1-10.

Adams, M.T., Schlatter, W., and Stabile, T. (2008). "Geosynthetic-reinforced soil integrated system." *EuroGeo4*, Paper No. 271, Edinburgh, UK.

Allen, T.M., and Bathurst, R. J. (2014a). "Design and performance of 6.3-m-high, block-faced geogrid wall designed using K-stiffness method." *Journal of Geotechnical and Geoenvironmental Engineering*, 142(2), 04013016.

Allen, T.M., and Bathurst, R.J. (2014b). "Performance of an 11 m high block-faced geogrid wall designed using the K-stiffness method." *Canadian Geotechnical Journal*, 51(1), 16-29.

Ambauen, S., Leshchinsky, B., Xie, Y., and Rayamajhi, D. (2016). "Service-state behavior of reinforced soil walls supporting spread footings: a parametric study using finite-element analysis." *Geosynthetics International*, 23(3), 156-170.

Bachus, R.C., Fragaszy, R.J., Jaber, M., Olem, K.L., Yuan, Z., and Jewell, R., (1992). Dynamic response of reinforced soil systems. *USAF Research Report F0 8635-90-C-0198*, 1 & 2, Air Force Civil Engineering Support Agency, Florida, USA.

Bathurst, R.J. (2006). "Reinforced soil retaining wall testing, modeling and design." *12th Indian Geotechnical Conference*, Madras, India, 21-32.

Bathurst, R.J., Allen, T.M., and Walters, D.L. (2002). "Short-term strain and deformation behavior of geosynthetic walls at working stress conditions." *Geosynthetics International*, 9(5-6), 451-482.

Bathurst, R.J., and Hatami, K. (1998). "Seismic response analysis of a geosynthetic reinforced soil retaining wall." *Geosynthetics International*, 5(1-2), 127-166.

Bathurst, R.J., and Hatami, K. (1999). "Numerical study of the influence of base shaking on geosynthetic reinforced retaining walls." *Geosynthetics'99*, Boston, MA, USA, 2, 963-976.

Bathurst, R.J., and Hatami, K. (2006a). "Parametric analysis of reinforced soil walls with different height and reinforcement stiffness." *8th International Conference on Geosynthetics*, Yokohama, Japan, 1343-1346.

Bathurst, R.J., and Hatami, K. (2006b). "Physical to computational modelling of reinforced soil walls under static loading." *2nd International Conference on Physical Modeling in Geotechnics*, Hong Kong, China, 1, 3-17.

Bathurst, R.J., Huang, B., and Hatami, K. (2008). "Numerical modeling of geosynthetic reinforced retaining walls." *12th International Conference of the International Association for Computer Methods and Advances in Geomechanics (IACMAG)*, Goa, India, 4071-4080.

Bathurst, R.J., Karpurapu, R.G., and Jarrett, P.M. (1992). "Finite element analysis of a geogrid reinforced soil wall." *ASCE GSP 30: Grouting, Soil Improvement and Geosynthetics*, 2, 1213-1224.

Bathurst, R.J., Nernheim, A., Walters, D.L., Allen, T.M., Burgess, P., and Saunders, D.D. (2009). "Influence of reinforcement stiffness and compaction on the performance of four geosynthetic reinforced soil walls." *Geosynthetics International*, 16(1), 43-59.

Bathurst, R.J., Vlachopoulos, N., Walters, D.L., Burgess, P.G., and Allen, T.M. (2006). "The influence of facing stiffness on the performance of two geosynthetic reinforced soil retaining walls." *Canadian Geotechnical Journal*, 43(12), 1225-1237.

Bathurst, R.J., Walters, D., Vlachopoulos, N., Burgess, P., and Allen, T.M. (2000). "Full scale testing of geosynthetic reinforced walls." *Advances in Transportation and Geoenvironmental Systems using Geosynthetics*, *GeoDenver 2000*, Denver, Colorado, 201-217.

Berg, R.R., Christopher, B.R., and Samtani, N.C. (2009). Design and construction of mechanically-stabilized earth walls and reinforced soil slopes – Volume I. *FHWA-NHI-10-024*, FHWA, U.S. Department of Transportation, Washington, D.C., USA.

Bolton, M. D. (1986). "The strength and dilatancy of sands." *Geotechnique*, 36(1), 65-78.

Boyle, S.R., Gallagher, M., and Holtz, R.D. (1996) "Influence of strain rate, specimen length and confinement on measured geotextile properties." *Geosynthetics International*, 3(2), 205-225.

Budhu, M., and Halloum, M. (1994). "Seismic external stability of geotextile reinforced walls." *5th International Conference on Geotextiles, Geomembranes and Related Products*, Singapore, 529-532.

Cai, Z., and Bathurst, R.J. (1995). "Seismic response analysis of geosynthetic reinforced soil segmental retaining walls by finite element method." *Computers and Geotechnics*, 17(4), 523-546.

Caltrans. (1994). *Memos to Designers 7-1*. California DOT, Sacramento, CA.

Chida, S., Minami, K., and Adachi, K. (1982). "Test de stabilité de remblais en Terre Armée". (translated from Japanese)

Collin, J.G., Chouery-Curtis, V.E., and Berg, R.R. (1992). "Field observation of reinforced soil structures under seismic loading." *Earth Reinforcement Practice*, 1, Balkema, Rotterdam, Netherlands, 223–228.

Damians, I.P., Bathurst, R.J., Josa, A., Lloret, A. (2014). "Numerical study of the influence of foundation compressibility and reinforcement stiffness on the behavior of reinforced soil walls." *International Journal of Geotechnical Engineering*, 8(3), 247-259.

Duncan, J.M., Byrne, P., Wong, K.S., and Mabry, P. (1980). Strength, stress-strain and bulk modulus parameters for finite element analysis of stresses and movements in soil masses. *Report No. UCB/GT/80-01*, University of California, Berkeley, CA, USA.

Ehrlich, M., and Mirmoradi, S.H. (2013). "Evaluation of the effects of facing stiffness and toe resistance on the behavior of GRS walls." *Geotextiles and Geomembranes*, 40, 28-36.

Ehrlich, M., Mirmoradi, S.H., and Saramago, R.P. (2012). "Evaluation of the effect of compaction on the behavior of geosynthetic-reinforced soil walls." *Geotextiles and Geomembranes*, 34, 108-115.

El-Emam, M., and Bathurst, R.J. (2004). "Experimental design, instrumentation and interpretation of reinforced soil wall response using a shaking table." *International Journal of Physical Modelling in Geotechnics*, 4(4), 13-32.

El-Emam, M., and Bathurst, R.J. (2005). "Facing contribution to seismic response of reduced-scale reinforced soil walls." *Geosynthetics International*, 12(5), 215-238.

El-Emam, M., and Bathurst, R.J. (2007). "Influence of reinforcement parameters on the seismic response of reduced-scale reinforced soil retaining walls." *Geotextiles and Geomembranes*, 25(1), 33-49.

El-Emam, M., Bathurst, R.J., and Hatami, K. (2004). "Numerical modeling of reinforced soil retaining walls subjected to base acceleration." *13th World Conference on Earthquake Engineering*, Vancouver, BC, Canada, Paper No. 2621.

Fakharian, K., and Attar, I.H. (2007). "Static and seismic numerical modeling of geosynthetic-reinforced soil segmental bridge abutments." *Geosynthetics International*, 14(4), 228-243.

Fairless, G.J. (1989). "Seismic performance of reinforced earth walls." *Ph.D. Thesis*, University of Canterbury, Christchurch, New Zealand.

FLAC Version 7.0. (2011). Itasca Consulting Group, Minneapolis, MN, USA.

Fox, P.J., Andrew, A.C., Elgamal, A., Greco, P., Isaacs, D., Stone, M., and Wong, S. (2015). "Large soil confinement box for seismic performance testing of geo-structures." *Geotechnical Testing Journal*, 38(1), 72-84.

Fox, P.J., Rowland, M.G., Scheithe, J.R., Davis, K.L., Supple, M.R., and Crow, C.C. (1997). "Design and evaluation of a large direct shear machine for geosynthetic clay liners." *Geotechnical Testing Journal*, 20(3), 279-288.

Fox, P.J., Nye, C.J., Morrison, T.C., Hunter, J.G., and Olsta, J.T. (2006). "Large dynamic direct shear machine for geosynthetic clay liners." *Geotechnical Testing Journal*, 29(5), 392-400.

Gebrenegus, T., Nicks, J., and Adams, M. (2015). "Large diameter triaxial testing of AASHTO open graded aggregates and the effect of relative density on strength." *IFCEE 2015, International Foundations Congress & Equipment Exposition 2015*, ASCE, Reston, VA, USA, 1870-1879.

Gotteland, P., Gourc, J.P., and Villard, P. (1997). "Geosynthetic reinforced structures as bridge abutments: Full scale experimentation and comparison with modelisations." *Mechanically Stabilized Backfill*, Balkema, Rotterdam, Netherland, 25-34.

Guler, E., Cicek, E., Demirkan, M.M., Hamderi, M. (2012). "Numerical analysis of reinforced soil walls with granular and cohesive backfills under cyclic loads." *Bulletin of Earthquake Engineering*, 10(3), 793-811.

Guler, E., and Enunlu, A.K. (2009). "Investigation of dynamic behavior of geosynthetic reinforced soil retaining structures under earthquake loads." *Bulletin of Earthquake Engineering*, 7(3), 737-777.

Guler, E., Hamderi, M., and Demirkan, M.M. (2007). "Numerical analysis of reinforced soil-retaining wall structures with cohesive and granular backfills." *Geosynthetics International*, 14(6), 330–345.

Guler, E., and Selek, O (2014). "Reduced-scale shaking table tests on geosynthetic-reinforced soil walls with modular facing." *Journal of Geotechnical and Geoenvironmental Engineering*, 10.1061/(ASCE)GT.1943-5606.0001102, 04014015.

Hatami, K., and Bathurst, R.J. (2000a). "Effect of structural design on fundamental frequency of reinforced-soil retaining walls." *Soil Dynamics and Earthquake Engineering*, 19(3), 137-157.

Hatami, K., and Bathurst, R.J. (2000b). "Investigation of seismic response of reinforced soil retaining walls." *4th International Conference on Recent Advances in Geotechnical Earthquake Engineering and Soil Dynamics*, San Diego, CA, USA, Paper No. 7.18.

Hatami, K., and Bathurst, R.J. (2005a). "Development and verification of a numerical model for the analysis of geosynthetic reinforced soil segmental walls under working stress conditions." *Canadian Geotechnical Journal*, 42(4), 1066-1085.

Hatami, K., and Bathurst, R.J. (2005b). "Verification of a numerical model for reinforced soil segmental retaining walls." *GeoFrontiers 2005: Slopes and Retaining Structures under Seismic and Static Conditions*, Austin, Texas, USA.

Hatami, K., and Bathurst, R.J. (2005c). "Parametric analysis of reinforced soil walls with different backfill material properties." *North American Geosynthetics Society 2005 Conference*, Las Vegas, Nevada, USA.

Hatami, K., and Bathurst, R.J. (2006). "Numerical model for reinforced soil segmental walls under surcharge loading." *Journal of Geotechnical and Geoenvironmental Engineering*, 132(6), 673-684.

Helwany, S.M.B., Budhu, M., and McCallen, D. (2001). "Seismic analysis of segmental retaining walls. I: Effects of facing details." *Journal of Geotechnical and Geoenvironmental Engineering*, 127(9), 750-756.

Helwany, S.M.B., and McCallen, D. (2001). "Seismic analysis of segmental retaining walls. II: Model verification." *Journal of Geotechnical and Geoenvironmental Engineering*, 127(9), 741-749.

Helwany, S.M.B., Reardon, G., and Wu, J.T.H. (1999). "Effects of backfill on the performance of GRS retaining walls." *Geotextiles and Geomembranes*, 17, 1-16.

Helwany, S.M.B., Wu, J.T.H., and Froessl, B. (2003). "GRS bridge abutments – an effective means to alleviate bridge approach settlement." *Geotextiles and Geomembranes*, 21, 177-196.

Helwany, S.M.B., Wu, J.T.H., and Kitsabunnarat, A. (2007). "Simulating the behavior of GRS bridge abutments." *Journal of Geotechnical and Geoenvironmental Engineering*, 133(10), 1129-1240.

Helwany, S.M.B., Wu, J.T.H., and Meinholz, P. (2012). Seismic design of geosynthetic-reinforced soil bridge abutments with modular block facing. *NCHRP Web-Only Document 187*, Transportation Research Board, Washington, D.C.

Ho, S.K., and Rowe, R.K. (1997). "Effect of wall geometry on the behaviour of reinforced soil walls." *Geotextiles and Geomembranes*, 14(10), 521-541.

Huang, B., Bathurst, R.J., and Hatami, K. (2009). "Numerical study of reinforced soil segmental walls using three different constitutive soil models." *Journal of Geotechnical and Geoenvironmental Engineering*, 135(10), 1486-1498.

Huang, B., Bathurst, R.J., Hatami, K., and Allen, T.M. (2010). "Influence of toe restraint on reinforced soil segmental walls." *Canadian Geotechnical Journal*, 47(8), 885-904.

Iai, S. (1989) "Similitude for shaking table tests on soil-structure-fluid models in 1 g gravitational fields." *Soils and Foundations*, 29(1), 105-118.

Iwamoto, M.K., Ooi, P.S., Adams, M.T., and Nicks, J.E. (2015). "Composite properties from instrumented load tests on mini-piers reinforced with geotextiles." *Geotechnical Testing Journal*, 38(4), 397-408.

Karpurapu, R.G., and Bathurst, R.J. (1995). "Behaviour of geosynthetic reinforced soil retaining walls using the finite element method." *Computers and Geotechnics*, 17(3), 279-299.

Ketchart, K., and Wu, J.T.H. (1997). "Performance of geosynthetic-reinforced soil bridge pier and abutment, Denver, Colorado, USA." *Mechanically Stabilized Backfill*, Balkema, Rotterdam, Netherland, 101-116.

Khosravi, A., Ghayoomi, M., McCartney, J.S., and Ko, H.-Y. (2010). "Impact of effective stress on the dynamic shear modulus of unsaturated sands." *GeoFlorida 2010: Advances in Analysis, Modeling & Design*, Orlando, FL, 410-419.

Koga, Y., Itoh, Y., Washida, S., and Shimazu, T. (1988). "Seismic resistance of reinforced embankment by model shaking tests." *International Geotechnical Symposium on Theory and Practice of Earth Reinforcement*, *IS-Kyushu'88*, Fukuoka, Balkema, Rotterdam, 413-418.

Koga, Y, and Washida, S. (1992). "Earthquake resistant design method of geotextile reinforced embankments." *International Geotechnical Symposium on Theory and Practice of Earth Reinforcement*, *IS-Kyushu'92*, Fukuoka, 255-259.

Koseki, J., Munaf, Y., Tatsuoka, F., Tateyama, M., Kojima, K., and Sato, T. (1998). "Shaking and tilt table tests of geosynthetic-reinforced soil and conventional-type retaining walls." *Geosynthetics International*, 5(1-2), 73-96.

Kost, A.D., Filz, G.M., Cousins, T., and Brown, M.C. (2014). "Full-scale investigation of differential settlements beneath a geosynthetic-reinforced soil bridge abutment." *Transportation Research Record*, No. 2462, 28-36.

Kramer, S. L., *Geotechnical Earthquake Engineering*, Prentice Hall, Upper Saddle River, NJ, 1996, 653pp.

Krishna, A.M., and Latha, G.M. (2009). "Seismic behavior of rigid-faced reinforced soil retaining wall models: reinforcement effect." *Geosynthetics International*, 16(5), 364-373.

Latha, G.M., and Krishna, A.M. (2008). "Seismic response of reinforced soil retaining wall models: Influence of backfill relative density." *Geotextiles and Geomembranes*, 26, 335-349.

Latha, G.M., and Santhanakumar, P. (2015). "Seismic response of reduced-scale modular block and rigid faced reinforced walls through shaking table tests." *Geotextiles and Geomembranes*, 43(4), 307-316.

Lee, K.Z.Z., and Chang, N.Y. (2012). "Predictive modeling on seismic performances of geosynthetic-reinforced soil walls." *Geotextiles and Geomembranes*, 35, 25-40.

Lee, K.Z.Z., Chang, N.Y., and Ko, H.Y. (2010). "Numerical simulation of geosynthetic-reinforced soil walls under seismic shaking." *Geotextiles and Geomembranes*, 28, 317-334.

Lee, W. (2000). "Internal stability of analyses of geosynthetic reinforced retaining walls." *Ph.D. Thesis*, University of Washington, Seattle, USA.

Lee, K.Z.Z., and Wu, J.T.H. (2004). "A synthesis of case histories on GRS bridge-supporting structures with flexible facing." *Geotextiles and Geomembranes*, 22(4), 181-204.

Leshchinsky, D, and Vulova, C. (2001). "Numerical investigation of the effects of geosynthetic spacing on failure mechanisms in MSE block walls." *Geosynthetics International*, 8(4), 343-365.

Ling, H.I. (2003). "Finite element applications to reinforced soil retaining walls – simplistic versus sophisticated analyses." *ASCE GSP 143: Geomechanics: Testing, Modeling and Simulation*, 217-236.

Ling, H.I., Cardany, C., Sun, L-X., and Hashimoto, H. (2000). "Finite element analysis of a geosynthetic-reinforced soil retaining wall with concrete-block facing." *Geosynthetics International*, 7(2), 137-162.

Ling, H.I., and Leshchinsky, D. (2003). "Finite element parametric studies of the behavior of segmental block reinforced soil retaining walls." *Geosynthetics International*, 10(3), 77-94.

Ling, H.I., Leshchinsky, D., and Chou, N.N.S. (2001). "Post-earthquake investigation on several geosynthetic-reinforced soil retaining walls and slopes during the Ji-Ji earthquake of Taiwan." *Soil Dynamics and Earthquake Engineering*, 21, 297-313.

Ling, H.I., Leshchinsky, D., Mohri, Y., and Wang, J. (2012). "Earthquake response of reinforced segmental retaining walls backfilled with substantial percentage of fines." *Journal of Geotechnical and Geoenvironmental Engineering*, 138(8), 934-944.

Ling, H.I., Liu, H., Kaliakin, V., and Leshchinsky, D. (2004). "Analyzing dynamic behavior of geosynthetic-reinforced soil retaining walls." *Journal of Engineering Mechanics*, 130(8), 911-920.

Ling, H.I., Mohri, Y., Leshchinsky, D., Burke, C., Matsushima, K., and Liu, H. (2005a). "Large scale shaking table tests on modular block reinforced soil retaining wall." *Journal of Geotechnical and Geoenvironmental Engineering*, 131(4), 465-476.

Ling, H.I., Liu, H., and Mohri, Y. (2005b). "Parametric studies on the behavior of reinforced soil retaining walls under earthquake loading." *Journal of Engineering Mechanics*, 131(10), 1056-1065.

Ling, H.I., Yang, S., Leshchinsky, D., Liu, H., and Burke, C. (2010). "Finite-element simulations of full-scale modular-block reinforced soil retaining walls under earthquake loading." *Journal of Engineering Mechanics*, 136(5), 653-661.

Liu, H., and Ling, H.I. (2012). "Seismic responses of reinforced soil retaining walls and the strain softening of backfill soils." *International Journal of Geomechanics*, 12(4), 351-356.

Liu, H., Wang, X., and Song, E. (2010). "Centrifuge testing of segmental geosynthetic-reinforced soil retaining walls subjected to modest seismic loading." *GeoFlorida 2010: Advanced in Analysis, Modeling & Design*, Florida, USA, 2992-2998.

Lu, N., Godt, J.W., and Wu, D.T. (2010). "A closed-form equation for effective stress in unsaturated soil." *Water Resources Research*, 46, W05515, 10.1029/2009WR008646.

Matsuo, O., Tsutsumi, T., Yokoyama, K., and Saito, Y. (1998). "Shaking table tests and analyses of geosynthetic-reinforced soil retaining walls." *Geosynthetics International*, 5(1-2), 97-126.

McCartney, J.S., Shing, P.B., Fox, P.J., Zheng, Y., and Rong, W. (2018). *Interaction of MSE abutments with bridge superstructures under seismic loading – Phase II*, California Department of Transportation (Caltrans), Sacramento, CA, USA (in preparation).

Mirmoradi, S.H., and Ehrlich, M. (2015). "Numerical evaluation of the behavior of GRS walls with segmental block facing under working stress conditions." *Journal of Geotechnical and Geoenvironmental Engineering*, 141(3), 04014109.

Mirmoradi, S.H., and Ehrlich, M. (2016). "Evaluation of the effect of toe resistance on GRS walls." *Transportation Geotechnics*, 8, 35-44.

Mirmoradi, S.H., and Ehrlich, M., (2017). "Effects of facing, reinforcement stiffness, toe resistance, and height on reinforced walls." *Geotextiles and Geomembranes*, 45(1), 67-76.

Mirmoradi, S.H., Ehrlich, M., and Dieguez, C. (2016). "Evaluation of the combined effect of toe resistance and facing inclination on the behavior of GRS walls." *Geotextiles and Geomembranes*, 44(3), 287-294.

Murata, O., Tateyama, M., Tatsuoka, F. (1994). "Shaking table tests on a large geosynthetic-reinforced soil retaining walls model." *Recent Case Histories of Permanent Geosynthetic-reinforced Soil Walls*, *Seiken Symposium*, Tokyo, 259-264.

Nagel, R.B., and Elms, D.G. (1985). "Seismic behavior of reinforced earth walls." *Research Report No. 85-4*, University of Canterbury, Christchurch, New Zealand.

Nicks, J.E., Adams, M.T., Ooi, P.S.K., and Stabile, T. (2013a). "Geosynthetic reinforced soil performance testing – axial load deformation relationships." *FHWA-HRT-13-066*, U.S. DOT, Washington, D.C.

Nicks, J., Adams, M., and Alzamora, D. (2013b). "Implications of MSE connection criteria for frictionally connected GRS structures." *Geosynthetics 2013*, IFAI, Roseville, MN, USA, 332-341.

Nicks, J.E., Esmaili, D., and Adams, M.T. (2016). "Deformations of geosynthetic reinforced soil under bridge service loads." *Geotextiles and Geomembranes*, 44(4), 641-653.

Nova-Roessig, L., and Sitar, N. (2006). "Centrifuge model studies of the seismic response of reinforced soil slopes." *Journal of Geotechnical and Geoenvironmental Engineering*, 132(3), 388-400.

Panah, A. K., Yazdi, M., and Ghalandarzadeh, A. (2015). "Shaking table tests on soil retaining walls reinforced by polymeric strips." *Geotextiles and Geomembranes*, 43(2), 148-161.

Ramakrishnan, K, Budhu, M., and Britto, A. (1998). "Laboratory seismic tests on geotextile wrap-faced and geotextile-reinforced segmental retaining walls." *Geosynthetics International*, 5(1-2), 55-71.

Ren, F., Zhang, F., Xu, C., Wang, G. (2016). "Seismic evaluation of reinforced-soil segmental retaining walls." *Geotextiles and Geomembranes*, 44(4), 604-614.

Richardson, G.N., Feger, D., Fong, A., and Lee, K.L. (1977). "Seismic testing of reinforced earth walls." *Journal of Geotechnical Engineering Division*, 103(1), 1–17.

Richardson, G.N., and Lee, K.L. (1975). "Seismic design of reinforced earth walls." *Journal of Geotechnical Engineering Division*, 101(2), 167–188.

Rowe, R.K., and Ho, S.K. (1997). "Continuous panel reinforced soil walls on rigid foundations." *Journal of Geotechnical and Geoenvironmental Engineering*, 123(10), 912-920.

Rowe, R.K., and Ho, S.K. (1998). "Horizontal deformation in reinforced soil walls." *Canadian Geotechnical Journal*, 35(2), 312-327.

Runser, D., Fox, P.J., and Bourdeau, P.L. (2001). "Field performance of a 17 m-high reinforced soil retaining wall." *Geosynthetics International*, 8(5), 367-391

Sabermahani, M., Ghalandarzadeh, A., and Fakher, A. (2009). "Experimental study on seismic deformation modes of reinforced-soil walls." *Geotextiles and Geomembranes*, 27(2), 121-136.

Sakaguchi, M. (1996). "A study of the seismic behavior of geosynthetic reinforced walls in Japan." *Geosynthetics International*. 3(1), 13–40.

Sakaguchi, M., Muramatsu, M., and Nagura, K. (1992). "A discussion on reinforced embankment structures having high earthquake resistance." *International Geotechnical Symposium on Theory and Practice of Earth Reinforcement*, *IS-Kyushu'92*, Fukuoka, 287-292.

Sandri, D. (1997). "A performance summary of reinforced soil structures in the Greater Los Angeles area after the Northridge Earthquake." *Geotextiles and Geomembranes*, 15(4-6), 235-253.

Segrestin, P., and Bastick, M. (1988). "Seismic design of reinforced earth retaining wall – the contribution of finite element analysis." *International Geotechnical Symposium on Theory and Practice of Earth Reinforcement*, Fukuoka, Kyushu, Japan, 577-582.

Siddharthan, R.J., Ganeshwara, V., Kutter, B.L., El-Desouky, M., and Whitman, R.V. (2004). "Seismic deformation of bar mat mechanically stabilized earth walls. I: Centrifuge tests." *Journal of Geotechnical and Geoenvironmental Engineering*, 130(1), 14-25.

Skinner, G.D., and Rowe, R.K. (2005). "Design and behavior of a geosynthetic reinforced retaining wall and bridge abutment on a yielding foundation." *Geotextiles and Geomembranes*, 23, 234-260.

Stein, W.J., and Neuman, T.R. (2007). Mitigation strategies for design exceptions. *FHWA-SA-07-011*, Federal Highway Administration, Washington, D.C., USA.

Sugimoto, M., Ogawa, S., and Moriyama, M. (1994). "Dynamic characteristics of reinforced embankments with steep slope by shaking model tests." *Recent Case Histories of Permanent Geosynthetic-Reinforced Soil walls*, *Seiken Symposium*, Tokyo, 271-275.

Takemura, J., and Takahashi, A. (2003). "Centrifuge modeling of seismic performance of reinforced earth structure." *Reinforced soil engineering: Advances in research and practice*, Marcel Dekker, New York, 417–442.

Talebi, M., Meehan, C.L., Cacciola, D.V., and Becker, M.L. (2014). "Design and construction of a geosynthetic reinforced soil integrated bridge system." *Geo-Congress 2014*, ASCE, Reston, VA, USA, 4176-4190.

Tatsuoka, F., Koseki, J., and Tateyama, M. (1997). "Performance of reinforced soil structures during the 1995 Hyogo-ken Nanbu earthquake," *Earth Reinforcement*, 2, Balkema, Rotterdam, Netherlands, 973-1008.

Telekes, G., Sugimoto, M., and Agawa, S., (1994). "Shaking table tests on reinforced embankment models." *13th International Conference on Soil Mechanics and Foundation Engineering*, New Delhi, 649-644.

Trautner, C.A., Zheng, Y., McCartney, J.S., and Hutchinson, T C. (2017). "An approach for shake table performance evaluation during repair and retrofit actions." *Earthquake Engineering and Structural Dynamics*, (in review).

Vahedifard, F., Leshchinsky, B., Sehat, S., and Leshchinsky, D. (2014). "Impact of cohesion on seismic design of geosynthetic-reinforced earth structures." *Journal of Geotechnical and Geoenvironmental Engineering*, 10.1061/(ASCE)GT.1943-5606.0001099, 04014016.

Vahedifard, F., Leshchinsky, B., Mortezaei, K., and Lu, N. (2015). "Active earth pressures for unsaturated retaining structures." *Journal of Geotechnical and Geoenvironmental Engineering*, 10.1061/(ASCE)GT.1943-5606.0001356, 04015048.

van Genuchten, M.T. (1980). "A closed-form equation for predicting the hydraulic conductivity of unsaturated soils." *Soil Science Society of America Journal*, 44(5), 892–898.

Vennapusa, P., White, D., Klaiber, W, and Wang, S. (2012). Geosynthetic reinforced soil for low-volume bridge abutments. *Report No. IHRB Project TR-621*, Iowa DOT, IA.

Vieira, C.S., Lopes, M.L., and Caldeira, L.M. (2013). "Sand–geotextile interface characterisation through monotonic and cyclic direct shear tests." *Geosynthetics International*, 20(1), 26-38.

Walters, D.L., Allen, T.M., and Bathurst, R.J. (2002). "Conversion of geosynthetic strain to load using reinforcement stiffness." *Geosynthetics International*, 9(5-6), 483-523.

Wolfe, W.E., Lee, K.L., Rea, D., and Yourman, A.M. (1978). "The effect of vertical motion on the seismic stability of reinforced earth walls." *Symposium on Earth Reinforcement*, ASCE, Reston, VA, 856-879.

Won, G.W., Hull, T., and De Ambrosis, L. (1996). "Performance of a geosynthetic segmental block wall structure to support bridge abutments." *Earth Reinforcement*, Vol. 1, Balkema, Rotterdam, Netherlands, 543–548.

Wu, J.T.H., Ketchart, K., and Adams, M. (2001). GRS bridge piers and abutments. *FHWA-RD-00-038*, U.S. DOT, Washington, DC.

Wu, J.T.H., Lee, K.Z.Z, Helwany, S.B., and Ketchart, K. (2006a). Design and construction guidelines for geosynthetic-reinforced soil bridge abutments with a flexible facing. *NCHRP Report 556*, Transportation Research Board, Washington, DC.

Wu, J.T.H., Lee, K.Z.Z, and Pham, T. (2006b). "Allowable bearing pressures of bridge sills on GRS abutments with flexible facing." *Journal of Geotechnical and Geoenvironmental Engineering*, 132(7), 830-841.

Wu, J.T.H., and Pham, T.Q. (2013). "Load-carrying capacity and required reinforcement strength of closely spaced soil-geosynthetic composites." *Journal of Geotechnical and Geoenvironmental Engineering*, 139(9), 1468-1476.

Wu, J.T.H., Pham, T.Q., and Adams, M.T. (2013). "Composite behavior of geosynthetic reinforced soil mass." *FHWA-HRT-10-077*, U.S. DOT, Washington, D.C.

Yang, K.-H., Zornberg, J.G., Liu, C.-N., and Lin, H.-D. (2012). "Stress distribution and development within geosynthetic-reinforced soil slopes." *Geosynthetics International*, 19(1), 62–78.

Yen, W.-H.P., Chen, G., Buckle, I., Allen, T., Alzamora, D., Ger, J., and Arias, J.G. (2011). Post-earthquake reconnaissance report on transportation infrastructure: Impact of the February 27, 2010, offshore Maule Earthquake in Chile, *FHWA-HRT-11-030*, U.S. DOT, Washington, D.C.

Yogendrakumar, M., and Bathurst, R.J. (1992). "Numerical simulation of reinforced soil structures during blast loadings." *Transportation Research Record 1336*, 1-8.

Yogendrakumar, M., Bathurst, R.J., and Finn, W.D.L. (1991). "Response of reinforced soil walls to earthquake loads." *IX Panamerican Conference on Soil Mechanics and Foundation Engineering*, Vina del Mar, Chile, 659-672.

Yogendrakumar, M., Bathurst, R.J. and Finn, W.D.L. (1992). "Dynamic response analysis of a reinforced soil retaining wall." *Journal of Geotechnical Engineering*, 118(8), 1158-1167.

Yu, Y., Bathurst, R.J., and Allen, T.M. (2016). "Numerical modeling of the SR-18 geogrid reinforced modular block retaining walls." *Journal of Geotechnical and Geoenvironmental Engineering*, 10.1061/(ASCE)GT.1943-5606.0001438, 04016003.

Zevgolis, I, and Bourdeau, P.L. (2007). Mechanically stabilized earth wall abutments for bridge support. *FHWA/IN/JTRP-2006/38*, Indiana Department of Transportation and Purdue University, West Lafayette, IN.

Zheng, Y., and Fox, P.J. (2016a). "Numerical investigation of geosynthetic-reinforced soil bridge abutments under static loading." *Journal of Geotechnical and Geoenvironmental Engineering*, 10.1061/(ASCE)GT.1943-5606.0001452, 04016004.

Zheng, Y., and Fox, P.J. (2016b). Closure to "Numerical investigation of geosynthetic-reinforced soil bridge abutments under static loading." By Yewei Zheng, and Patrick J. Fox. *Journal of Geotechnical and Geoenvironmental Engineering*, 10.1061/(ASCE)GT.1943-5606.0001623, 07016032.

Zheng, Y., and Fox, P.J. (2017). "Numerical investigation of the geosynthetic reinforced soil-integrated bridge system under static loading." *Journal of Geotechnical and Geoenvironmental Engineering*, 10.1061/(ASCE)GT.1943-5606.0001665, 04017008.

Zheng, Y., Fox, P.J., and McCartney, J.S. (2017). "Numerical study of compaction effect on the static behavior of geosynthetic reinforced soil-integrated bridge system." *Geotechnical Frontiers 2017*, Orlando, FL, USA, 33-43.

Zheng, Y., Fox, P.J., and McCartney, J.S. (2017). "Numerical simulation of load-deformation and failure behavior of geosynthetic-reinforced soil bridge abutments." *Journal of Geotechnical and Geoenvironmental Engineering*, (in review).

Zheng, Y., Fox, P.J., and Shing, P.B. (2014). "Numerical simulations for response of MSE wall-supported bridge abutment to vertical load." *GeoShanghai 2014, International Conference on Geotechnical Engineering 2014*, ASCE, Reston, VA, USA, 493-502.

Zheng, Y., Fox, P.J., and Shing, P.B. (2015a). "Numerical study of deformation behavior for a geosynthetic-reinforced soil bridge abutment under static loading." *IFCEE 2015, International Foundations Congress & Equipment Exposition 2015*, ASCE, Reston, VA, USA, 1503-1512.

Zheng, Y., Fox, P.J., and Shing, P.B. (2015b). "Verification of numerical model for static analysis of geosynthetic-reinforced soil bridge abutments." *Geosynthetics 2015*, IFAI, Roseville, MN, USA, 152-160.

Zheng, Y., Sander, A.C., Rong, W., Fox, P.J., Shing, P.B., and McCartney, J.S. (2017). "Shaking table test of a half-scale geosynthetic-reinforced soil bridge abutment." *Geotechnical Testing Journal*, (in press).